Research Topics

Volcanism in the central volcanic zone of the andes

Edited by
Felipe Aguilera, Gary Michelfelder, Pablo Grosse, Silvina Guzman and
Marco Taussi

Published in
Frontiers in Earth Science

ISSN 1664-8714
ISBN 978-2-8325-1513-6
DOI 10.3389/978-2-8325-1513-6

About Frontiers

Frontiers is more than just an open access publisher of scholarly articles: it is a pioneering approach to the world of academia, radically improving the way scholarly research is managed. The grand vision of Frontiers is a world where all people have an equal opportunity to seek, share and generate knowledge. Frontiers provides immediate and permanent online open access to all its publications, but this alone is not enough to realize our grand goals.

Frontiers journal series

The Frontiers journal series is a multi-tier and interdisciplinary set of open-access, online journals, promising a paradigm shift from the current review, selection and dissemination processes in academic publishing. All Frontiers journals are driven by researchers for researchers; therefore, they constitute a service to the scholarly community. At the same time, the *Frontiers journal series* operates on a revolutionary invention, the tiered publishing system, initially addressing specific communities of scholars, and gradually climbing up to broader public understanding, thus serving the interests of the lay society, too.

Dedication to quality

Each Frontiers article is a landmark of the highest quality, thanks to genuinely collaborative interactions between authors and review editors, who include some of the world's best academicians. Research must be certified by peers before entering a stream of knowledge that may eventually reach the public - and shape society; therefore, Frontiers only applies the most rigorous and unbiased reviews. Frontiers revolutionizes research publishing by freely delivering the most outstanding research, evaluated with no bias from both the academic and social point of view. By applying the most advanced information technologies, Frontiers is catapulting scholarly publishing into a new generation.

What are Frontiers Research Topics?

Frontiers Research Topics are very popular trademarks of the *Frontiers journals series*: they are collections of at least ten articles, all centered on a particular subject. With their unique mix of varied contributions from Original Research to Review Articles, Frontiers Research Topics unify the most influential researchers, the latest key findings and historical advances in a hot research area.

Find out more on how to host your own Frontiers Research Topic or contribute to one as an author by contacting the Frontiers editorial office: frontiersin.org/about/contact

Volcanism in the central volcanic zone of the andes

Topic editors
Felipe Aguilera — Catholic University of the North, Chile
Gary Michelfelder — Missouri State University, United States
Pablo Grosse — National Scientific and Technical Research Council (CONICET), Argentina
Silvina Guzman — CONICET Instituto de Bio y Geociencias del NOA (IBIGEO), Argentina
Marco Taussi — University of Urbino Carlo Bo, Italy

Citation
Aguilera, F., Michelfelder, G., Grosse, P., Guzman, S., Taussi, M., eds. (2023). *Volcanism in the central volcanic zone of the andes*. Lausanne: Frontiers Media SA. doi: 10.3389/978-2-8325-1513-6

Table of contents

frontiers | Frontiers in Earth Science

TYPE Editorial
PUBLISHED 17 January 2023
DOI 10.3389/feart.2023.1130976

Editorial: Volcanism in the Central Volcanic Zone of the Andes

Felipe Aguilera[1,2]*, Pablo Grosse[3,4], Silvina Guzmán[5,6], Gary Michelfelder[7] and Marco Taussi[8]

[1]Millennium Institute on Volcanic Risk Research—Ckelar Volcanoes, Antofagasta, Chile, [2]Departamento de Ciencias Geológicas, Universidad Católica del Norte, Antofagasta, Chile, [3]Consejo Nacional de Investigaciones Científicas y Técnicas (CONICET), Tucumán, Argentina, [4]Fundación Miguel Lillo, San Miguel de Tucumán, Argentina, [5]Instituto de Bio y Geo Ciencias del NOA (IBIGEO), Universidad Nacional de Salta—CONICET, Salta, Argentina, [6]National Institute of Oceanography and Applied Geophysics—OGS, Sgonico, Italy, [7]Department of Geography, Geology and Planning, Missouri State University, Springfield, MO, United States, [8]Dipartimento di Scienze Pure e Applicate, Università degli Studi di Urbino Carlo Bo, Urbino, Italy

KEYWORDS

volcanic monitoring, hazard/risk management, backarc volcanism, active volcanism, andean magmatism

EDITED AND REVIEWED BY
Valerio Acocella,
Roma Tre University, Italy

*CORRESPONDENCE
Felipe Aguilera,
feaguilera@ucn.cl

SPECIALTY SECTION
This article was submitted to Volcanology, a section of the journal Frontiers in Earth Science

RECEIVED 24 December 2022
ACCEPTED 11 January 2023
PUBLISHED 17 January 2023

CITATION
Aguilera F, Grosse P, Guzmán S, Michelfelder G and Taussi M (2023), Editorial: Volcanism in the Central Volcanic Zone of the Andes.
Front. Earth Sci. 11:1130976.
doi: 10.3389/feart.2023.1130976

Editorial on the Research Topic
Volcanism in the Central Volcanic Zone of the Andes

This Research Topic was born out of the 1st Symposium on the Central Volcanic Zone of the Andes (CVZA; carried out in virtual mode during 2021) which counted for the presence of geoscientists working in the volcanological, petrological and geochemical fields, among the others. Our objective was to bring together contributions focused on the evolution and impact of volcanism in the CVZA from its formation (Late Oligocene) up to present times, including specific and multidisciplinary studies, with both detailed and regional approaches. The CVZA is located in the western part of South America, as a consequence of the subduction of the Nazca plate under South American plate, and covers the northern Chile, northwestern Argentina, western Bolivia and southern Peru. The CVZA is characterized by the occurrence of massive explosive events, dominated by andesitic-to-dacitic products, and strongly influenced by the presence of a thick continental crust, which favors several processes as long-lasting magma storage, magma assimilation by crustal contamination, among others. One of the main scientific problems related to this volcanic area is to define what are the main processes that control the size and frequency of the major explosive eruptions. The nine articles published in this Research Topic cover a spectrum of topics applied in different areas of the CVZA, including poly- and monogenetic volcanism, the influence of the crust in magmatic processes, fluid geochemistry, volcano seismicity, petrology, geochronology, hazards assessment, relationships between volcanoes and archeology/anthropology/sociology.

Barry et al. compare the degassing processes between the Central and Southern volcanic zones of the Andes using He and carbon isotopes, and CO2/3He ratios obtained from gas and water samples related to fumaroles and thermal springs. They conclude that crustal thickness exerts a primary control on the extent of fluid-crust interaction, as helium and other volatiles rise through the upper plate in the Andean convergent margin, with more significant crustal inputs in the CVZA due its thicker crust. Additionally, CO2 removal related to calcite precipitation (probably associated with biological processes) and gas dissolution was observed in shallow hydrothermal systems of both volcanic zones.

Burns and de Silva present a regional study along the CVZA. They show that during the past 10 Myr, the CVZA records two distinct types of intermediate magmas: 1) Andesitic magmas generated/fractionated in the lower crust associated with major composite cones and small centers of the Quaternary arc, or 2) andesitic magmas resulting from hybridization of mantle-derived basalts and upper crustal lithologies related to 6–1 Ma ignimbrites and lava domes.

Salisbury et al. present new geochemical (major/trace elements and radiogenic isotopes) and geochronological data of a transect along the Bolivian Intersalar Range. They identify two distinct pulses of rear-arc magmatism: 1) a 20–14 Ma phase that corresponds to local compressional shortening, and 2) a 5–1 Ma phase that postdates structural deformation in the region. Additionally, they suggest melting in the region is triggered by the breakdown of Nb-rich hydrous minerals within foundering (delaminating) mantle lithosphere.

Aguilar et al. study the evolution of the previously poorly known Yura monogenetic field (Southern Perú) using geological mapping, stratigraphic logs, petrography, geochemistry and geochronology. They find that volcanic activity was concentrated during the Middle-Upper Pleistocene (*ca.* 195–54 ka) and was characterized by phreatomagmatic, Strombolian and effusive eruptions, which produced small scoria cones, maars, and lava flows/coulées.

McFarlin et al., determined the distribution and classified seismic data recorded at the Lazufre Volcanic System (northern Chile). Most of the events occur beneath Lastarria volcano with almost no activity observed beneath the Cordón del Azufre volcano. Five classes of seismic events were recognized: volcano-tectonic, two types of long-period, hybrid, and others whose origin remains unknown. Based on their spatial distribution and b-values, it was inferred that seismic activity is driven mainly by movement of fluids and gases associated with the regional magma zones and inflation centers.

Two articles deal with volcanic hazards assessment. Bertin et al. investigated new approaches to quantify the hazards of long-term active and complex settings at a regional scale (22.5–28°S), being one of the few hazard assessments carried out at a regional scale worldwide. The study was based on the estimation of 1) spatial probability of future volcanic activity (based on kernel density estimation using a new volcanic geospatial database), 2) temporal probability of future volcanic events, and 3) areas susceptible to volcanic flow and fall processes (based on computer modeling), from which several hazard maps were produced. Alcozer et al. carried out a local GIS-based multi-hazard assessment of the San Pedro volcano (northern Chile). They considered the size of eruptions to co-parameterize the size of the accompanying phenomena (e.g., mass flows) in a given eruptive scenario. The novelty of the study is the use of intra-scenarios (i.e., subdivisions of eruptive scenarios) to explore the size variability of explosive volcanic phenomena. The size of intra-scenarios was extrapolated from the largest-size deposits of each type of phenomenon from the geologic record. This work produced several single-event hazard maps, and an integrated hazard map.

The last two articles explore the relationship between volcanism and the ancient-to-present indigenous societies. Loyola et al., using petrographical techniques and archaeological knowledge, studied rocks used for stone tools and other artifacts in the Salar de Atacama basin area (22–24°S/67–68°W), to classify lithic assemblages and their sources. A diversity of volcanic and subvolcanic rocks were identified (e.g. pumice, micro-diorites, obsidians) from several sites including craters, maars, caldera-domes, lava flows, hydrothermal deposits, and ignimbrites. Ramos Chocobar and Tironi examine the volcanological understandings of the Lickanantay people in the Salar de Atacama Basin, called by the authors as "Atacameño volcanology". They describe the volcanological notions arising from the Lickanantay ancestral knowledge-volcanic formation, functions, and behavior. Finally, they present a delineation of some relevant elements of human–volcano interactions and volcanic risk management from an Atacameño perspective.

This Research Topic is a first effort to put together contributions that increase the knowledge of the CVZA, which is still limited, and we expect that the local/regional and international volcanological community looks to this area, which could provide several answers for critical volcanic processes, especially considering the very good preservation of their volcanic deposits as a consequence of the presence of arid-to-hyper arid environment.

Author contributions

All authors listed have made a substantial, direct, and intellectual contribution to the work and approved it for publication.

Conflict of interest

The authors declare that the research was conducted in the absence of any commercial or financial relationships that could be construed as a potential conflict of interest.

Publisher's note

frontiers | Frontiers in Earth Science

ORIGINAL RESEARCH
published: 13 June 2022
doi: 10.3389/feart.2022.897267

The Helium and Carbon Isotope Characteristics of the Andean Convergent Margin

P. H. Barry[1]*, J. M. De Moor[2,3], A. Chiodi[4], F. Aguilera[5,6], M. R. Hudak[1], D. V. Bekaert[1], S. J. Turner[7], J. Curtice[1], A. M. Seltzer[1], G. L. Jessen[8,9], E. Osses[8], J. M. Blamey[10], M. J. Amenábar[10], M. Selci[11], M. Cascone[11], A. Bastianoni[11], M. Nakagawa[12], R. Filipovich[4], E. Bustos[4], M. O. Schrenk[13], J. Buongiorno[14], C. J. Ramírez[15], T. J. Rogers[16], K. G. Lloyd[16] and D. Giovannelli[1,11,12,17]

[1]Marine Chemistry and Geochemistry Department, Woods Hole Oceanographic Institution, Woods Hole, MA, United States, [2]Observatorio Vulcanológico y Sismológico de Costa Rica (OVSICORI), Universidad Nacional, San Jose, Costa Rica, [3]Department of Earth and Planetary Sciences, University of New Mexico, Albuquerque, NM, United States, [4]Instituto de Bio y Geociencias del NOA (IBIGEO, UNSa-CONICET), Salta, Argentina, [5]Millennium Institute on Volcanic Risk Research—Ckelar Volcanoes, Antofagasta, Chile, [6]Departamento de Ciencias Geológicas, Universidad Católica del Norte, Antofagasta, Chile, [7]Department of Geosciences, University of Massachusetts Amherst, Amherst, MA, United States, [8]Instituto de Ciencias Marinas y Limnológicas, Universidad Austral de Chile, Valdivia, Chile, [9]Centro de Investigación Oceanográfica COPAS COASTAL, Universidad de Concepción, Concepción, Chile, [10]Fundación Biociencia, Universidad de Santiago de Chile, Santiago, Chile, [11]Department of Biology, University of Naples "Federico II", Naples, Italy, [12]Earth-Life Science Institute, Tokyo Institute of Technology, Tokyo, Japan, [13]Department of Earth and Environmental Sciences, Michigan State University, East Lansing, MI, United States, [14]Division of Natural Sciences, Maryville College, Maryville, TN, United States, [15]Servicio Geológico Ambiental (SeGeoAm), Heredia, Costa Rica, [16]Department of Microbiology, University of Tennessee, Knoxville, TN, United States, [17]National Research Council, Institute of Marine Biological Resources and Biotechnologies—CNR-IRBIM, Ancona, Italy

Edited by:
Franco Tassi,
University of Florence, Italy

Reviewed by:
Walter D'Alessandro,
National Institute of Geophysics and Volcanology, Italy
Dario Tedesco,
Biologiche e Farmaceutiche, Italy
Mariano Agusto,
University of Buenos Aires, Argentina

***Correspondence:**
P. H. Barry
pbarry@whoi.edu

Specialty section:
This article was submitted to Volcanology, a section of the journal Frontiers in Earth Science

Received: 15 March 2022
Accepted: 19 May 2022
Published: 13 June 2022

Citation:
Barry PH, De Moor JM, Chiodi A, Aguilera F, Hudak MR, Bekaert DV, Turner SJ, Curtice J, Seltzer AM, Jessen GL, Osses E, Blamey J, Amenábar MJ, Selci M, Cascone M, Bastianoni A, Nakagawa M, Filipovich R, Bustos E, Schrenk MO, Buongiorno J, Ramírez CJ, Rogers TJ, Lloyd KG and Giovannelli D (2022) The Helium and Carbon Isotope Characteristics of the Andean Convergent Margin. Front. Earth Sci. 10:897267. doi: 10.3389/feart.2022.897267

Subduction zones represent the interface between Earth's interior (crust and mantle) and exterior (atmosphere and oceans), where carbon and other volatile elements are actively cycled between Earth reservoirs by plate tectonics. Helium is a sensitive tracer of volatile sources and can be used to deconvolute mantle and crustal sources in arcs; however it is not thought to be recycled into the mantle by subduction processes. In contrast, carbon is readily recycled, mostly in the form of carbon-rich sediments, and can thus be used to understand volatile delivery *via* subduction. Further, carbon is chemically-reactive and isotope fractionation can be used to determine the main processes controlling volatile movements within arc systems. Here, we report helium isotope and abundance data for 42 deeply-sourced fluid and gas samples from the Central Volcanic Zone (CVZ) and Southern Volcanic Zone (SVZ) of the Andean Convergent Margin (ACM). Data are used to assess the influence of subduction parameters (e.g., crustal thickness, subduction inputs, and convergence rate) on the composition of volatiles in surface volcanic fluid and gas emissions. He isotopes from the CVZ backarc range from 0.1 to 2.6 R_A ($n = 23$), with the highest values in the Puna and the lowest in the Sub-Andean foreland fold-and-thrust belt. Atmosphere-corrected He isotopes from the SVZ range from 0.7 to 5.0 R_A ($n = 19$). Taken together, these data reveal a clear southeastward increase in ^{3}He/^{4}He, with the highest values (in the SVZ) falling below the nominal range associated with pure upper mantle helium (8 ± 1 R_A), approaching the mean He isotope value for arc gases of (5.4 ± 1.9 R_A). Notably, the lowest values are found in the CVZ, suggesting more significant crustal inputs (i.e., assimilation of ^{4}He) to the helium budget. The crustal thickness in the CVZ (up to

70 km) is significantly larger than in the SVZ, where it is just ~40 km. We suggest that crustal thickness exerts a primary control on the extent of fluid-crust interaction, as helium and other volatiles rise through the upper plate in the ACM. We also report carbon isotopes from (n = 11) sites in the CVZ, where $\delta^{13}C$ varies between −15.3‰ and −1.2‰ [vs. Vienna Pee Dee Belemnite (VPDB)] and $CO_2/^3He$ values that vary by over two orders of magnitude (6.9×10^8–1.7×10^{11}). In the SVZ, carbon isotope ratios are also reported from (n = 13) sites and vary between −17.2‰ and −4.1‰. $CO_2/^3He$ values vary by over four orders of magnitude (4.7×10^7–1.7×10^{12}). Low $\delta^{13}C$ and $CO_2/^3He$ values are consistent with CO_2 removal (e.g., calcite precipitation and gas dissolution) in shallow hydrothermal systems. Carbon isotope fractionation modeling suggests that calcite precipitation occurs at temperatures coincident with the upper temperature limit for life (122°C), suggesting that biology may play a role in C-He systematics of arc-related volcanic fluid and gas emissions.

Keywords: helium, carbon, SVZ, CVZ, Andes (Argentina and Chile)

1 INTRODUCTION

Helium has two stable isotopes: ^3He and ^4He. ^3He is primordial and has been stored in the mantle since Earth's accretion, whereas ^4He is continuously produced in Earth's crust due to the radioactive decay of U and Th. Earth reservoirs have characteristic $^3He/^4He$ values (typically reported relative to air; R_A = air $^3He/^4He = 1.382 \times 10^{-6}$; Clarke et al., 1976; Mabry et al., 2013). For example, the upper mantle typically has a $^3He/^4He$ value that is ~8 ± 1 times the atmospheric ratio (R_A; Graham, 2002). The continental lithospheric mantle has lower $^3He/^4He$, approximately 6.1 ± 2.1 R_A (Dunai and Baur, 1995; Gautheron and Moreira, 2002; Day et al., 2015), presumably due to radiogenic addition from the U and Th rich lithosphere. Crustal material is dominated by radiogenic ^4He production and has a $^3He/^4He$ = 0.05 R_A (Andrews, 1985). The mean He isotope ratio for arc gases is ~5.4 ± 1.9 R_A (Hilton et al., 2002), likely reflecting radiogenic additions from the surrounding crust. As a result, the $^3He/^4He$ in geothermal fluids provides information about the origin of volatiles (i.e., mantle vs. crust derived).

High CO_2 concentrations have been observed in volcanic arcs as well as in other volcanic regions with high heat flow and mantle partial melting (e.g., Hilton and Porcelli, 2003). Typically, C isotopes of CO_2 in volcanic arcs are interpreted to be an admixture between magmatic sources [mantle $\delta^{13}C$ is between −5‰ and −8‰ vs. Vienna Pee Dee Belemnite (VPDB); Javoy et al., 1986] and subduction inputs (Sano and Marty, 1995), which can vary from 0‰ in marine carbonates down to ~−30‰ in organic carbon-rich sediments (Hayes et al., 1999; Plank and Manning, 2019). Together, $^3He/^4He$, $CO_2/^3He$, and C isotopes of CO_2 can be used to determine the volatile provenance of gas and fluid emissions (Sano and Marty, 1995), as well as secondary processes that affect emissions (e.g., Barry et al., 2019a).

Several prior studies have characterized He-C isotope systematics in volcanic and geothermal systems in the Andes (**Figure 1**; e.g., Hilton et al., 1993; Hoke et al., 1994; Varekamp et al., 2006; Sepúlveda et al., 2007; Aguilera, 2008; Ray et al., 2009; Tassi et al., 2009; Tassi et al., 2010; Capaccioni et al., 2011; Tassi et al., 2011; Aguilera et al., 2012; Agusto et al., 2013; Benavente et al., 2013; Chiodi et al., 2015; Aguilera et al., 2016; Benavente et al., 2016; Roulleau et al., 2016; Tardani et al., 2016; Tassi et al., 2016; Arnold et al., 2017; Tassi et al., 2017; Lopez et al., 2018; Chiodi et al., 2019; Arnold et al., 2020; Inostroza et al., 2020; Robidoux et al., 2020; Lages et al., 2021; Tardani et al., 2021; Filipovich et al., 2022) to understand the source of the volcanic fluid and gas emissions. These studies demonstrate the co-occurrence of mantle ($^3He/^4He$ up to ~8 R_A) and crustal ($^3He/^4He$ ~0.05 R_A) He sources. In this contribution, we report new fluid and gas He-C isotope and relative abundance data, which we combine with previously published data to determine the extent of magmatic vs. crustal contributions across the Andean Convergent Margin (ACM). One of the main objectives of this study is to compare He-C systematics in the Central Volcanic Zone (CVZ) and the Southern Volcanic Zone (SVZ) regions in order to assess the influence of subduction parameters (e.g., crustal thickness, subduction inputs, convergence rate) on the composition of volatiles emitted at the surface. Determining volatile pathways is fundamental for ascertaining the dominant processes in each volcanic region as well as for differentiating volcanic source features from secondary modification processes (e.g., gas dissolution, calcite precipitation and/or crustal assimilation).

2 GEOLOGICAL BACKGROUND

Subduction of the Nazca Plate beneath the South America Plate resulted in the formation of the ACM and the South American Volcanic Arc (Dewey and Bird, 1970; James, 1971; Jordan et al., 1983). The ACM accounts for about 17% of the total length of the "Ring of Fire" and active volcanism occurs within three main segments: 1) the Northern Volcanic Zone (5°N–2°S), 2) Central Volcanic Zone (20°S–27°S), and 3) Southern Volcanic Zone (33°S–39°S) (Thorpe and Francis, 1979; Thorpe, 1982; Harmon et al., 1984; Ray et al., 2009). A fourth segment (Austral Volcanic

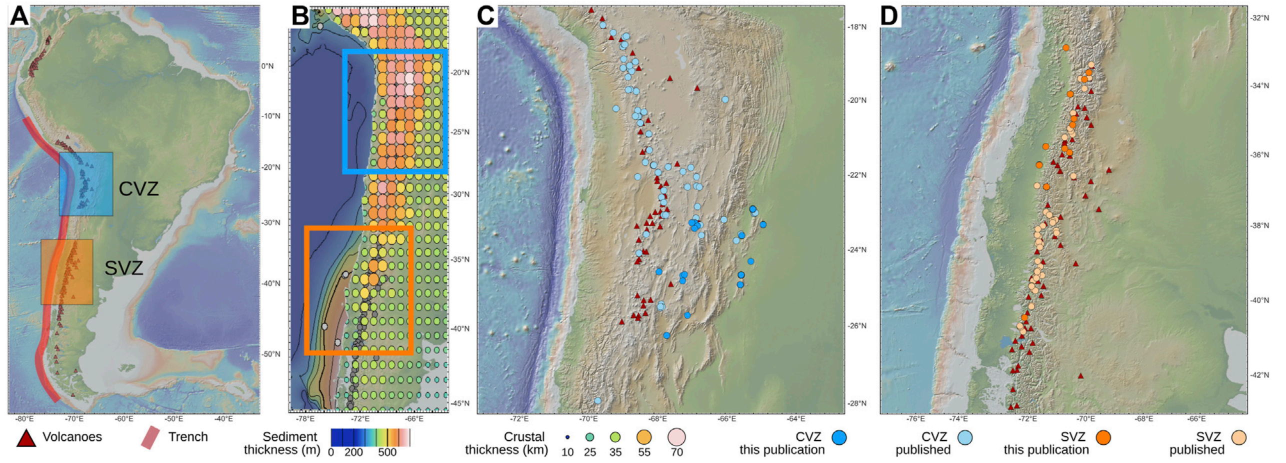

FIGURE 1 | Map sampling locations and subduction parameters. **(A)** Map of South America showing the relative location of the two sampling locations: the Central Volcanic Zone (CVZ) and the Southern Volcanic Zone (SVZ), which span across the ACM in Chile and Argentina. **(B)** Map showing offshore sediment thickness (see color bar) and crustal thickness (dot sizes) in the overriding plate. **(C)** Zoomed in view of the CVZ, with the location of all samples from this study (bright blue circles) and previously published studies (light blue circles) as well as the location of volcanic centers (red triangles). **(D)** Zoomed in view of the SVZ, with the location of all samples from this study (bright orange circles) and previously published studies (light orange circles) as well as the location of volcanic centers (red triangles). Published data are from Hilton et al. (1993), Hoke et al. (1994), Varekamp et al. (2006), Sepúlveda et al. (2007), Aguilera (2008), Ray et al. (2009), Tassi et al. (2009), Tassi et al. (2010), Capaccioni et al. (2011), Tassi et al. (2011), Aguilera et al. (2012), Agusto et al. (2013), Benavente et al. (2013), Chiodi et al. (2015), Aguilera et al. (2016), Benavente et al. (2016), Roulleau et al. (2016), Tardani et al. (2016), Tassi et al. (2016), Arnold et al. (2017), Tassi et al. (2017), Lopez et al. (2018), Chiodi et al. (2019), Arnold et al. (2020), Inostroza et al. (2020), Robidoux et al. (2020), Lages et al. (2021), Tardani et al. (2021), Filipovich et al. (2022) in this figure, as well as in subsequent figures.

Zone; 49°S–55°S) is located in the southernmost part of South America, and is related to the subduction of the Antarctica plate under the South American Plate (Stern, 2004). These are separated by gaps in magmatism associated with ridge subduction (the Nazca Ridge, to the north of the CVZ, and the Juan Fernandez Ridge, to the south) and shallow slab angles (e.g., Kay and Mpodozis, 2002; Newell et al., 2015). The current phase of subduction of the Nazca plate beneath the northern Andes began about 80 Myr ago (Ma) and propagated southwards reaching the SVZ about 55 Myr ago (Chen et al., 2019). The subducting plate is slightly older in the CVZ compared with the SVZ region (~45 Ma vs. 30 Ma; Syracuse and Abers, 2006), whereas the angle of subduction is slightly shallower (24° in the CVZ vs. 28° in the SVZ).

The CVZ is primarily composed of andesitic stratovolcanoes, which erupted from the Neogene until historic times (Robidoux et al., 2020). Crustal thickness varies drastically along this north to south transect, from ~30 to 70 km. The depth of the Benioff zone beneath the arc front varies from 80 to 120 km. Convergence rates are 7–9 cm/year on average (DeMets et al., 2010). Sediments are delivered to the arc at the trench and sediment thickness also varies significantly from north to south, with the CVZ being sediment-poor compared to the SVZ (**Figure 1B**) (Völker et al., 2013; Clift, 2017; Lages et al., 2021).

Volcanic activity in the CVZ consist mostly of andesites and dacites which have trace element and radiogenic isotope compositions (e.g., $^{87}Sr/^{86}Sr$ and $^{143}Nd/^{144}Nd$) consistent with nearly ubiquitous contamination during their prolonged ascent through the thick (~70 km; Thorpe, 1982) continental crust (De Silva, 1989; Mamani et al., 2010; Godoy et al., 2019). Hydrothermal activity occurs throughout the CVZ, expressed as major geothermal fields and intermittent thermal springs, particularly in the vicinity of volcanic centers such as Taapaca, Guallatiri, Isluga, and Putana (Tassi et al., 2010).

The SVZ extends from central to southern Chile-Argentina. It is composed of numerous stratovolcanoes and monogenetic cones (López-Escobar et al., 1995). The crust is significantly thinner in the SVZ compared to the CVZ, increasing from only ~30 km in the southernmost region to ~50 km near the northern segment terminus (Tassara and Echaurren, 2012), however there are several carbon-rich sedimentary basins (e.g., Neuquén Basin) adjacent to the SVZ (Howell et al., 2005). SVZ volcanic compositions consist mostly of basalts and andesites, though basaltic compositions become less common as crustal thickness increases (Tormey et al., 1991). Radiogenic isotope compositions of SVZ volcanics are variable and have been largely attributed to variations in mantle components where the crust is thin, with both mantle and crustal contributions apparent among more differentiated lavas in the north, where the crust is thicker (Jacques et al., 2014; Turner et al., 2017; Wieser et al., 2019). Hydrothermal activity is widespread in the SVZ due to high geothermal gradients, ongoing magmatic activity, permeable host rocks and abundant recharge (Ray et al., 2009).

3 MATERIALS AND METHODS

3.1 Sample Collection

Gas and water samples in this study were collected at subaerial hot and warm springs, natural gas seeps and fumaroles using

TABLE 1 | Helium and carbon isotope and abundance ratios for newly reported data (this study). 1-sigma uncertainties are less than 5% for ^{4}He/^{20}Ne, R/R$_A$, R$_C$/R$_A$, δ^{13}C, and CO$_2$/^{3}He. The abbreviation n.a., not available.

Sample name	Sample ID	Volcanic zone	Lat. °N	Long. °E	^{4}He/ ^{20}Ne	δ^{13}CO$_2$	R/ Ra	Rc/ Ra	CO$_2$/^{3}He	Phase	pH	Temp. °C	Salinity g/L
Galan Fumarole	AR-GF190226-1	CVZ	−25.86	−66.99	197.9	n.a.	1.77	1.77	4.18E + 09	G	7.75	80	0.19
Galan Fumarole	AR-GF190226-2	CVZ	−25.86	−66.99	217.7	−6.2	1.79	1.79	4.13E + 09	G	7.75	80	0.19
Incachule	AR-IN190223	CVZ	−24.28	−66.47	106.7	−12	1.97	1.97	n.a.	G	6.52	46.9	1.54
La Colcha	AR-LC190226	CVZ	−26.03	−66.99	333.3	−7.5	1.45	1.45	2.22E + 10	G	6.94	84	6.1
La Colcha	AR-LC190226	CVZ	−26.03	−66.99	545.6	−7.5	2.58	2.58	6.86E + 08	G	6.94	84	6.1
Pio Perez	AR-PP190301	CVZ	−25.41	−64.59	1.7	−1.2	0.36	0.21	3.72E + 10	G	8.47	54.3	1.81
Tocomar	AR-TM190224	CVZ	−24.19	−66.55	72.3	−11.7	2.47	2.48	1.68E + 11	G	7.13	69.2	3.93
Fiambalá	FB210806	CVZ	−27.74	−67.548	215.3	n.a.	0.24	0.24	n.a.	G	n.a.	n.a.	n.a.
El Ceibal	EC-211106	CVZ	−26.149	−64.955	1.2	n.a.	0.71	0.63	n.a.	G	n.a.	n.a.	n.a.
Baños de Fleming	BF211031	CVZ	−24.592	−64.909	n.a.	n.a.	0.82	n.a.	n.a.	G	n.a.	n.a.	n.a.
Pizarro	PZ211029	CVZ	−24.237	−64.157	25.4	n.a.	0.51	0.51	n.a.	G	n.a.	n.a.	n.a.
Caimancito 1	CA211030-1	CVZ	−23.745	−64.518	1.4	n.a.	0.59	0.5	n.a.	G	n.a.	n.a.	n.a.
Caimancito 2	CA211030-2	CVZ	−23.744	−64.519	n.a.	n.a.	0.48	n.a.	n.a.	G	n.a.	n.a.	n.a.
Antuco	AR-AO190224	CVZ	−24.18	−66.67	99.8	−7.66	1.96	1.96	6.67E + 09	W	6.25	27.8	21.21
Botijuela Vista	AR-BJ190222	CVZ	−25.74	−67.82	64.5	n.a.	1.24	1.24	8.21E + 10	W	6.44	40	8.65
Aguas Calientes Galan	AR-GA190226	CVZ	−25.83	−66.92	177.3	−1.5	1.56	1.56	8.78E + 10	W	6.7	67	3.28
Incachule	AR-IN190223	CVZ	−24.28	−66.47	12.7	n.a.	1.77	1.79	1.97E + 10	W	6.52	46.9	1.54
Incachule	AR-IN190223	CVZ	−24.28	−66.47	8.8	n.a.	1.68	1.71	1.59E + 11	W	6.52	46.9	1.54
Pastos Grande	AR-PG190225	CVZ	−24.36	−66.57	107.7	−15.33	1.34	1.34	n.a.	W	8.74	44.9	0.61
Pio Perez	AR-PP190301	CVZ	−25.41	−64.59	1.4	−10.67	0.33	0.14	2.17E + 10	W	8.47	54.3	1.81
Pio Perez	AR-PP190301	CVZ	−25.41	−64.59	1.1	−10.67	0.36	0.11	4.86E + 09	W	8.47	54.3	1.81
Rosario de la Frontera	AR-RF190301	CVZ	−25.84	−64.93	6	−8.28	0.36	0.33	9.58E + 10	W	8.23	82	1.57
Villa Vil	AR-VV190228	CVZ	−27.11	−66.82	79.5	−13.28	0.9	0.89	8.83E + 09	W	9.09	38.2	0.4
Termas de Catillo	CH-CT200308	SVZ	−36.29	−71.65	0.3	n.a.	1.1	n.a.	n.a.	G	9.49	37.5	3
Campanario	CH-CP200307	SVZ	−35.93	−70.59	64.2	−8.72	5.01	5.03	1.00E + 10	G	5.89	53.2	25
Panamavida	CH-PM200308	SVZ	−35.76	−71.42	0.4	n.a.	1.12	1.43	n.a.	G	9.91	32.45	4
San Pedro baños termales	CH-SP200302-2	SVZ	−35.14	−70.48	40	−12.56	2.46	2.47	1.20E + 08	G	6.19	21.98	46.5
San Pedro baños termales	CH-SP200302-2	SVZ	−35.14	−70.48	59.5	−12.56	2.4	2.4	4.70E + 07	G	6.19	21.98	46.5
Termas del Flaco	CH-TF-200303	SVZ	−34.96	−70.43	4	−11.15	1.44	1.48	2.20E + 09	G	6.24	68.4	5
Termas del Flaco	CH-TF-200303	SVZ	−34.96	−70.43	0.6	−11.15	1.13	1.27	3.90E + 10	G	6.24	68.4	5
Termas de Cauquenes	CH-CQ200301	SVZ	−34.25	−70.56	68.9	−15.9	1.67	1.68	n.a.	G	8.47	47.67	7.72
Baño Morales	CH-BM-200312	SVZ	−33.82	−70.06	8.1	−8.64	1.61	1.63	n.a.	G	6.07	27.2	20
Termas del Plomo	CH-TP-200304	SVZ	−33.62	−69.91	9.2	n.a.	2.52	2.58	2.00E + 08	G	6.43	36.8	19
Termas del Plomo	CH-TP200304	SVZ	−33.62	−69.91	21.1	n.a.	2.32	2.34	1.20E + 08	G	6.43	36.8	19
Chillan	CH5	SVZ	−36.9	−71.4	n.a.	−8.5	6.32	n.a.	5.00E + 10	G	n.a.	n.a.	n.a.
Chillan	CH6	SVZ	−36.9	−71.4	n.a.	−8.3	6.23	n.a.	5.30E + 10	G	n.a.	n.a.	n.a.
Cordon Caulle	Las Sopas	SVZ	−40.49	−72.17	n.a.	−4.1	6.6	n.a.		G	n.a.	n.a.	n.a.

(Continued on following page)

TABLE 1 | (*Continued*) Helium and carbon isotope and abundance ratios for newly reported data (this study). 1-sigma uncertainties are less than 5% for $^4He/^{20}Ne$, R/R_A, R_C/R_A, $\delta^{13}C$, and $CO_2/^3He$. The abbreviation n.a., not available.

Sample name	Sample ID	Volcanic zone	Lat. °N	Long. °E	$^4He/^{20}Ne$	$\delta^{13}CO_2$	R/Ra	Rc/Ra	$CO_2/^3He$	Phase	pH	Temp. °C	Salinity g/L
									7.10E + 10				
Chillan	CH1	SVZ	−36.9	−71.4	n.a.	−7.9	n.a.	n.a.	n.a.	G	n.a.	n.a.	n.a.
Chillan	CH3	SVZ	−36.9	−71.4	n.a.	−7.9	n.a.	n.a.	n.a.	G	n.a.	n.a.	n.a.
Termas de Catillo	CH-CT200308	SVZ	−36.29	−71.65	25.3	−17.17	0.65	0.65	3.69E + 09	W	9.49	37.5	3
El Medano	CH-EM-200301	SVZ	−35.82	−70.76	0.4	−10.19	0.94	0.74	3.43E + 10	W	7.22	37.5	3.5
Panamavida	CH-PM200308	SVZ	−35.76	−71.42	0.4	−15.34	0.97	0.89	2.27E + 10	W	9.91	32.45	4
Termas del Flaco	CH-TF200303	SVZ	−34.96	−70.43	2.5	n.a.	1.35	1.4	1.37E + 11	W	6.24	68.4	5
Auco	CH-AU200310	SVZ	−32.89	−70.71	n.a.	−12.15	0.96	n.a.	1.71E + 12	W	8.09	20.2	3

standard inverted funnel sampling techniques (e.g., Hilton et al., 2002; Barry et al., 2013). Gases and fluids were first flushed through silicone tubing and into 3/8-inch copper tubes (Weiss, 1968). After ample flushing (i.e., approximately 10x the volume of the tubing), stainless steel clamps were closed on each end of the copper tubes, trapping the sample inside of the copper tubing, between the clamps (e.g., Barry et al., 2016). Gas seeps with low flow rates required >1 h of flushing to effectively remove any air from the system. To ensure no back flow of air into the sampling apparatus, the outflow portion of the silicon tubing was submerged in a bottle of water, allowing gas to flow only in one direction (i.e., through the sampling apparatus).

Gases from bubbling springs were also collected using the water-displacement method (e.g., Craig, 1953; Mazor and Wasserburg, 1965). In brief, a funnel was submerged in a spring and the entire sampling apparatus (i.e., funnel, silicone tubing and copper tube) was initially filled with spring water. The funnel was then inverted and placed over the rising gas bubbles. As the bubbles of gas were captured, they slowly displaced the water in the copper tube. Once all water was displaced by sample gas, the stainless steel clamps were closed in the same way as described above. This technique is particularly useful in low flow gas seeps, where prohibitively long flushing times would be required (e.g., Kimani et al., 2021; Mtili et al., 2021). Water samples require minimal flushing and can often be collected in a matter of minutes. Gas samples were also collected using standard Giggenbach bottle methods (Giggenbach et al., 1989) for C isotope analysis and $CO_2/^3He$ determination. Giggenbach bottles were collected from the same tubing used for Cu-tubes and thus flushed in the same way as described above. Giggenbach bottle samples were not collected in the SVZ and samples for C isotopes and CO_2 concentrations were instead collected by injecting gas into previously evacuated 120 ml septum vials using a three-way valve and 60 ml syringe.

Geothermal samples were collected from 33 geographically distinct localities (**Table 1**) in the SVZ and CVZ between 2019–2021. A total of 44 samples (29 gas, 15 water) were analyzed for He and/or C isotopes and abundances, 23 from the CVZ and 21 from the SVZ, including duplicates and triplicates. The temperature, pH, and salinity of each sampling site were obtained using a portable YSI Plus 6-Series Sonde Multimeter (YSI Incorporated, Yellow Springs, OH, United States) and are reported alongside He-C data in **Table 1**.

3.2 Analytical Techniques

Noble gas analyses were conducted in the Barry Lab at Woods Hole Oceanographic Institution (WHOI) using a Nu Instruments multi-collector Noblesse HR mass spectrometer. The Noblesse has the capability to determine the isotope ratios of all 26 stable noble gases, with mass separation between all carbon-based interferences and Ar, as well as $^{40}Ar^{++}$ interferences with $^{20}Ne^+$. It has a unique zoom optics system that allows for instantaneous switching between different isotope sets. The zoom optics permit the detectors to be fixed, greatly enhancing stability. The sensitivity and resolving power are also adjusted without the complexity of a movable source slit. The instrument is interfaced to a noble gas processing and purification inlet system that is fully automated and allows all of the noble gases to be isolated prior to their inlet into the mass spectrometer.

Carbon isotopes were measured in three laboratories in total: Observatorio Vulcanológico y Sismológico de Costa Rica (OVSICORI) at Universidad Nacional, Costa Rica, University of Naples "Federico II," Naples, Italy and the Earth-Life Science Institute, Tokyo Institute for Technology, Tokyo, Japan. Details are in **Section 3.2.3**.

3.2.1 Gas Sample Noble Gas Purification

Copper tube samples were connected to the extraction line using an O-ring connection and ~5 cm^3 of gas was expanded into the cleanup line. The pressure was measured using a capacitance manometer and then a small aliquot of gas was expanded into the cleanup portion of the line. Reactive gases were chemically removed by exposing gases to a titanium sponge held at 650°C. The titanium sponge was then cooled for 10 min to room temperature in order to getter hydrogen before gases were expanded to a dual hot (SAES ST707) and cold (SAES ST707) getter system, held at 250°C and room temperature, respectively. Another small aliquot of gas was then segregated for preliminary analysis on a quadrupole mass spectrometer (QMS). Noble gases were separated using a series of cryogenic traps, cooled using helium compressors. The heavy noble gases (Ar–Kr–Xe) were adsorbed at 30 K onto a nude stainless steel trap and He and Ne were adsorbed at 10 K on a charcoal trap. The temperature of the charcoal trap was then raised to 30 K, releasing only He, which was then inlet into the Noblesse mass spectrometer. Following He abundance and isotope determination, the temperature on the charcoal cryogenic trap was raised to 80 K for 15 min to release Ne, which was inlet into the Noblesse mass spectrometer. Following Ne isotope measurement, the nude and charcoal cryogenic traps were raised to 300 K for cleanup. Air-standards were analyzed daily from an air cylinder collected on the roof of the Clark Laboratory building on WHOI's Quissett campus on 15 September 2020. Air-standards are fully automated and run overnight, following sample analysis during the day. Air-standards were run for He and Ne using an identical method to the one employed for samples. Air-standards were measured over a concentration range which spanned two orders of magnitude, to account for any non-linearity of the system. Full procedural blanks were run weekly; average (mean) ^{4}He blanks and ^{20}Ne blanks were less than 5% of the sample size. Doubly-charged $^{40}Ar^{++}$ was monitored but because it can be resolved from ^{20}Ne, no correction was applied. Likewise, no CO_2^{++} correction was applied to ^{22}Ne, because CO_2 backgrounds were at the detection limit and thus corrections were considered insignificant.

3.2.2 Water Sample Noble Gas Purification Protocol

Water samples were processed on the same extraction line as gas samples; however the inlet procedure was slightly different. Cu tube samples were interfaced to the extraction system in an identical fashion. Approximately 13 ml of water was inlet and then degassed under vacuum using a magnetic stirrer in a glass bulb beneath the Cu tube inlet area. Noble gases were then quantitatively transferred into a smaller volume using the capillary method (Beyerle et al., 2000; Hunt, 2015; Tyne et al., 2019). Water vapor in the extraction line was cryogenically drawn across a capillary towards a stainless-steel cold trap cooled to liquid nitrogen temperature (−196°C). The consistent flow of water vapor towards the colder water trap effectively entrains the noble gases and quantitatively draws them into the cold trap, along with a small portion of the water vapor. The consistency of this flow prevents any backflow of noble gases, such that they are quantitatively transferred into this cold trap volume (Beyerle et al., 2000). He and Ne were then inlet into the purification portion of the line (i.e., with Ti and SAES getters) for cleanup and noble gas separation in an analogous fashion to what is described above for gas samples.

3.2.3 Carbon Isotope Analysis

Carbon isotope compositions of gas samples were analyzed at OVSICORI (Universidad Nacional, Heredia, Costa Rica) on a Picarro G2201-i. The 2019 samples were analyzed by the same methodology as that described in Barry et al. (2019a) on oxidized NaOH solution from Giggenbach bottles. The samples from 2020 were analyzed as gas phase samples collected in previously evacuated 120 ml septum vials and analyzed using methodology similar to that described in Malowany et al. (2017). Samples and gas phase standards were quantitatively diluted in ultra-high purity (UHP) N_2 using a 2 L gas syringe and transferred into a 2 L flexfoil bag which was then attached to the inlet of the Picarro. A 20 cm copper tube filled with copper wire was placed in line between the bag and the inlet of the Picarro to remove H_2S, which can create significant interference on the carbon isotope measurements of CO_2 (Malowany et al., 2015). $\delta^{13}C$ (vs. VPDB) values were calibrated against a set of in house gas standards with $\delta^{13}C$ values of −15.6‰, −3.8‰, and −8.3‰. Repeat analyses of standards yielded uncertainties of <0.3‰.

Carbon isotopes on dissolved inorganic carbon (DIC) were analyzed at the Giovannelli Lab at the University of Naples "Federico II" (Naples, Italy) and at the Earth-Life Science Institute (Tokyo, Japan). Fluid samples were collected at the spring source in the field using sterile 50 ml syringes. Samples were filtered through a 0.22 μm filter (Millipore) and directly injected into a pre-vacuumed 50 ml serum bottle sealed with butyl rubber septa and an aluminum crimp. DIC concentrations and $\delta^{13}C$ values were measured using CO_2 in the headspace of glass vials after a 3 h reaction with injected 0.5 ml H_3PO_4. The amount of CO_2 and the isotopic values were measured using an Elementar IsoFlow attached to a PrecisION IRMS (at the University of Naples Federico II) and using an Agilent 6890N gas chromatograph attached to a Thermo-Finnigan Delta XP^{Plus} (at the Earth-Life Science Institute). Two international standards ($\delta^{13}C$ = −13.90‰ and 2.52‰) were used for standardization, and the standard deviations were obtained from more than three measurements. To ensure comparable results, three calibrated internal laboratory standards were run independently, and their results were within the standard error of the standard ± 0.1‰.

3.2.4 Data Analysis and Visualization

Data were plotted using the R Statistical software (R 4.1.2, https://www.r-project.org/) and the ggplot2 (Wickham, 2016) and ggtern package (Hamilton and Ferry, 2018). The dataset composed of both the newly obtained measurements and the compilation from the literature together with the R code to reproduce the plots have been permanently archived on Zenodo at DOI: 10.5281/zenodo.6360624 (https://doi.org/10.5281/zenodo.6360624). The remaining figures have been produced using GeoMapApp (http://www.geomapapp.org, Ryan et al., 2009) and Inkscape (https://inkscape.org/).

4 RESULTS

Helium (**Figure 2**) and carbon isotopic and relative abundance ratios (**Figure 3**) are reported in **Table 1**. For comparison, we also

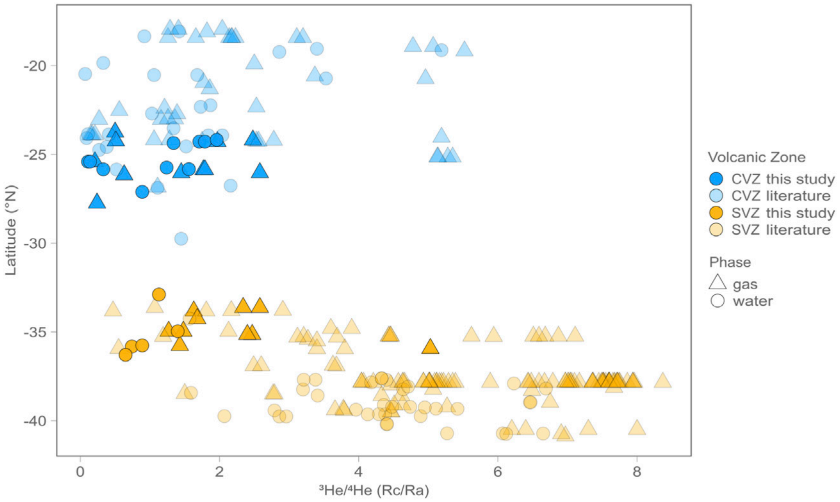

FIGURE 2 | Latitude versus air-corrected $^3He/^4He$ (R_C/R_A) values for gas (triangles) and water (circles) phase samples. Data from this study are shown as bright symbols, whereas data from previously published studies are represented by lighter colored symbols. On average CVZ samples have lower $^3He/^4He$ than SVZ samples, suggesting a larger crustal assimilation signature in the CVZ and a more pristine mantle signature in the SVZ.

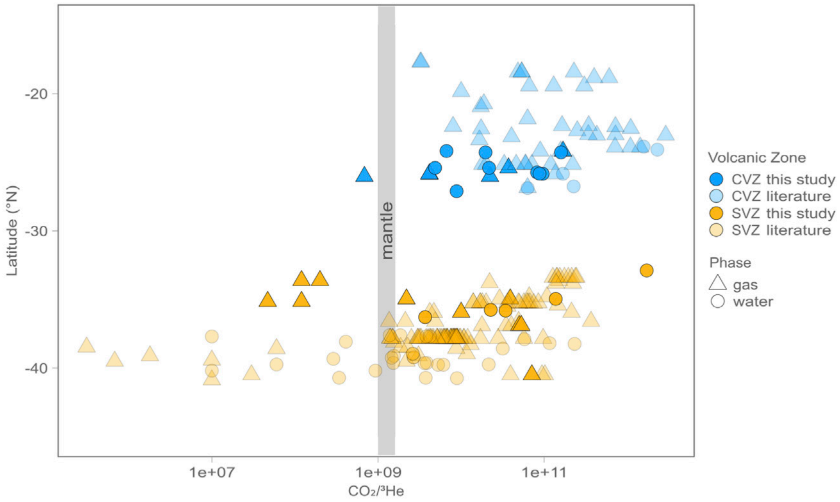

FIGURE 3 | Latitude versus $CO_2/^3He$ for gas (triangles) and water (circles) phase samples. Data from this study are shown in bright colors, whereas data from previously published studies are lighter in color. On average CVZ samples have higher $CO_2/^3He$ than SVZ samples, suggesting a larger subduction derived and/or crustal assimilation signature in the CVZ, and a more pristine mantle signature in the SVZ.

compile data from a number of previous studies (Hilton et al., 1993; Hoke et al., 1994; Varekamp et al., 2006; Sepúlveda et al., 2007; Aguilera, 2008; Ray et al., 2009; Tassi et al., 2009; Tassi et al., 2010; Tassi et al., 2011; Capaccioni et al., 2011; Aguilera et al., 2012; Agusto et al., 2013; Benavente et al., 2013; Chiodi et al., 2015; Aguilera et al., 2016; Benavente et al., 2016; Roulleau et al., 2016; Tardani et al., 2016; Tassi et al., 2016; Tassi et al., 2017; Arnold et al., 2017; Lopez et al., 2018; Chiodi et al., 2019; Arnold et al., 2020; Inostroza et al., 2020; Robidoux et al., 2020; Tardani et al., 2021; Lages et al., 2021; Filipovich et al., 2022; **Supplementary Table S1**). We also compute and report estimates of subduction and mantle derived inputs, after Sano and Marty (1995) (**Table 2**).

4.1 Helium Isotope ($^3He/^4He$)

Helium isotope results ($^3He/^4He$ of sample = R) from this study are reported relative to air (R_A), corrected for the occurrence of atmospheric He (to R_C/R_A) and blank contributions, which are consistently less than 5%. The $^4He/^{20}Ne$ value is used to apply an atmospheric correction to all samples, assuming ^{20}Ne is derived from air ($^4He/^{20}Ne = 0.32$) or air saturated water ($^4He/^{20}Ne = 0.26$ at 15°C; Ozima and Podosek, 2002; Hilton, 1996). As such,

TABLE 2 | Average carbon source (LSM) estimations from **Eqs 5**, **6**, **7**. Calculations were done for all gas samples compiled here as well as for samples with high He isotopes only (>5R_A). These calculations assume He–CO_2 characteristics (relative abundances and $\delta^{13}C$ systematics) can be used to resolve CO_2 contribution from three distinct sources: limestone (L) from subducted sediment and mineralized within slab basement, sedimentary (organic) carbon (S) from subducted sediment, and the mantle wedge (M). Each source is assumed to have a distinctive $CO_2/^3He$ (M = 2 × 10^9; L = 1 × 10^{13}; S = 1 × 10^{13}) and $\delta^{13}C$ (M = −5‰; L = 0‰; S = −30‰) signature. For reference, we also show the Clift (2017) estimates for inorganic to organic (L/S) carbon ratios in the bottom two rows.

Volcanic zone	N. samples	% L	% S	% M	L/S	(L/S)/M	Input/Output
CVZ (All)	46	70%	22%	8%	3.2	11.9	Output
SVZ (All)	107	55%	24%	21%	2.3	3.7	Output
CVZ (>5 RA)	12	73%	10%	17%	7.0	5.1	Output
SVZ (>5 RA)	28	54%	22%	24%	2.5	3.2	Output
CVZ Clift (2017)	—	—	—	—	5.0	—	Input
SVZ Clift (2017)	—	—	—	—	1.0	—	Input

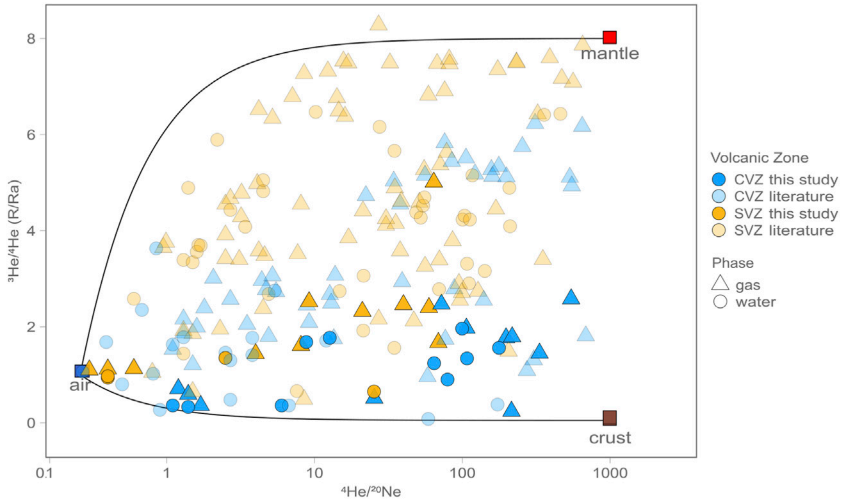

FIGURE 4 | Helium isotopes ($^3He/^4He$) vs. $^4He/^{20}Ne$ for gas (triangles) and water (circles) phase samples. Nearly all samples can be explained by three component mixing between air (blue square), mantle (red square) and crust (brown square). On average SVZ samples require more mantle contributions than CVZ samples, which display more radiogenic/crustal features.

the atmospheric He contribution can be calculated and then subtracted from the measured value (details and equations are given in **Section 5.1**). Notably, air corrections are small due to the fact that air contains only trace amounts of helium. $^4He/^{20}Ne$ values from this study are overlapping and vary by over four orders of magnitude in CVZ samples (**Table 1**; **Figure 4**) and by nearly three orders of magnitude in SVZ samples, with the highest values occurring in gas-phase samples. SVZ samples have the largest mantle contribution, whereas CVZ samples are dominated by radiogenic helium. We note duplicate sample analyses (i.e., same phase and locality) are in good agreement with respect to He isotopes; they deviate by less than 0.5 R_A for all samples except La Colcha, where duplicates vary by 1.13 R_A. In cases where there is a significant difference between He isotopes in duplicates we take the value with the highest $^4He/^{20}Ne$ to be most robust, because it indicates the lowest level of air contamination which is likely the culprit of any disagreement.

Across the CVZ, air-corrected helium isotope ratios range from 0.1 R_A to 2.6 R_A, and are slightly lower (more radiogenic) than recent reports of He isotopes from fluids and gases within the region (which range from 0.1 R_A to 5.5 R_A; Supplementary Table S1). Across the SVZ, air-corrected helium isotope ratios range from 0.7 R_A to 5.0 R_A, and are also generally lower (more radiogenic) than recent reports of He isotopes from the region (Agusto et al., 2013; Benavente et al., 2013; Roulleau et al., 2016; Tardani et al., 2016; Tassi et al., 2017; Lages et al., 2021; Tardani et al., 2021) which range from 0.5 R_A to 8.4 R_A (Supplementary Table S1).

Variations in He isotope (R_C/R_A) values are apparent between the CZV and SVZ, as well as within each region. These variations are most apparent when plotted against Lithosphere Asthenosphere Boundary (LAB) depths at each sample site (**Figure 5**), according to the model of Tassara and Echaurren (2012). High He isotope (R_C/R_A) values in each region occur where LAB depths are lowest. Though this result may in part reflect thin LAB model anomalies along the arc axis that arise due to high heat flow in regions of active volcanism, the correlation also persists across the entire data range. In summary, the most prominent characteristic of CVZ and SVZ helium isotope results is that all samples are characterized by an admixture of mantle

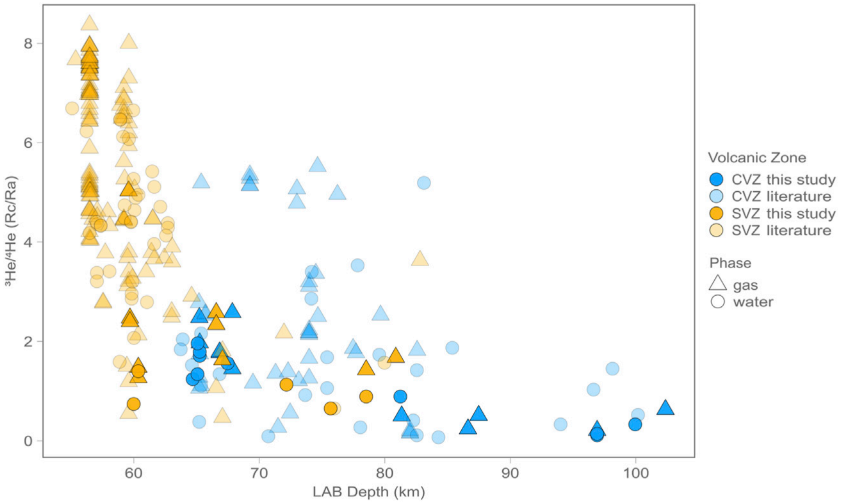

FIGURE 5 | Helium isotopes vs. Lithosphere Asthenosphere Boundary (LAB) depths according to the model of Tassara and Echaurren (2012) for gas (triangles) and water (circles) phase samples. Notably there is a negative correlation between He isotopes (R_C/R_A)and LAB depth.

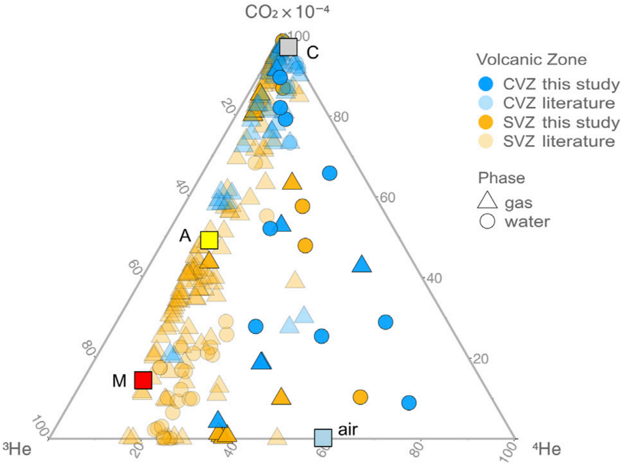

FIGURE 6 | Ternary plot of CO_2, ^3He, and ^4He for gas (triangles) and water (circles) phase samples from the CVZ and SVZ, illustrating the effects of crustal and radiogenic contamination of mantle-like volatiles. For reference, we plot "mantle" ($^3He/^4He = 8 \pm 1\ R_A$; $CO_2/^3He = 2 \times 10^9$) with a red square (M) (Marty and Jambon, 1987), average arc mantle ($^3He/^4He = 5.4 \pm 1.9\ R_A$; $CO_2/^3He = 1.2 \times 10^{10}$) with a yellow square (A) (Hilton et al., 2002), air ($^3He/^4He = 1\ R_A$; $CO_2/^3He = 5.5 \times 10^7$) with a blue square (air) and crust ($^3He/^4He = 0.05\ R_A$; $CO_2/^3He = 1 \times 10^{13}$) (Shaw et al., 2003; Barry et al., 2013) with a gray square (C). All gas samples fall on or are close to a binary mixing trajectory between mantle helium and variable amounts of crustal contamination. Fluid samples display lower $CO_2/^3He$ and helium isotope values, suggesting carbon removal (calcite precipitation). There is no evidence for degassing induced fractionation, as this would drive water samples in the opposite direction as observed trends.

and radiogenic (i.e., crustal) contributions. The highest values from this study plot well below the nominal range of values associated with upper mantle helium (8 ± 1 R_A) whereas the lowest ratios are approaching the radiogenic He production ratio (0.05 R_A) (e.g., Morrison and Pine, 1955). Lages et al. (2021) recently pointed out that He isotopes from fluid inclusion lava data retain higher He isotope values on average compared to the gas and water phase data presented here.

4.2 Carbon Isotopes [$\delta^{13}C$ (CO_2)]

C-isotope ratios ($\delta^{13}C$) range from −15.3‰ to −1.2‰ (versus VPDB) within CVZ samples, and from −17.2‰ to −4.1‰ (versus VPDB) within SVZ samples. On average, CVZ samples have higher $\delta^{13}C$ values (average = −8.7‰) compared to SVZ samples (average = −10.8‰).

4.3 $CO_2/^3He$ Values

$CO_2/^3He$ values vary over two orders of magnitude in CVZ samples, from ~6.9×10^8 (below MORB-like at 2×10^9) to higher values (~1.7×10^{11}) typically associated with input from crustal lithologies (e.g., O'nions and Oxburgh, 1988). The high $CO_2/^3He$ values are consistent with either subducted carbon contributions and/or crustal assimilation upon fluid ascent and storage in the crust (**Figure 6**). $CO_2/^3He$ varies by nearly five orders of magnitude in SVZ samples, from ~4.7×10^7 (well below MORB-like) to higher values (~1.7×10^{12}), well above the MORB range. The low $CO_2/^3He$ values in the SVZ suggest that carbon may be preferentially removed in the crustal system (see **Section 5.3.3** for details).

5 DISCUSSION

A number of processes can affect regional geothermal $^3He/^4He$ ratios, $\delta^{13}C$ values and associated He–CO_2 characteristics. Here we aim to determine which samples have $^3He/^4He$, $CO_2/^3He$, and $\delta^{13}C$ values most representative of the mantle source composition versus those that have been modified by secondary processes (e.g., carbon addition/loss, hydrothermal-related fractionation, and calcite precipitation) (**Figure 6**). Using such an approach, we are able to elucidate the sources and sinks of volatiles, as well as their pathways from the mantle/crustal source to the surface. Ultimately the goal is to understand how large-scale (i.e., margin-wide) tectonic processes control the stark He-C geochemical variability that we observe between the CVZ and the SVZ.

5.1 Helium

5.1.1 Helium Sources

Helium can be derived from the mantle, crust, and/or atmosphere, and the relative contributions of these different sources will ultimately control the $^3He/^4He$ of a given sample. When considering all geothermal data [i.e., our data (**Table 1**) and literature data (Supplementary Table S1)], we show that uncorrected He isotope (R/R_A) values range from 0.1 to 7.3 R_A in the CVZ ($n = 191$) and from 0.5 to 8.3 R_A in the SVZ ($n = 226$), which is consistent with previous findings (e.g., Lages et al., 2021). Air-corrected $^3He/^4He$ is much lower on average in the CVZ ($R_C/R_A = 1.8$ R_A; 1-sigma standard deviation = 1.4 R_A) relative to the SVZ ($R_C/R_A = 5.0$ R_A; 1 sigma S.D. = 2.1 R_A). Nearly all samples have $^4He/^{20}Ne$ values that are significantly higher than air (= 0.32) or air-saturated water (ASW) (= 0.26 at 15°C; **Figure 4**), suggesting negligible atmospheric contributions. For our data, we adopt the methods of Hilton, (1996) and use "*X*-values" to correct He isotope ratios for atmospheric contribution. For gas samples, the *X*-value is defined using **Eq. 1**:

$$(X)_{gas} = (^4He/^{20}Ne)_{measured}/(^4He/^{20}Ne)_{air} \quad (1)$$

Where $(^4He/^{20}Ne)_{measured}$ is the measured ratio and $(^4He/^{20}Ne)_{air}$ is the value of air.

For water samples, measured $^4He/^{20}Ne$ values are converted to *X* values using temperature-dependent Bunsen solubility coefficients (β; Weiss, 1971), following **Eq. 2**:

$$(X)_{fluid} = (^4He/^{20}Ne)_{measured}/(^4He/^{20}Ne)_{air} \times (\beta_{Ne}/\beta_{He}) \quad (2)$$

For pure fresh water at 15°C, $\beta_{Ne}/\beta_{He} = 1.22$ (Weiss, 1971).

The *X*-value can then be combined with measured He isotope values (R/R_A) to calculate a corrected He isotope value (R_C/R_A):

$$R_C/R_A = ((R/R_A \times X) - 1)/(X - 1) \quad (3)$$

Where R/R_A is the measured He isotope value, reported relative to air, and X is calculated using **Eqs 1**, **2**.

5.1.2 Helium Mantle-Crust Mixing

Once air contributions are quantified and corrected for, we use air-corrected He isotope (R_C/R_A) values to calculate the fraction of mantle-derived He, assuming a binary mixture between mantle and crustal endmembers (e.g., Barry et al., 2013):

$$\%\,\text{Mantle He} = (R_C/R_A - {}^3He/{}^4He_{Crust})/({}^3He/{}^4He_{Mantle} - {}^3He/{}^4He_{Crust}) \quad (4)$$

where, $^3He/^4He_{Mantle} = 8$ R_A (Graham, 2002; Lages et al., 2021), and $^3He/^4He_{Crust} = 0.05$ R_A (Morrison and Pine, 1955).

Using **Eq. 4**, we calculate that the CVZ is characterized by 21% mantle He and 79% crustal He on average. In contrast, we find that the SVZ is characterized by 62% mantle He and 38% crustal He on average. The extent of mixing between air, crustal and mantle components is most likely controlled by the thickness of the crust. We note that in the CVZ, where the crust is ~70 km thick on average, the $^3He/^4He$ is much lower (average (mean) $R_C/R_A = 1.8$ R_A) than in the SVZ (average (mean) $R_C/R_A = 5.0$ R_A), where the crust is only ~40 km thick on average. We hypothesize that, as fluids and gases migrate through thicker sections of crust in the overriding plate, they incorporate radiogenic ^4He due to interaction with the U- and Th-rich country rock (e.g., Hilton et al., 1993). This broad trend was recently pointed out by Lages et al., 2021, who presented a comprehensive He isotope compilation that included fluid and gas data as well as newly-reported He isotope data from fluid inclusions in minerals from lavas (mostly from the Northern Volcanic Zone). In total, the Lages et al. (2021) He isotope compilation reports 261 gas and water He isotope data points from the literature (spanning the NVZ, CVZ, and SVZ). Many of these data overlap with the compilation presented here, which focuses only on the CVZ and the SVZ, but contains (He and/or C isotope) data for 417 samples in total. The addition of C isotope data allows for interrogation of sources and processes affecting C cycling.

Several previous studies focused on He isotopes throughout the ACM (e.g., Hilton et al., 1993; Lages et al., 2021). Using fluid inclusion data, Lages et al., 2021 demonstrated that lavas retain mantle source signals (i.e., high $^3He/^4He$) more effectively than fluid and gas samples, with the most pristine lava samples yielding a He isotope endmember value of 8.0 R_A in the CVZ and 7.9 R_A in the SVZ. However, fresh lavas are only accessible in the volcanic arc, whereas geothermal fluids and gases provide a window into volatile cycling across the entire arc (forearc, arc, backarc). We thus adopt a mantle endmembers of 8.0 R_A for the above mixing calculation (**Eq. 4**). Notably, observed He isotope values below 8 R_A cannot be due to subduction of U- and Th-rich material, because radiogenic He-rich sediments would need to be far too old (i.e., >1890 Myr) to explain the observed data (Hilton et al., 1993; Lages et al., 2021). Instead, low He isotopes in the ACM are likely the result of either: 1) magma aging, or 2) fluid interaction/assimilation with the country rock. Hilton et al. (1993) showed that the latter scenario could explain He isotope trends if just 1% of country rock was assimilated from 10 million year old country rock. This would also satisfy observations in Sr and Pb isotope systematics (Hilton et al., 1993; Scott et al., 2018). An assimilation mechanism is preferred over magma aging, because in this scenario He isotope variability would be coupled with the age of the lowermost crust, thus predicting that SVZ samples would retain higher $^3He/^4He$ than CVZ samples, due to the relative thickness and antiquity of the crust.

5.2 Carbon

5.2.1 Carbon Sources

Carbon in geothermal samples can be derived from the mantle, the overlying crust, or introduced through subduction of carbon-laden sediments, which are released at depth and migrate to surface manifestations across the volcanic arc (e.g., Sano and Marty, 1995). $CO_2/^3He$ and $\delta^{13}C$ data can be used to differentiate between various carbon sources; however it is often difficult to definitively differentiate between the latter two processes. Here,

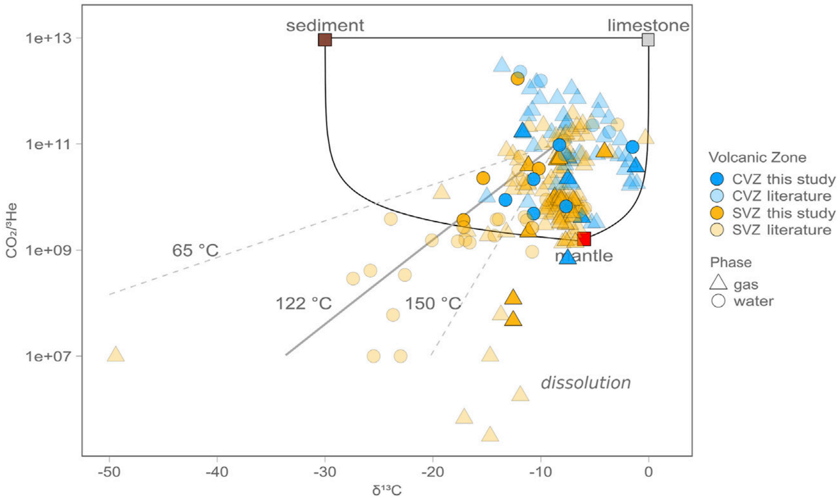

FIGURE 7 | $CO_2/{}^3He$ vs. $\delta^{13}CO_2$ for all gas (triangles) and water (circles) samples from this study (bright symbols) as well as from published studies (light symbols). Also plotted are subduction-related source end-member compositions for mantle (M), limestone (L), and sediment (S) for reference, along with mixing lines, after Sano and Marty (1995). Solid mixing lines represent binary mixtures between the three endmember values. The uncertainties on the $CO_2/{}^3He$ vs. $\delta^{13}CO_2$ data are lower than given by the size of the symbols. Predicted calcite fractionation model trends at 65°C, 122°C, and 150°C are also shown for fluid samples, assuming an initial $\delta^{13}C_i$ composition of –8.4‰ and $CO_2/{}^3He = 1.0 \times 10^{11}$, which are the average values from all gas samples. In contrast, gas samples with isotopically low $CO_2/{}^3He$ are likely affected by dissolution, which will drive $CO_2/{}^3He$ values down in gas samples.

we model $CO_2/{}^3He$ and $\delta^{13}C$ data for a total of 172 gas samples. These are mostly published data (n = 158) (Hilton et al., 1993; Hoke et al., 1994; Varekamp et al., 2006; Sepúlveda et al., 2007; Aguilera, 2008; Ray et al., 2009; Tassi et al., 2009; Tassi et al., 2010; Capaccioni et al., 2011; Tassi et al., 2011; Aguilera et al., 2012; Agusto et al., 2013; Benavente et al., 2013; Chiodi et al., 2015; Aguilera et al., 2016; Benavente et al., 2016; Roulleau et al., 2016; Tardani et al., 2016; Tassi et al., 2016; Arnold et al., 2017; Tassi et al., 2017; Lopez et al., 2018; Chiodi et al., 2019; Arnold et al., 2020; Inostroza et al., 2020; Robidoux et al., 2020; Lages et al., 2021; Tardani et al., 2021; Filipovich et al., 2022) and samples from this study (n = 14). We focus on gas samples in order to understand sources, as gases are less susceptible to fractionation processes than water phase samples. He–C isotope characteristics are similar to observations in other arcs worldwide (Sano and Marty, 1995; Sano and Williams, 1996), suggesting a prominent role of the subducting slab in supplying carbon to gas manifestations in both the CVZ and SVZ.

5.2.2 Subduction-Derived Carbon

Previous studies in the ACM have noted the role of sediment-derived fluids in melting the Sub-Andean mantle (e.g., Stern, 2007) and supplying volatiles to volcanically-derived samples (Ray et al., 2009). To quantify the extent of slab-derived CO_2, we adopt the approach of Marty et al. (1989), Varekamp et al. (1992), Sano and Marty (1995) which uses observed He-CO_2 characteristics to deconvolute mantle- versus subduction-derived (i.e., organic sediments and inorganic limestones) components. Specifically, this approach assumes that all deviations of volcanic gases from the mantle composition are subduction/mantle derived and that there is no crustal input from the overriding slab. Given these assumptions, He–CO_2 characteristics (relative abundances and $\delta^{13}C$ systematics) can be used to resolve CO_2 contribution from three distinct sources: limestone (L) from subducted sediment and mineralized within slab basement, sedimentary (organic) carbon (S) from subducted sediment, and the mantle wedge (M). Each endmember source component is assumed to have a distinctive $CO_2/{}^3He$ (M = 2×10^9; L = 1×10^{13}; S = 1×10^{13}) and $\delta^{13}C$ (M = −5‰; L = 0‰; S = −30‰) signature. In **Figure 7**, we plot the $CO_2/{}^3He$ ratios as a function of $\delta^{13}C$ for all gas samples, together with binary mixing trajectories. In order to quantify the relative proportions of CO_2 derived from each respective endmember component, mass fractions of three major sources of carbon are quantitatively calculated with **Eqs 5–7** below (Sano and Marty, 1995):

$$({}^{13}C/{}^{12}C)_O = f_M\,({}^{13}C/{}^{12}C)_M + f_L\,({}^{13}C/{}^{12}C)_L + f_S\,({}^{13}C/{}^{12}C)_S \tag{5}$$

$$1/({}^{12C}/{}^3He)_O = f_M/ = ({}^{12}C/{}^3He)_M + f_L/({}^{12}C/{}^3He)_L + f_S/({}^{12}C/{}^3He)_S \tag{6}$$

$$f_M + f_L + f_S = 1 \tag{7}$$

where subscripts L, S and M correspond to the end members limestone, sediment and mantle (**Table 2**) and subscript O = observed.

In this way we calculate that the average CO_2 provenance in the CVZ to be L:S:M = 70:22:8, whereas the average CO_2 provenance in the SVZ is L:S:M = 55:24:21 (**Table 2**). This suggests more significant mantle contributions to gases in the SVZ, which is consistent with the observation of higher ${}^3He/{}^4He$. These calculations equate to an average L/S of 3.2 and an average (L + S)/M of 11.9 for the CVZ, and an average L/S of 2.3 and an average (L + S)/M of 3.7 for the SVZ (**Table 2**). This estimate for the SVZ is broadly consistent with previous estimates by Ray et al. (2009) and findings at other arc-related geothermal systems (e.g., Sano and Marty, 1995).

If only gas samples with ^{3}He/^{4}He above 5 R_A are considered, the calculated L:S:M ratios change to 73:10:17 and 54:22:24 for the CVZ and SVZ, respectively. In this scenario, the mantle contribution is in better agreement between the two regions, which is not surprising considering that only high ^{3}He/^{4}He samples are being considered. Notably, slab-derived contributions dominate the CO_2 budget in both regions, irrespective of whether all samples or only those with high He isotope ratios are considered. Considering only samples with He isotopes >5 R_A, the average L/S is 7.0 and the average (L + S)/M is = 5.1 in the CVZ, and the average L/S is 2.5 and the average (L + S)/M is 3.2 in the SVZ. All L, S, M calculations are reported in **Table 2**.

We can directly compare estimates of L:S:M (**Table 2**) with input estimates of carbon concentrations in subducting lithologies (e.g., Clift, 2017). Carbon input estimates are compiled from scientific ocean drilling studies, which document the amount of carbonate and organic carbon subducted at convergent margins. Notably, the carbon input estimates from Clift (2017) factor in the erosional or accretionary nature of each margin when estimating how much carbon is delivered to the subduction zone. However, CVZ estimates remain poorly constrained due to lack of drill cores offshore of the CVZ. As noted above, the average output L/S in the CVZ and SVZ are 3.2 and 2.3, respectively. However, Clift (2017)'s L/S input estimates are 5.0 in the CVZ and 1.0 in the SVZ. Notably, if only samples with high He isotopes (>5 R_A) are considered (which equates to filtering out samples with a significant crustal contribution), then the L/S ratios increase from 3.2 to 7.0 and from 2.3 to 2.5 in the CVZ and SVZ, respectively (**Table 2**). In the CVZ, where crustal assimilation is more prevalent due to the exceedingly thick crust, this filtering exercise increases output L/S estimates by over a factor of two, presumably to a more representative input value [above estimates from Clift (2017)]. This suggests that the C contribution from the CVZ overriding plate is dominantly from organic rich sediments. In the SVZ, there is not a significant shift in L/S when a filter for only high He isotope samples is applied, due to the fact that the (thinner) crust does not have a significant impact on the L/S ratio.

In either scenario (with and without filtering), there is broad agreement between input L/S (Clift, 2017) and output estimates (this study) (**Table 2**). The fact that input and output estimates do not match perfectly may suggest that subducted C is actually being released over a much wider area than previously thought. We know from other studies (e.g., Barry et al., 2019a) that subducted carbon is likely released across the entire convergent margin (outer forearc, forearc, arc, backarc) and that adopting such a narrow view of where it could be released (i.e., only in the high He isotope arc) is likely an oversimplification. It is therefore important to sample across the entire arc system, so that carbon output estimates can be more systematically compared with input estimates. Additionally, the discrepancy between L/S inputs and outputs may suggest that C-bearing fluids are preferentially released from different slab lithologies at different subduction depths, similar to the process recently proposed for subducted sulfur by de Moor et al. (2022). Hence, one possible explanation for the difference between L/S inputs and outputs is that limestone-derived and organic sediment-derived C are not released in the same regions of the arc. The implication is that C isotope compositions of primary subduction-related fluids could vary significantly across the arc.

Similar disparities between input and output estimates have been observed at other arc-related localities, e.g., the Central America Volcanic Arc (CAVA), where output L/S estimates (3.8–5.6) were significantly lower than sedimentary input L/S estimates (11.5–13.6) (De Leeuw et al., 2007). The sense of the inputs-outputs discrepancy in the SVZ is in the opposite direction to CAVA [i.e., L/S output estimates (this study) are significantly higher (L/S = 2.3–2.5) than input estimates (L/S = 1.0; Clift, 2017) (**Table 2**)]. However, when only high (>5 R_A) samples are considered from the CVZ, the inputs-outputs discrepancy trends in the same direction as the SVZ (**Table 2**). The fact that L/S output estimates are lower than inputs in the CVZ suggests that there are relatively more organic contributions than what would be expected if all the C were quantitatively/proportionally released from the slab beneath the arc front. This could mean that limestone carbon is either preferentially 1) released in the forearc or 2) recycled to the deep mantle, whereas organic C is preferentially released beneath the volcanic arc. Notably, the latter scenario was recently suggested by Bouilhol et al. (2022), who noted decoupling of inorganic and organic carbon during subduction. Though speculative at this point, this topic may be of interest for future investigations. An alternative explanation for the general lack of agreement between carbon input and output estimates is that subducted sediment-derived C may not be entirely responsible for the observed variations in the gas chemistry data. In the following sections we explore alternative explanations for the variations in He-C characteristics.

5.2.3 Assimilation of Carbon From the Overriding Plate

The Sano and Marty (1995) approach assumes all He-C characteristics are controlled by subduction and mantle inputs and that there is no significant input of assimilated crustal CO_2. This assumption may be valid for high temperature arc samples marked by high ^{3}He/^{4}He, but here we report and compile data from across the entire arc system (i.e., forearc, arc, backarc). In such diverse tectonic settings He isotope ratios are highly variable (**Figure 8**) and often much lower, suggesting significant interaction with the crust. In **Section 5.1** we suggested that He isotope variations are primarily controlled by the thickness of the crust, with lower He-isotope values on average in the CVZ versus the SVZ. We surmise that similar processes could affect the carbon systematics, as $CO_2/^3$He is higher (2.9×10^{11}) on average in the CVZ (1-sigma standard deviation = 5.4×10^{11}) and lower (4.4×10^{10}) on average in the SVZ (1-sigma standard deviation = 1.4×10^{11}) (**Figure 8**). Additionally, δ^{13}C is −8.7‰ (1-sigma standard deviation = 4.5‰) on average in the CVZ and −10.8‰ (1-sigma standard deviation = 3.7‰) on average in the SVZ. Broadly speaking, the average $CO_2/^3$He in the SVZ is closer to the mantle range (vs. the CVZ), whereas the average carbon

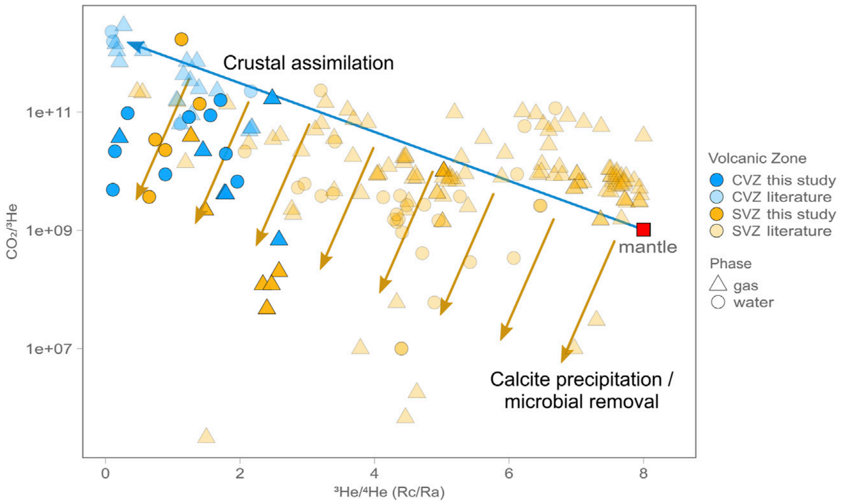

FIGURE 8 | $CO_2/^3He$ vs. He isotopes (R_C/R_A) for all samples. There is a notable trend (blue arrow) from the SVZ to the CVZ whereby samples range from nearly mantle-like to crustal (low He isotopes and higher $CO_2/^3He$). Yellow arrows indicate the effect of calcite precipitation and microbial removal. The fact that these arrows do not point straight down suggest that the residence time in the crust required for calcite removal is concomitant with time required to moderately lower He isotopes through ^4He addition.

isotope signature is farther from the canonical mantle range (vs. the CVZ). In **Section 5.3** we explore additional fractionation processes that could explain this apparent dichotomy.

5.3 Crustal Processes Acting to Modify He-C Characteristics

Carbon recycling and release from the subducted slab into volcanic fluids has been proposed to control the carbon isotope systematics across the ACM (Hilton et al., 1993; Ray et al., 2009). However, water samples suggest that secondary crustal processes are also at work in the region. This section therefore focuses on the additional processes that can modify the He–CO_2 of geothermal fluids, with the aim of determining if we can differentiate between source features (see **Sections 5.1**, **5.2**; mixing of mantle and slab-derived components) and secondary processes such as crustal overprinting (e.g., Mason et al., 2017; Karolytė et al., 2019), phase fractionation (e.g., Ray et al., 2009; Barry et al., 2013), gas dissolution and/or precipitation of calcite (Ray et al., 2009; Newell et al., 2015; Barry et al., 2019b). Likely, all of these processes exert some control on the observed He-C features.

5.3.1 Crustal Overprinting and Assimilation

As discussed in **Sections 5.1.2**, **5.2.3**, crustal overprinting appears to be pervasive in fluid and gas samples, particularly in lower temperature samples from the CVZ. He isotopes are highly variable, suggesting different amounts of assimilation with U- and Th- (and hence ^4He-) rich crust, consistent with radiogenic (i.e., Sr and Nd) observations (Hilton et al., 1993; Scott et al., 2018). Carbon appears to be similarly affected by interaction with the crust. Higher carbon isotope values on average in the CVZ indicate that isotopically heavy (i.e., inorganic) carbon is being preferentially assimilated in the CVZ versus the SVZ (**Figure 7**), suggesting that CVZ samples may be influenced by isotopically-heavy crustal/carbonate CO_2 dissolution (e.g., Mason et al., 2017; Karolytė et al., 2019) in addition to slab/MORB-like starting values. Notably, several previous He-C studies in acidic volcanic arc settings have suggested the release of previously sequestered CO_2 (Wehrmann et al., 2011; Dawson et al., 2016; de Moor et al., 2016; Mason et al., 2017). For example, Mason et al. (2017) attributed isotopically high C isotope values in mature continental arcs with accreted carbonate platforms (i.e., the CVZ) to the reworking of crustal limestone, effectively superimposing this signature on top of volcanic/subduction source features. Assimilation of carbon rich crustal material likely also occurs in the SVZ, but to a lesser extent. Alternatively, the elevated $CO_2/^3He$ (**Figure 6**) and non-mantle-like $\delta^{13}C$ values (**Figure 7**) could be entirely explained by subduction features as suggested in **Section 5.2**, but this would indicate that the much thicker crust in the CVZ versus the SVZ is not affecting the samples, which seems unlikely. A third explanation is that the carbon isotopes are controlled by additional secondary processes that induce fractionation, as is discussed in the following sections. We hypothesize that these competing processes together act to control volatile budgets not only in the Andes, but likely in arcs globally.

5.3.2 Degassing, Phase Fractionation, and Gas Dissolution

During degassing or boiling, a free gas phase separates from the fluid phase within the hydrothermal system. Helium partitions preferentially into the vapor phase relative to CO_2 as a consequence of its lower solubility in aqueous fluids (Ellis and Golding, 1963; Vogel et al., 1970; Ozima and Podosek, 1983; Ray et al., 2009; Barry et al., 2013).

For this reason, gas samples are often considered more representative of source features than water samples, as they are not subject to this additional fractionation mechanism. Accordingly, degassing and phase fractionation drive water $CO_2/^3He$ towards higher values (**Figure 6**) because CO_2 is more soluble in water than He. However, the opposite trend is observed in a subset of our data, as well as in the compiled literature data (i.e., we observe lower $CO_2/^3He$ in water samples versus gas samples on average; **Figure 6**). This strongly suggests that hydrothermal phase separation following degassing is not the dominant mechanism controlling He-C systematics between water and gas phase in the CVZ and SVZ, and that carbon is actively being removed from water samples. Low $\delta^{13}C$ values in the lowest $CO_2/^3He$ samples corroborate this explanation and we surmise that this is the result of calcite precipitation (see **Section 5.3.3** below; **Figure 7**).

Similarly, Gilfillan et al. (2009) and Güleç and Hilton (2016) showed that gas loss by dissolution in water can also result in $CO_2/^3He$ fractionation trends in both gas and water phase samples. Notably, the predicted fractionation gas trends are broadly similar to anticipated calcite precipitation trends (e.g., Güleç and Hilton, 2016). As gases ascend through bubbling springs towards the surface, they likely intersect one or more gas-undersaturated aquifers. When a gas phase comes into contact with such an aquifer, it preferentially loses the more soluble gas species (i.e., C) relative to the less soluble gas species (i.e., He), resulting in lower $CO_2/^3He$ in the gas phase which ultimately manifests at the surface (**Figure 7**). We surmise that this may have affected several of the gas samples in the SVZ (as noted on **Figure 7**). The opposite is true of water phase samples, which are ultimately left with elevated $CO_2/^3He$. Notably, a concomitate fractionation occurs in C-isotope of CO_2, resulting in a isotopically lower $\delta^{13}C$ values in residual gas phase sample. Such fractionation can sometimes be difficult to distinguish from that caused by calcite precipitation (e.g., Güleç and Hilton, 2016). The low $CO_2/^3He$ values observed in SVZ water samples suggests that carbon is actively being removed from the water and thus we attribute these signals to calcite precipitation (see **Section 5.3.3**).

5.3.3 Precipitation of Calcite

Secondary processes can be assessed using a CO_2-^3He-^4He ternary diagram (**Figure 6**), including the effects of carbon removal due to carbonate mineral formation in the crust. In **Figure 7**, $CO_2/^3He$ vs. $\delta^{13}C$ is plotted for all samples and it is clear that, on average, water and gas phase samples have broadly overlapping $CO_2/^3He$. However, we surmise that fluid samples in both regions may have experienced CO_2 loss by calcite precipitation at depth. In such a scenario, gases are dissolved in deep fluids that interact with country rock during transport through the hydrothermal system toward the surface. This migration results in the fluids becoming enriched in cations (e.g., Ca^{2+}, Mg^{2+}) (Spane and Webber, 1995; McLing and Johnson, 2002), especially where mafic rocks are prevalent. The CO_2-rich fluids emanating from the slab/mantle then react with these cations to precipitate carbonate minerals such as calcite or aragonite. During this reaction, CO_2 is retained in the carbonate mineral (e.g., $CaCO_3$, $MgCO_3$), resulting in lower $CO_2/^3He$ and more negative $\delta^{13}C$ in residual fluids as the heavier isotope of C is preferentially partitioned into the solid (carbonate) phase. Notably, this process is highly temperature-dependent, so by assuming a constant geothermal gradient, the extent of carbon isotope fractionation can be used to constrain the temperature (and depth) at which this process occurs. When considering data from this study together with published water data, we note that CVZ water samples exhibit higher $CO_2/^3He$ values on average, as well as the higher $\delta^{13}C$ values, only extending down to −18.7‰, whereas SVZ water samples exhibit the lower $CO_2/^3He$ values on average and $\delta^{13}C$ values as low as −27.4‰. Thus, the first order observation is that some samples in the SVZ, with very low $CO_2/^3He$ and $\delta^{13}C$, may reflect extreme carbon removal due to calcite precipitation (**Figure 8**).

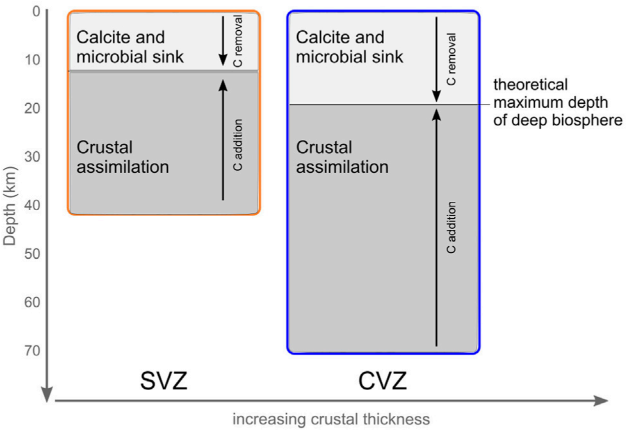

FIGURE 9 | Cartoon showing crustal thickness and the relative proportions of C removal (as calcite precipitation and potential microbial sink) vs. C addition (crustal assimilation) in the two volcanic zones. As the thickness of the crust increases from ~40 km in the SVZ to ~70 km in the CVZ, the depth to which biologically mediated calcite precipitation can occur, increases only marginally compared to crustal thickness. This disparity in crustal thickness results in different contributions of these competing processes. We hypothesize that these various processes each contribute to various extents to shape the volatile budget not just in the Andes, but likely in arcs globally.

In **Figure 7**, samples are plotted along with Rayleigh distillation fractionation lines for calcite precipitation at 65°C, 122°C, and 150°C. Notably, 65°C is the temperature at which calcite fractionation was proposed to occur in the Costa Rica forearc (Barry et al., 2019a). However, in the ACM, it appears that calcite precipitation occurs at higher temperatures, extending to temperatures as high as 150°C, which are consistent with observations from Baja, Mexico (Barry et al., 2020). Notably, 122°C is the estimated maximum temperature of cultured microorganisms (Takai et al., 2008), while 150°C has long been considered the theoretical upper limit for Life (Merino et al., 2019). The upper temperature limit of 150°C corresponds to a depth of ~6.8 km if a uniform geothermal gradient of ~22°C/km (Rothstein and Manning, 2003) is assumed. However, the actual depth for these temperatures might change in response to local heat flow, the type of rocks present, and the tectonic setting. For example, previous work has suggested a shallower geothermal gradient in the forearc of cold subduction zones, such that the 122°C isotherm might reach ~15 km or deeper (Plümper, et al., 2017). Fullerton et al. (2021) used a depth of 15 km to calculate the total biomass present in the Costa Rican Forearc crust. The CVZ and SVZ have different average heat flows and large heterogeneities (Hamza et al., 2005). Taking this into account, and using rock compositions ranging from andesite to rhyolite, the theoretical depths to the 150°C isotherms are 12 and 20 km for the SVZ and CSZ, respectively (**Figure 9**). Within this area, low temperature processes like calcite precipitation and microbial metabolism might remove significant amounts of carbon (Barry et al., 2019a; Fullerton et al., 2021). Previously, microbes have been shown to serve as nucleation sites for the precipitation of carbonate minerals across a wide range of temperatures (e.g., Fouke et al., 2000; Tsesarsky et al., 2016). The agreement between the best fit calcite precipitation temperature and the upper temperature limit for life (~122°C) is consistent with biological nucleation potentially being important for overcoming kinetic limitations on calcite precipitation (**Figure 9**), but could also simply be a coincidence.

In order to estimate how much carbon has potentially been removed due to calcite precipitation, we construct a simple model (after Ray et al., 2009; Barry et al., 2019a; Barry et al., 2020) assuming that CO_2 is released from the slab/mantle mixture and reacts with groundwater to form 1) an initial DIC pool (dissolved CO_2) and 2) a free CO_2 gas pool. The fractionation factor (α) at isotopic equilibrium for CO_2-HCO_3^--$CaCO_3$ is temperature dependent (**Eq. 8**) and can be derived from the empirically determined fractionation between DIC and calcite (Ohmoto and Rye, 1979).

$$\alpha = \mathrm{Exp}\left(\left(-8.914 \times 108/T^3 + 8.557 \times 10^6/T^2 - 18.11 \times 10^3/T + 8.27\right)/1000\right) \tag{8}$$

where T is the temperature in Kelvin.

In **Figure 7**, the initial $\delta^{13}C_i$ input is assumed to be homogenous at −8.4‰, which corresponds to the average value of all gas samples (Supplementary Table S1). The starting $CO_2/^3He$ is assumed to be 1.0×10^{11}, which is the average for all gas samples compiled here. We emphasize that assuming a single starting point is likely an oversimplification as we are dealing with a very large variety of thermal manifestations; however these assumptions are made for the purposes of presenting a unified model for all data. The fraction (f) of carbon loss can be calculated for any observed $\delta^{13}C_o$ value can be calculated using **Eq. 9** (Holloway and Blank, 1994; Barry et al., 2021).

$$f = 1 - \left[\left(\mathrm{Exp}\left(\mathrm{Ln}\left(\left(\delta^{13}C_o + 1000\right)/\left(\delta^{13}C_i + 1000\right)\right)/(\alpha - 1)\right)\right)\right] \tag{9}$$

Likewise the $CO_2/^3He$ can be calculated by accounting for the amount of carbon removed, assuming that no ^3He is lost, due to its inert nature (**Figure 7**). The fraction (f) of carbon loss increases as calcite forms and the residual DIC $\delta^{13}CO_2$ and $CO_2/^3He$ decrease. Given these assumptions (calcite precipitation temperature = 122°C; $\delta^{13}C_i$ = −8.4‰; $CO_2/^3He_i$ = 1.0×10^{11}), the model predicts that >99% of the original carbon must be lost from the most highly fractionated water samples in the SVZ, and >97% in the CVZ, resulting in low $CO_2/^3He$ and $\delta^{13}C$. On average, 90% of carbon was removed from water samples in the SVZ and 40% was removed from water samples in the CVZ. Notably, our assumed starting compositions are non-unique and if mantle-like starting values are assumed instead, a slightly different amount of fractionation would be required to explain the data (**Figure 7**). The fact that the signal associated with calcite precipitation appears to be stronger in the SVZ compared to the CVZ suggests that this process is most prominent in regions with thinner crust, and/or more mafic rocks, providing cations that promote calcite precipitation (**Figure 9**). Notably, in the CVZ, there is also significant calcite precipitation, but the overall prevalence of this process is not as apparent, perhaps due to greater contributions of crustal carbon from the overriding plate to hot spring emissions (i.e., higher starting $CO_2/^3He$ due to assimilation), which appears to be pervasive throughout the CVZ (**Figure 8**).

5.4 He-C and Along-Arc Properties

Large scale subduction-related parameters vary significantly along-strike, likely affecting surface volatile characteristics. Below, we briefly discuss how these large scale features may affect the He-C signatures that are observed across the CVZ and SVZ.

5.4.1 Sediment Composition and Thickness

The results from **Section 5.2.2** suggest that subduction of inorganic and organic carbon likely impact gas and fluid emissions across the arc. However, deciphering source features from secondary fractionation effects in the overriding plate remains somewhat enigmatic. Higher precipitation in the southern Andes leads to higher sedimentation rates offshore of the SVZ (**Figure 1A**). The physical barrier of the Juan Fernandez Ridge at ~32 °S inhibits northward sedimentary transport along the trench, resulting in a sediment-starved incoming plate and trench at the CVZ and a sediment-flooded trench offshore of the SVZ [offshore sediment thickness is ~150 m in the CVZ vs. ~500 m in the SVZ (Contreras-Reyes, 2008; Contreras-Reyes, 2010; Völker et al., 2013; **Figure 1B**)]. Because sediments contain structurally bound carbon, the amount of incoming carbon is likely much higher in the SVZ than in the CVZ; however there are no drill cores that are directly relevant to the CVZ. In the absence of significant sediments, altered oceanic crust (AOC) could deliver significant amounts of carbon to the margins, respectively (e.g., Bekaert et al., 2021).

While carbon L/S output estimates (this study) do not perfectly match L/S input estimates (Clift, 2017) (**Table 2**), we note that the trend is in the corresponding direction, suggesting more inorganic L relative to organic S in the CVZ versus the SVZ. The fact that the CVZ retains higher $CO_2/^3He$ (**Figure 8**) despite receiving an order of magnitude less C is critically important, because this suggests that He-C cannot be solely explained by mixing between subducted components and carbon from the mantle wedge. Instead the crust must be the source of a significant proportion of the carbon in the CVZ (**Figure 9**) through assimilation, which is supported by pervasively low He isotope ratios.

5.4.2 Slab Age, Subduction Rate and Angle

Along the Chile trench, the incoming plate is younger in the SVZ (~30 Ma) than in the CVZ (~45 Ma) (Syracuse and Abers, 2006); however convergence rates are steady between 7–9 cm/yr in each region. Because the amount of carbon delivered to the trench and the ratio of inorganic (L) to organic (S) carbon are almost entirely sediment-controlled, this moderate difference in slab age is not expected to make a significant difference to the budget of subducted C. However, the age difference between these two slabs may result in an initially warmer plate in the SVZ compared to the CVZ, which may promote melting at shallower depths. We surmise above that the disparity between our L/S estimates and the Clift (2017) estimates could be related to C being preferentially released in the forearc of SVZ, which in turn resulted in more calcite precipitation at lower temperatures in the overriding plate (e.g., Barry et al., 2019b). Furthermore, the subduction dip angle is steeper in the SVZ (28°) vs. the CVZ (24°), which likely affects carbon release depths. However, there is not sufficient resolution in the C isotope data to definitively postulate that subduction angle or slab age are primary drivers of He-C features in gas and fluid manifestations across the arc. Notably, previous studies have also estimated that the magmatic CO_2 flux from the CVZ is lower than in the SVZ (Aiuppa et al., 2019), which is broadly consistent with our findings. However, our results indicate that the total carbon flux (magmatic + crustal) may actually be higher in the CVZ, as an additional carbon pool is being mobilized in the CVZ.

6 SUMMARY

Carbon and other volatile elements are actively cycled between Earth reservoirs by plate tectonics at subduction zones, which has major implications for Earth's climate and habitability over geologic timescales. Here, we report He isotope ratios and abundance data for 42 deeply-sourced fluid and gas samples from the CVZ and the SVZ. He isotopes from the CVZ range from 0.1 to 2.6 R_A ($n = 23$), following correction for atmospheric contributions. Atmosphere-corrected He isotopes from the SVZ range from 0.7 to 5.0 R_A ($n = 19$). Taken together, these data reveal a clear southeastward increase in $^3He/^4He$, with the highest values (in the SVZ) plotting below the nominal range of values associated with pure upper mantle He (8 ± 1 R_A; Graham, 2002), approaching the mean He isotope value for arc gases of (5.4 ± 1.9 R_A; Hilton et al., 2002). Notably, the lowest values are found in the CVZ, suggesting more significant crustal contributions (i.e., assimilation) (**Figure 8**) to the He budget. The crustal thickness in the CVZ is up to 70 km, significantly larger than in the SVZ, where it is just ~40 km (Tassara and Echaurren, 2012; Assumpção et al., 2013) (**Figures 1B**, **9**). It thus appears that crustal thickness exerts a primary control on the extent of fluid-crust interaction, as helium and other volatiles rise through the upper plate in the ACM, which is broadly consistent with the findings of several previous studies (e.g., Lages et al., 2021). This suggests a masked mantle influence in the CVZ associated with thicker crust adding ^4He. Carbon isotope compositions ($\delta^{13}CO_2$) vary between −12.0‰ and −1.2‰ in the CVZ and $CO_2/^3He$ values vary over three orders of magnitude (9.0×10^8–1.1×10^{12}). In the SVZ, carbon isotopes ($\delta^{13}CO_2$) vary between −14.0‰ and −8.7‰ and $CO_2/^3He$ values vary by nearly three orders of magnitude (4.7×10^7–3.9×10^{10}). Lower $\delta^{13}CO_2$ and $CO_2/^3He$ values in the SVZ are consistent with calcite precipitation in shallow-level (upper ~20 km) hydrothermal systems (Ray et al., 2009; Barry et al., 2019a). We speculate that the coincidence of modeled calcite precipitation temperature (122°C) and the upper temperature limit for life may be consistent with biological nucleation being important for overcoming kinetic limitations on calcite precipitation. Taken together, the bimodal nature of the He-CO_2 data suggests fundamentally different volatile migration pathways in each volcanic region, indicating complex interplay between mantle degassing, sediment delivery, interaction with continental crust, and volatile sequestration *via* secondary processes. Finally, we emphasize that these competing processes are not unique to the Andes and that these models should be applied to understand the volatile budget in other arc settings around the world.

DATA AVAILABILITY STATEMENT

The datasets presented in this study can be found in online repositories. The names of the repository/repositories and accession number(s) can be found in the article/**Supplementary Material**. The complete dataset and the R code to reproduce the analysis have been permanently archived on Zenodo at DOI: 10.5281/zenodo.

AUTHOR CONTRIBUTIONS

All authors either helped collect samples or analyzed samples. All authors contributed to writing the manuscript.

FUNDING

This work was principally supported by the NSF-FRES award 2121637 to PB, KL, and JM. Field work was also supported by award G-2016-7206 from the Alfred P. Sloan Foundation and the Deep Carbon Observatory to PB, KL, DG, and JM. Additional support came from The National Fund for Scientific and Technological Development of Chile (FONDECYT) Grant 11191138 (The National Research and Development Agency of Chile, ANID Chile), and COPAS COASTAL ANID FB210021 to GJ. DG was partially supported by funding from the European Research Council (ERC) under the European Union's Horizon 2020 research and innovation program Grant Agreement No. 948972—COEVOLVE—ERC-2020-STG.

ACKNOWLEDGMENTS

We also acknowledge M. Correggia and L. Di Iorio for technical assistance with the water samples carbon data analysis at the University of Naples Federico II.

REFERENCES

Aguilera, F., Tassi, F., Darrah, T., Moune, S., and Vaselli, O. (2012). Geochemical Model of a Magmatic-Hydrothermal System at the Lastarria Volcano, Northern Chile. *Bull. Volcanol.* 74 (1), 119–134. doi:10.1007/s00445-011-0489-5

Aguilera, F., Cortes, J., González, C., and Layana, S. (2016). *Geología y geoquímica de fluidos del campo geotérmico de Cupo, Región de los Ríos, Chile*. Antofagasta, Chile: Private Report.

Aguilera, F. (2008). *Origen y naturaleza de los fluidos en los sistemas volcánicos, geotermales y termales de baja entalpía de la zona volcánica central (ZVC) entre los 17 43'S y 25 10'S*. Antofagasta, Chile: PhD Thesis: Universidad Católica del Norte.

Agusto, M., Tassi, F., Caselli, A. T., Vaselli, O., Rouwet, D., Capaccioni, B., et al. (2013). Gas Geochemistry of the Magmatic-Hydrothermal Fluid Reservoir in the Copahue–Caviahue Volcanic Complex (Argentina). *J. Volcanol. Geotherm. Res.* 257, 44–56. doi:10.1016/j.jvolgeores.2013.03.003

Aiuppa, A., Fischer, T. P., Plank, T., and Bani, P. (2019). CO2 Flux Emissions from the Earth's Most Actively Degassing Volcanoes, 2005-2015. *Sci. Rep.* 9 (1), 5442–5517. doi:10.1038/s41598-019-41901-y

Andrews, J. N. (1985). The Isotopic Composition of Radiogenic Helium and its Use to Study Groundwater Movement in Confined Aquifers. *Chem. Geol.* 49 (1-3), 339–351.

Arnold, Y. A., Cabassi, J., Tassi, F., Caffe, P. J., and Vaselli, O. (2017). Fluid Geochemistry of a Deep-Seated Geothermal Resource in the Puna Plateau (Jujuy Province, Argentina). *J. Volcanol. Geotherm. Res.* 338, 121–134. doi:10.1016/j.jvolgeores.2017.03.030

Arnold, Y. A., Franco, M. G., Tassi, F., Caffe, P. J., Jofre, C. B., Claros, M., et al. (2020). Geochemical Features of Hydrothermal Systems in Jujuy Province, Argentina: Hints for Geothermal Fluid Exploration. *J. S. Am. Earth Sci.* 101, 102627. doi:10.1016/j.jsames.2020.102627

Assumpção, M., Feng, M., Tassara, A., and Julià, J. (2013). Models of Crustal Thickness for South America from Seismic Refraction, Receiver Functions and Surface Wave Tomography. *Tectonophysics* 609, 82–96. doi:10.1016/j.tecto.2012.11.014

Barry, P. H., Hilton, D. R., Fischer, T. P., de Moor, J. M., Mangasini, F., and Ramirez, C. (2013). Helium and Carbon Isotope Systematics of Cold "Mazuku" CO_2 Vents and Hydrothermal Gases and Fluids from Rungwe Volcanic Province, Southern Tanzania. *Chem. Geol.* 339, 141–156. doi:10.1016/j.chemgeo.2012.07.003

Barry, P. H., Lawson, M., Meurer, W. P., Warr, O., Mabry, J. C., Byrne, D. J., et al. (2016). Noble Gases Solubility Models of Hydrocarbon Charge Mechanism in the Sleipner Vest Gas Field. *Geochimica Cosmochimica Acta* 194, 291–309. doi:10.1016/j.gca.2016.08.021

Barry, P. H., de Moor, J. M., Giovannelli, D., Schrenk, M., Hummer, D. R., Lopez, T., et al. (2019a). Forearc Carbon Sink Reduces Long-Term Volatile Recycling into the Mantle. *Nature* 568 (7753), 487–492. doi:10.1038/s41586-019-1131-5

Barry, P. H., Nakagawa, M., Giovannelli, D., Maarten de Moor, J., Schrenk, M., Seltzer, A. M., et al. (2019b). Helium, Inorganic and Organic Carbon Isotopes of Fluids and Gases across the Costa Rica Convergent Margin. *Sci. Data* 6 (1), 284–288. doi:10.1038/s41597-019-0302-4

Barry, P. H., Negrete-Aranda, R., Spelz, R. M., Seltzer, A. M., Bekaert, D. V., Virrueta, C., et al. (2020). Volatile Sources, Sinks and Pathways: A Helium-Carbon Isotope Study of Baja California Fluids and Gases. *Chem. Geol.* 550, 119722. doi:10.1016/j.chemgeo.2020.119722

Barry, P. H., Bekaert, D. V., Krantz, J. A., Halldórsson, S. A., de Moor, J. M., Fischer, T. P., et al. (2021). Helium-carbon Systematics of Groundwaters in the Lassen Peak Region. *Chem. Geol.* 584, 120535. doi:10.1016/j.chemgeo.2021.120535

Bekaert, D. V., Turner, S. J., Broadley, M. W., Barnes, J. D., Halldórsson, S. A., Labidi, J., et al. (2021). Subduction-driven Volatile Recycling: A Global Mass Balance. *Annu. Rev. Earth Planet. Sci.* 49, 37–70. doi:10.1146/annurev-earth-071620-055024

Benavente, O., Tassi, F., Gutiérrez, F., Vaselli, O., Aguilera, F., and Reich, M. (2013). Origin of Fumarolic Fluids from Tupungatito Volcano (Central Chile): Interplay between Magmatic, Hydrothermal, and Shallow Meteoric Sources. *Bull. Volcanol.* 75 (8), 1–15. doi:10.1007/s00445-013-0746-x

Benavente, O., Tassi, F., Reich, M., Aguilera, F., Capecchiacci, F., Gutiérrez, F., et al. (2016). Chemical and Isotopic Features of Cold and Thermal Fluids Discharged in the Southern Volcanic Zone between 32.5°S and 36°S: Insights into the Physical and Chemical Processes Controlling Fluid Geochemistry in Geothermal Systems of Central Chile. *Chem. Geol.* 420, 97–113. doi:10.1016/j.chemgeo.2015.11.010

Beyerle, U., Aeschbach-Hertig, W., Imboden, D. M., Baur, H., Graf, T., and Kipfer, R. (2000). A Mass Spectrometric System for the Analysis of Noble Gases and Tritium from Water Samples. *Environ. Sci. Technol.* 34 (10), 2042–2050. doi:10.1021/es990840h

Bouilhol, P., Debret, B., Inglis, E. C., Warembourg, M., Grocolas, T., Rigaudier, T., et al. (2022). Decoupling of Inorganic and Organic Carbon during Slab Mantle Devolatilisation. *Nat. Commun.* 13 (1), 308–310. doi:10.1038/s41467-022-27970-0

Capaccioni, B., Aguilera, F., Tassi, F., Darrah, T., Poreda, R. J., and Vaselli, O. (2011). Geochemical and Isotopic Evidences of Magmatic Inputs in the Hydrothermal Reservoir Feeding the Fumarolic Discharges of Tacora Volcano (Northern Chile). *J. Volcanol. Geotherm. Res.* 208 (3-4), 77–85. doi:10.1016/j.jvolgeores.2011.09.015

Chen, Y. W., Wu, J., and Suppe, J. (2019). Southward Propagation of Nazca Subduction Along the Andes. *Nature* 565 (7740), 441–447.

Chiodi, A., Tassi, F., Báez, W., Maffucci, R., Invernizzi, C., Giordano, G., et al. (2015). New geochemical and isotopic insights to evaluate the geothermal resource of the hydrothermal system of Rosario de la Frontera (Salta, northern Argentina). *J. Volcanol. Geotherm. Res.* 295, 16–25. doi:10.1016/j.jvolgeores.2015.03.001

Chiodi, A., Tassi, F., Báez, W., Filipovich, R., Bustos, E., Glok Galli, M., et al. (2019). Preliminary Conceptual Model of the Cerro Blanco Caldera-Hosted Geothermal System (Southern Puna, Argentina): Inferences from Geochemical Investigations. *J. S. Am. Earth Sci.* 94, 102213. doi:10.1016/j.jsames.2019.102213

Clarke, W. B., Jenkins, W. J., and Top, Z. (1976). Determination of Tritium by Mass Spectrometric Measurement of 3He. *Int. J. Appl. Radiat. isotopes* 27 (9), 515–522. doi:10.1016/0020-708x(76)90082-x

Clift, P. D. (2017). A Revised Budget for Cenozoic Sedimentary Carbon Subduction. *Rev. Geophys.* 55 (1), 97–125. doi:10.1002/2016rg000531

Contreras-Reyes, E., Grevemeyer, I., Flueh, E. R., and Reichert, C. (2008). Upper Lithospheric Structure of the Subduction Zone Offshore of Southern Arauco Peninsula, Chile, At~ 38 S. *J. Geophys. Res. Solid Earth* 113 (B07303), 1–19. doi:10.1029/2007JB005569

Contreras-Reyes, E., Flueh, E. R., and Grevemeyer, I. (2010). Tectonic Control on Sediment Accretion and Subduction off South Central Chile: Implications for Coseismic Rupture Processes of the 1960 and 2010 Megathrust Earthquakes. *Tectonics* 29 (TC6018), 1–27. doi:10.1029/2010TC002734

Craig, H. (1953). The Geochemistry of the Stable Carbon Isotopes. *Geochimica cosmochimica acta* 3 (2-3), 53–92. doi:10.1016/0016-7037(53)90001-5

Dawson, P., Chouet, B., and Pitt, A. (2016). Tomographic Image of a Seismically Active Volcano: Mammoth Mountain, California. *J. Geophys. Res. Solid Earth* 121 (1), 114–133. doi:10.1002/2015jb012537

Day, J. M. D., Barry, P. H., Hilton, D. R., Burgess, R., Pearson, D. G., and Taylor, L. A. (2015). The Helium Flux from the Continents and Ubiquity of low-3He/4He Recycled Crust and Lithosphere. *Geochimica Cosmochimica Acta* 153, 116–133. doi:10.1016/j.gca.2015.01.008

De Leeuw, G. A. M., Hilton, D. R., Fischer, T. P., and Walker, J. A. (2007). The He–CO_2 Isotope and Relative Abundance Characteristics of Geothermal Fluids

SUPPLEMENTARY MATERIAL

The Supplementary Material for this article can be found online at: https://www.frontiersin.org/articles/10.3389/feart.2022.897267/full#supplementary-material

in el Salvador and Honduras: New Constraints on Volatile Mass Balance of the Central American Volcanic Arc. *Earth Planet. Sci. Lett.* 258 (1-2), 132–146. doi:10.1016/j.epsl.2007.03.028

de Moor, J. M., Aiuppa, A., Avard, G., Wehrmann, H., Dunbar, N., Muller, C., et al. (2016). Turmoil at Turrialba Volcano (Costa Rica): Degassing and Eruptive Processes Inferred from High-Frequency Gas Monitoring. *J. Geophys. Res. Solid Earth* 121 (8), 5761–5775. doi:10.1002/2016jb013150

de Moor, J. M., Fischer, T. P., and Plank, T. (2022). Constraints on the Sulfur Subduction Cycle in Central America from Sulfur Isotope Compositions of Volcanic Gases. *Chem. Geol.* 588, 120627. doi:10.1016/j.chemgeo.2021.120627

De Silva, S. L. (1989). Altiplano-Puna Volcanic Complex of the Central Andes. *Geology* 17 (12), 1102–1106. doi:10.1130/0091-7613(1989)017<1102:apvcot>2.3.co;2

DeMets, C., Gordon, R. G., and Argus, D. F. (2010). Geologically Current Plate Motions. *Geophys. J. Int.* 181 (1), 1–80. doi:10.1111/j.1365-246x.2009.04491.x

Dewey, J. F., and Bird, J. M. (1970). Mountain Belts and the New Global Tectonics. *J. Geophys. Res.* 75 (14), 2625–2647. doi:10.1029/jb075i014p02625

Dunai, T. J., and Baur, H. (1995). Helium, Neon, and Argon Systematics of the European Subcontinental Mantle: Implications for its Geochemical Evolution. *Geochimica Cosmochimica Acta* 59 (13), 2767–2783. doi:10.1016/0016-7037(95)00172-v

Ellis, A. J., and Golding, R. M. (1963). The Solubility of Carbon Dioxide above 100 Degrees C in Water and in Sodium Chloride Solutions. *Am. J. Sci.* 261 (1), 47–60. doi:10.2475/ajs.261.1.47

Filipovich, R., Chiodi, A., Báez, W., Ahumada, M. F., Invernizzi, C., Taviani, S., et al. (2022). Structural Analysis and Fluid Geochemistry as Tools to Assess the Potential of the Tocomar Geothermal System, Central Puna (Argentina). *Geothermics* 98, 102297. doi:10.1016/j.geothermics.2021.102297

Fouke, B. W., Farmer, J. D., Des Marais, D. J., Pratt, L., Sturchio, N. C., Burns, P. C., et al. (2000). Depositional Facies and Aqueous-Solid Geochemistry of Travertine-Depositing Hot Springs (Angel Terrace, Mammoth Hot Springs, Yellowstone National Park, U.S.A.). *J. Sediment. Res.* 70 (3), 565–585. doi:10.1306/2dc40929-0e47-11d7-8643000102c1865d

Fullerton, K. M., Schrenk, M. O., Yücel, M., Manini, E., Basili, M., Rogers, T. J., et al. (2021). Effect of Tectonic Processes on Biosphere-Geosphere Feedbacks across a Convergent Margin. *Nat. Geosci.* 14 (5), 301–306. doi:10.1038/s41561-021-00725-0

Gautheron, C., and Moreira, M. (2002). Helium Signature of the Subcontinental Lithospheric Mantle. *Earth Planet. Sci. Lett.* 199 (1-2), 39–47. doi:10.1016/s0012-821x(02)00563-0

Giggenbach, W. F., and Goguel, R. L. (1989). *Methods for theCollection and Analysis of Geothermal and Volcanic Water and Gas Samples*. Petone, New Zealand: Dept. of Sci. and Ind. Res.

Gilfillan, S. M. V., Lollar, B. S., Holland, G., Blagburn, D., Stevens, S., Schoell, M., et al. (2009). Solubility Trapping in Formation Water as Dominant CO_2 Sink in Natural Gas Fields. *Nature* 458 (7238), 614–618. doi:10.1038/nature07852

Godoy, B., Taussi, M., González-Maurel, O., Renzulli, A., Hernández-Prat, L., le Roux, P., et al. (2019). Linking the Mafic Volcanism with the Magmatic Stages during the Last 1 Ma in the Main Volcanic Arc of the Altiplano-Puna Volcanic Complex (Central Andes). *J. S. Am. Earth Sci.* 95, 102295. doi:10.1016/j.jsames.2019.102295

Graham, D. W. (2002). Noble Gas Isotope Geochemistry of Mid-ocean Ridge and Ocean Island Basalts: Characterization of Mantle Source Reservoirs. *Rev. Mineralogy Geochem.* 47, 247. doi:10.2138/rmg.2002.47.8

Güleç, N., and Hilton, D. R. (2016). Turkish Geothermal Fields as Natural Analogues of CO_2 Storage Sites: Gas Geochemistry and Implications for CO_2 Trapping Mechanisms. *Geothermics* 64, 96–110.

Hamilton, N. E., and Ferry, M. (2018). Ggtern: Ternary Diagrams Using Ggplot2. *J. Stat. Softw. Code Snippets* 87 (3), 1–17. doi:10.18637/jss.v087.c03

Hamza, V. M., Dias, F. J. S. S., Gomes, A. J. L., and Terceros, Z. G. D. (2005). Numerical and Functional Representations of Regional Heat Flow in South America. *Phys. Earth Planet. Interiors* 152 (4), 223–256. doi:10.1016/j.pepi.2005.04.009

Harmon, R. S., Barreiro, B. A., Moorbath, S., Hoefs, J., Francis, P. W., Thorpe, R. S., et al. (1984). Regional O-, Sr-, and Pb-Isotope Relationships in Late Cenozoic Calc-Alkaline Lavas of the Andean Cordillera. *J. Geol. Soc.* 141 (5), 803–822. doi:10.1144/gsjgs.141.5.0803

Hayes, J. M., Strauss, H., and Kaufman, A. J. (1999). The Abundance of 13C in Marine Organic Matter and Isotopic Fractionation in the Global Biogeochemical Cycle of Carbon during the Past 800 Ma. *Chem. Geol.* 161 (1-3), 103–125. doi:10.1016/s0009-2541(99)00083-2

Hilton, D. R., and Porcelli, D. (2003). Noble Gases as Mantle Tracers. *Treatise Geochem.* 2, 568. doi:10.1016/b0-08-043751-6/02007-7

Hilton, D. R., Hammerschmidt, K., Teufel, S., and Friedrichsen, H. (1993). Helium Isotope Characteristics of Andean Geothermal Fluids and Lavas. *Earth Planet. Sci. Lett.* 120 (3-4), 265–282. doi:10.1016/0012-821x(93)90244-4

Hilton, D. R., Fischer, T. P., and Marry, B. (2002). Noble Gases and Volatile Recycling at Subduction Zones. *Rev. Mineralogy Geochem.* 47, 1–73. doi:10.2138/rmg.2002.47.9

Hilton, D. R. (1996). The Helium and Carbon Isotope Systematics of a Continental Geothermal System: Results from Monitoring Studies at Long Valley Caldera (California, U.S.A.). *Chem. Geol.* 127 (4), 269–295. doi:10.1016/0009-2541(95)00134-4

Hoke, L., Hilton, D. R., Lamb, S. H., Hammerschmidt, K., and Friedrichsen, H. (1994). 3He Evidence for a Wide Zone of Active Mantle Melting beneath the Central Andes. *Earth Planet. Sci. Lett.* 128 (3-4), 341–355. doi:10.1016/0012-821x(94)90155-4

Holloway, J. R., and Blank, J. G. (1994). Chapter 6. Application of Experimental Results to C-O-H Species in Natural Melts. *Rev. Mineralogy Geochem.* 30 (1), 187–230. doi:10.1515/9781501509674-012

Howell, J. A., Schwarz, E., Spalletti, L. A., and Veiga, G. D. (2005). The Neuquén Basin: an Overview. *Geol. Soc. Lond. Spec. Publ.* 252 (1), 1–14. doi:10.1144/gsl.sp.2005.252.01.01

Hunt, A. G. (2015). US Geological Survey Noble Gas Laboratory's Standard Operating Procedures for the Measurement of Dissolved Gas in Water Samples *(No. 5-A11)*. Reston, VA: US Geological Survey.

Inostroza, M., Tassi, F., Aguilera, F., Sepúlveda, J. P., Capecchiacci, F., Venturi, S., et al. (2020). Geochemistry of Gas and Water Discharge from the Magmatic-Hydrothermal System of Guallatiri Volcano, Northern Chile. *Bull. Volcanol.* 82 (7), 1–16. doi:10.1007/s00445-020-01396-2

Jacques, G., Hoernle, K., Gill, J., Wehrmann, H., Bindeman, I., and Lara, L. E. (2014). Geochemical Variations in the Central Southern Volcanic Zone, Chile (38–43°S): The Role of Fluids in Generating Arc Magmas. *Chem. Geol.* 371, 27–45. doi:10.1016/j.chemgeo.2014.01.015

James, D. E. (1971). Plate Tectonic Model for the Evolution of the Central Andes. *Geol. Soc. Am. Bull.* 82 (12), 3325–3346. doi:10.1130/0016-7606(1971)82[3325:ptmfte]2.0.co;2

Javoy, M., Pineau, F., and Delorme, H. (1986). Carbon and Nitrogen Isotopes in the Mantle. *Chem. Geol.* 57 (1-2), 41–62. doi:10.1016/0009-2541(86)90093-8

Jordan, T. E., Isacks, B. L., Ramos, V. A., and Allmendinger, R. W. (1983). Mountain Building in the Central Andes. *Episodes* 6 (3), 20–26. doi:10.18814/epiiugs/1983/v6i3/005

Karolytė, R., Johnson, G., Györe, D., Serno, S., Flude, S., Stuart, F. M., et al. (2019). Tracing the Migration of Mantle CO_2 in Gas Fields and Mineral Water Springs in South-East Australia Using Noble Gas and Stable Isotopes. *Geochimica Cosmochimica Acta* 259, 109–128. doi:10.1016/j.gca.2019.06.002

Kay, S. M., and Mpodozis, C. (2002). Magmatism as a Probe to the Neogene Shallowing of the Nazca Plate beneath the Modern Chilean Flat-Slab. *J. S. Am. Earth Sci.* 15 (1), 39–57. doi:10.1016/s0895-9811(02)00005-6

Kimani, C. N., Kasanzu, C. H., Tyne, R. L., Mtili, K. M., Byrne, D. J., Kazimoto, E. O., et al. (2021). He, Ne, Ar and CO_2 Systematics of the Rungwe Volcanic Province, Tanzania: Implications for Fluid Source and Dynamics. *Chem. Geol.* 586, 120584. doi:10.1016/j.chemgeo.2021.120584

Lages, J., Rizzo, A. L., Aiuppa, A., Robidoux, P., Aguilar, R., Apaza, F., et al. (2021). Crustal Controls on Light Noble Gas Isotope Variability along the Andean Volcanic Arc. *Geochem. Persp. Let.* 19, 45–49. doi:10.7185/geochemlet.2134

López-Escobar, L., Parada, M. A., Hickey-Vargas, R., Frey, F. A., Kempton, P. D., and Moreno, H. (1995). Calbuco Volcano and Minor Eruptive Centers Distributed along the Liquiñe-Ofqui Fault Zone, Chile (41–42 S): Contrasting Origin of Andesitic and Basaltic Magma in the Southern Volcanic Zone of the Andes. *Contributions Mineralogy Petrology* 119 (4), 345–361. doi:10.1007/BF00286934

Lopez, T., Aguilera, F., Tassi, F., de Moor, J. M., Bobrowski, N., Aiuppa, A., et al. (2018). New Insights into the Magmatic-Hydrothermal System and Volatile Budget of Lastarria Volcano, Chile: Integrated Results from the 2014 IAVCEI

CCVG 12th Volcanic Gas Workshop. *Geosphere* 14 (3), 983–1007. doi:10.1130/ges01495.1

Mabry, J., Lan, T., Burnard, P., and Marty, B. (2013). High-precision Helium Isotope Measurements in Air. *J. Anal. At. Spectrom.* 28 (12), 1903–1910. doi:10.1039/c3ja50155h

Malowany, K., Stix, J., Van Pelt, A., and Lucic, G. (2015). H_2S Interference on CO_2 Isotopic Measurements Using a Picarro G1101-I Cavity Ring-Down Spectrometer. *Atmos. Meas. Tech.* 8 (10), 4075–4082. doi:10.5194/amt-8-4075-2015

Malowany, K. S., Stix, J., de Moor, J. M., Chu, K., Lacrampe-Couloume, G., and Sherwood Lollar, B. (2017). Carbon Isotope Systematics of Turrialba Volcano, Costa Rica, Using a Portable Cavity Ring-Down Spectrometer. *Geochem. Geophys. Geosyst.* 18 (7), 2769–2784. doi:10.1002/2017gc006856

Mamani, M., Wörner, G., and Sempere, T. (2010). Geochemical Variations in Igneous Rocks of the Central Andean Orocline (13 S to 18 S): Tracing Crustal Thickening and Magma Generation through Time and Space. *GSA Bull.* 122 (1-2), 162–182. doi:10.1130/b26538.1

Marty, B., and Jambon, A. (1987). C/3He in Volatile Fluxes from the Solid Earth: Implications for Carbon Geodynamics. *Earth Planet. Sci. Lett.* 83 (1-4), 16–26. doi:10.1016/0012-821x(87)90047-1

Marty, B., Jambon, A., and Sano, Y. (1989). Helium Isotopes and CO2 in Volcanic Gases of Japan. *Chem. Geol.* 76 (1-2), 25–40. doi:10.1016/0009-2541(89)90125-3

Mason, E., Edmonds, M., and Turchyn, A. V. (2017). Remobilization of Crustal Carbon May Dominate Volcanic Arc Emissions. *Science* 357 (6348), 290–294. doi:10.1126/science.aan5049

Mazor, E., and Wasserburg, G. J. (1965). Helium, Neon, Argon, Krypton and Xenon in Gas Emanations from Yellowstone and Lassen Volcanic National Parks. *Geochimica Cosmochimica Acta* 29 (5), 443–454. doi:10.1016/0016-7037(65)90038-4

McLing, T. L., Smith, R. W., and Johnson, T. M. (2002). *Chemical Characteristics of Thermal Water beneath the.* Geology, Hydrogeology, and Environmental Remediation: Idaho National Engineering And Environmental Laboratory, Eastern Snake River Plain, Idaho, Special Paper 353. Boulder, CO, 205.

Merino, N., Aronson, H. S., Bojanova, D. P., Feyhl-Buska, J., Wong, M. L., Zhang, S., et al. (2019). Living at the Extremes: Extremophiles and the Limits of Life in a Planetary Context. *Front. Microbiol.* 10, 780. doi:10.3389/fmicb.2019.00780

Morrison, P., and Pine, J. (1955). Radiogenic Origin of the Helium Isotopes in Rock. *Ann. N. Y. Acad. Sci.* 62 (3), 71–92. doi:10.1111/j.1749-6632.1955.tb35366.x

Mtili, K. M., Byrne, D. J., Tyne, R. L., Kazimoto, E. O., Kimani, C. N., Kasanzu, C. H., et al. (2021). The Origin of High Helium Concentrations in the Gas Fields of Southwestern Tanzania. *Chem. Geol.* 585, 120542. doi:10.1016/j.chemgeo.2021.120542

Newell, D. L., Jessup, M. J., Hilton, D. R., Shaw, C. A., and Hughes, C. A. (2015). Mantle-Derived Helium in Hot Springs of the Cordillera Blanca, Peru: Implications for Mantle-To-Crust Fluid Transfer in a Flat-Slab Subduction Setting. *Chem. Geol.* 417, 200–209. doi:10.1016/j.chemgeo.2015.10.003

Ohmoto, H., and Rye, R. O., 1979. *Isotopes of Sulfur and Carbon*. New York, NY: Geochemistry of Hydrothermal Ore Deposits pp. 509–567

O'nions, R. K., and Oxburgh, E. R. (1988). Helium, Volatile Fluxes and the Development of Continental Crust. *Earth Planet. Sci. Lett.* 90 (3), 331–347. doi:10.1016/0012-821x(88)90134-3

Ozima, M., and Podosek, F. A. (2002). *Noble Gas Geochemistry*. Cambridge University Press, 160–249.

Ozima, M., and Podosek, F. A. (1983). *Geochemistry of Noble Gases*. Cambridge Univ. Press.

Plank, T., and Manning, C. E. (2019). Subducting Carbon. *Nature* 574 (7778), 343–352. doi:10.1038/s41586-019-1643-z

Plümper, O., King, H. E., Geisler, T., Liu, Y., Pabst, S., Savov, I. P., et al. (2017). Subduction Zone Forearc Serpentinites as Incubators for Deep Microbial Life. *Proc. Natl. Acad. Sci. U. S. A.* 114 (17), 4324–4329. doi:10.1073/pnas.1612147114

Ray, M. C., Hilton, D. R., Muñoz, J., Fischer, T. P., and Shaw, A. M. (2009). The Effects of Volatile Recycling, Degassing and Crustal Contamination on the Helium and Carbon Geochemistry of Hydrothermal Fluids from the Southern Volcanic Zone of Chile. *Chem. Geol.* 266 (1-2), 38–49. doi:10.1016/j.chemgeo.2008.12.026

Robidoux, P., Rizzo, A. L., Aguilera, F., Aiuppa, A., Artale, M., Liuzzo, M., et al. (2020). Petrological and Noble Gas Features of Lascar and Lastarria Volcanoes (Chile): Inferences on Plumbing Systems and Mantle Characteristics. *Lithos* 370-371, 105615. doi:10.1016/j.lithos.2020.105615

Rothstein, D. A., and Manning, C. E. (2003). Geothermal Gradients in Continental Magmatic Arcs; Constraints from the Eastern Peninsular Ranges Batholith, Baja California, Mexico. *Geol. Soc. Am. Special Pap.* 374, 337–354. doi:10.1130/0-8137-2374-4.337

Roulleau, E., Tardani, D., Sano, Y., Takahata, N., Vinet, N., Bravo, F., et al. (2016). New Insight from Noble Gas and Stable Isotopes of Geothermal/Hydrothermal Fluids at Caviahue-Copahue Volcanic Complex: Boiling Steam Separation and Water-Rock Interaction at Shallow Depth. *J. Volcanol. Geotherm. Res.* 328, 70–83. doi:10.1016/j.jvolgeores.2016.10.007

Ryan, W. B., Carbotte, S. M., Coplan, J. O., O'Hara, S., Melkonian, A., Arko, R., et al. (2009). Global Multi-Resolution Topography Synthesis. *Geochem. Geophys. Geosystems* 10 (3), Q03014. doi:10.1029/2008gc002332

Sano, Y., and Marty, B. (1995). Origin of Carbon in Fumarolic Gas from Island Arcs. *Chem. Geol.* 119 (1-4), 265–274. doi:10.1016/0009-2541(94)00097-r

Sano, Y., and Williams, S. N. (1996). Fluxes of Mantle and Subducted Carbon along Convergent Plate Boundaries. *Geophys. Res. Lett.* 23 (20), 2749–2752. doi:10.1029/96gl02260

Scott, E. M., Allen, M. B., Macpherson, C. G., McCaffrey, K. J. W., Davidson, J. P., Saville, C., et al. (2018). Andean Surface Uplift Constrained by Radiogenic Isotopes of Arc Lavas. *Nat. Commun.* 9 (1), 969–978. doi:10.1038/s41467-018-03173-4

Sepúlveda, F., Lahsen, A., and Powell, T. (2007). Gas Geochemistry of the Cordón Caulle Geothermal System, Southern Chile. *geothermics* 36 (5), 389–420. doi:10.1016/j.geothermics.2007.05.001

Shaw, A. M., Hilton, D. R., Fischer, T. P., Walker, J. A., and Alvarado, G. E. (2003). Contrasting He–C Relationships in Nicaragua and Costa Rica: Insights into C Cycling through Subduction Zones. *Earth Planet. Sci. Lett.* 214 (3-4), 499–513. doi:10.1016/s0012-821x(03)00401-1

Spane, F. A., Jr, and Webber, W. D. (1995). Hydrochemistry And Hydrogeologic Conditions within the Hanford Site Upper Basalt Confined Aquifer System *(No. PNL-10817)*. Richland, WA (United States); Pacific Northwest National Lab.PNNL.

Stern, R. J. (2004). Subduction Initiation: Spontaneous and Induced. *Earth Planet. Sci. Lett.* 226 (3-4), 275–292. doi:10.1016/s0012-821x(04)00498-4

Stern, R. J. (2007). When and How Did Plate Tectonics Begin? Theoretical and Empirical Considerations. *Chin. Sci. Bull.* 52 (5), 578–591. doi:10.1007/s11434-007-0073-8

Syracuse, E. M., and Abers, G. A. (2006). Global Compilation of Variations in Slab Depth beneath Arc Volcanoes and Implications. *Geochem. Geophys. Geosystems* 7 (5), Q05017. doi:10.1029/2005gc001045

Takai, K., Nakamura, K., Toki, T., Tsunogai, U., Miyazaki, M., Miyazaki, J., et al. (2008). Cell Proliferation at 122°C and Isotopically Heavy CH_4 Production by a Hyperthermophilic Methanogen Under High-Pressure Cultivation. *Proc. Natl. Acad. Sci. U.S.A.* 105, 10949–10954. doi:10.1073/pnas.0712334105

Tardani, D., Reich, M., Roulleau, E., Takahata, N., Sano, Y., Pérez-Flores, P., et al. (2016). Exploring the Structural Controls on Helium, Nitrogen and Carbon Isotope Signatures in Hydrothermal Fluids along an Intra-arc Fault System. *Geochimica Cosmochimica Acta* 184, 193–211. doi:10.1016/j.gca.2016.04.031

Tardani, D., Roulleau, E., Pinti, D. L., Pérez-Flores, P., Daniele, L., Reich, M., et al. (2021). Structural Control on Shallow Hydrogeochemical Processes at Caviahue-Copahue Volcanic Complex (CCVC), Argentina. *J. Volcanol. Geotherm. Res.* 414, 107228. doi:10.1016/j.jvolgeores.2021.107228

Tassara, A., and Echaurren, A. (2012). Anatomy of the Andean Subduction Zone: Three-Dimensional Density Model Upgraded and Compared against Global-Scale Models. *Geophys. J. Int.* 189 (1), 161–168. doi:10.1111/j.1365-246x.2012.05397.x

Tassi, F., Aguilera, F., Vaselli, O., Medina, E., Tedesco, D., Delgado Huertas, A., et al. (2009). The Magmatic- and Hydrothermal-Dominated Fumarolic System at the Active Crater of Lascar Volcano, Northern Chile. *Bull. Volcanol.* 71 (2), 171–183. doi:10.1007/s00445-008-0216-z

Tassi, F., Aguilera, F., Darrah, T., Vaselli, O., Capaccioni, B., Poreda, R. J., et al. (2010). Fluid Geochemistry of Hydrothermal Systems in the Arica-Parinacota, Tarapacá and Antofagasta Regions (Northern Chile). *J. Volcanol. Geotherm. Res.* 192 (1-2), 1–15. doi:10.1016/j.jvolgeores.2010.02.006

Tassi, F., Aguilera, F., Vaselli, O., Darrah, T., and Medina, E. (2011). Gas Discharges from Four Remote Volcanoes in Northern Chile (Putana, Olca, Irruputuncu and Alitar): a Geochemical Survey. *Ann. Geophys.* 54 (2), 2. doi:10.4401/ag-5173

Tassi, F., Agusto, M., Vaselli, O., and Chiodini, G. (2016). "Geochemistry of the Magmatic-Hydrothermal Fluid Reservoir of Copahue Volcano (Argentina): Insights from the Chemical and Isotopic Features of Fumarolic Discharges," in *Copahue Volcano* (Berlin, Heidelberg: Springer), 119–139. doi:10.1007/978-3-662-48005-2_6

Tassi, F., Agusto, M., Lamberti, C., Caselli, A. T., Pecoraino, G., Caponi, C., et al. (2017). The 2012–2016 Eruptive Cycle at Copahue Volcano (Argentina) versus the Peripheral Gas Manifestations: Hints from the Chemical and Isotopic Features of Fumarolic Fluids. *Bull. Volcanol.* 79 (10), 1–14. doi:10.1007/s00445-017-1151-7

Thorpe, R. S., and Francis, P. W. (1979). Variations in Andean Andesite Compositions and Their Petrogenetic Significance. *Tectonophysics* 57 (1), 53–70. doi:10.1016/0040-1951(79)90101-x

Thorpe, R. S. (1982). "The Andes," in *Andesites: Orogenic Andesites and Related Rocks*, 187–205.

Tormey, D. R., Hickey-Vargas, R., Frey, F. A., and López-Escobar, L. (1991). Recent Lavas from the Andean Volcanic Front (33 to 42°S); Interpretations of Along-Arc Compositional Variations. *Andean magmatism its Tect. setting* 265, 57–78. doi:10.1130/spe265-p57

Tsesarsky, M., Gat, D., and Ronen, Z. (2016). Biological Aspects of Microbial-Induced Calcite Precipitation. *Environ. Geotech.* 5 (2), 69–78.

Turner, S. J., Langmuir, C. H., Dungan, M. A., and Escrig, S. (2017). The Importance of Mantle Wedge Heterogeneity to Subduction Zone Magmatism and the Origin of EM1. *Earth Planet. Sci. Lett.* 472, 216–228. doi:10.1016/j.epsl.2017.04.051

Tyne, R. L., Barry, P. H., Hillegonds, D. J., Hunt, A. G., Kulongoski, J. T., Stephens, M. J., et al. (2019). A Novel Method for the Extraction, Purification, and Characterization of Noble Gases in Produced Fluids. *Geochem. Geophys. Geosyst.* 20 (11), 5588–5597. doi:10.1029/2019gc008552

Varekamp, J. C., Kreulen, R., Poorter, R. P. E., and Bergen, M. J. (1992). Carbon Sources in Arc Volcanism, with Implications for the Carbon Cycle. *Terra nova.* 4 (3), 363–373. doi:10.1111/j.1365-3121.1992.tb00825.x

Varekamp, J. C., deMoor, J. M., Merrill, M. D., Colvin, A. S., Goss, A. R., Vroon, P. Z., et al. (2006). Geochemistry and Isotopic Characteristics of the Caviahue-Copahue Volcanic Complex, Province of Neuquén, Argentina. *Special Papers-Geological Soc. Am.* 407, 317. doi:10.1130/2006.2407(15)

Völker, D., Geersen, J., Contreras-Reyes, E., and Reichert, C. (2013). Sedimentary Fill of the Chile Trench (32–46 S): Volumetric Distribution and Causal Factors. *J. Geol. Soc.* 170 (5), 723–736.

Vogel, J. C., Grootes, P. M., and Mook, W. G. (1970). Isotopic Fractionation between Gaseous and Dissolved Carbon Dioxide. *Z. Phys.* 230 (3), 225–238. doi:10.1007/bf01394688

Wehrmann, H., Hoernle, K., Portnyagin, M., Wiedenbeck, M., and Heydolph, K. (2011). Volcanic CO2 Output at the Central American Subduction Zone Inferred from Melt Inclusions in Olivine Crystals from Mafic Tephras. *Geochem. Geophys. Geosystems* 12 (6), Q06003. doi:10.1029/2010gc003412

Weiss, R. F. (1968). Piggyback Sampler for Dissolved Gas Studies on Sealed Water Samples. *Deep Sea Res. Oceanogr. Abstr.* 15 (6), 695–699. doi:10.1016/0011-7471(68)90082-x

Weiss, R. F. (1971). Solubility of Helium and Neon in Water and Seawater. *J. Chem. Eng. Data* 16 (2), 235–241. doi:10.1021/je60049a019

Wickham, H. (2016). *ggplot2: Elegant Graphics for Data Analysis*. New York: Springer-Verlag. 978-3-319-24277-4.

Wieser, P. E., Turner, S. J., Mather, T. A., Pyle, D. M., Savov, I. P., and Orozco, G. (2019). New Constraints from Central Chile on the Origins of Enriched Continental Compositions in Thick-Crusted Arc Magmas. *Geochimica Cosmochimica Acta* 267, 51–74. doi:10.1016/j.gca.2019.09.008

Conflict of Interest: The authors declare that the research was conducted in the absence of any commercial or financial relationships that could be construed as a potential conflict of interest.

frontiers | Frontiers in Earth Science

ORIGINAL RESEARCH
published: 27 June 2022
doi: 10.3389/feart.2022.875439

Probabilistic Volcanic Hazard Assessment of the 22.5–28°S Segment of the Central Volcanic Zone of the Andes

Daniel Bertin[1], Jan M. Lindsay[1], Shane J. Cronin[1], Shanaka L. de Silva[2], Charles B. Connor[3], Pablo J. Caffe[4], Pablo Grosse[5,6], Walter Báez[7], Emilce Bustos[7] and Robert Constantinescu[3]*

[1]School of Environment, University of Auckland, Auckland, New Zealand, [2]College of Earth, Ocean, and Atmospheric Sciences, Oregon State University, Corvallis, OR, United States, [3]School of Geosciences, University of South Florida, Tampa, FL, United States, [4]Instituto de Ecorregiones Andinas and Instituto de Geología y Minería (CONICET — Universidad Nacional de Jujuy), San Salvador de Jujuy, Argentina, [5]Consejo Nacional de Investigaciones Científicas y Técnicas (CONICET), Argentina, [6]Fundación Miguel Lillo, San Miguel de Tucumán, Argentina, [7]Instituto de Bio y Geociencias del NOA (IBIGEO, UNSa-CONICET), Salta, Argentina

Edited by:
Pablo Samaniego,
UMR6524 Laboratoire Magmas et Volcans (LMV), France

Reviewed by:
Alvaro Aravena,
Catholic University of the Maule, Chile
Suzanne Kay,
Cornell University, United States

***Correspondence:**
Daniel Bertin
daniel.bertin.u@gmail.com

Specialty section:
This article was submitted to Volcanology, a section of the journal Frontiers in Earth Science

Received: *14 February 2022*
Accepted: *31 May 2022*
Published: *27 June 2022*

Citation:
Bertin D, Lindsay JM, Cronin SJ, de Silva SL, Connor CB, Caffe PJ, Grosse P, Báez W, Bustos E and Constantinescu R (2022) Probabilistic Volcanic Hazard Assessment of the 22.5–28°S Segment of the Central Volcanic Zone of the Andes. Front. Earth Sci. 10:875439. doi: 10.3389/feart.2022.875439

Evaluation of volcanic hazards typically focusses on single eruptive centres or spatially restricted areas, such as volcanic fields. Expanding hazard assessments across wide regions (e.g., large sections of a continental margin) has rarely been attempted, due to the complexity of integrating temporal and spatial variability in tectonic and magmatic processes. In this study, we investigate new approaches to quantify the hazards of such long-term active and complex settings, using the example of the 22.5–28°S segment of the Central Volcanic Zone of the Andes. This research is based on the estimation of: 1) spatial probability of future volcanic activity (based on kernel density estimation using a new volcanic geospatial database), 2) temporal probability of future volcanic events, and 3) areas susceptible to volcanic flow and fall processes (based on computer modeling). Integrating these results, we produce a set of volcanic hazard maps. We then calculate the relative probabilities of population centres in the area being affected by any volcanic phenomenon. Touristic towns such as La Poma (Argentina), Toconao (Chile), Antofagasta de la Sierra (Argentina), Socaire (Chile), and Talabre (Chile) are exposed to the highest relative volcanic hazard. In addition, through this work we delineate five regions of high spatial probability (i.e., volcanic clusters), three of which correlate well with geophysical evidence of mid-crustal partial melt bodies. Many of the eruptive centres within these volcanic clusters have poorly known eruption histories and are recommended to be targeted for future work. We hope this contribution will be a useful approach to encourage probabilistic volcanic hazard assessments for other arc segments.

Keywords: Central Volcanic Zone, Chile, Argentina, MatHaz, volcanic hazards

INTRODUCTION

Traditionally, volcanic hazards are assessed at the scale of single volcanic systems, such as stratovolcanoes (e.g., Ogburn et al., 2020), or single volcanic fields (e.g., Connor and Hill, 1995). Motivation for hazard assessments typically stems from a perception of future risk, based on past eruptive casualties, rapid population and infrastructure growth, insights from new age or other geological information, and/or an increase in unrest indicators (e.g., Siebe and Macías, 2003; Bird et al., 2010; Sandri et al., 2014; Biass et al., 2016;Charbonnier et al., 2020; Jiménez et al., 2020). Volcanic hazard assessments depend upon assembling detailed information on eruption frequency, magnitude and style, integrating information from diverse geomorphic, structural, geochronological, geophysical, and geochemical data (e.g., Clavero et al., 2004; Harpel et al., 2011; Johnston et al., 2011; Alloway et al., 2017).

Different tools are required for assessing volcanic hazards at distributed volcanic fields (e.g., Bartolini et al., 2015; Sieron et al., 2021), volcanic islands (e.g., Becerril et al., 2014; Cappello et al., 2016), caldera systems (e.g., Bevilacqua et al., 2015; Charlton et al., 2020), and large complex multi-vent volcanoes (e.g., Cappello et al., 2012; Jiménez et al., 2018). The greatest problem in dealing with such complex volcanic systems is that the distribution of specific eruptive hazards needs to be examined in relation to the locations of possible vent opening (e.g., Sandri et al., 2018; Bevilacqua et al., 2021). In addition to investigating spatial variability, long-lived volcanism at complex sites generates strong temporal hazard variability, which is a challenge to understand in contemporary forecasts (e.g., Bebbington and Cronin, 2011; Lerner et al., 2019).

The problems of integrating spatial and temporal variations in hazard are compounded when examining larger areas of interest, such as volcanic arcs. Past regional-scale assessments typically analysed every volcano independently (e.g., Mullineaux, 1976; Miller, 1989; Lara et al., 2011; Amigo et al., 2012). However, this is only feasible when a handful of volcanoes in a region are considered. If dozens or hundreds of volcanic centres are analysed, new approaches and methods are needed. Techniques have been developed to forecast the location and timing of future volcanic vent opening in arc segments (Martin et al., 2004; Jaquet et al., 2012, Jaquet et al., 2017; Germa et al., 2013; Kósik et al., 2020; O'Hara et al., 2020), which is the first step towards regional assessments. There is a further need to integrate spatial and temporal histories into these types of analyses, along with a comprehensive and systematic methodology to evaluate different types, frequencies and scales of volcano processes associated with each vent/volcano. Another challenge when carrying out volcanic hazard assessments in large and complex volcanic regions is the inherent difficulty of collecting comprehensive data that are of similar quality and resolution across a broad area. Even data coverage, such as in age information, mapping or volume estimations are less likely (and less affordable) as the spatial scope increases to whole arcs or long-lived continental margin segments.

Despite the complex challenge that the assessment represents, evaluating volcanic hazards over very large areas can be useful for a first-order synoptic assessment to enable the targeting of limited resources for new investigations or mitigation efforts to the most important areas. Furthermore, a regional long-term analysis can help to understand larger system changes that may highlight critical features for future hazard, such as regional migration of volcanic focussing, arc-scale variations in volcanic flux, and other specific regional-based tectonic or other drivers for volcanic flare-ups.

In consequence, in this study we examine approaches to understand the relative spatial and temporal aspects of volcanic hazards within a large continental margin setting. This study is based on an area between latitudes 22.5–28°S along the Central Volcanic Zone of the Andes of South America (**Figure 1**). This region records ~35 Myr of uninterrupted volcanic activity, comprising a vast variety of activity types, volcanic landforms and erupted compositions. It includes the site of one of the largest (VEI 6+) Holocene explosive eruptions in the Andes, which occurred approximately 4.2 ka BP from the Cerro Blanco volcanic complex (26.8°S/67.7°W) (Báez et al., 2015; Fernández-Turiel et al., 2019; Báez et al., 2020a; de Silva et al., 2022), whereas the only confirmed historical (i.e., post ~1750 AD) eruptions in this arc segment occurred at Láscar (23.4°S/67.7°W), with the largest event (VEI of 3-4) in April 1993 (Gardeweg and Medina, 1994). However, much of the volcanic history of this area remains poorly constrained, even though many morphologically young volcanic features can be recognized throughout the region and several of these are considered potentially active (de Silva and Francis, 1991; González-Ferrán, 1995).

Here, we merge the MatHaz tool of Bertin et al. (2019) with a new volcanic geospatial database (Bertin et al., 2022) to generate the first probabilistic volcanic hazard assessment for the ~22.5–28°S segment of the Central Volcanic Zone of the Andes. MatHaz is an open-source computer code that performs an integrated probabilistic volcanic hazard assessment in regions characterized by distributed volcanism, whereas the Bertin et al. (2022) database collates, for the study area, all available late Cenozoic (<36 Ma) information on volcano types, vent locations, eruptive volumes and eruption ages. By integrating these two resources, we identify the most likely regions to host future volcanic activity, and delineate areas likely to be affected by pyroclastic density currents, ballistic projectiles, lava flows, debris flows, and tephra fallout. In doing so we are able to recognize, for the first time, order-of-magnitude variations in volcanic hazards across the region. After integrating these results into a single hazard map, we evaluate the relative volcanic hazard for all the settlements of the region. Overall, we hope the approach and results from our study will provide a guide for more targeted hazard and risk assessments in the future.

TECTONIC SETTING OF THE ~22.5–28°S SEGMENT

The ~22.5–28 S segment of the western margin of South America is part of the Central Volcanic Zone (CVZ) of the Central Andes

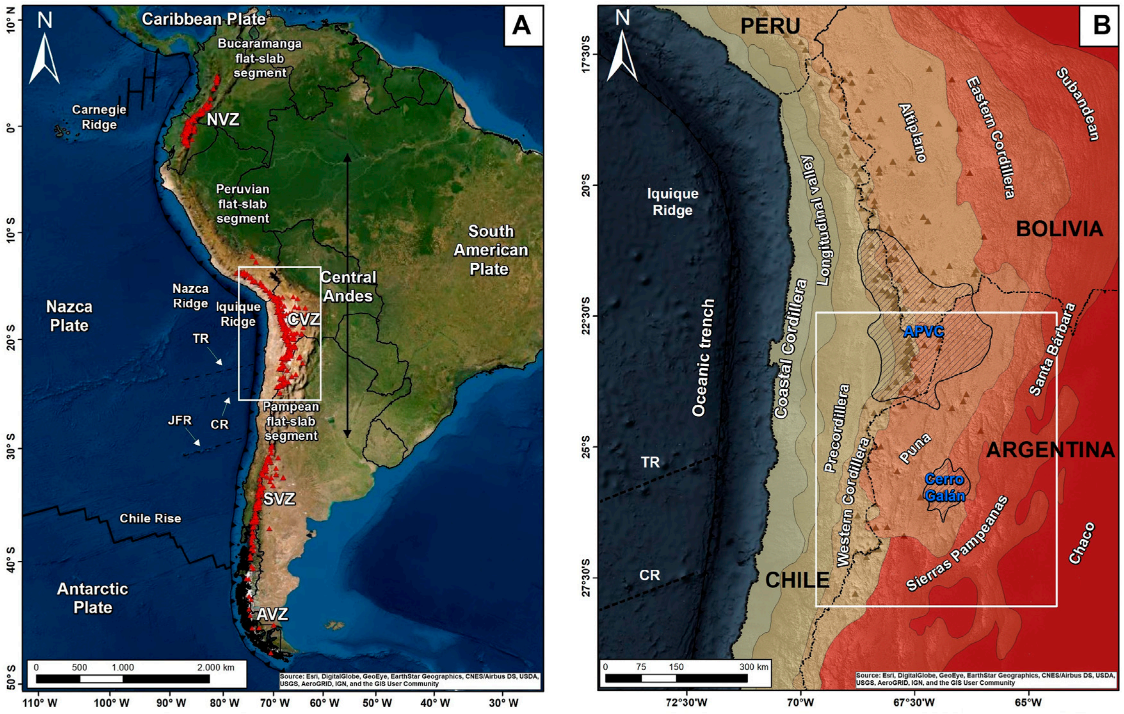

FIGURE 1 | (A) Location map of the Central Andes, showing the main tectonic elements. JFR = Juan Fernández, TR = Taltal, and CR = Copiapó ridges. NVZ = Northern Volcanic Zone, CVZ = Central Volcanic Zone, SVZ = Southern Volcanic Zone, and AVZ = Austral Volcanic Zone, according to Stern et al. (2007). **(B)** Main tectonomorphic regions of the Central Andes. White rectangle in **(B)** indicates our study area. Red triangles in **(A)** and grey triangles in **(B)** correspond to the Neogene-Quaternary volcanoes according to Siebert et al. (2010). The black striped regions in **(B)** show the Altiplano-Puna Volcanic Complex (APVC; de Silva, 1989) and the Cerro Galán (Kay et al., 2011) ignimbrite provinces.

(e.g., Stern et al., 2007) (**Figure 1A**). The Central Andes is an orogenic belt located between ~5 and −33°S that includes the CVZ and two flat slab segments (Peruvian to the north and Pampean to the south). The CVZ spans between ~13 and −28°S, and includes active and potentially active volcanoes of southern Peru, northern Chile, western Bolivia and northwestern Argentina. Volcanism in this region can be traced as far back as the Early Jurassic (190–180 Ma) (e.g., Parada et al., 2007; Ramos, 2009). Volcanic activity was semi-continuous since then, and its front migrated inland from the Coastal Cordillera (Early Jurassic-Late Cretaceous arc) to the Precordillera (Late Cretaceous-Paleogene arc), and then to the Western Cordillera (Neogene-Quaternary arc) (e.g., James and Sacks, 1999; Haschke et al., 2002; Charrier et al., 2007; Hoke and Lamb, 2007) (**Figure 1B**). During the middle Miocene, volcanic activity broadened to the east across much of the Altiplano-Puna (a hinterland plateau), and then progressively retreated back to the Western Cordillera during the upper Miocene and Pliocene (e.g., Coira et al., 1993; Allmendinger et al., 1997; Trumbull et al., 2006; Kay and Coira, 2009; Guzmán et al., 2014).

The magmatic broadening and narrowing event has been linked to a transient shallowing of the subduction zone due to the passage of the Juan Fernández Ridge (e.g., Trumbull et al., 2006; Kay and Coira, 2009; Freymuth et al., 2015; de Silva and Kay, 2018). This ridge, along with the Taltal and Copiapó oceanic ridges, earlier caused a flat slab event that affected a large segment of the Central Andean margin centred at ~18–20°S during the Eocene-Oligocene (45–25 Ma) (James and Sacks, 1999; O'Driscoll et al., 2012; Bello-González et al., 2018; Martinod et al., 2020). The passage of the Juan Fernández Ridge was followed 5–10 Myr later by a period of large-volume volcanism (e.g., Kay and Coira, 2009; Kay et al., 2010; Beck et al., 2015; Freymuth et al., 2015; Brandmeier and Wörner, 2016), which resulted in the Central Andean Neogene Ignimbrite Province (Kay et al., 2010; de Silva and Kay, 2018). In particular, the Altiplano-Puna Volcanic Complex (APVC; de Silva, 1989) and Cerro Galán (Kay et al., 2011) ignimbrite provinces are prominent foci in the study area (**Figure 1B**). The first-order correlation between the passage of the Juan Fernández Ridge and large-volume volcanism has given rise to the proposal that the southernmost segment of the CVZ (i.e., around ~27–28°S) has the potential to host a magmatic flare-up in the future (e.g., Kay and Coira, 2009; Beck et al., 2015; Ward et al., 2017). In addition, along with the arc broadening and narrowing, back-arc mafic magmatism also occurred in this region in response to lithospheric foundering events (e.g., Kay et al., 1994; Risse et al., 2013; Mulcahy et al., 2014; Maro et al., 2017; Chen et al., 2020; Gao et al., 2021). Collectively, volcanism has been controlled by a range of varying tectonic processes (e.g., Tibaldi et al., 2017; Naranjo et al., 2018; Morfulis et al., 2020).

Currently, Láscar is the most active volcano in this segment of the CVZ (**Figure 2**), with 34 eruptions recorded between 1848

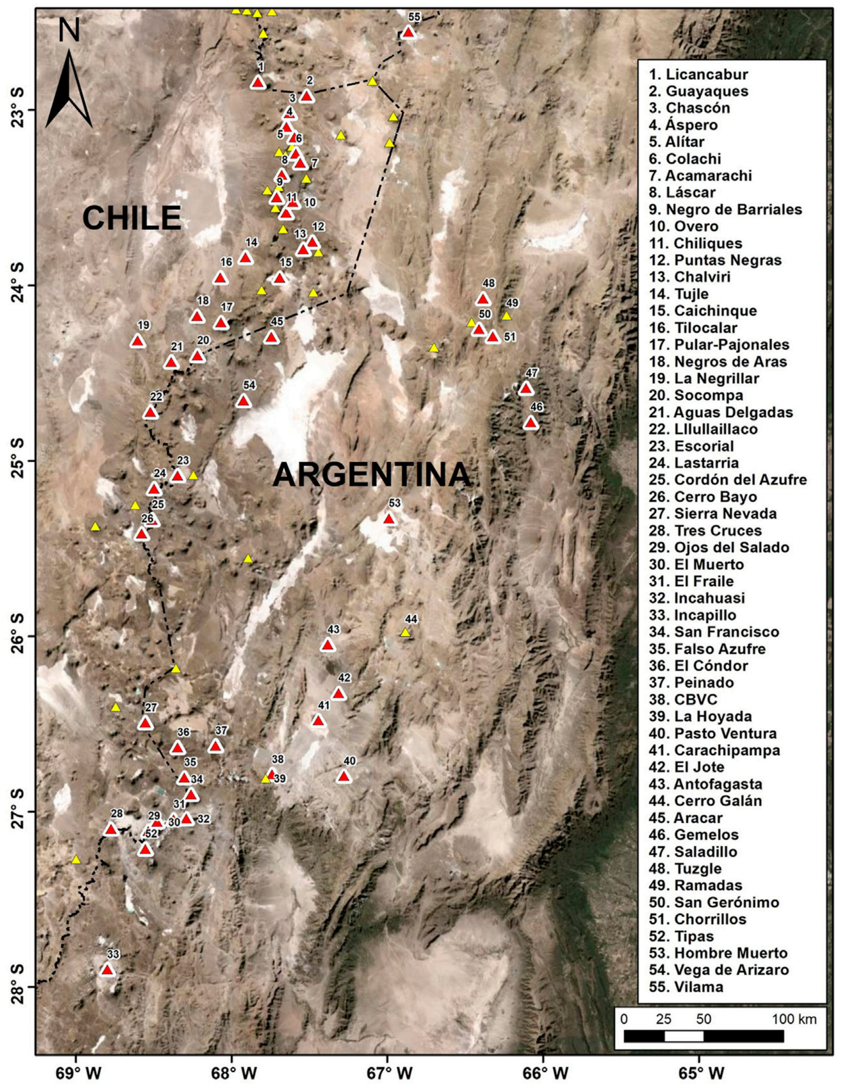

FIGURE 2 | The Central Volcanic Zone of the Andes of Chile and Argentina (~22.5–28°S). Yellow and red triangles correspond to the Plio-Pleistocene and Pleistocene-Holocene volcanoes in the region, respectively, modified from Siebert et al. (2010). Minor monogenetic fields/centres have been included as well. All the volcanoes of interest are labelled. CBVC = Cerro Blanco volcanic complex.

and October 2015 (Casertano, 1963; González-Ferrán, 1995; Petit-Breuilh, 2004; Global Volcanism Program, 2016). Láscar has also produced the only VEI 3-4 eruption in this arc segment in the historical record (i.e., since ~1750 AD), in April 1993. Other volcanoes with unconfirmed historical eruptions include (**Figure 2**): Llullaillaco, with seven events between 1854 and 1960 (Casertano, 1963; Petit-Breuilh, 2004); Aracar, with one event in March 1993 (Global Volcanism Program, 1993a); and Ojos del Salado, with one event in November 1993 (Global Volcanism Program, 1993b). Four volcanoes host long-term active fumarolic activity: Alítar, Láscar, Lastarria, and Ojos del Salado (de Silva and Francis, 1991; González-Ferrán, 1995), four are actively deforming: Lastarria, Cordón del Azufre, Cerro Bayo, and Cerro Blanco (Pritchard and Simons, 2002; Henderson and Pritchard, 2013), and nine have shown thermal anomalies detected by infrared satellite imagery: Licancabur, Alítar, Láscar, Chiliques, Púlar-Pajonales, Lastarria, Sierra Nevada, Falso Azufre, and Ojos del Salado (Jay et al., 2013). Only two of these volcanoes, Láscar and Lastarria, are currently actively monitored (Amigo, 2021; Aguilera et al., 2022).

Eruption histories of only a few volcanoes in the region have been comprehensively studied (e.g., Richards and Villeneuve, 2001; Richards et al., 2006; Naranjo, 2010; Gardeweg et al., 2011; Norini et al., 2014; Grosse et al., 2018, Grosse et al., 2022; Bustos et al., 2019); overall, they reveal a rich history of activity ranging in type (from effusive to explosive), volume (from $<10^{-3}$ to 10 s of km^3 of magma), and composition (from basaltic andesites to rhyolites). Specific vents at Láscar, Lastarria, and Cerro Blanco have been thoroughly studied and are known to pose high hazard (Perucca and Moreiras, 2009; Amigo et al., 2012;

Gardeweg and Amigo, 2015; Elissondo et al., 2016). However, these vents are a small fraction of the hundreds of youthful-looking existing vents in the area. The lack of detailed information on these other vents has hindered systematic regional hazard assessment. Recent studies have just begun to assess specific hazards in this area, including: pyroclastic density currents (Cerro Blanco; Báez et al., 2020a; Báez et al., 2020b), ballistic projectiles (Láscar; Bertin, 2017), lava flows (Chorrillos and San Gerónimo; Fernández-Turiel et al., 2021), debris flows (Lastarria; Rodríguez et al., 2020), and tephra fallout (Cerro Blanco; Fernández-Turiel et al., 2019). Building on this, a regional perspective on volcanic hazards is needed in order to identify which volcanic regions are most likely to become active in the future, which areas will be affected the most by future volcanic activity, and to motivate additional studies to better understand hazards at more detailed scales. The regional hazard assessment presented here is based on a comprehensive volcanic database and simplified tools for modeling volcanic hazards.

METHODS

Volcanic hazard assessments for specific segments of the CVZ (Perucca and Moreiras, 2009; Amigo et al., 2012; Ayala, 2014; Macedo et al., 2016) have typically analysed each volcano independently and conditional upon an eruption occurring. However, this approach is best suited for comparison of a handful of volcanoes. If hundreds of volcanic centres are analysed, as it is the case here, different approaches and methods are needed to take spatial and temporal variations in hazard into account. On the broadest scale, different techniques have been developed to forecast the location and timing of future volcanic activity in arc segments (e.g., Martin et al., 2004; Jaquet et al., 2012; Germa et al., 2013; Jaquet et al., 2017; Kósik et al., 2020; O'Hara et al., 2020). Of these, the approach of Martin et al. (2004) is particularly useful for the purposes of our application as it performs an estimation of the spatio-temporal hazard by modeling each volcanic vent as monogenetic or polygenetic. Hence, following the Martin et al. (2004) approach, we classified the volcanic vents within our study area (vents extracted from the Bertin et al., 2022 database) according to their categories (Németh and Kereszturi, 2015): monogenetic (single event in unique site), transitional-polycyclic (multiple events but each with a unique magma driver), or polygenetic (multiple events driven by a long-lived magmatic feeding system), based on the amount and type of different volcanic phenomena sourced from each vent (see **Supplementary Table S1** for the criteria followed). We concentrated our analysis on the last 36 Myr, postdating the latest major magmatic migration of the arc.

The Bertin et al. (2022) database lists 2,950 volcanic vents and 2,057 volcanic deposits (e.g., ignimbrite sheets, lava flows). For simplicity, to estimate vents for those volcanic deposits without an evident source location, 479 additional vents were mapped at the geometric centres of the deposits; thus 3,429 vents were identified in total (1,825 monogenetic, 133 transitional-polycyclic, 1,471 polygenetic). For every volcanic vent, maximum and minimum ages (expressed as a mean and two standard deviations) were assigned based on the radiometric ages of its associated volcanic deposits. For volcanic deposits lacking radiometric ages, estimations were conducted based on the ages of the adjoining deposits with a clear stratigraphic relationship. If this was not possible, a broad estimate was made based on the ages of all neighbouring deposits with similar geomorphic preservation. The volcanic vents layer thus created is available in geospatial vector data format in **Supplementary Material S1**.

From Vents to Events

A major challenge in volcano science is to unravel the eruptive histories of volcanoes from the geologic record (e.g., Damaschke et al., 2018; Lerner et al., 2019; Pure et al., 2020). On an arc-scale, we cannot hope, at least at this point in time, to successfully integrate the volcanic histories of hundreds of volcanoes. Therefore, here we estimate the average number of volcanic events per vent type over a fixed time interval assuming a fixed erupted volume.

An additional hindrance is that, even for 'monogenetic' vents, it is not certain that each volcanic vent represents a single eruptive episode (Runge et al., 2014; Báez et al., 2016; Bevilacqua et al., 2017; Connor et al., 2018; Gallant et al., 2021). This uncertainty, along with the likely presence of buried and eroded vents, can be examined through statistical (Runge et al., 2014), morphometric (Nieto-Torres and Martin Del Pozzo, 2019), and spatio-temporal clustering (Gallant et al., 2021) techniques. However, due to the large study area and the availability of age and volume information in the Bertin et al. (2022) database (each volcanic deposit includes an age and volume range), here we followed an alternative approach. For each volcanic deposit within the database (excluding voluminous ignimbrites), a specific volume was estimated from the known volume ranges assuming a uniform distribution. These volumes were summed to obtain a total erupted volume. Using a Monte Carlo approach, the volume estimations were repeated 10^6 times, constraining the total volume of the arc segment to be between 15,800 and 16,400 km^3. This volume range was then used to forecast the total number of volcanic events assuming the following: 1) age ranges were calculated for each vent by sampling their maximum and minimum ages; 2) every volcanic event had a volume of 0.1 km^3, which is the total dense rock equivalent (DRE) volume calculated for the Láscar 1993 eruption (Calder et al., 2000; Gardeweg et al., 2011); and 3) a fixed time interval of 10 kyr from 36 Ma to present (i.e., 3,600 time bins), deemed here as a sensible partition to evaluate event recurrence rates in detail without dramatically losing computational efficiency. Monogenetic vents were assumed to have only one eruption, polycyclic vents were assumed to have one eruption every 10 kyr, and polygenetic eruption rates were unknown. Hence, we estimated the polygenetic eruption rate by trial and error. That is, we started with an arbitrary polygenetic eruption rate and calculated the total number of events 10^4 times. When the mean of the total number of events, multiplied by 0.1 km^3, was within the range 15,800–16,400 km^3, then we kept that polygenetic eruption rate and repeated the exercise with a slightly different eruption rate until the whole volume range was covered. The code used to perform these calculations is available in **Supplementary Material S2**.

The results indicate a rate of 0.4433 (−0.0078/+0.0081) events per 10 kyr per polygenetic vent. This means that for all post-10 ka potentially active vents (137), an estimated 45.77 (−1.41/+1.35) events occurred, i.e., a 218 (−6/+7) year interval between 0.1 km^3 DRE events, a reasonable result taking into account that since AD ~1750, only one 0.1 km^3 eruption has been recorded in the region. The values obtained above, however, change when other event volumes are considered. This issue, and how it can influence the hazard analysis, is further addressed in the discussion.

Topographic Data

In order to provide a topographic digital base onto which conduct the hazard simulations, we compiled 135 ASTER GDEM v3 files (Advanced Spaceborne Thermal Emission and Reflection Digital Elevation Model; https://search.earthdata.nasa.gov). Each square degree tile has an average spatial resolution of ~30 m and a vertical accuracy of 7–14 m (Talchabhadel et al., 2021). Using Global Mapper v18 (https://www.bluemarblegeo.com/global-mapper/), we clipped out the region inside 22–30°S/70–64°W and reduced the spatial resolution to 1,000 m in order to generate a manageable file (<10 Mb). This pixel size was used to adjust the coordinates of each vent to make them compatible with the grid. Finally, the topography was exported as an Excel file (**Supplementary Material S3**) to be loaded in MatHaz.

Spatial and Temporal Volcanic Hazard Assessments

MatHaz provides a semi-automated probabilistic volcanic hazard assessment in regions characterized by distributed volcanism (**Supplementary Material S7**). The spatial analysis was conducted using an elliptical bivariate Gaussian kernel function, which transforms the point location of every volcanic event into a 2D probability density function (e.g., Connor et al., 2018). Elliptical kernels are well suited to situations where tectonism exerts a strong control on volcanism (e.g., rift settings or arcs) (e.g., Connor et al., 2018; Bertin et al., 2019). To obtain the dominant ellipse axes and orientations, the bandwidth matrices have to be calculated first (e.g., Connor et al., 2018). Amongst the many methods to estimate a bandwidth matrix, the $\hat{H}_{PI,AMSE}$ selector (PI: plug-in; AMSE: asymptotic mean squared error) was used in this case study due to its fast convergence to an optimal bandwidth (see Duong, 2005; Bertin et al., 2019). The influence of other bandwidth selectors on the kernel are addressed in the *Discussion* section.

MatHaz generates as many probability density functions as volcanic events, and groups them according to their age into different time bins. Here 36 time bins of 1 Myr each, spanning the range 36 Ma to Present, were defined in order to optimize simulation times. This required calculating the cumulative number of events per vent type for as long the vent was active with the restriction that no extra eruptions were added if the activity lasted more than 1 Myr. Thus, a rate of 44.33 (+0.78/−0.81) events per 1 Myr per polygenetic vent was obtained after extrapolating the eruption rates calculated above (see *From Vents to Events*). Similarly, a rate of 25.17 (−0.57/+0.56) events per 1 Myr was calculated for each polycyclic vent, and monogenetic vents were assigned a single event each. Finally, each vent was assigned to the time bin(s) representative of its period of activity (**Supplementary Material S4**).

For the temporal analysis it was assumed that future events will have a volume of 0.1 km^3, with a mean recurrence rate of 45.77 events/10 kyr (see *From Vents to Events*). Spatial and temporal data were assumed to be independent (e.g., Connor et al., 2013), so multiplying them together was used to obtain the spatio-temporal matrix. The spatio-temporal probability at present was calculated based on the last 36 Myr record of volcanic activity following an age-weighting procedure using an exponentially decreasing function, with higher (lower) weights assigned to younger (older) volcanoes (for example, 10 Myr-old-vents contribute ~$4{\cdot}10^{-5}$ whereas 20 Myr-old-vents contribute ~$2{\cdot}10^{-9}$ to the final spatial density map; see **Supplementary Material S7** for a detailed explanation on this). The probability of at least one volcanic event within a specific area (in km^2) for a specific forecasting time interval (in years) was obtained by integrating the spatio-temporal matrix over a finite region. In order to work with a cumulative probability as close to 1 as possible (that is, at least one volcanic eruption is expected in the time interval of interest), a period of 10,000 years was deemed as a suitable forecasting time interval. Such a long time interval also eliminates the differences that arise when other event volumes are considered. This is further addressed in the *Discussion* section.

Volcanic Hazards

The most relevant volcanic hazards in the study area are: pyroclastic density currents, ballistics, lava flows (including lava domes), debris flows, and tephra fallout. The near-vent environment, with hazards associated with vent opening, short-lived phreatic explosions and toxic gas emissions, which are extremely difficult to model, are expected to be included in the ballistic ejecta zone, deemed here as an approximation of the proximal hazard zone. We did not model debris avalanches because it is unclear whether the debris avalanche deposits exposed in the study area were generated during an eruption or not (e.g., van Wyk de Vries et al., 2001; Norini et al., 2020; Rodríguez et al., 2020).

MatHaz uses an energy cone model for pyroclastic density currents (Malin and Sheridan, 1982), a two-dimensional analytical model for ballistic projectiles (Bertin, 2017), a flow inundation model for lava flows and debris flows (Connor et al., 2012), and a two-segment linear approximation for tephra fallout (Fierstein and Nathenson, 1992) (see **Supplementary Material S7** for in-depth explanations about each technique). The input parameters of each model (e.g., volumes, thicknesses) were extracted from the Bertin et al. (2022) database and modeled as normal, lognormal or uniform distributions (**Supplementary Figures S1–S5**). The input parameters of each simulation were randomly sampled from these distributions. We ran simulations for as many different source locations as possible, which were convolved with the probabilities of a new eruption at those source

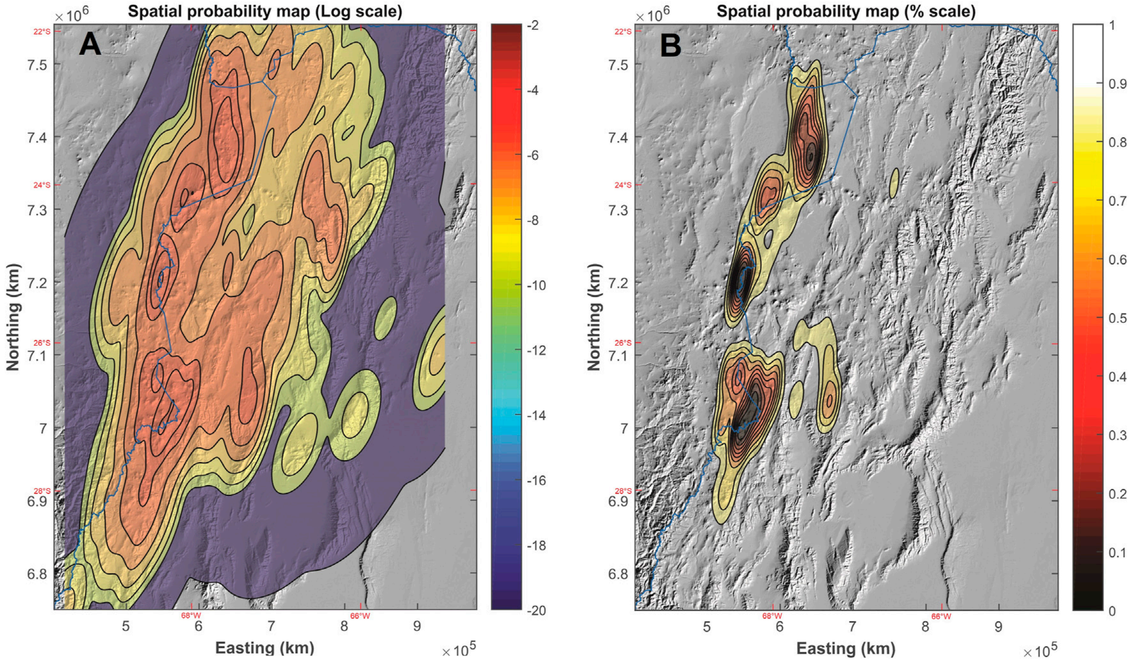

FIGURE 3 | Spatial probability maps of volcanic activity for our study area: **(A)** Raw probabilities. Probability density functions were obtained after applying the kernel density estimation method and are shown as probability isocontours on a logarithmic scale to illustrate order-of-magnitude changes. **(B)** Cumulative probabilities. Given a volcanic event, there is a 50% chance it will occur within the area defined by the 0.5 isocontour. The locations of the five clusters defined in this work are indicated. Main coordinate grid is in UTM units (zone 19 S) as MatHaz works in a plane coordinate grid system. Legend units are events/km^2. The political border between Chile, Argentina and Bolivia is depicted for reference (blue line). ASTER Digital elevation model used as a background image follows a greyscale colour scheme: the whiter the pixel, the higher the elevation.

locations within the time interval of interest (cf. Bertin et al., 2019). Results were then summed and normalized to obtain the probabilistic zoning for each volcanic hazard. We repeated this exercise ten times for each volcanic hazard to compare the outputs for the same inputs, and found that probabilities above ~5×10^{-5} can be confidently defined (**Supplementary Figures S6–S9**). Finally, we combined the five modeling results into a single map (cf. Javidan et al., 2021) with an even weighting for each volcanic hazard. The choice of equal weighting was made in the absence of additional evidence to define specific relative weights for the different volcanic phenomena considered in our case study, although the interested reader can assign other weights (e.g., based on expert knowledge) using the files provided in **Supplementary Material S5**. The limitations of the code are addressed in the *Discussion* section.

RESULTS

Spatial Analysis

Considering the 10^{-6} (events/km^2) probability isocontour as a conservative boundary of volcanism at any time, most of the volcanic activity in the region is represented by a well-defined magmatic arc and small zones of back-arc activity (**Figure 3A**). In addition, we delineate five regions of relatively high spatial probability of future volcanic activity (above 10^{-5} events/km^2), named here as clusters, which can be more clearly recognized if the spatial probabilities are shown following a cumulative scale (**Figure 3B**). These regions are:

1) Láscar cluster is N-S oriented and includes the Láscar, Colachi, Acamarachi, Chiliques, and Caichinque stratovolcanoes, the Alítar maar, the Chascón and Áspero domes, and the Chalviri and Puntas Negras volcanic chains.
2) Socompa cluster is roughly circular and includes the Socompa stratovolcano, the Púlar-Pajonales volcanic complex, and numerous distributed lava flows and cinder cones around Socompa, such as Negros de Aras/El Negrillar and Aguas Delgadas.
3) Lazufre cluster is elliptical with a NNE-SSW axis, and includes the Lastarria, Cordón del Azufre, and Cerro Bayo stratovolcanoes.
4) Incahuasi cluster is the largest of the five and includes several stratovolcanoes and volcanic complexes that straddle the Chile-Argentina border at around ~27°S, such as Ojos del Salado, Tres Cruces, El Muerto, El Fraile, Tipas, Incahuasi, Falso Azufre, Sierra Nevada, El Cóndor, and Peinado.
5) The Antofagasta cluster is the most diffuse and the only one located in the back-arc. It includes the Cerro Blanco volcanic complex and several monogenetic mafic centres and isolated

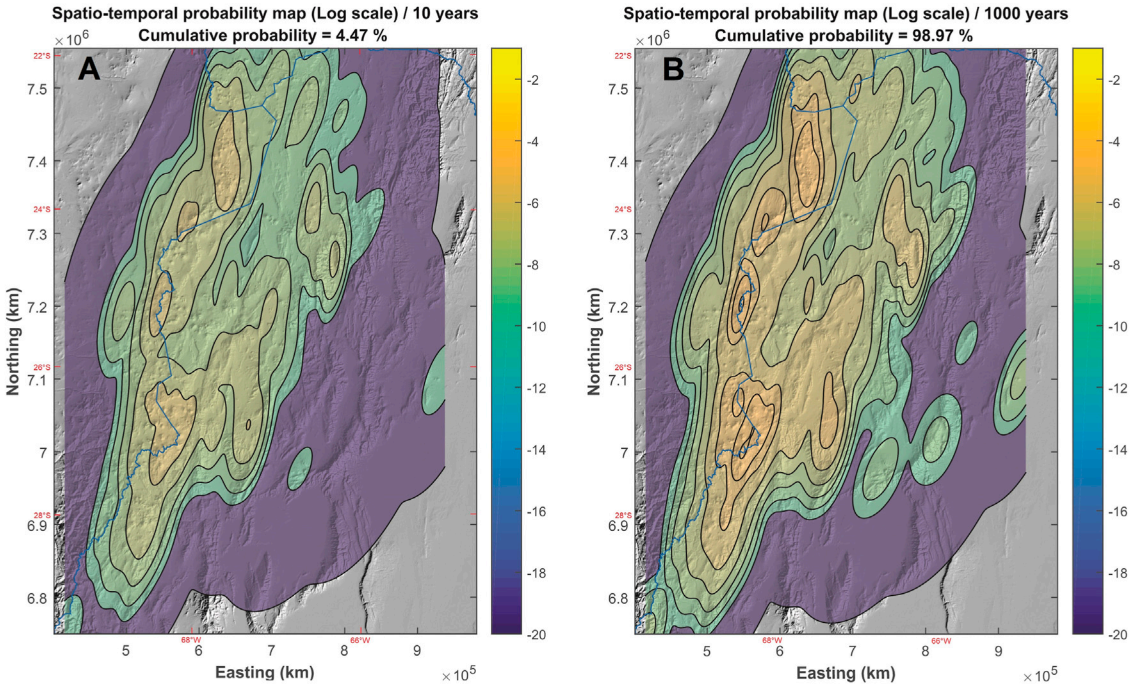

FIGURE 4 | Spatio-temporal probability maps of future volcanic activity for our study area at different forecasting time intervals. Probabilities were obtained after multiplying the spatial probability map shown in **Figure 3A** by the event recurrence rate (45.77 events per 10 kyr) modeled as a homogeneous Poisson point process, and are shown as probability isocontours on a logarithmic scale to illustrate order-of-magnitude changes. Above each plot we include the cumulative probabilities of occurrence of at least one Láscar 1993-like (i.e., 0.1 km^3) eruption for the next: **(A)** 10 years, and **(B)** 1,000 years, with 1993 taken as 'year zero'. Legend units are events/time interval/km^2. The political border between Chile, Argentina and Bolivia is depicted for reference (blue line). ASTER Digital elevation model used as a background image follows a greyscale colour scheme: the whiter the pixel, the higher the elevation.

lava flows, such as Carachipampa, Pasto Ventura, and those in the Antofagasta de la Sierra region.

Spatio-Temporal Analysis

Two spatio-temporal probability maps, generated for time intervals of 10 and 1,000 years (**Figures 4A,B**), show broadly similar areas of event location, with cumulative probabilities of ~5% and ~99%, respectively. The cumulative probability curve over time (**Figure 5**) indicates that a 50% probability of at least one 0.1 km^3 eruption occurring anywhere in the study area is estimated within ~150 years after the last 0.1 km^3-event. Cumulative probability curves constructed using other volumes are shown in **Supplementary Figure S14** and are further discussed in the next section.

Probabilistic Volcanic Hazard Analysis

The probabilistic hazard map for pyroclastic density currents (**Figure 6A**) was obtained by using the energy cone model to forecast runout from individual volcanoes. The shape of the probability isocontours for pyroclastic density currents generally mimics the spatial distribution of volcanism due to the simple modeling approach. The lowlands within <20–30 km from the most active volcanic regions (cf. **Figure 6F**) show the highest probabilities for pyroclastic density currents, of which the maximum (~10^{-4} pyroclastic density currents per km^2 per 10 kyr) occurs along the northern flanks of Ojos del Salado and El Muerto volcanic complexes (Incahuasi cluster). The pyroclastic density currents related to back-arc volcanic centres, such as around the Cerro Blanco volcanic complex and the Tuzgle stratovolcano, have probabilities up to 1.5 orders of magnitude lower than those estimated for the volcanic arc.

The probabilistic hazard map for ballistic projectiles (**Figure 6B**), which also encompasses the near-vent hazards, highlights the five volcanic clusters identified during the spatial analysis (cf. **Figure 6F**). In this map, probabilities rapidly decrease away from the main loci of activity, and just like the pyroclastic density currents, attain their maxima in the Incahuasi cluster. The lava flow and debris flow probabilistic hazard maps (**Figures 6C,D**, respectively) highlight the influence of topography. High probabilities for lava flows (~10^{-4} lavas per km^2 per 10 kyr) occur within depressions or valleys, usually at <5–15 km from the summits of young stratovolcanoes. Despite a similar general appearance in the figure scale, the debris flow probabilistic hazard map (**Figure 6D**) highlights twice as many small ravines and catchments compared with the lava flow map. This difference is due to the lower aspect ratio (higher dispersal) of debris flows in general, as indicated by their modeling parameters. Consequently, high probabilities for debris flows (~10^{-4} debris flows per km^2 per 10 kyr) extend up to 30–40 km from the major summits in the area. The highest probabilities for lava flows and debris flows (>10^{-4}) occur

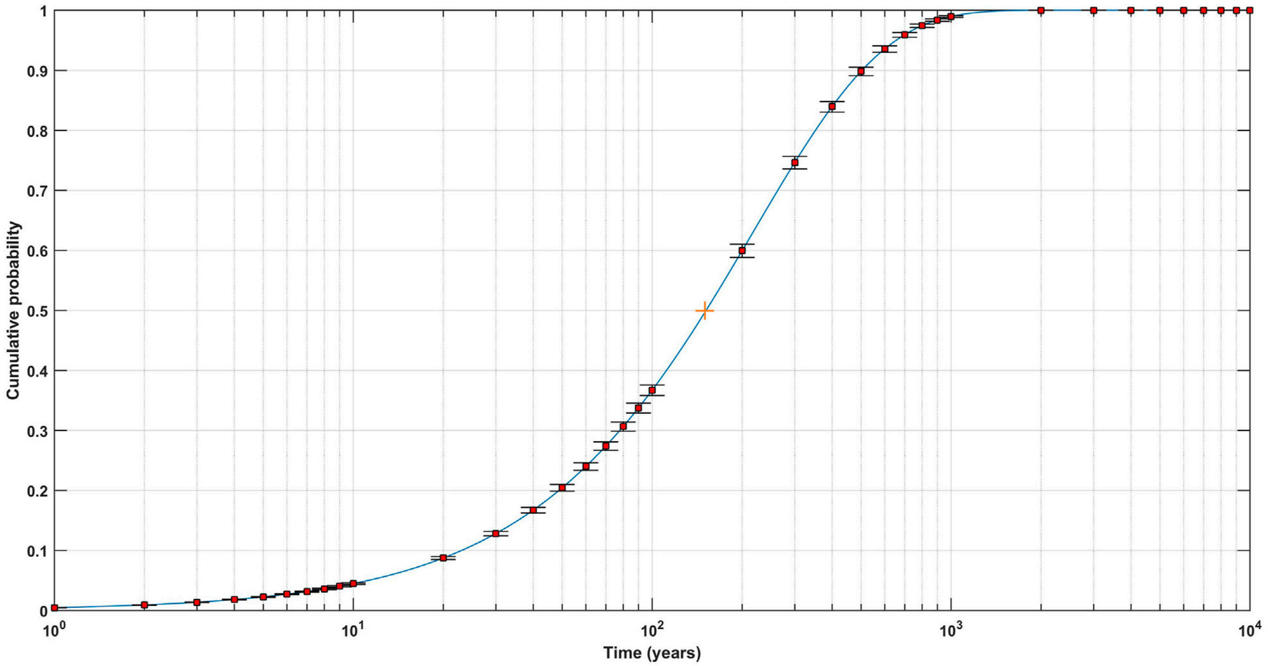

FIGURE 5 | Cumulative probability of occurrence versus forecasting time interval for a Láscar 1993-like (i.e., 0.1 km^3) eruption occurring anywhere within the study area. The curve was calculated for a mean recurrence rate of 45.77 events per 10 kyr and modelled as a homogeneous Poisson point process. Ranges of probabilities (black intervals) are illustrated at specific times (red squares) for the minimum and maximum recurrence rates calculated, which vary between 44.36 and 47.12 events per 10 kyr, respectively. Orange cross indicates the time when a cumulative probability of 50% is achieved. Another plot considering different recurrence rates is provided in **Supplementary Figure S14**.

between the Ojos del Salado and Falso Azufre volcanic complexes, and between the El Cóndor and Peinado stratovolcanoes (Incahuasi cluster). Also highlighted by this analysis are moderate probability (~10^{-5}) zones running along the main river valleys that drain the Puna plateau towards the foreland.

Tephra fallout probabilities (normalized thickness per km^2 per 10 kyr; **Figure 6E**) are greatest in the prevailing downwind areas to the east of the main volcanic vents. The individual influence of each volcanic cluster (cf. **Figure 6F**) is well defined at probabilities >10^{-5} (cumulative probability of ~50%), but they merge at probabilities <$10^{-5.5}$. The extent of the $10^{-5.5}$ probability east of the main arc clusters are due to the influence of the back-arc Antofagasta cluster, as well the Tuzgle stratovolcano and nearby monogenetic centres. The Incahuasi cluster generates the highest probabilities for tephra fallout (~$10^{-4.5}$) between the El Fraile and Falso Azufre volcanoes.

Integrated Hazard Map

Integrating the individual volcanic hazards with an even weighting (**Figure 7A**) shows that most of the late Cenozoic volcanism is included within the 10^{-7} probability isocontour (defined here as the probability that an area of 1 km^2 is impacted by any volcanic hazard in a 10 kyr time frame). This region defines an overall ~700 km-long and ~300 km-wide NNE oriented ellipse. At higher probabilities, patterns are more complex. The 10^{-6} isocontour includes most Quaternary volcanic products; that of $10^{-5.5}$ encloses most late Pleistocene-Holocene products, while all volcanic clusters are included within the 10^{-5} isocontour. The $10^{-4.7}$ isocontour defines the 50% boundary, which means that if a given volcanic phenomenon occurs somewhere, there is a 50% chance it will affect the area enclosed by that isocontour. Probabilities >10^{-4} are only found in very small regions related to the Láscar, Lazufre and Incahuasi volcanic clusters. The highest probability calculated, $10^{-3.5}$, occurs midway between the Ojos del Salado and Falso Azufre volcanic complexes, in the Incahuasi cluster.

Classifying probabilities as percentiles (**Figure 7B**; see **Supplementary Figures S10–S13** for zoomed-in excerpts that highlight each volcanic cluster), three relative hazard zones are defined: high (0%–25%; >$10^{-4.4}$), moderate (25%–50%; $10^{-4.7}$–$10^{-4.4}$), and low (50%–75%; $10^{-5.2}$–$10^{-4.7}$) hazard. This means that, for instance, in the high hazard zone, an overall 25% of the volcanic hazard occurs in areas enclosed by the $10^{-4.4}$ probability isocontour. Whilst these bins are relatively arbitrary, our choice was guided by the desire to only show three zones (rather than many); in practice the interested reader can select other divisions by using the files provided in **Supplementary Material S5**.

Coupling the Probabilistic Volcanic Hazards Assessment With Exposure Information

The integrated volcanic hazard map shown in **Figure 7A** was used to calculate the relative hazard of the 692 settlements in the region (from INDEC, 2010; INE Chile, 2017) (see **Table 1** for the

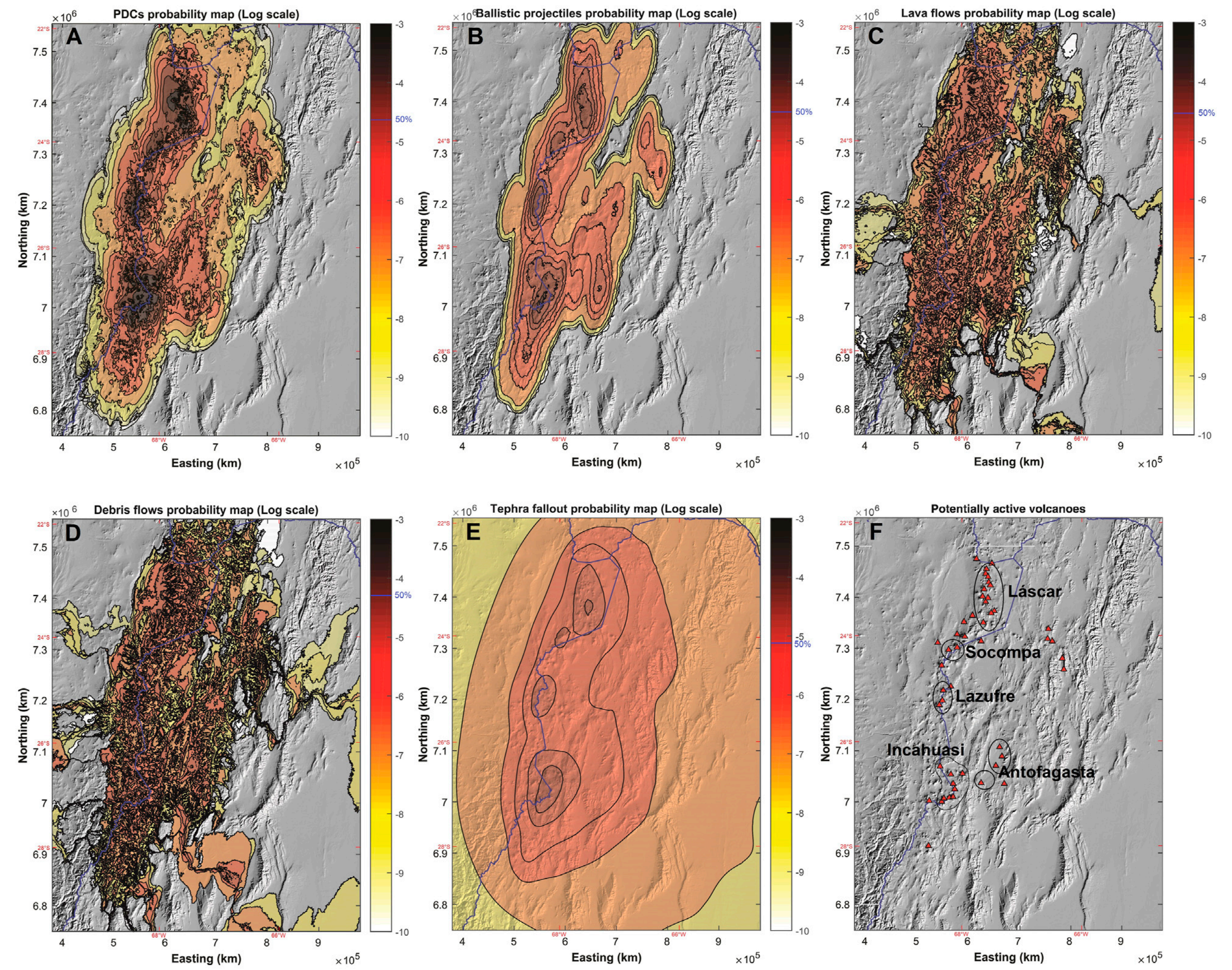

FIGURE 6 | Probabilistic volcanic hazard maps for the Central Volcanic Zone of Chile and Argentina (~22.5–28°S), obtained after empirical, semi-empirical or analytical modeling of: **(A)** Pyroclastic density currents, **(B)** Ballistic projectiles (which encompass near-vent hazards), **(C)** Lava flows, **(D)** Debris flows, and **(E)** Tephra fallout, based on the spatio-temporal probability assessment for a forecasting time interval of 10,000 years. Legend shows the probability of a 1 km^2 area be affected by a given volcanic phenomenon during the next 10 kyr, shown as probability isocontours on a logarithmic scale to illustrate order-of-magnitude changes. Light blue horizontal lines drawn in each legend depict the 50% boundary, which means that if a given volcanic phenomenon occurs somewhere, there is a 50% probability it will affect the area enclosed by that boundary. **(F)** Depicts the Pleistocene-Holocene volcanoes of **Figure 2** as well as the approximate boundary of each volcanic cluster, based on **Figure 3B**, which can be used as a spatial reference. The political border between Chile, Argentina and Bolivia is depicted for reference (blue line). ASTER Digital elevation model used as a background image follows a greyscale colour scheme: the whiter the pixel, the higher the elevation.

top 20; **Supplementary Material S6** for the complete list). Most of the 10 settlements with the highest relative hazard of being impacted by a volcanic phenomenon are small villages/hamlets, administration buildings, mountain camps or mining camps. Touristic villages Antofagasta de la Sierra, El Peñón, and La Poma, rank 14th, 15th and 18th, respectively. More populous touristic towns such as San Antonio de los Cobres, in Argentina, and San Pedro de Atacama, in Chile, rank 23rd and 62nd, respectively. The three highest ranked provincial capitals are Salta (177th), San Salvador de Jujuy (219th), and San Miguel de Tucumán (353rd), in Argentina. For Chile, the three highest ranked cities are El Salvador (357th), Diego de Almagro (433rd), and Calama (642nd). In addition, the probability of a specific location being affected by any volcanic phenomenon (calculated using the integrated volcanic hazard map shown in **Figure 7A**) can be plotted against the spatial probability of a future volcanic event occurring directly at that location (calculated using the spatial probability map shown in **Figure 3A**). **Figure 8** shows this exercise repeated for the 692 settlements in the region, using logarithmic scales on both axes to illustrate order-of-magnitude changes. Some settlements show low probabilities of hosting a volcanic event, but higher probabilities of being affected by any volcanic phenomenon (especially tephra fallout) (e.g., Tinogasta).

Results shown in **Table 1** and **Figure 8** could be useful for prioritizing hazard mitigation actions, or more detailed location-specific risk analysis, such as that of Reyes-Hardy et al. (2021)

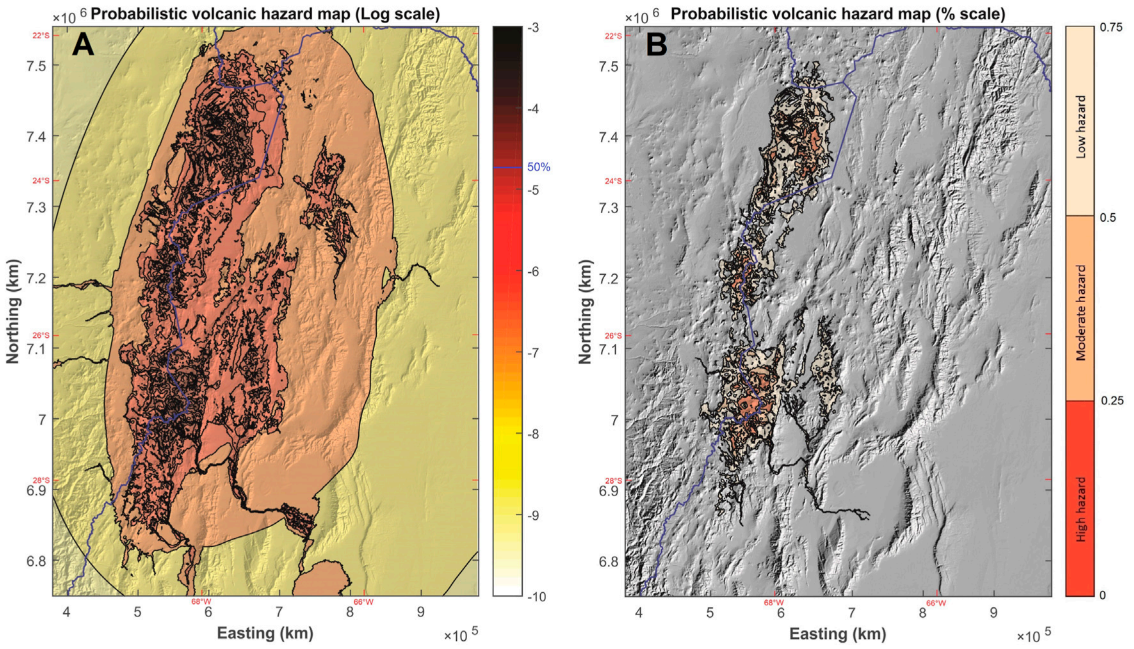

FIGURE 7 | (A) Integrated quantitative volcanic hazard map, constructed by adding each probability map (**Figures 6A–E**), weighted evenly. Legend shows the probability of a 1 km^2 area to be affected by any of the five volcanic phenomena during the next 10 kyr, shown as probability isocontours on a logarithmic scale to illustrate order-of-magnitude changes. Light blue horizontal line drawn in the legend depicts the 50% boundary, which means that if a volcanic phenomenon occurs somewhere, there is a 50% probability it will affect the area enclosed by that boundary. **(B)** Integrated volcanic hazard map, based on the results obtained in **(A)**, depicting three cumulative probability intervals: 0%–25%, 25%–50%, and 50%–75%, interpreted as relatively high, moderate, and low hazard regions, respectively. Zoomed-in excerpts highlighting some key regions are provided in **Supplementary Figures S10–S13**. The political border between Chile, Argentina and Bolivia is depicted for reference (blue line). ASTER Digital elevation model used as a background image follows a greyscale colour scheme: the whiter the pixel, the higher the elevation.

TABLE 1 | The 20 settlements most likely to be affected by any volcanic phenomenon in case an eruption occurs in the study region. For the complete list of settlements analysed, the reader is referred to **Supplementary Material S6**.

Locality	Country	Latitude (°)	Longitude (°)	Spat. Prob[a]	Haz. Prob[b]
Ojos del Salado	Chile	−26.931	−68.592	$6.1\cdot10^{-5}$	$7.5\cdot10^{-5}$
Las Grutas	Argentina	−26.911	−68.131	$9.0\cdot10^{-7}$	$5.3\cdot10^{-5}$
Talabre	Chile	−23.316	−67.886	$1.1\cdot10^{-5}$	$2.9\cdot10^{-5}$
Tilomonte	Chile	−23.793	−68.108	$3.2\cdot10^{-5}$	$2.7\cdot10^{-5}$
Socaire (village)	Chile	−23.595	−67.887	$9.5\cdot10^{-6}$	$2.2\cdot10^{-5}$
Socaire (customs office)	Chile	−23.824	−67.442	$4.6\cdot10^{-7}$	$2.1\cdot10^{-5}$
Las Papas	Argentina	−26.987	−67.782	$5.2\cdot10^{-8}$	$1.8\cdot10^{-5}$
Socompa	Chile	−24.451	−68.289	$7.5\cdot10^{-6}$	$1.8\cdot10^{-5}$
El Laco	Chile	−23.863	−67.491	$6.7\cdot10^{-7}$	$1.7\cdot10^{-5}$
Peine	Chile	−23.685	−68.058	$2.7\cdot10^{-5}$	$1.6\cdot10^{-5}$
Soncor	Chile	−23.330	−67.932	$6.4\cdot10^{-6}$	$1.5\cdot10^{-5}$
Camar	Chile	−23.405	−67.958	$6.8\cdot10^{-6}$	$1.2\cdot10^{-5}$
Punta del Agua	Argentina	−27.210	−67.731	$3.0\cdot10^{-9}$	$1.2\cdot10^{-5}$
Antofagasta de la Sierra	Argentina	−26.060	−67.406	$9.1\cdot10^{-6}$	$1.1\cdot10^{-5}$
El Peñón	Argentina	−26.478	−67.263	$1.6\cdot10^{-5}$	$1.1\cdot10^{-5}$
Toconao	Chile	−23.193	−68.006	$1.9\cdot10^{-6}$	$1.0\cdot10^{-5}$
Los Balverdi	Argentina	−28.276	−67.107	$5.6\cdot10^{-16}$	$1.0\cdot10^{-5}$
La Poma	Argentina	−24.712	−66.199	$5.7\cdot10^{-7}$	$9.6\cdot10^{-6}$
Fiambalá	Argentina	−27.656	−67.608	$1.4\cdot10^{-11}$	$9.1\cdot10^{-6}$
Medanitos	Argentina	−27.523	−67.580	$1.8\cdot10^{-10}$	$6.9\cdot10^{-6}$

[a] *Probability of a volcanic event taking place in the settlement over the next 10 kyr.*

[b] *Probability that the settlement is affected by any volcanic phenomenon over the next 10 kyr.*

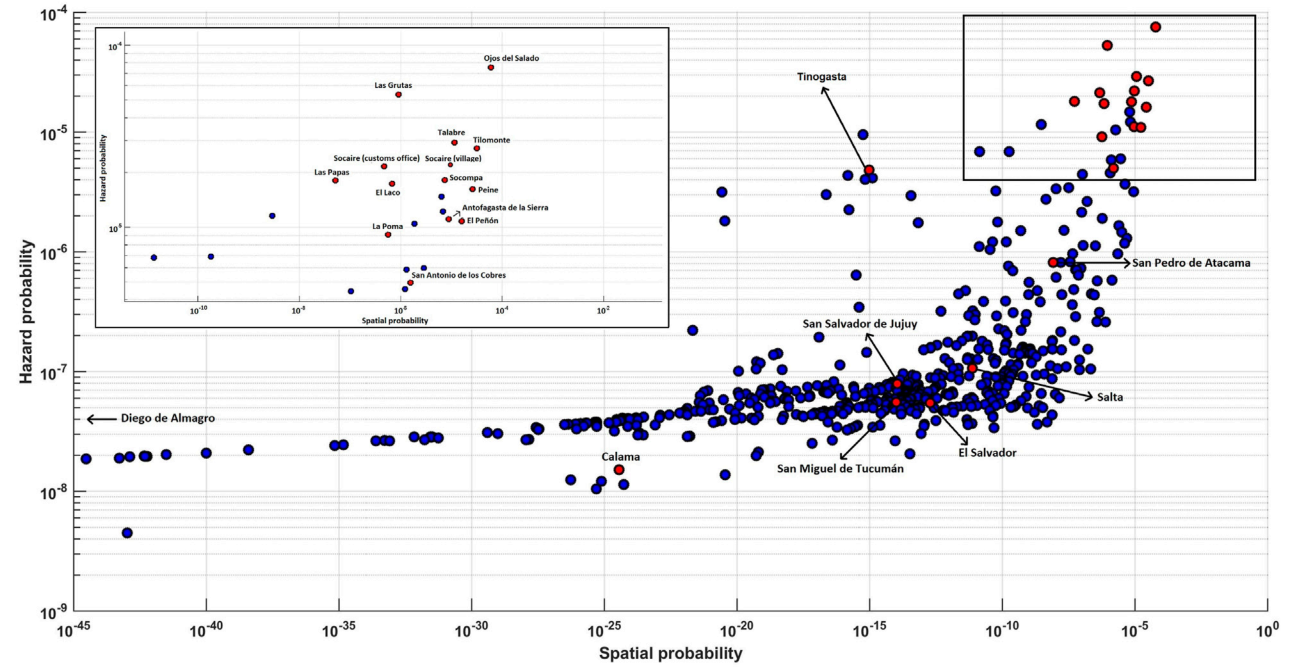

FIGURE 8 | Probability of a volcanic event occurring at any of the 692 populated sites in the study area over the next 10 kyr (calculated using the spatial probability map shown in **Figure 3A**), plotted against the probability that this same location be affected by any volcanic phenomenon over the same period (calculated using the integrated quantitative volcanic hazard map shown in **Figure 7A**). Red dots highlight the ten highest-ranked settlements listed in **Table 1** and all those mentioned in the text. The list with all the settlements can be found in **Supplementary Material S6**.

examining settlements in relation to Guallatiri volcano (18.5°S/69°W).

DISCUSSION

Volcanic Clusters, Magma Bodies and Thermal Anomalies

The volcanic clusters identified in this work can be indicative of subvolcanic processes that could lead to large-volume volcanism in the future (cf. George et al., 2016). In our study region, geophysical studies have identified large-scale crustal anomalies related to shallow (~2–10 km) partial melt bodies (Ward et al., 2013, Ward et al., 2017; Pritchard et al., 2018) (**Figure 9**). These include the Altiplano-Puna Magma Body (~21–24°S; Chmielowski et al., 1999; Ward et al., 2014; Pritchard et al., 2018), which is a ~500,000 km^3 mid-crustal body with an average 15%–22% partial melt (Schilling et al., 2006; Comeau et al., 2016; Pritchard et al., 2018; Spang et al., 2021). The Láscar volcanic cluster is located in its southern portion, also recognized by Díaz et al. (2012) using magnetotelluric data. The Láscar cluster may therefore represent a subdomain of the broader magma body with higher melt fractions. The Socompa cluster identified here lies outside the known boundaries of the Altiplano-Puna Magma Body to the south and may either represent a previously undocumented southern extension of it, or some other source anomaly such as a small zone of recent lithospheric delamination (Beck et al., 2015; DeCelles et al., 2015; Schoenbohm and Carrapa, 2015).

Further south, the Southern Puna Magma Body (~25–27.5°S; Bianchi et al., 2013) comprises at least four separate mid-to-upper crustal magma bodies: Lazufre, Incahuasi, Cerro Galán, and Incapillo-Bonete (**Figure 9**), with a cumulative volume of ~90,000 km^3 (Delph et al., 2017, Delph et al., 2021; Ward et al., 2017). The Lazufre and Incahuasi volcanic clusters overlap with the eponymous magma bodies, although the latter volcanic cluster is much larger than the magma body identified. The Incapillo-Bonete and Cerro Galán magma bodies do not appear to be linked to volcanic clusters. The Cerro Galán magma body is related to the eponymous caldera, which records at least ~4 Myr of ignimbrite-forming eruptions (Folkes et al., 2011; Kay et al., 2011), yet there has been no late Pleistocene-Holocene volcanic activity at this centre. The Incapillo-Bonete magma body is deeper than the others (~30–50 km; Goss et al., 2011; Ward et al., 2017) and may need to grow or rise before large-volume volcanism starts. The Antofagasta volcanic cluster identified here is, apparently, not associated with a previously defined magma body nor mid-to-upper crustal region of partial melt (Ward et al., 2017), although it is an actively deforming region, hosting the only known active caldera in the CVZ (Cerro Blanco) (Pritchard and Simons, 2002; Henderson and Pritchard, 2013; Vélez et al., 2021; de Silva et al., 2022).

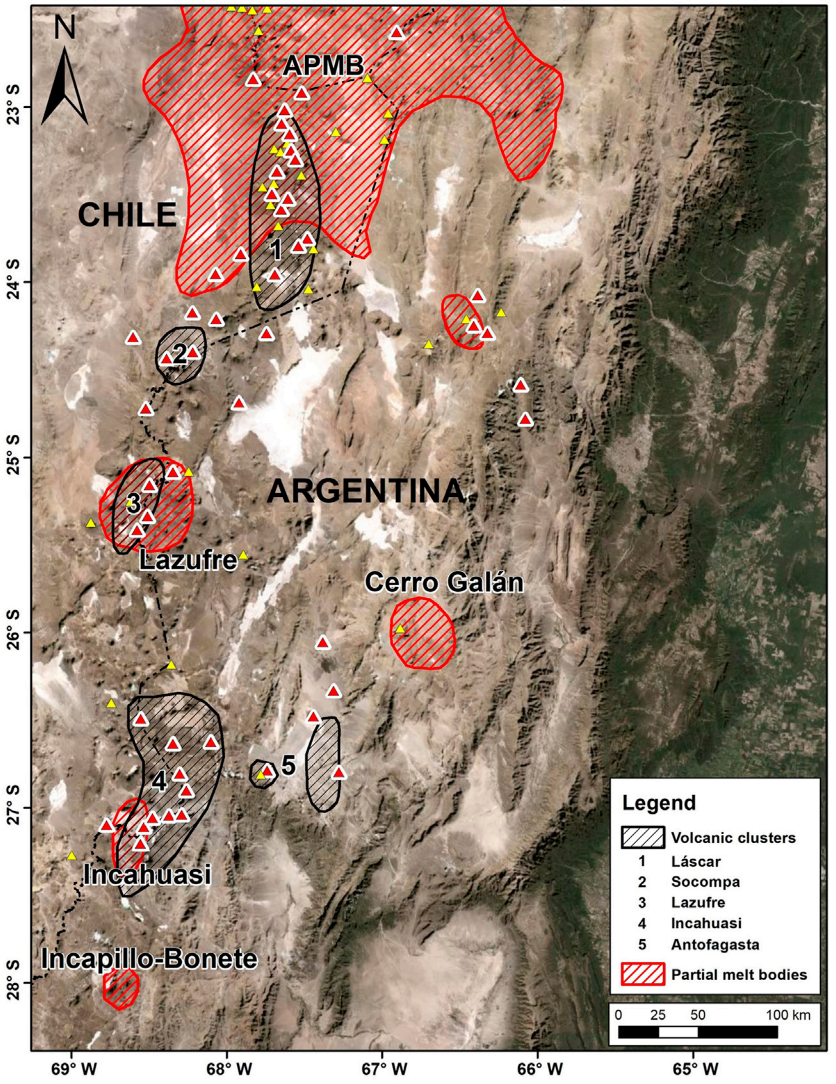

FIGURE 9 | The approximate extent of the five clusters identified in this work (black striped regions, based on the 0.6 probability isocontours from **Figure 3B**), along with the mid-to-upper crustal partial melt bodies identified in the region by Ward et al. (2017) (red striped labelled regions; APMB: Altiplano-Puna Magmatic Body). Yellow and red triangles correspond to the Plio-Pleistocene and Pleistocene-Holocene volcanoes in the region, respectively, modified from Siebert et al. (2010). Minor monogenetic fields/centres have been included as well.

Surface thermal anomalies have been detected through infrared satellite imagery at nine volcanoes: Licancabur, Alítar, Láscar, Chiliques, Púlar-Pajonales, Lastarria, Sierra Nevada, Falso Azufre, and Ojos del Salado (Jay et al., 2013). Of these, all but Licancabur are either on or near the edges of the volcanic clusters identified here, and four of them (Alítar, Láscar, Lastarria and Ojos del Salado) host permanent fumarolic activity. Volcanoes analysed by Jay et al. (2013), however, were only those selected from the Siebert and Simkin (2002-2010) catalogue, thus some volcanoes with the potential for thermal anomalies (i.e., with crater lakes and/or sulphur deposits) were not analysed (e.g., Chalviri, Tres Cruces, Cerro Blanco, El Fraile, El Muerto). Some of those volcanoes should be the focus of future field studies as they lie within the clusters identified here.

Arc vs. Back-Arc Distinction

In the Puna plateau, there was a kinematic shift from compression to strike-slip and minor extension at 12–10 Ma (Marrett et al., 1994; Schoenbohm and Strecker, 2009; Daxberger and Riller, 2015). The oldest back-arc mafic lavas in this region to have erupted since this shift have been dated at ~7.3 Ma (Risse et al., 2008) (although other undated lavas might be older), whereas the youngest ones are some extremely well preserved lava flows and cinder cones in the Antofagasta de la Sierra region (Risse et al., 2008; Fernández-Turiel et al., 2021). Based on the spatial probability map of volcanic activity (**Figure 3A**), the current volcanic back-arc can be delineated within the $10^{-5.4}$ probability isocontour (**Figure 10**). Matching the western boundary of the back-arc with the eastern boundary

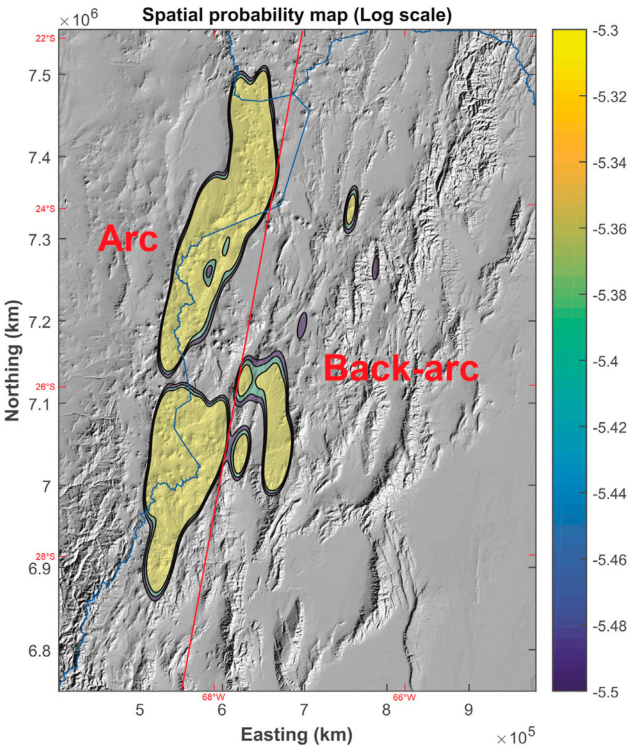

FIGURE 10 | Spatial distribution of the volcanism showing the current arc and back-arc regions. The probability isocontour $10^{-5.4}$ events/km^2 was used to define the boundary between these two regions (thick red line). Figure constructed using data from **Figure 3A**. The political border between Chile, Argentina and Bolivia is depicted for reference (blue line). ASTER Digital elevation model used as a background image follows a greyscale colour scheme: the whiter the pixel, the higher the elevation.

of the volcanic arc, these two regions can be compared to analyse their respective contributions to the volcanism by integrating the probabilities enclosed by each region. Thus, in terms of the probable locations of future volcanic activity, the arc contributes 88% and the back-arc 12%, whereas in terms of areas likely to be affected by future volcanic activity, the arc contributes 81% and the back-arc 19%. We therefore conclude that the arc is seven times more likely to host volcanic activity than the back-arc, and four times more likely to be affected by volcanic phenomena than the back-arc.

Sensitivity Analysis and Limitations of Our Study

The hazard assessment conducted in this study follows a sequential methodology that relies upon some assumptions. For instance, the estimation of volcanic events per vent type depended on the assumption of a fixed volume of 0.1 km^3 per event. Even though this volume can be deemed reasonable for the purposes of our application, considering that the large majority (>90%) of explosive volcanic eruptions in the world are of small-to-moderate size (VEIs of 0–3), and that ~20% of Holocene eruptions have VEIs of 3–4 (e.g., Siebert et al., 2010; Papale, 2018), it is necessary to test the influence of other volumes on the estimated eruption rates. We therefore tested order-of-magnitude differences in volume: 0.01 and 1 km^3. A volume of 0.01 km^3 led to a polygenetic eruption rate of 4.5855 (−0.0801/+0.0802) events per 10 kyr and an estimated 183.23 (−10.21/10.90) events for all post−10 ka active vents. For a volume of 1 km^3, the polygenetic eruption rate was 0.0315 (-0.0008/0.0008) events per 10 kyr and the eruption rate for all post-10 ka active vents was 32.06 (−0.80/+0.84) events. When the cumulative probabilities calculated from these eruption rates are projected into the future and plotted alongside the cumulative probabilities used throughout our case study (**Supplementary Figure S14**), we see that at large (>2,000 years) forecasting time intervals, all curves have attained cumulative probabilities very close to 1. Thereby, the forecasting interval of 10 kyr used during our hazard assessment can be considered as a reasonable and conservative value because the cumulative probabilities sum to near unity irrespective of the event recurrence rate.

Two main sources of uncertainty can affect the spatial probabilistic analysis (Bertin et al., 2019). The first refers to how bandwidth selectors can change the shape of the probability isocontours in the spatial probability map. Here, besides the $\hat{H}_{\mathrm{PI,AMSE}}$ selector used in our case study, we also tested the influence of two other commonly used bandwidth selectors, $\hat{H}_{\mathrm{PI,SAMSE}}$ (PI: plug-in; SAMSE: sum of asymptotic mean squared errors) and $\hat{H}_{\mathrm{SCV}}$ (SVC: smoothed cross validation) (see Duong, 2005; Bertin et al., 2019), on the spatial probability map shown in **Figure 3A**. Results (**Supplementary Figure S15**) show that the largest discrepancies are found towards the lowest probability isocontours ($<10^{-10}$ in our case), so the location and extent of the spatial clusters, which were defined at the highest probabilities, do not change when other bandwidth selectors are used. The second source of uncertainty is related to the distribution of vents into different time bins according to their modeled ages (ages sampled from normal distributions). Here we compared the distribution of vents used during our analysis to the range of distributions obtained after repeating the vent-grouping exercise 10^4 times. If we plot the minimum and maximum number of vents grouped within each time bin (**Supplementary Figure S16**), we see differences no higher than ~3% compared to the number of vents per time bin used during our study. Further, if we extract the minimum and maximum number of vents for the most recent time bin (<1 Ma) and model the ellipses of their respective bandwidths (calculated using the $\hat{H}_{\mathrm{PI,AMSE}}$ selector), it is found that the orientation (i.e., azimuth) of the ellipses differ by less than 0.3% compared to the orientation of the ellipse used during the spatial analysis. Similarly, a minor difference (<0.4%) is obtained when the areas of these ellipses are compared to each other. In conclusion, other bandwidth selectors and different vent-grouping age distributions do not affect the spatial probability map to any significant extent.

MatHaz has been developed as a tool to help deal with the real and practical complications of assessing hazard for large volcanic areas (Bertin et al., 2019). In order to achieve this task within reasonable simulation times, and unlike other hazard simulation tools, MatHaz has not been developed to model the physics of volcanic eruptions and their products, or to model the details of specific eruptive scenarios (Bertin et al., 2019). This strategy focuses on simplified models that are easy to manage and replicate and quick to execute, acknowledging that by meeting these conditions model resolution is lost. Nevertheless, even the simplest models considered in MatHaz have their own assumptions. For example, tephra fallout modeling was performed by drawing elliptical isopachs assuming a deposit that thins exponentially away from the source, an approach that is not necessarily true based on well-documented eruptions (e.g., Bonadonna and Costa, 2012; Kawabata et al., 2013). Debris flows and lava flows are modelled based on a simple 'flow-routing' code, so an important limitation is that the hazard areas will always follow the thalweg of the valley and will never overbank.

The simulation times of each model tested are also strongly influenced by the pixel size, which determines the level of spatial detail of the assessment. In our case study application, a pixel size of 1,000 m was used, which is ~0.1% of the longest side of the study area. This proportion was deemed adequate by Bertin et al. (2019) after testing the pixel size/computational efficiency trade-off for different pixel sizes, as any improvement on the spatial resolution of the assessment was far more computationally intensive but with little reward, in that the shapes of the main probability isocontours did not differ significantly for pixel size/study area ratios lower than 0.1%.

For the modeling methodology, it was assumed that every volcanic phenomenon had its source in a single pixel of fixed size. This is an oversimplification, especially for lava flows, since these can also start erupting from a fissure, which may or may not evolve into a single vent (e.g., Valentine and Gregg, 2008). In MatHaz, simulation of fissure eruptions adds a major complexity to the model due to the many assumptions about which additional source vents will have to be considered. In spite of these limitations, for a future application of MatHaz a potential user can edit the code to include other modeling algorithms and simulation tools. Another possibility might be running more sophisticated numerical models for those regions where the highest spatial probabilities were obtained.

Summarizing, our approach is, at least, effective in providing a first-order assessment of volcanic hazards for large and complex volcanic regions. In addition, even though we acknowledge that our results are mostly valid at a large (regional) scale, they can be used to guide targeted hazard assessments at more detailed scales.

Improving Future Hazard Assessments With Structural, Geophysical, and Geochronological Datasets

Probabilistic volcanic hazard assessments can be improved by including robust volcano-structural, seismic and thermal datasets at more detailed scales (e.g., Bartolini et al., 2014; Bertin et al., 2019). This information is however still patchy and incomplete for the area considered in the present study. For instance, apart from two volcanoes (Láscar and Lastarria), there is no permanent seismic network in the region (Amigo, 2021; Aguilera et al., 2022). Other isolated seismicity has been considered tectonic, but could have magmatic influences; for instance, Mulcahy et al. (2014) identified two brief, shallow (<5 km) swarms east of Falso Azufre and at Cerro Galán.

There is a large catalogue of faults, fractures, fissures and lineaments for this area (5,887 structures; extracted from the Bertin et al., 2022 database) (**Supplementary Material S4**), although these are mainly mapped in basement units, with structures unrecognised beneath most of the volcanic centres. To gain insight into how the structures can influence a future hazard analysis, we tested the incorporation of this patchy structural data into the probabilistic spatial assessment following the methodology described in Bertin et al. (2019). Results (**Figure 11**) show that even conservative weightings on structures (~20%) distort the probability isocontours towards regions far away from known volcanism. Hence, it appears that homogenous and high-resolution structural information (e.g., Becerril et al., 2013; Bartolini et al., 2014; Bertin et al., 2019; Bevilacqua et al., 2021) is required before it becomes useful, especially in order to discriminate between those structures that have interacted with ascending magmas in the past, and those that have not. In other words, regional-scale structural data do not seem to improve the assessment.

Data indicative of persistent thermal anomalies and/or zones of active surface deformation could also be used to improve future hazard assessments, although homogeneity of data coverage must be considered. Low enthalpy geothermal springs have been mapped in Chile (Hauser, 1997) and Argentina (Pesce and Miranda, 2003), although these are mostly in places accessible by road. Fumarolic activity at some volcanoes (e.g., Tassi et al., 2009, Tassi et al., 2011; Aguilera et al., 2016; Chiodi et al., 2019), together with geological evidence of young (i.e., Quaternary) phreatomagmatic activity at others (e.g., van Alderwerelt, 2017; Filipovich et al., 2019, Filipovich et al., 2020;Ureta et al., 2020, Ureta et al., 2021), most of which fall within the volcanic clusters identified here, should be coupled with high-resolution thermal surveys to improve the spatial coverage of potential current magmatic anomalies. On the other hand, there are long-term ground deformation anomalies identified in InSAR time series, tilt meter data, GPS/GNSS permanent stations and ground surveying at some active volcanoes (Pritchard and Simons, 2002; Henderson and Pritchard, 2013; Amigo, 2021; Vélez et al., 2021; Aguilera et al., 2022). This information could be used to guide high-resolution geodetic studies, following on from some targeted surveys that have been conducted at Cerro Blanco (Di Filippo et al., 2008; Brunori et al., 2013; Chiodi et al., 2019; Lamberti et al., 2020; Vélez et al., 2021).

Improvement of the geochronological data will definitely help constrain the periods of activity of individual volcanic vents. Summing all available data into a geochronological database (Bertin et al., 2022) is robust over long time periods (10s of Myr), or better in some areas, but there is a paucity of data to effectively characterise the late Pleistocene-Holocene volcanic record, especially when many morphologically young volcanic deposits remain undated. A desirable future goal would be to gain enough new accurate and high-precision age determinations to improve the temporal resolution of this modeling approach ten-

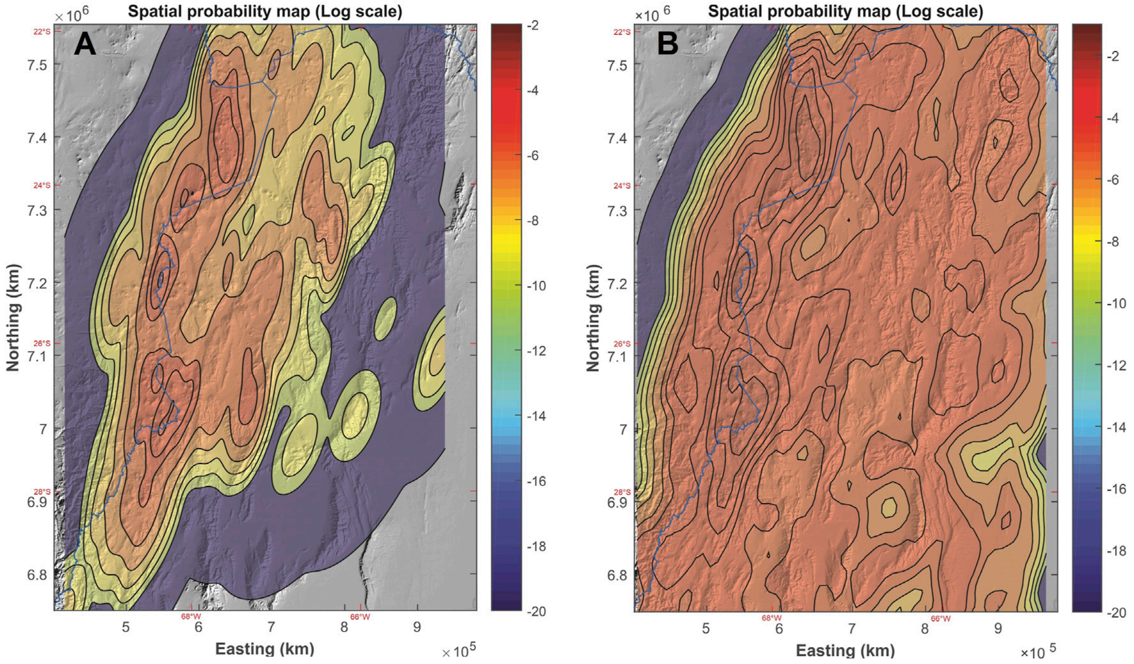

FIGURE 11 | Spatial probability analysis considering: **(A)** volcanic events, and **(B)** volcanic events (80%) and structural data (20%). Probability density functions were obtained after applying the kernel density estimation method, and are shown as probability isocontours on a logarithmic scale to illustrate order-of-magnitude changes. The political border between Chile, Argentina and Bolivia is depicted for reference (blue line). ASTER Digital elevation model used as a background image follows a greyscale colour scheme: the whiter the pixel, the higher the elevation.

fold (i.e., from 1 Myr to 100 kyr analysis windows). This will require targeting well-preserved recent volcanic deposits with state-of-the-art dating techniques to have the best chance of defining robust probability density functions for shorter time intervals, especially because the youngest time window is the one that contributes the most to the spatial probability map.

Recommendations for Future Work

Our study area is too large to expect a uniform high-resolution assessment of the volcanic eruption record. However, targeted analyses on particularly active parts of the region could lead to a much improved hazard assessment. We suggest high-resolution studies on the Puntas Negras and Chalviri volcanic chains (Láscar cluster), the Socompa and Púlar-Pajonales volcanoes (Socompa cluster), as well as the many volcanoes within the Incahuasi cluster (e.g., Ojos del Salado, El Fraile, Tipas, Peinado). The Incahuasi region shows the highest event probabilities (**Figures 3**, **4**), and has been addressed in only a few studies (González-Ferrán et al., 1985; Baker et al., 1987; Mpodozis et al., 1996; Gardeweg et al., 2000; Grosse et al., 2018, Grosse et al., 2020, Grosse et al., 2022; Naranjo et al., 2019). In addition, at least two <1 ka BP tephras mapped in Argentina (Fauqué and Tchilinguirian, 2002; Hermanns and Schellenberger, 2008), were likely erupted from the Incahuasi cluster (Sampietro-Vattuone et al., 2018, Sampietro-Vattuone et al., 2020; Fernández-Turiel et al., 2019). Additional permanent seismic monitoring networks should also be considered at Socompa, Tres Cruces, Ojos del Salado, and Cerro Blanco.

We recommend conducting a comprehensive evaluation of the erupted volume and volcanic eruption rates for this arc segment, as it could allow for an in-depth reconstruction of the spatio-volumetric-temporal evolution of volcanism in the region (e.g., how volcanism in terms of intensity and magnitude has varied over time). To achieve this goal, however, will require the development of a model that explicitly integrates the spatial, temporal, and volumetric components of hazard. Sophisticated spatio-temporal (Bebbington, 2013) and spatio-volumetric (Bebbington, 2015) hazard models have been developed for distributed volcanic fields, but their applicability to arc segments is yet to be tested. The inclusion of a volumetric component into a well-tested spatio-temporal model may shed further light on how much each volcanic cluster identified here contributes in terms of erupted volume. This will, in our opinion, highlight the Antofagasta cluster, particularly due to the presence of the Cerro Blanco volcanic complex, which has long been recognized as the source of at least two eruptions on the scale of the largest eruptions to have occurred on Earth since the late Pleistocene (Báez et al., 2015; Báez et al., 2020a; Báez et al., 2020b; Fernández-Turiel et al., 2019; de Silva et al., 2022).

CONCLUSION

We developed a long-term probabilistic volcanic hazard assessment of the Chilean-Argentinian segment of the Central Volcanic Zone of the Andes (~22.5–28°S). Through this we provide a first-order framework on which to build a detailed understanding of arc-scale/regional volcanic hazard. We recognize five regions of high spatial probability of future volcanic activity: Láscar, Socompa, Lazufre, Incahuasi, and Antofagasta. The largest clusters (Láscar, Lazufre and Incahuasi) correlate well with geophysical evidence of mid-crustal partial melt bodies, but the smallest two (Socompa and Antofagasta) do not. The Socompa and Antofagasta clusters should therefore be considered for further targeted thermal and other geophysical studies. We estimate a probability of 50% for an eruption of the scale of the Láscar 1993 event ($0.1\ km^3$) by the year ~2150. Our results suggest an ~80% probability that the next $0.1\ km^3$ eruption will occur from within one of the five volcanic clusters. The lack of a robust late Pleistocene-Holocene eruption record in this area is still a major hindrance for accurate short-term hazard assessments.

Five volcanic phenomena (pyroclastic density currents, ballistic projectiles, lava flows, debris flows and tephra fallout) were modeled for the whole region. Considering these collectively in an integrated volcanic hazards map, a relative hazard exposure was established for population centres in the region. This showed that the settlements with the highest relative likelihood of being affected by any of the volcanic phenomena mentioned above are small towns or similar, some of which are popular tourist destinations. Our results suggest that any major efforts towards improving volcanic hazard knowledge for this region should concentrate on improving volcanic event records within each of the five volcanic clusters identified here, especially the Incahuasi and Antofagasta clusters. In addition, examining the volcanic risk associated with the largest population centres that were defined in our exposure analysis should be pursued, especially San Antonio de los Cobres in Argentina and San Pedro de Atacama in Chile.

We suggest that the sequential methodology developed here could be tested in other volcanically active regions, as the results of such regional analysis can be used to identify areas to be prioritised for future volcanological research. Future efforts should also seek to explicitly add the erupted volume to the spatio-temporal framework in order to better understand other arc-scale processes that can impinge upon volcanic hazards.

DATA AVAILABILITY STATEMENT

The original contributions presented in the study are included in the article/**Supplementary Material**, further inquiries can be directed to the corresponding author.

AUTHOR CONTRIBUTIONS

DB conceived the study, developed methods, wrote and run all code, wrote the manuscript and prepared all relevant figures and complements. This work was supported and supervised by JL, SC, SdS, CC, and PC, who also contributed to the interpretation and edited the manuscript with several inputs from PG, WB, EB, and RC. All authors read and approved the final manuscript.

FUNDING

This work was partially funded through a CONICYT-Becas Chile PhD scholarship held by DB (2018–2021: Folio 72170365) and supported by the University of Auckland. SC and JL were supported by Transitioning Taranaki to a Volcanic Future MBIE Endeavour Project UOAX 1913. PC was supported by project PUE CONICET (Grant PUE-INECOA 22920170100027CO). PG was supported by Project PICT-2017-2798 of the Agencia Nacional de Promoción Científica y Tecnológica, and by Fundación Miguel Lillo. WB was supported by the PICT-2016/1359 grant.

ACKNOWLEDGMENTS

We thank Eliana Arango, Esteban Bertea, Alfredo Esquivel and Cristian Montonaro for their valuable help in several field campaigns throughout the region. The author acknowledges Danielle Charlton for helping with map designs, as well as Felipe Aguilera and Guadalupe Maro for discussions about Andean magmatism. Further data for this paper, if needed, are available by contacting the corresponding author at daniel.bertin.u@gmail.com. Chief Editor, Valerio Acocella, Associate Editor, Pablo Samaniego, and reviewers Alvaro Aravena and Suzanne Kay are deeply thanked for their insightful comments and suggestions that substantially improved the quality and structure of this paper.

SUPPLEMENTARY MATERIAL

The Supplementary Material for this article can be found online at: https://www.frontiersin.org/articles/10.3389/feart.2022.875439/full#supplementary-material

REFERENCES

Aguilera, F., Apaza, F., Del Carpio, J., Grosse, P., Jiménez, N., Ureta, G., et al. (2022). Advances in Scientific Understanding of the Central Volcanic Zone of the Andes: a Review of Contributing Factors. *Bull. Volcanol.* 84, 22. doi:10.1007/s00445-022-01526-y

Aguilera, F., Layana, S., Rodríguez-Díaz, A., González, C., Cortés, J., and Inostroza, M. (2016). Hydrothermal Alteration, Fumarolic Deposits and Fluids from Lastarria Volcanic Complex: A Multidisciplinary Study. *andgeo* 43 (2), 166–196. doi:10.5027/andgeov43n2-a02

Allmendinger, R. W., Jordan, T. E., Kay, S. M., and Isacks, B. L. (1997). The Evolution of the Altiplano-Puna Plateau of the Central Andes. *Annu. Rev. Earth Planet. Sci.* 25, 139–174. doi:10.1146/annurev.earth.25.1.139

Alloway, B. V., Pearce, N. J. G., Moreno, P. I., Villarosa, G., Jara, I., De Pol-Holz, R., et al. (2017). An 18,000 Year-Long Eruptive Record from Volcán Chaitén, Northwestern Patagonia: Paleoenvironmental and Hazard-Assessment Implications. *Quat. Sci. Rev.* 168, 151–181. doi:10.1016/j.quascirev.2017.05.011

Amigo, A., Bertin, D., and Orozco, G. (2012). "Peligros volcánicos de la zona norte de Chile," in *Servicio Nacional de Geología y Minería, Chile* (Santiago, Chile: Servicio Nacional de Geología y Minería), 17, 45. Serie Geología Ambiental.

Amigo, A. (2021). Volcano Monitoring and Hazard Assessments in Chile. *Volcanica* 4 (S1), 1–20. doi:10.30909/vol.04.s1.0120

Ayala, R. R. (2014). *Mapa preliminar de amenaza volcánica de Bolivia*. Cochabamba: XXI Congreso Geológico Boliviano, 241–251.

Báez, W., Arnosio, M., Chiodi, A., Ortiz-Yañes, A., Viramonte, J. G., Bustos, E., et al. (2015). Estratigrafía y evolución del Complejo Volcánico Cerro Blanco, Puna Austral, Argentina. *Rev. Mex. Ciencias Geol.* 32 (1), 29–49.

Báez, W., Bustos, E., Chiodi, A., Reckziegel, F., Arnosio, M., de Silva, S., et al. (2020a). Eruptive Style and Flow Dynamics of the Pyroclastic Density Currents Related to the Holocene Cerro Blanco Eruption (Southern Puna Plateau, Argentina). *J. S. Am. Earth Sci.* 98, 102482. doi:10.1016/j.jsames.2019.102482

Báez, W., Carraso Nuñez, G., Giordano, G., Viramonte, J. G., and Chiodi, A. (2016). “Polycyclic scoria cones of the Antofagasta de la Sierra basin, Southern Puna plateau, Argentina,” in *Monogenetic Volcanism*. Editors K. Németh, G. Carrasco-Núñez, J. J. Aranda-Gómez, and I. E. M. Smith (London, UK: Special Publication of the Geological Society of London), 446, 311–336. doi:10.1144/SP446.3

Báez, W., de Silva, S., Chiodi, A., Bustos, E., Giordano, G., Arnosio, M., et al. (2020b). Pulsating flow dynamics of sustained, forced pyroclastic density currents: insights from a facies analysis of the Campo de la Piedra Pómez ignimbrite, southern Puna, Argentina. *Bull. Volcanol.* 82, 53. doi:10.1007/s00445-020-01385-5

Baker, P. E., Gonzalez-ferran, O., and Rex, D. C. (1987). Geology and geochemistry of the Ojos del Salado volcanic region, Chile. *J. Geol. Soc.* 144, 85–96. doi:10.1144/gsjgs.144.1.0085

Bartolini, S., Bolós, X., Martí, J., Pedra, E. R., and Planagumà, L. (2015). Hazard Assessment at the Quaternary La Garrotxa Volcanic Field (NE Iberia). *Nat. Hazards* 78, 1349–1367. doi:10.1007/s11069-015-1774-y

Bartolini, S., Geyer, A., Martí, J., Pedrazzi, D., and Aguirre-Díaz, G. (2014). Volcanic Hazard on Deception Island (South Shetland Islands, Antarctica). *J. Volcanol. Geotherm. Res.* 285, 150–168. doi:10.1016/j.jvolgeores.2014.08.009

Bebbington, M. S. (2013). Assessing Spatio-Temporal Eruption Forecasts in a Monogenetic Volcanic Field. *J. Volcanol. Geotherm. Res.* 252, 14–28. doi:10.1016/j.jvolgeores.2012.11.010

Bebbington, M. S., and Cronin, S. J. (2011). Spatio-temporal Hazard Estimation in the Auckland Volcanic Field, New Zealand, with a New Event-Order Model. *Bull. Volcanol.* 73, 55–72. doi:10.1007/s00445-010-0403-6

Bebbington, M. S. (2015). Spatio-volumetric Hazard Estimation in the Auckland Volcanic Field. *Bull. Volcanol.* 77, 39. doi:10.1007/s00445-015-0921-3

Becerril, L., Bartolini, S., Sobradelo, R., Martí, J., Morales, J. M., and Galindo, I. (2014). Long-term Volcanic Hazard Assessment on El Hierro (Canary Islands). *Nat. Hazards Earth Syst. Sci.* 14, 1853–1870. doi:10.5194/nhess-14-1853-2014

Becerril, L., Cappello, A., Galindo, I., Neri, M., and Del Negro, C. (2013). Spatial Probability Distribution of Future Volcanic Eruptions at El Hierro Island (Canary Islands, Spain). *J. Volcanol. Geotherm. Res.* 257, 21–30. doi:10.1016/j.jvolgeores.2013.03.005

Beck, S. L., Zandt, G., Ward, K. M., and Scire, A. (2015). “Multiple Styles and Scales of Lithospheric Foundering beneath the Puna Plateau, Central Andes,” in *Geodynamics of a Cordilleran Orogenic System: The Central Andes of Argentina and Northern Chile*. Editors P. G. DeCelles, M. N. Ducea, B. Carrapa, and P. A. Kapp (McLean, VA: Geological Society of America Memoir), 212. doi:10.1130/2015.1212(03)

Bello-González, J. P., Contreras-Reyes, E., and Arriagada, C. (2018). Predicted Path for Hotspot Tracks off South America since Paleocene Times: Tectonic Implications of Ridge-Trench Collision along the Andean Margin. *Gondwana Res.* 64, 216–234. doi:10.1016/j.gr.2018.07.008

Bertin, D. (2017). 3-D Ballistic Transport of Ellipsoidal Volcanic Projectiles Considering Horizontal Wind Field and Variable Shape-dependent Drag Coefficients. *J. Geophys. Res. Solid Earth* 122 (2), 1126–1151. doi:10.1002/2016jb013320

Bertin, D., Lindsay, J. M., Becerril, L., Cronin, S. J., and Bertin, L. J. (2019). MatHaz: a Matlab Code to Assist with Probabilistic Spatio-Temporal Volcanic Hazard Assessment in Distributed Volcanic Fields. *J. Appl. Volcanol.* 8, 4. doi:10.1186/s13617-019-0084-6

Bertin, D., Lindsay, J. M., Cronin, S. J., de Silva, S., Connor, C., Caffe, P., et al. (2022). *Volcanic Geospatial Database of the Chilean-Argentinian Segment (22.5-29°S) of the Central Volcanic Zone of the Andes*. Auckland, NZ: The University of Auckland Dataset. doi:10.17608/k6.auckland.16894903.v3

Bevilacqua, A., Aravena, A., Neri, A., Gutiérrez, E., Escobar, D., Schliz, M., et al. (2021). Thematic Vent Opening Probability Maps and Hazard Assessment of Small-Scale Pyroclastic Density Currents in the San Salvador Volcanic Complex (El Salvador) and Nejapa-Chiltepe Volcanic Complex (Nicaragua). *Nat. Hazards Earth Syst. Sci.* 21, 1639–1665. doi:10.5194/nhess-21-1639-2021

Bevilacqua, A., Bursik, M., Bursik, M., Patra, A., Pitman, E., and Till, R. (2017). Bayesian Construction of a Long-Term Vent Opening Probability Map in the Long Valley Volcanic Region (CA, USA). *Siv* 31, 1–36. doi:10.5038/2163-338x.3.1

Bevilacqua, A., Isaia, R., Neri, A., Vitale, S., Aspinall, W. P., Bisson, M., et al. (2015). Quantifying Volcanic Hazard at Campi Flegrei Caldera (Italy) with Uncertainty Assessment: 1. Vent Opening Maps. *J. Geophys. Res. Solid Earth* 120 (4), 2309–2329. doi:10.1002/2014jb011775

Bianchi, M., Heit, B., Jakovlev, A., Yuan, X., Kay, S. M., Sandvol, E., et al. (2013). Teleseismic Tomography of the Southern Puna Plateau in Argentina and Adjacent Regions. *Tectonophysics* 586, 65–83. doi:10.1016/j.tecto.2012.11.016

Biass, S., Bonadonna, C., di Traglia, F., Pistolesi, M., Rosi, M., and Lestuzzi, P. (2016). Probabilistic Evaluation of the Physical Impact of Future Tephra Fallout Events for the Island of Vulcano, Italy. *Bull. Volcanol.* 78, 37. doi:10.1007/s00445-016-1028-1

Bird, D. K., Gisladottir, G., and Dominey-Howes, D. (2010). Volcanic Risk and Tourism in Southern Iceland: Implications for Hazard, Risk and Emergency Response Education and Training. *J. Volcanol. Geotherm. Res.* 189, 33–48. doi:10.1016/j.jvolgeores.2009.09.020

Bonadonna, C., and Costa, A. (2012). Estimating the Volume of Tephra Deposits: a New Simple Strategy. *Geology* 40, 415–418. doi:10.1130/g32769.1

Brandmeier, M., and Wörner, G. (2016). Compositional Variations of Ignimbrite Magmas in the Central Andes over the Past 26 Ma - A Multivariate Statistical Perspective. *Lithos* 262, 713–728. doi:10.1016/j.lithos.2016.07.011

Brunori, C. A., Bignami, C., Stramondo, S., and Bustos, E. (2013). 20 Years of Active Deformation on Volcano Caldera: Joint Analysis of InSAR and AInSAR Techniques. *Int. J. Appl. Earth Observation Geoinformation* 23, 279–287. doi:10.1016/j.jag.2012.10.003

Bustos, E., Báez, W., Norini, G., Arnosio, M., and de Silva, S. L. (2019). The Geological and Structural Evolution of the Long-Lived Miocene-Pleistocene La Hoyada Volcanic Complex in the Geodynamic Framework of the Central Andes, Argentina. *J. Volcanol. Geotherm. Res.* 385, 120–142. doi:10.1016/j.jvolgeores.2018.07.010

Calder, E. S., Sparks, R. S. J., and Gardeweg, M. C. (2000). Erosion, Transport and Segregation of Pumice and Lithic Clasts in Pyroclastic Flows Inferred from Ignimbrite at Lascar Volcano, Chile. *J. Volcanol. Geotherm. Res.* 104 (1-4), 201–235. doi:10.1016/S0377-0273(00)00207-9

Cappello, A., Ganci, G., Calvari, S., Pérez, N. M., Hernández, P. A., Silva, S. V., et al. (2016). Lava Flow Hazard Modeling during the 2014-2015 Fogo Eruption, Cape Verde. *J. Geophys. Res. Solid Earth* 121, 2290–2303. doi:10.1002/2015jb012666

Cappello, A., Neri, M., Acocella, V., Gallo, G., Vicari, A., and Del Negro, C. (2012). Spatial Vent Opening Probability Map of Etna Volcano (Sicily, Italy). *Bull. Volcanol.* 74, 2083–2094. doi:10.1007/s00445-012-0647-4

Casertano, L. (1963). *Catalogue of the Active Volcanoes of the World, Including Solfatara Fields, Part XV, Chilean Continent*. Rome, Italy: International Association of Volcanology, 55.

Charbonnier, S. J., Thouret, J.-C., Gueugneau, V., and Constantinescu, R. (2020). New Insights into the 2070calyrBP Pyroclastic Currents at El Misti Volcano (Peru) from Field Investigations, Satellite Imagery and Probabilistic Modeling. *Front. Earth Sci.* 8, 557788. doi:10.3389/feart.2020.557788

Charlton, D., Kilburn, C., and Edwards, S. (2020). Volcanic Unrest Scenarios and Impact Assessment at Campi Flegrei Caldera, Southern Italy. *J. Appl. Volcanol.* 9, 7. doi:10.1186/s13617-020-00097-x

Charrier, R., Pinto, L., and Rodríguez, M. P. (2007). “Tectonostratigraphic Evolution of the Andean Orogen in Chile,” in *The Geology of Chile*. Editors T. Moreno and W. Gibbons (London: The Geological Society), 21–114.

Chen, J., Kufner, S. K., Yuan, X., Heit, B., Wu, H., Yang, D., et al. (2020). Lithospheric Delamination beneath the Southern Puna Plateau Resolved by Local Earthquake Tomography. *J. Geophys. Res. Solid Earth* 125, e2019JB019040. doi:10.1029/2019jb019040

Chiodi, A., Tassi, F., Báez, W., Filipovich, R., Bustos, E., Glok Galli, M., et al. (2019). Preliminary Conceptual Model of the Cerro Blanco Caldera-Hosted Geothermal System (Southern Puna, Argentina): Inferences from

Geochemical Investigations. *J. S. Am. Earth Sci.* 94, 102213. doi:10.1016/j.jsames.2019.102213

Chmielowski, J., Zandt, G., and Haberland, C. (1999). The Central Andean Altiplano-Puna Magma Body. *Geophys. Res. Lett.* 26 (6), 783–786. doi:10.1029/1999gl900078

Clavero, J. E., Sparks, R. S. J., Pringle, M. S., Polanco, E., and Gardeweg, M. C. (2004). Evolution and Volcanic Hazards of Taapaca Volcanic Complex, Central Andes of Northern Chile. *J. Geol. Soc.* 161, 603–618. doi:10.1144/0016-764902-065

Coira, B., Kay, S. M., and Viramonte, J. (1993). Upper Cenozoic Magmatic Evolution of the Argentine Puna-A Model for Changing Subduction Geometry. *Int. Geol. Rev.* 35 (8), 677–720. doi:10.1080/00206819309465552

Comeau, M. J., Unsworth, M. J., and Cordell, D. (2016). New Constraints on the Magma Distribution and Composition beneath Volcán Uturuncu and the Southern Bolivian Altiplano from Magnetotelluric Data. *Geosphere* 12 (5), 1391–1421. doi:10.1130/ges01277.1

Connor, C. B., Connor, L. J., Germa, A., Richardson, J. A., Bebbington, M., and Saballos, J. A. (2018). How to Use Kernel Density Estimation as a Diagnostic and Forecasting Tool for Distributed Volcanic Vents. *Statistics Volcanol.* 4, 1–21. doi:10.5038/2163-338X.4.3

Connor, C. B., Connor, L. J., Jaquet, O., Wallace, L., Kiyosugi, K., Chapman, N., et al. (2013). "Spatial and Temporal Distribution of Future Volcanism in the Chuguku Region – a Partial Application of NUMO's ITM and Topaz Probabilistic Tectonic Assessment Methodology," in *Technical Report NUMO-TR-13-03* (Tokyo: Nuclear Waste Organization of Japan), 83.

Connor, C. B., and Hill, B. E. (1995). Three Nonhomogeneous Poisson Models for the Probability of Basaltic Volcanism: Application to the Yucca Mountain Region, Nevada. *J. Geophys. Res.* 100, 10107–10125. doi:10.1029/95jb01055

Connor, L. J., Connor, C. B., Meliksetian, K., and Savov, I. (2012). Probabilistic Approach to Modeling Lava Flow Inundation: a Lava Flow Hazard Assessment for a Nuclear Facility in Armenia. *J. Appl. Volcanol.* 1, 3. doi:10.1186/2191-5040-1-3

Damaschke, M., Cronin, S. J., and Bebbington, M. S. (2018). A Volcanic Event Forecasting Model for Multiple Tephra Records, Demonstrated on Mt. Taranaki, New Zealand. *Bull. Volcanol.* 80, 9. doi:10.1007/s00445-017-1184-y

Daxberger, H., and Riller, U. (2015). Kinematics of Neogene to Recent Upper-Crustal Deformation in the Southern Central Andes (23°-28°S) Inferred from Fault-Slip Analysis: Evidence for Gravitational Spreading of the Puna Plateau. *Tectonophysics* 642, 16–28. doi:10.1016/j.tecto.2014.12.003

de Silva, S. L. (1989). Altiplano-Puna Volcanic Complex of the Central Andes. *Geol* 17, 1102–1106. doi:10.1130/0091-7613(1989)017<1102:apvcot>2.3.co;2

de Silva, S. L., and Francis, P. W. (1991). *Volcanoes of the Central Andes*. Berlin: Spinger-Verlag, 216.

de Silva, S. L., and Kay, S. M. (2018). Turning up the Heat: High-Flux Magmatism in the Central Andes. *Elements* 14 (4), 245–250. doi:10.2138/gselements.14.4.245

de Silva, S. L., Roberge, J., Bardelli, L., Báez, W., Ortiz, A., Viramonte, J. G., et al. (2022). *Magmatic Evolution and Architecture of an Arc-Related, Rhyolitic Caldera Complex: The Late Pleistocene to Holocene Cerro Blanco Volcanic Complex, Southern Puna*. Argentina: Geosphere.

DeCelles, P. G., Carrapa, B., Horton, B. K., McNabb, J., Gehrels, G. E., and Boyd, J. (2015). "The Miocene Arizaro Basin, Central Andean Hinterland: Response to Partial Lithospheric Removal?," in *Geodynamics of a Cordilleran Orogenic System: The Central Andes of Argentina and Northern Chile*. Editors P. G. DeCelles, M. N. Ducea, B. Carrapa, and P. A. Kapp (McLean, VA: Geological Society of America Memoir), 212, 359–386. doi:10.1130/2015.1212(18)

Delph, J. R., Shimizu, K., and Ratschbacher, B. C. (2021). The Architecture of the Southern Puna Magmatic System: Integrating Seismic and Petrologic Observations with Geochemical Modeling. *J. Geophys. Res. Solid Earth* 126 (7). e2020JB021550. doi:10.1029/2020jb021550

Delph, J. R., Ward, K. M., Zandt, G., Ducea, M. N., and Beck, S. L. (2017). Imaging a Magma Plumbing System from MASH Zone to Magma Reservoir. *Earth Planet. Sci. Lett.* 457, 313–324. doi:10.1016/j.epsl.2016.10.008

Di Filippo, M., Di Nezza, M., Colombi, A., Viramonte, J. G., and Toro, B. (2008). *Estructura gravimétrica del Complejo Volcánico Cerro Blanco, Puna Austral Argentina*, 1. Jujuy: XVII Congreso Geológico Argentino, Actas, 203–204.

Díaz, D., Brasse, H., and Ticona, F. (2012). Conductivity Distribution beneath Lascar Volcano (Northern Chile) and the Puna, Inferred from Magnetotelluric Data. *J. Volcanol. Geotherm. Res.* 217-218, 21–29. doi:10.1016/j.jvolgeores.2011.12.007

Duong, T. (2005). *Bandwidth Selectors for Multivariate Kernel Density Estimation (PhD Thesis)*. Perth, Australia: University of Western Australia, 173.

Elissondo, M., Farías, C., and Collini, E. (2016). *Volcanic Risk Assessment in Argentina. Cities on Volcanoes, 09, Session 1.4.* Chile: Sernageomin.

Fauqué, L., and Tchilinguirian, P. (2002). "Villavil Rockslides, Catamarca Province, Argentina," in *Catastrophic Landslides: Effects, Occurrence, and Mechanisms*. Editors S. G. Evans and J. V. DeGraff (Boulder, CO: Geological Society of America Reviews in Engineering Geology), XV, 303–324. doi:10.1130/REG15-p303

Fernández-Turiel, J. L., Pérez-Torrado, F. J., Rodríguez-González, A., Saavedra, J., Carracedo, J. C., Rejas, M., et al. (2019). The Large Eruption 4.2 Ka Cal BP in Cerro Blanco, Central Volcanic Zone, Andes: Insights to the Holocene Eruptive Deposits in the Southern Puna and Adjacent Regions. *Estud. Geol.* 75 (1), e088. doi:10.3989/egeol.43438.515

Fernandez-Turiel, J. L., Saavedra, J., Perez-Torrado, F. J., Rodriguez-Gonzalez, A., Rejas, M., Guillou, H., et al. (2021). New ages, morphometric and geochemical data on recent shoshonitic volcanism of the Puna, Central Volcanic Zone of Andes: San Jerónimo and Negro de Chorrillos volcanoes. *J. S. Am. Earth Sci.* 109, 103270. doi:10.1016/j.jsames.2021.103270

Fierstein, J., and Nathenson, M. (1992). Another Look at the Calculation of Fallout Tephra Volumes. *Bull. Volcanol.* 54, 156–167. doi:10.1007/bf00278005

Filipovich, R., Báez, W., Bustos, E., Villagrán, A., Chiodi, A., and Viramonte, J. (2019). Eruptive Styles Related to the Monogenetic Mafic Volcanism of Pasto Ventura Región, Southern Puna, Argentina. *Andean Geol.* 46, 2. doi:10.5027/andgeov46n2-3091

Filipovich, R., Báez, W., Groppelli, G., Ahumada, F., Aldega, L., Becchio, R., et al. (2020). Geological Map of the Tocomar Basin (Puna Plateau, NW Argentina). Implication for the Geothermal System Investigation. *Energies* 13 (20), 5492. doi:10.3390/en13205492

Folkes, C. B., Wright, H. M., Cas, R. A. F., de Silva, S. L., Lesti, C., and Viramonte, J. G. (2011). A Re-appraisal of the Stratigraphy and Volcanology of the Cerro Galán Volcanic System, NW Argentina. *Bull. Volcanol.* 73, 1427–1454. doi:10.1007/s00445-011-0459-y

Freymuth, H., Brandmeier, M., and Wörner, G. (2015). The Origin and Crust/mantle Mass Balance of Central Andean Ignimbrite Magmatism Constrained by Oxygen and Strontium Isotopes and Erupted Volumes. *Contrib. Mineral. Pet.* 169, 58. doi:10.1007/s00410-015-1152-5

Gallant, E., Cole, L., Connor, C., Donovan, A., Molisee, D., Morin, J., et al. (2021). Modelling Eruptive Event Sources in Distributed Volcanic Fields. *Volcanica* 4 (2), 325–343. doi:10.30909/vol.04.02.325343

Gao, Y., Tilmann, F., Herwaarden, D. P., Thrastarson, S., Fichtner, A., Heit, B., et al. (2021). Full Waveform Inversion beneath the Central Andes: Insight into the Dehydration of the Nazca Slab and Delamination of the Back-Arc Lithosphere. *JGR Solid Earth* 126, e2021JB021984. doi:10.1029/2021JB021984

Gardeweg, M., Amigo, A., Matthews, S., Sparks, R. S. J., and Clavero, J. (2011). "Geología del volcán Láscar, Región de Antofagasta. Servicio Nacional de Geología y Minería, Carta Geológica de Chile," in *Serie Geología Básica* (Santiago, Chile: Sernageomin), 131, 1. mapa escala 1:50,000.40

Gardeweg, M., and Amigo, A. (2015). "Peligros del volcán Láscar, Región de Antofagasta. Servicio Nacional de Geología y Minería, Carta Geológica de Chile," in *Serie Geología Ambiental* (Santiago, Chile: Sernageomin), 22, 1. mapa escala 1:50,000.

Gardeweg, M., Clavero, J., Mpodozis, C., Pérez de Arce, C., and Villeneuve, M. (2000). "El Macizo Tres Cruces: un complejo volcánico longevo y potencialmente activo en la alta cordillera de Copiapó, Chile," in *IX Congreso Geológico Chileno*. Puerto Varas, Chile: Sociedad Geológica de Chile, Servicio Nacional de Geología y Minería, Universidad de Chile, 291–295.

Gardeweg, M., and Medina, E. (1994). *La erupción subpliniana del 19-20 Abril de 1993 del volcán Lascar, Norte de Chile*. Concepción, Chile: VII Congreso Geológico Chileno, 299–304.

George, O. A., Malservisi, R., Govers, R., Connor, C. B., and Connor, L. J. (2016). Is Uplift of Volcano Clusters in the Tohoku Volcanic Arc, Japan, Driven by Magma Accumulation in Hot Zones? A Geodynamic Modeling

Study. *J. Geophys. Res. Solid Earth* 121 (6), 4780–4796. doi:10.1002/2016jb012833

Germa, A., Connor, L. J., Cañon-Tapia, E., and Le Corvec, N. (2013). Tectonic and Magmatic Controls on the Location of Post-subduction Monogenetic Volcanoes in Baja California, Mexico, Revealed through Spatial Analysis of Eruptive Vents. *Bull. Volcanol.* 75, 782. doi:10.1007/s00445-013-0782-6

Global Volcanism Program (2016). "Report on Lascar (Chile) – July 2016," in *Bulletin of the Global Volcanism Network*. Editors A. E. Crafford and E. Venzke (Washington, DC: Smithsonian Institution), 41, 7.

Global Volcanism Program (1993a). "Report on Aracar (Argentina) – April 1993," in *Bulletin of the Global Volcanism Network*. Editor E. Venzke (Washington, DC: Smithsonian Institution), 18, 4. doi:10.5479/si.GVP.BGVN199304-355160

Global Volcanism Program (1993b). "Report on Ojos del Salado (Chile-Argentina) – November 1993," in *Bulletin of the Global Volcanism Network*. Editor R. Wunderman (Washington, DC: Smithsonian Institution), 18, 11. doi:10.5479/si.GVP.BGVN199311-355130

González-Ferrán, O., Baker, P. E., and Rex, D. C. (1985). Tectonic-volcanic Discontinuity at Latitude 27° South Andean Range, Associated with Nazca Plate Subduction. *Tectonophysics* 112, 423–441. doi:10.1016/0040-1951(85)90189-1

González-Ferrán, O. (1995). *Volcanes de Chile*. Santiago: Instituto Geográfico Militar, 640.

Goss, A. R., Kay, S. M., and Mpodozis, C. (2011). The Geochemistry of a Dying Continental Arc: the Incapillo Caldera and Dome Complex of the Southernmost Central Andean Volcanic Zone (~28°S). *Contrib. Mineral. Pet.* 161, 101–128. doi:10.1007/s00410-010-0523-1

Grosse, P., Guzmán, S. R., Nauret, F., Orihashi, Y., and Sumino, H. (2022). Central vs. Lateral Growth and Evolution of the < 100 ka Peinado Composite Volcano, Southern Central Volcanic Zone of the Andes. *J. Volcanol. Geotherm. Res.* 425, 107532. doi:10.1016/j.jvolgeores.2022.107532

Grosse, P., Ochi Ramacciotti, M. L., Escalante Fochi, F., Guzmán, S., Orihashi, Y., and Sumino, H. (2020). Geomorphology, Morphometry, Spatial Distribution and Ages of Mafic Monogenetic Volcanoes of the Peinado and Incahuasi Fields, Southernmost Central Volcanic Zone of the Andes. *J. Volcanol. Geotherm. Res.* 401, 106966. doi:10.1016/j.jvolgeores.2020.106966

Grosse, P., Orihashi, Y., Guzmán, S. R., Sumino, H., and Nagao, K. (2018). Eruptive History of Incahuasi, Falso Azufre and El Cóndor Quaternary Composite Volcanoes, Southern Central Andes. *Bull. Volcanol.* 80, 44. doi:10.1007/s00445-018-1221-5

Guzmán, S., Grosse, P., Montero-López, C., Hongn, F., Pilger, R., Petrinovic, I., et al. (2014). Spatial-temporal Distribution of Explosive Volcanism in the 25-28°S Segment of the Andean Central Volcanic Zone. *Tectonophysics* 636, 170–189. doi:10.1016/j.tecto.2014.08.013

Harpel, C. J., de Silva, S., and Salas, G. (2011). *The 2 Ka Eruption of Misti Volcano, Southern Peru – the Most Recent Plinian Eruption of Arequipa's Iconic Volcano*, 484. McLean, VA: Geological Society of America Special Paper, 1–72. doi:10.1130/2011.2484

Haschke, M., Siebel, W., Günther, A., and Scheuber, E. (2002). Repeated Crustal Thickening and Recycling during the Andean Orogeny in North Chile (21°-26°S). *J. Geophys. Res. Solid Earth* 107 (B1). doi:10.1029/2001jb000328

Hauser, A. (1997). *Catastro y caracterización de las fuentes de aguas minerales y termales de Chile*, 50. Santiago, Chile: Servicio Nacional de Geología y Minería, Boletín, 89.

Henderson, S. T., and Pritchard, M. E. (2013). Decadal Volcanic Deformation in the Central Andes Volcanic Zone Revealed by InSAR Time Series. *Geochem. Geophys. Geosystems* 14, 5. doi:10.1002/ggge.20074

Hermanns, R. L., and Schellenberger, A. (2008). Quaternary Tephrochronology Helps Define Conditioning Factors and Triggering Mechanisms of Rock Avalanches in NW Argentina. *Quat. Int.* 178, 261–275. doi:10.1016/j.quaint.2007.05.002

Hoke, L., and Lamb, S. (2007). Cenozoic Behind-Arc Volcanism in the Bolivian Andes, South America: Implications for Mantle Melt Generation and Lithospheric Structure. *J. Geol. Soc.* 164, 795–814. doi:10.1144/0016-76492006-092

INDEC (2010). *Censo Nacional de Población, Hogares y Viviendas 2010*. Buenos Aires, Argentina: Instituto Nacional de Estadística y Censos. https://www.indec.gob.ar/indec/web/Nivel4-Tema-2-41-135.

INE Chile (2017). Censo de Población y Vivienda 2017: Resultados Censo 2017. Available at: https://ine-chile.maps.arcgis.com/apps/webappviewer/index.html?id=c2155cac57d04032bf6ca5f151cddd6d (Accessed September 7, 2021).

James, D. E., and Sacks, I. S. (1999). "Cenozoic Formation of the Central AndesA Geophysical Perspective," in *Geology and Ore Deposits of the Central Andes*. Editor B. J. Skinner (Littleton, Colorado: Society of Economic Geologists, Special Publication No. 7), 1–25. doi:10.5382/sp.07.01

Jaquet, O., Lantuéjoul, C., and Goto, J. (2017). Probabilistic Estimation of Long-Term Volcanic Hazard under Evolving Tectonic Conditions in a 1 Ma Timeframe. *J. Volcanol. Geotherm. Res.* 345, 58–66. doi:10.1016/j.jvolgeores.2017.07.010

Jaquet, O., Lantuéjoul, C., and Goto, J. (2012). Probabilistic Estimation of Long-Term Volcanic Hazard with Assimilation of Geophysics and Tectonic Data. *J. Volcanol. Geotherm. Res.* 235-236, 29–36. doi:10.1016/j.jvolgeores.2012.05.003

Javidan, N., Kavian, A., Pourghasemi, H. R., Conoscenti, C., Jafarian, Z., and Rodrigo-Comino, J. (2021). Evaluation of Multi-Hazard Map Produced Using MaxEnt Machine Learning Technique. *Sci. Rep.* 11, 6496. doi:10.1038/s41598-021-85862-7

Jay, J. A., Welch, M., Pritchard, M. E., Mares, P. J., Mnich, M. E., Melkonian, A. K., et al. (2013). "Volcanic Hotspots of the Central and Southern Andes as Seen from Space by ASTER and MODVOLC between the Years 2000 and 2010," in *Geological Society, London, Special Publications*. Editors D. M. Pyle, T. A. Mather, and J. Biggs (London, UK: Special Publication of the Geological Society of London), 380, 161–185. doi:10.1144/sp380.1

Jiménez, D., Becerril, L., Bartolini, S., Escobar, D., and Martí, J. (2020). Making a Qualitative Volcanic-Hazards Map by Combining Simulated Scenarios: An Example for San Miguel Volcano (El Salvador). *J. Volcanol. Geotherm. Res.* 395, 106837. doi:10.1016/j.jvolgeores.2020.106837

Jiménez, D., Becerril, L., Bartolini, S., and Martí, J. (2018). Spatio-temporal Hazard Estimation in San Miguel Volcano, El Salvador. *J. Volcanol. Geotherm. Res.* 358, 171–183. doi:10.1016/j.jvolgeores.2018.04.003

Johnston, D., Becker, J., Jolly, G., Potter, S., Wilson, T., Stewart, C., et al. (2011). *Volcanic Hazards Management at Taranaki Volcano: Information Source Book*. Lower Hutt, Wellington, NZ: Institute of Geological and Nuclear Sciences Limited, 108. GNS Science Report 2011/37.

Kawabata, E., Bebbington, M. S., Cronin, S. J., and Wang, T. (2013). Modeling Thickness Variability in Tephra Deposition. *Bull. Volcanol.* 75, 738. doi:10.1007/s00445-013-0738-x

Kay, S. M., Coira, B. L., Caffe, P. J., and Chen, C.-H. (2010). Regional Chemical Diversity, Crustal and Mantle Sources and Evolution of Central Andean Puna Plateau Ignimbrites. *J. Volcanol. Geotherm. Res.* 198, 81–111. doi:10.1016/j.jvolgeores.2010.08.013

Kay, S. M., and Coira, B. L. (2009). "Shallowing and Steepening Subduction Zones, Continental Lithospheric Loss, Magmatism, and Crustal Flow under the Central Andean Altiplano-Plateau," in *Backbone of the Americas: Plateau Uplift, Shallow Subduction and Ridge Collision*. Editors S. M. Kay, V. A. Ramos, and W. R. Dickinson (McLean, VA: Geological Society of America Memoir), 229–259.

Kay, S. M., Coira, B., and Viramonte, J. (1994). Young Mafic Back Arc Volcanic Rocks as Indicators of Continental Lithospheric Delamination beneath the Argentine Puna Plateau, Central Andes. *J. Geophys. Res.* 99 (B12), 24323–24339. doi:10.1029/94jb00896

Kay, S. M., Coira, B., Wörner, G., Kay, R. W., and Singer, B. S. (2011). Geochemical, Isotopic and Single Crystal 40Ar/39Ar Age Constraints on the Evolution of the Cerro Galán Ignimbrites. *Bull. Volcanol.* 73, 1487–1511. doi:10.1007/s00445-010-0410-7

Kósik, S., Bebbington, M., and Németh, K. (2020). Spatio-temporal Hazard Estimation in the Central Silicic Part of Taupo Volcanic Zone, New Zealand, Based on Small to Medium Volume Eruptions. *Bull. Volcanol.* 82, 50. doi:10.1007/s00445-020-01392-6

Lamberti, M. C., Chiodi, A., Agusto, M., Filipovich, R., Massenzio, A., Baéz, W., et al. (2020). Carbon Dioxide Diffuse Degassing as a Tool for Computing the Thermal Energy Release at Cerro Blanco Geothermal System, Southern Puna (NW Argentina). *J. S. Am. Earth Sci.* 105, 102833. doi:10.1016/j.jsames.2020.102833

Lara, L. E., Orozco, G., Amigo, A., and Silva, C. (2011). "Peligros volcánicos de Chile. Servicio Nacional de Geología y Minería, Carta Geológica de Chile," in

Serie Geología Ambiental (Santiago, Chile: Sernageomin), 13, 34. 1 mapa escala 1:2.000.000.

Lerner, G. A., Cronin, S. J., Bebbington, M. S., and Platz, T. (2019). The Characteristics of a Multi-Episode Volcanic Regime: the Post-AD 960 Maero Eruptive Period of Mt. Taranaki (New Zealand). *Bull. Volcanol.* 81, 61. doi:10.1007/s00445-019-1327-4

Macedo, O., Taipe, E., Del Caripo, J., Ticona, J., Ramos, D., Puma, N., et al. (2016). *Evaluación del riesgo volcánico en el sur del Perú, situación de la vigilancia actual y requerimientos de monitoreo en el futuro. Observatorio Vulcanológico del Sur, Observatorio Vulcanológico del INGEMMET*. Arequipa, Perú: Observatorio Geofísico de la Universidad Nacional San Agustín, Informe técnico, 75.

Malin, M. C., and Sheridan, M. F. (1982). Computer-assisted Mapping of Pyroclastic Surges. *Science* 217, 637–640. doi:10.1126/science.217.4560.637

Maro, G., Caffe, P. J., Romer, R. L., and Trumbull, R. B. (2017). Neogene Mafic Magmatism in the Northern Puna Plateau, Argentina: Generation and Evolution of a Back-Arc Volcanic Suite. *J. Petrology* 58 (8), 1591–1617. doi:10.1093/petrology/egx066

Marrett, R. A., Allmendinger, R. W., Alonso, R. N., and Drake, R. E. (1994). Late Cenozoic Tectonic Evolution of the Puna Plateau and Adjacent Foreland, Northwestern Argentine Andes. *J. S. Am. Earth Sci.* 7 (2), 179–207. doi:10.1016/0895-9811(94)90007-8

Martin, A. J., Umeda, K., Connor, C. B., Weller, J. N., Zhao, D., and Takahashi, M. (2004). Modeling Long-Term Volcanic Hazards through Bayesian Inference: an Example from the Tohoku Volcanic Arc, Japan. *J. Geophys. Res. Solid Earth* 109, B10208. doi:10.1029/2004jb003201

Martinod, J., Gérault, M., Husson, L., and Regard, V. (2020). Widening of the Andes: An Interplay between Subduction Dynamics and Crustal Wedge Tectonics. *Earth-Science Rev.* 204, 103170. doi:10.1016/j.earscirev.2020.103170

Miller, C. D. (1989). "Potential Hazards from Future Volcanic Eruptions in California," in *U.S. Geological Survey Bulletin 1847*. Vancouver, Washington: United States Geological Survey, 17, 2. tables, 1 plate, scale 1:500,000.

Morfulis, M., Báez, W., Retamoso, S., Bardelli, L., Filipovich, R., and Sommer, C. A. (2020). Quantitative Spatial Distribution Analysis of Mafic Monogenic Volcanism in the Southern Puna, Argentina: Implications for Magma Production Rates and Structural Control during its Ascent. *J. S. Am. Earth Sci.* 104, 102852. doi:10.1016/j.jsames.2020.102852

Mpodozis, C., Kay, C., Gardeweg, M., and Coira, B. (1996). in *Geología de la región de Ojos del Salado (Andes Centrales, 27°S): implicancias de la migración hacia el este del frente volcánico Cenozoico Superior* (Buenos Aires: XIII Congreso Geológico Argentino, Actas), 3, 539–548.

Mulcahy, P., Chen, C., Kay, S. M., Brown, L. D., Isacks, B. L., Sandvol, E., et al. (2014). Central Andean Mantle and Crustal Seismicity beneath the Southern Puna Plateau and the Northern Margin of the Chilean-Pampean Flat Slab. *Tectonics* 33 (8), 1636–1658. doi:10.1002/2013tc003393

Mullineaux, D. R. (1976). "Preliminary Overview Map of Volcanic Hazards in the 48 Conterminous United States. Scale 1:7,500,000," in *U.S. Geological Survey Miscellaneous Field Studies Map MF-786*. Vancouver, Washington: United States Geological Survey.

Naranjo, J. A. (2010). "Geología del Complejo Volcánico Lastarria, Región de Antofagasta. Servicio Nacional de Geología y Minería, Carta Geológica de Chile," in *Serie Geología Básica*. (Santiago, Chile: Sernageomin), 123, 33. 1 mapa escala 1:25,000.

Naranjo, J. A., Hevia, F., Arcos, R., and Polanco, E. (2019). "Geología de las áreas Nevado Ojos del Salado y Cerro El Fraile, Región de Atacama. Servicio Nacional de Geología y Minería, Carta Geológica de Chile," in *Serie Geología Básica*. (Santiago, Chile: Sernageomin), 204-205, 1. mapa escala 1:100,000.96

Naranjo, J. A., Villa, V., Ramírez, C., and Pérez de Arce, C. (2018). Volcanism and Tectonism in the Southern Central Andes: Tempo, Styles, and Relationships. *Geosphere* 14 (2), 626–641. doi:10.1130/GES01350.110.1130/ges01350.1

Németh, K., and Kereszturi, G. (2015). Monogenetic Volcanism: Personal Views and Discussion. *Int. J. Earth Sci.* 104, 2131–2146. doi:10.1007/s00531-015-1243-6

Nieto-Torres, A., and Martin Del Pozzo, A. L. (2019). Spatio-temporal Hazard Assessment of a Monogenetic Volcanic Field, Near México City. *J. Volcanol. Geotherm. Res.* 371, 46–58. doi:10.1016/j.jvolgeores.2019.01.006

Norini, G., Bustos, E., Arnosio, M., Baez, W., Zuluaga, M. C., and Roverato, M. (2020). Unusual Volcanic Instability and Sector Collapse Configuration at Chimpa Volcano, Central Andes. *J. Volcanol. Geotherm. Res.* 393, 106807. doi:10.1016/j.jvolgeores.2020.106807

Norini, G., Cogliati, S., Baez, W., Arnosio, M., Bustos, E., Viramonte, J., et al. (2014). The Geological and Structural Evolution of the Cerro Tuzgle Quaternary Stratovolcano in the Back-arc Region of the Central Andes, Argentina. *J. Volcanol. Geotherm. Res.* 285, 214–228. doi:10.1016/j.jvolgeores.2014.08.023

O'Driscoll, L. L., Richards, M. A., and Humphreys, E. D. (2012). Nazca-South America Interactions and the Late Eocene-Late Oligocene Flat-Slab Episode in the Central Andes. *Tectonics* 31 (2), TC2013. doi:10.1029/2011TC003036

Ogburn, S. E., Norgaard, D., Charlton, D., Calder, E. S., Wright, H. M., Lindsay, J., et al. (2020). Volcanic Hazard Maps Database, V. 1.1 (20 September 2020) IAVCEI Commission on Volcanic Hazards and Risk. Available at: https://volcanichazardmaps.org (Accessed December 06, 2021).

O'Hara, D., Karlstrom, L., and Ramsey, D. W. (2020). Time-evolving Surface and Subsurface Signatures of Quaternary Volcanism in the Cascades Arc. *Geology* 48 (11), 1088–1093. doi:10.1130/G47706.1

Papale, P. (2018). Global Time-Size Distribution of Volcanic Eruptions on Earth. *Sci. Rep.* 8, 6838. doi:10.1038/s41598-018-25286-y

Parada, M. A., López-Escobar, L., Oliveros, V., Fuentes, F., Morata, D., Calderón, M., et al. (2007). "Andean Magmatism," in *The Geology of Chile*. Editors T. Moreno and W. Gibbons (London: The Geological Society), 115–146. doi:10.1144/GOCH.4

Perucca, L. P., and Moreiras, S. M. (2009). Seismic and Volcanic Hazards in Argentina. *Dev. Earth Surf. Process.* 13, 267–300. doi:10.1016/S0928-2025(08)10014-1

Pesce, A. H., and Miranda, F. J. (2003). *Catálogo de manifestaciones termales de la República Argentina, Volumen 1: Región Noroeste*, 36. Buenos Aires: Instituto de Geología y Recursos Minerales, Servicio Geológico Minero Argentino, Anales, 165.

Petit-Breuilh, M. E. (2004). *La historia eruptiva de los volcanes hispanoamericanos (Siglos XVI al XX)*. España: Servicio de Publicaciones del Exmo. Cabildo Insultar de Lanzarote – Casa de los Volcanes, 431.

Pritchard, M. E., de Silva, S. L., Michelfelder, G., Zandt, G., McNutt, S. R., Gottsmann, J., et al. (2018). Synthesis: PLUTONS: Investigating the Relationship between Pluton Growth and Volcanism in the Central Andes. *Geosphere* 14 (3), 954–982. doi:10.1130/ges01578.1

Pritchard, M. E., and Simons, M. (2002). A Satellite Geodetic Survey of Large-Scale Deformation of Volcanic Centres in the Central Andes. *Nature* 418, 167–171. doi:10.1038/nature00872

Pure, L. R., Leonard, G. S., Townsend, D. B., Wilson, C. J. N., Calvert, A. T., Cole, R. P., et al. (2020). A High Resolution 40Ar/39Ar Lava Chronology and Edifice Construction History for Tongariro Volcano, New Zealand. *J. Volcanol. Geotherm. Res.* 403, 106993. doi:10.1016/j.jvolgeores.2020.106993

Ramos, V. A. (2009). "Anatomy and Global Context of the Andes: Main Geologic Features and the Andean Orogenic Cycle," in *Backbone of the Americas: Plateau Uplift, Shallow Subduction and Ridge Collision*. Editors S. M. Kay, V. A. Ramos, and W. R. Dickinson (McLean, VA: Geological Society of America Memoir), 204, 31–65. doi:10.1130/2009.1204(02)

Reyes-Hardy, M.-P., Aguilera Barraza, F., Sepúlveda Birke, J. P., Esquivel Cáceres, A., and Inostroza Pizarro, M. (2021). GIS-based Volcanic Hazards, Vulnerability and Risks Assessment of the Guallatiri Volcano, Arica Y Parinacota Region, Chile. *J. S. Am. Earth Sci.* 109, 103262. doi:10.1016/j.jsames.2021.103262

Richards, J. P., Ullrich, T., and Kerrich, R. (2006). The Late Miocene-Quaternary Antofalla Volcanic Complex, Southern Puna, NW Argentina: Protracted History, Diverse Petrology, and Economic Potential. *J. Volcanol. Geotherm. Res.* 152, 197–239. doi:10.1016/j.jvolgeores.2005.10.006

Richards, J. P., and Villeneuve, M. (2001). The Llullaillaco Volcano, Northwest Argentina: Construction by Pleistocene Volcanism and Destruction by Sector Collapse. *J. Volcanol. Geotherm. Res.* 105, 77–105. doi:10.1016/S0377-0273(00)00245-6

Risse, A., Trumbull, R. B., Coira, B., Kay, S. M., and Bogaard, P. v. d. (2008). 40Ar/39Ar Geochronology of Mafic Volcanism in the Back-Arc Region of the Southern Puna Plateau, Argentina. *J. S. Am. Earth Sci.* 26, 1–15. doi:10.1016/j.jsames.2008.03.002

Risse, A., Trumbull, R. B., Kay, S. M., Coira, B., and Romer, R. L. (2013). Multi-stage Evolution of Late Neogene Mantle-Derived Magmas from the Central

Andes Back-Arc in the Southern Puna Plateau of Argentina. *J. Petrology* 54 (10), 1963–1995. doi:10.1093/petrology/egt038

Rodríguez, I., Páez, J., van Wyk de Vries, M., van Wyk de Vries, B., and Godoy, B. (2020). Dynamics and Physical Parameters of the Lastarria Debris Avalanche, Central Andes. *J. Volcanol. Geotherm. Res.* 402, 106990.

Runge, M. G., Bebbington, M. S., Cronin, S. J., Lindsay, J. M., Kenedi, C. L., and Moufti, M. R. H. (2014). Vents to Events: Determining an Eruption Event Record from Volcanic Vent Structures for the Harrat Rahat, Saudi Arabia. *Bull. Volcanol.* 76, 804. doi:10.1007/s00445-014-0804-z

Sampietro Vattuone, M. M., Peña Monné, J. L., Maldonado, M. G., Sancho Marcén, C., Báez, W., Sola, A., et al. (2018). Late Holocene Environmental Changes from Fluvio-Aeolian Morpho-Sedimentary Sequences (Santa María Valley, Northwest Argentina). *Bgm* 129 (4), 647–669. doi:10.21701/bolgeomin.129.4.004

Sampietro-Vattuone, M. M., Báez, W. A., Peña-Monné, J. L., and Sola, A. (2020). Chronological and Geomorphological Approach to the Holocene Tephras from Tafí and Santa María Valleys, NW Argentina. *Quat. Res.* 94, 14–30. doi:10.1017/qua.2019.78

Sandri, L., Thouret, J.-C., Constantinescu, R., Biass, S., and Tonini, R. (2014). Long-term Multi-Hazard Assessment for El Misti Volcano (Peru). *Bull. Volcanol.* 76, 771. doi:10.1007/s00445-013-0771-9

Sandri, L., Tierz, P., Costa, A., and Marzocchi, W. (2018). Probabilistic Hazard from Pyroclastic Density Currents in the Neapolitan Area (Southern Italy). *J. Geophys. Res. Solid Earth* 123, 3474–3500. doi:10.1002/2017jb014890

Schilling, F. R., Trumbull, R. B., Brasse, H., Haberland, C., Asch, G., Bruhn, D., et al. (2006). "Partial Melting in the Central Andean Crust: A Review of Geophysical, Petrophysical, and Petrologic Evidence," in *The Andes: Active Subduction Orogeny*. Editors O. Oncken, G. Chong, G. Franz, P. Giese, H.-J. Gotze, and V. A. Ramos, M.R. Strecker and P. Wigger (Berlin: Springer-Verlag), 459–474.

Schoenbohm, L. M., and Carrapa, B. (2015). "Miocene-Pliocene Shortening, Extension, and Mafic Magmatism Support Small-Scale Lithospheric Foundering in the Central Andes, NW Argentina," in *Geodynamics of a Cordilleran Orogenic System: The Central Andes of Argentina and Northern Chile*. Editors P. G. DeCelles, M. N. Ducea, B. Carrapa, and P. A. Kapp (Geological Society of America Memoir), 212, 167–180. doi:10.1130/2015.1212(09)

Schoenbohm, L. M., and Strecker, M. R. (2009). Normal Faulting along the Southern Margin of the Puna Plateau, Northwest Argentina. *Tectonics* 28, TC5008. doi:10.1029/2008tc002341

Siebe, C., and Macías, J. L. (2003). *Volcanic hazards in the Mexico City metropolitan area from eruptions at Popocatépetl, Nevado de Toluca, and Jocotitlán stratovolcanoes and monogenetic scoria cones in the Sierra Chichinautzin Volcanic Field*, 402. McLean, VA: Geological Society of America Special Paper, 253–329.

Siebert, L., Simkin, T., and Kimberly, P. (2010). *Volcanoes of the World*. 3rd ed. Berkeley: University of California Press, 551.

Siebert, L., and Simkin, T. (2002-2012). *Volcanoes of the World: An Illustrated Catalog of Holocene Volcanoes and Their Eruptions*. Washington, DC: Smithsonian Institution, Global Volcanism Program Digital Information Series. GVP-3.

Sieron, K., Juárez Cerrillo, S. F., González-Zuccolotto, K., Córdoba-Montiel, F., Connor, C. B., Connor, L., et al. (2021). Morphology and Distribution of Monogenetic Volcanoes in Los Tuxtlas Volcanic Field, Veracruz, Mexico: Implications for Hazard Assessment. *Bull. Volcanol.* 83, 47. doi:10.1007/s00445-021-01467-y

Spang, A., Baumann, T. S., and Kaus, B. J. P. (2021). A Multiphysics Approach to Constrain the Dynamics of the Altiplano-Puna Magmatic System. *J. Geophys. Res. Solid Earth* 126 (7), e2021JB021725. doi:10.1029/2021jb021725

Stern, C. R., Moreno, H., López-Escobar, L., Clavero, J. E., Lara, L. E., Naranjo, J. A., et al. (2007). "Chilean Volcanoes," in *The Geology of Chile*. Editors T. Moreno and W. Gibbons (London, UK: Geological Society of London), 149–180.

Talchabhadel, R., Nakagawa, H., Kawaike, K., Yamanoi, K., and Thapa, B. R. (2021). Assessment of Vertical Accuracy of Open Source 30m Resolution Space-Borne Digital Elevation Models. *Geomatics, Nat. Hazards Risk* 12 (1), 939–960. doi:10.1080/19475705.2021.1910575

Tassi, F., Aguilera, F., Vaselli, O., Darrah, T., and Medina, E. (2011). Gas Discharges from Four Remote Volcanoes in Northern Chile (Putana, Olca, Irruputuncu and Alitar): a Geochemical Survey. *Ann. Geophys.* 54, 2. doi:10.4401/ag-5173

Tassi, F., Aguilera, F., Vaselli, O., Medina, E., Tedesco, D., Delgado Huertas, A., et al. (2009). The Magmatic- and Hydrothermal-Dominated Fumarolic System at the Active Crater of Lascar Volcano, Northern Chile. *Bull. Volcanol.* 71, 171–183. doi:10.1007/s00445-008-0216-z

Tibaldi, A., Bonali, F. L., and Corazzato, C. (2017). Structural Control on Volcanoes and Magma Paths from Local- to Orogen-Scale: The Central Andes Case. *Tectonophysics* 699, 16–41. doi:10.1016/j.tecto.2017.01.005

Trumbull, R. B., Riller, U., Oncken, O., Scheuber, E., Munier, K., and Hongn, F. (2006). "The Time-Space Distribution of Cenozoic Volcanism in the South-Central Andes: a New Data Compilation and Some Tectonic Implications," in *The Andes: Active Subduction Orogeny*. Editors O. Oncken, G. Chong, G. Franz, P. Giese, H.-J. Gotze, V.A. Ramos, M.R. Strecker, and P. Wigger (Berlin: Springer-Verlag), 29–43.

Ureta, G., Aguilera, F., Németh, K., Inostroza, M., González, C., Zimmer, M., et al. (2020). Transition from Small-Volume Ephemeral Lava Emission to Explosive Hydrovolcanism: The Case of Cerro Tujle Maar, Northern Chile. *J. S. Am. Earth Sci.* 104, 102885. doi:10.1016/j.jsames.2020.102885

Ureta, G., Németh, K., Aguilera, F., Kósik, S., González, R., Menzies, A., et al. (2021). Evolution of a Magmatic to a Phreatomagmatic Volcanic System: The Birth of a Monogenetic Volcanic Field, Tilocálar Volcanoes, Northern Chile. *J. Volcanol. Geotherm. Res.* 414, 107243. doi:10.1016/j.jvolgeores.2021.107243

Valentine, G. A., and Gregg, T. K. P. (2008). Continental Basaltic Volcanoes - Processes and Problems. *J. Volcanol. Geotherm. Res.* 177, 857–873. doi:10.1016/j.jvolgeores.2008.01.050

van Alderwerelt, B. (2017). *Diverse Monogenetic Volcanism across the Main Arc of the Central Andes, Northern Chile* (Iowa City, Iowa: University of Iowa), 427. PhD Thesis.

van Wyk de Vries, B., Self, S., Francis, P. W., and Keszthelyi, L. (2001). A Gravitational Spreading Origin for the Socompa Debris Avalanche. *J. Volcanol. Geotherm. Res.* 105 (3), 225–247. doi:10.1016/S0377-0273(00)00252-3

Vélez, M. L., Bustos, E., Euillades, L., Blanco, M., López, J. F. S., Barbero, I., et al. (2021). Ground Deformation at the Cerro Blanco Caldera: A Case of Subsidence at the Central Andes Backarc. *J. S. Am. Earth Sci.* 106, 102941. doi:10.1016/j.jsames.2020.102941

Ward, K. M., Delph, J. R., Zandt, G., Beck, S. L., and Ducea, M. N. (2017). Magmatic Evolution of a Cordilleran Flare-Up and its Role in the Creation of Silicic Crust. *Sci. Rep.* 7, 9047. doi:10.1038/s41598-017-09015-510.1038/s41598-017-09015-5

Ward, K. M., Porter, R. C., Zandt, G., Beck, S. L., Wagner, L. S., Minaya, E., et al. (2013). Ambient Noise Tomography across the Central Andes. *Geophys. J. Int.* 194 (3), 1559–1573. doi:10.1093/gji/ggt166

Ward, K. M., Zandt, G., Beck, S. L., Christensen, D. H., and McFarlin, H. (2014). Seismic Imaging of the Magmatic Underpinnings beneath the Altiplano-Puna Volcanic Complex from the Joint Inversion of Surface Wave Dispersion and Receiver Functions. *Earth Planet. Sci. Lett.* 404, 43–53. doi:10.1016/j.epsl.2014.07.022

Conflict of Interest: The authors declare that the research was conducted in the absence of any commercial or financial relationships that could be construed as a potential conflict of interest.

frontiers | Frontiers in Earth Science

ORIGINAL RESEARCH
published: 05 July 2022
doi: 10.3389/feart.2022.897307

The Volcanic Landscapes of the Ancient Hunter-Gatherers of the Atacama Desert Through Their Lithic Remains

Rodrigo Loyola[1,2]*, Valentina Figueroa[1], Lautaro Núñez[1], Marco Vasquez[3], Christian Espíndola[4], Millarca Valenzuela[3,5] and Manuel Prieto[6]

[1]Instituto de Investigaciones Arqueológicas y Museo, Universidad Católica del Norte, San Pedro de Atacama, Chile, [2]UMR 8068 Technologie et Ethnologie des Mondes PréhistoriqueS, Université Paris Nanterre, Nanterre, France, [3]Departamento de Ciencias Geológicas, Universidad Católica del Norte, Antofagasta, Chile, [4]Comunidad Atacameña de Toconao, San Pedro de Atacama, Chile, [5]Millennium Institute of Astrophysics, Santiago, Chile, [6]Departamento de Ciencias Históricas y Geográficas, Facultad de Educación y Humanidades, Universidad de Tarapacá, Arica, Chile

Since ancient times Andean societies have formed an intimate relationship with volcanoes, the beginnings of which can be traced right back to the initial peopling of the region. By studying rocks used for stone tools and other everyday artifacts, we explore the volcanic landscapes of early hunter-gatherer groups (11,500–9,500 cal BP) of the highlands of the Atacama Desert (22–24°S/67–68°W). Petrological classification of the lithic assemblages of three Early Holocene archaeological sites showed the procurement of a great diversity of volcanic and subvolcanic rocks, including pumice, granitic rocks, micro-diorites, a large variety of tuffs and andesites, dacites, cherts, basalts, obsidians, among others. Field surveys enabled us to detect many of their sources related to volcanic features such as craters, maars, caldera-domes, lava flows, probable hydrothermal deposits, and ignimbrites. In these places, we also document large quarry-workshops and campsites from different periods, indicating intense and repeated human occupation over time. By comparing the artifacts with geological samples collected in the field, it was possible to assign the source of origin of a large part of the archaeological assemblages. Our data suggest that the volcanic features of the Atacama highlands were integrated into the mobility and interaction networks of ancient hunter-gatherer groups at an early date.

Keywords: volcanism, Andes mountains, hunter-gatherers, lithic raw materials, geoarchaeology

Edited by:
Gary Michelfelder,
Missouri State University,
United States

Reviewed by:
Marie-Noelle Guilbaud,
National Autonomous University of Mexico, Mexico
Hugo Nami,
Consejo Nacional de Investigaciones Científicas y Técnicas (CONICET), Argentina

Correspondence:
Rodrigo Loyola
rodarkeo@gmail.com

Specialty section:
This article was submitted to Volcanology,
a section of the journal
Frontiers in Earth Science

Received: *16 March 2022*
Accepted: *08 June 2022*
Published: *05 July 2022*

Citation:
Loyola R, Figueroa V, Núñez L, Vasquez M, Espíndola C, Valenzuela M and Prieto M (2022) The Volcanic Landscapes of the Ancient Hunter-Gatherers of the Atacama Desert Through Their Lithic Remains. Front. Earth Sci. 10:897307. doi: 10.3389/feart.2022.897307

1 INTRODUCTION

In the Andes region, volcanism is a multidimensional phenomenon that permeates different aspects of the everyday life and worldview of human societies. In the Andean cosmovision, volcanoes represent deities that are the subject of devotion and offerings during both ceremonial occasions and everyday prayers. As was remarked by Harris and Bouysse-Cassagne, they are mediators that allow communication between the surface and the underworld known as the "*mancca pasha*" (Bouysse-Cassagne and Bouysse, 1984; Bouysse-Cassagne and Harris, 1987; Harris, 1987; Bouysse-Cassagne and Bouysse, 1988). In Inka times, volcanoes and the high peaks of the Andes range were the scenario of complex rites and human sacrifices known as *capaccocha* (D'Altroy et al., 2007; Reinhard and Ceruti, 2010; Mignone, 2010; Mignone, 2015). Volcanic features were also used as geographic markers for the observation of astronomical events and the reproduction of the annual cycle as the case of the Llullaillaco Volcano (Sanhueza, 2004). For pre- and post-Columbian communities, they were also geographical landmarks used for spatial orientation, especially by travelers and caravans that crossed the mountain passes and the Atacama Desert (Núñez and Dillehay, 1979; Berenguer, 2004). Eruptions were not only catastrophic disasters; they were complex events that affected recurrently the cultural dynamics in the past (Bouysse-Cassagne and Bouysse, 1984; Bouysse-Cassagne and Bouysse, 1988; Pärssinen, 2015).

In the highlands of the Atacama Desert (south-central Andes), research carried out over the last 20 years into the early peopling has revealed abundant lithic industries in stratified deposits (Núñez et al., 2002; Núñez et al., 2005). The lithic assemblages recovered in various archaeological sites include a wide variety of stone tools used for different purposes: hunting large and small game; grinding plants; processing fur, wood and pigment, and the manufacture of ornaments (Loyola et al., 2019a). These objects were tremendously important not only for subsistence but also for the reproduction of social life; they were even included as offerings in ceremonies and mortuary rites in later periods or used as exchange goods (Loyola et al., 2021). The sources and diversity of these rocks, mainly of volcanic and subvolcanic origin, give us clues about the early links of these ancient populations with Andean volcanoes. Beyond the catastrophic effects of eruptions, this record allows us to approach the relationship between the first hunter-gatherer societies and volcanism in their daily lives.

Using an interdisciplinary and geo-archaeological approach, we studied the lithic assemblages recovered from three archaeological sites dated between 11,500 and 9,500 cal BP: Tuina-5, Tulán-67 and Tambillo-1 (Núñez et al., 2002; 2005). After lithological classification of the lithic raw materials, surveys were carried out on wide spatial scales which allowed us to document at least 10 sources of lithic procurement in an area

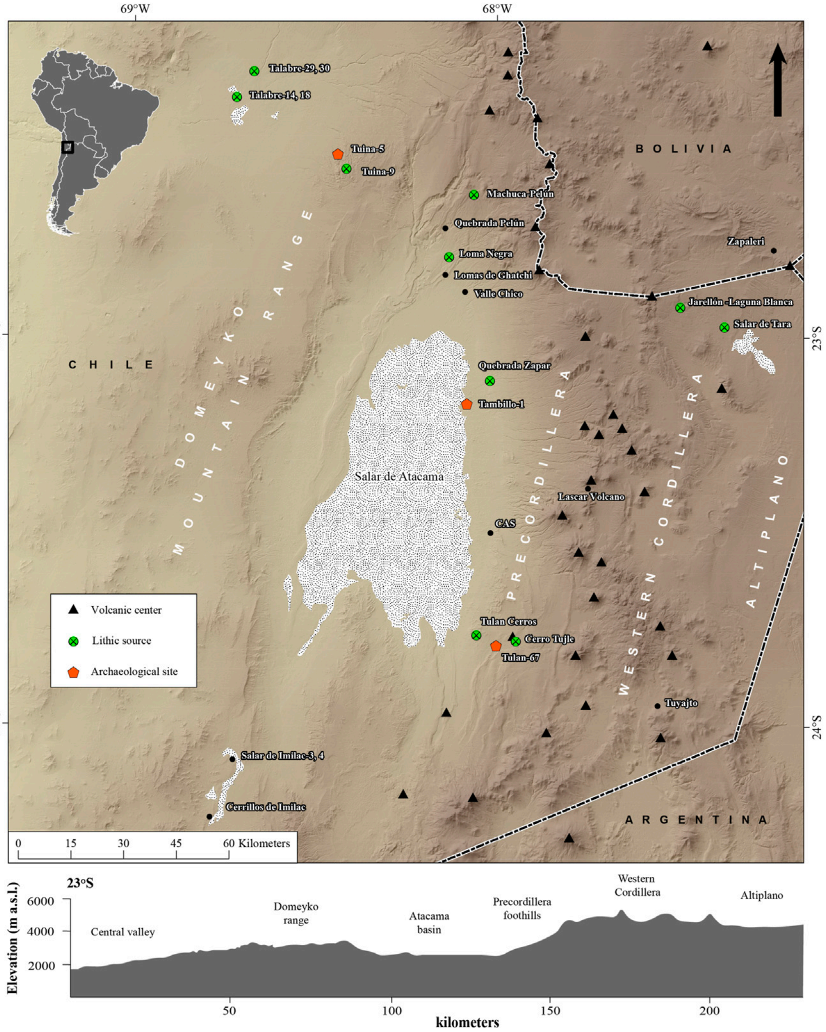

FIGURE 1 | Map of archaeological sites studied (red pentagons), lithic raw material sources (green circles), and principal volcanoes of the Atacama basin (black triangles).

TABLE 1 | Lithic assemblages studied, by archaeological site, stratigraphic layer, chronology and placement (after Núñez et al., 2005). Radiocarbon dates were calibrated using the ShCal020 curve (Hoggs et al., 2020) in OxCal software.

Site	Layer	^{14}C yr BP	Cal yr. BP	Site placement
Tuina-5	IV	10,060 + 70	11,830 – 11,260	Cave in dry ravine (3,200 m a.s.l)
		9.840 + 110	11,705 – 10,779	
Tambillo-1	I, II, and III	8,590 ± 130	10,119 – 9,144	Open-air campsite in border of salt-flat (2,200 m a.s.l)
		8,870 ± 70	10,178 – 9,631	
Tulán-67	VII	9,290 ± 100 BP	10,682 – 10,231	Rock-shelter in the border of Tulán ravine (2,580 m a.s.l)

of more than 10,000 km^2. Most of them correspond to volcanic and subvolcanic formations, resulting from the active volcanism of the Andes in different geological epochs. Comparison of the archaeological assemblages with geological samples recovered at the sources suggests the procurement and circulation of rocks across a vast high-mountain territory, and extending outside the region. The study of lithic industries will enable us to reveal a rich volcanic landscape that was frequented and internalized in the cognitive maps of the ancient human societies of the Atacama. Such episodes mark the beginning of a complex relationship between humans and volcanism, characterized by the resilience and innovation of Andean societies.

2 ARCHAEOLOGICAL BACKGROUND

Early hunter-gatherer societies inhabited the Atacama basin from 12,500 to 9,500 cal BP (Núñez et al., 2002; Núñez et al., 2005). Paleoenvironmental reconstructions indicate that during this period, the climate transitioned from the wetter conditions of the Late Pleistocene to a progressively more arid environment in the Holocene (Grosjean et al., 2001; Quade et al., 2008; Sáez et al., 2016). In this dynamic environment, pioneer Andean societies progressively populated the patches of available resources scattered over a contrasting environmental setting, ranging from 2,000 m a.s.l, where

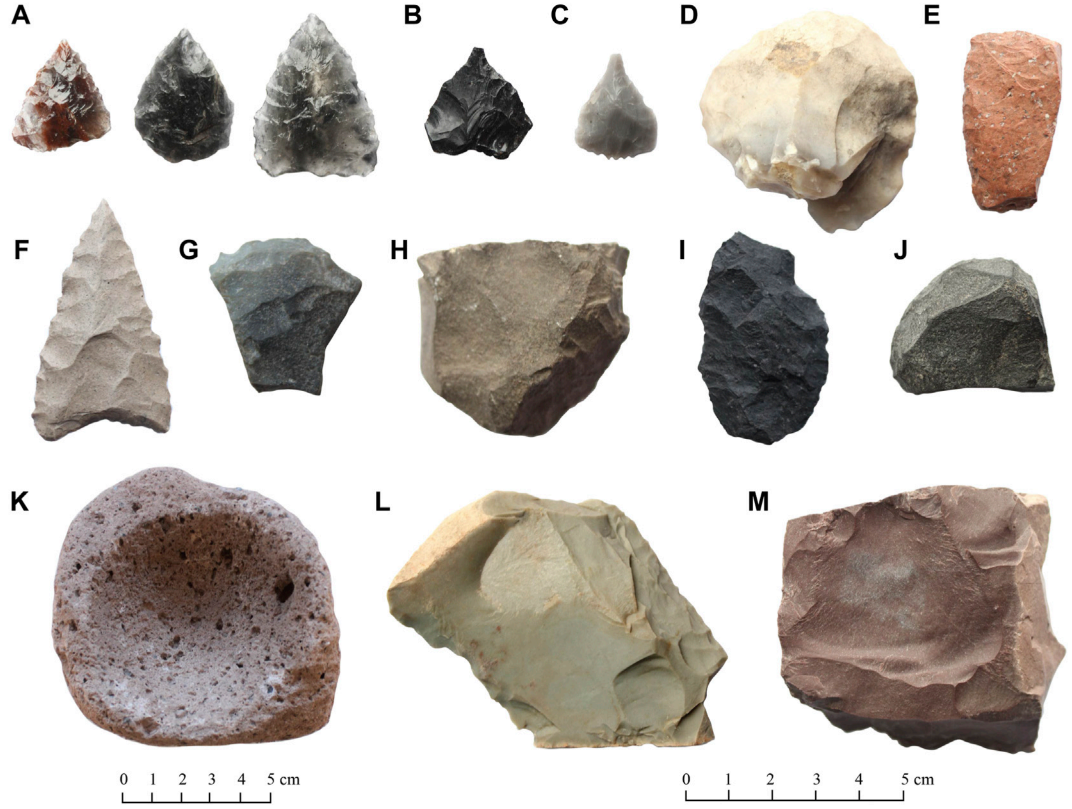

FIGURE 2 | Lithic assemblages and raw materials: **(A)** bifacial projectile points in gray translucent obsidian (Tuina-5 and Tambillo-1); **(B)** micro-perforator in shiny black obsidian (Tambillo-1); **(C)** bifacial perforator in opaque gray obsidian (Tulán-67); **(D)** end-scraper on white chert (Tuina-5); **(E)** side-scraper on red dacitic tuff (Tambillo-1); **(F)** bifacial projectile point on gray silicified tuff; **(G)** retouched flake on greenish ash dacitic tuff (Tambillo-1); **(H)** core on devitrified brown tuff (Tulán-67); **(I)** retouched piece on black andesite with crystals (Tambillo-1); **(J)** end-scraper on black aphiric andesite (Tulán-67); **(K)** container-mortar on gray-pink pumice (Tambillo-1); **(L)** retouched flake on epidotized siliceous rock (Tuina-5); **(M)** core on brown andesitic tuff (Tuina-5).

TABLE 2 | General rock classes and sub-varieties by archaeological site.

Rock classes and sub-varieties	**Tambillo-1**		**Tulán-67**		**Tuina-5**	
	n	**%**	***n***	**%**	***n***	**%**
Obsidian	1938	44.70	742	21.99	42	2,30
Translucent gray obsidian (OB-1)	429	9.89	14	0.41	39	2,14
Translucent brown obsidian (OB-2)	27	0.62	2	0.06		0
Opaque gray obsidian (OB-3)	33	0.76	659	19.53		0
Shiny black obsidian (OB-4)	1101	25.39	49	1.45	2	0,11
Shiny reddish-black obsidian (OB-5)	287	6.62		0		0
Shiny black-red obsidian (OB-6)	29	0.67	3	0.09		0
Translucent obsidian with fluid inclusions (OB-7)	5	0.12	4	0.12		0
Translucent obsidian (OB-8)	3	0.07		0		0
Translucent obsidian with black inclusions (OB-9)	2	0.05	3	0.09		0
Divers	18	0.42	8	0.24	1	0,05
Indeterminated	4	0.09		0		0
Siliceous rock	868	20.02	662	19.61	1296	70,97
White chert (SR-1)	553	12.75	108	3.20	407	22,29
Rock crystal (SR-2)		0	3	0.09		0
Green epidotized silicified rock (SR-3)	59	1.36	18	0.53	868	47,54
White chert with spots (dendritic habit) (SR-4)		0	2	0.06		0
White-yellow siliceous rock (SR-5)	1	0.02	310	9.19		0
Brown siliceous rock with reddish spots (SR-6)	2	0.05	33	0.98		0
Gray siliceous rock (SR-7)	44	1.01	24	0.71	3	0,16
Diverse	158	3.64	59	1.75	9	0,49
Thermo-altered	29	0.67	89	2.64	1	0,05
Indeterminated	22	0.51	16	0.47	8	0,44
Andesite	378	8.72	242	7.17	12	0,66
Black hornblende andesite (AN-1)	1	0.02	71	2.10		0
Black andesite white crystals (AN-2)	98	2.26	12	0.36		0
Black pyroxene andesite (AN-3)	78	1.80	2	0.06		0
Aphiric black andesite (AN-4)	8	0.18	121	3.59		0
Greenish hornblende andesite (AN-5)	122	2.81	2	0.06		0
Black andesite with tabular hornblendes (AN-6)	5	0.12	13	0.39		0
Divers	57	1.31	20	0.59	1	0,05
Indeterminated	9	0.21	1	0.03	11	0,60
Tuff	763	17.60	1483	43.94	324	17,74
Brown andesitic tuff (TF-1)	8	0.18		0	265	14,51
Devitrified cineritic tuff (TF-2)	187	4.31	1414	41.90	1	0,05
Red dacitic tuff with white crystals (TF-3)	300	6.92	11	0.33	53	2,90
Greenish brown dacitic tuff (TF-4)	81	1.87	2	0.06		0
Crystalline ash tuff (TF-5)	48	1.11		0		0
Pink tuff with flow (TF-6)	1	0.02		0		0
Gray-cream silicified tuff (TF-7)	26	0.60	11	0.33		0
Divers	100	2.31	9	0.27	4	0,22
Thermo-altered	3	0.07	14	0.41	1	0,05
Indeterminated	9	0.21	22	0.65		0
Dacite	35	0.81	5	0.15		0
Jaspoid	108	2.49	18	0.53	9	0,49
Quartzite	24	0.55	33	0.98		0
Basalt	38	0.88	89	2.64	33	1,81
Granitic rock	30	0.69	1	0.03		0
Micro-diorite	46	1.06		0	102	5,59
Mudstone	10	0.23	7	0.21	1	0,05
Pumice	16	0.37		0		0
Porphyry		0		0	3	0,16
Intrusive red rock	45	1.04		0		0
Green volcanic rock	2	0.05		0		0
Quartz	5	0.12	4	0.12	1	0,05
Thermo-altered	14	0.32	36	1.07	2	0,11
Indeterminate	16	0.37	53	1.57	1	0,05
Total	4336	100	3375	100	1826	100

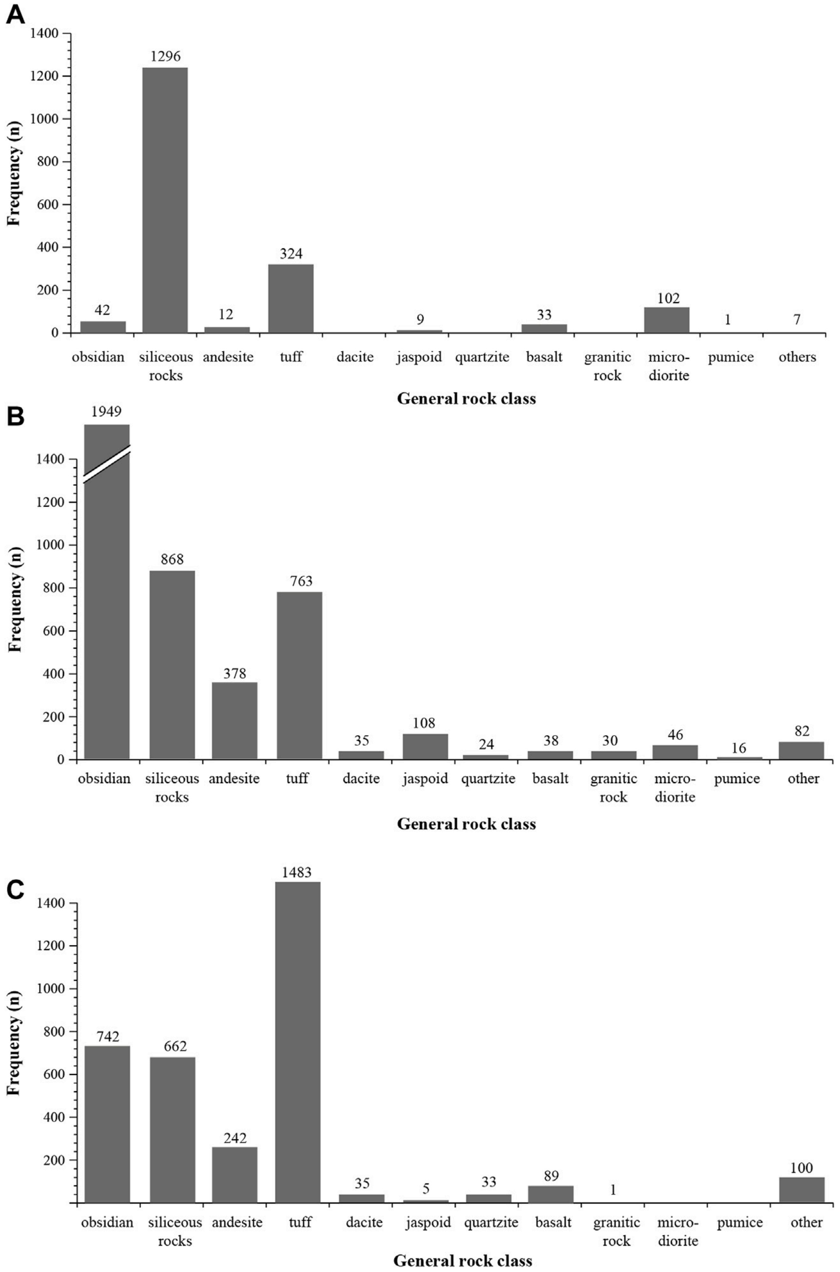

FIGURE 3 | Frequency of archaeological artifacts by rock class: **(A)** Tuina-5 (IV); **(B)** Tambillo-1; **(C)** Tulán-67(VII).

absolute desert predominates, to the more productive environmental patches of the Andes highlands above 4,000 m a.s.l. According to the evidence, the economy and subsistence of these groups were centered mainly on gathering plants in wetlands and hunting wild camelids such as the vicuña and the guanaco, as well as birds and rodents. Some evidence also reveals the consumption of the last remnants of extinct horse (Equidae) in Tuina-5 (Cartajena, 2003; Cartajena et al., 2006).

The Early Archaic Period is subdivided into two subphases. During the Tuina Phase (12,500 to 11,500 cal BP), the first human settlements occupied mainly caves and rock-shelters of the intermediate floors (2,700–3,200 m a.s.l) such as Tuina-1, Tuina-5, San Lorenzo-1, and Tulán-109 (Núñez et al., 2005). The evidence recovered at these sites suggests temporary occupations for logistical use as part of an initial peopling process (Loyola et al., 2019b). Diagnostic artifacts of this subphase are triangular non-stemmed Tuina projectile points and large retouched flake tools, anvils, and chopping tools. In the subsequent subphase Tambillo (11,500–9,500 cal BP), the human peopling process was consolidated. Archaeological sites of this period are more significant and denser due to more stable

TABLE 3 | Sources of lithic procurement identified in the Atacama basin.

Source	Rock class	Geoform	Geologic formation	Archaeologic evidence
Loma Negra–Puripica	Black hornblende andesite	Lava flow	Stratum-volcanoes III (Qv) (Pleistocene-Holocene)	Extensive area of workshops and knapping *loci*. An industry of blades and flakes, and circular structures were documented.
Machuca–Pelún	Gray and brown translucent obsidian	Caldera-dome (?)	Ignimbrite Puripicar (Pip)–Pliocene	Surface scatter of small nodules associated with ignimbritic formation. Scarce knapping evidence.
Jarellón–Laguna Blanca	Shiny reddish-black obsidian	Caldera-dome	Volcanic Complex II (c) (Plv)–Pliocene	Discrete knapping events of small nodules and blocks associated in some cases with stone structures and rock-shelters.
Salar de Tara	Shiny reddish-black obsidian	Ignimbritic flow	Filo Delgado ignimbrites (Plfd) (?)–Pliocene	Surface scatters of medium and small nodules in a large area with some evidence of *in situ* knapping.
Cerro Tujle	Black andesite	*Maar* crater	Volcanic Complex III (Qv)–Quaternary	Extensive quarry-workshop around the crater. Industry of flakes and blades in large blocks and fragments of black andesite.
Quebrada Zapar	Gray-pink Pumice	Ignimbritic flow	Cajón Ignimbrite (Pc)–Lower Pleistocene	Outcrop of subrounded and elongated pumice blocks on the edge of the Zapar ravine. No evidence of primary processing.
Tulán Cerros	Devitrified cineritic tuff	Outcrop on Hill top	Cerros Negros Formation (Pcn)–Pérmic?	Large, scattered quarry-workshops of variable extension of blade industry on block, circular structures and engraved plaquettes.
Salar de Talabre	Gray-cream silicified tuff	hydrothermal deposit (?)	Lasana Formation - Talabre Member (Ml2)/Middle Miocene–Lower Upper Miocene	Quarry workshops north of the salar (Talabre 29 and 30) and southeast of the current edge of the Salar de Talabre (Talabre 14 and 18). An industry of large flakes and bifaces predominates.
Cerros de Tuina	Green epidotized silicified rock and brown andesitic tuff	Hillside outcrop	Tuina Formation (Pt) (?)–Late Permian-Middle Triassic	Extensive quarry-workshop on a hillside with abundant material on the surface and a circular stone structure. Predominance of flake industry over medium size blocks and plaquettes.

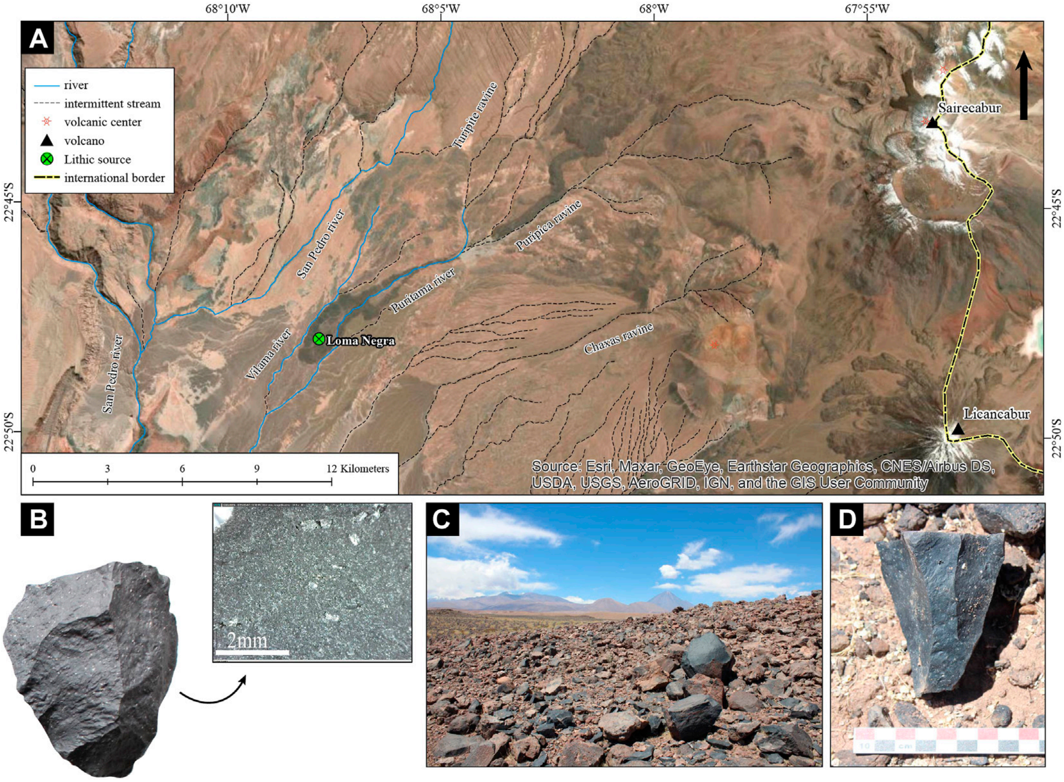

Source: Esri, Maxar, GeoEye, Earthstar Geographics, CNES/Airbus DS, USDA, USGS, AeroGRID, IGN, and the GIS User Community

FIGURE 4 | Loma Negra-Puripica source: **(A)** geological context; **(B)** raw material sample; **(C)** quarry-workshop site; **(D)** discarded blade core of black andesite.

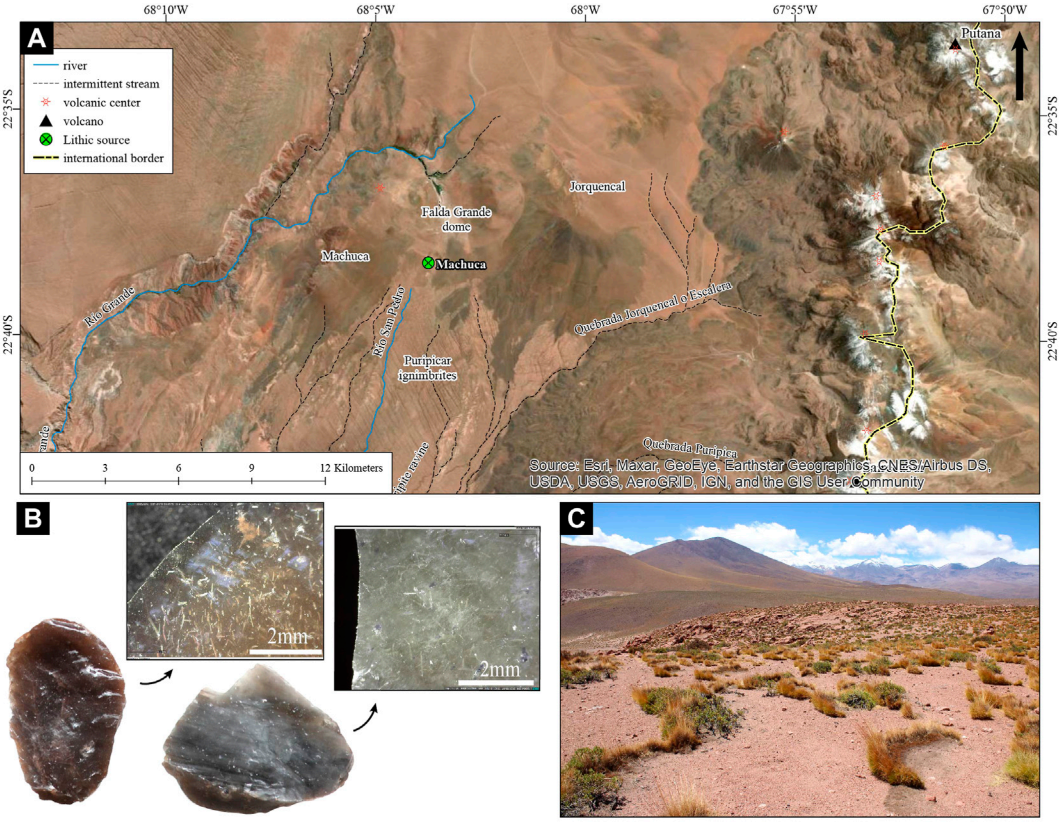

FIGURE 5 | Machuca-Pelún source: **(A)** geological context; **(B)** raw material samples; **(C)** scatter area of raw materials.

residential occupations (Núñez et al., 2016). During this phase, the settlement system incorporated a greater diversity of inhabited environments, complemented by seasonal mobility between the desert lowlands and the Andes highlands (Loyola et al., 2019a). Evidence of this has been recorded in various sites such as Tambillo-1, Tulán-67, Tulán-68, Tulán-109, Aguas Calientes-I-1, Tara-2 and Tuyajto-1 (Núñez et al., 2005). The excavation of these sites has allowed the recovery of a profuse lithic industry, represented by triangular projectile points, obsidian drills, small nail-scrapers, and abundant grinding tools.

3 STUDY AREA: GEOLOGICAL AND LITHOLOGICAL SETTING

The Atacama Basin (21–22°S/67–68°W) is located within what is now known, in Chile's political-administrative system, as the II Region of Antofagasta (northern Chile). It corresponds to an extensive basin of more than 3,000 km^2, limited by the Domeyko range to the west and the Andes Mountains to the east. Geomorphologically, it is inserted in the great depression of pre-Andean salt flats. The study area presents three climates at different altitudinal levels, according to the Köppen-Geiger classification: cold arid with dry winter [BWk(w)], cold semi-arid with dry winter [Bsk(w)], and tundra with dry winter [ET(w)]. At the base level of the basin are extensive saline deposits composed mainly of halite, with a surface area of 1,100 km^2 and a depth of 900 m, surrounded by a marginal zone of saline silt of about 2,000 km^2 that forms the great Salar de Atacama (Atacama salt flat) (Alonso and Risacher, 1996). This large saline crust results from the intense evaporation of surface waters, including ponds and shallow lagoons around its borders. At its phreatic level, the Salar de Atacama is fed by a dendritic drainage network that descends from the Andes Mountains through deep ravines. Some small salt flats and high saline lakes are formed in sub-basins above 4,000 m a.s.l, such as Aguas Calientes, Tuyajto, Tara and Miscanti (Risacher et al., 2003). The lithological components of the Atacama basin and the distribution of volcanic rocks can be understood through the general morphostructure of the basin, as shown in **Figure 1**.

3.1 The Domeyko Mountain Range

The Domeyko mountain range in northern Chile runs from north to south with an average altitude of 3,000 m a.s.l. The study area is characterized by mountainous features, pediplanes and alluvial fans (Ramírez and Gardeweg, 1982). The local lithology comprises Upper Carboniferous to Permian ignimbrites and rhyolitic domes, Triassic lacustrine fossiliferous strata, and

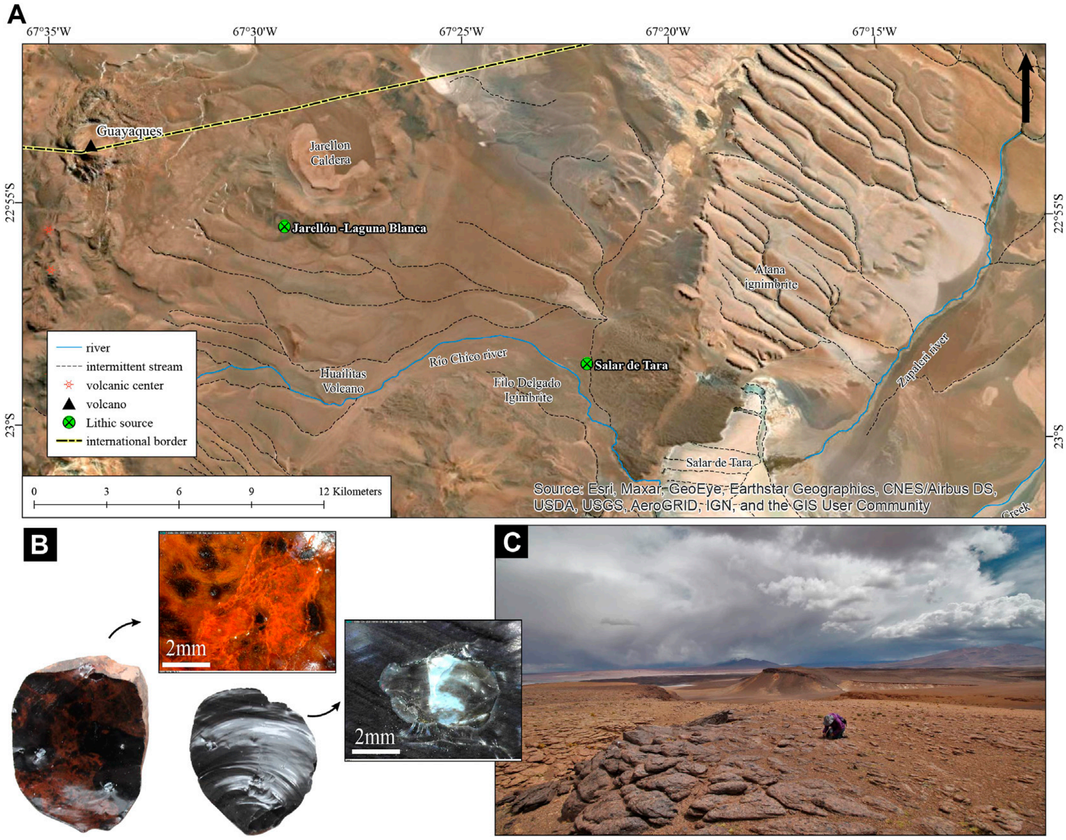

Source: Esri, Maxar, GeoEye, Earthstar Geographics, CNES/Airbus DS, USDA, USGS, AeroGRID, IGN, and the GIS User Community

FIGURE 6 | Jarellón-Laguna Blanca source: **(A)** geological context; **(B)** raw material sample; **(C)** scatter area of obsidian samples.

Cretaceous to Miocene continental sediments (Marinovic and Lahsen, 1984; Mpodozis et al., 2005). To the northwest of the study area, the Cerros de Tuina range is associated with a set of inverse faults (Henríquez et al., 2014).

3.2 The Precordillera Foothills

The Precordillera rises from the low, flat terrain of the Salar de Atacama to the Andes highlands. It presents irregular topography with a slope of 3-5°o̲, dissected by a dendritic drainage network of ravines up to 200 m deep (Ramírez and Gardeweg, 1982), and by ranges of small hills such as Cas, Peine and Lila hills. Lithologically, it is characterized by outcrops of Paleozoic, Mesozoic and Cenozoic rocks that include sandstones and shales, andesites, dacites, and tuffs (Niemeyer, 2013).

3.3 The Andes Mountain Range

The Andes consists of an imposing mountain range that extends longitudinally from north to south, formed by volcanic features, domes, and hills set on the rhyolitic plateau. In the study area, this unit includes: 1) The Western Cordillera that reaches 6,800 m a.s.l, consisting mainly of Cenozoic volcanic rocks and characterized by a strip of stratovolcanoes overlying older ignimbritic layers (Allmendinger et al., 1997); and 2) the Altiplano or Puna, an extensive ingimbritic *plateau* that extends through northeastern Chile, Argentina, Peru, and Bolivia at a mean altitude of 4,000 m a.s.l (Isacks, 1988). Locally, the volcanic deposits are formed mainly by ignimbrites, volcanic complexes, and aerial pyroclastic deposits from the Upper Miocene to the Quaternary. The ignimbrites are made up of tuffs of different degrees of welding, mainly dacitic and rhyolitic in composition (Gardeweg and Ramírez, 1985). The stratovolcanoes and stratified volcanic sequences show an andesitic and subordinately basaltic and dacitic composition and, to a lesser extent, pyroclastic cones, domes, and subcircular structures (craters) of rhyolitic composition. Upper pre-Miocene intrusive and folded sedimentary rocks appear in erosion windows and isolated hills (Gardeweg et al., 1998).

4 MATERIALS AND METHODS

The lithic assemblages studied in this work were recovered from stratigraphic layers of three archaeological sites: Tuina-5, Tambillo-1, and Tulán-67 (Núñez et al., 2002; Núñez et al., 2005) (**Table 1**). In the first stage, a petrographic classification of the complete archaeological lithic assemblages was carried out. The object of this was to define general groups based on general rock classes and sub-varieties according to variables such as color,

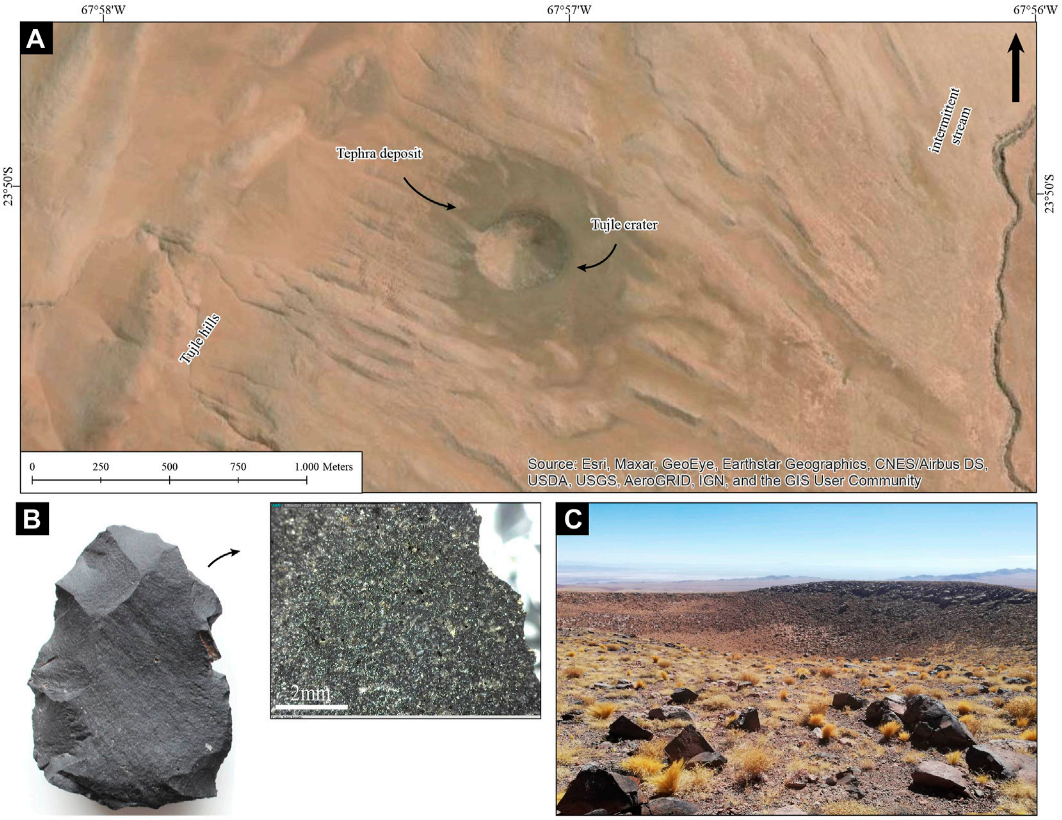

FIGURE 7 | Cerro Tujle source: **(A)** geological context; **(B)** raw material sample; **(C)** quarry-workshop site near to the crater border.

texture, granulometry, presence of impurities, and cortex, considering the existing local classifications[1,2,3].

The second stage consisted of locating and characterizing the raw material sources through directed surveys in the field. The archaeological and geological data of the Atacama basin and its surroundings were consulted to define areas of interest according to the lithologies observed and recognized in the archaeological lithic assemblages. The following data sourced were consulted: Calama sheet (1:250,000) (Marinovic and Lahsen, 1984), Zapaleri sheet (1:250,000) (Gardeweg and Ramírez, 1985), Toconao sheet (1:250,000) (Ramírez and Gardeweg, 1982), Chiu chart (1:50,000) (Blanco and Tomlinson, 2009), Lascar Volcano chart (1:50,000) (Gardeweg et al., 2011), San Pedro de Atacama chart (1:100,000) (Henríquez et al., 2014), Lila-Peine chart (1:100,000) (Niemeyer, 2013). Between 2019 and 2021, various field surveys were carried out and samples were taken from the sources identified. The archaeological artifacts and the geological samples recovered from the lithic procurement sources were compared in the third stage using a magnifying glass (30x) and a Dino-Lite digital microscope (30–250x). Lithological markers - understood as characteristic elements shared by rocks from the same outcrop-were defined that allowed the source of origin to be directly assigned.

5 RESULTS

5.1 Archaeological Assemblages and Lithic Raw Materials

The lithological classification of lithic assemblages identified a wide diversity of rocks, most of them of volcanic and subvolcanic origin, forming a rich and varied lithic assemblage (**Figure 2**). The main types identified were obsidian, cherts, and other siliceous rocks, andesites and tuffs, in addition to other minorities such as basalts, dacites, pumices, micro-diorites, and granitic and porphyritic rocks, among many others. A count of the rock classes and sub-varieties (with their respective codes used hereinafter) is presented in **Table 2**. Among the predominant rocks, obsidian was clearly much sought-after, being used mainly in the manufacture of projectile points and micro-perforators (**Figures 2A–C**). The

---

[1] Grosjean, M. 2003. Introduction to rock and mineral classification: a manual for archaeologist with an emphasis on the Atacama Desert, Chile. San Pedro de Atacama: Fondecyt 1020316. (Unpublished Report).

[2] Lau-Milla, R. 2007. Metodología y aplicación de geoarqueología para la caracterización litológica de sitios arqueológicos de la II Región. Antofagasta: Universidad Católica del Norte. Unpublished thesis.

[3] Vasquez, M. 2021. Caracterización y Procedencia de Materias Primas Líticas en sitios arqueológicos del Periodo Arcaico: Una Aproximación Geo-Arqueológica a los Paisajes Líticos del Desierto de Atacama. Antofagasta: Universidad Católica del Norte. Unpublished tesis.

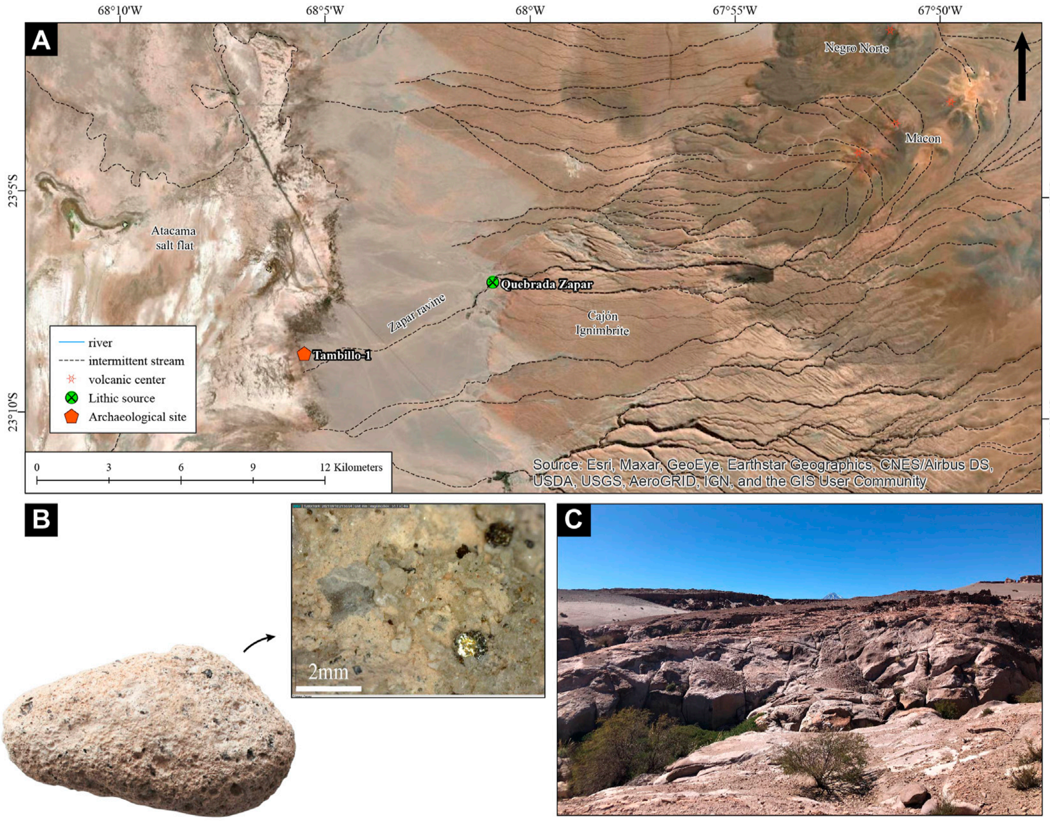

FIGURE 8 | Quebrada Zapar Source: **(A)** geological context; **(B)** pumice sample; **(C)** Zapar Ravine outcrops.

obsidian class breaks down into several sub-varieties, among which are shiny black (OB-4, **Figure 2B**), shiny reddish-black (OB-5), translucent gray (OB-1, **Figure 2A**), and opaque gray (OB-3, **Figure 2C**). The cherts and silicious rocks comprise several types of rocks but are mostly represented by a white chert with abundant vesicles and rough cortex (SR-1, **Figure 2C**), a white-yellow siliceous rock (SR-5), and a green epidotized silicified rock (SR-3, **Figure 2L**). They were used to produce retouched flake-tools and artifacts of various kinds such as end-scrapers, side-scrapers and also bifacial projectile points. The tuffs consist mainly of a red dacitic tuff with white crystals (TF-3, **Figure 2E**), a gray-cream silicified tuff with black inclusions (TF-7, **Figure 2F**), a brown andesitic tuff (TF-1, Figure 2m), a greenish brown dacitic tuff (TF-4, **Figure 2G**), and a devitrified cineritic tuff (TF-2, **Figure 2H**). The andesites are mostly composed of black hornblende andesites with white crystals (AN-1, **Figure 2I**), and aphiric black andesite (AN-4, **Figure 2J**). Another commonly present rock is the gray-pink pumice used in the manufacture of probable containers or mortars (**Figure 2K**).

There are important differences in the frequency of rock classes between sites. In Tuina-5, the predominant rocks are mainly white chert (SR-1), green epidotized siliceous rocks (SR-3) and red dacitic tuffs (TF-3) (**Figure 3A**). Obsidian is very scarce, occurring only in 31 pieces–all of the translucent gray variety (OB-1) with the exception of one shiny black (OB-4) obsidian flake. On the other hand, a greater diversity of rocks can be observed in Tambillo-1 (**Figure 3B**): obsidians are abundant, with shiny black (OB-4), translucent gray (OB-1), and opaque gray (OB-3) types predominating. Several varieties of chert, greenish ash tuff (TF-4), brown andesitic tuff (TF-1), and black hornblende andesite (AN-1), among others, were also recorded. Pumice artifacts, granitic rocks, and porphyries are present to a lesser extent. In Tulán-67, devitrified cineritic tuff (TF-2) and chert of the white-yellow (SR-5) variety predominate; there is also a significant frequency of aphiric black andesite (AN-4) and obsidian, particularly the opaque gray variety (OB-3) (**Figure 3C**).

5.2. Searching for the Volcanic Lithic Sources of the Atacama Basin

The directed surveys carried out based on geological and archaeological information have allowed us to document 10 lithic raw material procurement sources so far. Among the sources identified, various volcanic geoforms were distinguished: lava flows (Loma Negra-Puripica), volcanic domes and craters (Jarellón-Laguna Blanca and possibly Machuca-Pelún), maars (Cerro Tujle), ignimbrite flows (Quebrada Zapar and Ignimbrites of Filo Delgado), possible hydrothermal deposits (Salar de Talabre-14 and -18) as well as outcrops of continental sequences exposed in hilltops (Cerros de Tuina and Tulán Cerros). **Table 3** summarizes the lithic sources and their main characteristics. In all of them, we recorded evidence of primary processing in the form of cores, test

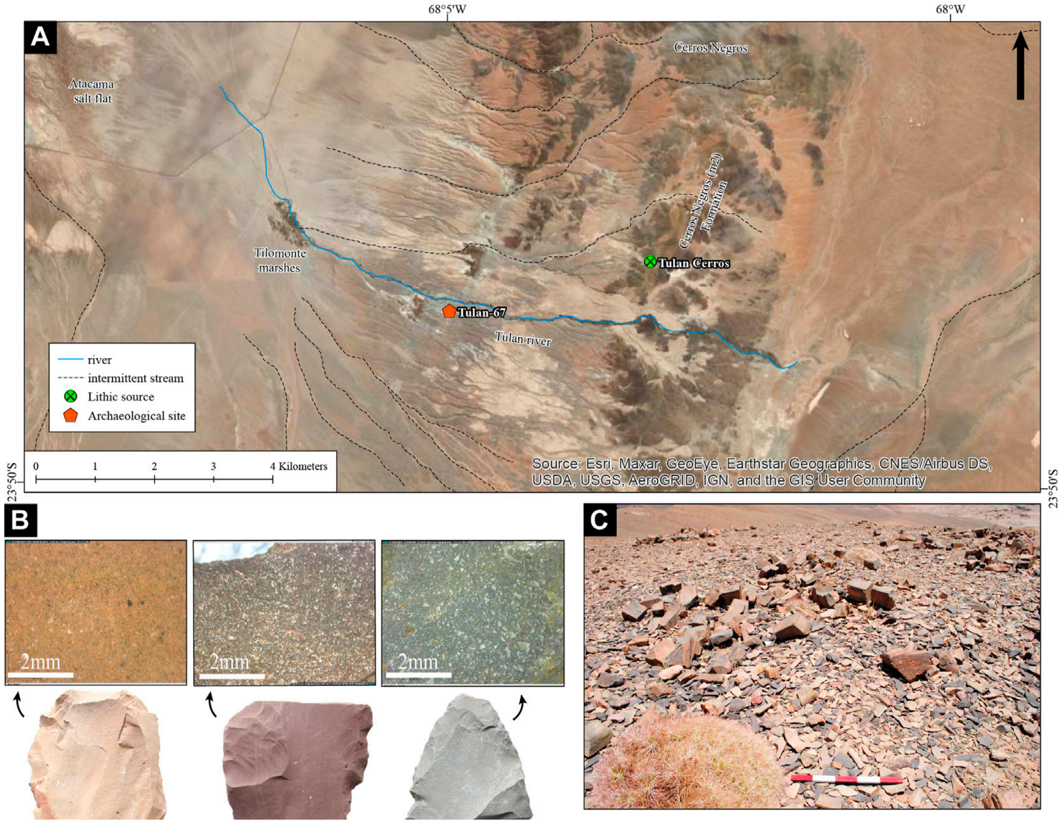

Source: Esri, Maxar, GeoEye, Earthstar Geographics, CNES/Airbus DS, USDA, USGS, AeroGRID, IGN, and the GIS User Community

FIGURE 9 | Tulán Cerros source complex: **(A)** geological context; **(B)** raw material samples; **(C)** Tulán Cerros-2 quarry-workshop site.

blocks, abundant flakes, blades, and in some cases, stone-hammers and retouched tools. Some of them, such as Loma Negra, Cerros de Tuina, Tulán Cerros, and Cerro Tujle, are large quarry-workshop sites formed by extensive anthropic floors of continuous lithic material.

5.2.1 Loma Negra-Puripica

The Loma Negra-Puripica source consists of an extensive lava flow of more than 20 km descending from Sairecabur volcano in a southwesterly direction (**Figure 4A**). The southern segment corresponds to the Loma Negra quarry initially studied by Gustavo Le Paige (Le Paige, 1958; Orellana, 1962; Le Paige, 1963; Le Paige, 1964; Le Paige, 1970; Agüero, 2005), while the northeastern segment houses the workshops reported near the Puripica archaeological sites (Núñez, 1981; Núñez et al., 1999; 2005). The raw material consists of a dark gray to black hornblende andesite with white crystals (**Figure 4B**). It comes in the form of large non-transportable blocks up to several meters long, medium-sized blocks, and smaller angular fragments that form a continuous raw material floor (**Figure 4C**). At the site, an industry of prismatic and pyramidal unidirectional blade cores (**Figure 4D**) and large flakes predominates, with a few large bifacial pieces. The evidence is concentrated around denser knapping *loci* and some circular stone structures of the same rock. Geologically, the lava flow is part of the stratum-volcano complex III (Qv) that groups Pleistocene-Holocene volcanoes and lava flows (Marinovic and Lahsen, 1984). The source could be related to the Machuca (4,460 m a.s.l) and Jorquencal (4,971 m a.s.l) stratovolcanoes; and/or to the Falda Grande lava-dome, which could be an ancient emission center (Henríquez et al., 2014).

5.2.2 Machuca-Pelún

The first descriptions of local obsidian come from surveys carried out by Gustavo Le Paige in Quebrada Pelún (Le Paige, 1964). A secondary source of small nodules was later reported in the lower part of the ravine (De Souza et al., 2002). Other works reported larger nodules at the head of the ravine near the town of Machuca in the highlands, scattered in large areas and also deposited in offerings structures or *apachetas* on the road (Pimentel, 2008), which were later characterized geochemically by Seelenfreund et al. (2010a). The surveyed area of greatest density was found in a deflated area of 4,000 m^2 on the southwestern edge of an ignimbrite outcrop (**Figure 5A**). Small rounded and sub-rounded nodules of maximum diameter 5–12 cm were observed scattered on the surface. The obsidian is very heterogeneous but with a predominance of translucent gray and translucent brown sub-varieties (**Figure 5B**). We did not observe dense areas of primary processing in the form of quarry workshops, except for very scattered, isolated evidence of

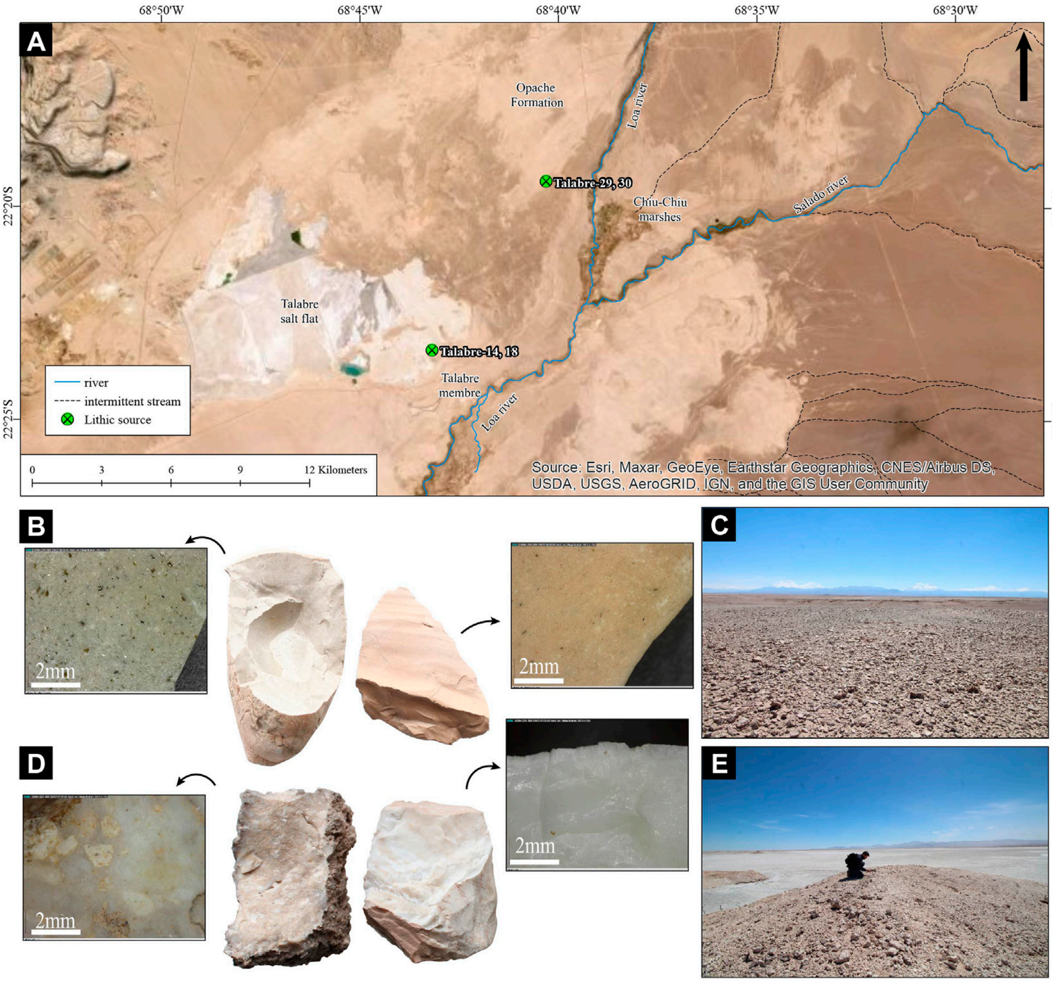

FIGURE 10 | Salar de Talabre source complex: **(A)** geological context; **(B)** raw material samples from Talabre-29 (left) and Talabre-30 (right) sites; **(C)** Talabre-30 quarry-workshop site; **(D)** raw material samples from Talabre-14 (right) and Talabre-18 (left) sources; **(E)** quarry-workshop site of Talabre-14.

knapping. The source appears to be spatially associated with an ignimbrite outcrop (**Figure 5C**) of the Puripica Formation (Guest, 1969; Henríquez et al., 2014).

5.2.3 Jarellón-Laguna Blanca and Salar de Tara

The Jarellón-Laguna Blanca obsidian source was first described by Seelenfreund et al. (2010b) as a primary source located on the slope of a collapsed caldera (**Figure 6A**). Geologically, the formation comprises dacitic and rhyolitic lavas (Gardeweg and Ramírez, 1985:63). Some interpretations suggest that the caldera formed due to a plinian eruption, which led to its collapse and the subsequent formation of the caldera (Seelenfreund et al., 2010b). Obsidian is available in eroded nodules of between 8 and 22 cm (**Figure 6B**) and blocks up to 70 cm near the flow edge of the northeast dome. Several knapping *loci*, stone parapets, and non-local obsidian offerings were recorded in the area (Seelenfreund et al., 2010b). A secondary source was also reported on the northwest edge of the Salar de Tara, located on a beach of lacustrine sedimentation (Seelenfreund et al., 2010a) (**Figure 6A**). We recorded several lithic scatters with abundant flakes, cores on natural nodules and bifacial projectile points on local obsidian. We sampled two areas to the northeast of the Hualitas volcano and recorded round nodules of shinny black and reddish-black obsidian (**Figure 6C**). We found slight evidence of exploitation in some lithic scatters associated with ephemeral stone structures. The obsidian nodules could be secondary transport from the Jarellón source, or could be related to the Hualitas stratum-volcano (5,010 masl) (Gardeweg and Ramírez, 1985).

5.2.4 Cerro Tujle

The Cerro Tujle source is a large quarry-workshop around a small volcanic crater 300 m in diameter and 70 m deep (**Figure 7A**). It was previously described as a meteorite crater (Ferrando, 1977), but later characterized as a maar-type volcanic crater produced by a phreatic-magmatic eruption (Ureta et al., 2018; Ureta et al., 2020a; Ureta et al., 2020b). The raw material occurs in large blocks and smaller angular fragments of black andesite available

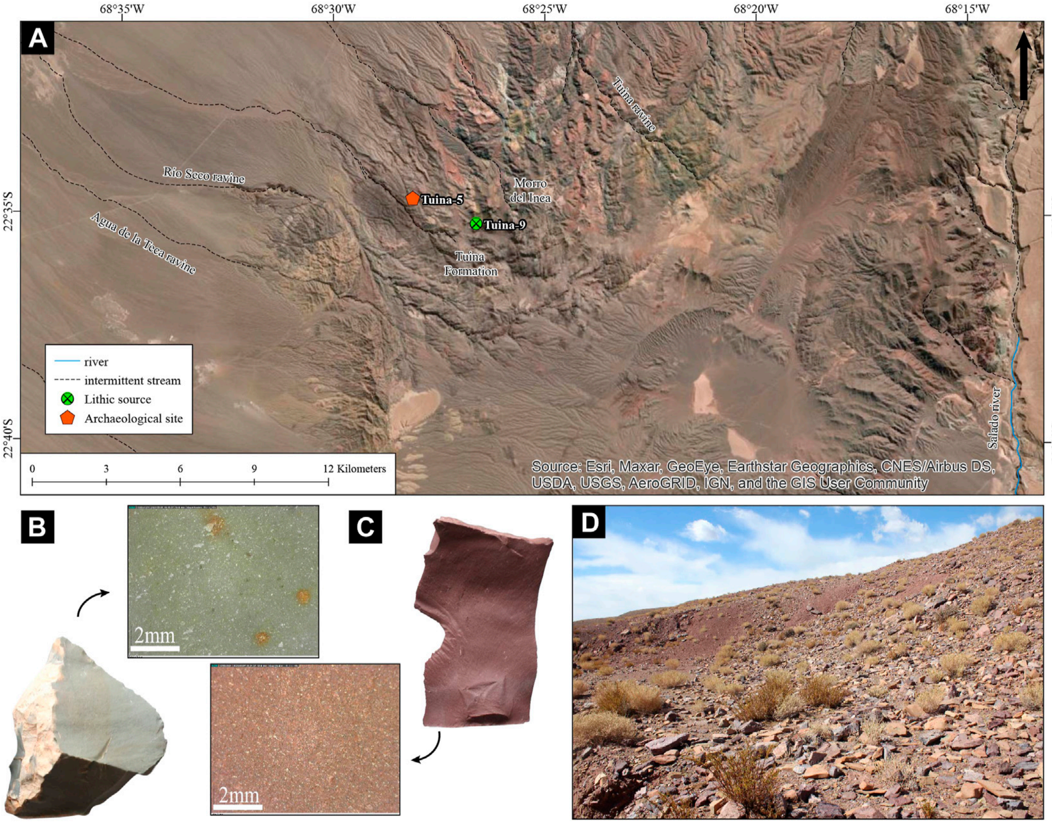

Source: Esri, Maxar, GeoEye, Earthstar Geographics, CNES/Airbus DS, USDA, USGS, AeroGRID, IGN, and the GIS User Community

FIGURE 11 | Cerros de Tuina: **(A)** geological context; **(B)** raw material samples; **(C)** raw material samples; **(D)** Tuina-9 quarry-workshop site.

around the tephra ring (**Figure 7B**). At the site, we observed many test blocks, cores, flakes, and especially large blades, and some bifacial pieces (**Figure 7C**). The formation was included within the set of stratum-volcanoes III of the Quaternary (Ramírez and Gardeweg, 1982).

5.2.4 Quebrada Zapar

On the eastern edge of Quebrada Zapar (**Figure 8A**), we found large, superficially scattered pumice fragments of up to 30–40 cm (**Figure 10B**). The fragments are of round and tabular morphology and consist of grey-pink pumice of dacitic composition (**Figure 8C**). The source would be linked to the Ignimbrite Cajón Formation (Pc) (Guest, 1968), which includes several levels of tuffs characterized by banded pumice (Henríquez et al., 2014). According to Marinovic and Lahsen (1984), the ignimbrite flows were emitted in a short period; they were attributed to the Purico volcano (5,703 masl) emission center, 30 km east of the site.

5.2.5 Tulán Cerros

Tulán Cerros consists of a large area north of Quebrada Tulán (2,850 masl), where veins form outcrops on top of the numerous hills of the landscape. More than 30 quarry-workshop sites have been reported in the upper part (Le Paige, 1964; Le Paige, 1970; Núñez, 1983) and several lithic scatters of the same raw material have been recorded in nearby areas (Barfield, 1969; Niemeyer and Schiapacasse, 1976) (**Figures 9A,B**). In recent surveys, we documented many quarry-workshop sites of variable extension where an industry of large bifaces, flakes, and blades predominates (**Figure 9C**). We observed lithic mortars on the surface, stone structures, and engraved plaquettes in some places. The raw material appears in erosion heights in the form of diaclassic blocks between 20 and 60 cm of green, reddish, brown, and light brown devitrified tuff (Loyola et al., 2016). The outcrop is probably related to the middle member of the Cerros Negros Formation (Pcn) (Niemeyer, 2013).

5.2.6 Salar de Talabre

The Salar de Talabre lithic workshops have been extensively studied (Le Paige, 1964; Lanning, 1967; Núñez 1967; Lanning, 1968; Lanning, 1970; Le Paige, 1970; Núñez 1983) (**Figure 10A**). The raw materials have been described as silicified tuff (Lewis-Johnson 1978) or vitreous rhyolitic tuff (Barfield, 1960), silicified limestone, and low-grade chert (Meltzer 1979). The Talabre-29 and 30 sites to the north of the basin (**Figure 10B**) consist of large open-air quarry-workshop sites on a plain where blocks and fragments of 20–40 cm of silicified gray, often cream, tuff form outcrops (**Figure 10C**). Geologically, the site is located in the Upper

TABLE 4 | Raw materials and assignment to local sources.

Raw material	Description	Assigned source	Code
Shiny black/reddish-black obsidian	Shiny black, fluid matrix with spherulitic devitrification, few plagioclase phenocrysts and cristobalite amygdales, often banded. Some samples show bands of iron oxide.	Tara /Jarellón-Laguna Blanca	OB-4 and OB-5
Translucent gray obsidian	The matrix is translucent, slightly yellowish gray to brown. It presents large violet plagioclase phenocrysts (0.5–1.5 mm), probably glass iron oxides, and elongated second generation plagioclase crystals often oriented. Some examples have dark and red dots. It shows scarce small greenish rectangular crystals, probably hornblendes altered to chlorites.	Machuca-Pelún	OB-1
Translucent brown obsidian	Brown translucent vitreous matrix with fluidal inclusions, brown spots, and scarce elongated plagioclase.	Machuca-Pelún	OB-2
Black hornblende andesite white crystals	Black to dark gray matrix with porphyritic, aphanitic texture, and characteristic white plagioclase phenocrysts in addition to subhedral hornblende and glass fragments. It shows moderate magnetic susceptibility and hornblendes had low alteration to chlorites.	Loma Negra-Puripica	AN-2
Aphiric black andesite	Black to dark gray matrix, aphiric texture with small plagioclase crystals and olivines.	Cerro Tujle	AN-4
Devitrified, cineritic tuff	Recrystallized cineritic tuff of light brown, brown, red and green color, with very fine grain size composed of quartz fragments, plagioclase, and crystals of calcite. In some cases, it presents dark minerals, probably biotites.	Tulán Cerros	TF-2
Green epidotized siliceous rock	Greenish gray texture with white spots, probably silicified plagioclase. Sometimes presents yellow patches of epidote.	Tuina-9	SR-3
Brown andesitic tuff	Brown matrix and fragmentary texture with pyroclasts of plagioclase, hornblende, and biotite. Present flow.	Tuina-9	TF-1
Gray-cream silicified tuff	Dacitic tuff with a greenish gray to pinkish color; presents fragmental texture with ash-sized pyroclasts of subhedral shape composed by plagioclase crystals, hornblende, biotite, embedded quartz and ferromagnesians with low alteration to iron oxides. The rock is generally silicified.	Talabre-29/30	TF-7
White chert	Greyish white matrix often with reddish spots of jarosite and abundant vesicles, chalcedony fillings, cleavages and a thick, rough cortex.	Talabre-14/18	SR-1
Pink pumice with flow	Greyish pink color and dacitic composition, with a vitroclastic texture, fragments of plagioclase, amphibole and pumice in a pumice matrix with glass fragments.	Quebrada Zapar (ignimbrite Cajón)	TF-6

Miocene-Upper Pliocene Opache Formation (MPo) (May et al., 2005; Blanco and Tomlinson, 2009). Some early work suggested that tuff formations originated from incandescent ash-falls on wet surfaces, probably lakes or swamps (Meltzer, 1979). The Talabre-14 and Talabre-18 quarry-workshops are located on the southeast margin of the current Talabre salt flat. In Talabre-14 (**Figure 10D**), we documented abundant evidence of knapping on waste-flakes and nodules of a white siliceous rock and beige chalcedony with significant impurities, vesicles, and very rough cortex (**Figure 10E**). In Talabre-18, large, semi-buried blocks of white chert of fair and mediocre quality were observed. The chert composition suggests a sedimentary origin, with possible recrystallization by low temperature hydrothermalism, but more studies are needed. Geologically, both sites are located in the Talabre Member (Ml2) of the Lasana Formation (Middle Miocene-Lower Upper Miocene) (Blanco and Tomlinson, 2009).

5.2.7 Cerros de Tuina (Tuina-9)

Tuina-9 consists of a workshop-quarry on the southern slope of Morro del Inca (3,608 masl) in the Tuina Mountain range (**Figure 11A**), where we find the most significant number of flakes and cores, and two stone structures. Diaclassic fragments and medium-sized plaquettes (20–40 cm) of an green epidotized siliceous rock are very abundant at the site (**Figure 11B**). We also documented a brown andesitic tuff in larger blocks (**Figure 11C**). The source seems to be related to the Lower Member of the Tuina Formation (PeTrt1) from the Upper Permian-Middle Triassic, mainly volcanic, consisting of andesites with frequent epidotization (**Figure 11D**) (Henríquez et al., 2014).

5.3 Identification of Lithic Raw Materials: Linking Sites and Sources

By comparing the archaeological artifacts with the raw material samples taken in the field we were able to assign the procurement sources. **Table 4** summarizes raw material assignments based on the recognition of the lithological markers defined in the geological samples. **Figure 12** shows the appearance of each variety at 50x. The shiny black obsidian (OB-4, **Figure 12A**) and reddish-black variety (OB-5, **Figure 12B**) was assigned to the Salar de Tara and Jarellón-Laguna Blanca sources, although it is impossible to separate them as they have the same geochemical signature and an identical visual appearance under the microscope. Together with the Zapaleri source (Yacobaccio et al., 2004), Jarellón-Laguna Blanca and Salar de Tara would form a homogeneous group of obsidian sources related to the same magmatic system (Seelenfreund et al., 2010a). In the case of Machuca-Pelún obsidian, two main sub-varieties were distinguished: OB-1 (**Figure 12C**) and OB-2 (**Figure 12D**) while the aphiric black andesite (AN-4, **Figure 12E**) corresponds to the Cerro Tujle maar. The devitrified cineritic tuff (TF-2, **Figure 12F**) in its three varieties (brown, light brown, and green) corresponds to the Tulán Cerros source complex. The green epidotized silicified rocks (SR-3) come primarily from the Tuina-9 source (**Figure 12G**), as does the brown andesitic tuff

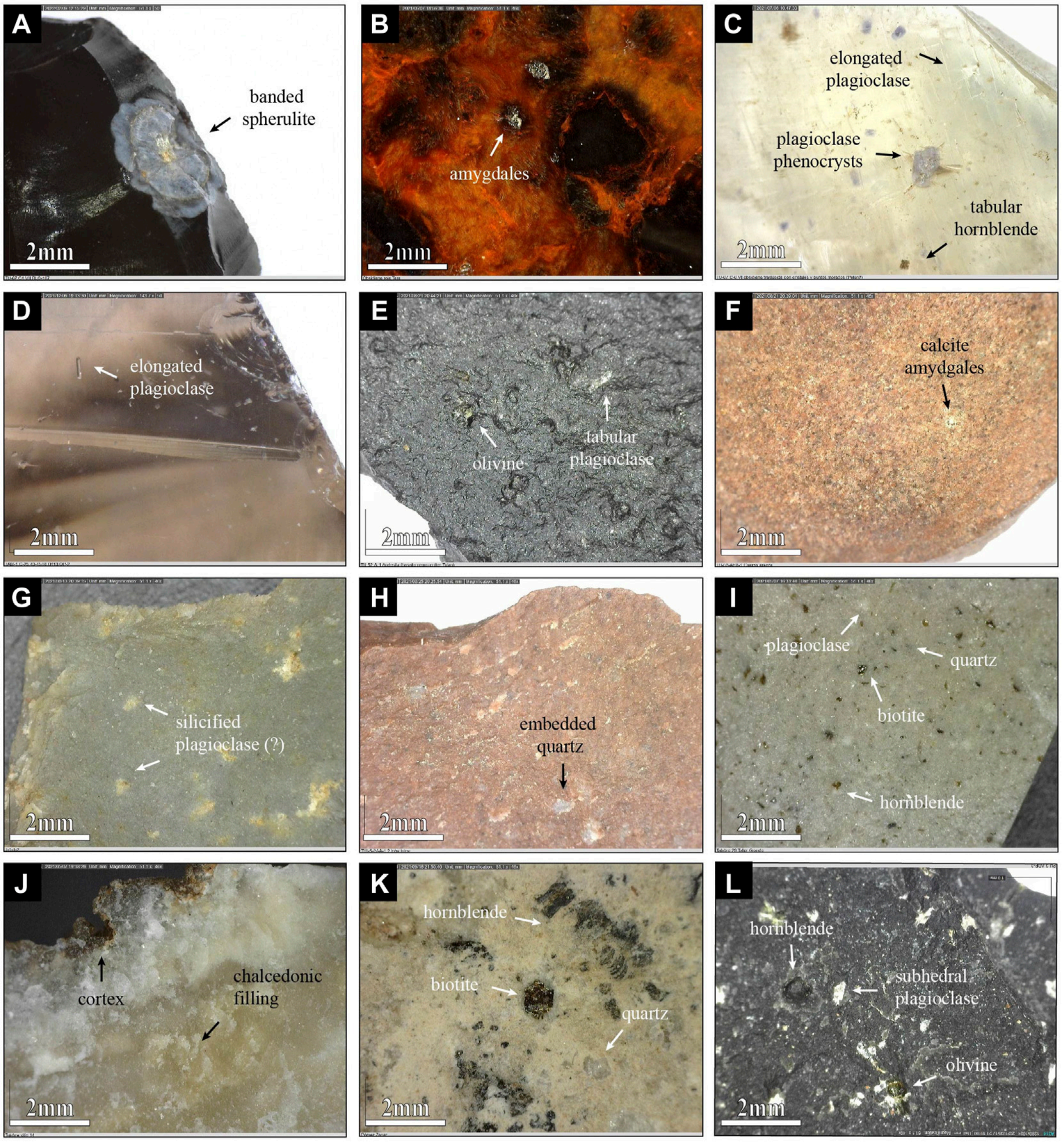

FIGURE 12 | Raw materials from known sources: **(A)**; shiny black obsidian (OB-4); **(B)** Shiny reddish-black obsidian (OB-5); **(C)** translucent gray obsidian (OB-1); **(D)** translucent brown obsidian (OB-2); **(E)** Aphiric black andesite (AN-4); **(F)** devitrified cineritic tuff (TF-2); **(G)** green epidotized silicified rock (SR-3); **(H)** brown andesitic tuff (TF-1); **(I)** gray-cream silicified tuff (TF-7); **(J)** white chert (SR-1); **(K)** gray-pink pumice; **(L)** black hornblende andesite (AN-1).

(TF-1, **Figure 12H**). The gray-cream silicified tuff (TF-7, **Figure 12I**) corresponds to the source of Talabre-29, 30. Among the wide variety of cherts, a good part of the white chert (SR1-1, **Figure 12J**) could be assigned to the Talabre-14 and 18 sources. The pumice, recorded in the Tambillo-1 site, was easily assigned to the Zapar source (**Figure 12K**) and the black hornblende andesites (AN-1, **Figure 12**L) are related to the Loma Negra-Puripica source.

Some lithic raw materials from unknown sources can be attributed to a local origin. The source of the opaque gray obsidian (OB-3, **Figure 13A**), recognized by its high content of hornblende and biotite, could be found near the Tulán ravine due to its higher frequency in Tulán sites. We also suspect that the black-red shiny obsidian (OB-6) with large grey amygdales (**Figure 13B**) comes from the Lascar volcano area (see **Figure 1**). Other obsidian pieces come from allochthonous sources in northwestern Argentina, as confirmed by XRF and NAA analyses (Loyola, 2020). The translucent obsidian (OB-8) shows reddish oxidized biotite crystals with a hexagonal shape (0.1–0.3 mm) that match with Salar del Hombre Muerto source (**Figure 13C**); while Ona-Las Cuevas obsidian presents characteristic fluid inclusions with biotite and oxidation (**Figure 12D**) and tabular hornblende crystals (**Figure 12E**) that match with our OB-7. Some few pieces of translucent obsidian with black inclusions (OB-9) of developed tabular hornblende (**Figure 12F**) come from the Alto Tocomar source

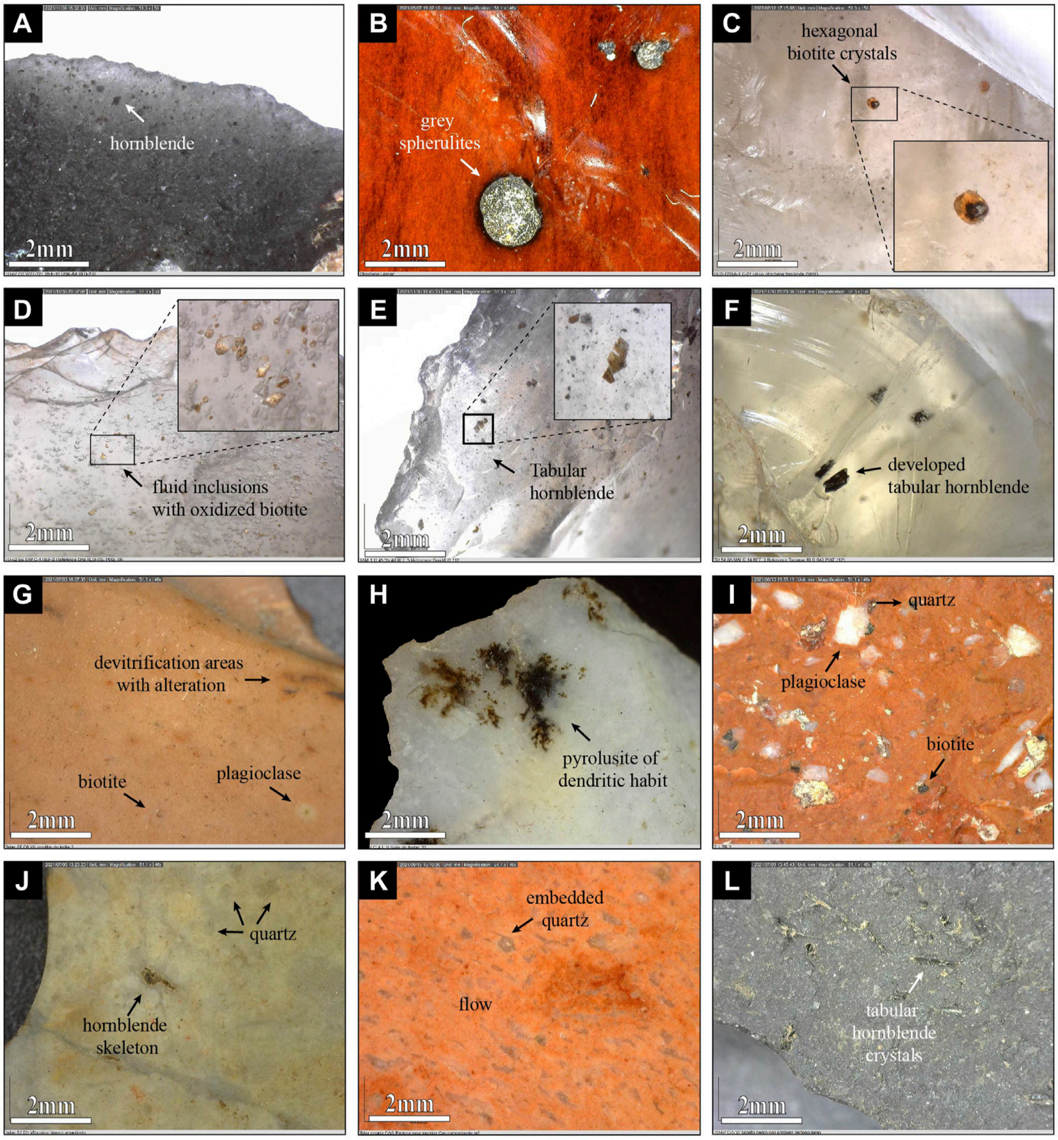

FIGURE 13 | Lithic raw materials from unknown and extra-local sources: **(A)**; opaque gray obsidian (OB-3); **(B)** Shiny black-red obsidian (OB-6); **(C)** translucent obsidian (OB-8); **(D)** translucent obsidian with fluid inclusions (OB-7); **(E)** translucent obsidian with inclusions (OB-7) **(F)** translucent obsidian with black inclusions (OB-9); **(G)** Brown siliceous rock with reddish spots (SR-6); **(H)** white chert with black spots (SR-4); **(I)** red dacitic tuff with white crystals (TF-3); **(J)** white-yellow silicified rock (SR-5); **(K)** Pink tuff whith flow (TF-6); **(L)** Black andesite with tabular hornblendes (AN-6).

in Salta, Argentina (see Yacobaccio et al., 2004). Two varieties of siliceous rocks–brown with reddish spots (SR-6, **Figure 12G**) and white with spots with dendritic habit (SR-4, **Figure 13H**) – were reported that would come from north of the Imilac basin (Cartajena et al., 2014; Loyola et al., 2019b). The source of the red dacitic tuff with white crystals (TF-3, **Figure 13I**) is also unidentified, but judging by its frequency it could be available at different points of the eastern border of the Atacama basin; it is most frequently found in archaeological sites near Tambillo and Aguas Blancas ravine (see **Figure 1**). The white-yellow siliceous rock (SR-5, **Figure 13J**) could come from a source located 5 km south of Tulán (Yacobaccio and Núñez, 1991). The pink tuff (TF-6, **Figure 13K**) is less abundant but probably comes from Cerros de CAS as well as a part of the gray basalt (Le Paige, 1970, see **Figure 1**). A common variety is a dark andesite with tabular hornblende crystals (AN-6, **Figure 13**L), the source of which is still unknown but presumably local. Finally, comparisons with museum collections make us think that the greenish brown dacitic tuff (TF-4) would come from the Lomas de Ghatchi (Le Paige, 1960; Le Paige 1963; Le Paige 1964) while the black pyroxene andesite (AN-3) is frequent in the quarry-workshops of Valle Chico ravine (Le Paige and Serracino 1974) (see **Figure 1**).

6 DISCUSSION

6.1 The Exploitation of Volcanic Rocks Among Early Andean Hunter-Gatherers

Analysis of the archaeological assemblages of Tuina-5, Tambillo-1, and Tulán-67 revealed that during the Early Archaic period, stone tools and other lithic objects were made from a wide variety of lithic raw materials of volcanic and subvolcanic origin. Such variability accounts for the use of rocks with different properties and qualities, from the sharpest and best quality, such as obsidian and siliceous rocks, to the most tenacious and resistant, such as andesite, tuffs and basalts, and even others as granite and pumice. Each of these rock classes seems to have been intended for particular categories of tools and objects, production of which required the application of specific know-how and knapping techniques, depending on its particular properties (see Nami, 2015).

However, several factors hindered lithological classification. One of them is the thermal alteration that introduces a series of physical-chemical changes in the artifacts that inhibit their identification, such as luster, rubefaction, calcination, cracking, plotids, and thermal fractures. Heat treatment is a technique widely used in prehistory to improve the quality of knappable rocks through controlled exposure to fire. However, thermal alterations can also result from accidental exposure to fire-pits or natural fires (Inizan and Tixier, 2000). In the sites, thermal alteration of lithic assemblages reaches 1,91% in Tambillo-1 (*n*=93), 0,82% (*n*=16) in Tuina-5 and 7,47% (*n*=247) in Tulán-67. Moreover, it is impossible at present to be sure whether this alteration is due to an intentional process to improve the quality of the raw material or is the involuntary result of exposure to heat sources, such as the several hearths documented at the sites. Further study is needed to explore how thermal alterations expressed in each

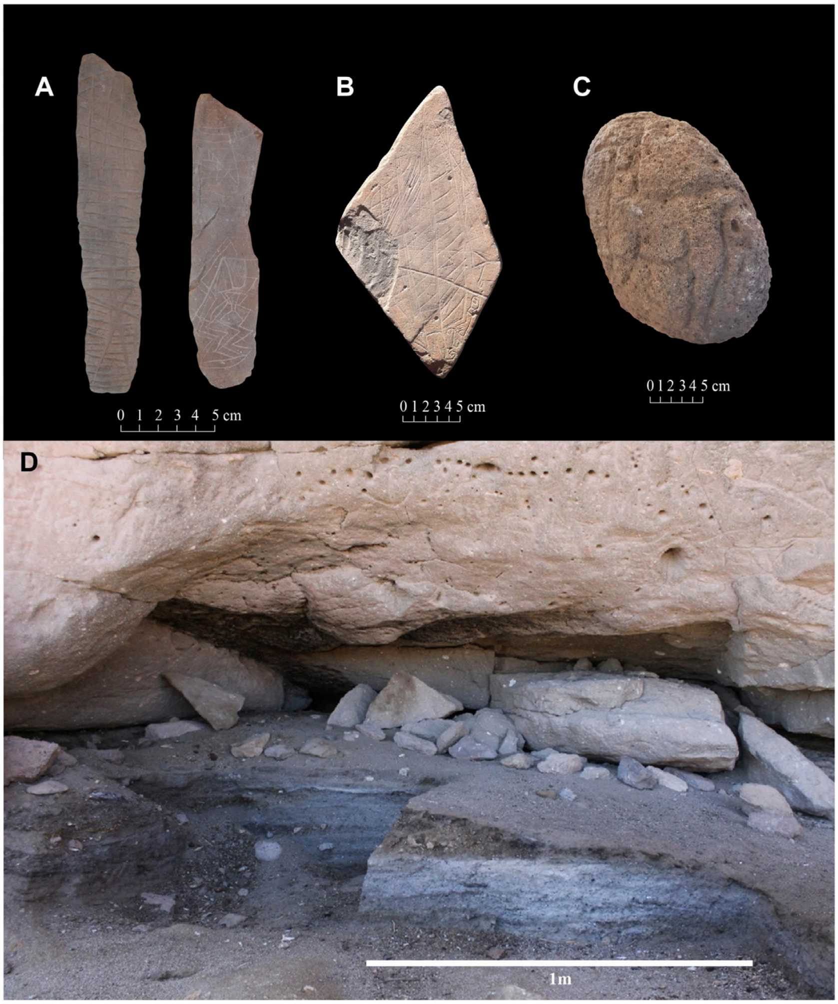

FIGURE 14 | Engraved lithics on volcanic rocks: **(A)** engraved blades with geometric motifs on devitrified cineritic tuff (Tulán Cerros-2 site); **(B)** engraved plaquettes from Tulán Cerros in devitrified cineritic brown tuff (collection of Gustavo Le Paige); **(C)** volcanic tuff with engraved camelid motif recovered from the initial occupation floor of the Puripica-1 site (Núñez 1983); **(D)** Late Early Archaic occupation in ash stratigraphic layer (light gray): site Tulán-109 (Núñez et al., 2005).

of the raw materials. On the other hand, assignment was also limited by the high fragmentation or small size of the samples: in some cases, the maximum length of the artifacts analyzed, such as pressure-retouching flakes, was no more than a few millimeters, preventing the conservation of lithic markers and other diagnostic features such as the cortex.

This high diversity of lithic raw materials probably reflects deep knowledge not only of the volcanic landscape and its rocks, but also the techniques necessary to work them. The exploitation of lithic resources among hunter-gatherers in the Atacama basin and adjacent basins has been addressed in various works (Le Paige, 1970; Serracino, 1975; Núñez et al., 2002; Loyola et al., 2021, among others). Judging by the descriptions and the availability of raw materials in the landscape, volcanic rocks have been a constant in Andean hunter-gatherer societies due to their wide availability and easy access, especially in high-altitude environments where their use persisted in later periods. The data obtained in this work suggest that human groups early integrated these resources into their social, economic, and technological sphere, developing a deep knowledge of their properties and characteristics. The application of technological and functional studies currently in progress will offer better understanding of raw material management, production techniques, and contexts of use.

6.2 The Procurement of Volcanic Rocks and the Lithic Sources

The procurement sources identified offer a first approach to the accessibility and availability of lithic resources in the Atacama basin. Several of these sources had been detected and characterized in different works dating back to the 1960s (Lanning, 1967; Lanning, 1968; Le Paige, 1970; Le Paige and Serracino, 1974; Núñez, 1983; Seelenfreund et al., 2010a; Seelenfreund et al., 2010b; Loyola et al., 2016); however, these works pursued other objectives and used different methodologies. Lithic studies of archaic sites have focused instead on understanding the technological management of resources and mobility patterns at site scale; we have little knowledge about sources of provenance. Conversely, there are several geochemical analyses and field characterizations in the case of obsidian (Seelenfreund et al., 2010a; Seelenfreund et al., 2010b) but with little application to early periods.

Our field surveys identified several lithic sources in the Atacama basin distributed in a vast and contrasting landscape ranging from 2000 to 4,500 m a.s.l. The sources detected are almost entirely volcanic and subvolcanic formations, such as lava flows, maars, craters, caldera-domes, ignimbrite flows, hydrothermal deposits, and outcrops of volcanic facies formed in different geological epochs. Each of them provides various kinds of rock. We documented large quarry-workshop sites in several of these places, with knapping evidence indicating intense and repeated human activity over several periods. The Loma-Negra and Puripica quarry-workshops are extensive areas of discarded material forming a continuous floor of lithic material, including stone structures. In Tulán Cerros, engraved plaquettes and blades have been recorded at the quarry-workshop sites; these provide evidence of symbolic practices (**Figures 14A,B**), although their chronology has not yet been well specified. Another exceptional engraved volcanic tuff was recovered from the initial occupation floor of Puripica-1 dated to 4,815 + 70 BP (5,651–5,320 cal BP) (**Figure 14C**), with one of the first manifestations of rock art in the area (Núñez, 1981; Núñez, 1983). The quarry-workshops of the Salar de Talabre are of medium intensity, but with an intense deposition of lithic materials. A similar pattern is found at Cerro Tujle, where the knapping activities were organized around the crater. The absence of evidence of exploitation in the Machuca-Pelún, Salar de Tara and Jarellón-Laguna Blanca sources is probably due to the greater dispersion of the raw material and to the fact that the nodules were collected and transported directly after being tested. Something similar could have happened in the case of the pumices that did not leave observable evidence of production.

The volcanic landscape of the Andean Puna provides a rich and diverse supply of lithic raw materials; however, these rocks are differentially available from limited sources, scattered throughout an arid and mountainous landscape. Human groups quickly integrated volcanic formations and their distribution into their cognitive maps; the archaeological evidence indicates that the sources were stable and recurrent nodes within the seasonal mobility cycle. These were not only spaces where hunter-gatherers carried out extractive activities, but were also occasions for social interaction and transmission of technical knowledge. Among early hunter-gatherers, obsidian appears to have been one of the most appreciated raw materials. The wide availability and distribution of obsidian allowed human groups to provision directly, both during their seasonal occupation of the highlands and from secondary sources on lower floors. This behavior persisted in societies that adopted agro-pastoralist ways of life in later periods. Thus, obsidian and other rocks continued to circulate and be exchanged over great distances (Berenguer, 2004; Yacobaccio, et al., 2004; Núñez, et al., 2007; Escola et al., 2016; Loyola et al., 2021).

6.3 The Volcanic Landscapes of the Early Hunter-Gatherers

By comparing the archaeological assemblages with samples collected in the field, potential sources of origin could be assigned to the lithic raw materials. This allows us to track the circulation of raw material between different microenvironments such as the Domeyko mountain range, the Precordillera foothills, the Altiplano, and even the eastern slope of the Andes. After a first evaluation, it can be suggested that the frequency of each raw material in the assemblages is directly related to the distance from its source. The lithic landscape, understood as the physical distribution and availability of rock resources (Gould and Saggers, 1985), offers a wide diversity of resources over variable distances. Most of the lithic raw materials come from sources in the immediate surroundings of the sites, whereas raw materials from more distant sources are transported to the settlements in smaller amounts and volumes. This differential distribution of raw materials can be directly related to the techno-economic zoning of the landscape. Sources in the immediate surroundings of the sites (<5 km) could be exploited as part of daily activities within the foraging area. The redundancy and intensity of activities in these spaces allowed the formation of large quarry-workshop sites such as Loma Negra, Tulán Cerros, and Cerros de Tuina. On the other hand, raw materials from more distant local sources (5–40 km), had to be supplied through other mechanisms; for example, through inter-settlement transport, within the seasonal mobility circuit, or even through specific logistical trips, leaving little evidence *in situ*, as is the case of Machuca-Pelún and Salar de Tara and Jarellón-Laguna Blanca. Rocks of allochthonous origin, especially trans-Andean obsidian, may have been obtained in smaller volumes by exchange or some other type of long-distance interaction.

The relationship between past societies and volcanism has generally been approached through the risk and impact of eruptive events (Torrence et al., 2000; Grattan et al., 2002; Shimoyama, 2002; Torrence and Grattan, 2002; Vanderhoek and Nelson, 2007; Torrence, 2014). In the Andes, a correlation between cultural changes and volcanic explosions in recent periods has been suggested (Bouysse-Cassagne and Bouysse, 1984; Pärssinen, 2015); however, we know little about early hunter-gatherer societies (Grosjean et al., 2007). Some works have discussed the consequences of volcanic events during the demographic bottleneck of the Middle Holocene period (Durán and Mikkan, 2009), and their effects on interaction networks and social organization (Aschero, 2016). Several catastrophic events and eruptions have occurred during the long sequence of human occupation in the Atacama Basin; in fact, volcanic ash layers interspersed with human occupations have been reported in Tulán-109 (2,900 m a.s.l) (**Figure 14D**), San Lorenzo-1 (3,000 m a.s.l), Tuina- 1 and -3 (3,000 m a.s.l), Miscanti-1 (4,200 m a.s.l) and Tambillo-6 (2000 m a.s.l), among others (Núñez et al., 2005; Núñez et al., 2018) but they have not yet been adequately studied. The Tulán-54 site, one of the oldest ceremonial centers in the region, was built on a dense layer of volcanic ash (Núñez et al., 2017). Local geological research has reported large-scale eruptions that could have formed the ash layers at archaeological sites. This is the case of the Tumbres eruption (9,100–9,300 cal BP), which produced an andesitic pumice fall deposit and a pyroclastic flow that extended for more than 10 km (Gardeweg et al., 1998). Likewise the Socompa devastating eruption (6,051 m a.s.l) produced a massive debris avalanche (7,200–6,200 cal BP) that extended for 40–50 km (van Wyk de Vries et al., 2001; Davies et al., 2010) with an ash fall area whose extent is still unknown. In the Argentine northwest, several Pleistocene and Holocene volcanic ash deposits have been reported, in some cases more than 4 meters thick (Fernández-Turiel et al., 2012).

These events must have occurred contemporaneously, and must have impacted early human societies not only through their direct consequences. Records of eruptions can persist for centuries in collective memory and oral tradition in the form of myths (Fox Hodgson, 2007). However, it has been argued that hunter-gatherer societies have a greater degree of resilience and tend to recover quickly from the sudden stress of explosive eruptions (Sheets 1999; Sheets, 2001). Volcanoes seem rather to have been recurrent nodes of interaction and mobility within the mobility cycle, and sources of raw materials from which to manufacture objects–not only tools for subsistence but also goods with a social and symbolic value, as in the case of rock art on ignimbrite formations (Núñez et al., 2017); obsidian projectile points were exchanged over great distances and deposited as offerings in ceremonies among late hunter-gatherers and early pastoralist groups (Loyola et al., 2020). Considering the continuity in the exploitation of these sources in later periods, knowledge of the landscape and its rocks must have been stored in oral tradition and shared cognitive maps in the long-term. It is therefore reasonable to suppose that this same knowledge probably laid the foundations for the development of the copper mining and lapidary technologies, for which the societies of the Atacama were widely recognized until recent times (Figueroa et al., 2013; Sapiains et al., 2022).

7 CONCLUSION

Andean societies developed and maintained a close relationship with volcanoes and high mountains from the beginning of peopling of the region in ancient times. Study of the lithic assemblages of three sites dated between 11,500 and 9,500 cal BP revealed the procurement and circulation of a wide variety of volcanic and subvolcanic rocks. These rocks were obtained from different formations and landforms, reflecting the high level of volcanism in the region both in the distant past and more recently that has modeled a steep relief with strong altitudinal contrasts. In these sites we also documented large quarry-workshop sites and even residential camps, evidence of the intensity of past human activities and their role within mobility and interaction networks.

The relationship between archaeological sites and procurement sources allows us for first time to trace the routes and distances traveled by individuals and groups during their daily activities and interactions in these landforms. From usual movements in the surroundings of the settlements or their seasonal displacements to the highlands, to the long-distance trips to the eastern slope of the Andes. Within these circulation networks at different scales, volcanoes were important nodes for their activities and movements. As it happens today, 10,000 years ago the volcanic features probably were already a fundamental part of the way of life of Andean societies in different dimensions–as sacred deities, economic resource areas, geographical and calendar markers, ritual settings and even recurrent habitats. Beyond the catastrophic consequences of eruptions, the andean societies and volcanism converge in still active and ancient "volcanic landscape", and the lithic record constitutes an exceptional archive of these social relations.

DATA AVAILABILITY STATEMENT

The original contributions presented in the study are included in the article/supplementary material, further inquiries can be directed to the corresponding author.

AUTHOR CONTRIBUTIONS

The authors contributed in the following areas: RL: research conception and planning; laboratory analysis; field study; general writing of the article. VF: Conception and research design; field work surveys and general writing of the article. Field coordination and logistics. LN: Theoretical-methodological development of the archaeological research; participation in field work and general drafting of the manuscript. MaV: Field work (source sampling) and laboratory analysis (study of geological samples). CE: Field work and anthropological-archaeological background analysis for the preparation of the manuscript. Logistics and planning in the field. MiV: Methodological development; direction of the analysis of samples in the laboratory; theoretical corpus and developement of the geological background. MP: Conception and research design; carthograpy; environmental contextualization; graphic work and editing of the manuscript.

FUNDING

Funding for fieldwork and analysis was made possible by Wenner-Gren Dissertation Fieldwork Grant 3770214982, Fondecyt 1201603, and ECOS C19H05.

ACKNOWLEDGMENTS

First of all, we would like to acknowledge that this research was conducted on the traditional lands of the Lickanantay People. Also, we thank the Instituto de Investigaciones Arqueológicas y Museo (IIAM-UCN) that sponsored this research. We thank the Comunidad Atacameña de Toconao (CAT) who provided us with field and logistical support during this research as part of the associative research agreement between CAT and IIAM. Special thanks to Jimena Cruz, Macarena Oviedo, Luciano Oviedo, and Pamela Cruz for the management of lithic collections. We thank the Comunidad Atacameña de Toconao especially the Presidents Yermin Basques (2019–2020), and Luzvenia Catur (2021–2022). Finally, we would like to thank to Dr. Thérèse Bouysse-Cassagne and Dr. Philippe Bouysse, whose pioneering work on Andean volcanoes, conversations and contributions inspired this work.

REFERENCES

Agüero, P. C. (2005). Aproximación al asentamiento humano temprano en los oasis de San Pedro de Atacama. *Estud. Atacam.* 30, 29–60. doi:10.4067/S0718-10432005000200003

Allmendinger, R. W., Jordan, T. E., Kay, S. M., and Isacks, B. L. (1997). The Evolution of the Altiplano-Puna Plateau of the Central Andes. *Annu. Rev. Earth Planet. Sci.* 25, 139–174. doi:10.1146/annurev.earth.25.1.139

Alonso, H., and Risacher, F. (1996). The Salar de Atacama Geochemistry, part 1: The origin of components and saline balance. *Rev. Geol. Chile* 23 (2), 113–122. doi:10.5027/andgeoV23n2-a01

Aschero, C. (2016). Cazadores-recolectores, organización social e interacciones a distancia. Un modelado del caso Antofagasta de la Sierra (Catamarca, Argentina). *Mundo Antes* 10, 43–71.

Barfield, L. (1960). A New Core-Axe Industry. *Antiquity* 34 (33), 1–60.

Barfield, L. (1969). A Primitive Stone Industry from Tilomonte. Prov, Antofagasta. B Mus Nac Hist. *Nat* 69, 81–87. doi:10.1021/cr60262a001

Berenguer, J. (2004). *Caravanas, interacción y cambio en el desierto de Atacama*. Santiago: Ediciones Sirawi/LOM Editores.

Blanco, N., and Tomlinson, A. (2009). *Carta Chiu Chiu, Región de Antofagasta. Carta Geológica de Chile no. 117*. Santiago: Servicio Nacional de Geología y Minería de Chile. escala 1:50.000.

Bouysse-Cassagne, T., and Bouysse, P. (1988). *Lluvias y Cenizas. Dos Pachacuti en la Historia*. La Paz: HISBOL.

Bouysse-Cassagne, T., and Bouysse, P. (1984). Volcan indien, volcan chrétien. À propos de l'éruption du Huaynaputina en l'an 1600 (Pérou méridional). *jsa* 70, 43–68. doi:10.3406/jsa.1984.2238

Bouysse-Cassagne, T., and Harris, O. (1987). "Pacha: En Torno Al Pensamiento Aymara," in *Tres reflexiones sobre el pensamiento andino*. Editors T. Bouysse, O. Harris, T. Platt, and T. Cereceda (La Paz: Hisbol), 11–57.

Cartajena, I. (2003). *Los conjuntos arqueofaunísticos del Arcaico Temprano en la Puna de Atacama, Norte de Chile* (Germany: Freie Universität Berlin). Dissertation's thesis.

Cartajena, I., Loyola, R., Núñez, L., and Faúndez, W. (2014). "Problemas y Perspectivas en la interpretación del Registro Espacial de Punta Negra Imilac," in *Distribución Espacial en Sociedades no Aldeanas: del Registro Arqueológico a la Interpretación Social*. Editors F. Falabella, L. Sanhueza, L. Cornejo, and I. Correa(Santiago: Serie Monográfica de la Sociedad Chilena de Arqueología 4), 143–162.

Cartajena, I., Núñez, L., and Grosjean, M. (2006). "Las Arqueofaunas del Arcaico Temprano en la vertiente Occidental de la Puna de Atacama," in *Actas del XVI Congreso Nacional de Arqueología Chilena*. Editor M. Massone (Santiago: Sociedad Chilena de Arqueología - Museo de Historia Natural de Concepción - Ediciones Escaparate), 507–517.

D'Altroy, T., Williams, V., and Lorandi, M. (2007). "The Inkas in the Southlands," in *Variations in the Expression of Inka Power*. Editors R. L. Burger, C. Morris, and R. Matos(Washington: Dumbarton Oaks Research Library and Collection), 85–133.

Davies, T., McSaveney, M., and Kelfoun, K. (2010). Runout of the Socompa Volcanic Debris Avalanche, Chile: a Mechanical Explanation for Low Basal Shear Resistance. *Bull. Volcanol.* 72, 933–944. doi:10.1007/s00445-010-0372-9

De Souza, P., Sinclaire, C., Molina, R., and Gallardo, F. (2002). Una nota sobre el hallazgo de una fuente secundaria de Obsidiana en la Quebrada de Pelun (Localidad de Machuca, San Pedro de Atacama). *Bol. Soc. Chil. Arqueol.* 33/34, 81–83.

Durán, V., and Mikkan, R. (2009). Impacto del volcanismo holocénico sobre el poblamiento humano del sur de Mendoza (Argentina). *Intersecc. Antropol.* 10, 295–310.

Escola, P. S., Hocsman, S., and Babot, M. P. (2016). Moving obsidian: The case of Antofagasta de la Sierra basin (Southern Argentinean Puna) during the late Middle and Late Holocene. *Quat. Int.* 422, 109–122. doi:10.1016/j.quaint.2016.04.048

Fernández-Turiel, J. L., Saavedra, J., Pérez-Torrado, F. J., Rodríguez-González, A., Alias, G., and Rodríguez-Fernández, D. (2012). Los depósitos de ceniza volcánica del Pleistoceno superior- Holoceno de la región de Tafí del Valle-Cafayate, Noroeste de Argentina. *Geo-Temas* 13, 871–873.

Ferrando, F. A. (1977). Two Unknown Meteor Craters in Antofagasta Region, Northern Chile. *Rev. Geográfica* 85, 210–212.

Figueroa, V., Salazar, D., Salinas, H., Núñez-Regueiro, P., and Manríquez, G. (2013). Pre-Hispanic Mining Ergology of Northern Chile: An Archaeological Perspective. *Chungará (Arica)* 45 (1), 61–81. doi:10.4067/S0717-73562013000100003

Fox Hodgson, S. (2007). "Obsidian: Sacred Glass from the California Sky," in *Myth and Geology*. Editors L. Piccardi and W. B. Masse(London: Geological Society, Special publications), 273, 295–313. doi:10.1144/gsl.sp.2007.273.01.23

Gardeweg, M., Amigo, A., Matthews, R., and Clavero, J. (2011). *Geología del Volcán Lascar, Región de Antofagasta. Carta Geológica de Chile, Serie Geología Básica 131*. Santiago: Servicio Nacional de Geología y Minería de Chile. escala 1:50.000.

Gardeweg, M. C., Sparks, R. S. J., and Matthews, S. J. (1998). Evolution of Lascar Volcano, Northern Chile. *J. Geol. Soc.* 155, 89–104. doi:10.1144/gsjgs.155.1.0089

Gardeweg, M., and Ramírez, C. F. (1985). *Hoja Río Zapaleri, II Región de Antofagasta. Carta Geológica de Chile*. Santiago: Servicio Nacional de Geología y Minería de Chile. Serie Geología Básica No. 66, escala 1:250.000.

Gould, R. A., and Saggers, S. (1985). Lithic Procurement in Central Australia: A Closer Look at Binford's Idea of Embeddedness in Archaeology. *Am. Antiq.* 50, 117–136. doi:10.2307/280637

Grattan, J., Brayshay, M., and Schüttenhelm, R. T. E. (2002). "The End Is Nigh? Social and Environmental Responses to Volcanic Gas Pollution," in *Natural Disasters and Cultural Change*. Editors R. Torrence and J. Grattan(London: Routledge), 87–106.

Grosjean, M., Santoro, C. M., Thompson, L. G., Núñez, L., and Standen, V. G. (2007). "Mid-Holocene Climate and Culture Change in the South Central Andes," in *Climate Change and Cultural Dynamics: A Global Perspective on Mid-holocene Transitions*. Editors D. G. Anderson, K. A. Maasch, and D. H. Sandweiss (San Diego, CA: Elsevier), 51–115. doi:10.1016/B978-012088390-5.50008-X

Grosjean, M., Van Leeuwen, J., Van der Knaap, W., Ammann, B., Tanner, W., Messerli, B., et al. (2001). A 22,000 14C Year BP Sediment and Pollen Record of Climate Change from Laguna Miscanti (23°S), Northern Chile. *Glob. Planet. Chang.* 28, 35–51. doi:10.1016/S0921-8181(00)00063-1

Guest, J. E. (1968). Banded Pumice in a Chilean Ignimbrite. *Geol. Mag.* 105 (2), 177–184. doi:10.1017/s0016756800052559

Guest, J. E. (1969). Upper Tertiary Ignimbrites in the Andean Cordillera of Part of the Antofagasta Province, Northern Chile. *Geol. Soc. Am. Bull.* 80, 337–362. doi:10.1130/0016-7606(1969)80[337:utiita]2.0.co;2

Harris, O. (1987). De la fin du monde. Notes depuis le Nord-Potos. *Cah. Des. Amériques Lat.* 6, 93–118.

Henríquez, S., Becerra, J., and Arriagada, C. (2014). *Geología del Área San Pedro de Atacama, Región de Antofagasta. Carta Geológica de Chile, Serie Geología Básica 171*. Santiago: Servicio Nacional de Geología y Minería. escala 1:100.000.

Hogg, A., Heaton, T., Hua, Q., Palmer, J., Turney, C., Southon, J., et al. (2020). SHCal20 Southern Hemisphere Calibration, 0–55,000 years cal BP. *Radiocarbon* 62 (4), 759–768. doi:10.1017/RDC.2020.59

Inizan, M.-L., and Tixier, J. (2000). L'émergence des arts du feu : le traitement thermique des roches siliceuses. *paleo* 26 (2), 23–36. doi:10.3406/paleo.2000.4707

Isacks, B. L. (1988). Uplift of the Central Andean Plateau and Bending of the Bolivian Orocline. *J. Geophys. Res.* 93, 3211–3231. doi:10.1029/JB093iB04p03211

Lewis-Johnson, L. (1978). "The Aguas Verdes Industry of Northern Chile," in *Advances in Andean Archaeology*. Editor D. Browman (The Hague-París: Mounton Publishers), 7–40. doi:10.1515/9783110810011.7

Lanning, E. P. (1967). "Informe previo de las investigaciones realizadas por la Columbia University Field Station durante el año 1966," in *Boletín Informativo* (Antofagasta: Universidad del Norte, Instituto de Ciencias Sociales), 4.

Lanning, E. P. (1968). "Informe previo de las investigaciones realizadas por la Columbia University Field Station durante el año I967," in *Revista de la Universidad del Norte*, 2, 63–68.

Lanning, E. (1970). Pleistocene Man in South America. *World Archaeol.* 2 (1), 90–111. doi:10.1080/00438243.1970.9979466

Le Paige, G. (1958). *Antiguas Culturas Atacameñas en la Cordillera chilena*, XLVII 22. Valparaíso: Revista Universitaria, 139–165. Época Paleolítica.

Le Paige, G. (1960). *Antiguas culturas atacameñas en la cordillera chilena. Época paleolítica (2o artículo)*, XLIV-XLV. Valparaíso: Revista Universitaria, 195–205.

Le Paige, G. (1964). *El precerámico en la cordillera atacameña y los cementerios del período Agroalfarero de San Pedro de Atacama*, 3. Antofagasta: Universidad del Norte. Anales de la Universidad del Norte.

Le Paige, G. (1963). *Ghatchi y su zona*, XLVIII. Santiago: Revista Universitaria, 177–193.

Le Paige, G. (1970). *Las industrias líticas de San Pedro de Atacama*. Santiago: Orbe-Universidad del Norte.

Le Paige, G., and Serracino, G. (1974). Informes de trabajo. *Estud. Atacameños* 2, 93–96. doi:10.22199/s07181043.1974.0002.00008

Loyola, R., De Souza, P., and Santander, B. (2016). "El Desbaste de Hojas Durante La Transición Arcaico Tardío-Formativo Temprano en Quebrada Tulán, II Región De Antofagasta," in *Actas del XIX Congreso de Arqueología Argentina. Serie Monográfica y Didáctica* (Tucumán: Universidad Nacional de Tucumán), 54, 1460–1466.

Loyola, R. (2020). El intercambio de obsidianas entre las sociedades cazadoras-recolectoras del Salar de Atacama: Una aproximación desde la etnografía. *Bol. Soc. Chil. Arqueol. Spec.* volume, 663–682.

Loyola, R., Núñez, L., and Cartajena, I. (2019b). Expanding the Edge: The Use of Caves and Rockshelters during the Late-Pleistocene Human Dispersal into the Central Atacama Highlands. *PaleoAmerica* 5 (4), 349–363. doi:10.1080/20555563.2019.1697919

Loyola, R., Núñez, L., and Cartajena, I. (2019a). What's it like Out There? Landscape Learning during the Early Peopling of the Highlands of the South-Central Atacama Desert. *Quat. Int.* 533, 7–24. doi:10.1016/j.quaint.2019.07.007

Loyola, R., Rivera, F., De Souza, P., Carrasco, C., Núñez, L., Glascock, M. D., et al. (2021). Hunting and Feasting in the Pre-columbian Andes: Exploring the Nature and Scale of Early Ceremonial Aggregations in Tulan Ravine (5300 to 2400 Yr Cal. BP) through the Circulation of Obsidian Artefacts. *J. Anthropol. Archaeol.* 64 (4), 101360. doi:10.1016/j.jaa.2021.101360

Marinovic, N., and Lahsen, A. (1984). "Hoja Calama, Región de Antofagasta," in *Carta Geológica de Chile* (Santiago: Servicio Nacional de Geología y Minería de Chile), 58. escala 1:250.000.

May, G., Hartley, A., Chong, G., Stuart, F., Turner, P., and Kape, S. (2005). Eocene to Pleistocene Lithoestratigraphy, Chonostratigraphy and Tectono-Sedimentary Evolution of the Calama Basin, Northern Chile. *Rev. Geol. Chile* 32 (1), 33–58. doi:10.4067/s0716-02082005000100003

Meltzer, S. (1979). *The Salar de Talabre, Northern Chile: The Utilization of a Paleoindian Locality*. New York, NY: Columbia University.

Mignone, P. (2015). Illas y Allicac: La capacocha del Llullaillaco y los mecanismos de ascenso social de los "Inkas de privilegio". *Bol. Mus. Chil. Arte Precolomb.* 20, 69–87. doi:10.4067/s0718-68942015000200005

Mignone, P. (2010). Ritualidad estatal, capacocha y actores sociales locales: El Cementerio del volcán Llullaillaco. *Estud. Atacam.* 40, 43–62. doi:10.2307/4155051010.4067/s0718-10432010000200004

Mpodozis, C., Arriagada, C., Basso, M., Roperch, P., Cobbold, P., and Reich, M. (2005). Late Mesozoic to Paleogene stratigraphy of the Salar de Atacama Basin, Antofagasta, Northern Chile: Implications for the tectonic evolution of the Central Andes. *Tectonophysics* 399, 125–154. doi:10.1016/j.tecto.2004.12.019

Nami, H. G. (2015). Experimental Observations on Some Non-optimal Materials from Southern South America. *Lithic Technol.* 40 (2), 128–146. doi:10.1179/2051618515Y.0000000004

Niemeyer, H. (2013). "Geología del Área Cerro Lila-Peine, Región de Antofagasta. Carta Geológica de Chile," in *Serie Geología Básica* (Santiago: Servicio Nacional de Geología y Minería de Chile), 147. escala 1: 100.000. doi:10.1179/2051618515Y.0000000004

Niemeyer, H., and Schiappacasse, V. (1976). in *Homenaje Al R.P. Gustavo Le Paige*. Editor H. Niemeyer (Antofagasta: Universidad del Norte), 31–57.*Los yacimientos arqueológicos de la laguna Meniques*

Núñez, A. L., Grosjean, M., and Cartajena, F. I. (1999). Un ecorefugio oportunístico en la puna de Atacama durante eventos áridos del Holoceno Medio. *Estud. Atacameños* 17, 125–174. doi:10.22199/S07181043.1999.0017.00008

Núñez, L. (1981). Asentamiento de cazadores recolectores tardíos en la Puna de Atacama: Hacia el sedentarismo. *Chungara* 8, 137–168.

Núñez, L., Cartajena, I., Carrasco, C., López Mendoza, P., De Souza, P., Rivera, F., et al. (2017). The Temple of Tulán-54: Early Formative Ceremonial Architecture in the Atacama Desert. *Antiquity* 91 (358), 901–915. doi:10.15184/aqy.2017.87

Núñez, L., De Souza, P., Cartajena, I., and Carrasco, C. (2007). "Quebrada Tulan: Evidencias de Interacción Circumpuneña durante el Formativo," in *Producción y circulación prehispánicas de bienes en el sur andino*. Editors A. M. Nielsen, C. Rivolta, V. Seldes, M. Vásquez, and P. Mercoli(Córdoba: Editorial Brujas), 287–304.

Núñez, L. (1967). *Descubrimiento arqueológico en el salar de Talabre, Norte de Chile*, 76. Santiago: Boletín de la Universidad de Chile, 4–12.

Núñez, L., and Dillehay, T. S. (1979). *Movilidad Giratoria, Armonía Social y Desarrollo en los Andes Meridionales: Patrones de Tráfico e Interacción Económica*. Antofagasta: Universidad Católica del Norte.

Núñez, L., Grosjean, M., and Cartajena, I. (2005). *Ocupaciones Humanas y Paleoambientes en la Puna de Atacama*. San Pedro de Atacama: Universidad Católica del Norte-Taraxacum.

Núñez, L., Jackson, D., Dillehay, T., Santoro, C., and Méndez, C. (2016). "Cazadores-recolectores tempranos y los primeros poblamientos en Chile hacia finales del Pleistoceno (ca. 13.000 a 10.000 años a.p," in *Prehistoria en Chile. Desde sus primeros habitantes hasta los Incas*. Editors F. Falabella, M. Uribe, L. Sanhueza, C. Aldunate, and J. Hidalgo(Santiago: Editorial Universitaria), 192–200.

Núñez, L., Loyola, R., Cartajena, I., López, P., Santander, B., Maldonado, A., et al. (2018). Miscanti-1: Human Occupation during the Arid Mid-holocene Event in the High-Altitude Lakes of the Atacama Desert, South America. *Quat. Sci. Rev.* 181 (1), 109–122. doi:10.1016/j.quascirev.2017.12.010

Núñez, L. (1983). *Paleoindio y Arcaico en Chile. Diversidad, Secuencia y Procesos. Ciudad de México*. Ciudad de México: Escuela Nacional de Antropología e Historia.

Nu´ñ̃ez, L., Grosjean, M., and Cartajena, I. (2002). Human occupations and climate change in the Puna de Atacama, Chile. *Science* 298, 821–824. doi:10.1126/science.1076449

Orellana, M. (1962). *Descripción de artefactos líticos de Ghatchi. El problema del Precerámico en el norte de Chile*. La Plata: Universidad Nacional de La Plata.

Pärssinen, M. (2015). "Chapter 15. Collasuyu of the Inka State," in *The Inka Empire: A Multidisciplinary Approach*. Editor I. Shimada (Austin, TX: University of Texas Press), 265–286. doi:10.7560/760790-016

Pimentel, G. (2008). Evidencias formativas en una vía interregional entre san pedro de Atacama y el Altiplano de Lípez. *Estud. Atacam.* 35, 7–33. doi:10.4067/S0718-10432008000100002

Quade, J., Rech, J. A., Betancourt, J. L., Latorre, C., Quade, B., Rylander, K. A., et al. (2008). Paleowetlands and Regional Climate Change in the Central Atacama Desert, Northern Chile. *Quat. Res.* 69 (3), 343–360. doi:10.1016/j.yqres.2008.01.003

Ramírez, C. F., and Gardeweg, M. (1982). *Hoja Toconao, Región de Antofagasta. Carta Geológica de Chile 54*. Santiago: Servicio Nacional de Geología y Minería. escala 1:250 000.

Reinhard, J., and Ceruti, C. (2010). *Inca Rituals and Sacred Mountains: A Study of the World's Highest Archaeological Sites*. Los Ángeles, CA: Cotsen Institute of Archaeology Press.

Risacher, F., Alonso, H., and Salazar, C. (2003). The Origin of Brines and Salts in Chilean Salars: A Hydrochemical Review. *Earth-Science Rev.* 63, 249–293. doi:10.1016/S0012-8252(03)00037-0

Sáez, A., Godfrey, L. V., Herrera, C., Chong, G., and Pueyo, J. J. (2016). Timing of Wet Episodes in Atacama Desert over the Last 15 Ka. The Groundwater Discharge Deposits (GWD) from Domeyko Range at 25°S. *Quat. Sci. Rev.* 145, 82–93. doi:10.1016/j.quascirev.2016.05.036

Sanhueza, C. T. (2004). Medir, Amojonar, Repartir: Territorialidades Y Prácticas Demarcatorias En El Camino Incaico De Atacama (Ii Región, Chile). *Chungará (Arica)* 36 (2), 483–494. doi:10.4067/S0717-73562004000200018

Sapiains, P., Figueroa, V., Hayashida, F., Salazar, D., Menzies, A., González, C., et al. (2022). Supergene Copper and the Ancient Mining Landscapes of the Atacama Desert: Refining the Protocol for the Study of Archaeological Copper Minerals through the Case Study of Pukara de Turi. *Minerals* 11, 1402. doi:10.3390/min11121402

Seelenfreund, A., Pino, M., Glascock, M. D., Sinclaire, C., Miranda, P., Pasten, D., et al. (2010b). Morphological and Geochemical Analysis of the Laguna Blanca/Zapaleri Obsidian Source in the Atacama Puna. *Geoarchaeology* 25 (2), 245–263. doi:10.1002/gea.v25:210.1002/gea.20306

Seelenfreund, A., Sinclaire, C., Dinator, M., Morales, J., Pasten, D., Miranda, P., et al. (2010a). "Negras y brillantes: explotación y distribución de obsidianas en la macro región del Salar de Atacama," in *Actas del XVII Congreso Nacional de Arqueología Chilena Tomo II* (Valdivia: Ediciones Kultrún), 813–824. Sociedad Chilena de Arqueología.

Serracino, G. (1975). Los movimientos de los cazadores y recolectores en la Cordillera de los Andes, entre la latitud 21° y 26° y longitud 67° 00" y 70° 22. *Estud. Atacameños* 3, 17–43.

Sheets, P. (1999). "The Effects of Explosive Volcanism on Ancient Egalitarian, Ranked, and Stratified Societies in Middle America," in *The Angry Earth: Disaster in Anthropological Perspective*. Editors A. Oliver-Smith and S. Hoffman (New York: Routledge), 36–58.

Sheets, P. (2001). "The Effects of Explosive Volcanism on Simple to Complex Societies in Ancient Middle America," in *Interhemispheric Climate Linkages*. Editor V. Markgraf (San Diego, CA: Academic Press), 73–86. doi:10.1016/B978-012472670-3/50008-2

Shimoyama, S. (2002). "Volcanic Disasters and Archaeological Sites in Southern Kyushu, Japan," in *Natural Disasters and Cultural Change*. Editors R. Torrence and J. Grattan(London: Routledge), 326–341.

Torrence, R., and Grattan, J. (2002). "The Archaeology of Disasters: Past and Future Trends," in *Living under the Shadow: Cultural and Environmental Impact of Volcanic Eruptions*. Editors R. Torrence and J. Grattan(Walnut Creek, CA: Left Coast Press), 1–18.

Torrence, R., Pavlides, C., Jackson, P., and Webb, J. (2000). Volcanic Disasters and Cultural Discontinuities in Holocene Time, in West New Britain, Papua New Guinea. *Geol. Soc. Lond. Spec. Publ.* 171, 225–244. doi:10.1144/GSL.SP.2000.171.01.18

Torrence, R. (2016). Social Resilience and Long-Term Adaptation to Volcanic Disasters: The Archaeology of Continuity and Innovation in the Willaumez Peninsula, Papua New Guinea. *Quat. Int.* 394, 6–16. doi:10.1016/j.quaint.2014.04.029

Ureta, G., Aguilera, F., Németh, K., Inostroza, M., González, C., Zimmer, M., et al. (2020b). Transition from Small-Volume Ephemeral Lava Emission to Explosive Hydrovolcanism: The Case of Cerro Tujle Maar, Northern Chile. *J. S. Am. Earth Sci.* 104, 102885. doi:10.1016/j.jsames.2020.102885

Ureta, G., Aguilera, F., Németh, K., and Menzies, A. (2018). "Cerro Tujle maar, southeast of the Salar de Atacama Basin, Chile: Morphological, petrographic and geochemical analysis," in 7th International Maar Conference, Olot, Spain, May 21–25, 2018. Editors X. Bolós and J. Martí, 130–891 131.

Ureta, G., Németh, K., Aguilera, F., González, R., González, R., González, C., et al. (2020a). Features that Favor the Prediction of the Emplacement Location of Maar Volcanoes: A Case Study in the Central Andes, Northern Chile. *Geosciences* 10 (12), 507. doi:10.3390/geosciences10120507

van Wyk de vries, B., Self, S., Francis, P. W., and Keszthelyi, L. (2001). A Gravitational Spreading Origin for the Socompa Debris Avalanche. *J. Volcanol. Geotherm. Res.* 105 (3), 225–247. doi:10.1016/S0377-0273(00)00252-3

Vanderhoek, R., and Nelson, R. E. (2007). "Ecological Roadblocks on a Constrained Landscape: the Cultural Effects of Catastrophic Holocene Volcanism on the Alaska Peninsula, Southwest Alaska," in *Living under the Shadow – the Cultural Impacts of Volcanic Eruptions*. Editors J. Grattan and R. Torrence (California: Left Coast Press), 133–152.

Yacobaccio, H. D., Escola, P. S., Pereyra, F. X., Lazzari, M., and Glascock, M. D. (2004). Quest for Ancient Routes: Obsidian Sourcing Research in Northwestern Argentina. *J. Archaeol. Sci.* 31 (2), 193–204. doi:10.1016/j.jas.2003.08.001

Yacobaccio, H., and Núñez, L. (1991). "Recursos y espacio en quebrada Tulán: el sitio Tulán 52 (Puna deAtacama)," in *Actas del XI Congreso Nacional de Arqueología Chilena*. Editor H. Niemeyer (Santiago: Museo Nacional de Historia Natural - Sociedad Chilena de Arqueología), 165–174.

Conflict of Interest: The authors declare that the research was conducted in the absence of any commercial or financial relationships that could be construed as a potential conflict of interest.

frontiers | Frontiers in Earth Science

ORIGINAL RESEARCH
published: 22 July 2022
doi: 10.3389/feart.2022.909967

An Inside Sun: Lickanantay Volcanology in the Salar de Atacama

Sonia Ramos Chocobar[1,2] *and Manuel Tironi*[3,4,5,6]*

[1]Fundación Ayllus Sin Fronteras, San Pedro de Atacama, Chile, [2]Indigenous Community of San Pedro de Atacama, San Pedro de Atacama, Chile, [3]Instituto de Sociología, Pontificia Universidad Católica de Chile, Santiago, Chile, [4]Instituto para el Desarrollo Sustentable, Pontificia Universidad Católica de Chile, Villarrica, Chile, [5]Centro para la Gestión Integrada de Riesgo de Desastres — CIGIDEN, Santiago, Chile, [6]Centro de Desarrollo Local, Pontificia Universidad Católica de Chile, Villarrica, Chile

The need of establishing more substantive dialogs between the mainstream and Indigenous knowledge on volcanoes has been increasingly recognized. To contribute to this endeavor, in this article we present the basic volcanological understandings of the Lickanantay people in the Salar de Atacama Basin. The Salar de Atacama Basin is an active volcanic territory within the Central Volcanic Zone of the Andes (CVZA). From the El Tatio geothermal field to Socompa volcano, more than 19 active volcanoes surround the territory that the Lickanantay (Atacameño) people have inhabited for more than 11,000 years. Living around and with the geological dynamism of the CVZA for millennia, the Lickanantay communities have accumulated rich observational and ceremonial data on volcanoes and volcanism. Paradoxically, however, while the Atacameño people have thoroughly characterized the CVZA, the volcanology community has not been properly introduced to the ancestral knowledge articulated in the territory. In order to make traditional Atacameño perspectives on volcanoes, volcanic risk, and geo-cosmic interdependence more amply available to the volcanology community, in this article, we present a basic description of what we call Atacameño volcanology. By Atacameño volcanology, we understand the ancestral principles by which volcanoes are known and understood as partaking in larger processes of a cosmo-ecological formation. Specifically, we describe the basic volcanological notions arising from the Lickanantay ancestral knowledge—volcanic formation, functions, and behavior. Second, we focus on the El Tatio geothermal field to offer a situated example. Finally, we delineate some relevant elements of human–volcano interactions and volcanic risk management from an Atacameño perspective. In our conclusions we suggest that volcanology, particularly in the context of the Andes, needs to engage more substantially with the Atacameño or other ancestral systems of knowledge production to expand volcanological insights and respond to the call for decolonizing science.

Keywords: Lickanantay, volcanology, indigenous knowledge, Salar de Atacama, risk management

Edited by:
Felipe Aguilera,
Catholic University of the North, Chile

Reviewed by:
Marie-Noelle Guilbaud,
National Autonomous University of Mexico, Mexico
Jon J Major,
(USGS), United States

***Correspondence:**
Manuel Tironi
metironi@uc.cl

Specialty section:
This article was submitted to Volcanology,
a section of the journal Frontiers in Earth Science

Received: *31 March 2022*
Accepted: *17 June 2022*
Published: *22 July 2022*

Citation:
Ramos Chocobar S and Tironi M (2022) An Inside Sun: Lickanantay Volcanology in the Salar de Atacama. Front. Earth Sci. 10:909967. doi: 10.3389/feart.2022.909967

1 INTRODUCTION

In the last few decades, important shifts have been made regarding the validation of Indigenous volcanological knowledge around the world. Earth scientists themselves have begun to recognize that the foundations of geology in general (Scarlett, 2022) and volcanology in particular (Pease, 2021; Scarlett et al., 2022) are inseparable from imperial colonialism, that is, that they have been shaped by the social and political issues and agendas of colonial expansion (Cartier, 2021). Acknowledging this legacy, there are growing calls for establishing more symmetrical, intercultural dialogues on volcanoes and volcanic processes.

The Salar de Atacama Basin (hereafter the Salar), home of the Lickanantay (Atacameño) people,[1] offers a powerful example. The Salar (23°30S 68°15′O/2,407 m.a.s.l.) is an active volcanic territory within the Central Volcanic Zone of the Andes (CVZA), in northern Chile. From the El Tatio geothermal field to Socompa volcano, more than 19 active volcanoes surround the territory that the Lickanantay people have inhabited for at least 11,000 years (Núñez, 1992). Over this period, different phases of occupations can be identified, each one characterized by specific patterns of resource utilization and human–land interactions, such as hunting, fishing, animal domestication, agriculture, animal husbandry, mining, commerce, and trade (Nuñez et al., 2010). Common to these phases, however, is the role of volcanoes articulating ecological, economic, and spiritual life in the puna (Grebe and Hidalgo, 1988; Berenguer, 2004; Valenzuela and Moyano, 2021).

This long history of volcano–human relations in the Salar has materialized into a robust knowledge system on volcanic activity and relations based on both observational and ceremonial knowledge-making. This includes general hypotheses on volcanic formations (Contreras, 1994; Barros, 1997), knowledge on climatic–volcanic interactions (Sanhueza, 2004; Moyano and Uribe, 2012), and on water–agriculture–cattle–volcanic nexuses (Redin, 2018). By all measures, then, the Lickanantay people have articulated their own geosciences.[2]

This knowledge, however, has been hardly recognized, let alone incorporated in Western volcanic research and policy. This is particularly troublesome when we recognize the twin histories of geological sciences and colonialism (Yusoff, 2019) and the concomitant imperative to treat Indigenous knowledge as proper, robust, and time-tested expertise (Liboiron, 2021).

Substantive collaborations between mainstream and Likanantay volcanologies are ever more important as the Salar de Atacama Basin is under intensive environmental pressure. A long history of extractivism in the area has materialized in the accumulation of multiple environmental effects. Copper and, more recently, lithium mining, have meant direct damage to aquifers, salt flats, rivers, and other geological formations and processes (Bolados and Babidge, 2017; Bustos–Gallardo et al., 2021). Consequently, conflicts between the state and corporations on one side, and communities on the other, have multiplied. In these conflicts, Atacameño hydrological understandings of the Salar, for example, have been largely neglected. So, at the heart of the frictions with the Indigenous communities lies not only the irreparable harm inflicted to unique ecosystems and Indigenous and peasant life projects, but also the systematic denial of Lickanantay geological knowledge, including knowledge about volcano–land–human relations that could be useful in water, land, and volcanic risk management.

This article is an attempt at bridging the gap between mainstream and Lickanantay volcanological knowledge. We do so by presenting what we call *Lickanantay volcanology*, or the ancestral principles by which volcanoes are known in the Salar and understood as partaking in larger processes of the cosmo-ecological formation. Our objective is not to give a definitive explanation of the Lickanantay knowledge on volcanoes—since such knowledge is always embodied and emplaced. It is neither to replace Western volcanological knowledge on the CVZA. Rather, our aim is to give a glimpse of some of the principles guiding Lickanantay volcanology and to present them to the volcanological community. This much-needed communication is crucial, we argue, in order to articulate more robust and just accounts on volcanic behavior and volcanic risk management in Indigenous territories.

The article is the collaboration between a Lickanantay elder and healer (Sonia Ramos) and a Chilean scholar (Manuel Tironi). The partnership is based on an ongoing relation of mutual learning over the last 4 years. In this period, we have established land-based protocols of intercultural collaboration and co-production, including joint fieldwork, co-writing, and ceremonies. We recognize that a scientific article does not problematize—actually it reinforces—current systems of knowledge-making. We also acknowledge that by presenting the basic features of Lickanantay volcanology in a scientific article, we are facilitating a first encounter between otherwise unconnected sets of expertise. Our objective is precisely to help in the cultivation of an inter-scientific dialogue for the articulation of an epistemologically plural strategy for volcanic risk management in the Salar and basins elsewhere. Our description can be helpful for the articulation of intercultural exchanges and plans in Perú, Ecuador, Colombia, and other volcanic zones in Latin America. By rendering visible Lickanantay volcanological knowledge, we also aim at hopefully limiting the increasing aggression to the Salar.

The article is organized as follows. In the next section, we introduce the Salar de Atacama's territory and the social challenges it faces in the words of Sonia Ramos as a Lickanantay elder. We also articulate a brief literature review to situate Lickanantay volcanology in the context of social, community, and Indigenous debates on volcanology and volcanic risk. In the third section, we present our materials and methods. In the fourth and main section, we present the basic features of Lickanantay volcanology as understood and

---

[1] Lickanantay is the kunza ethnonym of what in Chile is known as Atacameño people. It is composed by *lickan* (territory, country, or land) and *antay* (people), roughly translating as "people of the territory". The prefix *lickan* is appears extensively in Atacameño toponyms, for example Lickancabur ("Mountain of the people").

[2] If science is "the careful study of the structure and behavior of the physical world, especially by watching, measuring, and doing experiments", as defined by the Cambridge Dictionary, then the term should not be exclusive to Western knowledge, as argued by several Indigenous intellectuals (Deloria et al., 2018).

systematized by Sonia Ramos after decades of land-based and intergenerational observation and learning. Finally, in our conclusion, we reflect on the challenge of pluralizing volcanological knowledge when working in the CVZA and other Indigenous territories.

2 CASE STUDY AND LITERATURE REVIEW

2.1 The Salar de Atacama Basin: A Lickanantay Territory Under Pressure

The Salar is the central element around which the Lickanantay or Atacameño people have thrived for at least 11,000 years. The Lickanantay people speak *kunza* and have developed complex socio-cultural systems of knowledge-making and territorial occupation. From an ancestral perspective, the Salar is a complex entity interconnected with the surrounding volcanoes and the *aguadas* (water springs) that flow from mountains and volcanoes to the Salar. That is, the Salar is a embroiled eco-geological web that cannot be restricted to the figure of a salt flat. The Salar has been recognized as Indigenous land through the rights granted by the Indigenous Law of Chile (19.253) and Convention 169 on Indigenous and Tribal Peoples of the Labor Organization (ILO).

The process of *Chilenización*[3] since the late 19th century entailed the ever-increasing development of the mining industry in the Atacama Desert (Acuña and Tironi, 2021), disrupting the traditional agro-alimentary practices that otherwise sustain family economies in the Salar. Half of the copper mined in Chile comes from the Antofagasta region (Babidge and Bolados, 2018) and four of the largest operations are located in the surroundings of the Salar: Minera Escondida, Compañía Minera, Zaldívar, and CODELCO.

In the last few decades, the Salar has become the world's principal source of lithium (USGS, 2019), which has in turn increased current tensions. Lithium is industrially unearthed by pumping saline groundwater from beneath the Salar and extracting its dissolved lithium content (Bustos-Gallardo et al., 2021). The *salmuera* (brine) is then left to evaporate in shallow open-air ponds. For every ton of lithium, about two million liters of extracted water are needed to evaporate. This has not only radically changed the hydrological equilibrium of the Salar, but also disturbed fragile highland ecosystems and impacted ancestral sites and practices. From the perspective of Lickanantay knowledge, extractivism in the Salar affects the complex relational systems that connect humans, ancestors, and land—including surrounding volcanoes, rivers, and geothermal fields—in ways that Western science and policy-making are yet to fully appreciate.

2.2 Shifting Perspectives: From Social Volcanology to Indigenous Sovereignty

The colonial origins of the Earth sciences in general, and volcanology in particular, have been widely acknowledged (Stone, 1988; Home, 2006; Donovan et al., 2011; Atkinson, 2016; Kophamel, 2020; Pico et al., 2020; Cartier, 2021; Donovan, 2021; Scarlett, 2022). To survey, map, and ultimately exploit natural resources in colonized territories for the benefit of the empire was a crucial factor energizing geosciences as a scientific field in 17th century Europe (Driver, 1992; Stafford, 2017). Colonized societies had—and still have—their own geological and volcanological knowledge systems, articulated after millennia of close co-habitation and observation of terrestrial phenomena (Swanson, 2008). Indigenous knowledge, however, has been deemed as inferior, partial, magical, or, in the best of cases, supplemental by Western sciences (Whyte, 2020). As Haudenosaunee and Anishinaabe scholar Vanessa Watts (2013) suggests, Indigenous explanations of the world are often viewed as mythic by "modern" society, representing alternative modes of interpretation rather than "real" events. This neglect has been crucial for positioning Western science as the sole frame of reference for appraising reality. Aymara sociologist Silvia Rivera Cusicanqui (1993) coined the term "coloniality of knowledge" precisely to indicate that the process of universalizing a vision of the world after the principles of the Enlightenment Project[4] was sustained on epistemological impositions and erasures—and that the process, far from being in the past, is still ongoing with important ramifications.

These critiques do not aim at undermining the validity of Western volcanology. Rather, they call for the validation of other knowledge systems in the search for more diverse dialogues within the scientific field. And at least in the field of volcanology, there have been important progresses. An important development has been the integration of social and cultural perspectives on the production of socio-natural disasters (Quarantelli, 1987; Wisner et al., 2004; Hilhorst, 2006; Tierney, 2012; Bretton et al., 2018). This allowed the inclusion of notions such as geopolitics, vulnerability, and community into the understanding of volcanic hazards and their impacts (Cashman and Cronin, 2008; Chester et al., 2008; Haynes et al., 2008; Paton et al., 2008; Barclay et al., 2015; Donovan, 2019), giving birth to a sub-discipline sometimes called social volcanology (Donovan, 2010).

These approaches complement the anthropological research on the interpretation of volcanism according to Indigenous cosmovisions, the representations of volcanoes in belief systems, and the impacts of eruptions on traditions and

---

[3] "Chilenization" is the name given to the period between 1880 and 1930 in which the territory annexed after the war against Perú and Bolivia was culturally, institutionally, and socially incorporated to Chile. In the Lickanantay territory, this included the inculcation of national sentiments, the Christianization of the population, and the deliberate erasure of any Indigenous cultures (González, 2012).

[4] Referred to the European intellectual movement of the 17th and 18th centuries in which ideas concerning God, reason, nature, and humanity were synthesized into a worldview that gained wide assent in the West. Central to Enlightenment thought were the use and celebration of reason, the faith in progress, its focus on the scientific method, and reductionism—the breaking down of problems and systems into their components in order to find a solution and/or better understand how the system or problem works.

cultural identities (e.g., Peraldo and Mora, 1995; Skinner, 2004; Spoon, 2007; Aedo, 2008; Juárez, 2012; Moyano and Uribe, 2012; Schwartz-Marin et al., 2020; Socha et al., 2021). Importantly, this line of research attempts at problematizing the often rigid boundaries with which studies of volcanism and indigeneity are traditionally approached as two incompatible knowledge systems. It emphasizes the existence of a dual rather than a dichotomous relation between the symbolic—beliefs, norms, and imaginaries—and the material—natural and physical phenomena. From this vantage point, volcanoes are both physical entities *and* beings with volition and the capacity to intermediate in ecological, meteorological, and social relations (Juárez, 2012). For example, Moyano and Uribe (2012) showed that the Chiliques volcano (23°35′00″S 67°42′00″O) plays a central role within a system of sacred mountains that are invoked by the Atacameño community of Socaire during the canal cleaning ceremony, in which the volcano is invoked as an intermediator of meteorological phenomena.

Our attempt at presenting Lickanantay volcanology is aligned to these approaches, as it also points at opening volcanological research beyond strict scientificism. Inspired by the decolonial turn in the geosciences (Pico et al., 2020), we also diverge from these scholarships. Rather than trying to *interpret* what Lickanantay experts have to say about volcanism—restricting the labor of comparison to the Western scientists—the task of interpretation is conducted by Indigenous experts themselves (see for example Kopenawa and Albert, 2013). By doing this, we take Lickanantay volcanology as a proper, irreducible form of science that serves as a crucial source of guidance for Lickanantay resurgence. We aim to build a bridge between Western and Lickanantay volcanologies, neither by transforming the latter into "geomythology" (Donovan, 2010; Riede, 2015) nor massaging it to fit into an otherwise conventional science, but by validating it as a scientific system with ad hoc research questions and methods.

3 MATERIAL AND METHODS

The material of this article is the knowledge of Sonia Ramos and was collected during 4 years of conversations between the authors. This included formal interviews but also multiple exchanges during walks, meetings, and ceremonies in San Pedro de Atacama, El Tatio, Calama, and the Domeyko Cordillera. The records of these conversations were systematized and iteratively discussed in an open, collaborative process between the authors.

The methodology utilized is aligned with the Indigenous principles of knowledge and research (Smith, 1999). It takes conversation as the main method for data gathering, provided that, as in the Mapuche *güxam*,[5] conversation is not just a form of verbal exchange but an in-place process to communicate vernacular knowledge cultivated by the ancestors (Quilaqueo and Quintriqueo, 2017). It is also a process of sharing knowledge which, similar to what is known as *yarning* in the Australian context, is reliant upon relationships, responsibility, and accountability between the participants (Barlo et al., 2020). In this sense, the methodology of this article—including data collection, interpretation, and writing—is in itself a practice of historical and epistemological reclamation. For example, several conversations about volcanic and geothermal activities were conducted with volcanoes and geysers, traveling to their surroundings and invoking their presence through ceremonies—because in the Lickanantay epistemological systems, knowledge is always land-based or cultivated *in-place* (De la Cadena, 2015). Both Sonia Ramos and Manuel Tironi participated in these conversations, being guided by the former and recorded by the latter.

Following the Oral History methodology developed by Rivera Cusicanqui (1987), the conversational and relational methodologies we followed were aimed at coping with the ontological differences that constantly punctured the communication between a Lickanantay elder and a white scholar. This was also aimed at creating a systematic process of information feedback and validation in terms of the interests and expectations of doña Sonia as an ancestral authority. The process paid attention to doña Sonia's vision of history, society, and land. If some statements sound too politically charged, it is because Indigenous knowledge is always principled, that is, normative (oriented toward ethical and moral goals) and prescriptive (oriented toward informing conducts) (Teillier et al., 2018). In contrast to Western knowledge, there is no division between the observation of "what is" and the reflection of "what ought to be", and therefore between the objective and the subjective (González-Gálvez, 2016). To separate the factual and the normative in the results that follow would not only hamper a proper understanding of the Lickanantay volcanological principles presented here, but also the possibility of integrating Indigenous philosophies of science in their own right (Whyte, 2020). As discussed by Rivera Cusicanqui, what matters in the method of relational oral histories that we follow is not so much to identify "what happened" but *why* it happened and *how* what happened fits in the larger assessments of justice and *buen vivir*.[6]

4 RESULTS: LICKANANTAY VOLCANOLOGY

Following our methodological principles, the results that follow will not be presented as "findings", that is, as propositions

---

[5] *Güxam* is the Mapuche art of conversation in which an older person talks about his or her life and the history of his/her people, intertwining storytelling, memories, and teachings.

[6] *Buen vivir* ("good living") is the translation of *sumak kawsay* (Aymara), *suma qamaña* (Quechua), or *kume mongen* (Mapuche). It represents a fundamental philosophical pillar for Andean–Amazonian peoples by which there is an indissoluble and interdependent relationship between the universe, nature, and humanity that informs the ethical and practical bases of development and society (Acosta and Martínez, 2009).

analytically induced from observations and abstracted from their locus of enunciation. Instead, we present the words of doña Sonia herself. We have organized and edited them for consistency and to convey a coherent narration of what Lickanantay volcanology is—but they otherwise retain their situated and embodied meaning. As a result, arguments are not organized in a fully linear mode, but are articulated circularly, appearing in different passages throughout the narration. In addition, to retain the indigenous meaning of doña Sonia's words, all relevant commentaries, whether contextual explanations or engagements with archaeological, anthropological, and geological insights, will be presented as footnotes. It is important to note that we have retained the Spanish grammatical gender of those nouns whose meaning play a fundamental role in Lickanantay philosophy—and for which, neutralizing their gender would entail losing their significance. For example, "*naturaleza*" (nature) will be treated as feminine (*la naturaleza*, *la madre naturaleza*, and *la Pachamama*) and "*volcán*" (volcano) as masculine (*el volcán*).

The results are organized as follows. First, we present some of the main hypotheses and definitions articulating what we call Lickanantay volcanology. We then discuss Lickanantay volcanological knowledge within the broader Lickanantay philosophical system on nature and humans. Finally, we discuss what this knowledge reveals with regards to volcanic risk management from an Atacameño perspective. Taken together, these propositions need to be assessed as specific materializations of Lickanantay knowledge on the volcano–cosmos–human nexus, not as a comprehensive nor institutional articulation of a definitive Lickanantay canon on the matter.

4.1 Three Worlds: Lickanantay Volcanological Knowledge

4.1.1 The Above and Below: The Inside Sun

The universe that we see above is also below. Ancestrality refers to the cosmic, but also to that which is above is below. This is the basic unity-in-duality of ancestral knowledge, the doubling, and the pairs. We humans are in this intermediate layer. Let us call this intermediate the *visible* layer, the layer that we can see.

This is why we talk about three worlds: the world above, the human world, and the world beneath. But the above and below worlds have many great connections between them, and their gift to us is that they offer life to the intermediate world—a gift that we do not appreciate nor see. We break everything into pieces because we think that only science can see—but we do not dare to see these other worlds differently, interconnectedly.

So, as there is a sun above, there is an *inside Sun*, the one that exists below the land and that is able to give nature the needed energy to develop and create all the ecological systems. From an ancestral perspective, there is a constant interaction between the four elements: Earth, air, *puri*,[7] and fire. The fire element is an internal Sun, alive, situated in the bowels of the Earth. And this inside Sun is vital. It is this inside Sun which prevents the desert from becoming dead land, which gives us an adequate temperature, and which creates an equilibrium between the in-between world and the cosmic sun. We talk about the cosmic sun a lot, about its changes, waves, and explosions, but the same movements are being replicated in the interior of the Earth, which is giving us a seismic dynamism as an indicator of Earth movements, of *puri* movements in the planet.

It is this inside Sun that we need to start understanding, the one that is below us, and whose force some might call magma. Sometimes people talk about the infra-world—or the below world—as something dense and bad, but from our ancestral knowledge, we aim at trying to care for it and making it thrive. It is this inside Sun which prevents stagnation. And it is quite clear: if we have this inside Sun reverberating, nothing can be stagnant, it is us who hamper the free will of nature, and it is us humans that are stagnating and stopping the force of the inside Sun.

4.1.2 Body-Territory Circulations

Actually, the inside Sun moves through us, is a part of us. We have its magma in our bodies in the form of iron. In Lickanantay healing, we work a lot around those movements of the elements, because we are part of that wholeness. So, when nature is healthy, when the inside Sun is vibrant, we are healthy. This is what El Tatio teaches us.[8] El Tatio is a sacred place because it is an encounter of the four elements: fire, Earth, air, and *puri*. After a period of relentless change in the territory, the *abuelos*,[9] the ancient inhabitants of the territory returned to see if things had calmed after two thousand years of floods and inundations.[10] They needed to return because of the love for of their land and the need for balance and harmony. When they returned, they realized that the spiritual forces had put the four elements in one place, in El Tatio, to give humans an example of harmony.

El Tatio then teaches us how to harmonize our bodies, because we are also constituted by those four elements. When we de-harmonize a territory we also de-harmonize our bodies. Health is

---

[7] *Puri*, water in Kunza.

[8] El Tatio is the largest geyser field in the southern hemisphere and the third in the world, with more than 100 springs erupting at more than 4,000 m.a.s.l. in the Andes. It is located in the upper part of a tectonic pit about 4 km wide by 6 km long, which make up the El Tatio valley, and is flanked on the eastern sector by a tectonic massif called Serranía Tucle-Loma Lucero, composed of andesitic stratovolcanoes and that make up the natural geographical limit with Bolivia. To the west it is flanked by the so-called El Tatio Volcanic group, made up mainly of rhyolitic domes. The water reservoir of El Tatio is inside the volcanic rocks, covered by impermeable layers, with faults driving the hot waters to the surface. The heat source is unknown, but it may be magma or igneous intrusion.

[9] The concept of *abuelo* is central to Atacameño culture and sociability. Highly ambiguous and modulated by colonial relations, it refers to ancestors in multiple senses and represents the complex relation of Lickanantay people with the past. *Abuelos* include both ancestors in direct relation of kinship, as well as in archaeological reference to the "ancient ones" or *gentiles* about whom oral memory is no longer kept. *Abuelos* also refer to non-human forces—close to the figure of "spirit"— which at the same time animate and protect natural elements such as mountains and rivers (Ayala, 2008; Martínez, 2010; Villanueva et al., 2018).

[10] This episode is part of mythological Lickanantay stories and refers to pre-Hispanic times.

territory. So, how can we convince the sciences that "development" is, that we can find here in El Tatio for example, the answers for planetary challenges?

4.1.3 Basins, Mountains, and El Tatio

When this territory was formed it was just one block. It terraformed through time but it never lost its harmony nor its subterranean equilibrium. Today, the sciences separate the territory into basins, mountain ranges, and aquifers, but they are interconnected from below. And why do we talk about a subterranean equilibrium? Because, there is the inside Sun delivering its warmth, delivering life, and stitching the territory together.

We have also learnt that mountains are not just geological compounds. We say that some mountains communicate with the cosmos, with the above, and some others with the infra, with the below. Those that communicate with the infra, with the inside Sun, it is because the inside Sun renders a livable climate. The mission of the desert is to offer cold to the planet, to cool down the planet, but today the desert is unable to fulfill this mission because it has been extremely intervened.

Many volcanoes are our *maikos mayores*,[11] such as the Licancabur who is a living being, peaceful and kind with his people. He is in constant dialog with humans and allows for a harmonic living on the surface, in the intermediate world. Volcanoes are unique beings because they connect the above and the inside Suns. And they connect different elements, just like El Tatio. El Tatio is known as "The *abuelo* that cries",[12] also as the *abuelo* that sings for the beautiful sounds it makes when the wind blows. You can feel that there is something below here, something shining and warming that makes *puri* to appear [*asomarse*] as fumes. And that is energy. El Tatio is a very powerful energy field. There are other similar fields, but here, it presents itself non-violently because there is harmony between the four elements, there is an equilibrium. El Tatio shows us, every day, how we need to work with nature. When we arrived here, we saw new water springs and new small geysers. That is nature saying to humans that she can regenerate herself, that she does not need us. Mother Nature could be crying of pain for all the transgressions that she has suffered, but she does not; she is giving us answers to live well in the world instead.

This is the reason why El Tatio is such an important sacred place. This is what El Tatio teaches us and this is why it was saved from geothermal intervention. But not everyone can see that, not even some Indigenous communities. Why? Because, there is an installed colonialism [*colonialismo instalado*]. El Tatio is usually seen from the perspective of tourism as a landscape, and not as a consciousness.

4.2 *Buen vivir*: Human–Nature Relations

Crucial to understanding Lickanantay volcanology and creating meaningful collaborations, is to establish a new relation with ancestral knowledge. Ancestrality is not how the West sees it, as something pagan or folkloric. It is the real knowledge of nature. We need to talk from that vantage point. Spirituality is a science, a proper scientific endeavor based on systematic methods, evidence, data contrasting, and purpose. But people see it as something rather magical.

From a Lickanantay perspective, we have to reckon, to start with, that we are spirits in human disguises, and when we dissociate ourselves from that spirit, we dissociate from what we are, from our nature. There is much work to create a new path, because the path humans took is wrong; "industrialization" and "growth" have been wrong paths because they do not sustain nature. To the contrary, they destroy it. And that destruction of "the planet" is our destruction, we endanger our own survival. And Western science is not offering any answers. If we have survived in the desert, it is thanks to this ancestral knowledge, this work of integrality, this capacity to understand the balance between the four elements, and that we are part of them. If we do not realize this connection and what we are, we are destined to disappear.

It is, however, possible to create a *buen vivir*, to create good relations between humans and nature. And this is the relevance of understanding the inside Sun. How can we begin transforming volcanological research on the inside Sun into an inquiry about what we should be and rightly do? This is the fundamental question. By understanding the hydro–Sun connections, the internal, the sub-world, and the below, we can have great responses for these times, *pero la ciencia no está apapachando* [but science is not supporting this task].

El Tatio, again, as a sacred place in which the inside Sun makes itself visible in its interactions with *puri*, the Earth, and the atmosphere, is of great importance. If El Tatio had been destroyed, we would not have that opportunity to witness those interactions.[13] El Tatio is of paramount importance to think about—and find responses to—the changes that the planet is living through: the importance of understanding nature, how she protects us and gives us a *buen vivir*.

When El Tatio was intervened, you could only see the fumes, nothing else, barren. Now you can find water, again, sprouting. So, nature has the capacity and knows how to regenerate herself, how to create, she cannot be a dead being if she gives life. Take the thermophiles that abound in El Tatio. They are able to absorb the arsenic from *puri* and offer us drinkable water, *puri* that is good for humans. This demonstrates that *puri* is something alive, intelligent, self-creating, and searching for the means for human survival. This is crucial: from a Lickanantay

---

[11] *Maiko* or *mallku* is the name given to sacred mountains, which are in turn associated with spirits and *abuelos* or ancestors. *Maiko mayor* or *Tata-maiko* refers to an especially important ceremonial or tutelar sacred mountain (Grebe and Hidalgo, 1988; Valenzuela and Moyano, 2021). In this case, the Lickancabur (Mountain of the People) is a crucial spiritual figure who center-stages Atacameño ontogenetic narratives. The Fertilization of the Earth, the primary cosmological explanation in the Salar de Atacama, was produced by the copulation between the male Lickancabur and his female partner, Kimal, the largest mountain in the Domeyko Cordillera, parallel to the Andes (Contreras, 1994; Barros, 1997).

[12] *Tata-iu* in Kunza.

[13] The first geothermal exploration in El Tatio was carried out in 1908, and in 1931 two wells were drilled. In 1968 more systematic explorations were carried out in several areas of El Tatio. On 3 July 2008, the Regional Environmental Commission (Corema) of Antofagasta approved the first phase for the exploration of geothermal resources in an area located south of El Tatio. After intense resistance from Lickanantay communities, including a walk made by doña Sonia Ramos and Amelia Mamani from San Pedro de Atacama to Santiago to protest against the intervention of El Tatio, the exploration was stopped.

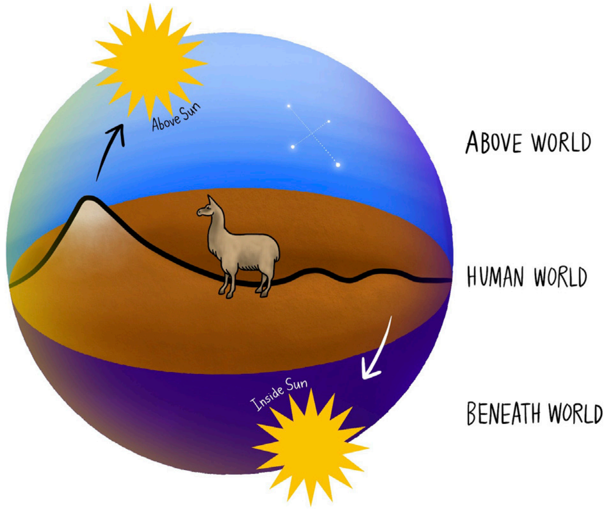

FIGURE 1 | Lickanantay organization of the three worlds. Design: Sergio Iacobelli.

perspective, nature—whether *puri*, volcanoes, plants, animals, and all their relations—is alive, sentient, and generous, creating and giving life abundantly. But we cannot feel it nor see it. It is as if humans were blind.

4.3 Offering as Volcanic Risk Management

Volcanoes are much related to climates, temperatures, and waters.[14] The inside Sun has to be thanked for that. Volcanoes are not something negative, totally to the contrary, it is thanks to them that we have good weather. Volcanoes are in charge of warming the cold desert, hence providing the needed warmth for ecological growth and conservation. Moreover, some volcanoes can attract the rain—the Sairecabur volcano means the Rain Mountain in Kunza (*saire* = rain, *caur/cabur* = mountain)—facilitating life in the world's driest desert. Maybe we have never shown our gratitude to the inside Sun and volcanoes, as they deserve, and we should. And that gratitude and care is the most crucial element to establish a communication channel with them.

Let us illustrate this with an anecdote. When the inside Sun heats the Putana volcano[15] and it manifests, Calama trembles. Some time ago, it would tremble every day in Calama. So people called me, "Doña Sonia, el Putana está tirando mucha fumarola y está temblando mucho así que *comuníquese*" [Doña Sonia, the Putana is emitting a lot of fumes and it's trembling a lot so *communicate yourself*"]. Ok, I said, I will talk to the volcano; I will try to ask him what is going on. So, I went with a cousin and my daughter. I did the offering to him (*ofrenda*), I talked to him, and what he said is that we, humans, were being too disrespectful with regards to his mission, in relation to the warmth that he gives us. So, I offered my apologies on behalf of Calama. When we were going back [to Calama], my cousin and daughter were in shock, saying that they could not believe it, that if they had not come, they would not believe it. The Putana began to calm down, the fumes began to decrease, and the weather changed.

It is this communication that ancestral people have always managed. Actually, I am not sure to call it "communication" since it is too aggressive—this *integrality* or completeness. Here, in the desert, one needs to learn integrality, to embrace integrality, otherwise you are lost, nature "*te hace pebre*" [destroys you]. Take, for example, the Lickancabur volcano. He is lovely and peaceful, and he is a water volcano because he attracts and creates water. So, we have to thank him, we owe him a lot of gratitude, and we need to give back to him—from gratitude. We do not have to go up to the Lickancabur to ask for money, for this or for that, no. We do not have to pay him as if we had a debt with him.[16] We need to thank him.

Thus, volcanic risk management, from an ancestral perspective, is not just about monitoring and evacuating. It is also about establishing *good relations* with volcanoes. It is about cultivating a more integral connection with them as kin, as beings that have feelings and proclivities, and without whom our life in the desert would be impossible. Actually, the notion of "volcanic risk" is misleading, because it assumes that the risk is the volcano himself. What is dangerous and risky is to sever our communication channels with him, to disrupt the warmth and the cycles of the inside Sun, for example by intervening it to extract energy and minerals. When the inside Sun is turned upside down, wretched and incapacitated, we will see the collapse of the Earth through the activity of our volcanoes. In addition, a volcanic eruption does not need to be dangerous. What we call "destruction" is often just nature regenerating herself. What is truly destructive is the overwhelming intervention to rivers, *bofedales* (high altitude wetlands), and *aguadas* (springs), disconnecting the three worlds and leaving behind a barren Earth unable to contain and absorb which are otherwise natural expressions of volcanoes. We need to worry more about extractivism than about volcanoes, which are beautiful creatures.

5 DISCUSSION

Lickanantay volcanology offers relevant insights that need to be considered if volcanology is to establish a respectful and caring relation with other knowledge in the CVZA, a transnational territory in which the Indigenous peoples have made observations

---

[14] Lickanantay communities have produced robust and time-tested knowledge on the linkages between volcanoes and climate and waters. For example, the Chiliques volcano plays a crucial role as a facilitator of meteorological phenomena (Moyano and Uribe, 2012), while the availability of water has always been related, ecologically and ceremonially, to *mallkus* (Grebe and Hidalgo, 1988; Valenzuela and Moyano, 2021).

[15] Also known as Jorgencal Volcano or Machuca Volcano, it is a stratovolcano located on the southern border between Bolivia and Chile (22°33′S 67°51′W) with an elevation of 5,890 m.a.s.l. and intense fumarolic activity at its summit.

[16] This is in relation to the *pago a la Tierra* (pay the Earth), or making an offering, a ritual guided by a logic of reciprocity between humans and deities. The *pago* is a tribute in exchange of benefits received from *Pachamama* and a propitiatory offering for new benefits requested (land fertility, cattle well-being, and water availability). It is a kind of agreement or an agreement to stay in good relations with the *Pachamama* (Carrasco, 2016; Grebe and Hidalgo, 1988; Ulmer, 2020).

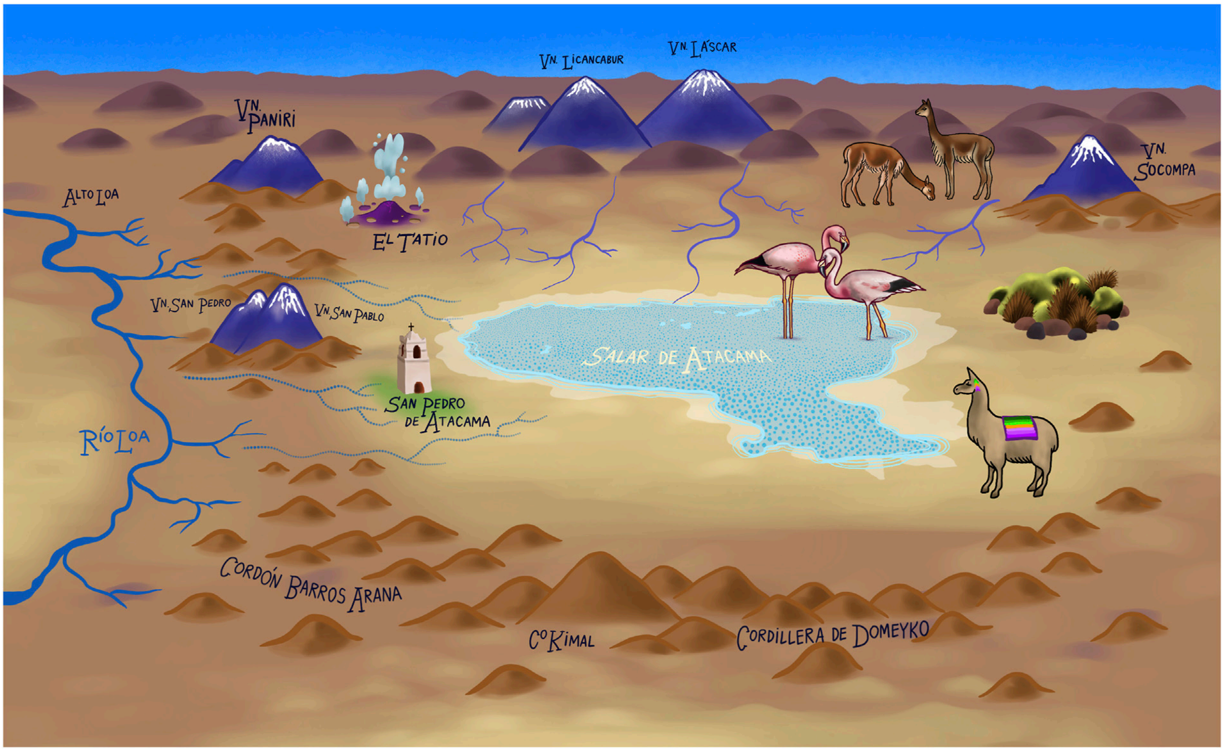

FIGURE 2 | Ancestral Lickanantay volcanic territory according to Sonia Ramos. Design: Sergio Iacobelli.

FIGURE 3 | El Tatio ancestral territory. Author: Manuel Tironi.

FIGURE 4 | Hécar (Iticunza) and Laguna Verde (Iticuna) volcanoes. Author: Manuel Tironi.

about, lived with, and intervened with volcanoes for millennia—and where extractivist damages are accumulating at a worrying speed. For example, Lickanantay volcanology teaches us that volcanoes need to be understood from a broader perspective, thus problematizing separations between volcanology and hydrogeology, ecological conservation, soil sciences, and climatology. Lickanantay volcanology also suggests that usual geological components—basins, aquifers, calderas, and ranges—might need to be revised in terms of their morphology in order to explore the possibility of accounting for subterranean connections that ancestral expertise assumes as extended beyond conventional geological demarcations. And that volcanology needs to integrate extractivism as a shaping geological stressor in its base lines and analyses, particularly for volcanic risk management. Hazards, Lickanantay volcanology suggests, are not related to eruptions or lahars, but due to the effect of extensive extractive operations on soils, waters, and social relations to land.

The most important contribution that Lickanantay volcanology has to offer, however, is epistemological. It renders visible that volcanology needs to understand itself as an open field in which different knowledge systems about volcanological dynamics can meet to co-produce better sciences and policies. This does not mean to invalidate what volcanology has achieved since von Humboldt's seminal observations of Chimborazo's eruption in Ecuador—but to take seriously other, even divergent practices and theories. This is especially important in the CVZA, where volcanological knowledge has been systematically produced for the last 10,000 years. This knowledge is built upon different definitions of what a volcano is and how it is connected to other biophysical systems, actually to where lays the demarcation between nature and culture, volcanology and cosmology, and geology and spirituality—and it is precisely for this kind of interconnections that it offers invaluable expertise. Mainstream volcanology can choose to extend the traditional scientific gesture, deeming the "beliefs" of Indigenous peoples as "mythological" or "folkloric", or it can explore new avenues of research and knowledge-making. Not long ago, the replacement of Indigenous knowledge systems with Western sciences was considered a civilizatory achievement. Today, in the face of the intractable planetary challenges we precisely face as a consequence of modern enlightenment, we need to cultivate an enhanced sense of humility and plurality, acknowledging the limits of our scientific methods—the ways in which the sciences mobilize and reinforce visions of the world that are far from universal. This is not a call to eliminate science as a method for knowledge production, but rather to assume the existence of other valid methods and to realize the urgent need for diverse dialogues among and across knowledge systems **Figures1–4**.

DATA AVAILABILITY STATEMENT

The datasets presented in this article are not readily available because this is qualitative data own by Indigenous elders. Requests to access the datasets should be directed to metironi@uc.cl.

ETHICS STATEMENT

The studies involving human participants were reviewed and approved by Comité Ético Científico en Ciencias Sociales Artes y Humanidades UC. The patients/participants provided their written informed consent to participate in this study.

AUTHOR CONTRIBUTIONS

SR contributed with: guiding ethical principles, territorial relations, planning of fieldwork, definition of main ideas, and revision of the final version. MT contributed with: writing the literature review, organizing the results section, organizing the discussion section, overall preparation of the manuscript, and translation into English.

FUNDING

This article was supported by FONDECYT 1190528, FONDECYT 1201373, and CIGIDEN (Research Center for Integrated Disaster Risk Management) ANID/FONDAP/15110017.

ACKNOWLEDGMENTS

We would like to express our gratitude to the *Pacha* for her sustenance, and especially to the *tata* El Tatio for being a constant source of guidance and knowledge. We also want to thank Natalia Toledo Ramos, Valentina Acuña, Gabriela Ramirez, and Juan Francisco Salazar for their support throughout the process of researching and writing this manuscript, and to Francisca Vergara for her assistance in the preparation of the literature review.

REFERENCES

Acosta A. and Martínez E. (Editors) (2009). *El buen vivir. Una vía para el desarrollo* (Santiago: Editorial Universidad Bolivariana).

Acuña, V., and Tironi, M. (2021). Extractivist Droughts: Indigenous Hydrosocial Endurance in Quillagua, Chile. *Extr. Industries Soc.* 9, 101027. doi:10.1016/j.exis.2021.101027

Aedo, J. (2008). Percepción del espacio y apropiación del territorio entre los Aymara de Isluga. *Estud. Atacameños* 36, 117–137. doi:10.4067/S0718-10432008000200007

Atkinson, D. (2016). Geographical Knowledge and Scientific Survey in the Construction of Italian Libya. *Mod. Italy* 8 (1), 9–29. doi:10.1080/1353294032000074052

Ayala, P. (2008). *Políticas del pasado: indígenas arqueólogos y Estado en Atacama*. Antofagasta: Universidad Católica del Norte.

Babidge, S., and Bolados, P. (2018). Neoextractivism and Indigenous Water Ritual in Salar de Atacama, Chile. *Lat. Am. Perspect.* 45 (5), 170–185. doi:10.1177/0094582x18782673

Barclay, J., Haynes, K., Houghton, B. F., and Johnston, D. (2015). "Social Processes and Volcanic Risk Reduction," in *Encyclopedia of Volcanoes*. Editors H. Sigurdsson, B. F. Houghton, H. Rymer, J. Stix, and S. R. McNutt (San Diego, CA: Academic Press). doi:10.1016/b978-0-12-385938-9.00069-9

Barlo, S., Boyd W (Bill), E., Pelizzon, A., and Wilson, S. (2020). Yarning as Protected Space: Principles and Protocols. *AlterNative: An International Journal of Indigenous Peoples* 16 (2), 90–98. doi:10.1177/1177180120917480

Barros, A. (1997). Pachamama y desarrollo: paisajes conflictivos en el Desierto de Atacama. *Estud. Atacameños* 13, 75–94. doi:10.22199/s07181043.1997.0013.00006

Berenguer, J. (2004). *Caravanas, Interacción Y Cambio En El Desierto De Atacama*. Santiago: Ediciones Sirawi/LOM Editores

Bolados, P., and Babidge, S. (2017). Ritualidad y extractivismo: la limpia de canales y las disputas por el agua en el Salar de Atacama, norte de Chile. *Estud. Atacameños*, 201–216.

Bretton, R. J., Gottsmann, J., and Christie, R. (2018). Hazard Communication by Volcanologists: Part 1 - Framing the Case for Contextualisation and Related Quality Standards in Volcanic Hazard Assessments. *J. Appl. Volcanol.* 7, 9. doi:10.1186/s13617-018-0077-x

Bustos-Gallardo, B., Bridge, G., and Prieto, M. (2021). Harvesting Lithium: water, brine and the industrial dynamics of production in the Salar de Atacama. *Geoforum* 119, 177–189. doi:10.1016/j.geoforum.2021.01.001

Carrasco, A. (2016). A Biography of Water in Atacama, Chile: Two Indigenous Community Responses to the Extractive Encroachments of Mining. *J. Lat. Am. Caribb. Anthropol.* 21, 130–150. doi:10.1111/jlca.12175

Cartier, K. M. S. (2021). Teaching Geoscience History in Context (Online). Available at: https://eos.org/articles/teaching-geoscience-history-in-context (Accessed 06 13, 22).

Cashman, K. V., and Cronin, S. J. (2008). Welcoming a Monster to the World: Myths, Oral Tradition, and Modern Societal Response to Volcanic Disasters. *J. Volcanol. Geotherm. Res.* 176 (3), 407e418. doi:10.1016/j.jvolgeores.2008.01.040

Chester, D. K., Duncan, A. M., and Dibben, C. J. L. (2008). The Importance of Religion in Shaping Volcanic Risk Perception in Italy, with Special Reference to Vesuvius and Etna. *J. Volcanol. Geotherm. Res.* 172 (3e4), 216e228. doi:10.1016/j.jvolgeores.2007.12.009

Contreras, E. (1994). Cultura y naturaleza en la cuenca del Salar de Atacama. *Estud. Atacameños* 11, 179–185. doi:10.22199/s07181043.1994.0011.00011

Cusicanqui, S. R. (1993). Anthropology and Society in the Andes. *Critique Anthropol.* 13 (1), 77–96. doi:10.1177/0308275x9301300104

De la Cadena, M. (2015). *Earth Beings: Ecologies of Practice Across Andean Worlds*. Durham, NC: Duke University Press.

Deloria, P. J., Lomawaima, K. T., Brayboy, B. M. J., Trahant, M. N., Ghiglione, L., and Blackhawk, D. N. (2018). Unfolding Futures: Indigenous Ways of Knowing for the Twenty-First Century. *Daedalus* 147 (2), 6–16. doi:10.1162/daed_a_00485

Donovan, A. (2019). Critical Volcanology? Thinking Holistically about Risk and Uncertainty. *Bull. Volcanol.* 81, 20. doi:10.1007/s00445-019-1279-8

Donovan, A. (2021). Colonising Geology: Volcanic Politics and Geopower. *Polit. Geogr.* 86, 102347. doi:10.1016/j.polgeo.2021.102347

Donovan, A., Oppenheimer, C., and Bravo, M. (2011). Rationalising a Volcanic Crisis through Literature: Montserratian Verse and the Descriptive Reconstruction of an Island. *J. Volcanol. Geotherm. Res.* 203, 87–101. doi:10.1016/j.jvolgeores.2011.03.010

Donovan, K. (2010). Doing Social Volcanology: Exploring Volcanic Culture in Indonesia. *Area* 42 (1), 117e126. doi:10.1111/j.1475-4762.2009.00899.x

Driver, F. (1992). Geography's Empire: Histories of Geographical Knowledge. *Environ. Plan. D.* 10 (1), 23–40. doi:10.1068/d100023

González, J. (2012). El Vicario Luis Silva Lezaeta y el proceso de "chilenización" en el Norte Grande: Las Experiencias de Antofagasta y Tarapacá. 1882-1897. *Tiempo Histórico* 5, 55–69.

González-Gálvez, M. (2016). *Los Mapuche y sus Otros: Persona, Alteridad y Sociedad en el Sur de Chile*. Santiago: Editorial universitaria.

Grebe, M. E., and Hidalgo, B. (1988). Simbolismo atacameño: un aporte etnológico a la comprensión de significados culturales. *Rev. Chil. Antropol.* 7, 75–97.

Haynes, K., Barclay, J., and Pidgeon, N. (2008). Whose Reality Counts? Factors Affecting the Perception of Volcanic Risk. *J. Volcanol. Geotherm. Res.* 172 (3e4), 259e272. doi:10.1016/j.jvolgeores.2007.12.012

Hilhorst, D. (2006). "Complexity and Diversity: Unlocking Social Domains of Disaster Response," in *Mapping Vulnerability: Disasters, Development, and People*. Editors G. Bankoff, G. Frerks, and D. Hilhorst (London: Earthscan).

Home, R. (2006). Scientific Survey and Land Settlement in British Colonialism, with Particular Reference to Land Tenure Reform in the Middle East 1920-50. *Plan. Perspect.* 21 (1), 1–22. doi:10.1080/02665430500397048

Juárez, A. (2012). Las montañas humanizadas: Los volcanes del altiplano central. *KinKaban* 1, 64–70.

Kopenawa, D., and Albert, B. (2013). *The Falling Sky*. Cambridge , MA: Words of Yanomami ShamanHarvard University Press.

Kophamel, W. (2020). Race and Soil. Geography, Ethnology, and Nazism. *Mètode Sci. Stud. J.* 10. doi:10.7203/metode.10.13560

Liboiron, M. (2021). Decolonizing Geoscience Requires More Than Equity and Inclusion. *Nat. Geosci.* 14, 876–877. doi:10.1038/s41561-021-00861-7

Martínez, J. L. (2010). "Somos resto de gentiles": El manejo del tiempo y la construcción de diferencias entre comunidades andinas. *Estud. Atacam.* 39, 57–70. doi:10.4067/s0718-10432010000100005

Moyano, R., and Uribe, C. (2012). El Volcán Chiliques Y El "Morar-En-El-Mundo" De Una Comunidad Atacameña Del Norte De Chile. *Estud. Atacam.* (43), 187–208. doi:10.4067/s0718-10432012000100010

Núñez, L. (1992). "Ocupación Arcaica en la Puna de Atacama: Secuencia, Movilidad y Cambio," in *Prehistoria sudamericana: Nuevas perspectivas*. Editor B. Meggers (Washington, DC: Taraxacum), 283–307.

Núñez, L., Grosjean, M., and Cartajena, I. (2010). Sequential Analysis of Human Occupation Patterns and Resource Use in the Atacama Desert. *Chungará (Arica)* 42 (2), 363–391. doi:10.4067/s0717-73562010000200003

Paton, D., Smith, L., Daly, M., and Johnston, D. (2008). Risk Perception and Volcanic Hazard Mitigation: Individual and Social Perspectives. *J. Volcanol. Geotherm. Res.* 172 (3e4), 179e188. doi:10.1016/j.jvolgeores.2007.12.026

Pease, R. (2021). Accusations of Colonial Science Fly after Eruption. *Science* 372 (6548), 1248–1249. doi:10.1126/science.372.6548.1248

Peraldo, G., and Mora, M. (1995). Las erupciones volcánicas como condicionantes sociales: casos específicos de América central. *Anu. Estud. Centroam.* 21 (1-2), 83–110.

Pico, T., Chen, C., Lau, H. C. P., Olinger, S., Wiggins, J. W., Austermann, J., et al. (2020). Geocontext: a Social and Political Context for Geoscience Education [online]. Available at: https://figshare.com/articles/online_resource/GeoContext_A_social_and_political_context_for_geoscience_education/14158457/1?file=26686871 (Accessed June 13, 2022). doi:10.6084/m9.figshare.14158457

Quarantelli, E. L. (1987). What Should We Study? Questions and Suggestions for Researchers about the Concept of Disasters. *Int. J. Mass Emergencies Disasters* 5, 7–32.

Quilaqueo, D., and Quintriqueo, S. (2017). *Métodos educativos mapuches: retos de la doble racionalidad educativa*. Temuco: Universidad Católica de Temuco.

Redin, G. (2018). Movimientos y continuidades de habitar y conocer ambientes vibrantes: Talabre en la puna atacameña. Master's Thesis. Santiago de Chile: Pontificia Universidad Catçólica de Chile.

Riede, F. (2015). Volcanic Eruptions and Human Vulnerability in Traditional Societies Past and Present. Denmark. Aarhus University Press.

Rivera Cusicanqui, S. (1987). El Potencial Epistemológico y Teórico de la Historia Oral: De la Lógica Instrumental a la Descolonización de la Historia. *Temas Sociales* 14, 49–75.

Sanhueza, C. T. (2004). Medir, Amojonar, Repartir: Territorialidades Y Prácticas Demarcatorias En El Camino Incaico De Atacama (Ii Región, Chile). *Chungará* 36 (2), 483–494. doi:10.4067/S0717-73562004000200018

Scarlett, J., Naismith, A., and Rushton, A. (2022). "Defining Disaster in Volcanology," in *Defining Disaster: Disciplines and Domains*. Editors M. Aronsson-Storrier, and R. Dahlberg (Cheltenham: Edward Elgar Publishing).

Scarlett, J. (2022). Researching Natural Hazards: the Harmful Legacy of Colonialism in Geoscience. Available at: https://eartharxiv.org/repository/view/3334/ (Accessed June 13, 2022). *EarthArXiv*, preprint doi:10.31223/X5B33P

Schwartz-Marin, E., Merli, C., Rachmawati, L., Horwell, C. J., and Nugroho, F. (2020). Merapi Multiple: Protection Around Yogyakarta's Celebrity Volcano through Masks, Dreams, and Seismographs. *Hist. Anthropol.*, 1–23. doi:10.1080/02757206.2020.1799788

Skinner, J. (2004). *Before the Volcano: Reverberations of Identity on Montserrat*. Kingston, Jamaica: Arawak Publishers.

Smith, L. T. (1999). *Decolonizing Methodologies: Research and Indigenous Peoples*. London: Zed Books.

Socha, D. M., Reinhard, J., and Perea, R. C. (2021). Inca Human Sacrifices from the Ampato and Pichu Pichu Volcanoes, Peru: New Results from a Bio-Anthropological Analysis. *Archaeol. Anthropol. Sci.* 13 (94). doi:10.1007/s12520-021-01332-1

Spoon, J. (2007). The 'Visions of Pele' Competition and Exhibit at Hawai'i Volcanoes National Park. *CRM J. Herit. Steward.* 4 (1), 72–74.

Stafford, R. A. (2017). "Annexing the Landscapes of the Past," in *Imperialism and the Natural World*. Editor J. M. MacKenzie (Manchester: Manchester University Press). doi:10.7765/9781526123671.00008

Stone, J. C. (1988). Imperialism, Colonialism and Cartography. *Trans. Inst. Br. Geogr.* 13, 57–64. doi:10.2307/622775

Swanson, D. A. (2008). Hawaiian Oral Tradition Describes 400 Years of Volcanic Activity at Kīlauea. *J. Volcanol. Geotherm. Res.* 176 (3), 427–431. doi:10.1016/j.jvolgeores.2008.01.033

Teillier, F., Llanquinao, G., and Salamanca, G. (2018). Epistemología de la lengua mapunzugun: definición conceptual de küpalme, rakizuam y güxam. *Papeles de Trabajo. Cent. Estud. Interdiscip. Etnolingüística Antropol. Socio-Cultural* 36, 100–122. doi:10.35305/.v0i36.16

Tierney, K. (2012). Disaster Governance: Social, Political, and Economic Dimensions. *Annu. Rev. Environ. Resour.* 37 (1), 341–363. doi:10.1146/annurev-environ-020911-095618

Ulmer, G. (2020). The Earth Is Hungry: Amerindian Worlds and the Perils of Gold Mining in the Peruvian Amazon. *J. Lat. Am. Caribb. Anthropol.* 25, 324–339. doi:10.1111/jlca.12495

USGS (2019). *Lithium. Mineral Commodity Summaries*. Washington, DC: US Geological Survey.

Valenzuela, A., and Moyano, R. (2021). "Ethnicity and Ritual in the *Atacameños* Andes: Water, Mountains, and Irrigation Channels in Socaire (Atacama, Chile)," in *Andean Foodways*. Editor J. E. Staller (Cheltenham: Springer).

Villanueva, J., Alonso, P., and Ayala, P. (2018). Arqueología de la ruptura colonial: mouros, chullpas, gentiles y abuelos en España, Bolivia y Chile en perspectiva comparada. *Estud. atacameños* 60, 9–30. doi:10.4067/S0718-10432018005001402

Watts, V. (2013). Indigenous Place-Thought and Agency Amongst Humans and Non Humans (First Woman and Sky Woman Go on a European World Tour!). *Decolonization Indig. Educ. Soc.* 2 (1), 20–34.

Whyte, K. (2020). "Sciences of Consent: Indigenous Knowledge, Governance Value, andResponsibility," in *Routledge Handbook of Feminist Philosophy of Science*. Editors K. Intemannand, and S. Crasnow (London and New York: Routledge), 117–130. doi:10.4324/9780429507731-12

Wisner, B., Blaikie, P., Cannon, T., and Davis, I. (2004). *At Risk: Natural Hazards, People's Vulnerability, and Disasters*. 2nd ed. London & New York: Routledge.

Yusoff, K. (2019). *A Billion Black Anthropocenes or None*. Minneapolis: University of Minnesota Press.

Conflict of Interest: The authors declare that the research was conducted in the absence of any commercial or financial relationships that could be construed as a potential conflict of interest.

Frontiers in Earth Science

TYPE Original Research
PUBLISHED 19 August 2022
DOI 10.3389/feart.2022.897315

OPEN ACCESS

EDITED BY
Karoly Nemeth,
Massey University, New Zealand

REVIEWED BY
Sam Poppe,
Vrije University Brussel, Belgium
Marta Della Seta,
Sapienza University of Rome, Italy

*CORRESPONDENCE
Nicolás Alcozer-Vargas,
nicolas.alcozer@alumnos.ucn.cl

SPECIALTY SECTION
This article was submitted to Geohazards and Georisks, a section of the journal Frontiers in Earth Science

RECEIVED 16 March 2022
ACCEPTED 28 June 2022
PUBLISHED 19 August 2022

CITATION
Alcozer-Vargas N, Reyes-Hardy M-P, Esquivel A and Aguilera F (2022), A GIS-based multi-hazard assessment at the San Pedro volcano, Central Andes, northern Chile.
Front. Earth Sci. 10:897315.
doi: 10.3389/feart.2022.897315

A GIS-based multi-hazard assessment at the San Pedro volcano, Central Andes, northern Chile

Nicolás Alcozer-Vargas[1,2,3,4]*, María-Paz Reyes-Hardy[1,5], Alfredo Esquivel[1,2,6] and Felipe Aguilera[1,2,3]

[1]Millennium Institute on Volcanic Risk Research—Ckelar Volcanoes, Antofagasta, Chile, [2]National Research Center for Integrated Natural Disaster Management (CIGIDEN), Santiago, Chile, [3]Departamento de Ciencias Geológicas, Universidad Católica del Norte, Antofagasta, Chile, [4]Programa de Magíster en Ciencias Mención Geología, Universidad Católica del Norte, Antofagasta, Chile, [5]Department of Earth Sciences, University of Geneva, Geneva, Switzerland, [6]Programa de Doctorado en Ciencias Mención Geología, Universidad Católica del Norte, Antofagasta, Chile

Recent advances in the modeling of volcanic phenomena have allowed scientists to better understand the stochastic behavior of volcanic systems. Eruptions can produce various types of volcanic phenomena of different sizes. The size of a given volcanic phenomenon dominates its spatial distribution and is commonly represented by volume/mass parameters in the models that reproduce their behavior. Multi-hazard assessments depend on first-order parameters to forecast hazards at a given geographic location. However, few multi-hazard assessments consider the size of the eruption (e.g., tephra fallout) to co-parameterize the size of the accompanying phenomena (e.g., mass flows) in a given eruptive scenario. Furthermore, few studies simulate multi-phenomenon eruptive scenarios with semi-continuous variations in their size, something that allows a better quantification of the aleatoric variability of the system. Here, we present a multi-hazard assessment of the San Pedro volcano, a high-threat volcano from northern Chile, that produced two large-size Plinian eruptions (VEI 5 and 6) in the last 16 ka, and ten Strombolian eruptions (VEI 2) between 1870 and 2021 CE, with the latest occurring on 2 December 1960 CE. We use intra-scenarios (i.e., subdivisions of eruptive scenarios) to explore the size variability of explosive volcanic phenomena. The size of intra-scenarios is extrapolated from the largest-size deposits of each type of phenomenon from the geologic record of the San Pedro volcano. We simulate explosive intra-scenarios for tephra fallout, concentrated PDCs, and lahars, and effusive scenarios for blocky lava flows. On the local scale, mass flows are likely (66–100%) to affect transport and energy infrastructure within a 14 km radius of the volcano. On the regional scale, large-size eruptions (VEI 5) in the rainy season are about as likely as not (33–66%) to accumulate 1 cm of tephra on energy, transport, and mining infrastructure over a 50 km radius, and these same eruptions are unlikely (10–33%) to accumulate 1 cm of tephra on the city of Calama. This work shows how multi-phenomenon intra-scenarios can be applied to better quantify the aleatoric variability of the type and size of volcanic phenomena in hazard assessments.

KEYWORDS

Northern Chile, Central Andes, hazard modeling, hazard simulation, volcanic hazard assessment

1 Introduction

The primary goal of volcanic hazard assessments is to forecast the occurrence of volcanic phenomena in a given geographical location (Decker, 1986; Blong, 2000; Newhall and Hoblitt, 2002; Marzocchi and Bebbington, 2012; Martí, 2017; Poland and Anderson, 2020). Volcanic systems have complex stochastic behaviors that can lead to the generation of various types of volcanic phenomena, such as tephra fallout, volcanic ballistic projectiles (VBPs), pyroclastic density currents (PDCs), water-sediment flows (lahars), and lava flows, among other types. During an eruption, volcanic phenomena can also be generated with different sizes. The spatial distribution of each volcanic phenomenon is dominated by their size, and it is directly related to the first-order parameters in the computational models used to reproduce their behavior. The spatial distribution of volcanic phenomena is controlled by external first-order parameters such as terrain elevation and atmospheric wind data. However, their spatial distribution is also dominated by internal first-order parameters, for example, tephra fallout is controlled by the erupted mass parameter in Tephra2 (Bonadonna et al., 2005); lahars by the volume parameter in Laharz-py (Schilling, 2014) and LaharFlow (Woodhouse et al., 2016); PDCs by the initial velocity and flow duration parameters in VolcFlow (Kelfoun et al., 2009; Kelfoun, 2017), and by the collapse height and mobility parameters in the Energy Cone model (Malin and Sheridan, 1982); VBPs by the initial velocity and launch angle parameters in Ballistics (Bertin, 2017); lava flows by the effusion rate and viscosity parameters in FlowGo/Q-LavHA (Harris and Rowland, 2001; Mossoux et al., 2016), and by the mean length parameter in Decreasing Probability/Q-LavHA (Bonne et al., 2008; Mossoux et al., 2016), among other examples. These parameters are related to the aleatoric variability of the volcanic system. Aleatoric variability comes from the random behavior of the system, and it is one of the uncertainties that can be quantified in volcanic hazard assessments (Marzocchi et al., 2004; Marzocchi et al., 2021).

The volume of a given volcanic phenomenon is a parameter that appears in some of these models, directly or indirectly. For instance, volume appears directly as a parameter in the lahar models, but it appears indirectly in the tephra fallout and PDCs models (i.e., it cannot be entered directly). Nonetheless, erupted mass can be converted to erupted volume by using a constant mean density value of 1,000 kg m^{-3} for pumice ash (Pyle, 2015), and volume can be approximated from the initial velocity and flow duration parameters in VolcFlow (Kelfoun et al., 2009). These conversions can be proven useful for producing a co-parameterization of the volume of multiple hazards in the same eruptive scenario. In this context, knowing the volume of each phenomenon produced during the largest eruption of a given volcano is crucial to co-parameterize the size of synchronous volcanic phenomena in the same eruptive scenario.

One of the most important sources of aleatoric variability in volcanic systems is the size of future volcanic phenomena. Many model-based volcanic hazard assessments do not explore the variability of the size of volcanic phenomena in their approaches. Most hazard assessments, subjectively, select and simulate a unique set of sizes (three or more) from the volcanic explosivity index (VEI) scale, this is known as the eruptive scenario methodology. However, this methodology does not account for many of the sizes that could occur for a given phenomenon within the same eruptive scenario selected, as previous works have proposed, for the case of tephra fallout (Sandri et al., 2016). This could be a byproduct of the use of the VEI scale, something that is done with two objectives, to reduce the computational time costs (by producing fewer simulations) and to better communicate the results (Selva et al., 2018). Nevertheless, hazard assessments should strive to obtain the spatial distribution probabilities of volcanic phenomena through the simulation of several scenarios that should be continuous or semi-continuous in size, and non-dependent on the major divisions of the VEI scale (e.g., Sandri et al., 2016; Biass et al., 2017; Charbonnier et al., 2020; Clarke et al., 2020; Tadini et al., 2022). Therefore, the gaps between the size of the selected and simulated scenarios should not differ by order of magnitude (e.g., 10^7, 10^8, 10^9 m^3), instead, the gaps should be smaller, and more scenarios should be produced.

In the last decade, a variety of computational frameworks have been published in the scientific literature that greatly improve the accessibility of methodologies and reduce computational time costs. For example, probabilistic toolboxes for analytical models of tephra fallout (Tephra2-TephraProb) (Bonadonna et al., 2005; Biass et al., 2016b), easily accessible statistical/empirical models of lava flows (Q-LavHA) (Felpeto et al., 2001; Bonne et al., 2008; Mossoux et al., 2016), and real-time deterministic numerical models for concentrated PDCs (VolcFlow) (Patra et al., 2005; Kelfoun et al., 2009) and lahars (LaharFlow) (Woodhouse et al., 2016). Even though the eruptive scenario methodology is done to reduce computational time costs, this could be no longer necessary in the future, as the computational power of personal computers and the advances in computational frameworks could be able to reduce simulation time costs, thus enabling the production of more scenarios.

The aleatoric variability within the volume of a volcanic phenomenon has been explored in various previous studies (Sandri et al., 2016; Biass et al., 2017; Charbonnier et al., 2020; Tadini et al., 2022). For example, Sandri et al. (2016) explore the intra-size variability of tephra fallout by following the discretization of the erupted mass parameters into bins with an interval of 0.1 on the magnitude (M) scale (Pyle, 2015); Biass et al. (2017) explore the intra-size variability of tephra fallout by producing thousands of simulations with different erupted mass values chosen stochastically (Monte Carlo method) from within a range of values; Tadini et al. (2022) explore the intra-size variability of tephra fallout by simulating a continuous distribution of erupted mass values; Charbonnier et al. (2020) explore the intra-size variability of PDCs by producing a discretization of the volume, by increasing by 10^6 m^3 the volume of all simulations.

Most model-based volcanic hazard assessments focus on a single type of volcanic phenomena, for example, tephra fallout (Biass and Bonadonna, 2013; Biass et al., 2014, 2016a, 2017; Bonasia et al., 2014; Sandri et al., 2016; Selva et al., 2018; Vásquez et al., 2019; Hayes et al., 2020; Michaud-Dubuy et al., 2021; Tadini et al., 2022; Titos et al., 2022) or PDCs (Sandri et al., 2018; Tierz et al., 2018; Charbonnier et al., 2020; Clarke et al., 2020; Esposti Ongaro et al., 2020; Flynn and Ramsey, 2020; Spiller et al., 2020). Double-hazard assessments focus on tephra fallout along with other types of volcanic phenomena, such as lava flows (Marrero et al., 2019; Gjerløw et al., 2022) or PDCs (Alcorn et al., 2013; Tennant et al., 2021). Multi-hazard assessments focus on three or more types of volcanic phenomena, such as tephra fallout, PDCs, lava flows, lahars, VBPs, or others (Felpeto et al., 2007; Capra et al., 2008; Scaini et al., 2012; Becerril et al., 2014, 2017; Sandri et al., 2014; Jiménez et al., 2020; Reyes-Hardy et al., 2021; Mead et al., 2022; Warwick et al., 2022). Multi-hazard assessments can quantify a wider range of the aleatoric variability of the behavior of a given volcanic system than single- or double-hazard assessments.

Here, we present a multi-hazard assessment of the San Pedro volcano, a high-threat volcano in northern Chile (Lara et al., 2011; SERNAGEOMIN, 2020). Even though San Pedro is a remote volcano, located in the middle of the Atacama Desert (21°S), a previous hazard assessment (Bertin and Amigo, 2015) has shown that the distribution of tephra fallout from large-size eruptions (VEI 5) could reach localities and infrastructure widely distributed throughout the northeastern quadrant of the Antofagasta region. Within a 100 km radius of the San Pedro volcano, the locality with the highest population density is the city of Calama (≈80 km SW), with an estimated population larger than ≈150,000 people (INE, 2017; MINVU and IDE, 2017). Plus, there are less populated localities, such as towns, villages, and railway stations located at different distances from the volcanic crater. Furthermore, there is transport (e.g., highways, railways, and airports), electrical (e.g., electrical transmission towers and a geothermal power plant), and some of the largest copper mining infrastructure in the world (e.g., El Abra, Radomiro Tomic, Chuquicamata, and Ministro Hales mines). A probabilistic tephra fallout assessment at the San Pedro volcano is essential for the copper mining industry, to estimate the likelihood of tephra accumulation on key infrastructures for the economic development of the country, as mining is the most important source of economic growth in Chile. Moreover, an analysis of the distribution of mass flows can be useful for land-use planning of future transport and energy infrastructure that is required to be constructed near the San Pedro volcano.

We evaluate four types of volcanic phenomena, three types of explosive phenomena (i.e., tephra fallout, concentrated PDCs, and lahars), and one effusive phenomenon (i.e., blocky lava flows). In the case of the explosive scenarios, we quantify the intra-variability of the size of a given volcanic phenomenon by formulating several eruptive scenarios that have continuous/semi-continuous volumes within the sizes of the VEI scale, which we call: eruptive intra-scenarios. The volume values of the different volcanic phenomena in these intra-scenarios are co-parameterized and correlate with each other. We based the size of the largest intra-scenario on the assumption that the largest deposits of the different explosive phenomena (tephra fallout, concentrated PDCs, and lahars) were created synchronously during the largest eruption in the geological record of the San Pedro volcano. We extrapolated volumes for concentrated PDCs and lahars from the volume of tephra fallout. Thus, the methodology is based on the volume of the largest deposit from each type of volcanic phenomenon generated by the volcano, a key parameter that could be possibly found in local stratigraphic field-based studies of volcanoes, or extrapolated from analogous volcanoes (Tierz et al., 2019).

Hazard assessments require the confection of maps to visualize and explain the likelihood of volcanic hazards to the governmental stakeholders and communities exposed to volcanic threats (Doyle et al., 2014; Lindsay and Robertson, 2018; Thompson et al., 2015, 2021). Hazard cartography is crucial for increasing resilience and mitigating volcanic disaster risk in vulnerable communities (Guimarães et al., 2021; Nieto-Torres et al., 2021). Volcanic systems often require hazard assessments with complementary approaches to bring forth alternative perspectives on hazard forecasting. For example, new studies can complement previous assessments through various means: 1) complement previous hazard zones of a given type of volcanic phenomena by using another computational model to produce simulations; 2) complement previous hazard zones by simulating a type of volcanic phenomena not simulated in previous hazard assessments, or 3) implement new hazard zones by simulating a type of volcanic phenomena not taken in consideration in previous hazard assessments. Our contribution is a complement to the current volcanic hazard assessment of the San Pedro volcano from these three perspectives (Bertin and Amigo, 2015).

The expansion and improvement of volcanic hazard assessments are relevant for future risk studies at high-threat volcanoes in northern Chile (e.g., Reyes-Hardy et al., 2021). The probabilistic methods employed in this study will robust the results of future risk assessments produced at the San Pedro volcano, and we hope it will be useful for volcanic hazard assessment at volcanoes in other data-scarce regions of the

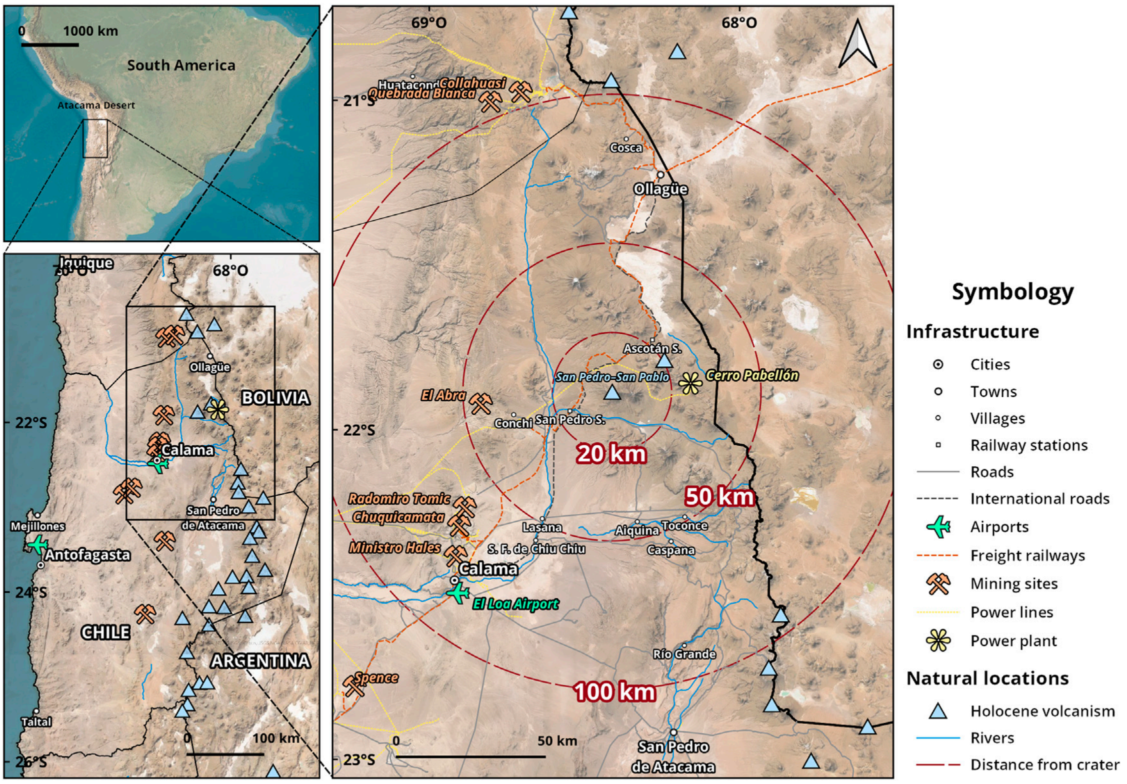

FIGURE 1
Ubication map showing locations and infrastructures at different radial distances from the San Pedro volcano. 'World imagery' and 'Terrain hillshade' base maps courtesy of ESRI and others. Volcanic data from Global Volcanism Program database, version 4.10.4 (GVP, 2013c). Additional cartography data was obtained from the OpenStreetMap database.

world. Another goal of this work is to show how to reproduce the methodology for volcanic hazard assessment, including a detailed description of the procedures and tools used to create the hazard maps with geographic information systems (GIS).

2 The San Pedro volcano

2.1 Overview

The San Pedro volcano (21°53′S; 68°24′W; code 355070) (GVP, 2013a) is a historically active Pleistocene–Holocene compound stratovolcano from the Central Volcanic Zone of the Andean volcanic arc (CVZA) (Stern, 2004; Tilling, 2009). San Pedro is in the northeastern quadrant of the Antofagasta Region of northern Chile, 35 km W of the Chile–Bolivia international border, and 80 km NE of the city of Calama (Figure 1).

Several types of studies have been carried out on the San Pedro volcano, for example, geological (Francis et al., 1974; O'Callaghan and Francis, 1986; Francis and Wells, 1988; De Silva and Francis, 1991; González-Ferrán, 1995), petrographic (Francis et al., 1974; O'Callaghan and Francis, 1986; Godoy et al., 2017; González-Maurel et al., 2019a; González-Maurel et al., 2020), geochronological (O'Callaghan and Francis, 1986; Mamani et al., 2008; Godoy et al., 2014, 2017; Delunel et al., 2016; Bertin and Amigo, 2019; González-Maurel et al., 2019b), historical eruption recordings (Casertano, 1963; González-Ferrán, 1995; Petit-Breuilh, 2004; Siebert et al., 2010; Bertin and Amigo, 2015, 2019), regional (Lara et al., 2011; Amigo et al., 2012) and local volcanic hazard assessments (Bertin and Amigo, 2015), emergency crisis plans (ONEMI, 2019), seismic (Pritchard et al., 2014), surface deformation (Pritchard and Simons, 2004; Pritchard et al., 2014), morphometric (Grosse et al., 2014; Aravena et al., 2015), spectral thermal anomalies (Jay et al., 2013), volatile fluxes (Aguilera et al., 2020), and glaciological (Barcaza et al., 2017). In northern Chile, model-based double-hazard assessments have been produced regionally for a series of volcanoes (Amigo et al., 2012). Besides, model-based multi-hazard assessments have been done for single volcanoes, such as Láscar (Gardeweg and Amigo, 2015), San Pedro (Bertin and Amigo, 2015), and Guallatiri (Jorquera et al., 2019; Reyes-Hardy et al., 2021).

The historical record of the San Pedro volcano comprises 11 eruptions between the years 1870–2021 CE (Siebert et al., 2010; GVP, 2013a; Bertin and Amigo, 2019), and the last eruption occurred more than 60 years ago, on 2 December 1960 CE (Casertano, 1963). However, the description of these events is incomplete, and only six eruptions have been confirmed and assigned the predetermined size of VEI 2 (Newhall and Self, 1982; GVP, 2013a). No geological record of historical eruptions has been found to date, and most eruptions are interpreted to be phreatic explosions by previous authors (Bertin and Amigo, 2015, 2019) as no significant details or visual descriptions of these events have been given in the literature. Despite this, the San Pedro volcano has the second-most abundant historical record of eruptions in northern Chile, just after the Lascar volcano—the most active volcano of the CVZA—which has a total of 29 confirmed eruptions in its record between the years 1848–2021 CE (GVP, 2013b).

The geologic record of the San Pedro volcano dates to *ca.* 310 ka (Bertin and Amigo, 2019). Recent geological studies have found that it has produced two Plinian eruptions in the last 16 ka (Sellés and Gardeweg, 2017; Bertin and Amigo, 2019). Estimations of the volume of tephra fallout deposits, yield eruptions of VEI5/M5.7 (*ca.* 15.45 ka BP) and VEI6/M6.0 (*ca.* 11.55 ka BP) (Bertin and Amigo, 2015, 2019). The M6.0 eruption is the largest in the geological record of the San Pedro volcano (Bertin and Amigo, 2019), and one of the largest tephra fallout deposits in the last 12 ka in northern Chile. Many authors interpret that this eruption generated PDCs as well, which traveled up to 14 km W and produced the 'El Encanto' ignimbrite (Francis et al., 1974; O'Callaghan and Francis, 1986; Bertin and Amigo, 2019). Two studies have provided estimates for the volume of the tephra fallout deposit by applying different methodologies. Francis et al. (1974) estimated a volume of 2 km^3, while Bertin and Amigo (2019) estimated, through different methodologies, a volume of 10 km^3 (Bonadonna and Houghton, 2005) and 26 km^3 (Sulpizio, 2005), although, the former value was selected to classify the eruption. This volume is comparable to the 1600 eruption of the Huaynaputina volcano in Peru, which has been classified as a VEI 6 eruption with an erupted volume of 11 km^3: the largest historical eruption in the CVZA (Tilling, 2009). In addition, the San Pedro volcano has produced at least four domes in the last 11 ka (Bertin and Amigo, 2019), from which two of these collapsed and generated PDCs toward the northern flank of the volcano. The recurrence and magnitude of these events positions San Pedro as one of the most geologically and historically active volcanoes of northern Chile and the CVZA (Lara et al., 2011).

According to hazard-related studies, volcanic phenomena such as tephra fallout, PDCs, lava flows, and VBPs are likely to occur in future eruptions of the San Pedro volcano (Lara et al., 2011; Amigo et al., 2012; Bertin and Amigo, 2015, 2019), whereas the perceived potential for the volcano to produce lahars is unlikely (Lara et al., 2011). Primarily, due to the absence of an ice cap (Bertin and Amigo, 2015) and the seasonal variation of the area covered by snow at the volcanic summit.

A priori, tephra fallout is one of the most important phenomena that could be produced by the San Pedro volcano, due to the large distances it can travel. Even though San Pedro is a remote volcano, and the population density of the Atacama Desert is small, previous volcanic hazard assessments (Bertin and Amigo, 2015) have shown that the distribution of tephra fallout from a large-size eruption (VEI 5–6) could reach localities and infrastructure widely distributed throughout the northeastern quadrant of the Antofagasta region.

Recent threat rankings placed San Pedro in 41st place out of a total of 92 geologically active volcanoes from all the country, including the Central, Southern, and Austral volcanic zones of the Andean volcanic arc. Nonetheless, it is in the fifth position out of 32 geologically active volcanoes in northern Chile (Lara et al., 2011; SERNAGEOMIN, 2020). Furthermore, a recent hazard ranking has placed San Pedro in fifth place out of 8 historically active volcanoes in northern Chile (Guimarães et al., 2021). Consequently, even though it is not considered a priority on a national scale, it is important on a local and regional scale (Antofagasta Region).

The volcano is currently being monitored by the Southern Andes Volcanological Observatory (in Spanish: Observatorio Volcanológico de Los Andes del Sur, OVDAS)[1] and monitoring reports are produced monthly (e.g., OVDAS, 2022; Amigo, 2021). Regarding monitoring studies, no deformation was detected during InSAR surveys (Pritchard and Simons, 2004), but there are records of seismic disturbances (Pritchard et al., 2014; OVDAS, 2022), small thermal anomaly hotspots (Jay et al., 2013), and fumarolic degassing (Aguilera et al., 2020). Moreover, a single gas plume has been observed by various authors in the modern western cone throughout the last 50 years (Francis et al., 1974; O'Callaghan and Francis, 1986; Bertin and Amigo, 2019; Aguilera et al., 2020).

Within a 20 km radius, less than ≈20 people are living at the maintenance stations of the Chile–Bolivia freight railway (San Pedro and Ascotán stations) (Figure 2) (INE, 2017; MINVU and IDE, 2017). Regarding electric infrastructure, there is a chain of high-voltage electrical transmission towers connecting the Cerro Pabellón geothermal power plant to the power grid of the Antofagasta Region (Figures 1, 2). Additionally, there are critical transport routes, such as the international highway (CH–21) and the trails of the Chile–Bolivia freight railway (Figures 1, 2).

---

[1] https://rnvv.sernageomin.cl/volcan-san-pedro/

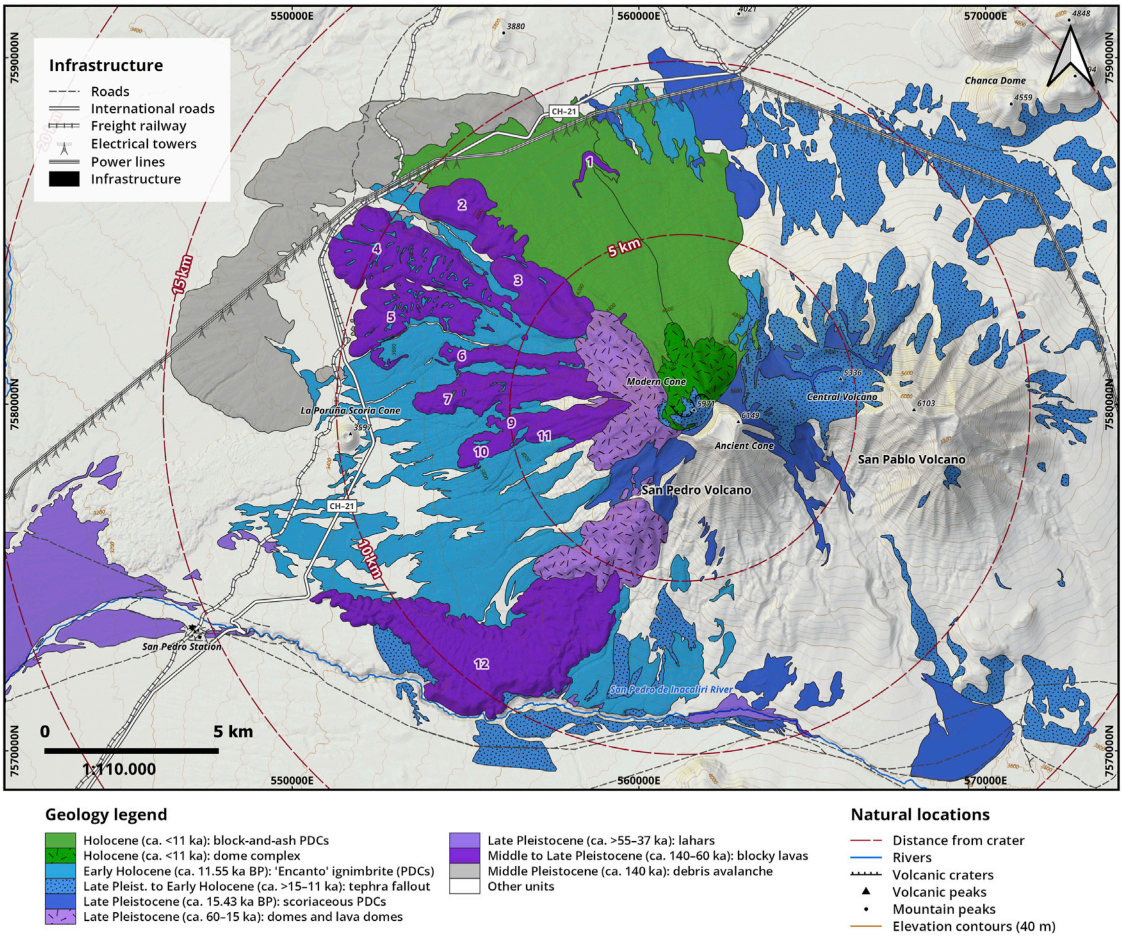

FIGURE 2
Simplified geological map of the San Pedro volcano. Map based on the mapping and geochronology produced by Bertin and Amigo (2019). This map shows in color the deposits of blocky lava flows, PDCs, tephra fallout, and lahars (*ca.* 140 ka–present) and in gray the volcanic avalanche deposit (*ca.* 140 ka) (1:110,000 scale). The 'Terrain: multi-directional hillshade' and the 'Terrain: hillshade' base maps are courtesy of ESRI and others, taken from the Living Atlas database (https://livingatlas.arcgis.com). Additional cartography data was obtained from the OpenStreetMap database with the QuickOSM plugin for QGIS (https://github.com/3liz/QuickOSM).

Within a 20–50 km radius, there are more than ≈150 people in the towns of Conchi (≈28 km SW), Ayquina (≈44 km S), Lasana (≈49 km W), and Toconce (≈49 km SE) (Figure 1) (MINVU and IDE, 2017). In addition, there are crucial mining and energy infrastructures: the Cerro Pabellón geothermal power plant (≈26 km E) and the El Abra open-pit copper mine (≈44 km W) (Figure 1).

Within a 50–100 km radius, more than ≈155,000 people are living mostly in the city of Calama (≈80 km SW), and in small localities such as Chiu Chiu (≈56 km SW), Caspana (≈55 km S), Ollagüe (≈75 km NE), and Río Grande (≈89 km W) (Figure 1) (INE, 2017; MINVU and IDE, 2017). Likewise, there are at least three copper mines within this distance from the volcano, including Radomiro Tomic (≈63 km SW), Chuquicamata (≈68 km SW), and Ministro Hales (≈76 km SW) (Figure 1). Further, mining activity generates a weekly high influx of workers traveling through the El Loa international airport (≈81 km SW), promoting a floating population in the city of Calama.

2.2 Geological time interval evaluated

The geological history of the San Pedro volcano is divided into Stage I (*ca.* 310–140 ka) and Stage II (*ca.* 140 ka to the present) (Francis et al., 1974; O'Callaghan and Francis, 1986; Bertin and Amigo, 2019). Its whole volcanic edifice is composed of two superimposed coalescent cones (Francis et al., 1974). The ancestral eastern cone (≈6,149 m a.s.l.) was built during San Pedro Stage I, while the modern western cone (≈5,971 m a.s.l.) was built during San Pedro Stage II (Figure 2) (Bertin and Amigo, 2019). These evolution stages are separated by the sector collapse of the ancestral eastern cone that occurred during the middle Pleistocene (*ca.* 140 ka) (O'Callaghan and Francis, 1986). This collapse produced a debris avalanche with an estimated volume of 6 km^3 that deposited volcanic materials up to 15 km NW of the volcano (Figure 2) (O'Callaghan and Francis, 1986; Bertin and Amigo, 2019). The products of the volcano cover an area between 124 and 150 km^2, while the whole edifice has an estimated volume between 40 and 56 km^3 (De Silva and Francis, 1991; Grosse et al., 2014; Aravena et al., 2015; Bertin and Amigo, 2019). In the following paragraphs, we only review Stage II of San Pedro, as it spans the same time interval evaluated in this assessment (*ca.* 140 ka to present).

The construction of the modern western cone begins during the middle to late Pleistocene when effusive eruptions occurred in the collapsed escarpment of the ancestral eastern cone. These eruptions produced at least twelve blocky lava flows with runout lengths between 7.2 and 12.4 km toward the NW and W, and between 20 and 100 m of front thicknesses (Figure 2) (Bertin and Amigo, 2019). These blocky lava flows have an andesitic to dacitic composition and an age constrained at *ca.* 140–60 ka by several authors through Ar^{40}/Ar^{36} geochronology (O'Callaghan and Francis, 1986; Mamani et al., 2008; Godoy et al., 2014, 2017; Delunel et al., 2016; Bertin and Amigo, 2019; González-Maurel et al., 2019b).

During the late Pleistocene (*ca.* >55–37 ka), at least four lahar discharges occurred toward the W and S. Two deposits stand out due to their length, reaching 20 and 25 km toward the W, and even impacting the Loa River valley (Figure 2) (Bertin and Amigo, 2019). At *ca.* 60–15 ka, a transition to more differentiated effusive products occurred, leading to five lava domes and six non-flowing domes (Bertin and Amigo, 2019). The lava domes have runout lengths between 1.5 and 6.5 km toward the NW and SW (Bertin and Amigo, 2019).

From the late Pleistocene to the early Holocene (*ca.* >15–11 ka), at least seven explosive eruptions formed tephra fallout deposits that can be found up to 25 km NE and SE of the volcano (Figure 2) (Bertin and Amigo, 2019). Some of these deposits have been identified near the Ascotán station (≈27 km NE) and near the Chile–Bolivia border (≈38 km SE) (Figure 1) (Bertin and Amigo, 2019). Previous works attribute the largest deposit to a VEI 6 Plinian eruption (M6.0) constrained at *ca.* 11.55 ka BP (through radiocarbon dating C^{14}), whereas the second-largest deposit is attributed to a VEI 5 Plinian eruption (M5.7) constrained at *ca.* 15.45 ka BP (C^{14}) (Bertin and Amigo, 2019). At *ca.* 15 ka, San Pedro produced PDCs that traveled up to 14 km toward the SE, and to the SW and N. This deposit has a thickness between 0.1 and 0.3 m and a scoriaceous composition (Bertin and Amigo, 2019). Previous authors propose that this deposit is synchronous with the tephra fallout deposits of the VEI 5 Plinian eruption (M5.7), whereas the other five deposits have smaller but unknown magnitudes (Bertin and Amigo, 2019).

During the early Holocene (*ca.* 11 ka), San Pedro produced large PDCs with a runout length of up to 14 km toward the W, that formed a pumice-rich deposit called 'El Encanto' ignimbrite (Figure 2) (Sellés and Gardeweg, 2017; Bertin and Amigo, 2019). Authors suggest that this deposit formed synchronously with the tephra fallout deposits of the Plinian VEI 6 eruption (M6.0) (Bertin and Amigo, 2019). The volume of the Encanto ignimbrite has been estimated at 1.5 km^3 (O'Callaghan and Francis, 1986) and 0.75 km^3 (Bertin and Amigo, 2019), being the largest PDCs deposit in the geological record of the volcano. At *ca.* <11 ka, three non-flowing dacitic domes and one lava dome were produced (Bertin and Amigo, 2019). The lava domes have runout lengths between 1.0 and 2.5 km toward the N, thicknesses between 130 and 150 m, and well-developed ogive structures (Bertin and Amigo, 2019). At least two of these domes collapsed partially during their emplacement, generating PDCs with runout lengths between 9 and 10 km toward the N, between 1 and 2 m thick, and a block-and-ash composition (Francis et al., 1974; Bertin and Amigo, 2019).

3 Methodology

We applied a methodology comprising four steps: 1) the selection of eruptive scenarios and intra-scenarios, 2) the selection of the computational models, 3) the parameterization of the models and simulations of the explosive intra-scenarios and effusive scenarios, and 4) the preparation and visualization of likelihood and hazard zone maps.

3.1 Eruptive scenarios and intra-scenarios

We separated the eruptive scenarios into explosive intra-scenarios and effusive scenarios. Explosive intra-scenarios account for tephra fallout, concentrated PDCs, and syn-eruptive lahars generated by snowcap melting, whereas effusive scenarios only account for blocky lava flows.

This methodology is based on the estimated volume of the largest deposits of each volcanic phenomenon produced by the volcano. This methodology assumes that the largest deposits of each phenomenon were created and deposited during the same eruption, i.e., the largest eruption in the geologic record of the volcano. Thus, we assume that the largest tephra fallout deposit is synchronous with the largest PDC and lahar deposits of the volcano. In the case of the San Pedro volcano, this is true for the largest tephra fallout and PDCs deposits that were created during the M6.0 Plinian eruption (*ca.* 11.55 ka BP) (Francis et al., 1974; O'Callaghan and Francis 1986; Bertin and Amigo, 2019). Even though the largest lahar deposit is thought to have an older age (*ca.* >55–37 ka), we assume that a M6.0 eruption is

TABLE 1 The volumes and magnitudes of the explosive volcanic phenomena simulated in this study.

Intrascenarios	Min. magnitude	Max. magnitude	Min. tephra vol. (m^3)	Max. tephra vol. (m^3)	Concentrated PDCs vol. (m^3)	Lahars vol. (m^3)
1	3.1	3.2	1.26×10^7	1.58×10^7	1.21×10^6	–
2	3.3	3.4	2.00×10^7	2.51×10^7	1.92×10^6	–
3	3.5	3.6	3.16×10^7	3.98×10^7	3.04×10^6	1.25×10^5
4	3.7	3.8	5.01×10^7	6.31×10^7	4.81×10^6	1.98×10^5
5	3.9	4.0	7.94×10^7	1.00×10^8	7.63×10^6	3.14×10^5
6	4.1	4.2	1.26×10^8	1.58×10^8	1.21×10^7	4.98×10^5
7	4.3	4.4	2.00×10^8	2.51×10^8	1.92×10^7	7.89×10^5
8	4.5	4.6	3.16×10^8	3.98×10^8	3.04×10^7	1.25×10^6
9	4.7	4.8	5.01×10^8	6.31×10^8	4.81×10^7	1.98×10^6
10	4.9	5.0	7.94×10^8	1.00×10^9	7.63×10^7	3.14×10^6
11	5.1	5.2	1.26×10^9	1.58×10^9	1.21×10^8	–
12	5.3	5.4	2.00×10^9	2.51×10^9	1.92×10^8	–
13	5.5	5.6	3.16×10^9	3.98×10^9	3.04×10^8	–
14	5.7	5.8	5.01×10^9	6.31×10^9	4.81×10^8	–
15	5.9	6.0	7.94×10^9	1.00×10^{10}	7.45×10^8	–
Estimated volume of the real deposit (m^3)	–	6.0	–	1.00×10^{10}	7.43×10^8	3.18×10^7

able to produce this large lahar deposit. The simulations produced in this work are based on the complete time interval of San Pedro Stage II (*ca*. 140 ka to present).

For better comprehension and communication of the results, we selected three explosive scenarios representing small-size (VEI 3), medium-size (VEI 4), and large-size eruptions (VEI 5). However, each explosive scenario is composed of various intra-scenarios (see Supplementary Material):

1) The small-size scenario (VEI 3) goes from magnitudes 3.0 to 4.0, and it is composed of 5 tephra fallout, 10 concentrated PDCs, and 3 lahar intra-scenarios.
2) The medium-size scenario (VEI 4) goes from magnitudes 4.0 to 5.0, and it is composed of 5 tephra fallout, 10 concentrated PDCs, and 5 lahar intra-scenarios.
3) The large-size scenario (VEI 5) goes from magnitudes 5.0 to 6.0, and it is composed of 5 tephra fallout and 10 concentrated PDCs intra-scenarios; it does not contain lahar intra-scenarios.

Most eruptive scenario methodologies select and simulate a low number of scenarios, as they use three to four values of the VEI scale (Newhall and Self, 1982). However, we produce a higher number of scenarios by selecting and simulating scenarios located within the values of the VEI scale, by using the magnitude scale (Pyle, 2015), as done by previous authors (Sandri et al., 2016). We divided explosive scenarios into intra-scenarios to quantify the intra-variability of the mass/volume of each phenomenon. The volume/mass parameters used in the simulations of these explosive intra-scenarios are presented in Table 1.

3.2 Selection of computational models

The following computational models were used to simulate the volcanic phenomena:

1) The Tephra2 model (v. 1.2)[2] within the TephraProb toolbox (v. 1.7)[3] for tephra fallout (Bonadonna et al., 2005; Biass et al. 2016b).
2) The VolcFlow single-fluid model (v. 3.5.0)[4] for concentrated PDCs (Kelfoun et al., 2009).
3) The LaharFlow[5] model for syn-eruptive or 'hot' lahars generated by snow cap melting (Woodhouse et al., 2016; Tierz et al., 2017; Espín Bedón et al., 2019).
4) The Decreasing Probability model within the Q-LavHA framework (v. 3.0)[6] for blocky lava flows (Felpeto et al., 2001; Bonne et al., 2008; Mossoux et al., 2016).

---

[2] https://github.com/geoscience-community-codes/tephra2

[3] https://github.com/e5k/TephraProb

[4] https://lmv.uca.fr/volcflow/

[5] https://www.laharflow.bristol.ac.uk

[6] https://we.vub.ac.be/en/q-lavha

Tephra2 is an analytical model (Folch, 2012) of tephra dispersal and accumulation (Bonadonna et al., 2005), and TephraProb is a framework of functions for MATLAB that uses the Tephra2 model (Biass et al., 2016b). TephraProb can produce complex probabilistic eruptive scenario simulations efficiently for the user, such as in the 'eruptive range scenario' setting (Biass et al., 2016b). In this setting, a Monte Carlo sampling approach is applied to obtain random values for the first-order parameters from within a range of input values given by the user. Then, TephraProb produces simulations using the sampled values of the first-order parameters of the Tephra2 model (Biass et al., 2016b). These first-order parameters are erupted mass (kg), column height (m a.s.l.), eruption duration (h), and total grain-size distribution (TGSD) (φ-scale) (Biass et al., 2017). The Tephra2 model has been selected due to its extensive use and validation in the literature. It has been applied to many volcanoes, including Hekla in Iceland (Biass et al., 2014), La Fossa in Italy (Biass et al., 2016b), Puyehue–Cordón Caulle in southern Chile (Biass et al., 2016b), and Sakurajima in Japan (Biass et al., 2017), among others.

PDCs have two transport regimes (Lube et al., 2020): concentrated PDCs and diluted PDCs. Concentrated PDCs are considered to follow the topography and are analogous to pyroclastic flows, whereas diluted PDCs do not necessarily follow the topography and they are analogous to pyroclastic surges (Kelfoun, 2017). VolcFlow single-fluid is a deterministic model for simulating concentrated PDCs over a Digital Elevation Model (DEM) (Kelfoun et al., 2009; Kelfoun, 2017). VolcFlow considers the friction within the flow and between the flow and the topography of the volcano (Ogburn and Calder, 2017), which is something that other models have included, such as Titan2D (Patra et al., 2005). Nonetheless, VolcFlow single fluid uses an empirically defined parameter called 'constant retarding stress' (Pa), which is interpreted to be better suited than a frictional behavior parameter for modeling concentrated PDCs (Charbonnier and Gertisser, 2012). Additionally, Ogburn and Calder (2017) found that VolcFlow is more suitable to model concentrated PDCs of larger size than Titan2D. We have selected VolcFlow because it is a real-time model from which its final volume is constrained by the initial velocity and the flow duration parameters. Furthermore, other parameters within the model had been clearly described by several studies, for example, VolcFlow has been used to reproduce PDCs at Tungurahua in Ecuador (Kelfoun et al., 2009), Merapi in Indonesia (Charbonnier and Gertisser, 2012; Charbonnier et al., 2013; Kelfoun et al., 2017), Soufrière Hills in Montserrat (Gueugneau et al., 2019), Mount Pélee in Martinique (Gueugneau et al., 2020), and El Misti in Peru (Charbonnier et al., 2020).

LaharFlow is a deterministic model that can produce real-time simulations of the distribution of lahars over a DEM (Woodhouse et al., 2016). It includes an empirical model for erosion and depositation and a phenomenological model for the variation of the basal stress as a function of the flow composition (Tierz et al., 2017). The parameters of LaharFlow were calibrated by using data from the 1985 Nevado del Ruiz lahar (Pierson et al., 1990). Even though LaharFlow is a relatively recent model, it has already been tested to model lahars in the literature (Tierz et al., 2017; Espín Bedón et al., 2019). The first-order parameters in LaharFlow are the DEM resolution and the volume. LaharFlow occupies the Shuttle Radar Topography Mission (SRTM) 30-m global DEM (Farr et al., 2007), which can be extrapolated to create lower-resolution DEMs, with the intent to decrease computational time costs. Other important parameters of the model are the erosion rate, the erosion depth, and the granular friction, although no published works have produced sensitivity analyses to identify the variability of results from the use of different values in these parameters (Tierz et al., 2017; Espín Bedón et al., 2019). We have selected LaharFlow because it is a real-time model that has an initial volume parameter, which can be used to co-parameterize the volume of different phenomena in the same intra-scenario.

Q-LavHA is a framework of four different models that can simulate the distribution of 'a'ā lava flows over a DEM (Mossoux et al., 2016). One of the reasons for its selection is the accessibility of Q-LavHA, as it is a free QGIS plug-in written in Python, that can integrate smoothly with the GIS tools used in this methodology. Q-LavHA simulates the spatial propagation of an 'a'ā lava flow and the terminal length of a channelized flow over a DEM (Mossoux et al., 2016), based on the probabilistic steepest slope method proposed by Felpeto et al. (2001). Q-LavHA improves on this method, by adding a second corrective factor (H_p) for calculating the path of lava flows. Q-LavHA hosts various models within its framework: the Manhattan Length, Euclidean Length, the Decreasing Probability, and the Thermo-rheological (FlowGo) models. We used the Decreasing Probability model that was devised and tested by Bonne et al. (2008) at Mount Cameroon in Cameroon. Other works have used this model by simulating 'a'ā flows in several volcanic vents of the Gran Canaria Island in Spain (Rodriguez-Gonzalez et al., 2021).

3.3 Simulation of explosive intra-scenarios

The explosive scenarios include tephra fallout, concentrated PDCs, and lahars. In this section, we describe how we obtained the volume/mass values of each phenomenon in the largest explosive intra-scenarios, i.e., the parameter values linking the three models used.

3.3.1 Tephra fallout

For the tephra fallout assessment, we applied the 'eruption range scenario' setting (TephraProb). This requires a range of

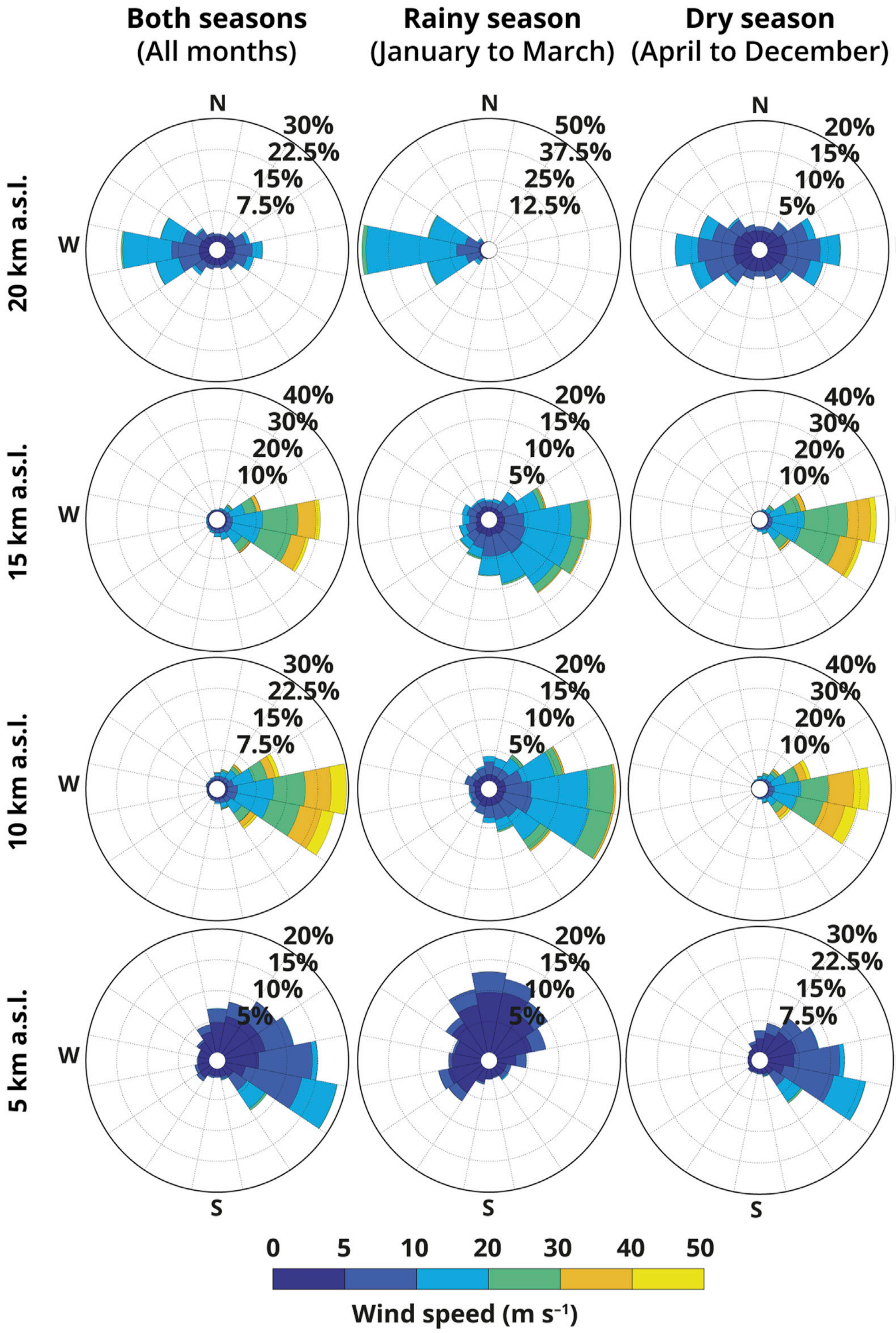

FIGURE 3
San Pedro ERA5 wind data set. The figure shows wind field data obtained from the ERA5 dataset and plotted with the TephraProb toolbox.

values as the input for the erupted mass parameter for each intra-scenario (i.e., minimum and maximum values).

To obtain the maximum erupted mass value of the largest tephra fallout intra-scenario, we considered the volume of the tephra fallout deposit from the Plinian VEI 6 eruption (M6.0) (Bertin and Amigo, 2019). Its erupted volume (V_{TF}, m^3) was converted into erupted mass (m, kg), by assuming a constant mean density (ρ, kg m^{-3}) value of 1,000 kg m^{-3} for the whole deposit by using Eq. (1) (following Bonadonna et al., 2005; Pyle, 2015; Biass et al., 2016b; 2017). This resulted in a maximum erupted mass value of 1.0 × 10^{13} kg (Table 1).

$$m = V_{TF} \cdot \rho \tag{1}$$

To obtain the minimum erupted mass value of the largest tephra fallout intra-scenario, we converted the maximum erupted mass value (1.0 × 10^{13} kg) to an integer of the magnitude scale (M, adimensional) following Eq. (2) (Pyle, 2015). This results in a maximum magnitude value of 6.0. Then, this value (6.0) was reduced by 0.1 to obtain a minimum magnitude value of 5.9. We converted this value to erupted mass by using Eq. (3) (Pyle, 2015). This resulted in a minimum erupted mass value of 7.9 × 10^{12} kg (Table 1).

$$M = log_{10}(m) - 7 \tag{2}$$

$$m = 10^{M+7} \tag{3}$$

This equation allowed us to select continuous values of magnitude/erupted mass for the other tephra fallout intra-scenarios (Supplementary Material). We selected a continuous range of erupted mass values for 30 intra-scenarios, ranging from M3.0–3.1 to M5.9–6.0, and we computed minimum and maximum erupted mass values for each one of these (Supplementary Material), following Sandri et al. (2016). Due to the high computational time cost of this methodology (Selva et al., 2018), we only produced probabilistic simulations for half the intra-scenarios (15). We selected the intra-scenarios that had an uneven value for the minimum magnitude (Table 1).

Regarding other tephra fallout parameters, the minimum and maximum column height values were obtained from Mastin et al. (2009) by using Eq. (4), with column height (H_{TF}, m a.s.l.) and erupted volume (V_{TF}, in this case, in km^3). We only simulated the climactic phase of the eruptions (following Sandri et al., 2016; Biass et al., 2017), with a chosen eruption duration of 1–6 h for all scenarios. All tephra fallout scenarios assume that a vent will open at the summit crater of the modern western cone San Pedro, as this location has a vent currently emitting a gas plume (Aguilera et al., 2020).

$$H_{TF} = (25.9 + 6.64 \cdot log_{10} V_{TF}) \cdot 1000 \tag{4}$$

The wind data were obtained from the European Center for Medium-Range Weather Forecasts (ECMWF) Re-Analysis 5 (ERA5) dataset. The ERA5 dataset has atmospheric wind direction (°) and velocity (m s^{-1}) data from the year 1979 to the present, it has a global spatial resolution of 32 km and a temporal resolution of 6 h. Additionally, there are 37 vertical vectorial wind fields (atmospheric pressures) between 4.9 and 30.1 km (a.s.l.). We selected 11 years of wind data, between 2008 and 2018. At 4 wind profiles per day, this time interval has 16,072 wind profiles. A visual representation of the mean values of this wind data set can be seen in Figure 3. The advised time interval for wind data is 10 years, used in most tephra fallout assessments (e.g., Scollo et al., 2013; Biass et al., 2014, 2016b, 2017; Sandri et al., 2016).

TephraProb can account for seasonality in the wind data by making a separate stochastic selection of wind conditions for rainy and dry seasons. Wind seasonality was evaluated in all tephra fallout scenarios. The wind data set was separated into two seasons: 1) the rainy season and 2) the dry season. The rainy season spans from January to March, whereas the dry season spans from April to December. At 10–15 km a.s.l., the E-ward winds of the dry season are considerably faster (<50 m s^{-1}) than in the rainy season (<30 m s^{-1}) (Figure 3). Besides, the rainy season has relatively low-velocity (<20 m s^{-1}) winds with W-ward, S-ward, and N-ward components, whereas these are negligible in the dry season (Figure 3). At 20 km a.s.l., the rainy season develops relatively moderate (<30 m s^{-1}) W-ward winds, whereas the dry season develops both E-ward and W-ward relatively low-velocity winds (<20 m s^{-1}). Wind seasonality in northern Chile has been attributed to the southward movement of the South American Summer Monsoon (SASM), which originates in the Amazonian rainforest (Garreaud, 2009; Cavalcanti, 2012; Carvalho, 2020).

3.3.2 Concentrated pyroclastic density currents

For the concentrated PDCs assessment, we used the estimated volume of the largest PDC deposit of the San Pedro volcano: the Encanto ignimbrite. The area covered by the Encanto ignimbrite was estimated to be a minimum of 4.95 × 10^7 m^2, based on the area of mapped deposits (Figure 2) (Bertin and Amigo, 2019). Bertin and Amigo (2019) estimated the volume of this deposit using a mean thickness of 15 m, resulting in a mean volume of 7.43 × 10^8 m^3. If the middle value of the volume of the largest tephra fallout intra-scenario is multiplied by 8.3%, we obtained a value similar (7.45 × 10^8 m^3) to the volume of the Encanto ignimbrite (7.43 × 10^8 m^3). We used the 8.3% value to estimate the volumes of the other 30 concentrated PDCs intra-scenarios (Table 1 and Supplementary Material).

We used an 11.91-m resolution DEM produced by the 'TerraSAR–X add-on for digital elevation measurement' (TanDEM–X) and developed by the German Aerospace Center (Deutsches Zentrum für Luft- und Raumfahrt, DLR).

---

7 https://github.com/drewstev/arcgridwrite

TABLE 2 Physical and geochemical data of the 12 lava flow deposits of the San Pedro volcano. [a]Francis et al. (1974a); [b]Bertin and Amigo (2019); [c]Mamani et al. (2008); [d]Godoy et al. (2014); [e]Godoy et al. (2017); [f]O'Callaghan and Francis (1986); [g]Delunel et al. (2016); [h]González-Maurel et al., 2019b. Front thickness measurements were taken from Bertin and Amigo (2019). Manhattan and Euclidean lengths were measured with QGIS. The Abbreviations: wt.% means weight percentage and SD means standard deviation.

Lava flow deposit	Direction	Manhattan length (m)	Euclidean length (m)	Front thickness[b] (m)	Composition	Min. SiO_2 (wt.%)	Max. SiO_2 (wt.%)	SiO_2 reference	Age (ka)	Age SD (ka)	Age reference
Lava flow 1	N	7,915	7,903	40	—	—	—	—	—	—	—
Lava flow 2	NW	9,855	9,647	100	Dacite	64.1	64.9	a, c, d	130	40	b
Lava flow 3	NW	7,104	6,890	100	Dacite	64.4	64.4	a, c, d	96	8	h
Lava flow 4	NW	11,374	11,272	60	Andesite, Dacite	63.2	65.5	b, d, e	60	6	b
Lava flow 5	W	10,638	9,870	80	Dacite	63.6	65.6	b, c, d	90	80	b
Lava flow 6	W	7,293	7,241	50	Dacite	63.7	63.7	a	—	—	—
Lava flow 7	W	7,822	7,775	70	Andesite	62.2	64.3	a, b, f	—	—	—
Lava flow 8	W	5,401	5,420	20	—	—	—	—	—	—	—
Lava flow 9	W	5,399	5,385	30	Andesite	57.2	57.2	a	—	—	—
Lava flow 10	W	6,754	6,723	40	Andesite, Dacite	63.1	63.1	a, b, d	140	40	b
Lava flow 11	SW	4,576	4,611	60	Andesite, Dacite	65.1	65.1	f	—	—	—
Lava flow 12	SW	15,642	12,103	60	—	—	—	—	107 96 68	23.2 36 27	g b b
Minimum	—	4,576	4,611	20	—	57	57	—	60	6	—
Maximum	—	15,642	12,103	100	—	65	66	—	140	80	—
Mean	—	8,314	7,903	59	—	63	64	—	104	33	—
SD	—	3,121	2,376	25	—	2	3	—	29	–	—

The flow duration and the initial velocity were changed accordingly to produce the expected final volumes for all concentrated PDCs intra-scenarios. The duration of the flow was set between 65 and 2,500 s, while the initial velocity was set between 0.05 and 0.35 m s^{-1} depending on the simulation volume (Kelfoun et al., 2009) (Supplementary Material). A constant retarding stress was selected at 5,000 Pa for all simulations (Kelfoun et al., 2009), and all other parameters in the model remained at constant values (Supplementary Material). Finally, we simulated all 30 intra-scenarios.

3.3.3 Lahars

For the lahar assessment, the area covered by the largest lahar deposit of the San Pedro volcano was estimated at 2.12 × 10^7 m^2, according to the area of mapped deposits produced by previous authors (Bertin and Amigo, 2019) (Figure 2). The mean thickness of this deposit is estimated at 1.5 m (Bertin and Amigo, 2019), resulting in an estimated lahar deposit volume of 3.18 × 10^7 m^3. We assume that this deposit was produced during the largest M6.0 Plinian eruption at the San Pedro volcano, along with the largest tephra fallout and PDCs deposits.

To estimate the volume of the largest lahar intra-scenario, we assume a volume of solids of 40% and a volume of water of 60% (Thouret et al., 2020), and we consider tephra as its only solid component. To estimate the volume of solids, we used the same principle as in the concentrated PDCs, although we multiplied the middle value of the volume of the largest tephra fallout intra-scenario by 0.14% (see Supplementary Material). This results in a volume of solids of 1.25 × 10^6 m^3, which corresponds to 40% of the final volume of the largest lahar intra-scenario. The other 60% of the final volume is estimated to be incorporated by melted water from the snow cap. This results in a water volume of 1.88 × 10^6 m^3 and a final volume of 3.14 × 10^7 m^3, analogous to the calculated volume of the largest lahar deposit described before (3.18 × 10^7 m^3). Finally, we used the 0.14% value to estimate the volumes of the other lahar intra-scenarios.

Landsat 8 images from 2018 to 2020 ($n = 50$) show that the extension of the present snow cap varies throughout the year, as its area changes depending on the season. Meanwhile, the literature suggests that the San Pedro volcano had an ice cap during the late Pleistocene, during the timespan when the largest lahar deposit is thought to have been formed (*ca.* >55–37 ka). This interpretation is supported by moraine deposits at *ca.* 3,000 m a.s.l. at the southern flank of the volcano (Francis et al., 1974), and rock glaciers near the summit of the volcano (Payne, 1998; Barcaza et al., 2017). In addition, previous assessments have mentioned that it is unlikely for syn-eruptive lahars to be generated in this decade, due to the lack of an ice cap on the volcano (Bertin and Amigo, 2015).

To obtain the estimated mean radius of the snow cap at the San Pedro volcano, we measured the mean radius of the snow cap by using Landsat 8 images ($n = 50$), resulting in a mean snowcap radius of 775 ± 381 m. Then, we estimated the mean volume of this snow cap, with an assumed maximum snow thickness of 0.40 m, which resulted in a volume of 7.54 × 10^5 m^3. This is the estimated volume of water that can be produced given the average current snow conditions at the summit of the San Pedro volcano. This water volume agrees with the volume of water (60%) obtained for the lahar intra-scenario number 8 (Table 1). Thus, we used a 775-m radius for the source cap in this scenario, and we calculated the radius (r) of the source caps in the other intra-scenarios by using an assumed maximum snow thickness (t) value of 0.4 m (see Supplementary Material) and the inverse of the cylinder volume (V_w) formula, shown in Eq. (5). We think that this is the maximum thickness value for the snow cap of the volcano, and we use it to not underestimate the amount of snow that could be produced at the volcano during anomalous snowing days. Nevertheless, due to the climatic conditions, a lower snow thickness could be likely at the summit of the San Pedro volcano.

$$r = \sqrt{\frac{V_w}{\pi \cdot t}} \tag{5}$$

It is important to note that the occurrence of the largest intra-scenario would be very unlikely because of the amount of ice/snow melted water needed to produce it. Because of this, we did not simulate the intra-scenarios of large-size (intra-scenarios 11–15). Instead, we simulated the medium and small-size scenarios (Table 1). Therefore, the medium-size scenario with the largest size has a lahar volume of 3.14 × 10^6 m^3 (i.e., intra-scenario 10), one order of magnitude lower than the volume of the largest lahar deposit (3.14 × 10^7 m^3). We simulated a total of 8 scenarios in 7 different cap source locations on top of the western and eastern cones of the volcano. We produced a hexagonal grid of 700 m in diameter, with their respective centroids, in the same way as for blocky lava flows (see Section 3.4 and Supplementary Material). We set the DEM resolution of the LaharFlow model to 40 m for all simulations with the intent of reducing computational time costs. All other parameters in the model remained at their predetermined values (Supplementary Material).

3.4 Simulation of effusive scenarios

3.4.1 Blocky lava flows

The effusive scenarios include only blocky lava flows. We used the 11.91-m resolution TanDEM–X DEM in all simulations. For each effusive scenario, a different vent was used at the summit crater of the modern western cone. To obtain the distribution of these vents, we produced a hexagonal tessellation grid on the summit crater of the modern western cone of the San Pedro volcano by using the GDAL function (create grid). Then, we produced centroids for each hexagon with the GDAL function (centroids) (Supplementary Material). We tested different diameters for the hexagonal polygons of the

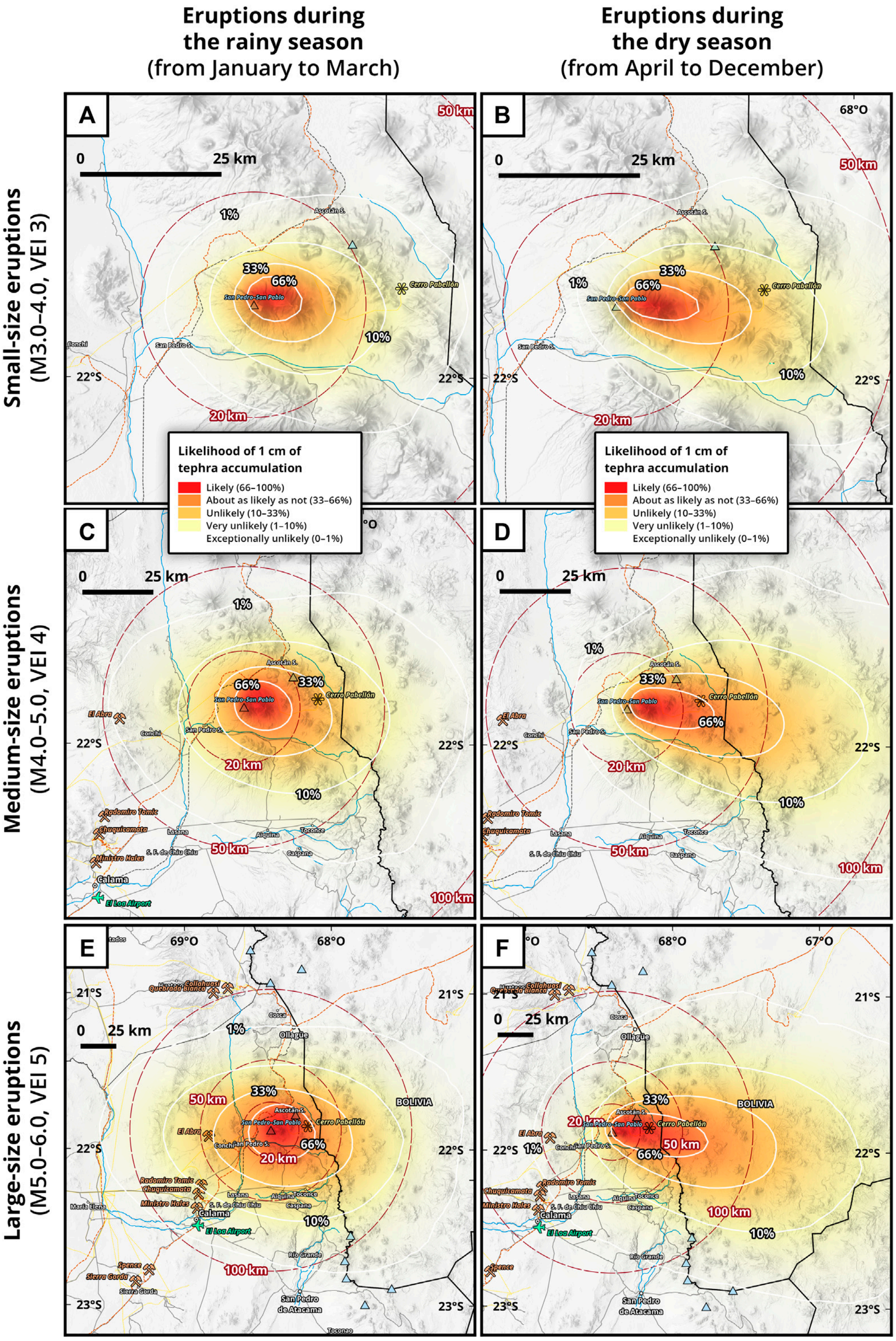

FIGURE 4
Likelihood maps of 1 cm of tephra fallout accumulation (alternatively: 10 kg m^{-2} or 10 mm). **(A,B)**, likelihood maps of small-size eruptions of magnitude 3.0–4.0 (VEI 3) (1:500,000 scale); **(C,D)**, likelihood maps of medium-size eruptions of magnitude 4.0–5.0 (VEI 4) (1:1,000,000 scale); **(E,F)**, likelihood maps for large-size eruptions of magnitude 5.0–6.0 (VEI 5) (1:2,000,000 scale). **(A,C,E)** represent eruptions during the rainy season (from January to March); **(B,D,F)** depict eruptions during the dry season (from April to December).

tessellation, but we decided to use a diameter of 200 m because this resulted in 32 source vent locations, a fair number of scenarios, and low computational time costs. All scenarios were simulated with the ‘point’ setting in the vent type parameter. The coordinates of the vent locations can be seen in Supplementary Material.

The simulations were made with the Decreasing Probability model and using the Euclidean length of the lava flow deposits. We measured the 12 blocky lava flow deposits identified by Bertin and Amigo (2019). We obtained a mean Euclidean length of 7,903 with a standard deviation of 2,376 (7,903 ± 2,376 m), with a minimum of 4,611 m (11th lava flow deposit, Figure 2), and a maximum of 12,103 m (12th lava flow deposit, Figure 2). All measurements can be seen in Table 2. The values used for the H_c and H_p parameters were 12 and 20 m for all simulations, respectively. Mossoux et al. (2016) estimated that these correction values can be associated with the minimum and maximum thickness of a lava flow. Bertin and Amigo (2019) describe a front thickness of 20 m for the eighth lava flow deposit (Figure 2; Table 2).

3.5 Preparation and visualization of maps

3.5.1 Probability rasters

Each cell of the probability rasters has values that range from 0 to 1, which are the conditional probabilities of a given volcanic phenomenon reaching a particular location (or the likelihood of phenomenon distribution). The probabilistic model-toolbox Tephra2-TephraProb outputs probabilistic rasters, therefore the mean of these rasters ($\bar{x}$) is easily done with the statistical mean formula shown in Eq. (6), following other volcanic hazard assessments (Sandri et al., 2016; Biass et al., 2016b; Charbonnier et al., 2020, among others). In Eq. (6), the sum of the rasters of each scenario (x_i) is divided by the number of simulations (n). However, the deterministic models (i.e., VolcFlow and LaharFlow), output thickness rasters that must be corrected by converting to one all the thickness values above zero—also known as the ‘hazard footprint’ (Loughlin et al., 2015)—to then obtain the mean of all the simulations through Eq. (6). In the case of the Decreasing Probability model, as it is not a numerical or analytical model, but a statistical/empirical model, its results have been treated as if they were from a deterministic model, this means that all probability values above zero have been converted to one, and then the mean has been obtained through Eq. (6). Finally, we give a uniform temporal occurrence probability to each simulated intra-scenario.

$$\bar{x} = \frac{\sum_{i=1}^{n} x_i}{n} \tag{6}$$

The probability rasters of each tephra fallout scenario are obtained by exporting the ESRI ASCII (.asc) probability rasters from MATLAB, using the TephraProb toolbox and importing them to QGIS. We selected the probability rasters with a tephra accumulation threshold of 10 kg m^{-2}. Then, these rasters are interpolated with the GRASS function (r.resamp.interp) from a low resolution (6.0, 4.0, and 2.5 km) to a higher resolution (2.0 km). For instance, the small-size tephra fallout scenario has five intra-scenarios. To obtain the probability raster of this scenario, we add the probability rasters of its five intra-scenarios and divide them by the total number of small-size intra-scenarios ($n = 5$) by using Eq. (6) with the GDAL raster calculator. The probability rasters of the medium and large-size scenarios are obtained following the same procedure.

The probability raster of concentrated PDCs is obtained by exporting ESRI ASCII (.asc) rasters from MATLAB by using the ArcGridWrite function[7]. Then, these rasters are loaded in ArcGIS ArcMap and corrected by flipping them upside down along the horizontal axis by using the ArcMap function (flip raster), because the ArcGridWrite function wrongfully flips the horizontal axis of the ASCII raster matrices, then, these raster matrices are imported to QGIS. All thickness values above zero are converted to one with the GDAL raster calculator (code: *‘raster’ > 0 = 1*). The mean probabilities of all 30 simulations of PDCs are obtained by using Eq. (6) with the GDAL raster calculator ($n = 30$). Then, the values are normalized with the SAGA function (raster normalization), so that all cells had values ranging from zero to one. Finally, we smoothed the values of the rasters with the GRASS function (r.neighbors).

The probability raster of lahars is obtained by downloading the ‘maximum height’ vector data files (.kml) from LaharFlow and importing them to QGIS. These files have an error in the thickness column as it is populated with text values (e.g., ‘h = 0.234’) instead of numbers. To correct this, a new column labeled ‘thickness’ with only the thickness value must be created. To eliminate the ‘*h_max =*’ portion we created a new column (code: *replace(Name, ‘h_max =’, ‘ ’)*). Then, these vector files are converted to raster format by using the GDAL function (rasterizer), with the ‘thickness’ column as the selected field value that will populate the cells of the raster. Then, Eq. (6) is applied (although, with $n = 56$). The same normalization and smoothing procedures described to the VolcFlow probability rasters are applied to the LaharFlow rasters.

The probability raster of blocky lava flows is obtained by filling with zeros the no-data cell values of the rasters by using the GRASS function (r.null). Then, all probability values above zero are converted to one with the GDAL raster calculator. Then, Eq. (6) is applied (although, with $n = 32$). Likewise, the same normalization and smoothing procedures used for the VolcFlow and LaharFlow probability rasters are applied to the Decreasing Probability/Q-LavHA rasters.

3.5.2 Likelihood (probability) maps

To communicate our results, we use the five-stage likelihood classification of the IPCC (Intergovernmental Panel on Climate

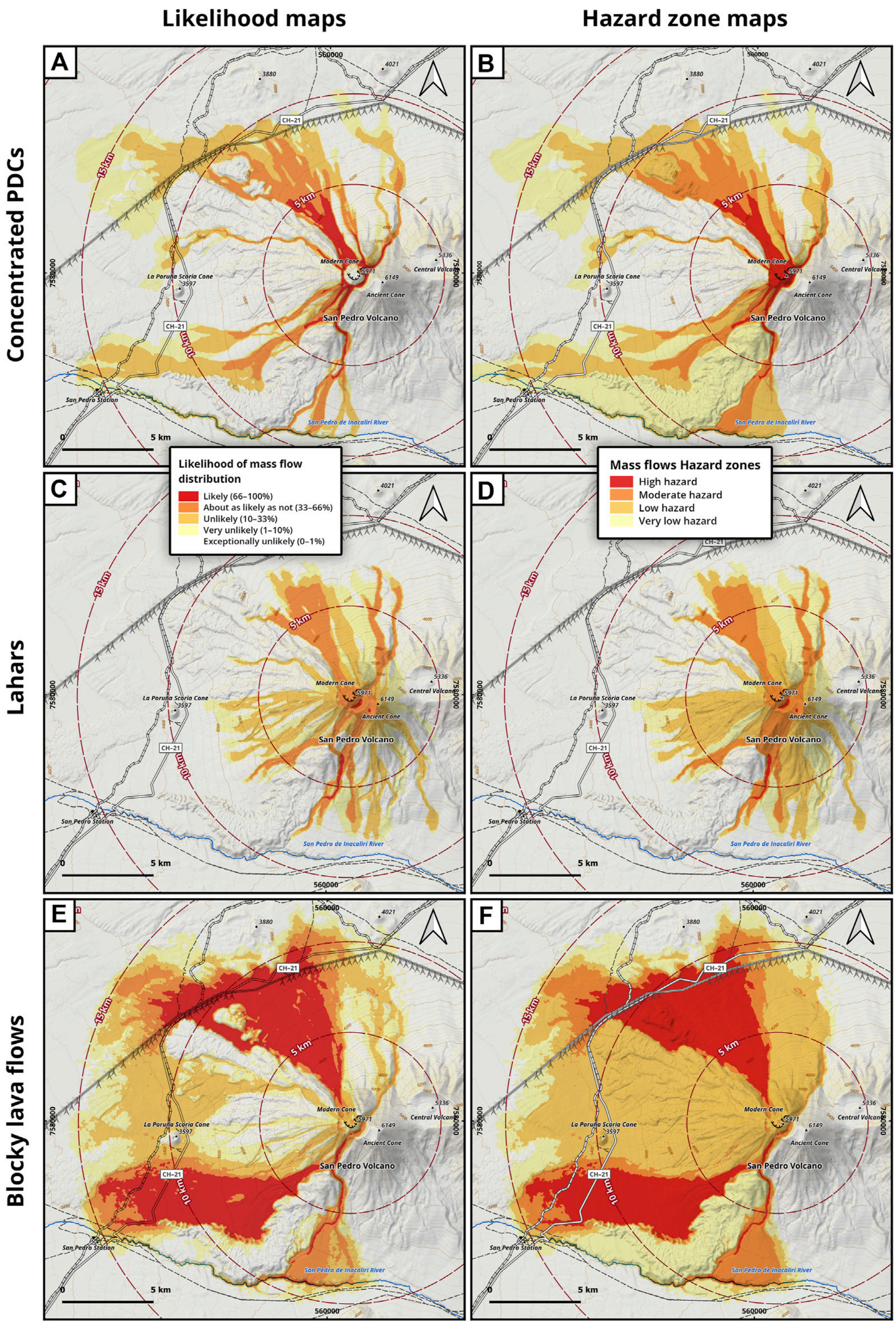

FIGURE 5
(A) likelihood map of concentrated PDCs. **(B)** hazard zone map of concentrated PDCs. **(C)** likelihood map of lahars. **(D)** hazard zone map of lahars. **(E)** likelihood map of blocky lava flows. **(F)** hazard zone map of blocky lava flows. (all maps in 1:100,000 scale).

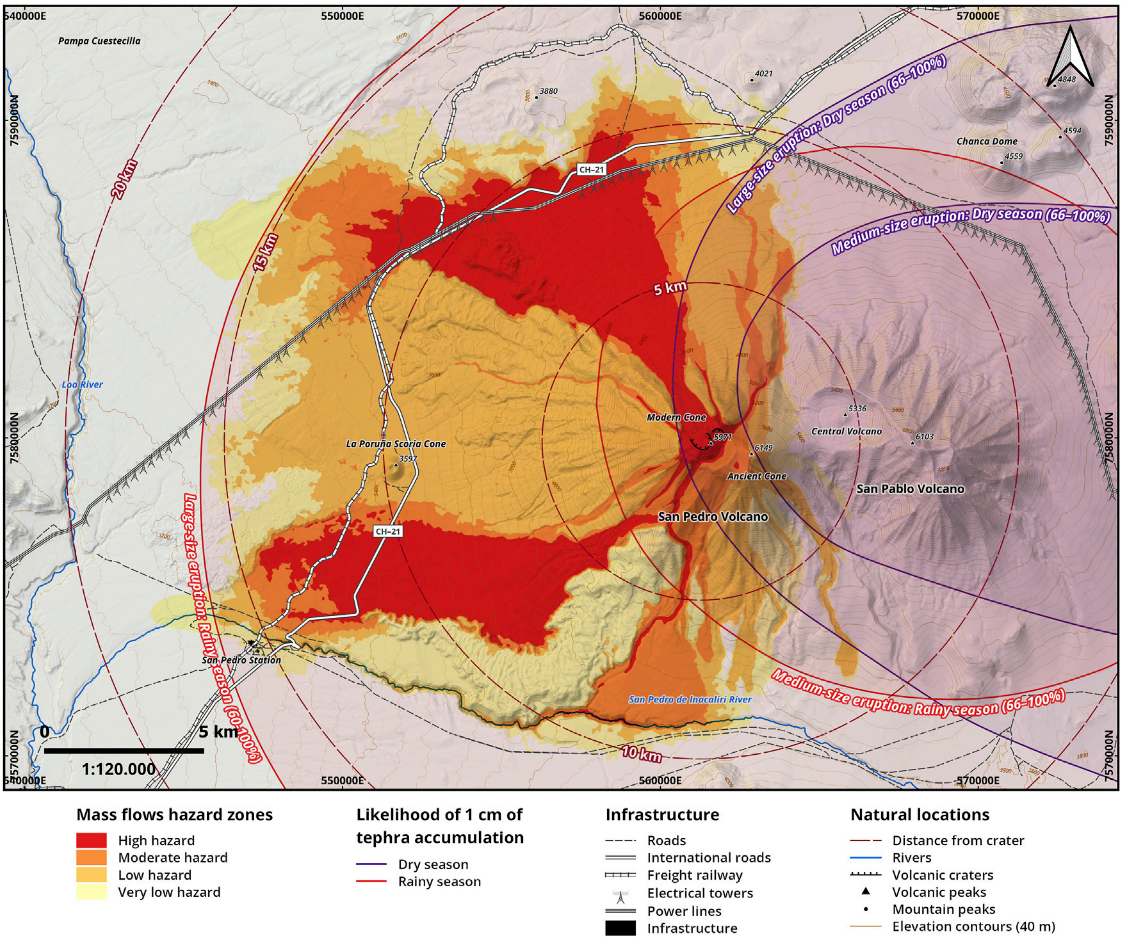

FIGURE 6
Final integrated multi-hazard zone map of tephra fallout and mass flows (1:120,000 scale).

Change) (Mastrandrea et al., 2010) to distinguish between hazard zones, as done in other works (Tierz et al., 2017). We assigned a five-color palette from ColorBrewer[8] to each hazard zone (Brewer, 2003), these zones are:

1) Likely (66–100%) or high hazard zone (red).
2) About as likely as not (33–66%) or moderate hazard zone (orange).
3) Unlikely (10–33%) or low hazard zone (yellow).
4) Very unlikely (1–10%) or very low hazard zone (light-yellow).
5) Exceptionally unlikely (0–1%) or exceptionally low hazard zone (white)

These maps represent the likelihood of phenomenon distribution, whether by inundation (lahars, blocky lava flows), invasion (concentrated PDCs), or accumulation (tephra fallout).

Figure 4 shows the likelihood (isarithmic) maps of 1 cm of tephra fallout accumulation. In these maps, four labeled contours (i.e., 1, 10, 33, and 66%) are used to draw the qualitative limits of the likelihood of tephra fallout distribution. Each one of these contours connects the raster points where the probabilities of 1 cm (or 10 kg m^{-2}) of tephra accumulation are equal. In this case, 10 kg m^{-2} equals 1 cm of tephra accumulation because we used a 1,000 kg m^{-3} density of pumice tephra in all simulations. Contours were computed with the GDAL function (contours). In addition to contours, a continuous color gradient was employed (red, orange, yellow, and light-yellow). Thompson et al. (2015) have shown that this way of representing the hazard of tephra fallout is better understood by both communities and stakeholders alike. In the case of mass flows, the likelihood maps of concentrated PDCs (Figure 5A), lahars (Figure 5C), and blocky lava flows (Figure 5E) are presented in Figure 5.

3.5.3 Single and multiple hazard zone maps

To create a final multi-hazard map, we decided to stack hazard zones of each phenomenon, instead of obtaining the mean of all the three probability rasters. To do this, vector polygons (e.g., shapefiles, .shp) are needed. For instance, to obtain the high hazard zone polygon from the probability raster of concentrated PDCs, we calculated a new raster where all the values above 66% were converted to one, and all values below 66% were converted to 0. Then, we converted this new raster to a vector polygon with the GDAL function (polygonize). Additionally, all gaps inside the limits of this high hazard zone polygon were included inside the high hazard zone to improve the readability of the map. All other hazard zones of PDCs were obtained in the same manner and following the same qualitative intervals from the likelihood classification presented above (Mastrandrea et al., 2010). We obtained the hazard zone maps of lahars and blocky lava flows following the same procedure. The hazard zone maps of concentrated PDCs (Figure 5B), lahars (Figure 5D), and blocky lava flows (Figure 5F) are presented in Figure 5, while Figure 6 shows the final multi-hazard map. The multi-hazard map was created by stacking the hazard zone polygons of each one of these single maps in the following manner: all three very low hazard zones polygons first, then the three low hazard zones, followed by the three moderate hazard zones, and finally the three high hazard zones. Furthermore, we included the conditional likelihoods of tephra accumulation from the medium and large-size eruptions of both seasons (Figures 4C–F). The rainy season eruptions were assigned a red color, while dry season eruptions were assigned a purple color to be easily distinguished (Figure 6).

4 Results

4.1 Tephra fallout

All three scenarios of tephra fallout considered the seasonality of wind conditions, i.e., the variations in wind direction and velocity between the rainy and dry seasons in northern Chile. The left column of the tephra fallout probability maps shows the results for the rainy season (January–March) (Figures 4A,C,E), while the right column shows the results for the dry season (April–December) (Figures 4B,D,F). The results show a higher likelihood of tephra accumulation in Chilean localities during the rainy season (January–March) than during the dry season (April–December) (Figures 4B,D,F).

Large-size eruptions in the rainy season (Figure 4E) are likely (66–100%) to accumulate 1 cm of tephra on the San Pedro and Ascotán stations; and on the Cerro Pabellón power plant. However, these eruptions are about as likely as not (33–66%) to settle 1 cm of tephra on the Conchi locality. Moreover, these eruptions are unlikely (10–33%) to deposit 1 cm of tephra on the Lasana, Chiu Chiu, Aiquina, Toconce, and Caspana localities; and on the El Abra Copper Mine. Furthermore, these eruptions are very unlikely (1–10%) to accumulate 1 cm of tephra on the Calama, Ollagüe, Río Grande localities; on the Radomiro Tomic, Chuquicamata, and Ministro Hales copper mines; and on the El Loa international airport.

Large-size eruptions in the dry season (Figure 4F) are likely (66–100%) to settle 1 cm of tephra on the Cerro Pabellón power plant, and about as likely as not (33–66%) to do so on the Ascotán station. Further, these eruptions are unlikely (10–33%) to deposit 1 cm of tephra on the Toconce locality and the San Pedro station. Besides, they are very unlikely (1–10%) to accumulate 1 cm of tephra in the Conchi, Caspana, Aiquina, Lasana, and Chiu Chiu localities; and on the El Abra copper mine.

Medium-size eruptions in the rainy season (Figure 4C) are about as likely as not (33–66%) to settle 1 cm of tephra on the Cerro Pabellón power plant and the electrical towers and power lines, whereas medium-size eruptions in the dry season (Figure 4D) are likely (66–100%) to do so.

Small-size eruptions in the rainy season (Figure 4A) are very unlikely (1–10%) to deposit 1 cm of tephra on the Cerro Pabellón power plant, although, small-size eruptions in the dry season (Figure 4B) are unlikely (10–33%) to do so.

During the rainy season, large-size eruptions are likely (66–100%) to accumulate 1 cm of tephra on the CH–21 highway, the freight railway, electrical towers, and power lines, whereas, medium-size eruptions are about as likely as not (33–66%) to do so, and small-size eruptions are very unlikely (1–10%) to do so.

Regarding highly populated centers, the accumulation of 1 cm of tephra in Calama after small to medium-size eruptions is exceptionally unlikely (0–1%) during both seasons (Figures 4A–D). Nonetheless, the accumulation of 1 cm of tephra in Calama after large-size eruptions is very unlikely (1–10%) during the rainy season (Figure 4E) and exceptionally unlikely (0–1%) during the dry season (Figure 4F).

Other localities such as Cosca, San Pedro de Atacama, Quillagüa, Huatacondo, María Elena, Sierra Gorda, Toconao, Tocopilla, and Antofagasta are exceptionally unlikely (0–1%) to be covered by 1 cm of tephra fallout after eruptions of all sizes in both seasons.

4.2 Mass flows

Concentrated PDCs produced by future eruptions are about as likely as not (33–66%) to invade the San Pedro de Inacaliri river valley; they are unlikely (10–33%) to invade the CH–21 highway, freight railway, and electrical towers surrounding the volcano; and very unlikely (1–10%) to invade the San Pedro station (Figures 5A,B).

Syn-eruptive lahars generated by future eruptions are exceptionally unlikely (0–1%) to inundate the San Pedro station, or the transport and energy infrastructure surrounding the volcano (Figures 5C,D).

Blocky lava flows produced during future effusive eruptions are likely (66–100%) to inundate the northern and southwestern flanks of the San Pedro volcano (Figures 5E,F). Further, blocky lava flows are likely (66–100%) to inundate various sections of the international highway, freight railway, along with some electrical transmission towers (Figures 5E,F).

5 Discussion

5.1 The differences with other multi-hazard assessments

Volcanic systems often require many hazard assessments with complementary approaches to bring forth alternative perspectives on hazard forecasting (Calder et al., 2015; Martí, 2017). The previous hazard assessment of the San Pedro volcano (Bertin and Amigo, 2015) produced simulations for tephra fallout by using the Tephra2 model (Bonadonna et al., 2005), and simulations of PDCs by using the Energy Cone model (Malin and Sheridan, 1982). However, the previous assessment did not produce simulations for lahars or blocky lava flows, the latter were not considered because the authors evaluated a different time interval (50 ka to present) in the geological history of the volcano (Bertin and Amigo, 2015).

Our tephra fallout assessment complements the 2015 hazard assessment (Bertin and Amigo, 2015) for multiple reasons. First, the 2015 assessment considered medium (VEI 4–5) and large-size (VEI 5–6) scenarios, whereas the present assessment considers 15 eruptive intra-scenarios from magnitudes 3.0 to 6.0, synthesized into three eruptive scenarios of small (VEI 3), medium (VEI 4), and large size (VEI 5). Second, the present work uses a different visualization of the hazard zones of tephra fallout than the previous hazard assessment, which aids stakeholders and the civil community to understand them, in agreement with previous works (Thompson et al., 2015). Moreover, the representation of wind seasonality is synthesized into only two seasons (rainy and dry seasons), whereas, in the 2015 assessment, this representation is done for the four standard climate seasons (summer, fall, winter, and spring). Third, the 2015 assessment simulated a greater time interval for wind data (16 years) than the present work (11 years), although the number of simulated wind profiles is greater in the present assessment than in the 2015 assessment. Even though both works used the same model (Tephra2), the probabilistic toolbox, TephraProb (Biass et al., 2016b), facilitated the production of a high number of simulations for each intra-scenario in the present assessment, something that was not available for the previous authors, as TephraProb was made available years after the development of the 2015 assessment.

The 2015 assessment used the Energy Cone model introduced by Malin and Sheridan (1982) to simulate PDCs (Bertin and Amigo, 2015). The main difference between the Energy Cone and the VolcFlow models is that the Energy cone is a statistical/empirical model, whereas VolcFlow is a numerical model. Even though the empirical relationships between the parameters of the Energy Cone model are well constrained (Newhall and Hoblitt, 2002), it does not consider the initial volume of the simulated deposits (Ogburn and Calder, 2017), which is crucial for the co-parameterization of phenomena size between the same intra-scenarios in the present assessment. Finally, the hazard zones PDCs in the present assessment are a complement to the hazard zones proposed in the 2015 assessment.

Our blocky lava flow assessment is an improvement because the previous assessment (Bertin and Amigo, 2015) did not simulate blocky lava flows. Even though the Decreasing Probability model simulates ‘a’ā lava flows more effectively, we think it can also simulate blocky lava flows because it was able to reproduce the length of the real lava flow deposits of the San Pedro volcano. Additionally, even though the recent geological history of the San Pedro volcano had migrated to higher-silica phenomena (i.e., lava domes), a blocky lava flow assessment can still be useful for the effusive phases of future eruptions.

Our lahar assessment can be seen as a complement to hazard zones proposed in the 2015 assessment because previous zones were not delimited with lahar models of any type because they were estimated from the distribution of geological deposits (Bertin and Amigo, 2015). In the present work, the probabilistic use of LaharFlow (Woodhouse et al., 2016), is an improvement in the forecasting of future lahars at the San Pedro volcano. The LaharFlow model allowed us to co-parameterize its volume with other models of volcanic phenomena within the same simulated intra-scenario.

5.2 The simulations of volcanic phenomena

We did not consider other volcanic phenomena, such as VBPs, diluted PDCs, and volcanic avalanches by sector collapse, as they are not within the scope of this study. In the case of VBPs, there are two limitations to their implementation in this methodology. First, mass/volume is not a parameter in models of VBPs (Mastin, 2001; Biass et al., 2016c; Bertin 2017). Second, recent works have demonstrated that the launch velocity of VBPs, one of the first-order parameters in VBPs models, does not correlate with the size of eruptions (Maeno et al., 2013; Taddeucci et al., 2017). Therefore, we could not integrate models of VBPs with the simulated explosive intra-scenarios in the present assessment. In the case of sector collapse, we did not produce simulations for volcanic avalanches because of the low recurrence of this phenomenon globally and regionally (Sandri et al., 2014). In the case of diluted PDCs, we only could produce an assessment with the single-fluid version of VolcFlow, which models concentrated PDCs, but not diluted PDCs (Kelfoun et al., 2009). Therefore, the results of these simulations are limited, as they are not representative of the whole areas that real PDCs could cover. However, they are representative of the areas where the largest portion of the volume of PDCs could be deposited (Ogburn and Calder, 2017). Even though the areas where diluted PDCs could be distributed are not simulated, the areas that this phenomenon could cover are delimited by the hazard zones of simulated blocky lava flows in the final multi-hazard map (Figure 6).

In the case of the distribution of tephra fallout, the rainy season has low-velocity winds with W-ward, S-ward, and N-ward components, which causes simulated tephra to be transported equally toward the W and E (Figures 4A,C,E). Conversely, the dry season has fast E-ward winds, causing simulated tephra to distribute toward the E (Figures 4B,D,F). Plus, the larger the size of the eruption, the more it is affected by wind conditions (see Figure 6). This is because larger size eruptions have higher column heights (Mastin et al., 2009), therefore, they are affected by the high-altitude high-velocity W-ward winds of the rainy season (Figure 3). The San Pedro and Ascotán freight railway stations have the highest likelihood of tephra accumulation of all localities evaluated in this study (Figure 4). From the results, we suggest that a special emphasis should be placed on the Toconce locality, due to its location, as it seems to have a similar likelihood of tephra accumulation after large eruptions independent of the season (Figures 4E,F); being unlikely (10–33%) to be covered by 1 cm of tephra in both seasons, something that does not happen in other localities.

Regarding the distribution of mass flows, the northern and southwestern flanks are likely to be the areas most affected by all types of mass flows. In the case of the northern flank, we think this is because it connects to the crater of the modern western cone with a high-slope angle. Meanwhile, the southern flank has an incision on the southwestern face of the summit of the modern western cone, again, with a high-slope angle. The current topography of the volcano promotes the distribution of mass flows toward the northern and southwestern flanks, which increases the probability of mass flows reaching those locations. However, the topography surrounding the volcano controls the probability of mass flow distribution at farther distances from the crater. The general trend of the topography surrounding the volcano is to decrease in elevation toward the W. Therefore, mass flows tend to have a W-ward distribution; this can be seen especially in the distribution of concentrated PDCs (Figures 5A,B) and blocky lava flows (Figures 5E,F). The current deposits of blocky lava flows will be key in containing, blocking, or redirecting the distribution of future mass flows, both in the northern and southwestern flanks of the San Pedro volcano (Figure 6). In the simulations, the fourth deposit of blocky lava flows bounds the distribution of mass flows on the northern flank (Figure 2). Likewise, the 12th lava flow interrupts the distribution of mass flows on the southwestern flank (Figure 2).

In the case of the estimation of probabilities, we treated the empirical/statistical Decreasing Probability model as a deterministic model. Thus, we obtained the mean probability raster through Eq. (6). This is done because one simulation of the Q-LavHA model reproduces the direction of a one pixel-wide lava flow event instead of the full-width of a lava flow event (hazard footprint), as analytical or numerical models do. Therefore, 5000 iterations were used to reproduce the distribution of one lava flow event. If we did not make this correction, the probabilities were anomalously concentrated between 0 and 10% in the probability raster, thus making the delimitation of hazard zones subjective. Our treatment of this model as deterministic agrees with how the probabilities of empirical/statistical models have been estimated in other hazard assessments, for example, for the Energy Cone model (Tierz et al., 2018; Clarke et al., 2020).

Regarding the source locations of phenomena, we suggest that a hexagonal tessellation is more efficient than a square tessellation at discretizing the volcanic crater area. This is because source locations are more equally distributed than in a square tessellation. Even though we did not test the influence of the hexagon diameters chosen (200 and 700 m), we selected these values considering that the number of hexagons that fitted inside the crater areas would result in a fair computational time cost for both models. Furthermore, we assumed that all possible source locations have a uniform probability of occurrence.

The thickness values of the blocky lava flow deposits are relatively high (Table 2). With the TanDEM–X DEM, we found that the larger thicknesses were found near the front of the lava flows. The simulation of these front thickness values would not be advisable because they are an overestimation of the front thickness of the lava flow as it is flowing down the volcano during an eruption. The TanDEM–X DEM shows that most thickness values of the largest lava flow deposits (fourth and fifth; Figure 2) are within the 20–40 m range if they are measured at half of their Manhattan length. The eighth deposit has almost half the Manhattan length of the fourth and fifth deposits, and its front thickness value is 20 m. Therefore, we used this field-measured value (20 m) as the maximum thickness corrective value (H_p). We think this value is a better representation of the front thickness a blocky lava flow would have as it is flowing down the flanks of the volcano during an effusive eruption.

6 Conclusion

The San Pedro volcano has the fifth highest-threat index among northern Chile volcanoes. Its historically active behavior and the magnitude of its recent eruptions have shown the importance of forecasting the potential distribution of future volcanic phenomena at this volcano. In this assessment, four types of volcanic phenomena were simulated using accessible computational models. This assessment helps to quantify the hazard through multi-phenomena eruptive scenarios with continuous sizes. The hazard zones proposed in this work are a complement to previous hazard assessments at the San Pedro volcano. The following conclusions were reached:

1) There is a higher likelihood of tephra impact in Chilean localities and infrastructure during the rainy season (January–March) than during the dry season (April–December).
2) Large-size eruptions (VEI 5) in the rainy season (January–March) are very unlikely (1–10%) to accumulate 1 cm of tephra in the city of Calama (and its surrounding mining sites).
3) Large-size eruptions (VEI 5) in the rainy season are exceptionally unlikely (0–1%) to deposit 1 cm of tephra in the cities of María Elena, Sierra Gorda, San Pedro de Atacama, Tocopilla, and Antofagasta.
4) Electrical (power lines and towers) and transport (highway and railways) infrastructure, along with river valleys surrounding the volcano, could be impacted by both tephra fallout and mass flows during future eruptions.
5) The Cerro Pabellón power plant has the highest likelihood of tephra fallout impact than any other infrastructure surrounding the volcano, and the likelihood is higher during the dry season.

Both vulnerable communities and governmental entities can help mitigate the impact of potential future eruptions by being aware of the hazards, educating the community, and developing an effective emergency plan for the San Pedro volcano. Volcanic hazard maps can provide preemptive information to governmental entities for future land-use planning, civil protection, and management of volcanic crises in the Antofagasta Region.

Data availability statement

The original contributions presented in the study are included in the article/Supplementary Material, further inquiries can be directed to the corresponding author.

Author contributions

NA-V conceived the study, produced the simulations, and wrote the manuscript with inputs from M-PR-H and AE. FA acquired funding for the research. All authors read, reviewed, and approved the final manuscript.

Funding

This research has been funded by the ANID FONDAP 15110017 project, National Research Center for Integrated Natural Disaster Management (CIGIDEN), granted by the Chilean National Agency for Research and Development (ANID) and the FIC–R BIP 30488832-0 project, Mitigation of Risk Associated to Volcanic Processes in the Antofagasta Region, granted by the Innovation Fund for Regional Competitiveness (FIC–R) of the Antofagasta Regional Government, Chile (GORE Antofagasta). M-PR-H is funded by the SNSF 188757 project, A new probabilistic framework for regional volcanic risk assessment including hazards interacting at multiple temporal and spatial scales, granted by the Swiss National Science Foundation (SNSF). AE is funded by the ANID 21192242 National PhD Grant.

Acknowledgments

We thank John Santibañez and Francisco Armijo for their insights about some aspects of the research. We thank Dr. Gabriel Ureta for providing access to the TanDEM–X digital elevation model through the DEM_GEOL2956 proposal and the German Aerospace Center (Deutsches Zentrum für Luft- und Raumfahrt, DLR) for the development of the TanDEM–X project. We thank reviewers Sam Poppe and Marta Della Setta who helped to improve the manuscript with their constructive revisions and feedback. Finally, we thank editor Karoly Nemeth for the editorial handling of the manuscript.

Conflict of interest

The authors declare that the research was conducted in the absence of any commercial or financial relationships that could be construed as a potential conflict of interest.

Publisher's note

Supplementary material

The Supplementary Material for this article can be found online at: https://www.frontiersin.org/articles/10.3389/feart.2022.897315/full#supplementary-material

References

Aguilera, F., Layana, S., Rojas, F., Arratia, P., Wilkes, T. C., González, C., et al. (2020). First measurements of gas flux with a low-cost smartphone sensor-based UV camera on the volcanoes of northern Chile. *Remote Sens.* 12 (13), 2122. doi:10.3390/rs12132122

Alcorn, R., Panter, K. S., and Gorsevski, P. V. (2013). A GIS-based volcanic hazard and risk assessment of eruptions sourced within Valles Caldera, New Mexico. *J. Volcanol. Geotherm. Res.* 267, 1–14. doi:10.1016/j.jvolgeores.2013.09.005

Amigo, A. (2012). Volcano monitoring and hazard assessments in Chile. *Volcanica* 4 (S1), 1–20. doi:10.30909/vol.04.S1.0120

Amigo, Á., Bertin, D., and Orozco, G. (2012). *Peligros volcánicos de la zona norte de Chile, Regiones de Arica y Parinacota, Tarapacá, Antofagasta y Atacama. Carta Geológica de Chile, Serie Geología Ambiental, 17.* Santiago: Servicio Nacional de Geología y Minería SERNAGEOMIN.

Aravena, D., Villalón, I., and Sánchez, P. (2015). Igneous related geothermal resource in the Chilean Andes. *Proc. World Geotherm. Congr.* 2015, 401. doi:10.1016/0375-6505(88)90068-5

Barcaza, G., Nussbaumer, S. U., Tapia, G., Valdés, J., García, J.-L., Videla, Y., et al. (2017). Glacier inventory and recent glacier variations in the Andes of Chile, South America. *Ann. Glaciol.* 58 (75pt2), 166–180. doi:10.1017/aog.2017.28

Becerril, L., Bartolini, S., Sobradelo, R., Martí, J., Morales, J. M., Galindo, I., et al. (2014). Long-term volcanic hazard assessment on El Hierro (Canary Islands). *Nat. Hazards Earth Syst. Sci.* 14 (7), 1853–1870. doi:10.5194/nhess-14-1853-2014

Becerril, L., Martí, J., Bartolini, S., and Geyer, A. (2017). Assessing qualitative long-term volcanic hazards at Lanzarote Island (Canary Islands). *Nat. Hazards Earth Syst. Sci.* 17 (7), 1145–1157. doi:10.5194/nhess-17-1145-2017

Bertin, D. (2017). 3-D ballistic transport of ellipsoidal volcanic projectiles considering horizontal wind field and variable shape-dependent drag coefficients. *J. Geophys. Res. Solid Earth* 122 (2), 1126–1151. doi:10.1002/2016JB013320

Bertin, D., and Amigo, Á. (2019). *Geología del Volcán San Pedro, Región de Antofagasta. Carta Geológica de Chile, Serie Geología Básica, 201.* Santiago: Servicio Nacional de Geología y Minería SERNAGEOMIN.

Bertin, D., and Amigo, Á. (2015). *Peligros del Volcán San Pedro, Región de Antofagasta. Carta Geológica de Chile, Serie Geología Ambiental, 25.* Santiago: Servicio Nacional de Geología y Minería SERNAGEOMIN.

Biass, S., and Bonadonna, C. (2013). A fast GIS-based risk assessment for tephra fallout: The example of Cotopaxi volcano, Ecuador, Part I: Probabilistic hazard assessment. *Nat. Hazards (Dordr).* 65 (1), 477–495. doi:10.1007/s11069-012-0378-z

Biass, S., Bonadonna, C., Connor, L., and Connor, C. (2016b). TephraProb: A Matlab package for probabilistic hazard assessments of tephra fallout. *J. Appl. Volcanol.* 5 (1), 10. doi:10.1186/s13617-016-0050-5

Biass, S., Bonadonna, C., di Traglia, F., Pistolesi, M., Rosi, M., Lestuzzi, P., et al. (2016a). Probabilistic evaluation of the physical impact of future tephra fallout events for the Island of Vulcano, Italy. *Bull. Volcanol.* 78 (5), 37. doi:10.1007/s00445-016-1028-1

Biass, S., Falcone, J. L., Bonadonna, C., Di Traglia, F., Pistolesi, M., Rosi, M., et al. (2016c). Great balls of fire: A probabilistic approach to quantify the hazard related to ballistics—a case study at La Fossa volcano, Vulcano Island, Italy. *J. Volcanol. Geotherm. Res.* 325, 1–14. doi:10.1016/j.jvolgeores.2016.06.006

Biass, S., Scaini, C., Bonadonna, C., Folch, A., Smith, K., Höskuldsson, A., et al. (2014). A multi-scale risk assessment for tephra fallout and airborne concentration from multiple Icelandic volcanoes – Part 1: Hazard assessment. *Nat. Hazards Earth Syst. Sci.* 14 (8), 2265–2287. doi:10.5194/nhess-14-2265-2014

Biass, S., Todde, A., Cioni, R., Pistolesi, M., Geshi, N., Bonadonna, C., et al. (2017). Potential impacts of tephra fallout from a large-scale explosive eruption at Sakurajima volcano, Japan. *Bull. Volcanol.* 79 (10), 73. doi:10.1007/s00445-017-1153-5

Blong, R. (2000). "Volcanic hazard and risk management," in *The encyclopedia of volcanoes*. Editor H. Sigurdsson. 1st ed. (Academic Press), 1215–1227.

Bonadonna, C., Connor, C. B., Houghton, B. F., Connor, L., Byrne, M., Laing, A., et al. (2005). Probabilistic modeling of tephra dispersal: Hazard assessment of a multiphase rhyolitic eruption at Tarawera, New Zealand. *J. Geophys. Res.* 110 (B3), B03203. doi:10.1029/2003JB002896

Bonadonna, C., and Houghton, B. F. (2005). Total grain-size distribution and volume of tephra-fall deposits. *Bull. Volcanol.* 67 (5), 441–456. doi:10.1007/s00445-004-0386-2

Bonasia, R., Scaini, C., Capra, L., Nathenson, M., Siebe, C., Arana-Salinas, L., et al. (2014). Long-range hazard assessment of volcanic ash dispersal for a Plinian eruptive scenario at Popocatépetl volcano (Mexico): Implications for civil aviation safety. *Bull. Volcanol.* 76 (1), 789. doi:10.1007/s00445-013-0789-z

Bonne, K., Kervyn, M., Cascone, L., Njome, S., Van Ranst, E., Suh, E., et al. (2008). A new approach to assess long-term lava flow hazard and risk using GIS and low-cost remote sensing: The case of Mount Cameroon, West Africa. *Int. J. Remote Sens.* 29 (22), 6539–6564. doi:10.1080/01431160802167873

Brewer, C. A. (2003). A transition in improving maps: The ColorBrewer example. *Cartogr. Geogr. Inf. Sci.* 30 (2), 159–162. doi:10.1559/152304003100011126

Calder, E., Wagner, K., and Ogburn, S. E. (2015). "Volcanic hazard maps," in *Global volcanic hazards and risk*. Editors S. C. Loughlin, S. Sparks, S. K. Brown, S. F. Jenkins, and C. Vye-Brown. 1st ed. (Cambridge: Cambridge University Press), 335–342. doi:10.1017/CBO9781316276273.022

Capra, L., Norini, G., Groppelli, G., Macías, J. L., and Arce, J. L. (2008). Volcanic hazard zonation of the Nevado de Toluca volcano, México. *J. Volcanol. Geotherm. Res.* 176 (4), 469–484. doi:10.1016/j.jvolgeores.2008.04.016

Carvalho, L. M. V. (2020). Assessing precipitation trends in the Americas with historical data: A review. *WIREs Clim. Change* 11 (2). doi:10.1002/wcc.627

Casertano, L. (1963). *Catalogue of the active volcanoes and solfatara fields of the Chilean continent. Catalogue of the active volcanoes of the world, including solfatara fields, 15.* Rome: International Volcanological Association.

Cavalcanti, I. F. A. (2012). Large scale and synoptic features associated with extreme precipitation over South America: A review and case studies for the first decade of the 21st century. *Atmos. Res.* 118, 27–40. doi:10.1016/j.atmosres.2012.06.012

Charbonnier, S. J., Germa, A., Connor, C. B., Gertisser, R., Preece, K., Komorowski, J.-C., et al. (2013). Evaluation of the impact of the 2010 pyroclastic density currents at Merapi volcano from high-resolution satellite imagery, field investigations and numerical simulations. *J. Volcanol. Geotherm. Res.* 261, 295–315. doi:10.1016/j.jvolgeores.2012.12.021

Charbonnier, S. J., and Gertisser, R. (2012). Evaluation of geophysical mass flow models using the 2006 block-and-ash flows of Merapi Volcano, Java, Indonesia: Towards a short-term hazard assessment tool. *J. Volcanol. Geotherm. Res.* 231, 87–108. doi:10.1016/j.jvolgeores.2012.02.015

Charbonnier, S. J., Thouret, J.-C., Gueugneau, V., and Constantinescu, R. (2020). New insights into the 2070 cal yr BP pyroclastic currents at El Misti volcano (Peru) from field investigations, satellite imagery and probabilistic modeling. *Front. Earth Sci. (Lausanne).* 8, 557788. doi:10.3389/feart.2020.557788

Clarke, B., Tierz, P., Calder, E., and Yirgu, G. (2020). Probabilistic volcanic hazard assessment for pyroclastic density currents from pumice cone eruptions at Aluto Volcano, Ethiopia. *Front. Earth Sci. (Lausanne).* 8, 348. doi:10.3389/feart.2020.00348

De Silva, S. L., and Francis, P. (1991). *Volcanoes of the Central Andes*. New York: Springer-Verlag.

Decker, R. W. (1986). Forecasting volcanic eruptions. *Annu. Rev. Earth Planet. Sci.* 14, 267–291. doi:10.1146/annurev.ea.14.050186.001411

Delunel, R., Blard, P.-H., Martin, L. C. P., Nomade, S., and Schlunegger, F. (2016). Long term low latitude and high elevation cosmogenic ^{3}He production rate inferred from a 107 ka-old lava flow in northern Chile: 22°S–3400 m a.s.l. *Geochimica Cosmochimica Acta* 184, 71–87. doi:10.1016/j.gca.2016.04.023

Doyle, E. E. H., McClure, J., Johnston, D. M., and Paton, D. (2014). Communicating likelihoods and probabilities in forecasts of volcanic eruptions. *J. Volcanol. Geotherm. Res.* 272, 1–15. doi:10.1016/j.jvolgeores.2013.12.006

Espín Bedón, P. A., Mothes, P. A., Hall, M. L., Valverde Arcos, V., and Keen, H. (2019). The "Mera" lahar deposit in the upper Amazon basin: Transformation of a late Pleistocene collapse at Huisla volcano, central Ecuador. *J. Volcanol. Geotherm. Res.* 385, 103–119. doi:10.1016/j.jvolgeores.2018.10.008

Esposti Ongaro, T., Komorowski, J.-C., Legendre, Y., and Neri, A. (2020). Modelling pyroclastic density currents from a subplinian eruption at La Soufrière de Guadeloupe (West Indies, France). *Bull. Volcanol.* 82 (12), 76. doi:10.1007/s00445-020-01411-6

Farr, T. G., Rosen, P. A., Caro, E., Crippen, R., Duren, R., Hensley, S., et al. (2007). The shuttle radar topography mission. *Rev. Geophys.* 45 (2), RG2004. doi:10.1029/2005rg000183

Felpeto, A., Araña, V., Ortiz, R., Astiz, M., and García, A. (2001). Assessment and modelling of lava flow hazard on Lanzarote (Canary Islands). *Nat. hazards* 23 (2), 247–257. doi:10.1023/a:1011112330766

Felpeto, A., Martí, J., and Ortiz, R. (2007). Automatic GIS-based system for volcanic hazard assessment. *J. Volcanol. Geotherm. Res.* 166 (2), 106–116. doi:10.1016/j.jvolgeores.2007.07.008

Flynn, I. T. W., and Ramsey, M. S. (2020). Pyroclastic density current hazard assessment and modeling uncertainties for Fuego volcano, Guatemala. *Remote Sens.* 12 (17), 2790. doi:10.3390/rs12172790

Folch, A. (2012). A review of tephra transport and dispersal models: Evolution, current status, and future perspectives. *J. Volcanol. Geotherm. Res.* 235–236, 96–115. doi:10.1016/j.jvolgeores.2012.05.020

Francis, P. W., Roobol, M. J., Walker, G. P. L., Cobbold, P. R., and Coward, M. (1974). The San Pedro and San Pablo volcanoes of northern Chile and their hot avalanche deposits. *Geol. Rundsch.* 63 (1), 357–388. doi:10.1007/BF01820994

Francis, P. W., and Wells, G. L. (1988). Landsat thematic mapper observations of debris avalanche deposits in the Central Andes. *Bull. Volcanol.* 50 (4), 258–278. doi:10.1007/BF01047488

Gardeweg, M., and Amigo, Á. (2015). *Peligros del volcán Láscar, Región de Antofagasta. Carta Geológica de Chile, Serie Geología Ambiental, 22.* Santiago: Servicio Nacional de Geología y Minería SERNAGEOMIN.

Garreaud, R. D. (2009). The Andes climate and weather. *Adv. Geosci.* 22, 3–11. doi:10.5194/adgeo-22-3-2009

Gjerløw, E., Höskuldsson, Á., Bartolini, S., Biass, S., Mossoux, S., Gilbert, J., et al. (2022). The volcanic hazards of Jan Mayen Island (North-Atlantic). *Front. Earth Sci. (Lausanne).* 10, 730734. doi:10.3389/feart.2022.730734

Godoy, B., Wörner, G., Kojima, S., Aguilera, F., Simon, K., Hartmann, G., et al. (2014). Low-pressure evolution of arc magmas in thickened crust: The San Pedro–Linzor volcanic chain, Central Andes, Northern Chile. *J. S. Am. Earth Sci.* 52, 24–42. doi:10.1016/j.jsames.2014.02.004

Godoy, B., Wörner, G., Le Roux, P., de Silva, S., Parada, M. Á., Kojima, S., et al. (2017). Sr- and Nd-isotope variations along the Pleistocene San Pedro–Linzor volcanic chain, N. Chile: Tracking the influence of the upper crustal Altiplano-Puna Magma Body. *J. Volcanol. Geotherm. Res.* 341, 172–186. doi:10.1016/j.jvolgeores.2017.05.030

González-Ferrán, Ó. (1995). *Volcanes de Chile*. 1st ed. Santiago: Instituto Geográfico Militar.

González-Maurel, O., Deegan, F. M., le Roux, P., Harris, C., Troll, V. R., Godoy, B., et al. (2020). Constraining the sub-arc, parental magma composition for the giant Altiplano-Puna Volcanic Complex, northern Chile. *Sci. Rep.* 10 (1), 6864. doi:10.1038/s41598-020-63454-1

González-Maurel, O., Godoy, B., le Roux, P., Rodríguez, I., Marín, C., Menzies, A., et al. (2019a). Magmatic differentiation at La Poruña scoria cone, Central Andes, northern Chile: Evidence for assimilation during turbulent ascent processes, and genetic links with mafic eruptions at adjacent San Pedro volcano. *Lithos* 338–339, 128–140. doi:10.1016/j.lithos.2019.03.033

González-Maurel, O., le Roux, P., Godoy, B., Troll, V. R., Deegan, F. M., Menzies, A., et al. (2019b). The great escape: Petrogenesis of low-silica volcanism of Pliocene to Quaternary age associated with the Altiplano-Puna Volcanic Complex of northern Chile (21°10′-22°50′S). *Lithos* 346–347, 105162. doi:10.1016/j.lithos.2019.105162

Grosse, P., Euillades, P. A., Euillades, L. D., and van Wyk de Vries, B. (2014). A global database of composite volcano morphometry. *Bull. Volcanol.* 76 (1), 784. doi:10.1007/s00445-013-0784-4

Gueugneau, V., Kelfoun, K., Charbonnier, S., Germa, A., and Carazzo, G. (2020). Dynamics and impacts of the May 8th, 1902 pyroclastic current at Mount Pelée (Martinique): New insights from numerical modeling. *Front. Earth Sci. (Lausanne).* 8, 279. doi:10.3389/feart.2020.00279

Gueugneau, V., Kelfoun, K., and Druitt, T. (2019). Investigation of surge-derived pyroclastic flow formation by numerical modelling of the 25 June 1997 dome collapse at Soufrière Hills Volcano, Montserrat. *Bull. Volcanol.* 81 (4), 25. doi:10.1007/s00445-019-1284-y

Guimarães, L. F., Nieto-Torres, A., Bonadonna, C., and Frischknecht, C. (2021). A new inclusive volcanic risk ranking, Part 2: Application to Latin America. *Front. Earth Sci. (Lausanne).* 9, 757742. doi:10.3389/feart.2021.757742

GVP (2013b). "Lascar (355100) [data set]," in *Volcanoes of the world, v. 4.10.4 (09 December 2021).* Editor E. Venzke (Washington: Smithsonian Institution, Global Volcanism Program). Available at: https://volcano.si.edu/gvp_votw.cfm?vn=355100.

GVP (2013a). "San Pedro–San Pablo (355070) [data set]," in *Volcanoes of the world, v. 4.10.4 (09 December 2021)*. Editor E. Venzke (Washington: Smithsonian Institution, Global Volcanism Program). Available at: https://volcano.si.edu/volcano.cfm?vn=355070.

GVP (2013c). *Volcanoes of the world* version 4.10.4 *(09 December 2021).* Editor E. Venzke (Washington: Smithsonian Institution, Global Volcanism Program).

Harris, A. J., and Rowland, S. (2001). FLOWGO: A kinematic thermo-rheological model for lava flowing in a channel. *Bull. Volcanol.* 63 (1), 20–44. doi:10.1007/s004450000120

Hayes, J. L., Wilson, T. M., Deligne, N. I., Lindsay, J. M., Leonard, G. S., Tsang, S. W. R., et al. (2020). Developing a suite of multi-hazard volcanic eruption scenarios using an interdisciplinary approach. *J. Volcanol. Geotherm. Res.* 392, 106763. doi:10.1016/j.jvolgeores.2019.106763

INE (2017). *Censo 2017, Chile*. Santiago: Instituto Nacional de Estadísticas INE.

Jay, J. A., Welch, M., Pritchard, M. E., Mares, P. J., Mnich, M. E., Melkonian, A. K., et al. (2013). Volcanic hotspots of the central and southern Andes as seen from space by ASTER and MODVOLC between the years 2000 and 2010. *Geol. Soc. Lond. Spec. Publ.* 380 (1), 161–185. doi:10.1144/SP380.1

Jiménez, D., Becerril, L., Bartolini, S., Escobar, D., and Martí, J. (2020). Making a qualitative volcanic-hazards map by combining simulated scenarios: An example for San Miguel Volcano (El Salvador). *J. Volcanol. Geotherm. Res.* 395, 106837. doi:10.1016/j.jvolgeores.2020.106837

Jorquera, C., Rodriguez, I., Bertin, L. J., and Flores, F. (2019). *Peligros del volcán Guallatiri, Región de Arica y Parinacota. Carta Geológica de Chile, Serie Geología Ambiental, 35.* Santiago: Servicio Nacional de Geología y Minería SERNAGEOMIN.

Kelfoun, K. (2017). A two-layer depth-averaged model for both the dilute and the concentrated parts of pyroclastic currents: A model for pyroclastic currents. *J. Geophys. Res. Solid Earth* 122 (6), 4293–4311. doi:10.1002/2017JB014013

Kelfoun, K., Gueugneau, V., Komorowski, J.-C., Aisyah, N., Cholik, N., Merciecca, C., et al. (2017). Simulation of block-and-ash flows and ash-cloud surges of the 2010 eruption of Merapi volcano with a two-layer model. *J. Geophys. Res. Solid Earth* 122 (6), 4277–4292. doi:10.1002/2017JB013981

Kelfoun, K., Samaniego, P., Palacios, P., and Barba, D. (2009). Testing the suitability of frictional behaviour for pyroclastic flow simulation by comparison with a well-constrained eruption at Tungurahua volcano (Ecuador). *Bull. Volcanol.* 71 (9), 1057–1075. doi:10.1007/s00445-009-0286-6

Lara, L., Orozco, G., Amigo, Á., and Silva, C. (2011). *Peligros volcánicos de Chile. Carta Geológica de Chile, Serie Geología Ambiental, 13*. Santiago: Servicio Nacional de Geología y Minería SERNAGEOMIN.

Lindsay, J. M., and Robertson, R. E. A. (2018). Integrating volcanic hazard data in a systematic approach to develop volcanic hazard maps in the Lesser Antilles. *Front. Earth Sci. (Lausanne).* 6, 42. doi:10.3389/feart.2018.00042

Loughlin, S. C., Sparks, S., Brown, S. K., Jenkins, S. F., and Vye-Brown, C. (Editors) (2015). *Global volcanic hazards and risk*. (Cambridge: Cambridge University Press). doi:10.1017/CBO9781316276273

Lube, G., Breard, E. C. P., Esposti-Ongaro, T., Dufek, J., and Brand, B. (2020). Multiphase flow behaviour and hazard prediction of pyroclastic density currents. *Nat. Rev. Earth Environ.* 1 (7), 348–365. doi:10.1038/s43017-020-0064-8

Maeno, F., Nakada, S., Nagai, M., and Kozono, T. (2013). Ballistic ejecta and eruption condition of the vulcanian explosion of Shinmoedake volcano, Kyushu, Japan on 1 February, 2011. *Earth Planets Space* 65 (6), 609–621. doi:10.5047/eps.2013.03.004

Malin, M. C., and Sheridan, M. F. (1982). Computer-assisted mapping of pyroclastic surges. *Science* 217 (4560), 637–640. doi:10.1126/science.217.4560.637

Mamani, M., Tassara, A., and Wörner, G. (2008). Composition and structural control of crustal domains in the Central Andes. *Geochem. Geophys. Geosyst.* 9, Q03006. doi:10.1029/2007gc001925

Marrero, J. M., García, A., Berrocoso, M., Llinares, Á., Rodríguez-Losada, A., Ortiz, R., et al. (2019). Strategies for the development of volcanic hazard maps in monogenetic volcanic fields: The example of La Palma (Canary Islands). *J. Appl. Volcanol.* 8 (1), 6. doi:10.1186/s13617-019-0085-5

Martí, J. (2017). *Assessing volcanic hazard*, 1. Oxford University Press. doi:10.1093/oxfordhb/9780190699420.013.32

Marzocchi, W., and Bebbington, M. S. (2012). Probabilistic eruption forecasting at short and long-time scales. *Bull. Volcanol.* 74 (8), 1777–1805. doi:10.1007/s00445-012-0633-x

Marzocchi, W., Sandri, L., Gasparini, P., Newhall, C., and Boschi, E. (2004). Quantifying probabilities of volcanic events: The example of volcanic hazard at Mount Vesuvius: Quantifying volcanic hazard. *J. Geophys. Res.* 109, B11201. doi:10.1029/2004JB003155

Marzocchi, W., Selva, J., and Jordan, T. H. (2021). A unified probabilistic framework for volcanic hazard and eruption forecasting. *Nat. Hazards Earth Syst. Sci.* 21 (11), 3509–3517. doi:10.5194/nhess-21-3509-2021

Mastin, L. G. (2001). *A simple calculator of ballistic trajectories for blocks ejected during volcanic eruptions*. Open-File Report 2001–0045. Reston, VA: U.S. Geological Survey. doi:10.3133/ofr0145

Mastin, L. G., Guffanti, M., Servranckx, R., Webley, P., Barsotti, S., Dean, K., et al. (2009). A multidisciplinary effort to assign realistic source parameters to models of volcanic ash-cloud transport and dispersion during eruptions. *J. Volcanol. Geotherm. Res.* 186 (1–2), 10–21. doi:10.1016/j.jvolgeores.2009.01.008

Mastrandrea, M. D., Field, C. B., Stocker, T. F., Edenhofer, O., Ebi, K. L., Frame, D. J., and Zwiers, F. W. (2010). Guidance note for lead authors of the IPCC fifth assessment report on consistent treatment of uncertainties. Available at: https://www.ipcc.ch/site/assets/uploads/2018/05/uncertainty-guidance-note.pdf.

Mead, S., Procter, J., Bebbington, M., and Rodriguez-Gomez, C. (2022). Probabilistic volcanic hazard assessment for national park infrastructure proximal to Taranaki Volcano (New Zealand). *Front. Earth Sci. (Lausanne).* 10, 832531. doi:10.3389/feart.2022.832531

Michaud-Dubuy, A., Carazzo, G., and Kaminski, E. (2021). Volcanic hazard assessment for tephra fallout in Martinique. *J. Appl. Volcanol.* 10 (1), 8. doi:10.1186/s13617-021-00106-7

MINVU and IDE (2017). *Áreas urbanas consolidadas* [Data set]. Ministerio de Vivienda y Urbanismo (MINVU) and Infraestructura de Datos Geoespaciales (IDE). Gobierno de Chile. Available at: https://www.ide.cl/descargas/capas/minvu/Area_Urbana_Consolidada.

Mossoux, S., Saey, M., Bartolini, S., Poppe, S., Canters, F., Kervyn, M., et al. (2016). Q-LavHA: A flexible GIS plugin to simulate lava flows. *Comput. Geosciences* 97, 98–109. doi:10.1016/j.cageo.2016.09.003

Newhall, C. G., and Hoblitt, R. (2002). Constructing event trees for volcanic crises. *Bull. Volcanol.* 64 (1), 3–20. doi:10.1007/s004450100173

Newhall, C. G., and Self, S. (1982). The Volcanic Explosivity Index (VEI) an estimate of explosive magnitude for historical volcanism. *J. Geophys. Res.*, 87 (C2), 1231–1238. doi:10.1029/JC087iC02p01231

Nieto-Torres, A., Guimarães, L. F., Bonadonna, C., and Frischknecht, C. (2021). A new inclusive volcanic risk ranking, Part 1: Methodology. *Front. Earth Sci. (Lausanne).* 9, 697451. doi:10.3389/feart.2021.697451

O'Callaghan, L. J., and Francis, P. W. (1986). Volcanological and petrological evolution of San Pedro volcano, provincia EI Loa, north Chile. *J. Geol. Soc.* 143 (2), 275–286. doi:10.1144/gsjgs.143.2.0275

Ogburn, S. E., and Calder, E. S. (2017). The relative effectiveness of empirical and physical models for simulating the dense undercurrent of pyroclastic flows under different emplacement conditions. *Front. Earth Sci. (Lausanne).* 5, 83. doi:10.3389/feart.2017.00083

ONEMI (2019). *Plan específico de emergencia por variable de riesgo: Erupciones volcánicas, Región de Antofagasta*. Santiago: Oficina Nacional de Emergencia del Ministerio del Interior y Seguridad Pública (ONEMI). Gobierno de Chile.

OVDAS (2022). Reporte de actividad volcánica, enero 2022, Región de Antofagasta *(No. 1). Observatorio Volcanológico de los Andes del Sur OVDAS.* Santiago: Servicio Nacional de Geología y Minería SERNAGEOMIN.

Patra, A. K., Bauer, A. C., Nichita, C. C., Pitman, E. B., Sheridan, M. F., Bursik, M., et al. (2005). Parallel adaptive numerical simulation of dry avalanches over natural terrain. *J. Volcanol. Geotherm. Res.* 139 (1–2), 1–21. doi:10.1016/j.jvolgeores.2004.06.014

Payne, D. (1998). Climatic implications of rock glaciers in the arid western cordillera of the Central Andes. *Glacial Geol. Geomorphol.* rp03/1998.

Petit-Breuilh, M. (2004). *La historia eruptiva de los volcanes hispanoamericanos (siglos XVI al XX): El modelo Chileno*. Lanzarote: Servicio de Publicaciones, Cabildo Insular de Lanzarote.

Pierson, T. C., Janda, R. J., Thouret, J.-C., and Borrero, C. A. (1990). Perturbation and melting of snow and ice by the 13 November 1985 eruption of Nevado del Ruiz, Colombia, and consequent mobilization, flow and deposition of lahars. *J. Volcanol. Geotherm. Res.* 41 (1–4), 17–66. doi:10.1016/0377-0273(90)90082-Q

Poland, M. P., and Anderson, K. R. (2020). Partly cloudy with a chance of lava flows: Forecasting volcanic eruptions in the Twenty-First Century. *J. Geophys. Res. Solid Earth* 125, e2018JB016974. doi:10.1029/2018JB016974

Pritchard, M. E., Henderson, S. T., Jay, J. A., Soler, V., Krzesni, D. A., Button, N. E., et al. (2014). Reconnaissance earthquake studies at nine volcanic areas of the Central Andes with coincident satellite thermal and InSAR observations. *J. Volcanol. Geotherm. Res.* 280, 90–103. doi:10.1016/j.jvolgeores.2014.05.004

Pritchard, M. E., and Simons, M. (2004). An InSAR-based survey of volcanic deformation in the Central Andes. *Geochem. Geophys. Geosyst.* 5, Q02002. doi:10.1029/2003GC000610

Pyle, D. (2015). "Sizes of volcanic eruptions," in *The encyclopedia of volcanoes*. Editor H. Sigurdsson. 2nd ed. (Elsevier), 257–264. doi:10.1016/B978-0-12-385938-9.00013-4

Reyes-Hardy, M.-P., Aguilera, F., Sepúlveda, J. P., Esquivel, A., and Inostroza, M. (2021). GIS-based volcanic hazards, vulnerability and risks assessment of the Guallatiri Volcano, Arica y Parinacota Region, Chile. *J. S. Am. Earth Sci.* 109, 103262. doi:10.1016/j.jsames.2021.103262

Rodriguez-Gonzalez, A., Aulinas, M., Mossoux, S., Perez-Torrado, F. J., Fernandez-Turiel, J. L., Cabrera, M., et al. (2021). Comparison of real and simulated lava flows in the Holocene volcanism of Gran Canaria (Canary Islands, Spain) with Q-LavHA: Contribution to volcanic hazard management. *Nat. Hazards (Dordr).* 107 (2), 1785–1819. doi:10.1007/s11069-021-04660-6

Sandri, L., Costa, A., Selva, J., Tonini, R., Macedonio, G., Folch, A., et al. (2016). Beyond eruptive scenarios: Assessing tephra fallout hazard from Neapolitan volcanoes. *Sci. Rep.* 6 (1), 24271. doi:10.1038/srep24271

Sandri, L., Thouret, J.-C., Constantinescu, R., Biass, S., and Tonini, R. (2014). Long-term multi-hazard assessment for El Misti volcano (Peru). *Bull. Volcanol.* 76 (2), 771. doi:10.1007/s00445-013-0771-9

Sandri, L., Tierz, P., Costa, A., and Marzocchi, W. (2018). Probabilistic hazard from pyroclastic density currents in the Neapolitan area (Southern Italy). *J. Geophys. Res. Solid Earth* 123 (5), 3474–3500. doi:10.1002/2017JB014890

Scaini, C., Folch, A., and Navarro, M. (2012). Tephra hazard assessment at Concepción volcano, Nicaragua. *J. Volcanol. Geotherm. Res.* 219–220, 41–51. doi:10.1016/j.jvolgeores.2012.01.007

Schilling, S. P. (2014). *Laharz_py: GIS tools for automated mapping of lahar inundation hazard zones*. Open-File report No. 2014–1073. Reston, VA: U.S. Geological Survey. doi:10.3133/ofr20141073

Scollo, S., Coltelli, M., Bonadonna, C., and Del Carlo, P. (2013). Tephra hazard assessment at Mt. Etna (Italy). *Nat. Hazards Earth Syst. Sci.* 13 (12), 3221–3233. doi:10.5194/nhess-13-3221-2013

Sellés, D., and Gardeweg, M. (2017). *Geología del área Ascotán–Cerro Inacaliri, Región de Antofagasta. Carta Geológica de Chile, Serie Geología Básica, 190*. Santiago: Servicio Nacional de Geología y Minería SERNAGEOMIN.

Selva, J., Costa, A., De Natale, G., Di Vito, M. A., Isaia, R., Macedonio, G., et al. (2018). Sensitivity test and ensemble hazard assessment for tephra fallout at Campi Flegrei, Italy. *J. Volcanol. Geotherm. Res.* 351, 1–28. doi:10.1016/j.jvolgeores.2017.11.024

SERNAGEOMIN (2020). Ranking de riesgo específico de volcanes activos de Chile 2019. *Red Nacional de Vigilancia Volcánica (RNVV)*. Santiago: Servicio Nacional de Geología y Minería SERNAGEOMIN.

Siebert, L., Simkin, T., and Kimberly, P. (2010). *Volcanoes of the world*. 3rd ed. Washington, DC: Smithsonian Institution.

Spiller, E. T., Wolpert, R. L., Ogburn, S. E., Calder, E. S., Berger, J. O., Patra, A. K., et al. (2020). Volcanic hazard assessment for an eruption hiatus, or post-eruption unrest context: Modeling continued dome collapse hazards for Soufrière Hills volcano. *Front. Earth Sci. (Lausanne).* 8, 535567. doi:10.3389/feart.2020.535567

Stern, C. R. (2004). Active Andean volcanism: Its geologic and tectonic setting. *Rev. Geol. Chile* 31 (2), 161–206. doi:10.4067/s0716-02082004000200001

Sulpizio, R. (2005). Three empirical methods for the calculation of distal volume of tephra-fall deposits. *J. Volcanol. Geotherm. Res.* 145 (3–4), 315–336. doi:10.1016/j.jvolgeores.2005.03.001

Tadini, A., Azzaoui, N., Roche, O., Samaniego, P., Bernard, B., Bevilacqua, A., et al. (2022). Tephra fallout probabilistic hazard maps for Cotopaxi and Guagua Pichincha volcanoes (Ecuador) with uncertainty quantification. *J. Geophys. Res. Solid Earth* 127, e2021JB022780. doi:10.1029/2021JB022780

Taddeucci, J., Alatorre-Ibargüengoitia, M. A, Cruz-Vázquez, O., Del Bello, E., Scarlato, P., and Ricci, T. (2017). In-flight dynamics of volcanic ballistic projectiles. *Rev. Geophys.* 55, 675–718. doi:10.1002/2017RG000564

Tennant, E., Jenkins, S. F., Winson, A., Widiwijayanti, C., Gunawan, H., Haerani, N., et al. (2021). Reconstructing eruptions at a data limited volcano: A case study at Gede (West Java). *J. Volcanol. Geotherm. Res.* 418, 107325. doi:10.1016/j.jvolgeores.2021.107325

Thompson, M. A., Lindsay, J. M., and Gaillard, J. (2015). The influence of probabilistic volcanic hazard map properties on hazard communication. *J. Appl. Volcanol.* 4 (1), 6. doi:10.1186/s13617-015-0023-0

Thompson, M. A., Lindsay, J. M., Leonard, G. S., Lutteroth, C., Bostrom, A., Corballis, P., et al. (2021). Volcanic hazard map visualisation affects cognition and crisis decision-making. *Int. J. Disaster Risk Reduct.* 55, 102102. doi:10.1016/j.ijdrr.2021.102102

Thouret, J.-C., Antoine, S., Magill, C., and Ollier, C. (2020). Lahars and debris flows: Characteristics and impacts. *Earth-Science Rev.* 201, 103003. doi:10.1016/j.earscirev.2019.103003

Tierz, P., Loughlin, S. C., and Calder, E. S. (2019). VOLCANS: an objective, structured and reproducible method for identifying sets of analogue volcanoes. *Bull. Volcanol.* 81, 76. doi:10.1007/s00445-019-1336-3

Tierz, P., Stefanescu, E. R., Sandri, L., Sulpizio, R., Valentine, G. A., Marzocchi, W., et al. (2018). Towards quantitative volcanic risk of pyroclastic density currents: Probabilistic hazard curves and maps around Somma-Vesuvius (Italy). *J. Geophys. Res. Solid Earth* 123, 6299. doi:10.1029/2017JB015383

Tierz, P., Woodhouse, M. J., Phillips, J. C., Sandri, L., Selva, J., Marzocchi, W., et al. (2017). A framework for probabilistic multi-hazard assessment of rain-triggered lahars using Bayesian belief networks. *Front. Earth Sci. (Lausanne).* 5, 73. doi:10.3389/feart.2017.00073

Tilling, R. I. (2009). Volcanism and associated hazards: The Andean perspective. *Adv. Geosci.* 22, 125–137. doi:10.5194/adgeo-22-125-2009

Titos, M., Martínez Montesinos, B., Barsotti, S., Sandri, L., Folch, A., Mingari, L., et al. (2022). Long-term hazard assessment of explosive eruptions at Jan Mayen (Norway) and implications for air traffic in the North Atlantic. *Nat. Hazards Earth Syst. Sci.* 22 (1), 139–163. doi:10.5194/nhess-22-139-2022

Vázquez, R., Bonasia, R., Folch, A., Arce, J. L., and Macías, J. L. (2019). Tephra fallout hazard assessment at Tacaná volcano (Mexico). *J. S. Am. Earth Sci.* 91, 253–259. doi:10.1016/j.jsames.2019.02.013

Warwick, R., Williams-Jones, G., Kelman, M., and Witter, J. (2022). A scenario-based volcanic hazard assessment for the Mount Meager volcanic complex, British Columbia. *J. Appl. Volcanol.* 11 (1), 5. doi:10.1186/s13617-022-00114-1

Woodhouse, M. J., Johnson, C. G., Hogg, A. J., Phillips, J. C., Espín Bedón, P. A., Almeida, S., et al. (2016). LaharFlow: A web-based lahar hazard model. Cities on Volcanoes 9, Puerto Varas, Chile. doi:10.13140/RG.2.2.35597.95201

frontiers | Frontiers in Earth Science

TYPE Original Research
PUBLISHED 22 August 2022
DOI 10.3389/feart.2022.890998

OPEN ACCESS

EDITED BY
Pablo Grosse,
Consejo Nacional de Investigaciones Científicas y Técnicas (CONICET), Argentina

REVIEWED BY
Kevin Michael Ward,
South Dakota School of Mines and Technology, United States
Stephanie Prejean,
United States Geological Survey (USGS), United States

*CORRESPONDENCE
Heather McFarlin,
hlmcfarlin@alaska.edu

SPECIALTY SECTION
This article was submitted to Volcanology, a section of the journal Frontiers in Earth Science

RECEIVED 07 March 2022
ACCEPTED 20 July 2022
PUBLISHED 22 August 2022

CITATION
McFarlin H, Thompson G, McNutt SR, Braunmiller J and West ME (2022), Classification of seismic activity at the Lazufre Volcanic System, based on 2011 to 2012 data.
Front. Earth Sci. 10:890998.
doi: 10.3389/feart.2022.890998

Classification of seismic activity at the Lazufre Volcanic System, based on 2011 to 2012 data

Heather McFarlin[1,2]*, Glenn Thompson[1], Stephen R. McNutt[1], Jochen Braunmiller[1] and Michael E. West[2]

[1]School of Geosciences, University of South Florida, Tampa, FL, United States, [2]Geophysical Institute, University of Alaska Fairbanks, Fairbanks, AK, United States

The Lazufre Volcanic System (LVS), on the border of northern Chile and Argentina, is an active complex of two volcanoes, Lastarria to the north and Cordón del Azufre to the south. The LVS is not regularly monitored with any scientific equipment despite being recognized as a top ten volcanic hazard in Argentina by the Observatorio Argentino de Vigilancia Volcánica of the Servicio Geológico y Minero Argentino. The system has shown unusual inflation signatures observed in InSAR but the level of seismic activity and its spatial and temporal distribution were unknown due to the lack of a permanent local seismic network. The PLUTONS Project deployed eight broadband seismic stations throughout the LVS between November 2011 and March 2013. This study shows event locations and types from November 2011 through March 2012. We analyze 591 seismic events within 20 km of Lastarria. Most events cluster tightly beneath Lastarria and almost no activity is observed beneath Cordón del Azufre or the primary inflation center. All events are reviewed manually, and located using a velocity model that assimilates prior studies and accounts for hypocenters within the edifice up to 5 km above sea level. More than 90% of the resulting hypocenters are shallower than 10 km below sea level. The waveforms have characteristics similar to those observed at many other volcanoes, suggesting five classes of events: volcano-tectonic (VT), long-period 1 (LP1), long period 2 (LP2), hybrid (HY), and unknown (X). Frequency-magnitude analysis reveals distinct b-values ranging from 1.2 for VT events to 2.5 for LP1 events. Based on the spatial distribution of events and the b-values, we infer that seismic activity is driven mainly by movement of fluids and gases associated with the regional magma zones and inflation centers. The seismic activity is energetic at times, and quieter at others, suggesting the presence of episodic magmatic and/or hydrothermal activity, focused at Lastarria. Our findings indicate that the previously observed inflation signals are indeed volcanic in origin. These results also demonstrate the potential for success of a future seismic monitoring system and provide a framework for interpreting the subsequent observations, both of which are critical to assessing the volcanic risk of the northern Chile-Argentina region.

KEYWORDS

Lastarria, Lazufre, volcano seismology, Central Andes, PLUTONS project

Introduction

One requirement for a volcanic risk assessment is data showing the baseline level of seismic activity at a volcano. Understanding where, and what types of earthquakes are occurring at a volcano is essential. The Lazufre Volcanic System (LVS, centered at ~25.252°S, 68.514°W; Figure 1), on the border of northern Chile and Argentina, was recently classified as a top ten volcanic hazard in Argentina (Garcia and Badi, 2021), even though the types, locations, and frequency of volcanic earthquakes were unknown.

InSAR studies have shown large deformation signatures at numerous volcanoes in the Central Andes (Pritchard and Simons, 2002). One of the most prominent of these signatures is between two volcanoes, Lastarria to the north and Cordón del Azufre to the south, on the northern border between Chile and Argentina (Figure 1). Pritchard and Simons (2002) refer to the study region as "Lazufre", a blend of the names of the two volcanoes surrounding the deformation. We refer to it as the Lazufre Volcanic System. The LVS is in the Central Volcanic Zone of the Andes, approximately 300 km east of the subduction trench, on the northern edge of the Southern Puna Magma Body (SPMB) and lies in the modern volcanic arc (Bianchi et al., 2013).

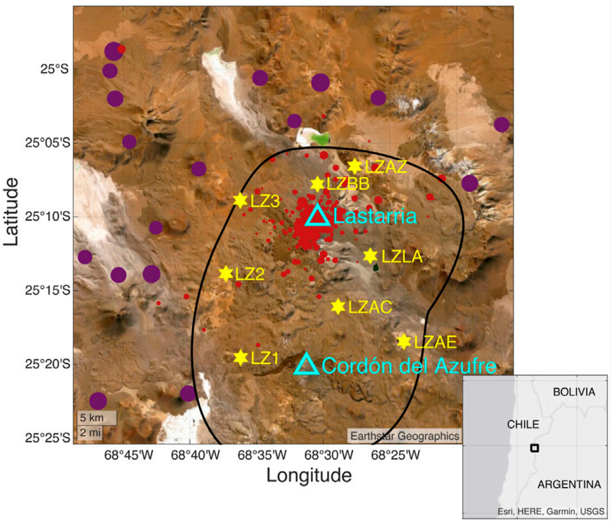

FIGURE 1
Map showing locations of Lastarria and Cordón del Azufre volcanoes (cyan triangles; Smithsonian Global Volcanism Program), seismic stations (yellow stars), regional seismicity (purple circles) and seismic events analyzed and located in this study (red circles). Circle radius is proportional to magnitude, with regional events from M_b3.5 to M_b6.1 from the International Seismology Center from 1960–2020 (ISC, 2022). Black line shows approximate extent of deformation due to LMB, as estimated from Spica et al. (2015). The base map is a satellite image from Earthstar Geographics. Inset map shows location of the main map as a black square on the border between Northern Chile and Argentina (north is up).

The SPMB is a region of partial melt that includes smaller melt bodies such as the Lazufre Magma Body (LMB), the Cerro Galán Magma Body, and the Incahuasi Magma Body (Ward et al., 2013; Ward et al., 2017; Delph et al., 2017; Pritchard et al., 2018). The LMB has been inflating at ~2.5 cm/yr since at least 1998, over an NNE-oriented ellipsoidal region that is ~45 x 37 km^2 (Pritchard and Simons, 2002) and centered at ~25.259°S, ~68.483°W (Henderson et al., 2017). The current hypothesis is that this inflation is due to a magma reservoir at 5–10 km below sea level (bsl) as evidenced by receiver functions (McFarlin et al., 2014), low V_s at ~5 km bsl (Ward et al., 2013) and geobarometry (Stechern et al., 2017); the latter also indicates multiple storage zones at > 20 km depth, likely connected by a system of dikes and sills with the shallower reservoir. While the LMB inflation has been continuous, it does appear to vary by ±1.5 cm in approximately 5–7-year cycles (e.g., Ruch et al., 2009; Henderson and Pritchard, 2013; Pearse and Lundgren, 2013; Remy et al., 2014; Henderson et al., 2017; Pritchard et al., 2018). The current study covers a period of decreased inflation rate of ~1.5 cm/yr, down from the previous years of ~3 cm/yr.

Due to the remoteness of these volcanoes, no permanent geophysical monitoring stations exist. The closest permanent seismic station is GO02, part of the Chilean National Seismic Network, about 110 km west of the LVS. The International Seismological Center (ISC) Bulletin only contains a few regional, mainly intermediate-depth earthquakes in this area above magnitude 3.0, but no small magnitude, shallow events local to the LVS. Recently, because of the large amount of inflation found at this volcanic system, and other research showing the potential for volcanic activity, such as a suggested shallow magma intrusion based on magnetotelluric data (Díaz et al., 2015), the Observatorio Argentino de Vigilancia Volcánica (OAVV) of the Servicio Geológico y Minero Argentino (SEGEMAR) classified Lastarria as a top ten potential hazard in the northern region of Argentina (Garcia and Badi, 2021). Because a detailed study of the seismicity of these volcanoes has never been conducted, the activity levels and states of the volcanoes are essentially unknown.

Despite evidence of inflation, and associated speculation about gas and magma movement in the LVS, there has been no on-site observation of seismic activity to corroborate ongoing volcanic activity and elevated risk at the LVS. Without local seismic records, it is impossible to identify local earthquakes and their spatial and temporal patterns. If Lastarria or Cordón del Azufre are seismically active, then this activity can be used to infer: 1) where, and at what depths, crustal magmatic activity might be most vigorous; 2) whether seismic activity is driven primarily by fluids and gases, or by stresses and tectonics in the surrounding crust; 3) and whether the movement of magma and gas is episodic or more steady state. These questions are societally important because they lay the foundation for any future monitoring efforts and can inform volcanic hazard analyses for the larger region. Here, we present a characterization of the seismic activity for the LVS based on a 5-month deployment of local seismic stations (Figure 1).

Geologic setting

Lastarria (25.168°S, 68.507°W) and Cordón del Azufre (25.336°S, 68.521°W) are each within 10 km of the inflation center associated with the LMB (Figure 1). Lastarria is more active than Cordón del Azufre and is a polygenetic volcanic complex with a summit at 5,706 m above sea level (asl) (De Silva and Francis, 1991; Tamburello et al., 2014). The volcano consists of four semi-nested craters that trend NNW (approximately perpendicular to the orientation of the NNE-trending LMB inflation signal), with the youngest being the farthest north (De Silva and Francis, 1991). Lastarria is an andesitic-dacitic volcano that has not erupted in 2,500 years (Naranjo, 2010; Lopez et al., 2018), but has four extensive, active fumarole fields with evidence of liquid sulfur flows (Naranjo, 1985; Naranjo, 1988; De Silva and Francis, 1991) and vigorous degassing (Lopez et al., 2018).

Two small and shallow sources of inflation have recently been discovered directly beneath Lastarria, with the sources approximately 4 km asl and 1 km bsl. Both correspond to low velocity zones (decreases in P and S velocities in Figure 2, denoted as ULVZ A and ULVZ B in Figure 3; Spica et al., 2015). The shallower of the two (ULVZ A, ~4 km asl, Figure 3) is thought to be related to the hydrothermal system, with a low Vs. of 1.25 km/s (Figure 2; Spica et al., 2015) and very low resistivity of ~1–10 Ωm (Díaz et al., 2015). The heat flow in this area is high (>700 mW/m^2; Pritchard et al., 2018), and is evident at the surface by fumarole temperatures and liquid sulfur flows (80–408°C; Aguilera et al., 2012; Zimmer et al., 2017; Pritchard et al., 2018). The deeper inflation source from 2 km asl to 1 km bsl (ULVZ B, Figure 3) is thought to be a shallow magma chamber based on low Vs. (1.25 km/s; Spica et al., 2015), low resistivity (~5–10 Ωm, Díaz et al., 2015) and high HCl and HF concentrations, which are indicative of shallow magma degassing (Tamburello et al., 2014; Lopez et al., 2018; Pritchard et al., 2018). This deeper inflation has been modeled as a spherical over-pressurized source that has been inflating at ~9 mm per year since ~2003 over a 6 km^2 area (e.g., Pritchard and Simons, 2002; Froger et al., 2007; Ruch et al., 2009; Pritchard et al., 2018).

Between 2009 and 2012, a change in gas chemistry of the fumaroles from a hydrothermal to a more magmatic signature occurred (Aguilera et al., 2012; Lopez et al., 2018). This might indicate that heat from ascending magma ‘dries out’ the hydrothermal system, or that ascending magma stalls out and degasses due to isobaric crystallization (Aguilera et al., 2012). Current thoughts are that the Lastarria fumarole fields may serve as a pressure valve for the inflating LMB (Froger et al., 2007; Spica et al., 2015; Pritchard et al., 2018).

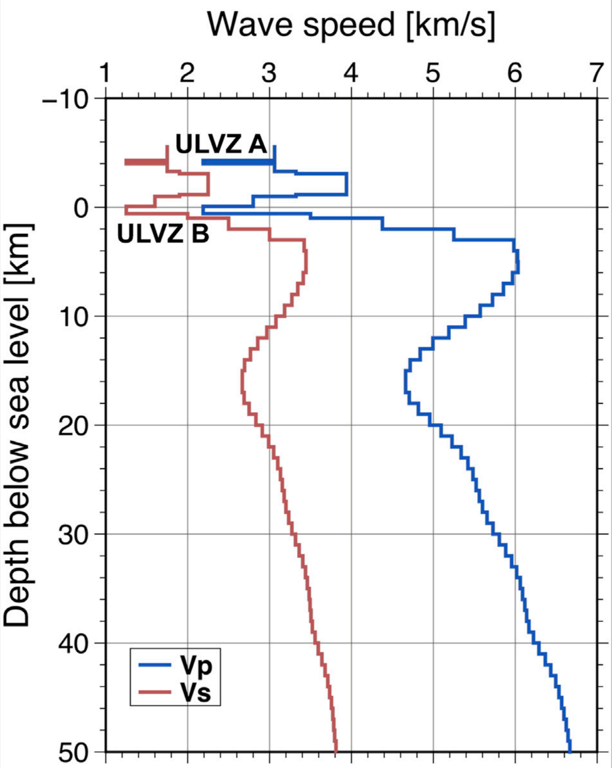

FIGURE 2
Velocity model used in this study, as combined and modified from Ward et al. (2017) and Spica et al. (2015). Red line is the S-wave velocity. Blue line is the P-wave velocity. Depths start at 5.706 km above sea level (at the surface and shown as negative depths). The model includes the two shallow ULVZs (labelled ULVZ A and ULVZ B) from Spica et al. (2015) and a deeper, broad low velocity zone from ~5−33 km bsl based on Ward et al. (2017). Supplementary Table S1 lists Vp, Vs., and Vp/Vs. with depth; Supplementary Table S2 lists alternate model with low velocity zones eliminated.

Cordón del Azufre is also an andesitic-dacitic volcano, with a summit elevation of 5,481 m asl. It is less active than Lastarria, with its most recent eruptions between 0.6 and 0.3 Ma (Naranjo et al., 2018). Activity consisted of pyroclastic and lava flows, and domes, mostly towards the NE side of the volcano (De Silva and Francis, 1991). Each lava flow is less than 1 km in length, but the cluster is large (~45 km^2; De Silva and Francis, 1991) and of a dacitic composition. The older craters of Cordón del Azufre trend N-S, with a total of 4 craters in a 5 km-long chain (De Silva and Francis, 1991).

Data and methods

The PLUTONS project (Pritchard et al., 2018) deployed eight seismic stations in the Lazufre region between November 2011 and March 2013 (Figure 1). Five of these stations, LZAZ, LZBB, LZ3,

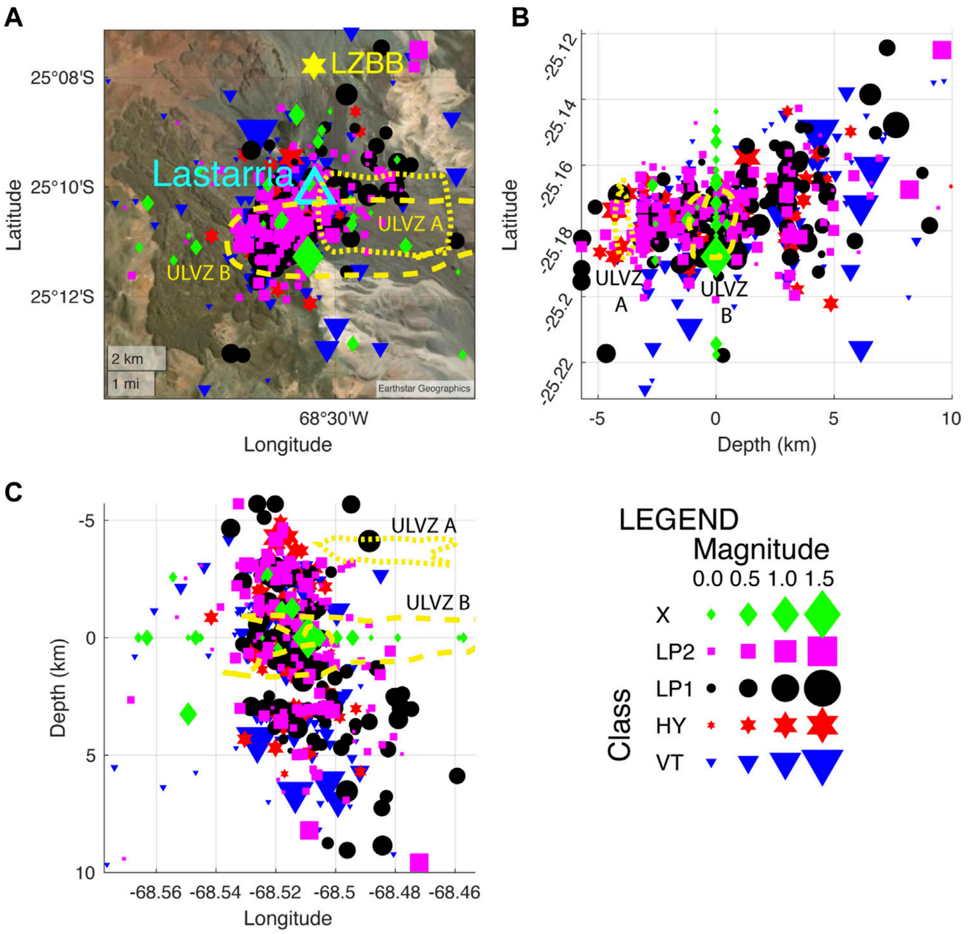

FIGURE 3
Hypocenters of events located in this study, within ~5 km of Lastarria, from 11 November 2011 to 31 March 2012. Symbols indicate event types, and are sized by magnitude, as shown in the legend on the lower right. Ultra-low velocity zones A (ULVZ A) and B (ULVZ B), estimated from Spica et al. (2015) are shown as dotted and dashed yellow lines, respectively. (A) Map view. Lastarria volcano shown as cyan triangle. Cordón del Azufre is off the map, as are the seismic stations except for LZBB. The map is approximately 11 x 11 km and north is up. In (B) Latitude vs. Depth, and (C) Depth vs. Longitude plots. Negative depths are above sea level.

LZ2, LZ1 (all towards the west) consisted of Güralp 3T-120 sec 3-component broadband seismometers with RT-130 digitizers. The remaining three stations, LZLA, LZAC, LZAE (all towards the east) were Güralp 6TD 3-component broadbands with integrated digitizers. A ninth station (LZ6) was installed but was not operational for the entirety of the deployment. In this study, we examine data between November 2011 and March 2012; the remaining data have yet to be analyzed.

We built an initial LVS seismic event catalog using the BRTT Antelope suite (Vernon et al., 2021). We began our analysis by visually inspecting a subset of the waveform data and developing a classification scheme specific for the events observed. We then tuned the Antelope program *dbdetect* STA/LTA (short-term average/long-term average) parameters (Butterworth filter 1.0–20 Hz, STA = 0.5 s, LTA = 60 s, detection "on" threshold = 4.0, detection "off" threshold = 2.0), to capture these events. Auto-locations were computed with the *GENLOC* library (Pavlis et al., 2004), which is packaged with Antelope. We used the velocity model *utu03* (Hutchinson, 2015) for initial locations.

The velocity model used for manual review is a combination of the models from Ward et al. (2017) and Spica et al. (2015) (Figure 2), modified to account for the ~5 km of crust asl. We used the Spica et al. (2015) model for the depths above 3 km bsl and the Ward et al. (2017) model for depths below 3 km bsl. The two studies had different scales and focused on different depths. Combining them thus provides a detailed velocity model for the shallowest depths, and a more generalized model at larger depths (Supplementary Table S1). Both models are V_s models, and we used a constant V_p/V_s ratio of 1.75 to obtain V_p Sea level is chosen as the 0 km reference depth for the combined velocity model, and the surface in this region is at ~5 km asl, so shallow events have negative depths between -5.6 and 0 km asl. The resulting velocity model includes the two low velocity zones under Lastarria (ULVZ A and ULVZ B) and the deeper low velocities of the LMB (Figures 2, 3).

Manual review of the tuned catalog consisted of visual analysis of each auto-detected event with the Antelope program *dbloc2*, adjusting P and S picks, adding any additional P and S picks, re-locating the event (with *GENLOC*), and re-calculating M_L. We used the zoom function in the *dbpick* window to find where an emergent earthquake signal started and adjusted the P phase pick uncertainty accordingly. We also made use of the Antelope command *dbspgram* to aid in identification of phase arrivals and frequency content of the waveforms. If an S phase was difficult to identify for a given event, then we did not add an S pick to that station for that event. In general, S phase pick uncertainties are larger than those for P phase picks, and the pick phase uncertainty for emergent, low frequency events is higher than for impulsive, high frequency events. The eastern stations (LZLA, LZAC, LZAE) exhibited higher noise levels than the rest of the network. It is unclear whether the higher noise reflects site conditions or the instrumentation. The impact, however, is that phases were more difficult to identify and had larger errors in the east. For some events this introduced large azimuthal gaps and location errors in the east side of the array. Events with fewer than 4 P picks and 3 S picks were rejected. Default *dbevproc* parameters were used to calculate local magnitudes (M_L). Analyses of event counts and event rates were performed with the GISMO Toolbox for MATLAB (Thompson and Reyes, 2018).

Results

Catalog overview

Our final catalog consists of 613 located events between 11 November 2011 and 31 March 2012. Of these, 591 are within 20 km of Lastarria, corresponding to an average of 4.2 events per day within the 142-day period. But activity is episodic; we find an average of 4.8 events per day for the first 59 days, then 0.5 events per day for the next 33 days, and 5.8 events per day for the final 50 days, reaching a maximum of 26 events on 25 March 2012.

Classification scheme

We identified five different classes of event types in our catalog, based on analysis of event waveforms and corresponding spectra. These are in general agreement with terminology and classifications used widely in volcano seismology. There is no single agreed-upon global terminology. Rather, basic event types are identified but local terminology is modified to remedy characteristics of the particular stations, events, and geography. See McNutt et al. (2015) and Wasserman (2012) for reviews.

- Volcano-Tectonic (VT) events show an impulsive P arrival and a clear S wave (Figure 4A), and they have a broad frequency spectrum from ~2–20 Hz (Figure 4B). A total of 202 VT events are in our catalog, an average rate of 1.4 events per day. There is an apparent lull in VT activity from 8 January to 10 February 2012, with only four events in this period (Figure 5). 58% of VT events occurred in the final 50 days.
- Hybrid (HY) events have a high frequency onset, and decay to lower frequencies in the coda (Figures 4C,D). A total of 66 HY events are in our catalog, an average of 0.47 events per day. 68% of HY events occurred in the final 50 days (Figure 5), with only three events between 8 December 2011, and 10 February 2012.
- There are also two types of events with lower frequencies than VT and hybrid events. We termed these two types Long Period 1 (LP1) and Long Period 2 (LP2), based on their frequency content. Both LP types were completely missed by the initial autodetection but were identified visually, and then detected using revised STA/LTA parameters. The S phase picks for the long period events are not true S phases. We put the S pick on the first large amplitude of the event after the initial onset and used *dbspgram* to look at the strength of the frequency content with time to aid in phase identification and event classification.

  LP1 events have a dominant frequency of 3–4 Hz and are monochromatic (Figures 4E,F). A total of 130 LP1 events are in our catalog. The P arrival is emergent (error bars on each P pick are adjusted to account for emergence and uncertainty in arrival onset). The event rate is fairly constant, except for 8 January to 10 February 2012, when only three LP1 events occurred (Figure 5).

  LP2 events are quasi-monochromatic, with a dominant frequency of ~4–6 Hz (Figures 4G,H). A total of 165 LP2 events are in our catalog. 58% of these events occurred before 8 January 2012, and 39% occurred after 10 February 2012 (Figure 5).
- Unknown events: We identified additional events with frequencies and waveforms inconsistent with the classification scheme discussed above. We label these as "X" events. Most have no discernable S phases. Many of these events had a curious, reverse-hybrid look to their waveform with a low frequency onset and high frequency coda. These resemble LP-rockfall events seen at Soufriere Hills Volcano, Montserrat (Luckett et al., 2002), though we have no evidence of a similar mechanism. A total of 50 X events are in our catalog, and examples can be found in Supplementary Figure S7. Their rate of occurrence varied from 0.15 to 0.4 events per day.

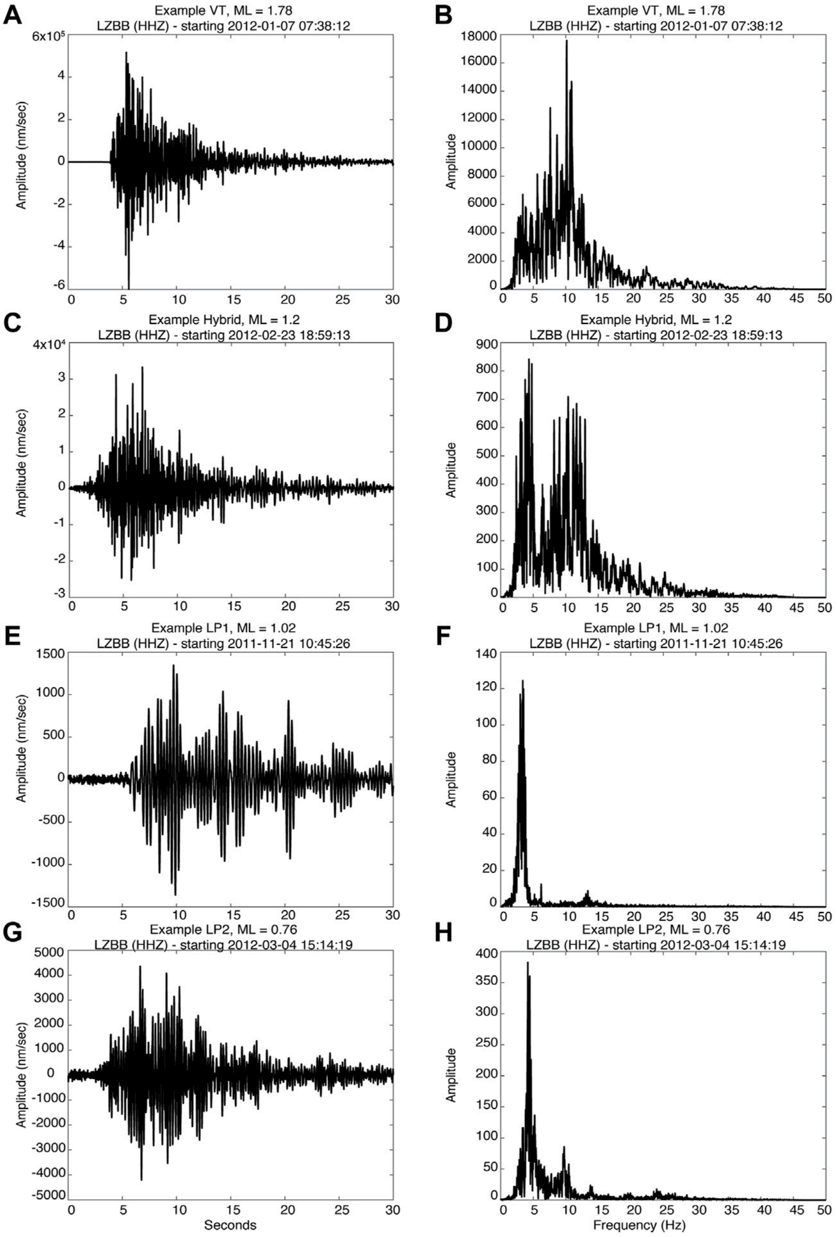

FIGURE 4

Example vertical component waveforms and associated spectra for each event type at station LZBB. Horizontal (E–W) waveforms and associated spectra can be found in Supplementary Figure S7. All waveforms have a time window of 30 s, have been detrended and filtered with a 1 Hz 2-pole high pass filter. **(A)** VT event. Event occurred on 01/07/2012 07:38:12 UTC at 25.1499°S, 68.5262°W, and depth of 4.3 km bsl, with M_L = 1.78. **(B)** Spectra from seismogram in **(A)**. **(C)** Hybrid event. Event occurred on 02/23/2012 18:59:13 UTC at 25.1737°S, 68.5198°W, and depth of 4.3 km asl, with M_L= 1.2. **(D)** Spectra from seismogram in **(C)**. **(E)** Long Period Type 1 (LP1) event. Event occurred on 11/21/2011 10:45:26 UTC at 25.1478°S, 68.4311°W, and depth of 7.6 km bsl, with M_L = 1.02. **(F)** Spectra from seismogram in **(E)**. **(G)** Long Period Type 2 (LP2) event. Event occurred on 03/04/2012 15:14:19 UTC at 25.1692°S, 68.5030°W, and depth of 2.9 km bsl, with M_L = 0.76. **(H)** Spectra from seismogram in **(G)**.

Hypocenters

Hypocenters cluster close to Lastarria (Figures 1, 3, Supplementary Figure S9) and appear to extend from its summit down to approximately the top of the LMB at ~10 km bsl (Supplementary Figure S8) with 90% of events shallower than 6 km bsl and 96.5% shallower than 10 km bsl. The average epicenter of all events is at 25.174°S, 68.514°W (Table 1), which is <1 km southwest of the summit of Lastarria. Of the 613 events in our catalog, 591 are within 20 km, 581 are within 10 km, and 540 are within 5 km of the average epicenter indicating tight clustering. Generally, events trend further to the northeast with increasing

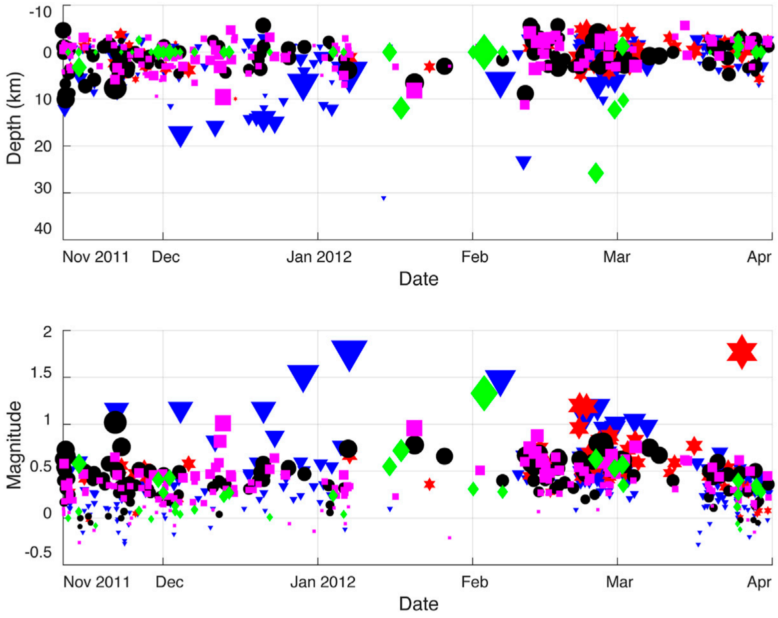

FIGURE 5
Time series of depth and magnitude for events. Symbols and colors depict event types and are the same as in Figure 3. There is an apparent lull in activity across all event types from early January to early February 2012.

TABLE 1 Summary event catalog statistics by event type. Column 2: Number of events within 20 km horizontal distance of the average epicenter (25.174°S, 68.514°W). Column 3: Mean residual time errors between observed and predicted phase arrival times. Columns 4–6: Mean latitude, longitude, and depth of all events (per event type). Column 7–9: Largest event M_L, Mc, and b-value. Plus/minus errors represent one standard deviation. No b-value was estimated for X events due to sample size.

Type	No. of events	Residual (s)	Latitude (°S)	Longitude (°W)	Depth (km)	Largest M_L (±0.1)	Mc (±0.1)	b-value
VT	191	0.48	25.173 ± 0.026	68.518 ± 0.037	1.6 ± 5.1	1.8	0.2	1.2 ± 0.1
Hybrid	66	0.43	25.175 ± 0.010	68.513 ± 0.023	0.2 ± 3.2	1.8	0.5	1.6 ± 0.2
LP1	130	0.39	25.173 ± 0.014	68.509 ± 0.015	0.9 ± 3.1	1.0	0.5	2.5 ± 0.2
LP2	164	0.40	25.174 ± 0.012	68.513 ± 0.015	0.2 ± 3.1	1.0	0.3	1.8 ± 0.1
X	40	0.67	25.178 ± 0.046	68.525 ± 0.047	1.3 ± 5.0	1.3	N/A	N/A
All	591	0.45	25.174 ± 0.021	68.515 ± 0.028	0.9 ± 4.0	1.8	0.3	1.5 ± 0.1

depth, consistent with a feature dipping at about 20° to the vertical. We found little to no activity in the immediate vicinity of Cordón del Azufre; this result does not appear to be an artifact of the network geometry. Most VT, HY, LP1 and LP2 events have 4–6 P-phase picks, and 4–6 S-phase picks (Figure 6, Supplementary Figures S1–S5). Only 2.5% of these events locate further south than 25.2°S.

Hypocenter distributions and uncertainties show little dependence on event class (Table 1; Supplementary Figure S9). The epicentral distributions of each event class are statistically identical. For example, the average epicenter of VT events is within 0.4 km of the average epicenter of HY events, which is only 10–20% of one standard deviation. Mean differences between predicted and observed arrival times range from 0.39 s for LP1 events to 0.48 s for VT events, again showing little variation.

Depth distributions also overlap but show some separation. The average depths are 0.2 km for HY and LP2 events, 0.9 km for LP1 events, and 1.6 km for VT events. These mean depth differences are well within one standard deviation (3.1–5.2 km; Table 1). 95% of HY events are shallower than 5.0 km bsl, increasing to 5.9 km for LP2 events, 6.8 km for LP1 events, and 12.0 km for VT events.

Only 14 of 50 X events have discernable S-phases, so X hypocenters are poorly constrained (particularly depths). For X events without S-phases, we fixed depths to 0 km. We also tried fixing depths to -5 km, but then only eight X

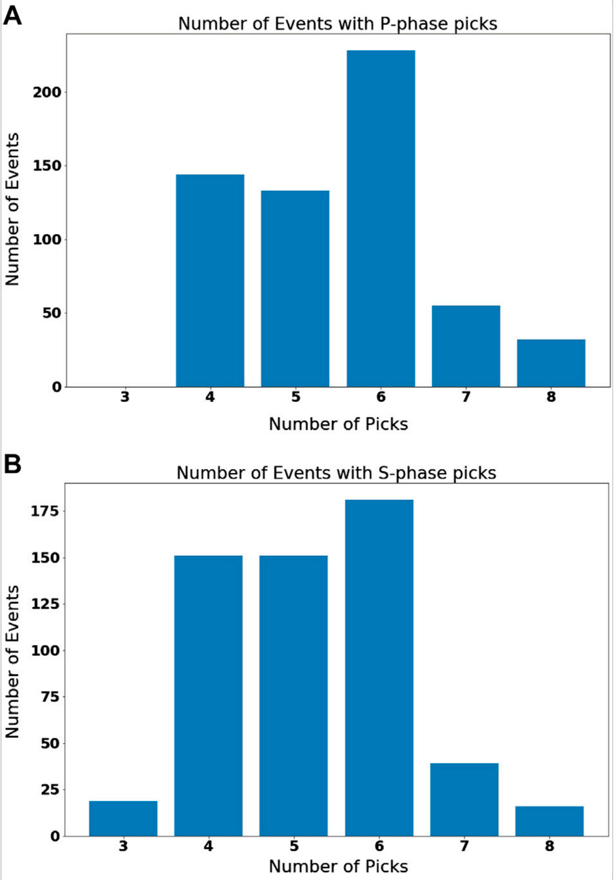

FIGURE 6
Histograms showing the number of events versus number of P phase picks **(A)**, and S phase picks on the **(B)**, for all event types. A breakdown by event type can be found in the Supplementary Figures S1–S5.

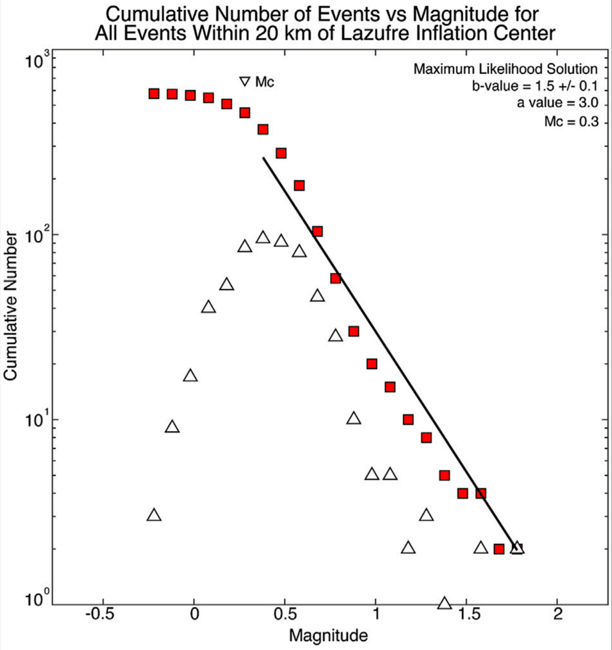

FIGURE 7
Frequency-magnitude distribution for events in Figure 3. Mc = magnitude of completeness. For consistency, the Maximum Likelihood method was used for b-value estimation for all event types (separate distributions for each event type are shown in Supplementary Figures S6A–S6D). This plot is for all events and shows a b-value ~ 1.5 and an Mc ~ 0.3. White triangles indicate the number of events for each magnitude bin, red squares indicate the cumulative number of events. The upside-down triangle indicates Mc, and the line is the regression of the cumulative number of events from which the b- and a-values are calculated.

events locate within the Figure 1 region, suggesting these events are not related to surficial processes.

Magnitudes

Local magnitudes (M_L) in our catalog range from −0.3 to 1.8. The largest VT was a M_L=1.8 event in early January 2012 (Figure 5). The largest hybrid event was also M_L=1.8 (in late March 2012). The largest LP1 and LP2 events were only M_L=1.0.

All b-values in this study (Table 1; Figure 7, Supplementary Figure S6) were calculated using the maximum likelihood solution for curve-fitting. The b-value for VT events is 1.2 ± 0.1 (Supplementary Figure S6A). This is a typical value for VT earthquakes near volcanoes (i.e., Roberts et al., 2015; McNutt, 1996). We estimate a magnitude of completeness (Mc) of 0.2 for VT events. The b-value for hybrid events is 1.6 ± 0.2 with Mc = 0.5 ± 0.1 (Supplementary Figure S6B). The b-value for LP1 events is 2.5 ± 0.2, with Mc = 0.5 ± 0.2 (Supplementary Figure S6C). This b-value is quite high but is comparable to LP events at other volcanoes (Glazner and McNutt, 2021). The b-value for LP2 events is 1.8 ± 0.1 with Mc=0.3 ± 0.1 (Supplementary Figure S6D). These b-values may not be statistically robust given the small spread in M_L.

We note that there is an inverse correlation between b-value and frequency content: LP1 events have the lowest frequency content, and a high b-value. The opposite is true for VT events.

Discussion

The manually reviewed events occurring within the LVS from November 2011 through March 2012 mainly occur in a 5-km-radius cylindrical zone whose axis is just southwest of the Lastarria summit at the surface, dipping to the NE at about 20° off vertical with increasing depth. The shallow events near and southwest of Lastarria cluster close to the shallow magma chambers that have been identified from ambient seismic noise analysis (Spica et al., 2015) and resistivity modeling of magnetotelluric data (C1 and C2 low resistivity anomalies, Díaz et al., 2015). The C1 anomaly of Díaz et al. (2015) is the shallower of the two, extending down to approximately 4 km asl and is centered around Lastarria. This coincides with the ULVZ A of Spica et al. (2015). Díaz et al. (2015) attributes this upper body to fumarolic activity. The C2 resistivity anomaly of Díaz et al. (2015) is deeper, extending to 2–3 km bsl south of Lastarria. This is coincident with the ULVZ B of Spica et al. (2015), and Díaz et al. (2015) attribute C2 to magmatic fluids, which they speculate are heating fumaroles for the C1 body. Without clear supporting evidence, we suggest the event locations in map and cross-sectional views are consistent with activity on a series of dikes that extend from near the Lastarria summit to the shallow magma chamber and perhaps down to the ceiling at the northern edge of the Lazufre inflation body (Figure 3). VT events are on average deeper than low frequency events (HY, LP1, and LP2) with 5% of VT events deeper than 12 km bsl, and 5% of low frequency events deeper than 5.8 km bsl.

The epicentral locations are stable, but depths vary depending on the velocity model as is common. We found relatively few hypocenters with depths of 0–2 km bsl (Figure 3, Supplementary Figure S8). This 'depth gap' may be related to ULVZ B which extends from -1 to 1 km depth in our model. To examine if this is real, we relocated all hypocenters based on an alternate velocity model that eliminates ULVZ A and B (Supplementary Table S2). Not surprisingly, this alternate model pushed hypocenters an average of 1.7 km deeper (from 0.9 to 2.6 km bsl) and 5% of events are deeper than 11.5 km, since wave speeds are on average higher. The depth gap is reduced, which suggests it is an artifact of the presence of the low-velocity zone in the model. Crucially however, the epicenters do not change much between the two velocity models. Our choice for the shallow part of the velocity model is based on the ULVZs identified by Spica et al. (2015) directly beneath Lastarria. These ULVZs have limited spatial extent such that some, but not all, rays from events to stations pass through them (Supplementary Figure S10). The "true" depth distribution is thus likely a mix of results shown for the two velocity models—the two models likely represent endmembers of the possible model space (Supplementary Figures S11, S12). Since we are using a 1D velocity model in a region with 3D properties, a 3D velocity model with topography could potentially provide better resolved hypocenters but is not trivial to derive or use for the LVS given the scant data.

Seismicity was relatively high from November 2011 to early January 2012, and from mid-February until 31 March 2012 (Figure 5). This contrasts with the period from mid-January to mid-February 2012, when the event rate was 5-times lower. The network operations did not change in any significant way throughout the study period and the observed lull in activity is a real feature. This suggests an episodic nature of activity that likely reflect changes in the magmatic system at depth, indicating that the system itself is not in steady state, resulting in a variable stress/strain environment. This perhaps suggests that all the seismicity is responding to the same external events, such as pulses of magma injection or gas release.

The b-value for the entire catalog is approximately b=1.5 ± 0.1 (Figure 7) and Mc is approximately 0.3 ± 0.1. In general, the b-value is a useful metric to characterize groups of earthquakes. The b-value for tectonic earthquakes is generally ~1.0 whereas volcanoes often show higher values. Complementary lab studies show that b-values are affected by fluids (Wyss, 1973), thermal gradients (Warren and Latham, 1970), stresses (Scholz, 1968), and material heterogeneities (Mogi, 1962), so we can use b-values to make inferences about the state of the crust where earthquakes occur. See Glazner and McNutt (2021) for a recent review and compilation. For the LVS, the VT events have a b-value of 1.2, near the worldwide tectonic average, and likely represent shear failure on faults. The hybrid, LP1 and LP2 events have higher b-values of 1.6–2.5 suggesting the presence of mobile fluids, as supported by active fumarole fields and overall high heat flow in the LVS (Pritchard et al., 2018).

The high b-values across three event types (Figure 7, Supplementary Figure S6) provide further support for an area with a high thermal gradient (Wiemer and McNutt, 1997), or alternatively with either a low stress environment or a highly fractured heterogeneous area (i.e., Eyre and van der Baan, 2015; Schorlemmer et al., 2005; Mogi, 1962). The seismograms within each event type are not identical, indicating that the events are occurring in different places and are not repetitive. Thus, we envision a plexus of cracks, dikes, and/or sills near each other, but cannot resolve this with our data.

Current volcanic activity at the LVS consists of seismicity, extensive and highly active fumarole fields, deformation, and degassing. Gas compositions changed between 2009 and 2012 from a hydrothermal signature to a magmatic signature (Lopez et al., 2018). This is the same time frame that the inflation rate of the deeper mush body, the Lazufre Magma Body (LMB), decreased by half (Henderson et al., 2017; Lopez et al., 2018, Pearse and Lundgren, 2013) perhaps suggesting that ascending magma is stalling out and degasses due to isobaric crystallization (Aguilera et al., 2012). However, without concurrent long-term geophysical and geochemical monitoring, a deeper understanding of the state of the LVS might be out of reach, and a full volcanic risk assessment for this region cannot be made with confidence.

Summary and conclusion

We conducted the first study of seismic activity at the LVS based on local observations. No information about the level of activity or its distribution with respect to the Lastarria and Cordón del Azufre volcanic centers or to an InSAR-observed inflation center located between the volcanoes existed prior to our study. Our ~5-month catalog from November 2011 to March 2012 includes 591 events within 20 km of Lastarria corresponding to about four events per day. The seismic events cluster close to the summit of Lastarria and occur mainly at depth from ~5 km asl to ~6 km bsl (Figure 3). We find little to no evidence for seismicity directly beneath the

Cordón del Azufre volcano and the Lazufre Magma Body inflation center (about mid-way between Lastarria and Cordón del Azufre).

Lastarria is seismically active, and we observed different event types that are characteristic of seismicity at many volcanoes. Our event classes consist of VT, Hybrid, and long period LP1 and LP2 events, all of which tend to occur close to Lastarria above the top of the northern edge of the inflation due to the Lazufre Magma Body (LMB). We found a lull in activity across all event types from mid-January to mid-February 2012 (Figure 5) suggesting the magmatic system is not in steady state. This perhaps indicates that all seismicity might be responding to the same external events, such as episodic pulses of magma injection or gas release at depth beneath the LVS.

The locations of the various events are consistent with the idea that the LMB is "feeding" the shallow, localized inflation center active beneath the summit of Lastarria. These events could be indicative of fluid movement through a series of dikes from the LMB up to the summit of Lastarria (Figure 3). Supporting evidence includes: 1) event depths bottoming out near the top of the LMB (~10 km bsl), with 95% of events being shallower than 6 km depth, 2) most events locating close to Lastarria, rather than to Cordón del Azufre, and are coinciding with previously imaged shallow magma bodies, and 3) high b-values for HY, LP1, and LP2 events, indicating the presence of mobile fluids.

Future work could include identification of additional events (e.g., using cross-correlation, machine learning) to improve the statistical significance of parameters in Table 1 (e.g., b-values) and estimation of 'X' event mechanisms to understand their sources. Relative event relocation (e.g., HypoDD) could be used to delineate boundaries of potential magma/mush bodies or pipes/conduits. Similarly, analysis of the radiation patterns of low frequency events, and modeling based on cracks or pipes could improve understanding of the plumbing system of the LVS. Future seismic studies could include more stations for better network geometry.

Our study shows that the LVS is an active volcanic system that undergoes episodic changes in seismicity. Results from seismicity analysis presented here, combined with observed cycles of varying inflation rates from InSAR and changes in gas composition from geochemical studies, highlight the dynamic nature of the system and the importance for continued and improved long-term monitoring efforts of the LVS. Such efforts are crucial to improve understanding of the volcanic hazards for the larger region.

Data availability statement

The raw data supporting the conclusion of this article will be made available by the authors, without undue reservation.

Author contributions

HM performed the bulk of this work as part of her dissertation. GT wrote code, provided Antelope support, and prepared Figures 1, 3, 5 using GISMO, a seismic toolbox for MATLAB (Thompson and Reyes, 2018). GT, SM, JB, and MW provided funding, training, mentorship, and edited the manuscript.

Funding

Partial funding was provided by the NSF Continental Dynamics Program via a subcontract from UAF to USF, with the project #0909254.

Acknowledgments

The authors would like to acknowledge Matt Gardine for extensive assistance with the BRTT Antelope Suite, along with Alexandra Farrell, Lea Gardine, Dara Merz, and Danielle Molisee for discussions, technical expertise with MATLAB programming, and moral support. Scott Stihler is acknowledged for showing the "proper way" to locate low frequency volcanic events. Jamie Farquharson is acknowledged for processing and providing precipitation data in the Supplement. The authors thank Pablo Grosse for guest editing this special issue, and the two reviewers for their kind and helpful comments.

Conflict of interest

Publisher's note

Supplementary material

The Supplementary Material for this article can be found online at: https://www.frontiersin.org/articles/10.3389/feart.2022.890998/full#supplementary-material

References

Aguilera, F., Tassi, F., Darrah, T., Moune, S., and Vaselli, O. (2012). Geochemical model of a magmatic-hydrothermal system at the Lastarria volcano, northern Chile. *Bull. Volcanol.* 74, 119–134. doi:10.1007/s00445-011-0489-5

Bianchi, M., Heit, B., Jakovlev, A., Yuan, X., Kay, S. M., Sandvol, E., et al. (2013). Teleseismic tomography of the southern Puna plateau in Argentina and adjacent regions. *Tectonophysics* 586, 65–83. doi:10.1016/j.tecto.2012.11.016

De Silva, S. L., and Francis, P. (1991). *Volcanoes of the central Andes*, 219. Berlin: Springer-Verlag.

Delph, J. R., Ward, K. M., Zandt, G., Ducea, M. N., and Beck, S. L. (2017). Imaging a magma plumbing system from MASH zone to magma reservoir. *Earth Planet. Sci. Lett.* 457, 313–324. doi:10.1016/j.epsl.2016.10.008

Díaz, D., Heise, W., and Zamudio, F. (2015). Three-dimensional resistivity image of the magmatic system beneath Lastarria volcano and evidence for magmatic intrusion in the backarc (northern Chile). *Geophys. Res. Lett.* 42, 5212–5218. doi:10.1002/2015GL064426

Eyre, T. S., and van der Baan, M. (2015). Overview of moment-tensor inversion of microseismic events. *Lead. Edge* 34 (8), 882–888. doi:10.1190/tle34080882.1

Froger, J.-L., Rémy, D., Bonvalot, S., and Legrand, D. (2007). Two scales of inflation at Lastarria-Cordón del Azufre volcanic complex, Central Andes, revealed from ASAR-ENVISAT interferometric data. *Earth Planet. Sci. Lett.* 255, 148–163. doi:10.1016/j.epsl.2006.12.012

Garcia, S., and Badi, G. (2021). Towards the development of the first permanent volcano observatory in Argentina. *Volcanica* 4 (S1), 21–48. doi:10.30909/vol.04.s1.2148

Glazner, A. F., and McNutt, S. R. (2021). Relationship between dike injection and b-value for volcanic earthquake swarms. *JGR. Solid Earth* 126, 12. doi:10.1029/2020JB021631

Henderson, S. T., Delgado, F., Elliot, J., Pritchard, M. E., and Lundgren, P. R. (2017). Decelerating uplift at Lazufre volcanic center, Central Andes, from A.D. 2010 to 2016, and implications for geodetic models. *Geosphere* 13, 1489–1505. doi:10.1130/GES01441.1

Henderson, S. T., and Pritchard, M. E. (2013). Decadal volcanic deformation in the Central Andes Volcanic Zone revealed by InSAR time series. *Geochem. Geophys. Geosyst.* 14, 1358–1374. doi:10.1002/ggge.20074

Hutchinson, L. (2015). Double-difference relocation of earthquakes at Uturuncu volcano, Bolivia, and Interior Alaska. dissertation. Fairbanks: University of Alaska Fairbanks.

International Seismological Centre (2022). *On-line Bulletin*. Thatcham: Berkshire. doi:10.31905/D808B830

Lopez, T., Aguilera, F., Tassi, F., Maarten de Moor, J., Bobrowski, N., Aiuppa, A., et al. (2018). New insights into the magmatic-hydrothermal system and volatile budget of Lastarria volcano, Chile: integrated results from the 2014 IAVCEI CCVG 12th volcanic gas workshop. *Geosph. (Boulder).* 14, 983–1007. doi:10.1130/GES01495.1

Luckett, R., Baptie, B., and Neuberg, J. (2002). The relationship between degassing and rockfall signals at Soufriere Hills Volcano, Montserrat. *Geol. Soc. Lond. Memoirs* 21, 1. doi:10.1144/GSL.MEM.2002.021.01.28

McFarlin, H. L., Christensen, D. H., Thompson, G., McNutt, S. R., Ryan, J. C., Ward, K. M., et al. (2014). Receiver Function Analyses of Uturuncu Volcano, Bolivia and Lastarria/Cordon del Azufre Volcanoes, Chile. *AGU Fall Meet. Abstr.* 2014, V31E–V4792.

McNutt, S. R. (1996). “Seismic monitoring and eruption forecasting of volcanoes: a review of the state-of-the-art and case histories,” in *Monitoring and mitigation of volcano hazards* (Berlin, Heidelberg: Springer). doi:10.1007/978-3-642-80087-0_3

McNutt, S. R., Thompson, G., Johnson, J., De Angelis, S., and Fee, D. (2015). “Seismic and infrasonic monitoring,” in *The encyclopedia of volcanoes* (New York, NY: Academic Press), 1071–1099.

Mogi, K. (1962). On the time distribution of aftershocks accompanying the recent major earthquakes in and near Japan. *Bull. Earthq. Res. Inst. Univ. Tokyo* 40 (1), 107–124.

Naranjo, J. A. (1988). Coladas de azufre de los volcanes Lastarria y bayo en el norte de Chile: reologia, génesis e importance en geologia planetaria. *Rev. Geol. Chile* 15 (1), 3–12.

Naranjo, J. A. (2010). *Geología del Complejo Volcánico Lastarria, Región de Antofagasta*. Santiago: Servicio Nacional de Geología y Minería, Carta Geológica de Chile. 72. 1:250,000 scale, 1 sheet.

Naranjo, J. A. (1985). Sulphur flows at Lastarria volcano in the north Chilean Andes. *Nature* 313, 778–780. doi:10.1038/313778a0

Naranjo, J. A., Villa, V., Ramírez, C., and Ramirez, C. A. (2018). Miocene to Holocene geological evolution of the Lazufre segment in the Andean volcanic arc. *Geosph. (Boulder).* 14, 47–59. doi:10.1130/GES01352.1

Pavlis, Gary L., Vernon, F., Harvey, D., and Quinlan, D. (2004). The generalized earthquake-location (GENLOC) package: an earthquake-location library. *Comput. Geosciences* 30, 1079–1091. doi:10.1016/j.cageo.2004.06.010

Pearse, J., and Lundgren, P. (2013). Source model of deformation at Lazufre volcanic center, Central Andes, constrained by InSAR time series. *Geophys. Res. Lett.* 40, 1059–1064. doi:10.1002/grl.50276

Pritchard, M. E., de Silva, S. L., Michelfelder, G., Zandt, G., McNutt, S. R., Gottsmann, J., et al. (2018). Synthesis: plutons: investigating the relationship between pluton growth and volcanism in the central Andes. *Geosph. (Boulder).* 14, 954–982. doi:10.1130/GES01578.1

Pritchard, M. E., and Simons, M. (2002). A satellite geodetic survey of large-scale deformation of volcanic centres in the central Andes. *Nature* 418, 167–171. doi:10.1038/nature00872

Remy, D., Froger, J. L., Perfettini, H., Bonvalot, S., Gabalda, G., Albino, F., et al. (2014). Persistent uplift of the Lazufre volcanic complex (Central Andes): new insights from PCAIM inversion of InSAR time series and GPS data. *Geochem. Geophys. Geosyst.* 15, 3591–3611. doi:10.1002/2014GC005370

Roberts, N. S., Bell, A. F., and Main, I. G. (2015). Are volcanic seismic b-values high, and if so when? *J. Volcanol. Geotherm. Res.* 308, 127–141. doi:10.1016/j.jvolgeores.2015.10.021

Ruch, J., Manconi, A., Zeni, G., Solaro, G., Pepe, A., Shirzaei, M., et al. (2009). Stress transfer in the Lazufre volcanic area, central Andes. *Geophys. Res. Lett.* 36, L22303. doi:10.1029/2009GL041276

Scholz, C. H. (1968). Microfractures, aftershocks, and seismicity. *Bull. Seismol. Soc. Am.* 58 (3), 1117–1130.

Schorlemmer, D., Wiemer, S., and Wyss, M. (2005). Variations in earthquake-size distribution across different stress regimes. *Nature* 437 (7058), 539–542. doi:10.1038/nature04094

Spica, Z., Legrand, D., Iglesias, A., Walter, T. R., Heimann, S., Dahm, T., et al. (2015). Hydrothermal and magmatic reservoirs at Lazufre volcanic area, revealed by a high-resolution seismic noise tomography. *Earth Planet. Sci. Lett.* 421, 27–38. doi:10.1016/j.epsl.2015.03.042

Stechern, A., Just, T., Holtz, F., Blume-Oeste, M., and Namur, O. (2017). Decoding magma plumbing and geochemical evolution beneath the Lastarria volcanic complex (northern Chile)—evidence for multiple magma storage regions. *J. Volcanol. Geotherm. Res.* 338, 25–45. doi:10.1016/j.jvolgeores.2017.03.018

Tamburello, G., Hansteen, T. H., Bredemeyer, S., Aiuppa, A., and Tassi, F. (2014). Gas emissions from five volcanoes in northern Chile and implications for the volatiles budget of the Central Volcanic Zone. *Geophys. Res. Lett.* 41, 4961–4969. doi:10.1002/2014GL060653

Thompson, G., and Reyes, C. (2018). Gismo - a seismic data analysis toolbox for MATLAB (Version 1.20b) [software package]. Available at: http://geoscience-community-codes.github.io/GISMO/(Accessed Feb 11, 2022). doi:10.5281/zenodo.1404723

Vernon, F., Lindquist, K., and Harvey, D. (2021). Antelope 5.11. [software package]. Available at: https://brtt.com/software/latest-release/(Accessed February 13, 2022).

Ward, K. M., Delph, J. R., Zandt, G., Beck, S. L., and Ducea, M. N. (2017). Magmatic evolution of a Cordilleran flare-up and its role in the creation of silicic crust. *Sci. Rep.* 7, 9047. doi:10.1038/s41598-017-09015-5

Ward, K. M., Porter, R. C., Zandt, G., Beck, S. L., Wagner, L. S., Minaya, E., et al. (2013). Ambient noise tomography across the central Andes. *Geophys. J. Int.* 194, 1559–1573. doi:10.1093/gji/ggt166

Warren, N. W., and Latham, G. V. (1970). An experimental study of thermally induced microfracturing and its relation to volcanic seismicity. *J. Geophys. Res.* 75 (23), 4455–4464. doi:10.1029/jb075i023p04455

Wasserman, J. (2012). “volcano seismology,” in *New Manual of seismological observatory practice 2 (NMSOP-2)*. Editor P. Bormann (Potsdam: Deutsches GeoForschungsZentrum GFZ), 1–77. doi:10.2312/GFZ.NMSOP-2_ch13

Wiemer, S., and McNutt, S. R. (1997). Variations in the frequency-magnitude distribution with depth in two volcanic areas: Mount St. Helens, Washington and Mt. Spurr, Alaska. *Geophys. Res. Lett.* 24 (2), 189–192. doi:10.1029/96gl03779

Wyss, M. (1973). Towards a physical understanding of the earthquake frequency distribution. *Geophys. J. Int.* 31 (4), 341–359. doi:10.1111/j.1365-246x.1973.tb06506.x

Zimmer, M., Walter, T. R., Kujawa, C., Gaete, A., and Franco-Marin, L. (2017). Thermal and gas dynamic investigations at Lastarria volcano, Northern Chile. The influence of precipitation and atmospheric pressure on the fumarole temperature and the gas velocity. *J. Volcanol. Geotherm. Res.* 346, 134–140. doi:10.1016/j.jvolgeores.2017.03.013

frontiers | Frontiers in Earth Science

TYPE Original Research
PUBLISHED 28 September 2022
DOI 10.3389/feart.2022.904914

Quaternary volcanism in the Yura Monogenetic Field near Arequipa city, southern Peru

Rigoberto Aguilar[1]*, David Arteaga[1,2], Nélida Manrique[1], Benjamin van Wyk de Vries[3], Kevin Cueva[1], Edu Taipe[1], Hervé Guillou[4] and Vincent Scao[4]

[1]Instituto Geológico Minero y Metalúrgico, Observatorio Vulcanológico del INGEMMET, Arequipa, Perú, [2]Universidad Nacional de San Antonio Abad del Cusco, Facultad de Ingeniería Geológica, Minas y Metalúrgica, Cusco, Perú, [3]Université Clermont Auvergne, Laboratoire Magmas et Volcans UMR 6524 CNRS, OPGC IRD, Campus Universitaire des Cézeaux, Aubière, France, [4]Laboratoire des Sciences du Climat et de l'Environnement, CEA-CNRS-UVSQ, Université Paris-Saclay, Gif sur Yvette, France

Arequipa (Peru) is an area where volcanic activity has been persistent during the Quaternary. Studies carried out in this area have highlighted the emplacement of ignimbrite deposits, large volcanic clusters and stratovolcanoes. Monogenetic volcanism is also present, although poorly explored and studied. Due to its location over an ignimbrite plain and poor state of preservation, the only identified monogenetic cone in the Arequipa basin was the Nicholson volcano, while other monogenetic centers remained unknown. This lack of information about the recent volcanism can lead to inadequate definition of scenarios in a hazard assessment in the region. The present study has investigated monogenetic volcanism in the northwestern edge of the Arequipa basin based on geological survey, geochronology and geochemical data. Here, we report for the first time five small volcanic centers such as Yura Viejo, Ccapua, Uyupampa, El Chiral and Patacocha, which together with the Nicholson volcano form the Yura Monogenetic Field. Stratigraphic considerations and new $^{40}Ar/^{39}Ar$ ages allow us to place the eruptive activity in the Middle–Upper Pleistocene (*c.* 195–54 ka). Phreatomagmatic, Strombolian and effusive eruptions characterize the monogenetic activity of the field. As a result of these eruptions, small scoria cones, maars, and lava flows/coulées were generated. The eruptive products show ubiquitous olivine phenocryst-rich (<10 vol%) set in a fine pilotaxitic groundmass, suggesting rapid ascent of basaltic magmas to the surface controlled by the tectonic setting. The analyzed rocks lie in a narrow range of basaltic-andesite composition (50.9–55.6 wt% SiO_2) being the most mafic Pleistocene - Recent volcanic products identified in the Arequipa basin, along with the least differentiated magmas from the nearby Chachani volcanic cluster. This work shows how monogenetic volcanism can occur contemporaneous and closely spaced to larger volcanic clusters and active stratovolcanoes. We hope the information provided here will contribute to improve the risk management by highlighting the scenario of monogenetic eruptions that should be considered in the hazard assessment.

OPEN ACCESS

EDITED BY
Silvina Guzman,
CONICET Instituto de Bio y Geociencias del NOA (IBIGEO), Argentina

REVIEWED BY
Karoly Nemeth,
Massey University, New Zealand
Dario Pedrazzi,
Spanish National Research Council (CSIC), Spain

*CORRESPONDENCE
Rigoberto Aguilar,
raguilar@ingemmet.gob.pe

SPECIALTY SECTION
This article was submitted to Volcanology, a section of the journal Frontiers in Earth Science

RECEIVED 26 March 2022
ACCEPTED 22 August 2022
PUBLISHED 28 September 2022

CITATION
Aguilar R, Arteaga D, Manrique N, van Wyk de Vries B, Cueva K, Taipe E, Guillou H and Scao V (2022), Quaternary volcanism in the Yura Monogenetic Field near Arequipa city, southern Peru. *Front. Earth Sci.* 10:904914.
doi: 10.3389/feart.2022.904914

KEYWORDS

monogenetic field, central volcanic zone, Yura, Arequipa, Peru

1 Introduction

Monogenetic volcanic fields are important manifestations of volcanic activity that usually consist of a set of separate vents (volcanic emission centers) including several volcanic geoforms such as scoria cones, maars, tuff cones, tuff rings, lava domes, and lava flows (e.g., Connor and Conway, 2000; Connor et al., 2000; Németh, 2010; Németh and Kereszturi, 2015). The term 'monogenetic volcano' is used to designate a volcano that erupts during a single period of time (weeks, months or years) in which there is no evidence of a significant or long-lasting temporary interruption in eruptive activity (Macdonald, 1972; Williams and McBirney, 1979; Connor and Conway, 2000). It is important to note that even within a day the accumulating tephra may suffer some syn-eruptive erosion and remobilization of pyroclasts. This is especially valid in areas where rainfall or heavy wind action may coincide with the eruption. The generally small volume of magma emitted is produced by one short, sustained period of activity, then the volcano becomes extinct, and any further activity occurs through a different magma intrusion and new locations. Usually, in monogenetic volcanoes, the magma body rises rapidly (within hours to days) to the surface, so there is little interaction with crustal rocks; it is for this reason that most of these volcanoes emit basaltic magmas (Valentine and Gregg, 2008).

Small volumes and low-silica contents usually characterize monogenetic volcanism. Wörner et al. (2018) described four main constructional volcano types in the Central Volcanic Zone of the Andes (Figure 1C): 1) andesitic and dacitic composite stratovolcanoes, 2) large volcanic clusters that have erupted relatively wide compositional ranges from mafic andesites to dacites, 3) voluminous rhyodacitic ignimbrite fields, and 4) scarce, volumetrically insignificant, basaltic or basaltic andesitic, monogenic fields. In the southern Peruvian Andes, recent studies have focused on the understanding of Pleistocene-Holocene stratovolcanoes (e.g., Thouret et al., 2001; Harpel et al., 2011; Rivera et al., 2014: Samaniego et al., 2016), large volcanic clusters (Mariño et al., 2020; Aguilar et al., 2022) and ignimbrite fields (e.g., Paquereau-Lebti et al., 2006, 2008; Thouret et al., 2016). However, there are few studies on monogenetic volcanism (e.g., Siebe et al., 2006; Delacour et al., 2007; Galas, 2011). Regional scale geological maps published by INGEMMET (Geological Survey of Peru) indicate the presence of some single monogenetic centers of probable Quaternary age (e.g., Marhuas volcano, Chivay lava field) to the north of Arequipa (>90 km), but their eruptive histories remain unknown. In addition, it is likely that many other monogenetic centers have not yet been discovered.

Monogenetic volcanism in the Arequipa region has been important in terms of volume and extension, as is the case of the Andahua (composed of at least 22 cones), Huambo and Orcopampa monogenetic fields (e.g., Delacour et al., 2007, their Figure 1; Galas, 2011) compared to other monogenetic fields in southern Peru. In the Arequipa tectonic depression, only the Nicholson monogenetic volcano was previously known to exist (Delacour et al., 2007; Global Volcanism Program, 2013). Emplaced over the Arequipa Airport Ignimbrite (Paquereau-Lebti et al., 2006), this scoria cone is easily recognizable in aerial photographs or satellite images (Figures 1, 5). Tephra-fall deposits cropping out near the Uyupampa town were mapped as part of older deposits of the Chachani volcanic cluster (Aguilar et al., 2022) since there was not an identified source and because these tephra layers were covered by lava flows from one of the Chachani's edifices.

In this work, we present an overview of the Quaternary monogenetic volcanism near the Arequipa basin. We herein document for the first time the Yura Viejo, Ccapua, Uyupampa, El Chiral and Patacocha volcanoes, which together with the Nicholson cone may form what we name the "Yura Monogenetic Field". These small volcanoes composing the monogenetic field, the Chachani volcanic cluster and Misti stratocone border the Arequipa basin following a NW-SE trend (Figure 1B). Based on detailed fieldwork, satellite images and photogrammetry, whole-rock geochemistry and petrographic descriptions we characterize Nicholson, Ccapua, Yura Viejo, and Uyupampa volcanoes. Due to inaccessibility, we carried out a remotely-based analysis of El Chiral and Patacocha volcanic centers. Furthermore, combining field data and morphometric parameters we propose the eruption style and classification of each volcano in this monogenetic field, contributing to the understanding of monogenetic volcanism in southern Peru.

The Yura Monogenetic Field, located along the border of a tectonic basin, where the small monogenetic volcanoes were emplaced over ignimbrite deposits and near the Chachani large volcanic cluster and Misti stratovolcano, constitutes a very interesting example of monogenetic activity occurring in a temporal and spatial proximity to polygenetic volcanism with larger explosive and effusive eruptions. Reconstructing the history of volcanic activity around urban areas is fundamental for constraining the hazard scenarios and risk assessment.

2 Geological and tectonic setting

The magmatic and volcanic activity in the Peruvian segment of the Andean Central Volcanic Zone is ongoing since the Lower Jurassic (~190 Ma) until present (e.g., Mamani et al., 2010), but increased in Cenozoic times, especially during the uplift of the Andes after 40 Ma (e.g., Thouret et al., 2016). At the regional

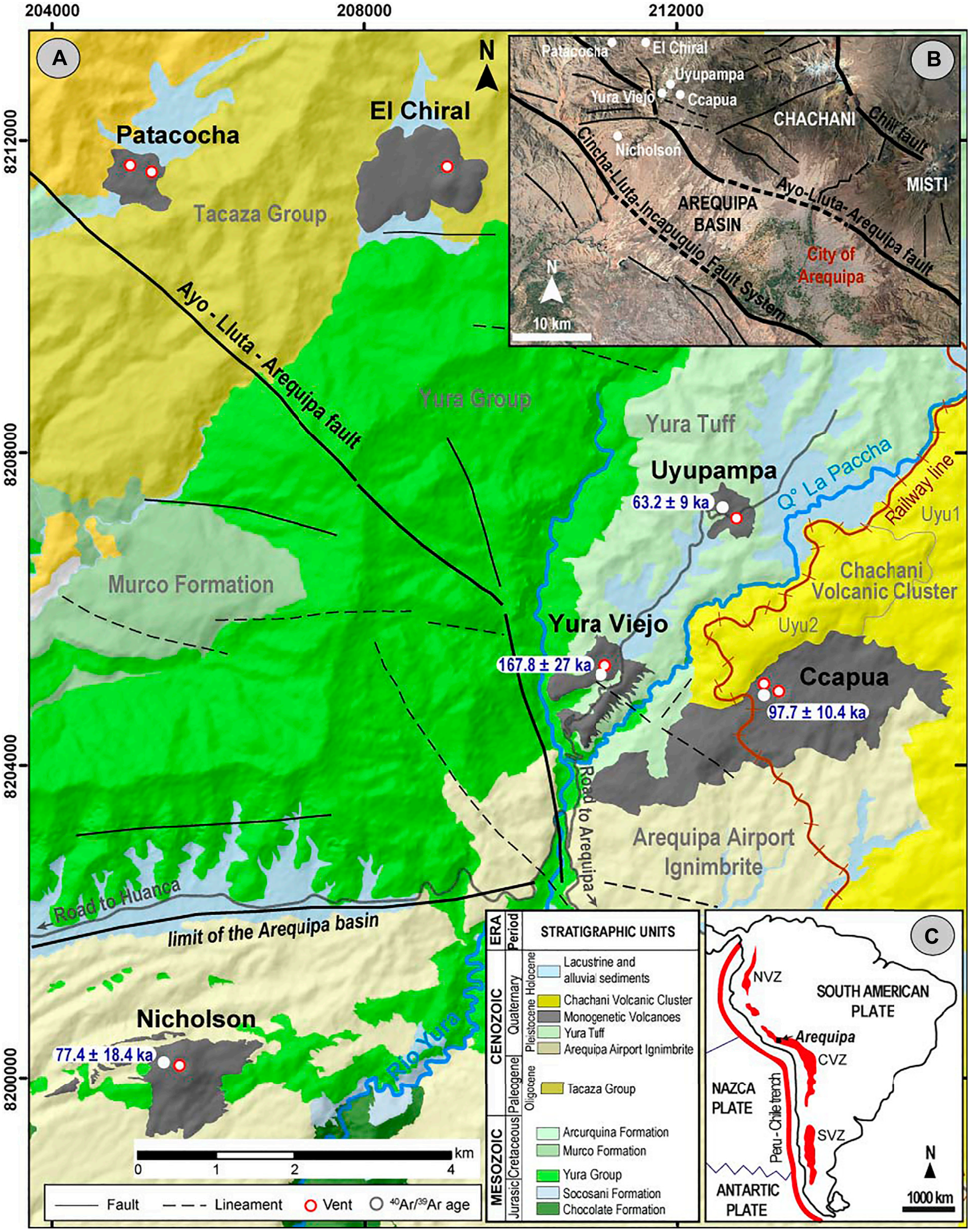

FIGURE 1
(A) Geological map of the Yura Monogenetic Field, northeastern of the Arequipa basin. Lithological data was taken from GEOCATMIN, INGEMMET (2014) and Paquereau-Lebti et al. (2006). Relief of image taken from Arc Map World Imagery Service. **(B)** Inset of a schematic map of the structural setting of the Arequipa basin and surrounding areas. **(C)** Inset of the subduction zone and convergence between Nazca and South American plates are indicated. Red polygons indicate the Northern (NVZ), Central (CVZ) and Southern (SVZ) Volcanic Zones respectively. Continuous and thick red line indicates the Peru-Chile Trench.

scale, Mamani et al. (2010) described the magmatism and geochemical evolution since 91 Ma, with overlap and migration of seven magmatic arcs during different periods. Tectonic shortening and magmatism allowed the thickening of the continental crust (Ramos, 2010; Armijo et al., 2015). The seven successive arcs are: 1) Toquepala (91–45 Ma), 2) Andahuaylas-Anta (45–30 Ma), 3) Tacaza (30–24 Ma), 4) Huaylillas (24–10 Ma), 5) Lower Barroso (10–3 Ma), 6) Upper Barroso (3–1 Ma) and 7) the Frontal Arc or Present-day Arc (<1 Ma). The active magmatic arc or "Frontal Arc" in southern Peru results from eruptive activity since ~1.3 Ma. The Pleistocene Frontal Arc (e.g., Mamani et al., 2010) is located 220–250 km east of the Peru-Chile Trench and above a 30°dipping slab (Thorpe et al., 1982; Wilson, 1986; Stern, 2004) (Figure 1). The present-day range of active, dormant and extinct volcanoes that grew upon the Western Cordillera along a N130° and N160°orientation parallels the Peru-Chile Trench (15° 15′-17° 30′S and 70° 00′-73° 30′W).

The geodynamic context includes an active continental margin and an archetypal Andean subduction (Thorpe et al., 1982; Wilson, 1986). However, in southern Peru, the continental magmatic arc is also obliquely convergent (i.e., the plate margin is at about N74 ± 4°E angle to the subduction direction; Norabuena et al., 1998). This oblique convergence is accommodated since at least the Neogene by sinistral faults (Mering et al., 1996; Sempere et al., 2014). Neogene to Recent volcanism is often associated with trans-tensional regimes because these areas offer less resistance through normal and strike-slip faults, through which the magma can rise more easily to the surface (e.g., van Wyk de Vries and Merle 1998; Acocella et al., 1999).

The WNW-ESE oriented Arequipa depression (Figure 1B) has been interpreted as a pull-apart basin associated with regional ~N130° transtensive faults (Mering et al., 1996; Thouret et al., 2001; Benavente et al., 2017). The basin is filled by Middle Miocene to Early Pleistocene ignimbrites (e.g., Paquereau-Lebti et al., 2006), and more recent volcanoclastic deposits and alluvial deposits. The basin boundary is formed by the Cincha-Lluta-Incapuquio Fault System (Figure 1B) which has experienced different tectonic regimes (Vicente et al., 1982), delineating the western limit of the Western Cordillera, and has influenced the sedimentation of the Arequipa basin (e.g., Carlotto et al., 2009). Studies conducted around the Arequipa basin have shown that this fault system has operated during the Mesozoic in successive extensional and reverse regimes (e.g., Acosta et al., 2010). The system was interpreted as transpresive faults (Vicente et al., 1982), which now act in a trans-tensional regime.

The N130° oriented Ayo-Lluta-Arequipa Fault (also known as Huanca fault) is a regional structure that was formerly a thrust fault. This structure brings into contact Mesozoic sedimentary units (including the Yura Group) with the Cenozoic volcano-sedimentary units (Figure 1). During the Cenozoic, the area was affected by major compressive phases. Since the Middle Miocene, extensional tectonics has had a major influence on volcanism in the Western Cordillera (Huaman Rodrigo et al., 1985 in Mering et al., 1996). Since the Pliocene, the Ayo-Lluta-Arequipa system has acted as a normal and sinistral fault (Mering et al., 1996; Sempere and Jacay, 2006).

2.1 The bedrock stratigraphy of Yura Monogenetic Field

Several of the pyroclastic deposits in the Yura Monogenetic Field contain rock fragments extracted from the substrate on which the volcanoes were emplaced. In the area surrounding the Yura town, the bedrock is formed of Mesozoic sedimentary and Neogene volcanic deposits (Figure 1). A summary of stratigraphic units of the bedrock is presented in Table 1.

3 Methods

3.1 Geological mapping and sample collection

Fieldwork was carried out during short field campaigns between June 2018 and November 2021. We visited 114 field sites distributed in the monogenetic field along the Yura Valley (Figure 1). The source of individual lava flows and pyroclastic deposits was distinguished by using stratigraphic and volcanological relationships between deposits and geoforms (scoria cones, maars, fissures that fed flows or topographic highs). Mapping of eruptive units (1:25000 scale) included lithologic criteria (type, size, and abundance of mineral phases) and morphologic criteria (e.g., Condit and Connor, 1996). Outcrops in natural surfaces together with road-cuts and quarries served to carry out the facies observations and descriptions. Four stratigraphic logs were measured in outcrops with greater exposure of stratigraphic units. The geological maps of the Yura Monogenetic Field were digitized using ArcMap® 10.1 (https://desktop.arcgis.com) at 1:25000 scale, the same scale used by INGEMMET (Instituto Geológico Minero y Metalúrgico) for geological maps of active volcanoes in Peru. The coordinate system of all maps presented herein are UTM WGS84, Zone 19S. Polygons delimiting the volcanoes were used to calculate their surface areas in ArcMap. In some areas, high-resolution digital elevation models (UTM-WGS84 DEM, 60-cm spatial resolution) were obtained by oblique photogrammetry with a Phantom-4PRO drone. The methodology of photogrammetry was similar to that described by Diefenbach et al. (2012) and James et al. (2020). We used AgiSoft Photoscan® software (https://www.agisoft.com) for photogrammetric analysis. Morphometric parameters described by Wood (1979) such as cone basal diameter, crater diameter and cone height were obtained from fieldwork data and high-resolution DEMs

TABLE 1 Bedrock in the surrounding areas of the Yura Monogenetic Field.

Unit	Description	Age	Reference
Chachani Volcano Cluster	Consist of at least twelve volcanic edifices forming a group of stratovolcanoes, dome coulées and blocky-lava flow fields. Their deposits overly the Arequipa Airport Ignimbrite and the Yura Tuff, and a lava flow in its western flank partially covers the Ccapua monogenetic volcano.	1012 ± 53–56.5 ± 31.6 ka	Aguilar et al. (2022)
Yura Tuff	Non-welded pumice and ash pyroclastic flows the volume of which was estimated at ~1.5 km^3. Yura Tuff outcrops are restricted to the north and west sides of Chachani complex. They fill a north-south elongated depression between sediments of the Yura Group and Pre-Chachani lava bedrock	1.278 ± 46 Ma	Paquereau-Lebti et al. (2006, 2008). Aguilar et al. (2022)
Arequipa Airport Ignimbrite	Consists of two units (18 km^3), a white indurated massive ash-and-lapilli tuff overlain by a pink non-welded, massive and lithic-rich lapilli tuff. The source of this ignimbrite is buried under the Chachani Volcano Cluster, as indicated by Anisotropy of Magnetic Susceptibility measurements and the size of lithic fragments, which increases towards the north	1.65 ± 0.04 Ma	Paquereau-Lebti et al. (2006, 2008)
Tacaza Group	Composed of volcanic breccia and andesitic lavas. These volcanic rocks crop out in the northwestern part of the study area	Oligocene	Jenks (1946)
Arcurquina Fm	Composed of marine, regularly-bedded, thickening-upward, grey to black, organic rich micritic limestones. These rocks are found to the northwestern side of the study area	Middle to Upper Cretaceous (Albian to Cenomanian)	Jenks (1948); Callot et al. (2008)
Murco Fm	Mainly composed of dark shales and soft chert with a predominance of variegated sandstones. These sequences are found forming the flanks of the anticlines and synclines of the area. The outcrops of this formation are found in the western part of the monogenetic field	Middle Cretaceous	Wilson (1963)
Yura Group	Sedimentary rocks from floodplain deposits and lateral accretion of point-bar deposits sited on a semi-flat topography. The outcrops are found in the central part, near the monogenetic volcanoes	Middle to Late Jurassic (Callovian to Tithonian)	Benavides (1962); Alván et al. (2018)
Socosani Fm	Consist of shales interbedded with fossiliferous limestones. These rocks crop out along the Río Yura, to the southeast of Nicholson volcano.	Middle—Upper Jurassic	Benavides (1962)
Chocolate Fm	Composed of purplish volcanic and sedimentary (sandstone and limestone) rocks, some of which have been affected by metamorphism. The outcrops of Chocolate Fm. are found in the southern part of the area	Lower Jurassic	Vargas (1970)

using ArcMap. The average flank slopes were calculated trigonometrically using the morphometric parameters (e.g., Hasenaka and Carmichael, 1985).

3.2 Petrography, geochemistry and geochronology

Twelve lava and scoria samples were used for petrographic descriptions. Thin sections of those samples were studied in order to describe representative rocks from the volcanic centers. Ten of them have been taken in volcanic deposits (bombs and lavas), while two are xenoliths included in tephra-fall deposits. Given that the mineral assemblage is quite homogeneous, the number of samples is deemed representative. All analyzed samples are fresh, or at least show no conspicuous weathering. Modal analyses of the sample set are given in Table 2. The abundance of each main mineral phase in thin section was determined by using images taken with a polarized microscope in the most representative zones. Using Adobe® Illustrator (https://www.adobe.com/la/products/illustrator.html), the images were examined to determine the percentage of each mineral. For determining the frequency (modal analysis), we used the point-counting method (e.g., Rodríguez Rey et al., 2004) following five steps: 1) we consider a rectangular frame inside the image to restrict the crystal counting to this area. Two sides of the frame have dashed lines and the other have continue lines. 2) All crystals that were completely included within the frame and the crystals that have some portion inside the dashed lines were counted (point counting). 3) Into the rectangular frame, we added a grid of 600 points. 4) Each point intersecting a crystal was manually counted to calculate the number of crystals contained in the frame. 5) The % abundance is obtained by: (# of crystals/Area of rectangular frame) × 100.

Major and trace element analyses of whole-rock samples were performed by ICP-AES and ICP-MS respectively, with an analytical precision (2σ) less than 1% for major elements and around 5% for trace elements at Instituto Geológico Minero y Metalúrgico (INGEMMET) in Peru. For these analyses, agate-crushed powders of seventeen samples were mixed with $LiBO_2$, placed in a graphite crucible, and melted in an induction oven at 1050°C for 4.5 min, resulting in a homogeneous glass bead. The glass was then

TABLE 2 Summary of the petrographic characteristics of the Yura monogenetic field. Pl: plagioclase, Px: pyroxene, Amph: amphibole, Qz: quartz, Op: opaques, Cb: carbonates, Kfd: potasic feldspar. % values in parentheses represents the percentage of crystal content as phenocrysts (>500 μm) and micro-phenocrysts (100–500 μm) and microlites (<100 μm) in the groundmass.

Volcano	Sample	Mineral assemblage				Texture		Deposit type	Rock type (modal classification)	Observations
		Crystals		Groundmass (% vol.)	Alteration mineral (% vol.)	Whole rock	Mineral			
		Phenocryst (% vol.)	Accessory (% vol.)							
Nicholson	CHA-VR21-010	Ol (~9)	Op (~4)	Px (~42) ± Pl (~38) ± glass (~2) ± vesicles (~5)	-	Porphyritic, pilotaxitic groundmass	Ol skeletal growth, glomeroporphyritic	Scoria fall	Basaltic andesite	Irregular vesicles, xenoliths (volcanic)
Ccapua	CHA-VR21-001	Ol (~7)	Op (~4)	Pl (~32) ± Px (~25) ± glass (~4) ± vesicles (~27)	clay (~1)	Porphyritic, pilotaxitic groundmass	Ol skeletal growth, glomeroporphyritic	Scoria fall	Basaltic andesite	Irregular vesicles
	CHA-18-25	Ol (~8)	Op (~3)	Pl (~30) ± Px (~22) ± Ol (~5) ± glass (~5) ± vesicles (~27)	-	Porphyritic, pilotaxitic groundmass	Ol skeletal growth, glomeroporphyritic	Lava flow	Basaltic andesite	Sub-rounded vesicles
	CHA-18-50	Ol (~10)	Op (~4)	Pl (~31) ± Px (~23) ± glass (~4) ± vesicles (~28)	Fe ox (traces)	Porphyritic, pilotaxitic groundmass	Ol skeletal growth, glomeroporphyritic	Scoria fall	Basaltic andesite	Irregular vesicles
	CHA-19-51	Ol (~9)	Op (~4)	Pl (~34) ± Px (~26) ± glass (~2) ± vesicles (~25)	Fe ox (traces)	Porphyritic, pilotaxitic groundmass	Ol skeletal growth, glomeroporphyritic	Scoria fall	Basaltic andesite	Irregular vesicles
Yura Viejo	CHA-VR21-002	Ol (~6)	Op (~4)	Px (~34) ± Pl (~25) ± glass (~3) ± vesicles (~28)	clay (traces) ± Fe ox (traces)	Porphyritic, pilotaxitic groundmass	Ol skeletal growth, glomeroporphyritic	Scoria fall	Basaltic andesite	Irregular vesicles
	CHA-18-46	Ol (~9)	Op (~4)	Px (~28) ± Pl (~26) ± glass (~4) ± vesicles (~29)	clay (traces)	Porphyritic, pilotaxitic groundmass	Ol skeletal growth, glomeroporphyritic	Scoria fall	Basaltic andesite	Irregular vesicles, volcanic enclaves
	CHA-VR21-004	Ol (~9)	Op (~3) ± Amph (traces)	Px (~34) ± Pl (~31) ± glass (~2) ± vesicles (~21)	opacite (traces) ± clay (traces)	Porphyritic, trachytic groundmass	Ol skeletal growth, glomeroporphyritic	Scoria fall	Basaltic andesite	Irregular vesicles
	CHA-VR21-003A	Qz (~87)	Op (~2) ± Kfd (~1) ± zr (traces)	clay (~4) ± Cb (~2)	-	Clastic	-	sedimentary xenolith	quartz sandstone	Volcanic lithic fragments, Siliceous lithic fragments
	CHA-VR21-003B	Qz (~85)	Kfd (~1) ± Op (traces) ± zr (traces)	clay (~11)	-	Clastic	-	sedimentary xenolith	quartz sandstone	Volcanic lithic fragments
Uyupampa	CHA-VR21-009	Ol (~8)	Op (~6)	Pl (~53) ± Px (~20) ± glass (traces) ± vesicles (~13)	-	Porphyritic, trachytic groundmass	Ol skeletal growth, coronitic	Lava flow	Basaltic andesite	Irregular vesicles
	CHA-18-26	Ol (~9)	Op (~3)	Pl (~32) ± Px (~28) ± glass (~2) ± vesicles (~26)	clay (traces) ± opacite (traces)	Porphyritic, pilotaxitic groundmass	Ol skeletal growth, coronitic	Scoria fall	Basaltic andesite	Irregular vesicles, sedimentary xenolith

dissolved in a solution of deionized water and nitric acid (HNO_3) and finally diluted by a factor of 2000. For comparison with surrounding volcanic products, these new data (Table 3) were combined with previously analysed rock samples from Chachani volcano cluster (Mamani et al., 2010; Aguilar et al., 2022), Arequipa Airport Ignimbrite and Yura Tuff (Paquereau-Lebti et al., 2006).

The chronology of volcanic activity in the Yura Monogenetic Field was constrained using the $^{40}Ar/^{39}Ar$ dating method at the Laboratoire des Sciences du Climat et de l'Environnement (LSCE/IPSL, Gif-sur-Yvette, France). Groundmass in the samples from Yura Viejo, Uyupampa, Ccapua and Nicholson volcanoes were used for age determinations. $^{40}Ar/^{39}Ar$ ages are summarized in Table 4, whereas, the corresponding analytical procedures and results are detailed in the Supplementary Material S1, S2.

4 Volcanism and crustal structure in the yura monogenetic field

4.1 Volcanic activity

The Yura Monogenetic Field is composed of six volcanic centers; three of them (Patacocha, Yura Viejo and Ccapua) are

TABLE 3 Major, trace and REE analyses of samples from Arequipa Airport Ignimbrite (AAI), Yura Tuff and Yura Monogenetic Field obtained during this work. All Fe is given as Fe_2O_3. The coordinates of the sample locations are indicated in UTM WGS84, Zone 19S.

Unit	AAI	Yura tuff								Ccapua				Nicholson	Uyupampa		Yura Viejo									
Sample	CHA-18-19	CHA-18-58B	CHA-18-27	CHA-18-52	CHA-18-53	CHA-19-48	CHA-19-45	CHA-19-47	CHA-VR21-005	CHA-18-25	CHA-19-50	CHA-19-51	CHA-VR21-001	CHA-19-52	CHA-18-26	CHA-R21-009	CHA-VR21-002	CHA-VR21-004	CHA-VR21-012a	CHA-VR21-012b	CHA-VR21-012c	CHA-VR21-012d	CHA-VR21-012e	CHA-VR21-012f	CHA-R21-012g	CHA-R21-012h
Type	pumice	pumice	pumice	pumice	pumice	pumice	pumice	pumice	pumice	scoria	scoria	lava flow	scoria	lava flow	scoria	lava flow	scoria	lava flow	scoria	scoria	scoria	scoria	scoria	scoria	scoria	scoria
East	214187	218335	214839	9214864	9214864	214275	212382	214770	218032	211989	213177	213207	213209	205935	212710	212688	210536	211218	211280	211280	211280	211280	211280	211280	211280	211280
North	8201556	8216174	8212280	8210161	8210161	8213944	8204788	8220951	8213226	8204176	8204984	8205007	8205215	8200162	8207154	8207175	8204358	8205159	8205224	8205224	8205224	8205224	8205224	8205224	8205224	8205224
SiO_2	72.5	69.9	71.4	71.7	71.5	72.1	68.3	67.9	67.1	50.9	53.5	54.4	55.6	51.3	53.3	55.0	55.6	53.2	54.5	54.2	54.0	54.5	54.2	54.5	54.4	54.9
TiO_2	0.15	0.20	0.18	0.19	0.20	0.12	0.29	0.27	0.56	1.56	1.43	1.40	1.36	1.48	1.37	1.46	1.40	1.39	1.32	1.35	1.36	1.37	1.35	1.37	1.37	1.36
Al_2O_3	12.7	13.3	13.3	12.6	12.5	13.7	14.2	14.4	13.1	16.4	16.8	16.8	15.6	15.7	16.5	15.6	14.8	15.6	16.8	16.9	16.8	16.8	16.7	16.6	16.6	16.8
Fe_2O_3	1.03	1.15	1.12	1.23	1.21	0.91	1.95	1.85	3.44	10.26	8.28	8.40	8.26	9.88	8.79	8.58	8.93	8.86	8.55	8.55	8.76	8.62	8.73	8.69	8.64	8.68
MnO	0.08	0.05	0.08	0.07	0.07	0.07	0.06	0.06	0.06	0.14	0.10	0.10	0.11	0.13	0.13	0.12	0.12	0.12	0.15	0.14	0.15	0.14	0.16	0.16	0.15	0.15
MgO	0.24	0.35	0.31	0.38	0.41	0.16	0.70	0.61	1.74	5.31	4.48	4.49	4.07	5.95	4.94	4.40	4.62	4.49	4.27	4.12	4.31	4.14	4.18	4.29	4.33	4.14
CaO	0.88	1.15	1.06	1.45	1.31	1.01	2.05	1.59	2.86	8.19	7.61	7.57	7.02	8.08	7.56	7.11	7.25	7.16	7.50	7.50	7.53	7.50	7.54	7.59	7.64	7.51
Na_2O	3.73	3.04	3.53	3.47	3.70	3.92	4.17	3.66	2.91	3.87	4.35	4.21	3.96	3.47	3.96	4.00	3.58	3.95	4.03	4.02	4.03	4.06	4.08	4.14	4.09	3.99
K_2O	4.03	4.80	4.45	4.08	4.02	4.05	3.87	4.20	4.01	1.77	2.01	1.99	1.81	1.60	1.79	1.84	1.58	1.81	1.88	1.90	1.84	1.87	1.88	1.87	1.91	1.89
P_2O_5	0.07	0.06	0.10	0.08	0.08	<0.01	0.11	0.09	0.18	0.40	0.45	0.40	0.42	0.33	0.42	0.43	0.34	0.41	0.41	0.42	0.45	0.42	0.42	0.44	0.45	0.44
LOI	3.48	6.01	4.08	3.74	4.07	3.12	4.18	4.54	2.59	0.78	0.33	0.15	<0.01	0.71	0.46	0.10	0.17	0.95	0.42	0.50	0.43	0.38	0.23	0.37	0.47	0.12
Rb		141		54	76	110	85	104	115		35	35	50	25	44	31	41	43	47	41	41	45	45	46	45	45
Sr	111	205	186	155	170	167	311	202	428	881	953	982	913	886	892	900	844	943	870	755	824	823	824	852	778	824
Y	15	10	16	16	16	14	15	15	22	20	17	16	17	18	18	37	18	31	20	19	18	17	17	17	16	16
Nb	10.3	9.1	10.4	11.1	11.2	11.7	8.6	10.6	8.5	5.1	6	5.8	7	5.2	5.7	7.6	6.4	6.7	6.7	6.4	6	6.1	6	5.8	6.1	6.6
Zr	110	165	121	144	140	110	127	174	172	155	91	110	145	89	161	176	164	173	188	160	124	150	139	129	146	178
Cs	1.56	3.82	1.81	1.67	1.68	2.49	1.45	1.69	2.27	0.42	0.51	0.44	0.4	0.83	0.49	0.37	0.49	0.37	0.59	0.83	0.63	0.57	0.68	0.59	0.73	0.61
Ba	1092	1094	1186	757	959	930	1079	889	1064	740	898	913	767	630	836	786	630	786	907	798	868	848	873	883	809	839
Hf	3.6	4.6	3.7	4	4	3.7	3.9	5.2	5.4	3.8	3.9	3.8	4	3.4	4	4.9	4.6	4.7	4.8	4.1	3.2	4	3.5	3.2	3.6	4.1
Th	10.1	17.8	10	10.4	10.5	9.9	7.7	9.7	9.1	1.8	2.6	2.4	3.3	2	2.2	3.3	3.1	2.9	2.9	2.8	2.7	2.7	2.8	2.6	2.6	3.2
U	1.4	3.1	1.4	1.4	1.3	1.5	1.2	1.2	1.4	0.4	0.5	0.5	0.5	0.4	0.4	0.5	0.5	0.4	0.6	0.6	0.6	0.6	0.6	0.5	0.6	0.6
La		43		15	27	24	33	27	37		36	36	33	28	33	32	29	34	39	33	36	36	37	38	34	36
Ce	86.3	90.6	78.8	84	82.4	83	75.7	84.9	78.5	68.5	80.5	79.5	81.1	59.4	76.6	78.4	71.6	80.9	82.4	81.5	81.2	78.8	81.3	79.3	83	81.5
Pr	8.5	8.6	7.5	8.3	8.1	8.8	8.1	8.9	9	7.6	10	9.7	10.1	7.7	8.2	10.2	9	10.2	10.1	10	9.8	9.8	9.9	9.6	10.1	9.8
Nd	31.4	28.3	28.2	27.5	27.1	30.1	28.2	30.7	31.8	36.4	40	40.1	40.6	32.4	38.1	40.7	37.8	40.8	41.3	40.1	40.5	39.9	40.5	39.4	40.3	39.8
Sm	4.4	4	4.2	4.3	4.1	5	4.2	4.8	5.1	6.4	7.2	7.2	7.3	6.6	6.7	7.3	7.2	7.2	6.9	6.9	6.7	6.8	6.7	6.8	6.8	7
Eu	0.8	0.8	0.8	0.8	0.8	0.9	1	0.9	1	1.8	1.9	1.8	1.8	1.7	1.7	1.8	1.7	1.8	2	1.9	1.8	1.8	1.8	1.9	1.9	1.8
Gd	3.3	2.8	3.2	3.4	3.1	3.4	3.2	3.5	3.9	5.9	6	5.7	5.9	5.6	5.4	5.9	6.4	5.7	6	6	5.8	5.7	5.7	5.7	5.7	5.9
Tb	0.4	0.3	0.4	0.4	0.5	0.5	0.4	0.5	0.5	0.8	0.8	0.7	0.8	0.8	0.7	0.8	0.9	0.8	0.8	0.8	0.8	0.7	0.7	0.7	0.7	0.7
Dy	2.5	1.8	2.7	2.6	2.5	2.8	2.6	2.9	2.4	4.4	4.2	4.1	3.7	4.3	3.9	3.7	4.2	3.7	3.8	3.8	3.5	3.6	3.7	3.5	3.6	3.6
Ho	0.4	0.3	0.4	0.5	0.5	0.5	0.5	0.5	0.5	0.7	0.7	0.7	0.7	0.8	0.6	0.7	0.8	0.7	0.7	0.7	0.7	0.7	0.7	0.7	0.7	0.7
Er	1.4	0.9	1.5	1.4	1.4	1.5	1.4	1.6	1.4	2	2	1.9	1.8	2.2	1.7	1.8	2.2	1.8	1.8	1.7	1.7	1.6	1.6	1.6	1.6	1.6
Tm	0.2	0.1	0.2	0.2	0.2	0.2	0.2	0.2	0.2	0.3	0.2	0.2	0.2	0.3	0.2	0.3	0.3	0.2	0.2	0.2	0.2	0.2	0.2	0.2	0.2	0.2
Yb	1.5	0.8	1.7	1.6	1.5	1.5	1.4	1.5	1.4	1.8	1.5	1.5	1.5	1.8	1.5	1.6	1.7	1.5	1.4	1.4	1.5	1.5	1.5	1.4	1.4	1.5
Lu	0.2	<0.15	0.21	0.21	0.2	0.22	0.21	0.23	0.21	0.22	0.23	0.22	0.21	0.26	0.2	0.21	0.25	0.21	0.21	0.2	0.2	0.22	0.2	0.2	0.21	0.21

TABLE 4 Summary of $^{40}Ar/^{39}Ar$ data from incremental heating experiments on groundmass splits.

Sample Lab file #	Volcano	Type of deposit	UTM Easting	UTM Northing	wt. (mg)	K/Ca (total)	Total FusionAge (ka)	Age Spectrum				Isochron analysis				
								Increments used (°C)	^{39}Ar (%)	Age ± $2\sigma^{(1)}$ (ka)	$^{40}Ar/^{36}Ar$ ± $2\sigma^{(1)}$ MSWD	n/N	MSWD	$^{40}Ar/^{36}Ar$ ± $2\sigma^{(1)}$ intercept	Age ± $2\sigma^{(1)}$ (ka)	F Spreading Factor
CHA-VR21-09																
FG-2995 to FG-3003	Uyupampa	lava flow	213209	8205215	131	0.36	51.6 ± 10.6	726–1081	88.3	**63.2 ± 9.0**	0.37	7 of 9	0.67	298.3 ± 2.4	65.3 ± 17.5	3.4%
CHA-VR21-010																
FG-3004 to FG-3013	Nicholson	scoria fall	205497	8200259	131	0.28	79.7 ± 20.8	663–1083	98.0	**77.4 ± 18.4**	0.24	8 of 10	0.43	299.5 ± 2.0	63.4 ± 31.8	1.4%
CHA-VR21-001																
FG-2984 to FG-2993	Ccapua	scoria fall	213209	8205215	124	0.41	99.5 ± 13.8	725–1167	98.7	**97.7 ± 10.4**	0.16	8 of 10	0.20	299.0 ± 3.3	95.8 ± 19.6	6.7%
CHA-VR21-004																
FG-3014 to FG-3023	Yura Viejo	lava flow	211218	8205159	121	0.23	133.9 ± 28.0	788–1168	84.4	**167.8 ± 27.0**	0.32	7 of 9	0.52	298.8 ± 3.3	164.6 ± 59.8	2.9%

Ages calculated relative Acs-2 at 1.1891 Ma (Niespolo et al., 2017) and the total ^{40}K decay constant of Renne et al. (2011). (1): Full external error. n/M: number of crystals retained in the age calculation over the number of analyzed crystals. F: Spreading factor of Jourdan et al. (2009). Values in bold indicate the ages considered for each volcano.

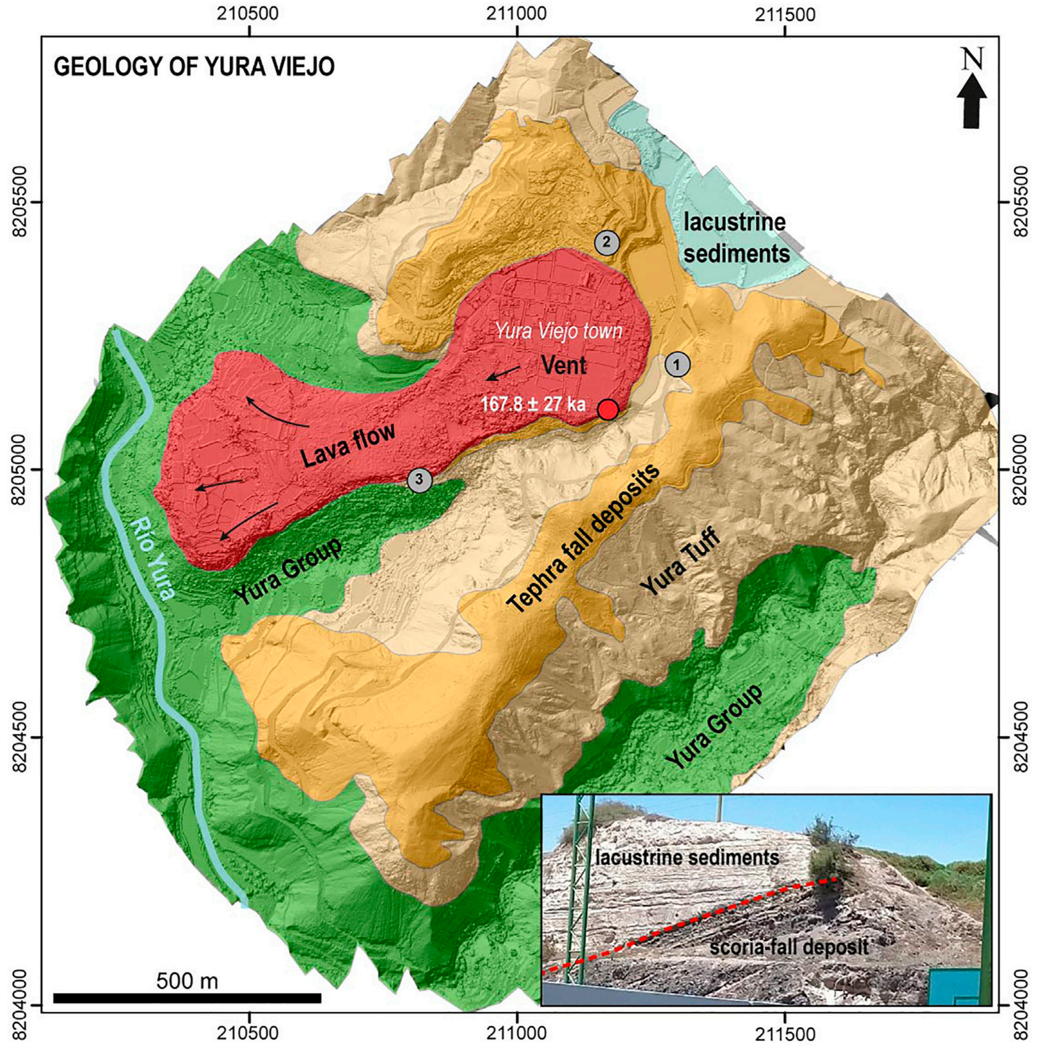

FIGURE 2
Geological map of the Yura Viejo volcano, embedded on a 60-cm resolution digital Elevation Model (DEM) map. Gray numbered dots indicate the location of stratigraphic sections shown in Figure 5. In the lower-right corner, a photograph of tephra fallout beds covered by lacustrine sediments.

distributed along ~10 km in a N130° direction, and two volcanic centers (El Chiral and Uyupampa) follow a N140° trend separated by 6 km, aligned with the Ayo-Lluta-Arequipa Fault. The Nicholson volcano is located near the northwestern limit of the Arequipa basin. Eruptive activity has been characterized by eruptions that generated scoria flows, pyroclastic fallout and lava flow emissions.

4.1.1 Yura Viejo

This volcano was built above Yura Tuff and Mesozoic sedimentary rocks of the Yura Group (Figure 2). The crater (~520 m diameter) is situated in the current location of the town of Yura Viejo, which is marked by a semi-circular structure opened to the southwest. The preserved deposits cover an area ~0.74 km^2 surrounding the emission center. Three stratigraphic columns in the crater ring allowed us to describe its eruptive history, which is characterized by a succession of pyroclastic (PDC) scoria flows, scoria fallouts and reworked ash layers, ending with a lava flow deposit (Figures 2, 3). The pyroclastic components are mainly the same in all of the deposits, distributed in different sizes and proportions.

In the eastern flank (Figure 3, profiles 1 and 2), the lower successions, up to 12.50 m thick (thickness from the surveyed profiles), directly overlie the Yura Tuff along an erosional surface, and form the basal part of the ejecta ring on the eastern flank. These successions are characterized by scoria flows (10–150 cm thick), interbedded with bombs and lapilli fallout (20–80 cm thick), and ash layers (2–18 cm thick).

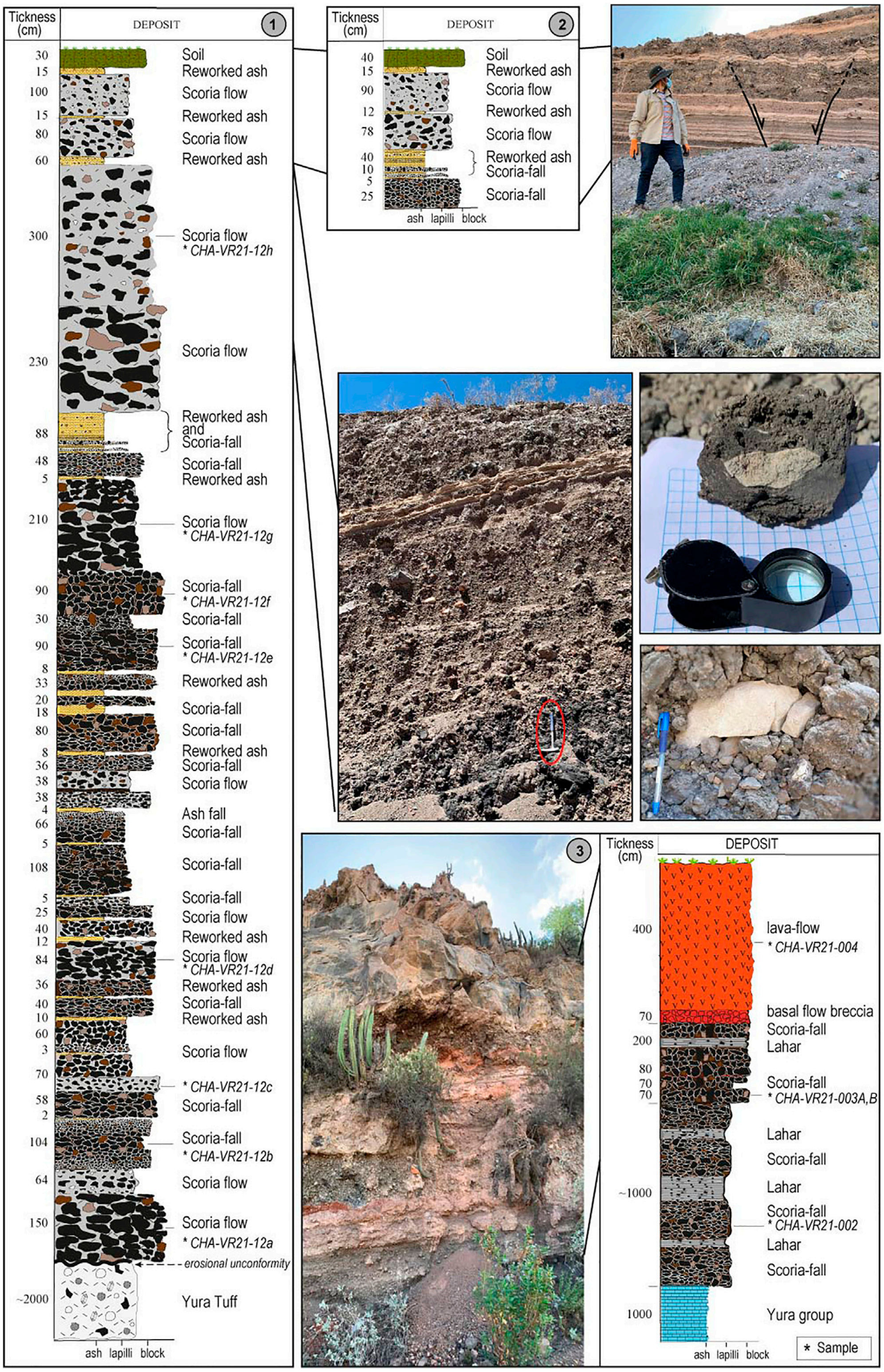

FIGURE 3
Stratigraphic sections described in outcrops of the Yura Viejo volcano. Photographs of outcrops of stratigraphic columns and the xenoliths included in the scoria blocks and fallout deposit. Black clasts in the deposits indicate the scoria, whereas the other colors indicate the lithics (sedimentary and rare ignimbrite lithics). The numbers (1, 2 and 3) indicate the location of the sections in Figure 2.

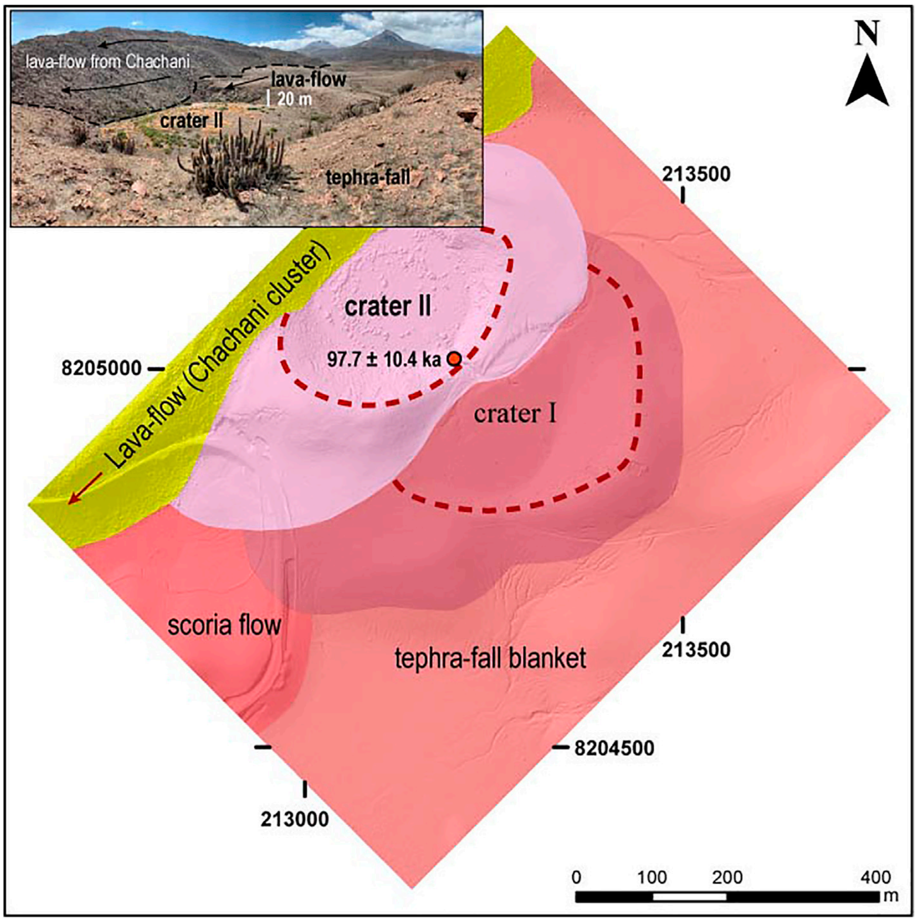

FIGURE 4
Geological map of Ccapua maar, embedded on a 60-cm resolution digital Elevation Model (DEM) map. On the upper-left corner, a photograph of crater II partially covered by a blocky lava flow from Chachani volcano cluster (Aguilar et al., 2022).

The scoria-flow deposits are composed of moderately to weakly indurated, unsorted, dark gray in color, and mostly clast-supported deposits. Sub-angular blocks (40–80%) are embedded in a medium-to-coarse ash matrix (20–60%). Juvenile clasts consist of scoria blocks (20–75%, 12–70 cm maximum size), dense lava blocks (<3%, <8 cm diameter), and bread-crust bombs (<2%, <200 cm diameter). Lithics are composed of quartz-sandstone, shale, and rare ignimbrite fragments (3–8%, 3–40 cm maximum size), which are found both included in scoria blocks (xenoliths) and loose fragments (Figure 3).

Block and lapilli fallout beds are moderately to well sorted, clast-supported, non-agglutinated, and have variable thicknesses (20–80 cm). The juvenile scoria of these layers are dark gray; the size of scoria fragments varies from 2 to 50 cm, and rare dense lava fragments (1–10 cm) are also found. The lithics are composed of quartz sandstone and shale from Yura Group, with variable maximum size (10–40 cm) and scarce ignimbrite fragments depending on the layer's thickness. These rocks are also incorporated as xenoliths in juvenile blocks. The ash layers are pinkish-gray in color, and have variable thickness in the log, from 2 to 18 cm in the lower layers, and up to 18 cm in the upper layers.

The upper succession is 11.60 m thick (from surveyed profiles), and consists predominantly of scoria flows, interbedded with ash-fall (mainly remobilized) and few block-and-lapilli fallout layers. The scoria flows are massive, unsorted, matrix-supported and dark gray deposits composed of blocks (30–40%) embedded in a fine matrix (60–70%). Blocks are scoria (22–30%, 15–60 cm maximum size), and quartz-sandstone and shale lithics (3–10%, 20–75 cm maximum size). Two block-fallout deposits are 48 cm and 90 cm thick respectively. Scoria blocks have maximum sizes of 7 and 50 cm, while sedimentary lithics are 20 cm in diameter. Ash fall layers are pinkish gray in color, moderately welded, and their thickness vary from 5 to 62 cm. Bread-crust scoria bombs reaching diameters up to 50 cm are found at ~1 km from the vent.

Described (successions) pyroclastic deposits in the eastern flank are not well-preserved in the southwestern flank (Figure 3, profile 3). However, scoria block fallouts interbedded with lahar flow deposits crop out over dark shale and sandstones strata from the Yura Group (Figures 2, 3) in a topographic low in this zone. Scoria-fall deposits are similar to those described above, whereas lahar flow deposits (1–2 m thick) are matrix-supported, compacted, pink and contain scoria fragments embedded in a muddy fine matrix. Superimposed on these deposits, a massive, dark-gray, a'a lava flow (~15 m thick) dated by ^{40}Ar/^{39}Ar at 167.8 ± 27.0 ka (Table 4) was emplaced filling a small valley oriented to the southwest, reaching a distance of ~1 km from the crater (Figure 2). This lava flow shows a brown basal breccia of <70 cm thick. This volcano was probably emplaced in an ancient riverbed, forming a dam where lacustrine sediments were accumulated. These sediments overlap the scoria-fall deposits in the northeastern side of the volcano (Figure 2).

Due to its resistance to erosion, the lava emitted by the Yura Viejo volcano is well preserved, and the ravine that previously existed in the area opened up on its sides, forming an elevated plateau (relief inversion process). On the other hand, the tephra generated by the explosions are readily eroded, and are currently found only in the upper part of the surrounding hills. Deposits of Yura Viejo are cut by NW-SE active faults, in areas close to the vent (Figure 3).

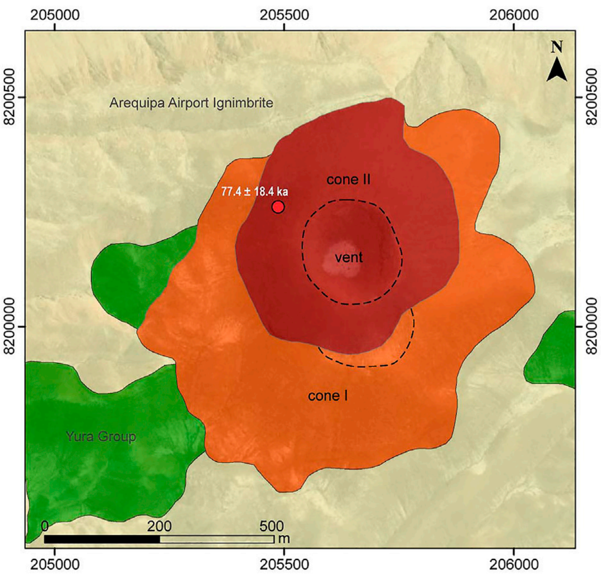

FIGURE 5
Geological map of Nicholson cone embedded on a Google Earth image.

4.1.2 Ccapua

This eruptive center (4.39 km^2) overlies the Arequipa Airport Ignimbrite. It is formed by two overlapping structures of low height, with two craters that lie below the surrounding ground level (Figure 4). The first emission center (crater I in Figure 4) has a cone basal diameter (Wco) of 640 m, the crater diameter (Wcr) reaches 360 m, and the average cone height (Hco) is 15 m, while the average flank slope is 6°. A basal deposit covering the ignimbrite is composed of scoria with mainly lapilli and scarce bombs (<1-m diameter), followed by a massive, unsorted, dark gray, and clast-supported (~70% blocks) deposit. The thickness of the ejecta ring is variable, with a major concentration in the southeastern flank.

The second emission center covers the northwestern half of the first crater, and is also partially covered on its northwestern edge by a blocky lava flow deposit (Uyu2) from the Chachani volcanic cluster (Uyupampa lava field; Aguilar et al., 2022). The Wco reaches 480 m, the Wcr is 320 m, the average Hco is 10 m, and the average flank slope is 10°. Lava flows and agglutinated scoria blocks form the rim of the crater (Figure 4). The base of the ejecta ring has moderately laminated layers of lapilli embedded in a whitish ash size matrix, overlain by a non-stratified deposit of dark red and black scoria blocks immersed in a medium to coarse brown ash matrix. The thickness of the uppermost scoria blocks deposit is irregular, and has its maximum value on the southwestern flank (~40 m). This last scoria deposit yielded a ^{40}Ar/^{39}Ar age of 97.7 ± 10.4 ka (Table 4). The floors of both craters are partially filled with fine sediments (sand and silt) suggesting the presence of water in the past. One km west of the craters, a ~20-m thick and dark-gray a'a lava flow crops out beneath tephra-fallout layers. The front and the upper surface of this lava flow is visible only along 120 m, making it difficult to determine the source vent. However, based on its proximity to the craters, the flow direction and the similarity in mineral content (mostly olivine phenocrysts) we assume that it was emitted from Ccapua volcano.

In addition, a massive deposit of dark brown and black scoria blocks and bombs embedded in a fine matrix was emplaced following a southwestern direction, and reaches distances as far as 2 km. This deposit has a maximum thickness of 60 m at 1.2 km from the vent. Ballistic bread-crust bombs attributed to Ccapua, mantle the Arequipa Airport Ignimbrite in the surrounding areas at distances as far as 2 km.

4.1.3 Nicholson

Nicholson volcano (1.42 km^2) was built at the southwestern edge of the Yura Monogenetic Field on a plain formed by the ~1.65 Ma Arequipa Airport Ignimbrite (Paquereau-Lebti et al., 2008; Figure 5), which is cut by the Yura River to the east. The volcanic edifice consists of two superimposed scoria cones. The older cone has a mean Wco of 540 m, Wcr of 200 m, Hco of 90 m, and average flank slope of 28°. The younger cone is located in the northern part, and its cone morphology is characterized by semi-circular outlines, with a very well defined circular shape crater. This cone has a 520 m Wco, 210 m Wcr, 75-m Hco, and 26° average flank slope. Both cones were built by massive accumulations of black to dark red, poorly welded, unsorted, and clast-supported deposits, lacking any internal bedding. The constituents of these deposits are reddish and dark scoria clasts

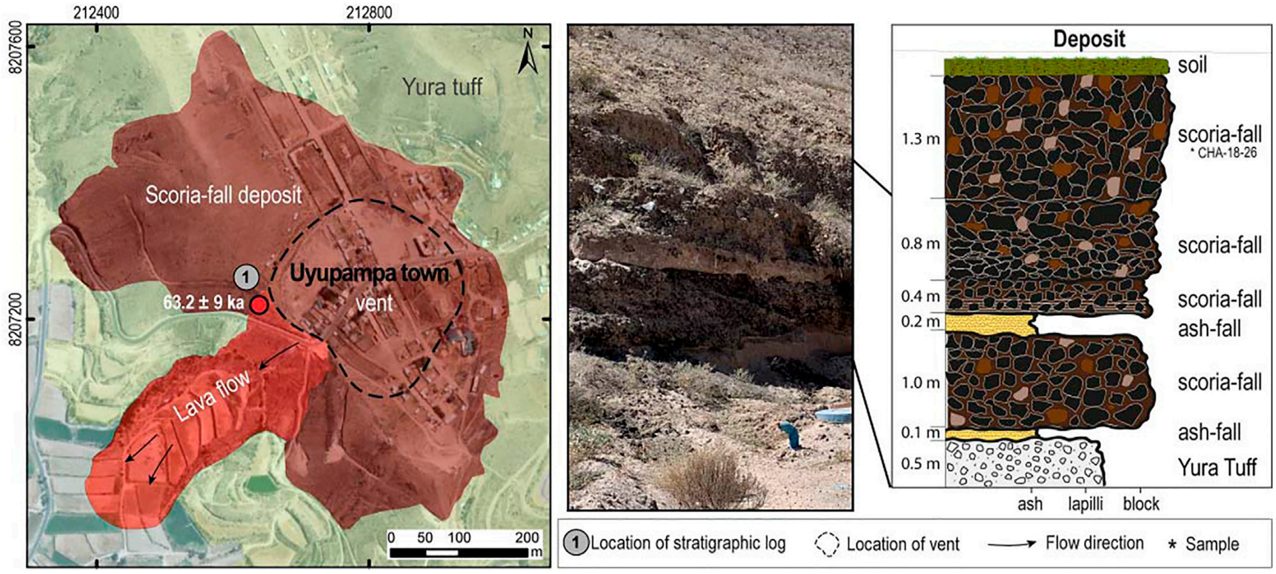

FIGURE 6
Geological map of Uyupampa volcano, showing a stratigraphic section and a picture of the outcrop where the section was described.

with lapilli to block sizes (<3-m diameter). Lava flow deposits border the northern and eastern side of the younger crater, while agglutinated blocks of scoria are found all around the crater rim. Ballistic fragments of ~30 cm can be found up to 900 m away from the vent. A scoria fall deposit of the younger cone was ^{40}Ar/^{39}Ar dated at 77.4 ± 18.4 ka (Table 4). In the lower part of the southeastern flank, 40–60 cm thick muddy and matrix-supported (50% of matrix) lahar deposits are observed, which incorporated angular scoria fragments (<10 cm in diameter). In most of its extension, Nicholson volcano is covered by a layer of reworked ash (~7–10 cm thick) from the 1600 B.P. eruption of Huaynaputina volcano, located 104 km to the southeast (e.g., Japura, 2018; Prival et al., 2020).

4.1.4 Uyupampa

Uyupampa volcano overlies the Yura Tuff, and its deposits cover 0.30 km^2. This volcanic center seems to be strongly eroded and its deposits were used as quarries for housing construction. However, a semicircular structure of ~300 m diameter is found in the present location of the town of Uyupampa, which may indicate the crater of the volcanic center. It is important to note that this monogenetic volcano is not related to the younger “Uyupampa lava-field” (blocky lavas) belonging to the Chachani Volcano Cluster (e.g., Aguilar et al., 2022) cropping out to the left side of La Paccha ravine (Figure 1).

The basal deposits of Uyupampa monogenetic volcano were emplaced over the Yura Tuff (Figure 6), and consist of pinkish ash layers (10–20 cm thick) interbedded with dark gray, moderately sorted scoria blocks/bombs - lapilli (35–130 cm thick) fallout deposits. At ~120 m east of the crater, pinkish ash-fall layers with scarce scoria fragments (<10 cm diameter) grade to unsorted, clast-supported, brown-black scoria block/bomb fallout deposits (up to 70 cm size and 95% blocks). These layers are overlain by diffusely laminated and dark gray scoria and lithic ash-lapilli layers. The upper units consist of an accumulation of unsorted, clast-supported, brown and black scoria block/bombs layers. Most of the pyroclastic deposits contain bread-crust and cauliflower texture bombs that reach up to 100 cm in diameter (at 300 m from the crater). Scoria bombs and other tephra fall deposits have quartz-sandstone and shale xenoliths and loose clasts (<30 cm).

The eruptive activity of this volcanic center culminated with the emplacement of a massive, olivine-rich a’a lava flow dated by ^{40}Ar/^{39}Ar method at 63.2 ± 9.0 ka (Table 4) which reached up to 500 m from the vent, following a southwest topographic low (Figure 6).

4.1.5 El Chiral

This volcanic unit was emplaced near the Ayo-Lluta-Arequipa Fault, covering 1.54 km^2. It is formed by a lobular-shaped lava dome (Figure 7), which is cut by a ~50-m thick and ~1.60 km long lava flow deposit. This lava flow fills a small NE-SW depression where volcanic deposits of the Tacaza Group and quartz sandstones (Hualhuani Formation) of the Yura Group crop out. The geoforms of the vent and lava bodies of El Chiral suggest a cylindrical shape conduit, and emplacement of the lava in a gently inclined topography (e.g., Murcia and Németh, 2020).

4.1.6 Patacocha

This eruptive center (~0.45 km^2) shows an irregularly shaped and complex edifice formed by two coalescing cones and three

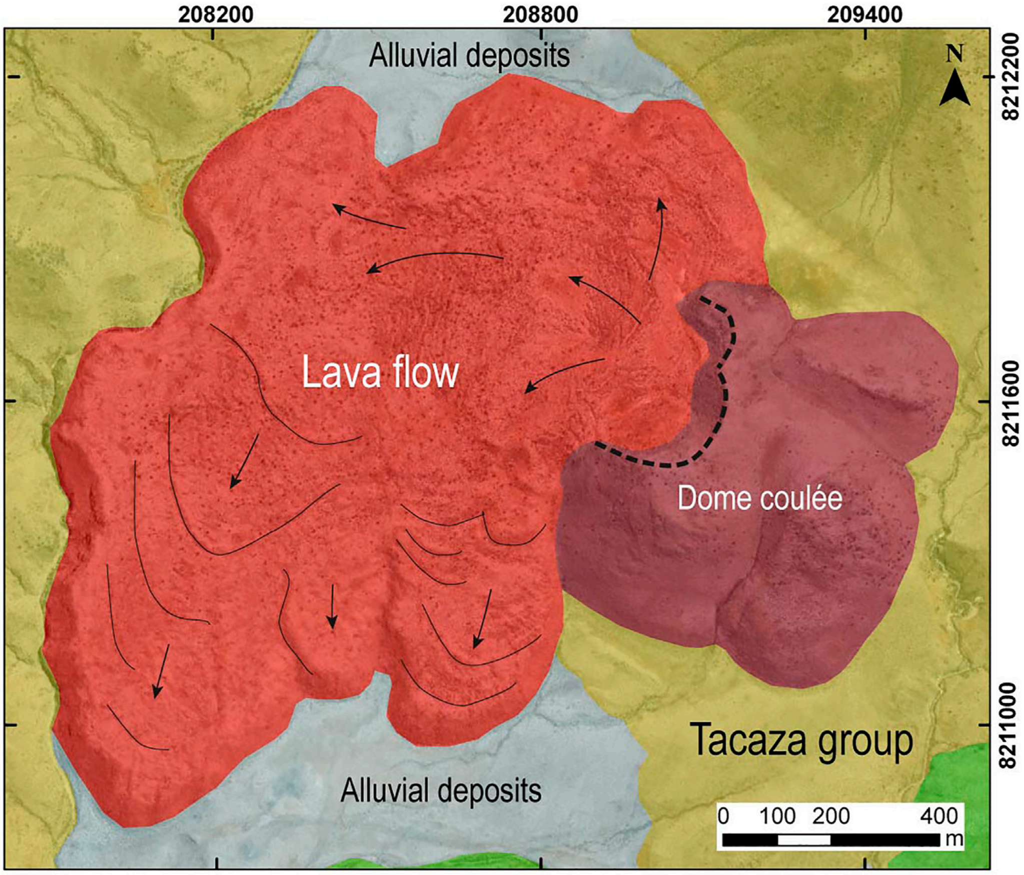

FIGURE 7
Geological map of El Chiral volcanic center, showing two units of dome coulée and lava flow deposits.

craters. The northwestern cone is capped by two coalescing craters (craters II and III), whereas the southeastern cone (crater I) has only one crater (Figure 8). Using Google Earth images and GIS software, we estimated the morphological parameters of the two cones: 1) Wco of 420 m, Wcr of 220 m, Hco of 24 m, and average flank slope of 14° for the northwestern cone. The smaller crater of 80-m diameter cuts the first larger crater. 2) Wco of 380 m, Wcr of 135 m, Hco of 40 m, and the average flank slope is 18° for the southeastern cone. The material expelled by this volcano covers deposits of the Tacaza Group, and apparently closed the channel of a stream, causing the damming of water and the formation of a lagoon called Patacocha (highland lagoon in Quechua). Due to the difficulty in accessing this area, it was not possible to take samples for laboratory analysis.

4.2 Volcano-structural setting

The local tectonic setting in which the Yura Monogenetic Field was emplaced consists of four groups of faults: N130°, N160°, N80° and N20°. This configuration is similar to the nearby Chachani volcano cluster described by Aguilar et al. (2022).

1) On satellite images, a N130° oriented lineament cuts the Potrero-Airport domes and coincides with the collapse scar of the middle unit of this group of domes (Aguilar et al., 2022). The N120°-130° faults extend to the east of the city of Arequipa and offset pyroclastic deposits at the base of El Misti volcano (Upper Pleistocene) in the Chiguata zone (Thouret et al., 2001). Another remarkable fault is the dextral and normal fault that cuts across the western flank of El Misti volcano (Thouret et al., 2001) and extends towards the east flank of Estribo stratovolcano with a N130° orientation.
2) At a regional scale, N120°-130° and N160° faults and lineaments display an *en-echelon* fault system, which extends to El Misti stratocone and Pichu-Pichu volcanic complex. In the eastern central part of the Chachani volcanic cluster, this system cuts these edifices. The orientation of these lineaments is probably controlled by perpendicular N80° faults.

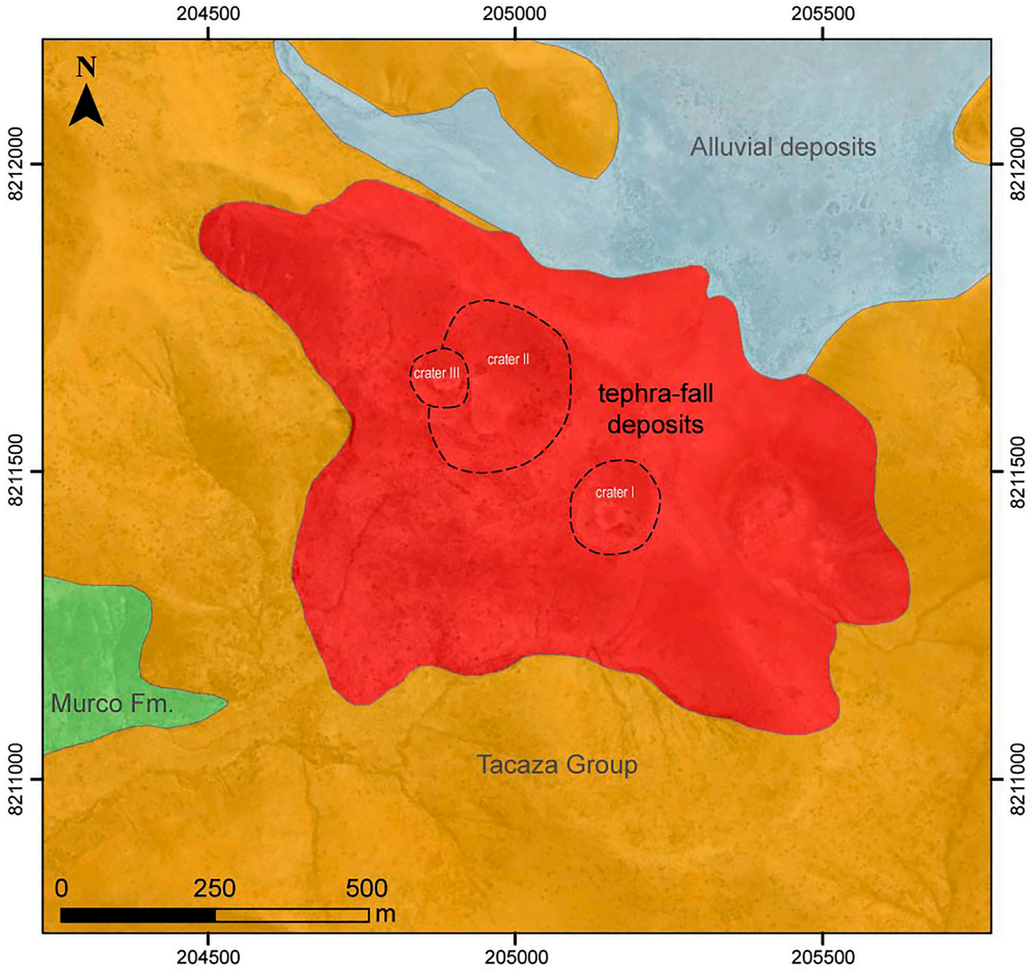

FIGURE 8
Geological map of Patacocha volcano, showing at least three identified vents.

3) A group of long faults and lineaments (~20 km), with a prevailing N80° direction, allow us to define a NE-SW structure which delimits the northwestern edge of the Arequipa basin (Mering et al., 1996; Thouret et al., 2001; Benavente et al., 2017). This fault intersects the Ayo-Lluta-Arequipa Fault (~N130° strike-slip and normal fault; Figure 1B).
4) Finally, the last group of short lineaments follows a N20-40° direction observed in the southern sector of the Chachani volcanic cluster. A remarkable feature in this area is the N20-40° predominant orientation of the majority of small eruptive vents, which have built the voluminous Airport-Potrero dome coulées. Uyupampa and Yura Viejo volcanoes in the Yura Monogenetic Field follow a similar trend.

The extensional zone along N80°- and N135°-trending faults is associated with fissures that allow the ascent of magmas to the surface (e.g., Huaman-Rodrigo et al., 1993). Magnetic measurement data for Nicholson volcano identified two E-W trending tabular bodies beneath the edifice, suggesting dyke-shaped feeding conduits (Rivera, 2021). E-W lineaments are also observed between Ccapua and Yura Viejo Volcanoes, and El Chiral and Patacocha volcanoes. Uyupampa and Yura Viejo volcanoes are aligned following a N40° trend. In the southwestern flank of Chachani, several small vents are also aligned along N10° and N40° eruptive fissures (Aguilar et al., 2022).

The N130° and N80° structures that we identified in the Yura Monogenetic Field and Chachani Volcano Cluster resemble those described by Huaman-Rodrigo et al. (1993) in the region of the Río Colca - Nevado Ampato-Sabancaya volcano, located about 50 km northwest of Yura (Maca and Huambo faults). In the area near Huambo NW of Yura, and in the northern flank of Chachani Volcano Cluster, N80° normal faults (Huaman-Rodrigo et al., 1993; Sempere and Jacay, 2006; Aguilar et al., 2022) are considered active because they cut recent

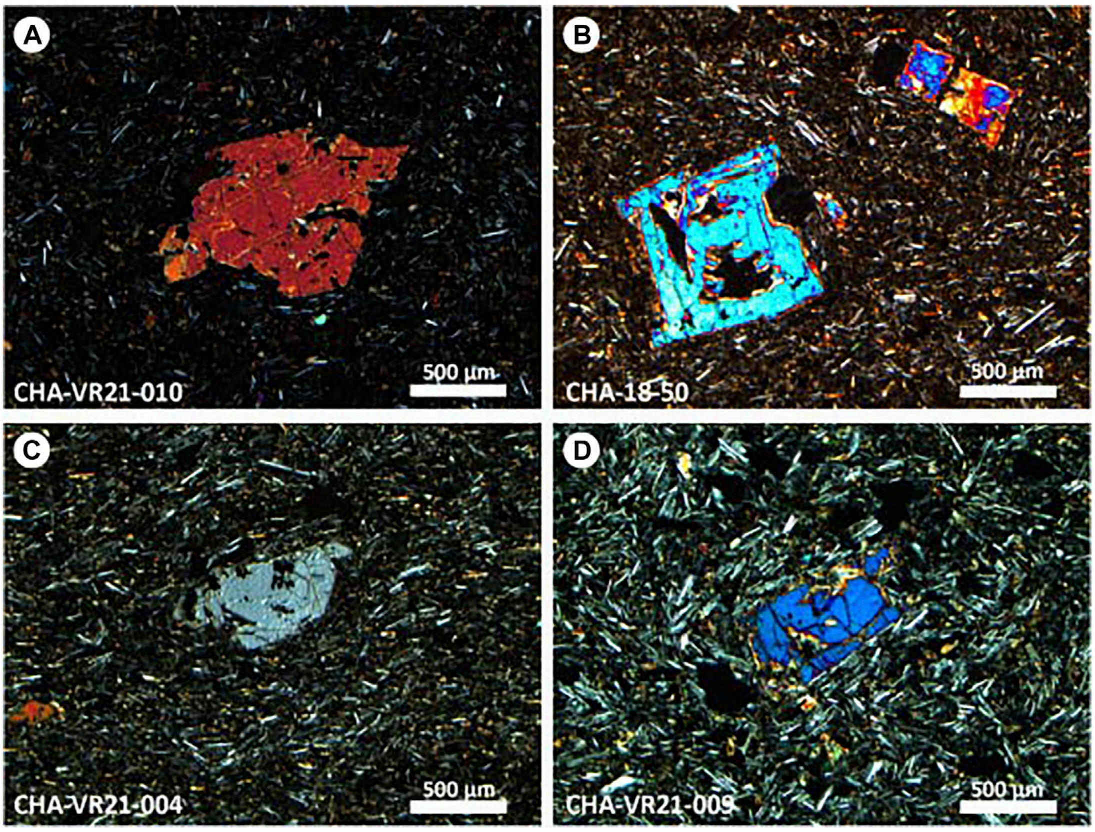

FIGURE 9
Observed textures in thin sections of the Yura monogenetic volcanoes. Olivine phenocryst is a ubiquitous mineral phase in all analyzed samples. **(A)** Subhedral olivine phenocryst in microlithic groundmass from Nicholson cone; **(B)** Skeletal texture observed in olivine in sample from Ccapua volcano; **(C)** Olivine phenocryst in microlithic groundmass in Yura Viejo volcano rocks; **(D)** Subhedral olivine phenocryst in Uyupampa lavas.

Late Pleistocene lava flows and Holocene colluvial deposits. A destructive earthquake took place on one of them at Maca, on the left bank of the Río Colca canyon in 1992 (e.g., Antayhua et al., 2001). Other similar events occurred in August 2016 and March 2022, damaging houses and infrastructure.

5 Petrography and geochemistry

5.1 Modal mineralogy

The mineral content of all analyzed samples from the volcanic centers of Yura Monogenetic Field is similar (Figure 9 and Table 2). All analyzed samples are porphyritic (7–10 vol%) and vesicular. In all samples, the dominant mineral is olivine, while the groundmass contains ortho- and clinopyroxene, plagioclase and glass.

Olivine (7–10 vol%; ≤2 mm) occurs as subhedral phenocrysts with subrounded and embayed edges. In some cases, it has skeletal and breakdown textures (Figure 9). Pyroxene is present only in the groundmass (20–42 vol%; <400 μm; clinopyroxene > orthopyroxene) together with plagioclase microlites (26–53 vol %; <300 μm), giving the matrix a pilotaxitic texture by almost all samples (Table 2). Volcanic glass (<5 vol%) is found encompassing the microlites. The opaque minerals (<5 vol%; <800 μm) present anhedral and subhedral forms, and occur as accessory minerals as inclusions in olivine, or as replacement in crystal molds and disseminated in the groundmass (Table 2). The vesicles (5–29 vol %) have irregular shapes.

5.2 Whole-rock major and trace element chemistry

Analyzed samples are given in Table 3. The scoria and lavas consist of high-K (1.60–2.01 wt% K_2O) calc-alkaline rocks, which is a typical characteristic of the modern volcanic arcs in the Central Volcanic Zone (e.g., Wilson, 1986). Basaltic-andesite is an ubiquitous composition throughout the entire volcanic field, ranging from 50.9 to 55.6 wt% SiO_2 (Peccerillo and Taylor, 1976;

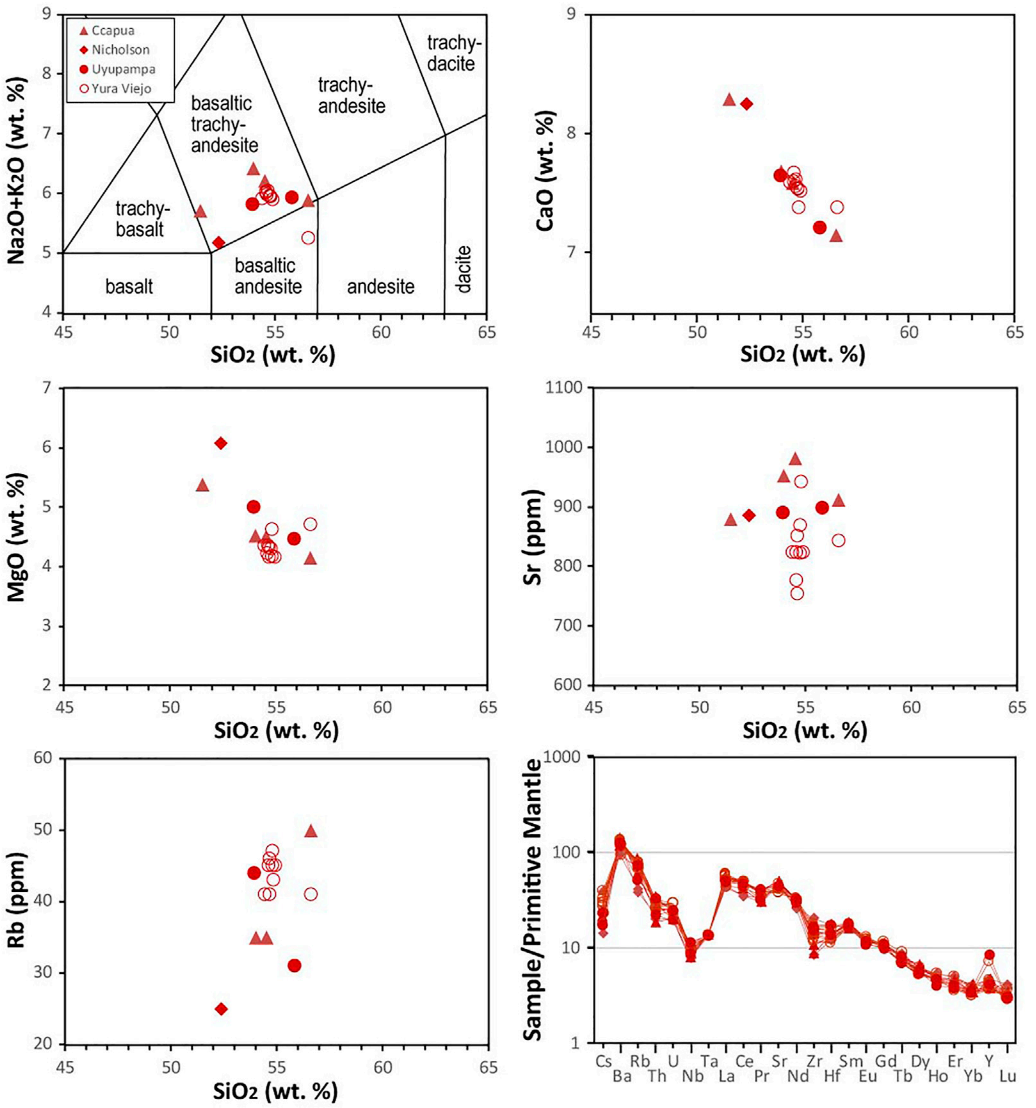

FIGURE 10
Chemical composition of Yura monogenetic volcanoes. Total Alkali-Silica versus SiO_2 diagram (Le Bas et al., 1986) showing the classification of Nicholson, Ccapua, Yura Viejo and Uyupampa volcanoes. Major oxides are shown as recalculated volatile-free values. Ca, MgO, Sr, and Rb versus SiO_2 diagrams show the compositional variation. Multi-element diagrams normalized to primitive mantle (Sun and McDonough, 1989) showing trace element patterns of rock samples.

Figure 10). The least differentiated olivine-rich samples are found in the Ccapua and Nicholson volcanic centers. In Harker diagrams, some of which are shown in Figure 10, MgO, CaO, Fe_2O_3 contents show negative correlation with SiO_2 indicating a common differentiation trend. Similarly, transition elements (e.g., Ni, Cr, V) and Dy are negatively correlated to SiO_2 suggesting that fractional crystallization is the major differentiation process in these magmas. Most incompatible elements such as Rb, U and Th together with Sm are positively correlated with increasing SiO_2.

A multi-element diagram normalized to primitive mantle (Sun and McDonough, 1989; Figure 10) displays a similar pattern for all analyzed samples: enrichment in LILE (Cs, Rb, Ba, Sr) relative to HFSE (Nb, Ta). The patterns for scoria and lavas from Yura Monogenetic Field are similar to those observed for other monogenetic volcanoes in the region such as Andahua-Huambo-Orcopampa (e.g., Delacour et al., 2007; Mamani et al., 2010; Galas, 2011) and for Central Volcanic Zone rocks (e.g., Wilson, 1986; Davidson et al., 1991; Stern, 2004).

TABLE 5 Summary of characteristics and morphologic parameter for volcanic centers in the Yura Monogenetic Field.

Volcano name	Volcano-sedimentary process	Typical deposits	Morphology parameters					Observations	Eruption style	Classification
			Wco (m)	Wcr (m)	Hco (m)	Wcr/ Wco	Hco/ Wco			
Nicholson	Proximal fallout and ballistics, rootless lava flow	Ash to block accumulation in the flanks, tephra blanket in the distal areas	Cone I: 616 Cone II: 520	200 210	90 75	0.32 0.40	0.15 0.14	vent migration	Strombolian	Scoria cone
Ccapua	Fallout from eruptive column, PDC, lava flow, ballistics	Ash to block/ bomb, agglutinated scoria in the ejecta ring	Crater I: 640 Crater II: 480	360 320	~15 ~10	0.56 0.67	0.02 0.02	vent migration, crater filled with post-eruption sediments	Phreatomagmatic - Strombolian	Maar
Yura Viejo	Fallout from eruptive column, PDC, ballistics. Lava flow, lahar flow	Ash to block/ bomb beds in the ejecta ring, tephra blanket in distal areas	~800	520	~25	0.65	0.03	lava infill the crater, relief inversion. Crater below the surrounding surface	Phreatomagmatic - Strombolian	Maar (?)
Uyupampa	Fallout from eruptive column, PDC, ballistics. Lava flow	Ash to block/ bomb beds in the ejecta ring, bread-crust and cauliflower bombs	~510	~300	-	-	-	tephra blanket in distal areas	Phreatomagmatic - Strombolian	Tuff ring/ Maar (?)
Patacocha	Fallout from eruptive column (?)	Tephra fallout	Cone I: 380 Cone II: 420	135 220	~40 ~24	0.36 0.52	0.11 0.05	accumulation of tephra dammed the ravine forming the Patacocha lagoon	no information	Scoria cone
El Chiral	lava flow	Lava rock	Dome coulée: length: 420 m, width: 265 m, thickness: ~105 m Lava flow: length: 1600 m, thickness ~50						Effusive	Dome coulée and lava flow

Wco, cone basal diameter; **Wcr**, crater diameter; **Hco**, cone height.

6 Discussion

6.1 Eruptive style and classification of volcanoes in the yura monogenetic field

At monogenetic volcanoes, the internal magma dynamics that occurs at shallow depths and the characteristics (form and dimension) of the conduit are linked to the way that magma is released at the surface, and the volcanic edifice construction (Murcia and Németh, 2020, and references therein). The topography where the magma is deposited also plays a role in the geoform of the volcano. The eruptive activity forming the monogenetic volcanoes usually consist of magmatic or phreatomagmatic explosions and in many cases accompanied by effusive emissions (Németh and Kereszturi, 2015). Field observations and description of the deposits in the Yura Monogenetic Field allow us to suggest: 1) Nicholson (and probably Patacocha) volcanoes were built by Strombolian (magmatic) eruptions. 2) Ccapua, Yura Viejo and Uyupampa volcanoes show ash to block particle sizes embedded in a muddy matrix, which suggests the interaction between magma and water, generating phreatomagmatic eruptions. However, accumulation of mainly scoria blocks/bombs and lava flows suggests Strombolian eruption phases. 3) El Chiral is composed of lava flows and coulées. Due to the lack of field data, it is not possible to characterize the type of eruption, although it was probably mainly effusive.

Basic measurements of morphometric parameters such as the cone basal diameter (Wco), crater diameter (Wcr) and cone height (Hco) allow obtaining morphometric signatures for classification of monogenetic volcanoes (e.g., Wood, 1979; Németh and Kereszturi, 2015). This classification includes spatter cones (Wco = 0.08 km, Wcr/Wco = 0.36 km and Hco/Wco = 0.22 km), scoria/cinder cones (Wco = 0.8 km, Wcr/Wco = 0.4 km and Hco/Wco = 0.18 km), as well as maars and tuff rings (Wco = 1.38 km, Wcr/Wco = 0.6 km and Hco/Wco = 0.02 km) from average dimensions (Wood, 1979). Based on characterization parameters described by Németh and

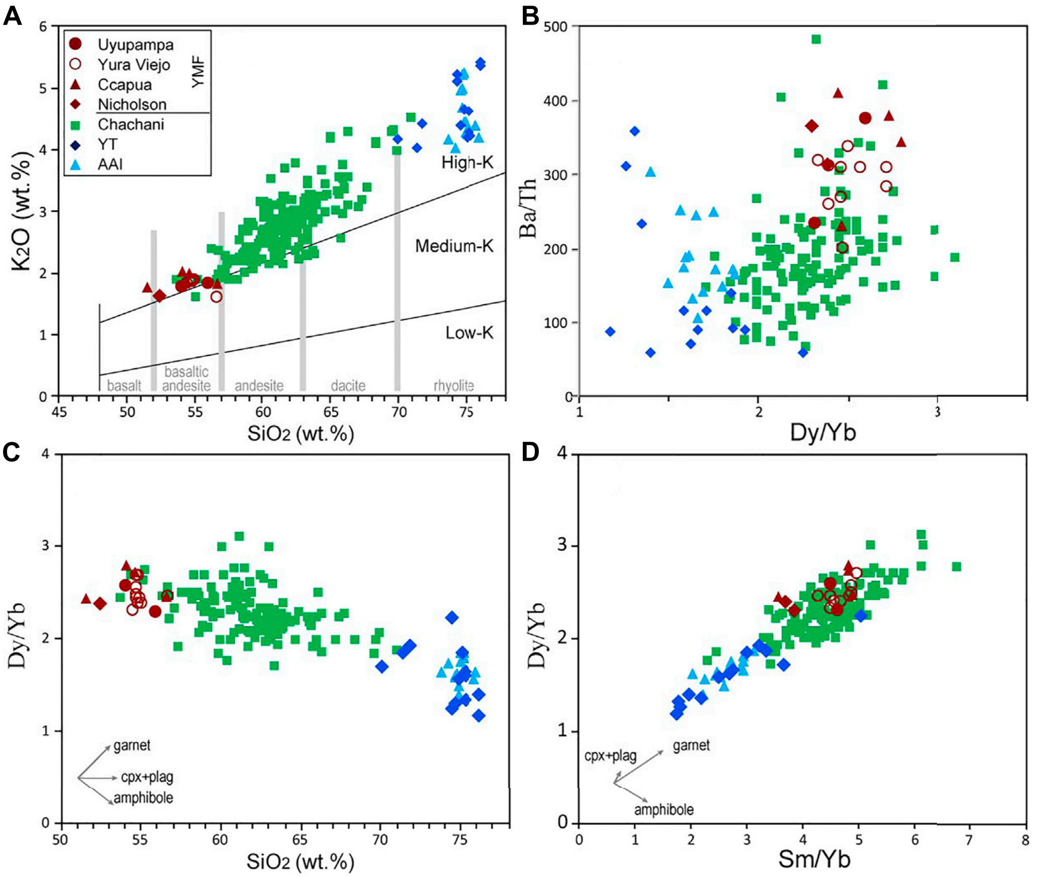

FIGURE 11
SiO_2 versus K_2O diagram (after Peccerillo and Taylor, 1976; **(A)**, and trace element signatures **(B, C, D)** in the Yura Monogenetic Field rocks for the purpose of comparison with available datasets of nearby Yura Tuff, Arequipa Airport Ignimbrite and Chachani volcanic Cluster (Paquereau-Lebti et al., 2006; Mamani et al., 2010; Aguilar et al., 2022). The inset trends of evolution in **(C)** and **(D)** were taken from Wörner et al. (2018). Cpx: clinopyroxene, plag: plagioclase.

Kereszturi (2015), and Wood (1979), we suggest that the eruptive activity in the study area produced scoria cones (Nicholson and Patacocha), maars (Ccapua, Yura Viejo and Uyupampa), and a dome coulée and lava flow (El Chiral). A summary of the main characteristics and morphologic parameters is presented in Table 5.

6.2 Chemical comparison with surrounding volcanoes

Figure 11 shows the comparison of Yura Monogenetic Field with surrounding Pleistocene volcanic rocks. Major element oxides show similar patterns among Yura Field, Chachani cluster, Yura Tuff and Arequipa Airport Ignimbrite. The Yura Field samples are the least differentiated magmas in the Arequipa basin; only some lava and scoria samples from the Chachani cluster exhibit similar composition. The Chachani volcanic cluster shows an intermediate and wider compositional range from basaltic andesite to rhyolite (54–71 SiO_2 wt%). The most differentiated samples belong to the Arequipa Airport Ignimbrite, which has a homogeneous silica content (74–76 SiO_2 wt%; Paquereau-Lebti et al., 2006). The Yura Tuff also shows highly differentiated compositions, but with a less homogeneous silica content (70–76 SiO_2 wt%).

Incompatible-element ratios such as Ba/Th vs. Dy/Yb and Dy/Y vs. Sm/Yb (Figure 11) exhibit overlapping fields with higher values in Ba/Th and Dy/Yb in the Yura Monogenetic Field and Chachani cluster. By contrast, the more evolved magmas of Arequipa Airport Ignimbrite and Yura Tuff show lower Dy/Yb and Sm/Yb values.

Due to the proximity of their sources, magmas generating the ignimbrites, the Chachani cluster and the Yura Monogenetic Field, could have a similar source and have passed through a similar substrate in their way to the surface, so they would have similar contaminants (e.g., sedimentary rocks of the Yura

Group). However, the abundance of xenoliths and subangular bedrock fragments found in the Yura Monogenetic Field deposits indicate that the assimilation process was much less effective in them. These monogenetic rocks and less differentiated lavas from Chachani cluster show similar basaltic-andesite compositional patterns (Figure 11). In general, rocks from the Yura Monogenetic Field may represent the mafic end-member of the Pleistocene-Holocene volcanic products in the Arequipa basin and surrounding areas (e.g., Aguilar et al., 2022). At a regional scale, these magmas show one of the least differentiated magmas in the Central Volcanic Zone (e.g., Delacour et al., 2007; Mamani et al., 2010; Torres et al., 2020).

6.3 Chronology of monogenetic volcanism in the yura valley

Magmatic activity in the Arequipa region occurred continuously during the Pleistocene. The Arequipa Airport Ignimbrite marks a moderate to large magnitude explosive event (~18 km^3) that occurred *c.* 1.65 Ma (Paquereau-Lebti et al., 2006). This event emplaced pyroclastic density currents that filled the Arequipa depression, and caused the formation of a possible caldera (García et al., 1997). The geographic location of the ignimbrite source is likely covered by the edifices composing the Chachani volcano cluster (Paquereau-Lebti et al., 2006, 2008; Aguilar et al., 2022). After caldera formation, andesitic lava flows were emplaced in the western edge of Chachani, with outcrops now located in the Quebrada La Paccha (Figure 1). Yura Tuff (*c.* 1.28 Ma; Paquereau-Lebti et al., 2006) overlies those lavas and fills the Yura valley (formed between the current northwestern side of Chachani and the wall formed by Yura Group units; Figure 1). The Chachani volcanic cluster started its activity at ~1.01 Ma on the northeastern side, having recorded continuous activity until *c.* 641.8 ka with a possible hiatus that lasted until *c.* 463 ka. After *c.* 463 ka, the eruptive activity migrated to the central and southern part of the whole cluster (Aguilar et al., 2022). Towards the lower western flank of Chachani volcanic cluster and covering ignimbrite deposits, the Uyupampa lava field is composed of porphyritic lava flows, one of which yield an age of *c.* 232 ka. The youngest dated rock in the Chachani Volcanic Cluster belong to a block-and-ash deposit from Cabreria dome (*c.* 56.5 ka; Aguilar et al., 2022).

The oldest lithological units, on which the volcanoes of the Yura Monogenetic Field (e.g., El Chiral and Patacocha) were emplaced, belong to the Tacaza Group (*c.* 30–24 Ma; e.g., Mamani et al., 2010) in the northwestern sector of the field. However, the degree of preservation of volcanic structures such as the craters (cones), lobes and ridges (lava flows) suggests that Patacocha and El Chiral are much younger than c. 24 Ma. The ages obtained for the Yura Viejo, Ccapua, Nicholson and Uyupampa volcanoes match the stratigraphy of the area since they cover older deposits of the Arequipa Airport Ignimbrite and the Yura Tuff. The *c.* 168 ka age of Yura Viejo is in accordance with the degree of preservation of its deposits. Nicholson and Ccapua volcanoes were built over deposits of the Arequipa Airport Ignimbrite, while the Uyupampa and Yura Viejo volcanoes directly overlie the Yura Tuff. Based on the degree of preservation of the Patacocha scoria cones and El Chiral lava flow-dome coulée, we suggest that these volcanoes are relatively contemporaneous to the dated ones. Thus, the Yura Monogenetic Field would have been active in a time window of 141 kyr, between *c.* 195 ka and *c.* 54 ka. We note that this range of ages is younger than expected since the second crater of Ccapua volcano was partially covered by a lava flow from the Uyupampa field (Chachani volcanic cluster, Figure 1). Detailed fieldwork however, allowed us to determine that Ccapua was formed after the emplacement of the lava flow (Uyu1) dated by ^{40}Ar/^{39}Ar at 231.7 ± 36.2 (on groundmass; Aguilar et al., 2022), and was later covered by another lava flow (Uyu2) which should be younger than 97.7 ± 10.4 ka. The new ages obtained allow us to suggest that the eruptive activity of the Yura Monogenetic Field temporally coincided with the youngest edifices of Chachani volcanic cluster (Aguilar et al., 2022) and the basal units of the Misti composite cone (≤112 ka; Thouret et al., 2001). Future radiometric dating of the volcanic products from Patacocha and El Chiral are necessary to better constrain the age and duration of the magmatism in this monogenetic field.

6.4 Yura monogenetic field as potential geosite for education and awareness of volcanic hazards

Recent volcanic activity in southern Peru has caused significant impacts to the population and economic activity for the communities settled in surrounding areas. Recent volcanic eruptions of the Ubinas volcano (2006–2009, 2014–2017 and 2019) have affected agriculture, critical infrastructure, and forced authorities to evacuate the people to shelters in safe areas (e.g., Rivera et al., 2010). The Sabancaya volcano began a new long-lasting vulcanian eruption process in 2016, and continues to this day, with no signs of ending in the near future. The ash emitted by frequent explosions of Sabancaya have caused damage to agriculture, livestock, and has even affected air traffic in the city of Arequipa (e.g., Aguilar, 2019; INGEMMET, 2021). In addition, during rainy seasons, the occurrence of lahars in the ravines that descend from the Misti and Chachani volcanoes has caused the destruction of homes, damage to basic infrastructure, and casualties (e.g., Rivera et al., 2018). These events remind us that volcanic eruptions and associated processes can negatively impact the development of communities; therefore, it is necessary that the population and decision-makers develop measures to reduce the impact of these hazards. According to the record of eruptive activity, the hazards related to monogenetic volcanoes in the Yura Monogenetic Field are tephra-fall, ballistic fall, scoria flow, lava flow and lahar. Thus, the study of structures and deposits of the Yura Monogenetic Field can allow the identification of potential geosites for scientific, educational and geoturism uses and related to volcanic hazards. Nicholson is an easily accessible volcano to explain Strombolian eruptions and the formation of scoria cones. Ccapua volcano clearly shows the superposition of two craters and the formation of a maar which is partially covered by a younger lava flow. The Yura Viejo volcano shows explosive Strombolian-type activity combined with lahar flows, culminating with the emplacement of a lava flow. In addition, outcrops of ignimbrites that represent violent explosive eruptions can be seen in the area, as well as very representative sequences of sedimentary rocks of the Yura Group. The small monogenetic volcanoes also provide superb views of the surrounding larger volcanoes, and this, combined with their accessible outcrops and clear geology, provides an especially rich educational and geotouristic resource. This is especially important for communicating and understanding hazards and risk, as the urban centers and human infrastructure are visible in the landscape. In recently published press releases, it was indicated that the town of Yura Viejo is located in the crater of an extinct monogenetic volcano. This information was well-received by the local inhabitants and has attracted the attention of visitors, whose flow is increasing, not only to Yura Viejo, but also to the nearby Ccapua waterfalls (La Paccha ravine near Ccapua maar; Figure 1).

Due to its proximity to the urban area of Arequipa, and the good preservation of its deposits, the Yura Monogenetic Field has a great potential to promote geotourism for recreational, scientific and educational purposes in the face of the volcanic hazards (e.g., Galas et al., 2018; Arias et al., 2021). The valorization of these geosites could help in the popularization of these places and above all in their preservation by using an information simple to understand. There are examples of monogenetic fields that are growing tourist attractions, such as the Andagua monogenetic volcanoes (e.g. Galas et al., 2018), which are located within the Peruvian “Colca and Andagua Volcanoes” UNESCO Global Geopark. Other geosites are La Garrotxa monogenetic field in Spain (e.g., Planagumà-Guàrdia et al., 2022), and the Chaine de Puys in Clermont-Ferrand, France (e.g. Vereb et al., 2020).

7 Concluding remarks

The study of the eruptive history of monogenetic volcanic centers is useful to define the sequence of events and the dynamics of the eruptions that built these volcanic edifices. Such volcanoes are key for understanding the geological evolution of an area, as they reflect the magma dynamics, the tectonics and the subsequent surface processes. Therefore, the combination of volcanic stratigraphy, geochemical and petrographic studies of volcanic activity in the Yura Monogenetic Field is important to better understand the evolution of volcanism in southern Peru. The study of the deposits has allowed us to reconstruct the history of this monogenetic field emplaced after medium-size ignimbrites formation in the Arequipa tectonic depression. Our new data suggest that volcanism in the Yura Monogenetic Field was active between *c.* 195 ka and *c.* 54 ka, which is more recent than previously expected (*c.* 1278 ka–*c.* 232 ka). The stratigraphic position and the degree of preservation of cone craters, lobes and ridges in lava flow/coulées indicate that El Chiral and Patacocha are much younger than Tacaza Group (Oligocene) as they cover volcanic units assigned to this group (Figure 1). However, due to their geographical proximity, similarity in their petrographic and chemical characteristics these volcanoes are contemporaneous to the dated ones. Hence, the volcanism in the area lasted for ~141 ka, beginning with the Yura Viejo volcano and probably finishing with Uyupampa volcano.

Bulk-rock major and trace elements highlight the fact that compositions have not varied with the locations of vents along the monogenetic field. These volcanic centers have relatively homogeneous basaltic-andesite compositions (50.9–55.6 wt% SiO_2), being among the least differentiated Quaternary rocks in the surrounding areas of the Arequipa basin. The dynamic of eruptions is marked by Strombolian and phreatomagmatic explosive activity, combined with scattered lava flows and small pyroclastic density current deposits (scoria flows). In most of the volcanoes, scoria flows including glassy bread-crust and cauliflower bombs suggest phreatomagmatic activity that crop out together with lahar deposits.

The Yura Viejo volcano shows one of the most complex histories in the Yura Monogenetic Field. The observed deposits indicate that its activity began with phreatomagmatic evolving to Strombolian eruptions, which expelled rock fragments (tephra) up to 1 km away from the crater. Subsequently, it generated a lava flow that was emplaced in a small gorge reaching a distance of ~1 km towards the current Yura River, ending its eruptive activity.

This contribution has revealed the presence of a monogenetic field in the northwestern edge of the Arequipa basin by locating, studying and dating unknown volcanic centers. The results obtained provide important information to improve the knowledge of recent volcanic activity in the Arequipa region, which is relevant for volcanic hazard assessment and related risk management. This information could be also useful for the knowledge of the territory and identification of geosites, promote their conservation and propose new areas for education about geohazards and risk.

Data availability statement

The original contributions presented in the study are included in the article/Supplementary Material, further inquiries can be directed to the corresponding author.

Author contributions

RA, DA and NM worked in the conception, design of the study, and drafted the original manuscript. The first three authors together with BV, carried out the fieldwork and mapping. KC and ET worked in photogrammetry for high-resolution images. HG and VS prepared the samples, analyzed and drafted the $^{40}Ar/^{39}Ar$ data. All authors reviewed the manuscript.

Acknowledgments

We thank the editor, S. Guzman, reviewers K. Németh and Dario Pedrazzi for their comments and constructive suggestions made on the early version of the manuscript, which helped to improve its content. This work stems from the research studies developed by Instituto Geológico Minero y Metalúrgico (INGEMMET) through the project “GA-17D: Estudio de peligros del Complejo Volcánico Chachani”. The work was carried out within the framework of UNESCO - IGCP 692 Project: Geoheritage for Geohazard Resilience Project. Fieldwork of BV was supported by the Agence Nationale de la Recherche of the French government through the program Investissements d’Avenir (16-IDEX-0001 CAP 20-25). We thank the staff of the analytical chemistry and sample preparation units of the INGEMMET laboratories. T. Flaherty is also acknowledged for the English improvement of a previous version of the text.

Conflict of interest

The authors declare that the research was conducted in the absence of any commercial or financial relationships that could be construed as a potential conflict of interest.

Publisher’s note

Supplementary material

The Supplementary Material for this article can be found online at: https://www.frontiersin.org/articles/10.3389/feart.2022.904914/full#supplementary-material

References

Acocella, V., Salvini, F., Funiciello, R., and Faccenna, C. (1999). The role of transfer structures on volcanic activity at Campi Flegrei (Southern Italy). *J. Volcanol. Geotherm. Res.* 91 (2–4), 123–139. doi:10.1016/s0377-0273(99)00032-3

Acosta, H., Mamani, M., Alvan, A., Oviedo, M., and Rodriguez, J. (2010). “Actividad tectónica del sistema de fallas Incapuquio durante la formación de la cuenca Arequipa en el Jurásico”. *XV congreso peruano de Geología. CD Resúmenes extendidos.*

Aguilar, R. (2019). “Exposure-based risk assessment of tephra-fall associated with long-lasting Vulcanian eruptions at Sabancaya volcano, Peru,” in *These de Specialisation in the assessment and management of geological and climate related risk - cerg-C 2018* (Geneva: University of Geneva).

Aguilar, R., Thouret, J.-C., Samamniego, P., Wörner, G., Jicha, B., Paquette, J.-L., et al. (2022). Growth and evolution of long-lived, large volcanic clusters in the central Andes: The Chachani Volcano cluster, southern Peru. *J. Volcanol. Geotherm. Res.* 426, 107539. doi:10.1016/j.jvolgeores.2022.107539

Alván, A., Jacay, J., Caracciolo, L., Sánchez, E., and Trinidad, I. (2018). Sedimentary facies analysis of the Mesozoic clastic rocks in Southern Peru (Tacna, 18°S): Towards a paleoenvironmental Redefinition and stratigraphic Reorganization. *J. S. Am. Earth Sci.* 84, 399–421. doi:10.1016/j.jsames.2018.04.014

Antayhua, Y., Tavera, H., and Bernal, I. (2001). Análisis de la actividad sísmica en la región del volcán Sabancaya (Arequipa). *Bol. Soc. Geol. Perú* 92, 78–79.

Arias, C., Manrique, N., Aguilar, R., and van Wyk de Vries, B. (2021). “Geosite assessment in Arequipa city - Peru: UNESCO IGCP 692 project ’geoheritage for geohazard resilience,” in The 23rd EGU General Assembly.

Armijo, R., Lacassin, R., Coudurier-Curveur, A., and Carrizo, D. (2015). Coupled tectonic evolution of Andean orogeny and global climate. *Earth. Sci. Rev.* 143, 1–35. doi:10.1016/j.earscirev.2015.01.005

Benavente, C., Delgado, F., García, B., Aguirre, E., and Audin, L. (2017). Neotectónica, Evolución y Peligro Sísmico en la Región Arequipa. *INGEMMET, Bol. Ser. Geodinámica Ing. Geol. N°* 64, 395.

Benavides, V. (1962). Estratigrafía pre-terciaria de la Región de Arequipa. *Bol. Soc. Geol. del Perú, Tomo* XXXVI, 58.

Callot, P., Sempere, T., Odonne, F., and Robert, E. (2008). Giant submarine collapse of a carbonate platform at the Turonian-Coniacian transition: The Ayabacas Formation, southern Peru. *Basin Res.* 20 (3), 333–357. doi:10.1111/j.1365-2117.2008.00358.x

Carlotto, V., Quispe, J., Acosta, H., Rodríguez, R., Romero, D., Cerpa, L., et al. (2009). Dominios geotectónicos y metalogénesis del Perú. *Bol. Soc. Geol. Perú* 103, 1–89.

Condit, C. D., and Connor, C. B. (1996). Recurrence rates of volcanism in basaltic volcanic field: An example from the Springerville volcanic field, Arizona. *Geol. Soc. Am. Bull.* 108, 1225–1241. doi:10.1130/0016-7606(1996)108<1225:rrovib>2.3.co;2

Connor, C. B., and Conway, F. M. (2000). “Basaltic volcanic fields,” in *Encyclopedia of volcanoes: San diego.* Editor H. Sigurdsson (Academic Press), 331–343.

Connor, C. B., Stamatakos, J. A., Ferrill, D. A., Hill, B. E., Ofoegbu, G. I., Conway, F. M., et al. (2000). Geologic factors controlling patterns of small-volume basaltic volcanism: Application to a volcanic hazards assessment at Yucca Mountain, Nevada. *J. Geophys. Res.* 105, 417–432. doi:10.1029/1999JB900353

Davidson, J. P., Harmon, R. S., and Wörner, G. (1991). “The source of Central Andean magmas; some considerations,” in *Andean magmatism and its tectonic* *setting geol soc amer spec paper*. Editors R. S. Harmon and C. W. Rapela, 265, 233–244.

Delacour, A., Gerbe, M.-C., Thouret, J.-C., Wörner, G., and Paquereau, P. (2007). Magma evolution of quaternary minor volcanic centres in southern Peru, central Andes. *Bull. Volcanol.* 69 (6), 581–608. doi:10.1007/s00445-006-0096-z

Diefenbach, A., Crider, J., Schilling, S., and Dzurisin, D. (2012). Rapid, low-cost photogrammetry to monitor volcanic eruptions: An example from mount st. Helens, Washington, USA. *Bull. Volcanol.*, 74. 579–587. doi:10.1007/s00445-011-0548-y

Galas, A., Paulo, A., Gaidzik, K., Zavala, B., Kalicki, T., Churata, D., et al. (2018). Geosites and geotouristic attractions proposed for the project geopark Colca and volcanoes of Andagua, Peru. *Geoheritage* 10 (4), 707–729. doi:10.1007/s12371-018-0307-y

Galas, A. (2011). The extent and volcanic structures of the Quaternary Andahua Group, Andes, southern Peru. *Ann. Soc. Geol. Pol.* 81, 1–19.

García, F., Chorowicz, J., and Legros, F. (1997). La caldera Chachani, gran centro explosivo plioceno-holoceno del sur del perú? Identificación y evolución en imagenes landsat y radar ERS. *Soc. Geol. Perú* 1, 449–454.

Harpel, C., da Silva, S., and Salas, G. (2011). The 2-ka eruption of Misti volcano, southern Peru -The most recent plinian eruption of Arequipa's iconic volcano. *Geol. Soc. Amer Spec. Pap.* 484, 1–72.

Hasenaka, T., and Carmichael, I. S. (1985). The cinder cones of Michoacán-Guanajuato, central Mexico: Their age, volume and distribution, and magma discharge rate. *J. Volcanol. Geotherm. Res.* 25, 105–124. doi:10.1016/0377-0273(85)90007-1

Huaman-Rodrigo, D., Chorowicz, J., Guillande, R., Antallaca, A., Caceres, R., and Aguilar, A. (1993). "Remote Sensing contribution on seismotectonic hazard in a volcanic active area (Nevado Sabancaya, southern Peru)," in *Int. Symp. Andean geodynamics ISAG*, 373–376.

INGEMMET (2014). GEOCATMIN, Sistema de Información Geológico y Catastral Minero. *Ingemmet, Manual de Uso* 36.

INGEMMET (2021). Evaluación de peligros volcánicos por caída de ceniza en el Distrito de Lluta. Distrito de Lluta, provincia de Caylloma, departamento Arequipa: Lima. *Ingemmet, Inf. Técnico N°* 7205, 40.

James, M. R., Carr, B., D'Arcy, F., Diefenbach, A., Dietterich, H., Fornaciai, A., et al. (2020). Volcanological applications of unoccupied aircraft systems (UAS): Developments, strategies, and future challenges. *Volcanica* 3 (1), 67–114. doi:10.30909/vol.03.01.67114

Japura, S. (2018). *Estudio estratigráfco y sedimentológico del depósito de caída pliniana de la erupción del volcán Huaynaputina del año 1600 d.C. Tesis de Ingeniero Geólogo*. Puno: Universidad Nacional del Altiplano, 192.

Jenks, W. (1948). *Geología de la hoja de Arequipa al 200000*. Boletín: Carta Nacional.

Jenks, W. (1946). Tertiary and Quaternary vulcanism in southern Peru. *Geol. Soc. Am. Bull.* 57, 1209.

Jourdan, F., Renne, P. R., and Reimold, W. U. (2009). An appraisal of the ages of terrestrial impact structures. *Earth Planet. Sci. Lett.* 286, 1–13. doi:10.1016/j.epsl.2009.07.009

Le Bas, M. J., Le Maitre, R. W., Strakeisen, A., and Zanettin, B. (1986). A chemical classification of volcanic rocks based on Total Alkali Silica Diagram. *J. Pet..* 27, 745–750.

Macdonald, G. A. (1972). *Volcanoes*. Englewood Cliffs, New Jersey, Prentice-Hall. 87.

Mamani, M., Wörner, G., and Semperé, T. (2010). Geochemical variation in igneous rocks of the central andean orocline (13 °S to 18 °S): Tracing crustal thickening and magmas generation through time and space. *Geol. Soc. Amer Bull.* 97, 241–254.

Mariño, J., Thouret, J. C., Cabrera, M., Aguilar, R., Manrique, N., Edwards, B., et al. (2020). *Geología y evaluación de los peligros del complejo volcánico Nevado Coropuna*. Lima: Boletín Geológico, INGEMMET, 145.

Mering, C., Huaman-Rodrigo, D., Chorowicz, J., Deffontaines, B., and Guillande, R. (1996). New data on the geodynamics of southern Peru from computerized analysis of SPOT and SAR ERS-1 images. *Tectonophysics* 259, 153–169. doi:10.1016/0040-1951(96)00034-0

Murcia, H., and Németh, K. (2020). "Effusive monogenetic volcanism." in *Updates in Volcanology - transdisciplinary nature of volcano science*. (London: IntechOpen). doi:10.5772/intechopen.94387

Németh, K., and Kereszturi, G. (2015). Monogenetic volcanism: Personal views and discussion. *Int. J. Earth Sci.* 104, 2131–2146. doi:10.1007/s00531-015-1243-6

Németh, K. (2010). "Monogenetic volcanic fi elds: Origin, sedimentary record, and relationship with polygenetic volcanism," in *What is a volcano?* Editors E. Cañón-Tapia and A. Szakács (Boulder: Geological Society of America Special Paper), 470, 43–66. doi:10.1130/2010.2470(04

Niespolo, E. M., Rutte, D., Deino, A. L., and Renne, P. R. (2017). Intercalibration and age of the Alder Creek sanidine 40Ar/39Ar standard. *Quat. Geochronol.* 39, 205–213. doi:10.1016/j.quageo.2016.09.004

Norabuena, E., Leffier-Griffin, L., Mao, A., Dixon, T., Stein, S., Sacks, S., et al. (1998). Space geodetic observations of nazca-south America convergence across the central Andes. *Science* 279, 358–362. doi:10.1126/science.279.5349.358

Paquereau-Lebti, P., Fornari, M., Roperch, P., Thouret, J.-C., and Macedo, O. (2008). Paleomagnetic, magnetic fabric properties, and ^{40}Ar/^{39}Ar dating, of Neogene - Quaternary ignimbrites in the Arequipa area, Southern Peru. Flow directions and implications for the emplacement mechanisms. *Bull. Volc* 70, 977–997.

Paquereau-Lebti, P., Thouret, J.-C., Wörner, G., and Fornari, M. (2006). Neogene and quaternary ignimbrites in the area of Arequipa, southern Peru: Stratigraphical and petrological correlations. *J. Volcanol. Geotherm. Res.* 154, 251–275. doi:10.1016/j.jvolgeores.2006.02.014

Peccerillo, A., and Taylor, S. R. (1976). Geochemistry of Eocene calc-alkaline volcanic rocks from the Kastamonu area, northern Turkey. Contrib. *Mineral. Pet.* 58, 63–81.

Planagumà-Guàrdia, L., Martí-Molist, J., and Vila-Subirós, J. (2022). Conservation of the geological heritage of volcanic fields: La Garrotxa volcanic zone natural park, Spain. *Geoheritage* 14, 39. doi:10.1007/s12371-022-00677-w

Prival, J. M., Thouret, J-C., Japura, S., Gurioli, L., Bonadonna, C., Mariño, J., et al. (2020). New insights into eruption source parameters of the 1600 CE Huaynaputina Plinian eruption, Peru. *Bull. Volcanol.* 82, 7. doi:10.1007/s00445-019-1340-7

Ramos, V. (2010). The tectonic regime along the Andes: Present-day and mesozoic regimes. *Geol. J.* 45 (1), 2–25. doi:10.1002/gj.1193

Renne, P. R., Balco, G., Ludwig, K. R., Mundil, R., and Min, K. (2011). "Response to the comment by W.H. Schwarz et al. on," in *Joint determination of 40K decay constants and 40Ar */40K for the Fish Canyon sanidine standard, and improved accuracy for 40Ar/39Ar geochronology*. Editors, 75, 5097–5100.*Geochimica Cosmochimica Acta*17

Rivera, L. (2021). "Mapeo Tridimensional del volcán Nicholson, Perú, mediante la inversión del vector magnético esparcido en coordenadas esféricas," in *Report (unpubl.), IGCP-692 project: Geoheritage for geohazard resilience*, 93.

Rivera, M., Thouret, J.-C., Mariño, J., Berolatti, R., and Fuentes, J. (2010). Characteristics and management of the 2006–2008 volcanic crisis at the Ubinas volcano (Peru). *J. Volcanol. Geotherm. Res.* 198 (1-2), 19–34. doi:10.1016/j.jvolgeores.2010.07.020

Rivera, M., Thouret, J.-C., Samaniego, P., and Le Pennec, J. L. (2014). The 2006–2009 activity of the Ubinas volcano (Peru): Petrology of the 2006 eruptive products and insights into Genesis of andesite magmas, magma recharge and plumbing system. *J. Volcanol. Geotherm. Res.* 270, 122–141. doi:10.1016/j.jvolgeores.2013.11.010

Rivera, M., Vílchez, M., and Vela, J. (2018). *Peligros por huaicos en la ciudad de Arequipa. En: Taller Internacional Fortalecimiento de capacidades para mitigar los impactos de huaicos en Perú, Lima y Arequipa, Perú, 15-19 octubre 2018: Libro de Resúmenes*. Arequipa: INGEMMET, 45–49.

Rodríguez Rey, A., Calleja, L., Suárez del Río, L., Ruiz de Argandoña, V., Díez Sarriá, I., and Sánchez Delgado, N. (2004). Procedimiento estereológico para la cuantificación del tamaño de grano de rocas en 2-D: Aplicación a la interpretación petrofísica de la velocidad de corte de granitos con útiles diamantados. *Trab. Geol.* 24, 147–152.

Samaniego, P., Rivera, M., Mariño, J., Guillou, H., Liorzou, C., Zerathe, S., et al. (2016). The eruptive chronology of the Ampato-Sabancaya volcanic complex (southern Peru). *J. Volcanol. Geotherm. Res.* 323, 110–128. doi:10.1016/j.jvolgeores.2016.04.038

Sempere, T., and Jacay, J. (2006). *Estructura tectónica del Sur del Perú (Antearco, arco y Altiplano suroccidental)*. Lima: XIII Congreso Peruano de Geología, Extended Abstracts, 324–327.

Sempere, T., Noury, M., Garcia, F., and Bernet, M. (2014). "Elementos para una actualización de la estratigrafía del Grupo Moquegua, sur del Perú," in *XVII congreso peruano de Geología, Lima, extended abstracts, digital file "Sempere* (Lima: T", Soc Geol Perú).

Siebe, C., Schaaf, P., Carlotto, V., and Gomez, J. C. (2006). Radiocarbon ages and composition of holocene-late Pleistocene monogenetic kimsachata and oroscocha volcanoes in cusco, Peru. *Cities Volcanoes* 4, 23–27.

Stern, C. R. (2004). Active andean volcanism: Its geologic and tectonic setting. *Rev. Geol. Chile* 31 (2), 161–206. doi:10.4067/s0716-02082004000200001

Sun, S., and McDonough, W. F. (1989). Chemical and isotopic systematics of oceanic basalts: Implications for mantle composition and processes. *Geol. Soc. Amer Spec. Pap.* 42, 313–345. doi:10.1144/gsl.sp.1989.042.01.19

Thorpe, R. S., Francis, P. W., Hammil, M., and Baker, M. B. (1982). in *The Andes*. Editor R. S. Thorpe (New York: Andesites), 187–205.

Thouret, J.-C., Finizola, A., Fornari, M., Legeley-Padovani, A., Suni, J., and Frechen, M. (2001). Geology of el Misti volcano near the city of Arequipa, Peru. *Geol. Soc. Am. Bull.* 113 (12), 1593–1610. doi:10.1130/0016-7606(2001)113<1593:goemvn>2.0.co;2

Thouret, J.-C., Jicha, B., Paquette, J.-L., and Cubukcu, E. (2016). A 25 Myr chronostratigraphy of ignimbrites in South Peru. Implications for the volcanic history of the Central Andes. *J. Geol. Soc. Lond.* 173, 734–756. doi:10.1144/jgs2015-162

Torres, I., Németh, Ká., Ureta, G., and Aguilera, F. (2020). Characterization, origin, and evolution of one of the most eroded mafic monogenetic fields within the central Andes: The case of El País lava flow field, northern Chile. *J. S. Am. Earth Sci.* 105, 102942. doi:10.1016/j.jsames.2020.102942

Valentine, G. A., and Gregg, T. K. P. (2008). Continental basaltic volcanoes - processes and problems. *J. Volcanol. Geotherm. Res.* 177, 857–873. doi:10.1016/j.jvolgeores.2008.01.050

van Wyk de Vries, B., and Merle, O. (1998). Extension induced by volcanic loading in regional strike-slip zones. *Geol.* 26, 983–986. doi:10.1130/0091-7613(1998)026<0983:eibvli>2.3.co;2

Vargas, L. (1970). Geología del Cuadrángulo de Arequipa. *Boletín del Servicio de Geología y Minería* 24, 64.

Global Volcanism Program (2013). in *Cerro Nicholson (354008) in volcanoes of the World*. Editor E. Venzke (Smithsonian Institution). Downloaded https://volcano.si.edu/volcano.cfm?vn=354008 (Accepted Jun 30, 2022).

Vereb, V., van Wyk de Vries, B., Guilbaud, M-N., and Karátson, D. (2020). The urban geoheritage of clermont-ferrand: From inventory to management. *Quaest. Geogr.* 39 (3), 5–31. doi:10.2478/quageo-2020-0020

Vicente, J.-C., Sequeiros, F., Valdivia, M., and Zavala, J. (1982). El sobre-escurrimiento de Cincha-lluta: Elemento del accidente mayor andino al NW de Arequipa. *Bol. Soc. Geol. Perú* 61, 67–99.

Williams, H., and McBirney, A. R. (1979). *Volcanology*. San Francisco: Freeman, 397.

Wilson, J. J. (1963). Cretaceous stratigraphy of the central Andes of Peru. *Am. Assoc. Petrol. Geol. Bull.* 47, 1–34.

Wilson, M. (1986). *Igneous petrogenesis*. London: Unwyn Hyman, 456.

Wood, C. A. (1979). “Monogenetic volcanoes in terrestrial planets,” in Proceedings of the 10 th Lunar and Planetary Science Conference.

Wörner, G., Mamani, M., and Blum-Oeste, M. (2018). Magmatism in the central Andes. *Elem. (Que).* 14, 237–244. doi:10.2138/gselements.14.4.237

frontiers | Frontiers in Earth Science

TYPE Original Research
PUBLISHED 03 October 2022
DOI 10.3389/feart.2022.917488

^{40}Ar/^{39}Ar ages and geochemistry of the Intersalar Range of the Bolivian Altiplano: A volcanological transect spanning the arc and reararc of the Central Andean Plateau

Morgan J. Salisbury[1]*, Néstor Jiménez[2] and Dan Barfod[3]

[1]Department of Earth Sciences, Durham University, Durham, United Kingdom, [2]Universidad Mayor de San Andrés, Instituto de Investigaciones Geológicas y del Medio Ambiente, La Paz, Bolivia, [3]NEIF Argon Isotope Laboratory, SUERC, East Kilbride, United Kingdom

The volcanic Intersalar Range of western Bolivia provides a unique opportunity to examine geochemical variations spanning the arc and reararc regions of the Central Andean Plateau. In this study we report 23 new ^{40}Ar/^{39}Ar ages, 15 whole-rock Sr-Nd-Pb isotope analyses, and 50 whole-rock major and trace element analyses from samples collected across ~115 km of the Intersalar Range. Most samples are classified as trachyandesites and trachydacites, with the most mafic lavas (slightly alkaline, basaltic trachyandesites) erupting from the Pliocene Coracora volcano in the central Altiplano. We identify two distinct pulses of reararc magmatism: a Miocene phase between 20 Ma and 14 Ma that corresponds with local compressional shortening, and a Plio-Pleistocene phase between 5 and 1 Ma that postdates observed structural deformation in the region. ^{87}Sr/^{86}Sr values (0.70512–0.70600) and ^{143}Nd/^{144}Nd values (0.51226–0.51255) are generally higher, and lower, respectively, in the younger phase, whereas Pb isotopes (^{206}Pb/^{204}Pb = 17.7315–18.5095; ^{207}Pb/^{204}Pb = 15.5714–15.6279; ^{208}Pb/^{204}Pb = 37.7862–38.6156) show little variation with age. Isotope values are only loosely correlated with distance from the modern Central Volcanic Zone. Higher Sr/Y, Dy/Yb, and $[La/Yb]_N$ values in the Plio-Pleistocene samples are consistent with homogenization at the base of a thicker continental crust compared to the Miocene samples. Nb concentrations show the strongest correlation with distance into the reararc compared to all other trace elements (arc Nb = 6–16 ppm; reararc Nb = 12–26 ppm). Nb/Nb* values (a measurement of the depth of the negative Nb anomaly) correspondingly increase into the reararc (indicating smaller anomalies), reaching a maximum at Coracora volcano before decreasing in the far rear arc region. Compiled data across the Central Andean Plateau reveal a strong correlation between Nb/Nb* and the presence of intact mantle lithosphere beneath the central Altiplano. We interpret this distinct Nb signal to reflect melting triggered by the breakdown of Nb-rich hydrous minerals within foundering (delaminating) mantle lithosphere. In conjunction with spatiotemporal data, Nb systematics provide the clearest indication of mantle lithosphere in regions where mafic samples are not present.

OPEN ACCESS

EDITED BY
Pablo Grosse,
Consejo Nacional de Investigaciones Científicas y Técnicas (CONICET), Argentina

REVIEWED BY
Osvaldo González-Maurel,
University of Cape Town, South Africa
Axel Karl Schmitt,
Heidelberg University, Germany

*CORRESPONDENCE
Morgan J. Salisbury,
msalisbury@lowercolumbia.edu

SPECIALTY SECTION
This article was submitted to Geochemistry, a section of the journal Frontiers in Earth Science

RECEIVED 11 April 2022
ACCEPTED 24 August 2022
PUBLISHED 03 October 2022

CITATION
Salisbury MJ, Jiménez N and Barfod D (2022), ^{40}Ar/^{39}Ar ages and geochemistry of the Intersalar Range of the Bolivian Altiplano: A volcanological transect spanning the arc and reararc of the Central Andean Plateau.
Front. Earth Sci. 10:917488.
doi: 10.3389/feart.2022.917488

KEYWORDS

Central Andes, volcanism, whole-rock and isotope geochemistry, 40Ar/39Ar age dating, Bolivia Altiplano

Introduction

The Central Andean Plateau, also known as the Altiplano-Puna Plateau, is the second largest crustal plateau on Earth and the only to coincide with active continental arc volcanism. Its enigmatic formation at a subduction boundary in the absence of continental collision has led numerous researchers to examine the complex temporal, structural, and magmatic history of the plateau (see Oncken et al., 2006; Trumbull et al., 2006; Barnes and Ehlers, 2009 for reviews). Despite numerous advances, the mantle sources, and their melting triggers, across much of the plateau remain poorly constrained, particularly in regions that lack mafic volcanism. A considerable factor limiting our knowledge of the intimate relationship between magmatism and orogeny in the Central Andes is an incomplete dataset of the ages and compositions of the abundant plateau volcanism. The rare mafic magmatism in the dominantly compressive Central Andes further complicates our understanding of petrogenesis in the region. In this context, radiometric ages of volcanism are an essential piece of the puzzle, as they provide unequivocal data revealing the time and location of melting events. In this study we evaluate spatial, temporal, and geochemical data of an arc-normal transect along the Intersalar Range of western Bolivia (~19.5–20.0°S, ~67.5–68.7°W) and the broader plateau at this latitude to address the primary sources and melting triggers of the Central Andean Plateau at this latitude. Despite limitations, geochemical data of non-basaltic volcanism can provide significant insight, particularly when considered within a broader spatiotemporal framework.

The intersalar range

The Intersalar Range (*Serranía Intersalar* in Spanish on Bolivian geologic maps) is named after its location between two of the world's largest salt flats (Salar de Uyuni and Salar de Coipasa) on the Bolivian Altiplano. The Intersalar Range is a series of composite volcanic centers, flat lava domes known as tortas, and extensive ignimbrites that extend eastward from the Western Cordillera into the central Altiplano of Bolivia (Figures 1–3). The western portion of the Intersalar Range blends into the north-south trending Central Volcanic Zone (CVZ) arc along the Bolivia/Chile border. The eastern extent of the range is loosely defined by the composite centers of Coracora and Tunupa, with volcanism extending further east in the form of structurally aligned monogenetic magmatism of the central and eastern Altiplano (Davidson and de Silva, 1992, 1995), and the immense Los Frailes volcanic complex (Jiménez and López-Velásquez, 2008) near the fold and thrust belt of the Eastern Cordillera (Figure 1). This arc-perpendicular trend of volcanism coincides with the axis of topographic symmetry dividing the northern and southern portions of the Bolivian Orocline, and also marks the widest extent of the Central Andean Plateau (Allmendinger et al., 2005). In total, this arc-normal volcanic transect is among the most extensive of the entire plateau and coincides with one of its better structurally constrained sections (e.g., Beck and Zandt, 2002; Yuan et al., 2002; McQuarrie et al., 2005), thus allowing a detailed examination of the relationship between magmatism, plateau geometry, and structural deformation.

Prior to a geochemical and temporal analysis of lavas from Tunupa volcano (Salisbury et al., 2015), only limited geochemical and age information was available for the Intersalar Range. This range was mapped by Leytón and Jurado (1995) (Salinas de Garci Mendoza quadrangle, 1:250,000 scale) as consisting primarily of Miocene to Pleistocene lavas overlying extensive and gently folded pyroclastic deposits that crop out in both the eastern and western portions of the range (Figure 3). A potential collapse caldera was mapped by Leytón and Jurado (1995) near Cerro Mokho, however detailed analysis of ignimbrite stratigraphy and related structures will be necessary to confirm this hypothesis. Age estimates of Leytón and Jurado (1995) were based primarily on 12 dispersed K/Ar ages ranging from 17.6 ± 0.2 Ma to 1.8 ± 0.2 Ma and the relative amounts of erosion experienced by the volcanic centres. Hoke and Lamb (2007) added one geochemical analysis and a K/Ar age (2.57 ± 0.45 Ma) within the confines of the Intersalar Range as defined in the present study.

The results from Tunupa volcano demonstrated significant geochemical differences from volcanoes of the CVZ arc, and served as the impetus for the current study, which aims to use age-constrained geochemical data collected across the Intersalar Range and the broader plateau to evaluate various proposed reararc melting mechanisms and mantle sources. In the present study, we provide a strategic reconnaissance of ^{40}Ar/^{39}Ar ages, Sr-Nd-Pb isotope data, and whole-rock geochemical analyses of the Intersalar Range of western Bolivia. We then consider this dataset within the broader context of regional magmatism and the lithospheric geometry of the Central Andean Plateau revealed by geophysical data.

Geologic setting

The Intersalar Range is oriented orthogonally to both the Peru-Chile trench and the main trend of the CVZ arc of the Western Cordillera, extending ~120 km from the Chile/Bolivia border into the center of the internally drained Altiplano basin in

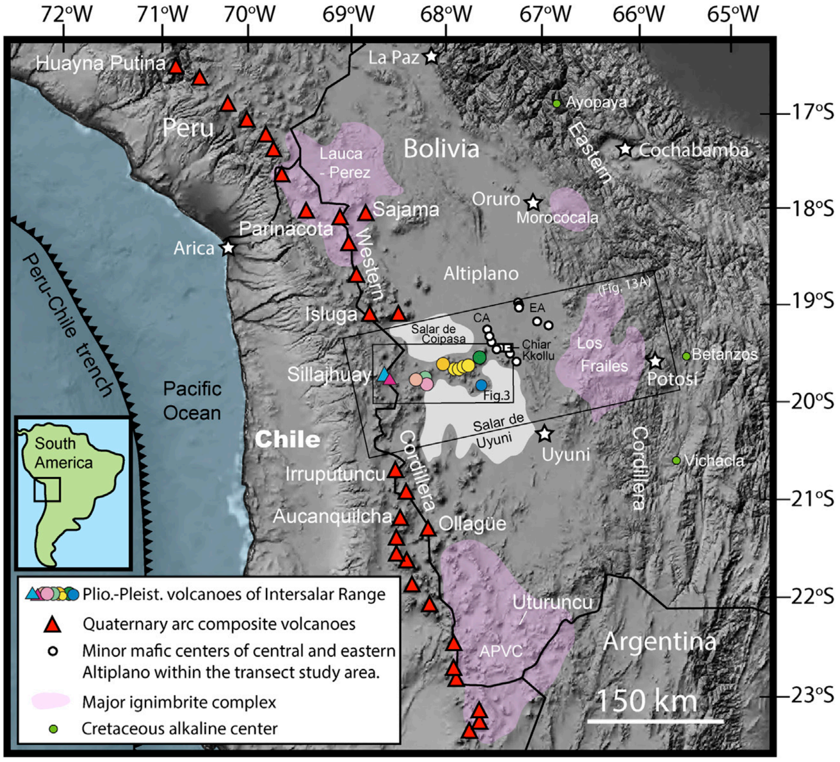

FIGURE 1
Location of the Intersalar Range volcanoes (colored symbols) of the Bolivian Central Andean Plateau in South America. Symbols are consistent in all subsequent figures. The labeled minor mafic centers of the central Altiplano (CA), eastern Altiplano (EA), and the Cretaceous-rifting related alkaline rocks of Ayopaya, Betanzos, and Vichacla are discussed in the text and included in subsequent figures for comparison with the data of this study. Not all volcanic centers in the map region are labeled in this figure. References in subsequent figures and text. Shaded relief digital elevation model (DEM) background image derived from 90 m resolution SRTM data.

Bolivia (Figure 1). The immense Central Andean Plateau is an elevated region between 14°S and 28°S, defined by a contour greater than 3,000 m. a.s.l. With individual peaks approaching 7,000 m. a.s.l. (Barnes and Ehlers, 2009). The plateau is morphologically divided at ~22°S into the northern Altiplano and the southern Puna regions, and from west to east into the Precordillera, Western Cordillera, Altiplano/Puna basins, Eastern Cordillera, Interandean zone, and the Subandean Range. The Quaternary CVZ arc is located along the Western Cordillera and spans nearly the entire extent of the plateau from 14°S to 27°S. In the latitude of the Intersalar Range, Wörner et al. (1992) recognized a relative lack of Quaternary composite volcanism in the Alto de Pica region between Isluga and Irruputuncu volcanoes, which coincides with a change in Pb isotopic compositions that are interpreted to reflect interaction of magmas with domains of different crustal type and age. Although later investigation would identify Quaternary complexes in both Chile (Polanco and Gardeweg, 2000; Correa, 2011) and Bolivia (this study), this segment of the arc, known as the "Pica Gap" is notable for an apparent lack of Late Pleistocene to Holocene volcanism, and for a lack of tectonic horsts, which are typical for the entire CVZ both to the north and south (Wörner et al., 1994). See Gardeweg and Sellés (2017) for a discussion of the Pica Gap in northern Chile.

The continental crust of the Central Andes is among the thickest in the world (up to 80 km) and Moho depths vary significantly throughout the plateau (Yuan et al., 2002; McGlashan et al., 2008). At the latitude of the Intersalar Range (~19–20°S), the Western Cordillera and Eastern Cordillera are underlain by ~70 km, and ~80 km-thick-crust, respectively, although the crust only reaches to depths of ~57 km beneath the eastern portion of the Intersalar Range in the central Altiplano (Yuan et al., 2002). The geophysical data further suggest that this crust is dominantly felsic with very little, if any, mafic component (Beck and Zandt, 2002; Yuan et al., 2002). Lithospheric thickness variations follow an inverted pattern compared to the crust at 19–20°S: Beck and Zandt (2002) identified a root of mantle lithosphere that extends to depths of ~150 km beneath the central Altiplano, but is essentially absent beneath both the Western and Eastern Cordilleras. These values are in stark contrast to the ~200 km thick lithosphere of the Brazilian craton and are interpreted to

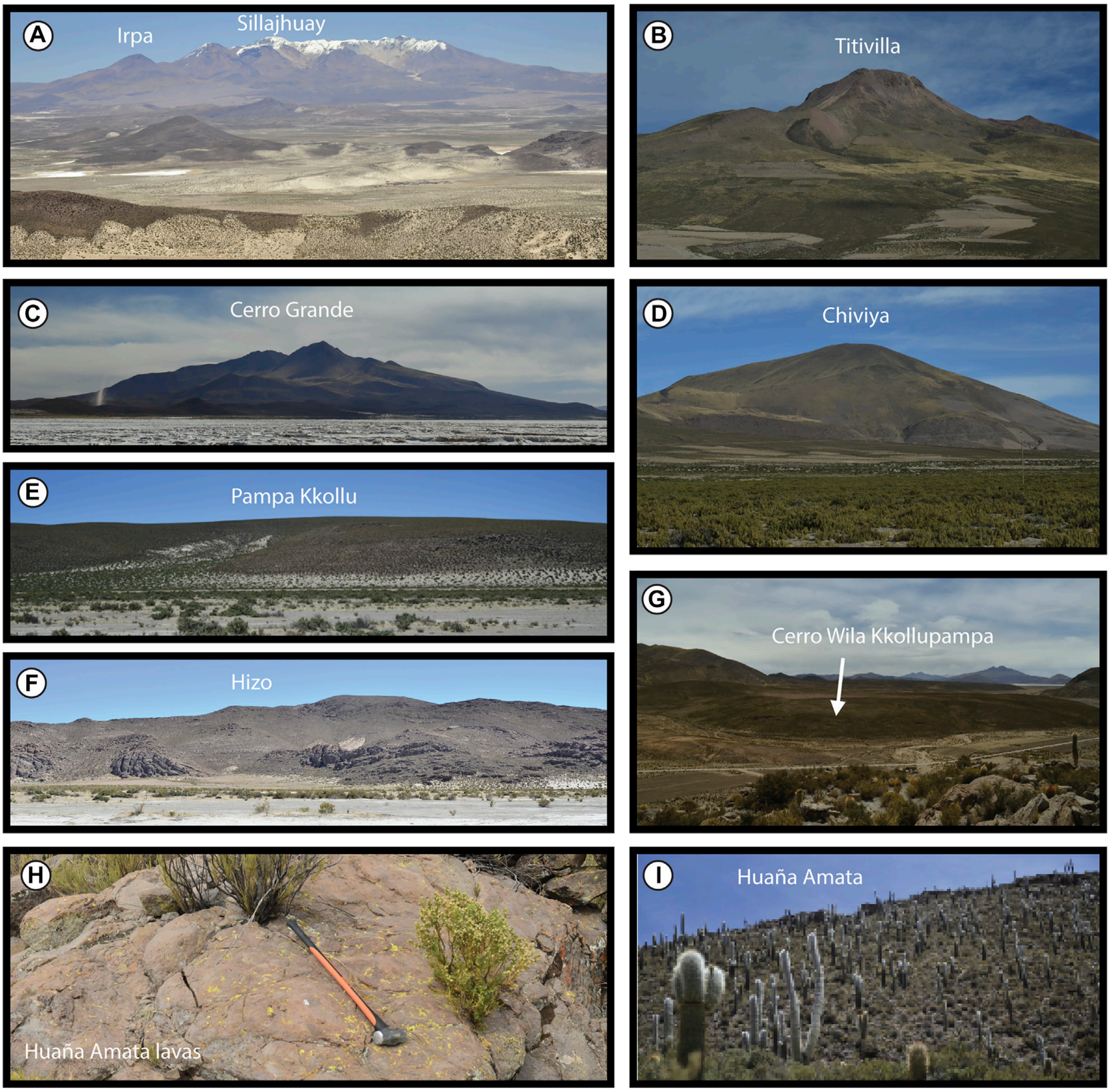

FIGURE 2
Field photographs showing examples of Intersalar Range volcanism. **(A)** View towards the arc composite centers of Sillajhuay and Irpa volcanoes along the Bolivia/Chile Border, image taken from Chiviya volcano. **(B–D)** Rear arc composite centers Titivilla, Grande, and Chiviya. **(E–F)** Smaller silicic centers in the western Intersalar Range: Pampa Kkollu and a previously unnamed center near estancia Hizo. **(G)** Cerro Wila Kkollupampa, one of the five, broad, flat-topped, relatively mafic tortas sampled in the eastern Intersalar Range. **(H–I)** Miocene Huaña Amata volcanic center showing typical examples of weathering and vegetation of the Intersalar Range.

result from piecemeal foundering (delamination) of the mantle lithosphere and mafic lower crust (Beck and Zandt, 2002).

Although few exposed structures exist within the Intersalar Range, our data can be interpreted within the framework of deformation recorded by nearby structures and related sedimentation. Southwest of the study area in the western flank of the Western Cordillera and Precordillera (20–21°S, 69°W), deformation is interpreted to have occurred in two stages, the first between ~45 and ~37 Ma, and the second between ~17 and ~10 Ma (Victor et al., 2004). This second stage of deformation is largely coincident with shortening related to the Yazón Anticline (20.4°S, 67.9°W) between

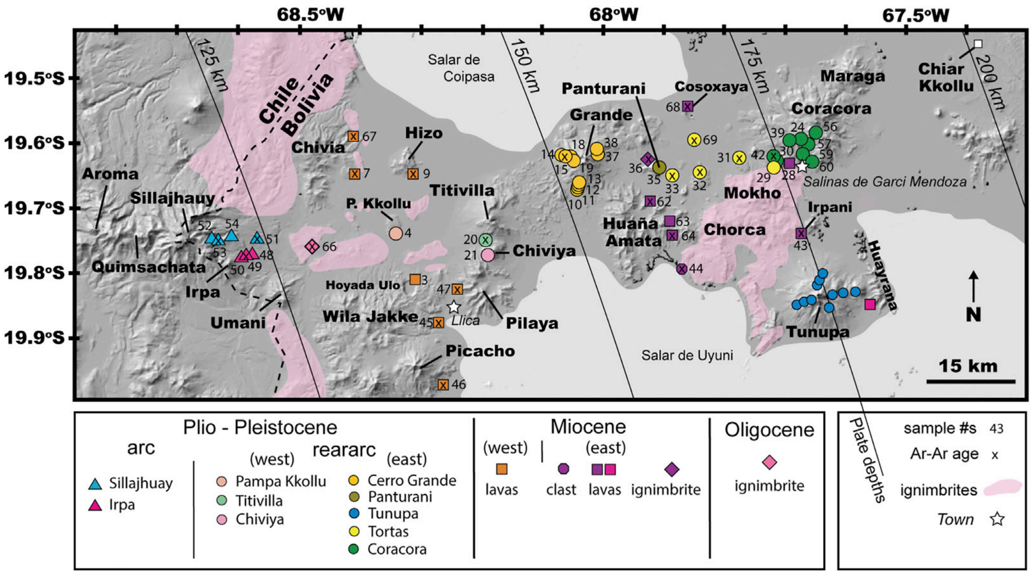

FIGURE 3
Locations of sample collection sites shown on a digital topographic map of the Intersalar Range (SRTM 90 data). All samples shown are from this study except for those of Tunupa and Huayrana (Salisbury et al., 2015) and Chiar Kkollu (Davidson and de Silva, 1995; Hoke and Lamb, 2007). Whole-rock geochemical data analyzed for all newly collected samples, with $^{40}Ar/^{39}Ar$ age determinations marked with x. Triangles indicate samples from arc volcanoes, circles are rearare Pliocene-Pleistocene lavas, squares are Miocene lavas, octagon is Miocene breccia clast, and diamonds are pyroclastic deposits. Ages of undated samples are based on stratigraphic relations with dated samples and/or geologic mapping by Leytón and Jurado (1995). For Plio-Pleistocene centers, colors represent samples from individual volcanic centers. For Miocene centers, colors indicate western and eastern groups. Symbol shapes and colors are consistent in all figures. Plate depths from Cahill and Isacks (1992).

~21 and ~11 Ma with maximum rates at ~15 Ma, whereas structures exposed in the region of Uyuni indicate shortening between ~35 and 10 Ma in the eastern Altiplano (Elger et al., 2005). Also in the eastern Altiplano, ~30 km east of the Intersalar Range, the numerous reverse faults and folds of Tambo Tambillo (19–20°S, 68°W) indicate shortening in the central Altiplano between ~14 and ~5 Ma, which largely overlaps with ~14 to ~9 Ma deformation of the Corque syncline ~160 km to the north (Kennen et al., 1995). As the observed structural deformation of the Altiplano is apparently insufficient to account for its extreme crustal thickness, ductile flow of hot, lower crust from the Eastern Cordillera may have contributed up to 40% of the Altiplano crust (Husson and Sempere, 2003).

Proposed petrogenetic models of Bolivian Altiplano volcanism

Cenozoic rearare magmatism of Bolivia has long been of interest to Andean researchers as the large distances from the CVZ arc suggest an intriguing relationship between the construction of the Central Andean Plateau and rearare magmatism. However, the primary melting triggers and the relative contributions of mantle asthenosphere, mantle lithosphere, and continental crust in the genesis of plateau magmas remain difficult to constrain (e.g., Hildreth and Moorbath, 1988; Rogers and Hawkesworth, 1989; Davison and de Silva, 1992; Davison and de Silva, 1995; Hoke and Lamb, 2007; Jiménez and López-Velásquez, 2008; Salisbury et al., 2015). In a study of 15 volumetrically minor, monogenetic lavas of the central and eastern Altiplano (Figure 1), Davidson and de Silva (1995) favored a petrogenetic model where low degrees of partial melting of the asthenosphere is triggered by dehydration of the Nazca plate in the far rearare region, where these melts are then subject to significant geochemical modification at the base of the thick continental crust. Hoke and Lamb (2007) took advantage of a more comprehensive dataset and significant advances in geophysical measurements of the region and argued that magmatism of the Bolivian Altiplano was strongly influenced by a widespread lithospheric removal event in the Late Oligocene/Early Miocene that created irregular depths of the mantle lithosphere and allowed long-term decompression melting of the asthenosphere beneath the Los Frailes volcanic complex and lateral melt migration to centers beneath the central Altiplano and the eastern Intersalar Range. In contrast, Salisbury et al. (2015) proposed that the high Nb concentrations in the Pleistocene lavas from Tunupa volcano more likely signaled a strong influence of melted hydrated mantle lithosphere, triggered by localized piecemeal foundering. Each of these models are evaluated below in the Discussion section.

Sample collection and analytical methods

Field collection

Sampling of the Bolivian Intersalar Range was carried out during three field campaigns to the western Altiplano in 2012 (Figure 3). In total, 72 samples were collected with 50 samples later selected for detailed chemical analyses, which are reported in this study. Of the 50 new analyses, 47 are from effusive lava flows, 2 are from explosive eruptions, and one is from an intrusive stock collected from Coracora volcano. Ignimbrite matrix (sample #66) was collected ~23 km east of the summit of Sillajhuay, near Rio Cancosa, from a widespread, and apparently large-volume, ignimbrite of the western Altiplano. Pumice (sample #36) was extracted from a small-volume, and apparently locally sourced, ignimbrite on the northwest flank of Panturani. The 47 samples of lava were collected from 22 individual centers from both the arc and reararc regions, spanning ~115 km. Multiple samples were collected from morphologically distinct lava flows from the composite centers of Sillajhuay, Irpa, Chivia, Grande, Huaña Amata and Coracora, whereas only single samples were collected from the composite centers of Wila Jakke, Hoyada Ulo, Picacho, Pilaya, Titivilla, Chiviya, and Panturani. Single samples were also collected from the flat-topped, apparently monogenetic tortas of Wila Kkollupampa, Tenica Loma, Jachcha Pallallí, Uta Kkollu, and Tuju Tujuni that erupted between Grande and Coracora, as well as the smaller, relatively isolated centers of Hizo, Pampa Kkollu, Cosoxaya, and Irpani. The lavas of Cosoxaya and Irpani were not mapped by Leytón and Jurado (1995) and are named here based on local landmarks. The Hizo center is enigmatic as there are apparent flow structures reminiscent of a vent location of large-volume ignimbrites (e.g., Salisbury et al., 2011), however, detailed field and laboratory investigation is necessary to better understand this center. A dark, angular clast (sample #44) was removed from a sedimentary breccia containing a homogenous load of 15–30 cm cobbles on the northern shore of Salar de Uyuni south of Huaña Amata. As chemical alteration is common in the Intersalar Range, care was taken to find the least-altered samples in the field and to remove weathering rinds when necessary. Appropriate samples for age and geochemical analyses were selected following thin-section analysis.

^{40}Ar/^{39}Ar geochronology

In total, 23 samples representing 21 different volcanic centers were selected to provide a comprehensive overview of the age of Intersalar Range volcanism. Petrographic analysis was used to identify potassium-bearing phases and to select suitable samples with low degrees of alteration for ^{40}Ar/^{39}Ar dating.

Sanidine was prioritized, although only available for analysis in four samples. Plagioclase phenocrysts were selected for nine samples, and unaltered, phenocryst-free groundmass consisting of glass and plagioclase microlites were chosen for the 10 samples without suitable potassium-bearing phenocrysts. Eighteen samples (groundmass or feldspar) were run as step-heating experiments and presented in plateau and inverse isochron diagrams. Seven samples of feldspar were run as sets of single grain total-fusion experiments and presented as probability density function plots. Two of these (#66, 68) were analyzed by both methods. Samples and neutron flux monitors were stacked in quartz tubes with the relative positions of packets precisely measured for later reconstruction of neutron flux gradients. The sample package was irradiated in the Oregon State University reactor, Cd-shielded facility. Alder Creek sanidine (1.1891 ± 0.0008, Ma, 1σ, Niespolo et al., 2017) was used to monitor ^{39}Ar production and establish neutron flux values (J) for the samples.

^{40}Ar/^{39}Ar data were collected at the Scottish Universities Environmental Research Centre (SUERC) NERC Argon Isotope Facility (East Kilbride) on a GVi instruments ARGUS V multi-collector mass spectrometer using a variable sensitivity Faraday collector array in static collection (non-peak hopping) mode (Sparks et al., 2008; Mark et al., 2009) for step heating, and an MAP-215–50 single-collector instrument equipped with an electron multiplier for single grain analyses. Gas was extracted from samples via step-heating using a mid-infrared (10.6 μm) CO_2 laser with a non-gaussian, uniform energy profile and a variable beam diameter. The samples were loaded into a copper planchette, housed in a doubly-pumped ZnS-window laser cell, evacuated to UHV conditions. Liberated argon was purified of active gases (e.g., CO_2, H_2O, H_2, N_2, CH_4) using three Zr-Al getters; one at 16°C and two at 400°C. Time-intensity data were regressed to t_0 with second-order polynomial fits to the data. The average total system blank (±2σ) for laser extractions, measured between each sample run over the temperature range where age information is extracted, was $8.9 \pm 6.4 \times 10^{-16}$ mol ^{40}Ar, $1.1 \pm 2.3 \times 10^{-16}$ mol ^{39}Ar, $2.7 \pm 3.8 \times 10^{-17}$ mol ^{36}Ar (ARGUS) and $1.2 \pm 0.8 \times 10^{-15}$ mol ^{40}Ar, $0.8 \pm 4.6 \times 10^{-17}$ mol ^{39}Ar, $1.2 \pm 0.3 \times 10^{-17}$ mol ^{36}Ar (MAP). Mass discrimination was monitored daily, between sample runs by analysis of an air standard aliquot delivered by an automated pipette system over the course of the 2-month analysis period. ARGUS: for n=306 air standards the mass fractionation factor (D) was determined to be 0.9994 ± 0.0019. MAP: for n=314 air standards the mass fractionation factor (D) was determined to be 1.0109 ± 0.0029. See raw data in Supplementary Material for D values applied to individual steps.

Plateau ages were identified by the following criteria: (1) Steps overlap in age within 2σ uncertainty; (2) a minimum ^{39}Ar content for a step is ≥0.1% of total ^{39}Ar release; (3) the plateau consists of at least five contiguous steps; (4) a minimum of 50% of ^{39}Ar in the chosen steps; (5) the inverse isochron formed by the plateau steps yields an age indistinguishable from the plateau age at 2σ uncertainty; (6) the trapped component composition, derived from the inverse isochron, is indistinguishable from the composition of air at the 2σ uncertainty level; (7) age and uncertainty (SEM) were calculated using the mean weighted by the inverse variance of each step; (8) for replicated samples, a plateau for each aliquot was independently calculated and the accepted steps for each aliquot combined into a composite isochron and composite plateau; and (9) the dispersion of data points, as indicated by MSWD, on the isochron and plateau diagrams are comparable to the expected analytical scatter for a given number of steps (Wendt and Carl 1991).

Peak age distributions in probability density function plots were defined by determining the best contiguous group of individual grain analyses that conforms to a Gaussian distribution with the expected scatter as indicated by the value of MSWD (Wendt and Carl 1991). Grains with large age uncertainties of >100% or low radiogenic yields of <20% $^{40}Ar^*$ were rejected prior to calculating the probability distributions. All blank, interference, and mass discrimination calculations were performed with the *MassSpec* software package version 8.058 (Deino, 2015). Plateau ages, or composite plateau ages for replicated samples, were chosen as the best estimates of the emplacement ages. Ages are reported with 2σ analytical uncertainties.

Whole-rock analyses

50 new analyses of whole-rock major- and trace-elements were performed at the Geo-Analytical Laboratory at Washington State University–Pullman under the direction of Richard Conrey, Laureen Wagoner, and Charles Knaak in 2013. Whole-rock major-element concentrations were analyzed by X-ray fluorescence (XRF) using lithium tetraborate fused beads and a Rigaku 3,370 spectrometer with a Rh target. Trace-element concentrations were measured by XRF and inductively coupled plasma–mass spectrometry (ICP-MS). Repeat analysis of standard GSP-2 over the analysis period suggests long term precision and accuracy of <2% for all major elements analyzed by XRF, except FeO* where accuracy is <3%. For trace elements analyzed by XRF precision and accuracy is <10% for all elements except for Sc (<16%), and U (<70%). Repeat analysis of samples by ICP-MS show precision <1%–5% for all elements analyzed. In cases where the same element was measured by both methods, such as Sc and U, ICP-MS results are reported. See Johnson et al. (1999) and Knaack et al. (1994) for detailed analytical methodology. The whole-rock major and trace element data collected by Salisbury et al. (2015) used the same laboratory and methods as the present study and are included in the figures of this study. The Tunupa study provides context on the range of data expected at individual composite centers.

Fourteen of the samples dated by $^{40}Ar/^{39}Ar$, and one undated sample of presumed Pleistocene age, were analyzed for Sr, Nd, and Pb isotopes using a ThermoElectron Neptune multi-collector ICP-MS system at the Arthur Holmes Isotope Geochemistry Laboratory at the University of Durham in 2014 under the guidance of Dr. Geoff Nowell. Details of the operating procedures and instrument configuration are described in detail in Handley et al. (2007) and references therein. Data quality was monitored by frequent analysis of standard reference materials throughout each analytical session. Measurement of isotope standards returned the following values: NBS-987 $^{87}Sr/^{86}Sr = 0.710264 \pm 0.000016$ (2s) (n = 16); J&M Nd isotope standard 0.511106 ± 0.00012 (2s) (n=15); and NBS-981 $^{206}Pb/^{204}Pb = 16.9415 \pm 0.0011$ (2s), $^{207}Pb/^{204}Pb$ 15.4987 + 0.0011 (2s), $^{208}Pb/^{204}Pb = 36.7258 \pm 0.0037$ (2s), $^{207}Pb/^{206}Pb = 0.94185 \pm 0.00003$, $^{208}Pb/^{206}Pb = 2.16742 \pm 0.00012$ (2s) (n=8).

Results

$^{40}Ar/^{39}Ar$ age determinations

The twenty-three new $^{40}Ar/^{39}Ar$ ages presented here (Supplementary TableS1) range from Late Oligocene to Pleistocene (Figure 4). Plateau age spectra criteria were met for seventeen samples (ten groundmass, four plagioclase, and three sanidine). Probability density function ages are preferred for six samples. A high level of precision (2σ < 1.4% of age) was achieved for 14 of the plateau ages including those from sanidine, plagioclase, and groundmass, whereas a lower level of precision (2σ = 1.5%–14% of age) is reported for three of the plagioclase plateau ages and the six probability ages (Supplementary TableS1; Figure 5). Most of the newly reported ages can be grouped into either an Early to Mid-Miocene phase between ~19.4 Ma and 14.0 Ma, or a Pliocene to Pleistocene phase between ~5 Ma and 1 Ma. The exceptions to these groups in the Intersalar Range are lavas from the silicic center of Picacho (9.49 ± 0.77 Ma), the ~8 Ma stock of Cerro Mokho (Leytón and Jurado, 1995), and the ~11 Ma lavas of Huayrana (Salisbury et al., 2015). The Miocene lavas are further divided into western and eastern groups (Figure 3 and subsequent figures).

The oldest dated sample of this study is from the ignimbrite matrix (sample #66) collected near Rio Cancosa on the western Altiplano. As suitable clasts of pumice could not be extracted, we acquired single-crystal fusion data for this sample that show an age peak of 24.87 ± 0.39 Ma. Three slightly older grains were rejected in this treatment, suggesting the presence of a minor population of foreign crystals in the ignimbrite and that the plateau age may be slightly biased toward an older age. We take the younger probability density function age as the best estimate of the timing of emplacement. If this age is reliable, it represents one of the oldest known eruptions at this latitude of western Bolivia and may correlate with ignimbrites in Chile of similar age (Sellés et al., 2016). We report an age of 15.626 ± 0.021 Ma for the

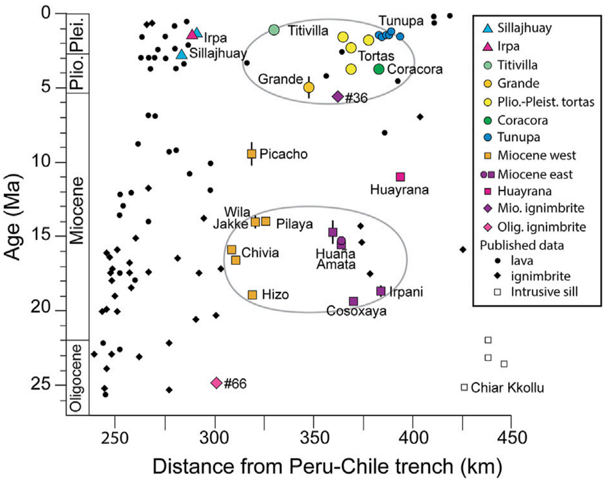

FIGURE 4
^{40}Ar/^{39}Ar age data of this study as colored symbols, including Huayrana and Tunupa of Salisbury et al. (2015), plotted against distance from the Peru-Chile subduction trench. Black circles (effusive lavas) and black diamonds (ignimbrite deposits) represent published data from the literature collected within the area shown in Figure 3 (Baker and Francis, 1978; Davidson and de Silva, 1995; Kennen et al., 1995; Hoke and Lamb, 2007; Jiménez and López-Velásquez, 2008; Mamani et al., 2010; Correa, 2011; McLeod et al., 2012; Sellés et al., 2016). For this study, all two sigma errors are smaller than symbol size except where otherwise noted with vertical bars. Reararc volcanism within the Intersalar Range generally fall into two groups, either a Miocene or a Plio-Pleistocene phase as shown by grey outlines. Miocene eruptions are further divided into western and eastern groups.

breccia clast collected south of the Oligocene to Miocene ignimbrite field of Cerro Chorca. Because of the homogeneity of the deposit, the angular clasts suggesting limited transportation, and similar ages (14.72 ± 0.79 and 15.31 ± 0.11 Ma) reported for two lavas collected from the nearby Huaña Amata center, this breccia clast is considered to be derived from a local source, most likely Huaña Amata.

Lavas from Titivilla volcano gave the youngest ^{40}Ar/^{39}Ar age (1.19 ± 0.11 Ma), although we note that the error for this plagioclase plateau age is higher than most of the other ages of this study. The four dated samples from the apparently low viscosity tortas between Grande and Coracora range between 3.785 ± 0.018 Ma (Jachcha Pallallí) and 1.611 ± 0.022 Ma (Uta Kkollu). The Jachcha Pallallí lavas (3.740 ± 0.018 Ma) are similar in age, morphology, and petrography to the lavas from the western flank of Coracora (sample #42), suggesting that these lavas may be related to the same eruptive episode. For the CVZ arc, our two sanidine plateau ages for Sillajhuay lava flows separated by 500 m of elevation indicate effusive volcanism on the eastern flanks of this large composite volcano at 2.7147 ± 0.0068 Ma and 1.335 ± 0.014 Ma. A plagioclase probability age of 1.457 ± 0.045 Ma for lavas from Irpa further suggest abundant arc activity at these centers in the Late Pliocene and Pleistocene.

Our age results are generally consistent with the relative age estimates of Leytón and Jurado (1995), with some noticeable exceptions: the lavas of Hizo were mapped as Pliocene or younger but gave a sanidine age of 18.877 ± 0.016 Ma; and samples from Sillajhuay and Titivilla gave Pleistocene ages, although they were mapped as Miocene-Pliocene. The Pleistocene Tunupa volcano was also mapped as Miocene-Pliocene although ages from seven individual eruptions indicate a Pleistocene history (1.6–1.2 Ma) for this edifice (Salisbury et al., 2015). We note that although the Salinas de Garci Mendoza quadrangle of Leytón and Jurado (1995) uses a Pliocene/Pleistocene boundary of 1.6 Ma, the ^{40}Ar/^{39}Ar ages mentioned above would still classify as Pleistocene under this scheme. Additionally, the tortas west of Coracora were mapped as Pleistocene to Holocene (younger than 1.6 Ma), although our age results from four of these tortas range from 3.84 to 1.63 Ma. The discrepancy between age estimates based on erosion and our new ^{40}Ar/^{39}Ar ages underscores the importance of precise radiometric age dating in the arid Central Andes. We use the boundary of 2.58 Ma for the Pliocene/Pleistocene throughout this manuscript.

Petrographic overview

Textures of Pliocene to Pleistocene Intersalar Range lavas generally fall into two categories (Supplementary TableS2; Figure 6) that correlate with the composition and type of volcanic center from which they erupted. Lavas from the more silicic (wt% SiO_2 = ~60%–65%) composite centers from both the main arc trend and the reararc region tend to be porphyritic (20%–35% phenocrysts) and are dominated by phenocrysts (~2–7 mm) of plagioclase, or sanidine (Figure 6A). These lavas also contain abundant phenocrysts of biotite (5%–7%) and amphibole (4%–9%) with lesser amounts (≤1%) of orthopyroxene and clinopyroxene. Embayed quartz xenocrysts with pyroxene reaction coronas are present in some samples as are glomerocrysts with the same phenocryst assemblages as the host lavas. The groundmass is dominated by abundant plagioclase microphenocrysts and microlites, often with a hyalopilitic texture. Apatite is a common accessory mineral in all samples. The more mafic (wt% SiO_2 = ~57%–59%) lavas associated with the smaller, monogenetic tortas are generally phenocryst poor (<5%–17%) and contain olivine (3%–5%, ~0.2–1.0 mm) as the primary phenocryst phase with lesser amounts of orthopyroxene, clinopyroxene, and partially to completely opacitized amphibole and biotite (Figures 6B,C). Partially resorbed quartz xenocrysts with pyroxene reaction coronas are also common in these samples. Glomerocrysts are common and are comprised dominantly of olivine. Groundmass textures are strongly hyalopilitic with abundant aligned microlites of plagioclase with some samples also containing microlites of olivine and pyroxene. Miocene lavas show petrographic diversity, although most are porphyritic with

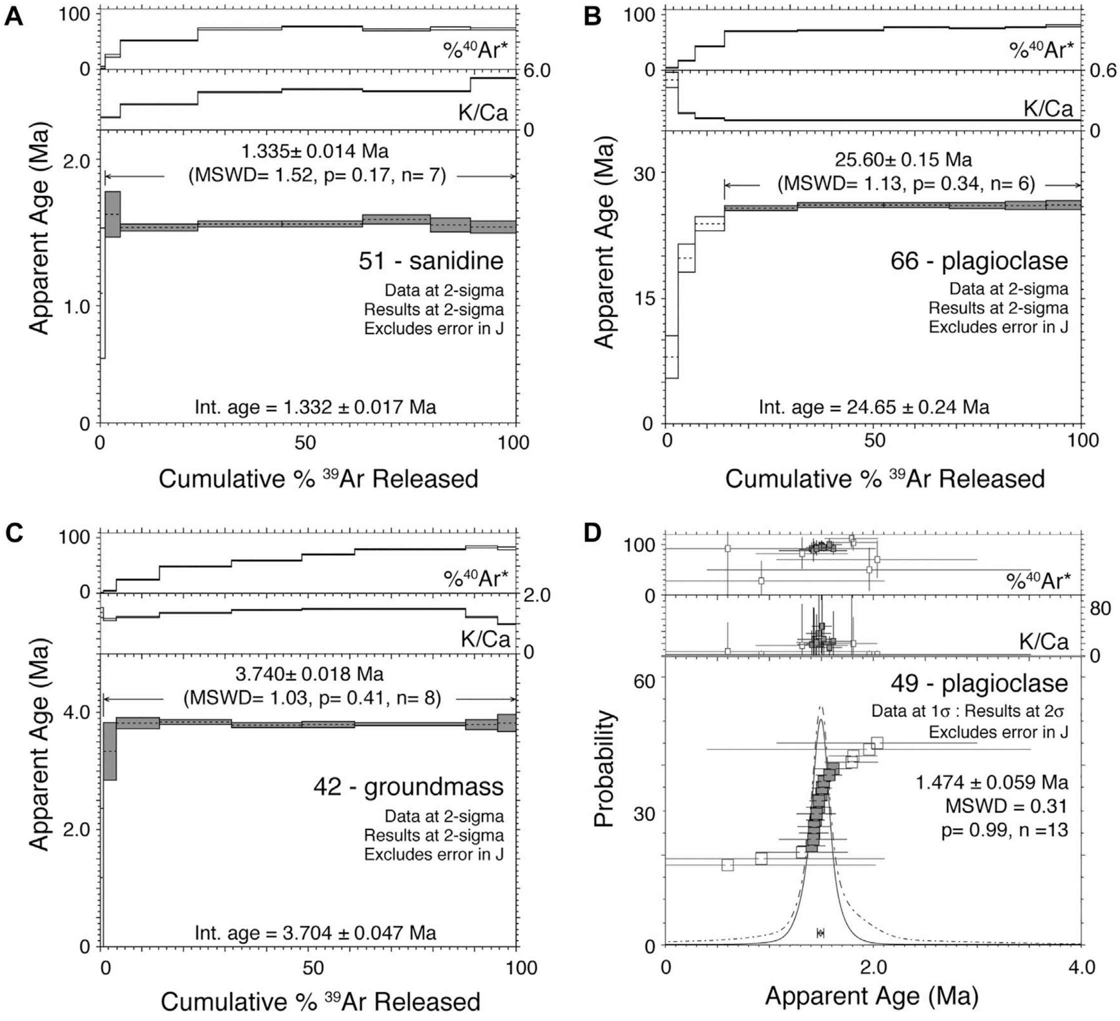

FIGURE 5
Typical plateau age spectra showing representative analyses of Intersalar Range lavas: **(A)** sanidine plateau age (sample #51) **(B)** plagioclase plateau age (sample #66) **(C)** phenocryst-free groundmass age (sample #42); and **(D)** plagioclase probability age (sample #49).

abundant phenocrysts of plagioclase (10%–20%) and pyroxenes (2%–13%). The more mafic samples from Chivia located near the modern CVZ arc also contain olivine phenocrysts, whereas the Cosoxaya lavas from the eastern Intersalar Range contain a significant amount of amphibole (~6%) and biotite (~2%) phenocrysts. Mafic minerals from the Late Oligocene ignimbrite sample near Rio Cancosa were too altered for identification.

Whole-rock geochemistry

The volcanic rocks analyzed in this study (Supplementary Material) range from 53.7 to 76.4 wt% SiO_2 with most samples classified as trachyandesites to trachydacites on a total alkalis-silica (TAS) diagram (Le Maitre et al., 1989) (Figure 7A). The most mafic samples of this study are basaltic trachyandesites collected from the Pliocene Coracora volcano, basaltic andesites from the Miocene Chivia lavas, and the trachyandesites of the Pliocene monogenetic tortas. Consistent with morphology indicating higher viscosity flows, the lavas of the composite centers are mostly trachyandesites to trachydacites. The most silicic samples are rhyolitic. Most Intersalar Range samples plot as subalkaline, with the more mafic Coracora lavas and nearby tortas plotting slightly alkaline (Irvine and Baragar, 1971). On a SiO_2 vs K_2O diagram, Intersalar Range samples plot almost entirely as high-K, calc-alkaline, with only a few of the most silicic samples plotting as shoshonitic (Figure 7B). On Harker diagrams with samples examined as a single suite, MgO, CaO, Al_2O_3, FeO, and TiO_2 are negatively correlated with silica

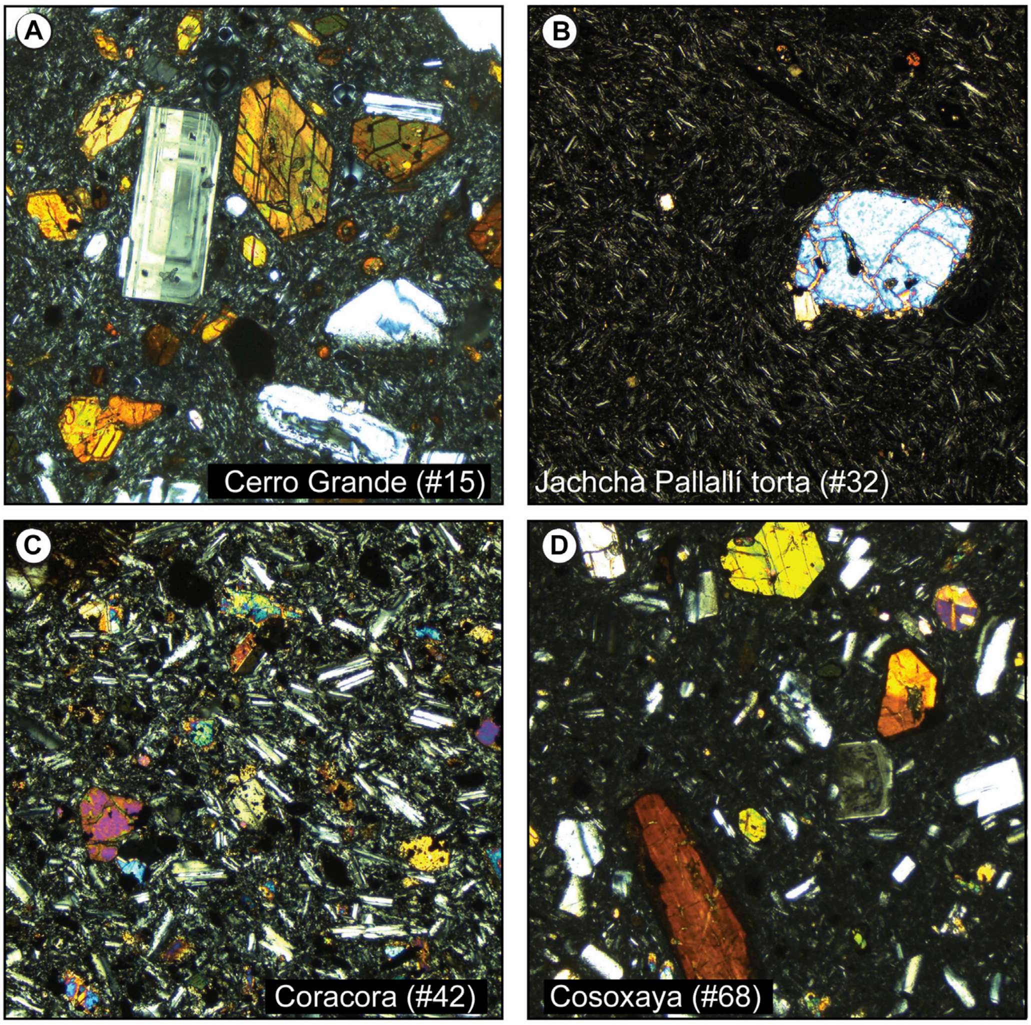

FIGURE 6
Photomicrographs in cross-polarized light of representative petrographic features of Intersalar Range lavas. Field of view is approximately 2 mm for each image. **(A)** Highly porphyritic lava from Pliocene Cerro Grande lavas (sample #15) with phenocrysts of plagioclase and amphibole, typical of silicic composite centers. **(B)** Olivine phenocryst and groundmass from the Pliocene phenocryst-poor trachyandesite Jachcha Pallalí torta (sample #32), typical of lavas from the relatively mafic monogenetic centers of the central Altiplano. **(C)** Olivine-bearing basaltic trachyandesite from the Pliocene Coracora center (sample #42). **(D)** Miocene reararc amphibole- and biotite-bearing trachyandesite lavas of Cosoxaya (Sample #68).

(Figures 8A–D), K_2O is positively correlated, and Na_2O and MnO show little to no variation.

Overall, major and trace element compositions (Supplementary Material, Figure 8) of Intersalar Range lavas show broad similarities with the CVZ arc, with the notable exceptions of the Intersalar Range lavas containing significantly higher concentrations of Nb, Ta, and TiO_2. Considering the entire geochemical suite: Rb, Pb, Th, Y, U, and Cs are positively correlated with silica, whereas Sr, Ni, Cr, V, Cu, Zn, Sc, Sm, and Eu are negatively correlated. In contrast, the high field strength elements (HFSEs), notably Nb, and all other analyzed trace elements show little to no correlation with silica. All Intersalar Range lavas are characterized by typical arc-like trace element signatures with enrichments in Rb, Ba, Th, and K and relative depletions in Nb, Ta, and Ti compared to N-type MORB (Figure 9A). On a chondrite normalized rare earth element (REE) diagram, the younger volcanoes are characterized by steeper slopes and correspondingly higher normalized La/Yb ratios (Figure 9B). Variations in major and trace element data were analyzed with respect to both age and across-arc distance, measured here as distance from the Peru-Chile trench, with the most notable observations shown in Figure 10. These systematic geochemical differences are evaluated below in the Discussion section.

In Intersalar Range samples, $^{87}Sr/^{86}Sr$ values (0.70512–0.70600) show a much smaller range compared to

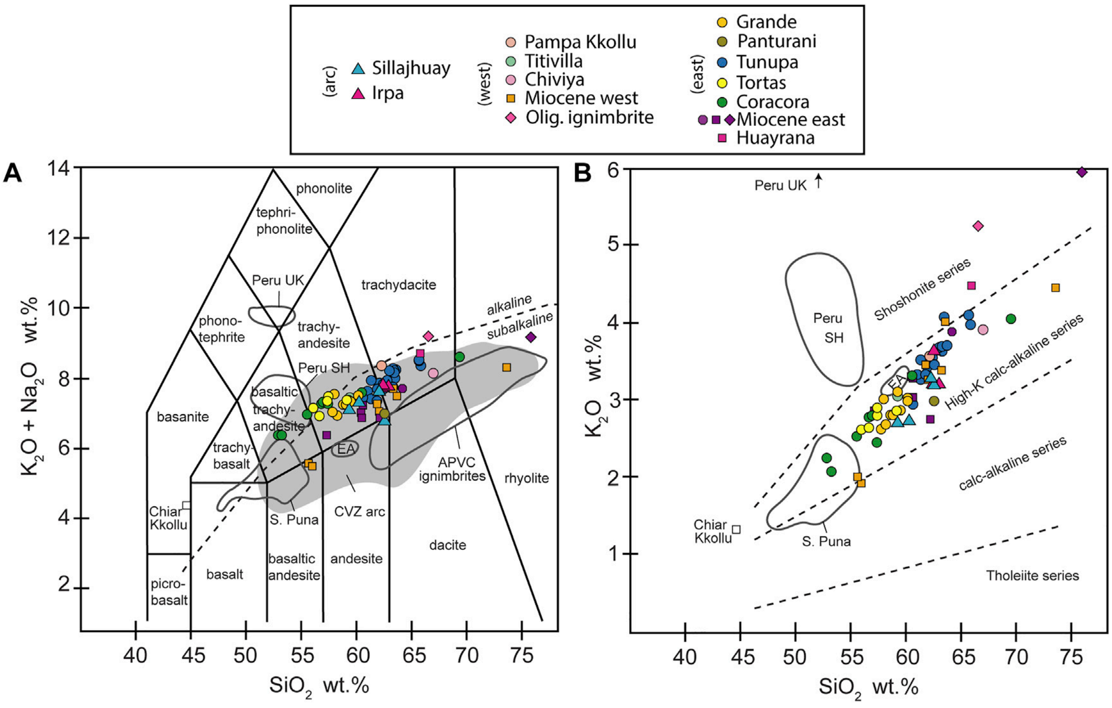

FIGURE 7
Whole-rock geochemical classification for the 50 samples analyzed in this study with examples of relevant plateau volcanism shown for reference. Samples of Tunupa volcano (Salisbury et al., 2015) are included in this diagram and show the range of compositions from a single composite center. **(A)** Total Alkali-Silica (TAS) diagram with classification from Le Maitre et al. (1989) and alkaline/subalkaline fields of Irvine and Baragar (1971). Solid grey field shows the entire distribution of CVZ Quaternary arc lavas (Mamani et al., 2010). Chiar Kkollu (Hoke and Lamb, 2007) and grey outlines show distribution of comparative examples of reararc volcanism discussed in the text: mafic volcanic rocks of the southern Puna (Drew et al., 2009; Risse et al., 2013); shoshonitic (SH) and ultrapotassic (United Kingdom) reararc lavas from the northern Altiplano of Peru (Carlier et al., 2005); Quillacas volcano (EA) of the Bolivian eastern Altiplano (McLeod et al., 2012), and the ignimbrites of the Miocene to Pleistocene Altiplano-Puna volcanic complex (APVC; Salisbury et al., 2011). **(B)** Classification of samples using the SiO$_2$ vs K$_2$O diagram (Irvine and Baragar, 1971; Peccerillo and Taylor, 1976). Distribution of reararc lavas from the literature are the same references as in **(A)**. Ultrapotassic lavas from the Peruvian northern Altiplano plot off the graph (wt% SiO$_2$ = 50–54%; wt% K$_2$O = 7.0–8.1).

^{143}Nd/^{144}Nd (0.51226–0.51255) (Figure 11). Many of the ^{87}Sr/^{86}Sr values are lower compared to the nearby CVZ arc of the northern Altiplano (Parinacota to Ollagüe) and are significantly lower than the lavas of the eastern Altiplano and the large-volume ignimbrite centers of Los Frailes and the Altiplano- Puna Volcanic Complex. ^{143}Nd/^{144}Nd values of the Intersalar Range sample set tend to be somewhat higher than the eastern Altiplano lavas and ignimbrite complexes. In the reararc volcanoes of the Intersalar Range, ^{87}Sr/^{86}Sr values generally increase, and ^{143}Nd/^{144}Nd values decrease, from the Miocene to the Plio-Pleistocene with some exceptions (Figures 12A,B). ^{87}Sr/^{86}Sr values show little correlation with distance from the arc in either age group (Figure 12D), whereas ^{143}Nd/^{144}Nd values of the western Miocene samples are higher than those in the east (Figure 12E). With increasing SiO$_2$, ^{87}Sr/^{86}Sr and ^{143}Nd/^{144}Nd show only moderate positive and negative correlation, respectively. ^{206}Pb/^{204}Pb, ^{207}Pb/^{204}Pb, and ^{208}Pb/^{204}Pb values of Intersalar Range samples range from 17.7315–18.5095, 15.5714–15.6279, and 37.7862–38.6156, respectively. The ^{206}Pb/^{204}Pb values are consistent with Mamani et al. (2010) and nearly all fall within the range of the Arequipa crustal domain ($16.083 < {}^{206}$Pb/^{204}Pb < 18.453) with two of the samples plotting just outside the Arequipa field. Among the reararc samples, Pb isotope values show significantly more systematic variation with respect to east/west distance from the arc (Figure 12F) than with age (Figure 12C). Pb isotopes of Intersalar Range samples show no systematic variation with SiO$_2$.

Discussion

The new dataset presented in this study allows an evaluation of the timing and processes of magmatism in the Intersalar Range of western Bolivia and its relationship to the development of the Central Andean Plateau. Below, we use the term 'arc' volcanism to refer to typical subduction volcanism related to dehydration of the subducting oceanic plate and "non-arc" volcanism to refer to any

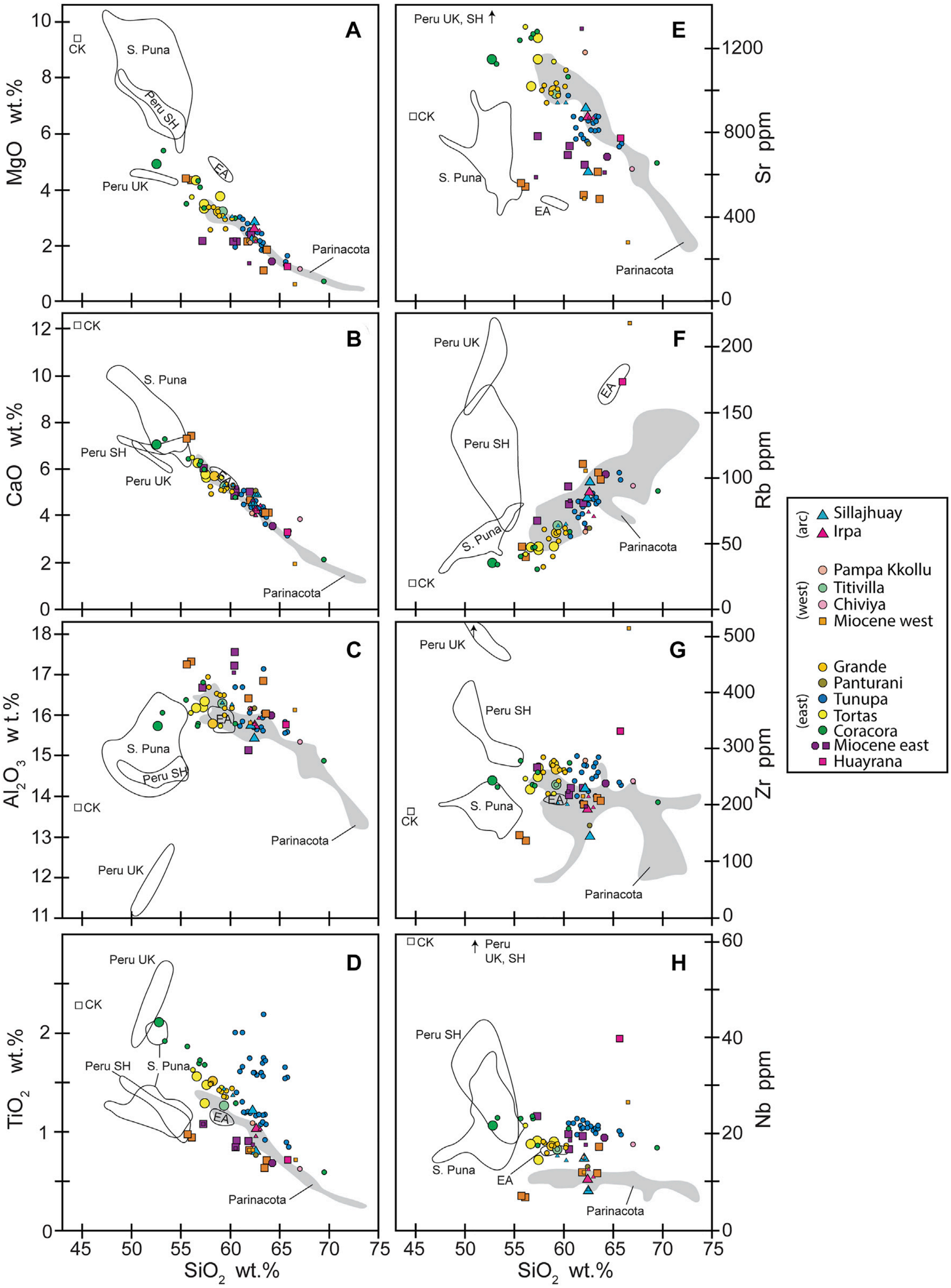

FIGURE 8
Selected Harker diagrams of Intersalar Range lavas. Compositional field of Parinacota volcano shown for comparison to a well-studied CVZ composite volcano of the main arc (Hora et al., 2009). Select reararc lavas of the plateau are also shown for comparison (same references as Figure 7). Reararc TiO_2 and Nb values exhibit the largest deviation from the Parinacota array. Note that shoshonitic (SH) and ultrapotassic (United Kingdom) lavas from the Peruvian reararc (Carlier et al., 2005) are extremely enriched in trace elements and plot off the diagrams of Sr, Zr, and Nb. Larger symbols from the current study represent data with $^{40}Ar/^{39}Ar$ age control.

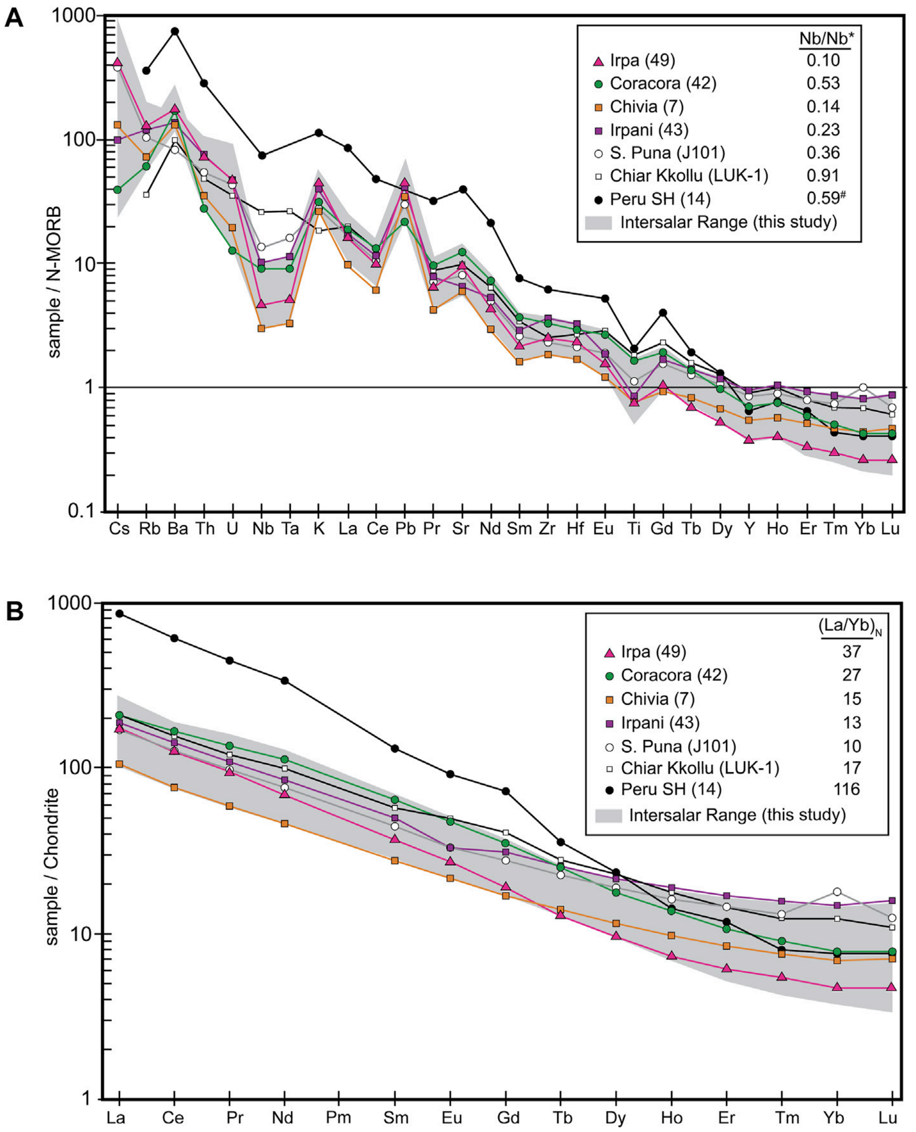

FIGURE 9
Normalized abundances (Sun and McDonough, 1989) of trace elements for representative Intersalar Range samples: Plio-Pleistocene arc (Irpa) and reararc (Coracora); Miocene arc (Chivia) and reararc (Irpani). Prominent reararc lavas shown for reference and discussed in text (references as in Figure 7). Sample numbers in parentheses. **(A)** Spidergram showing incompatible element enrichment patterns relative to the primitive mantle. Notice the wide range in Nb and Ta values. The depth of the negative Nb anomaly shown as values of Nb/Nb*, calculated relative to U and K (#note that Peru shoshonites were not analyzed for U and the value of Nb/Nb* is calculated based on the curve of the pattern shown on this graph). Reararc lavas of both Plio-Pleistocene and Miocene lavas are characterized by smaller negative Nb anomalies (higher Nb/Nb* values) compared to the arc. **(B)** Chondrite-normalized REE patterns. In contrast to Nb/Nb*, the most pronounced differences in REE patterns correlate with age: Pliocene-Pleistocene samples (e.g., Irpa and Coracora) are characterized by steeper slopes and higher La/Yb ratios compared to the Miocene samples (e.g., Chivia and Irpani).

other type of magmatic trigger. Arc volcanism along the western edge of central South America extends to at least the Jurassic and has been more or less continuous in the Western Cordillera at the latitude of the Intersalar Range since the Late Oligocene, following an ~10 m.y. Volcanic hiatus between ~35 and 25 Ma that is attributed to an episode of flat-slab subduction (James and Sacks 1999). Although it is unresolved precisely how far arc volcanism extends eastward into the reararc region, we consider typical subduction-related flux melting unlikely to explain the entirety of Intersalar Range volcanism due to the large distances (>100 km) from the arc front. We also consider the hypothesis of decompression melting and lateral melt migration from beneath Los Frailes (Hoke and Lamb, 2007) as an implausible explanation for the volcanoes of the central Altiplano including those of the eastern

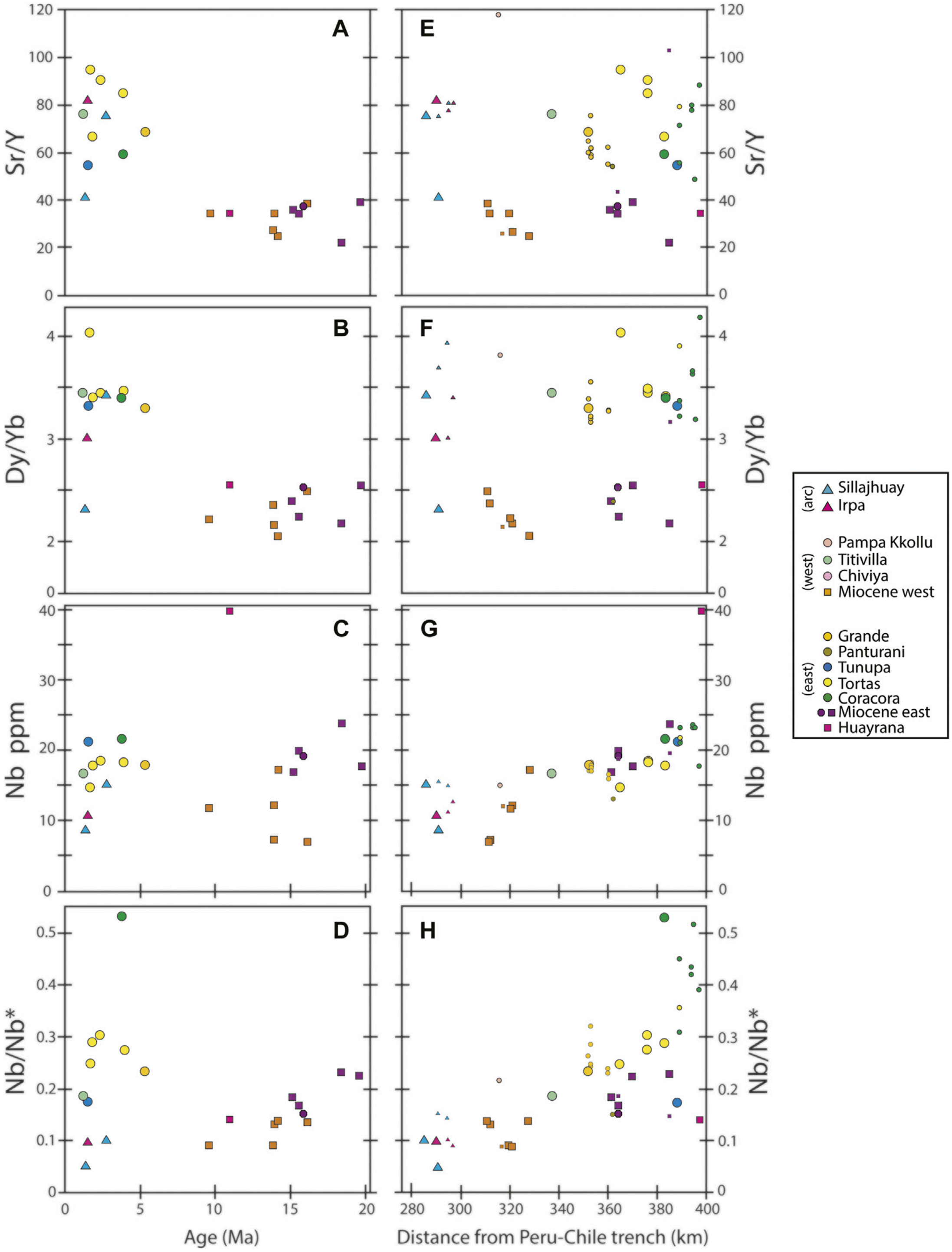

FIGURE 10
Geochemical data from the Intersalar Range plotted against age **(A–D)** and distance from the Peru-Chile trench **(E–H)**. Larger symbols indicate samples with ^{49}Ar/^{39}Ar age control. Nb exhibits the best correlation with distance for all elements analyzed. Nb/Nb* is a measure of the depth of the negative Nb anomaly compared to U and K. See text for details.

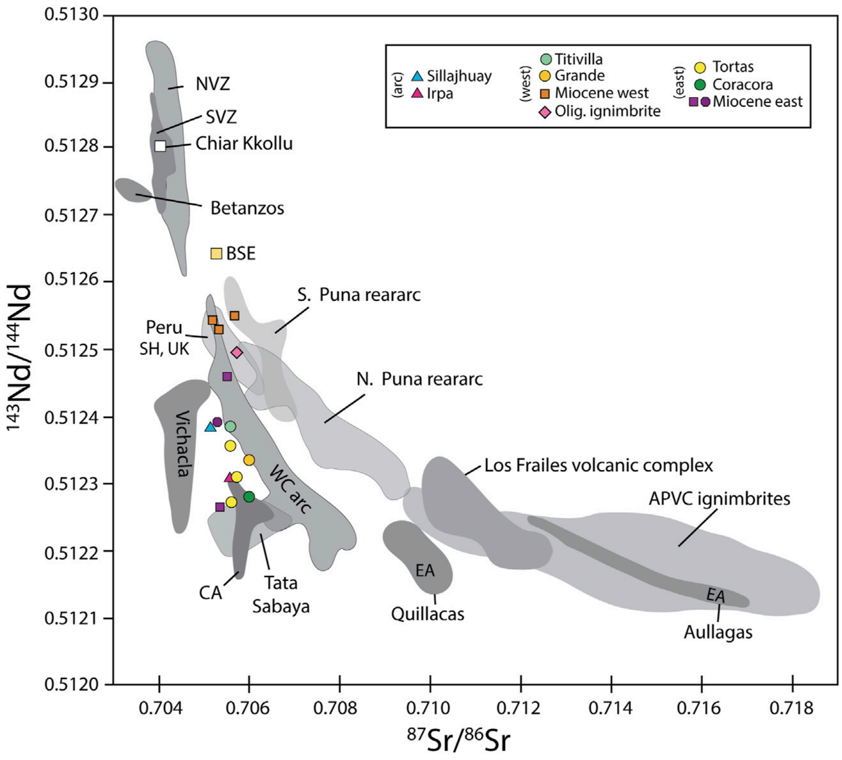

FIGURE 11

$^{87}Sr/^{86}Sr$ and $^{143}Nd/^{144}Nd$ data from the Intersalar Range with select Central Andean igneous rocks for reference. The Western Cordillera (WC) arc array includes Pleistocene centers of Pomerape, Irruputuncu, El Rojo Norte, Olca (Mamani et al., 2010); Aucanquilcha, La Poruñita (Walker 2011); and Ollagüe (Feeley and Davidson, 1994). Reararc centers include Tata Sabaya (de Silva et al., 1993); Chiar Kkollu and other small volume mafic rocks of the central Altiplano (CA; Davidson and de Silva, 1995) and eastern Altiplano (EA; McLeod et al., 2012). Reararc mafic rocks from the central Altiplano (Chiar Kkollu southern Puna in Argentina (Kay et al., 1994; Drew et al., 2009; Risse et al., 2013), the northern Puna in Argentina (Maro et al., 2017), and the northern Altiplano in Peru (Carlier et al., 2005) are shown for reference. Northern Volcanic Zone (NVZ) and Southern Volcanic Zone fields compiled from the GeoROC database 2012 (http://georoc.mpch-mainz.gwdg.de/georoc). Cretaceous rifting-related volcanism of Betanzos and Vichacla from the Bolivian Eastern Cordillera (Lucassen et al., 2007), and the dominantly crustal-derived ignimbrites of Los Frailes (Kato, 2013) and the Altiplano Puna volcanic complex (Lindsay et al., 2001; Kay et al., 2010) are also shown for comparison. Bulk Silicate Earth (BSE) from Rollinson (1993).

Intersalar Range. Such a model would require the lateral melt migration of more than 100 km and is also inconsistent with the apparent pulsing of magmatism in the Intersalar Range, in contrast with the more consistent eruptions of the Los Frailes region since the Early Miocene (Figure 13B).

The onset of widespread reararc volcanism at ~25 Ma across much of the footprint of the Central Andean Plateau, is strongly suggestive of a causal relationship between reararc magmatism and the physical processes related to plateau construction (James and Sacks, 1999; Trumbull et al., 2006). The most likely hypothesis of a reararc melting trigger in the Central Andean Plateau is related to delamination, or foundering, of the mantle lithosphere and mafic lower crust (e.g., Kay and Kay, 1993; Allmendinger et al., 1997; DeCelles et al., 2015). However, the details related to the timing, scale, and mechanisms of foundering remain unconstrained. Removal of the lower crust and lithosphere can induce magmatism by multiple mechanisms, including return flow of the asthenosphere (decompression melting) around the foundering block; conductive heating of the foundering and/or newly exposed mantle lithosphere and crust; and dehydration melting of the asthenosphere and/or mantle lithosphere caused by the pressure-induced breakdown of hydrous minerals as the block descends to greater pressures and depths (e.g., Elkins-Tanton, 2005). In the case of dehydration melting, an arc-like trace element signature would be expected. Assimilation of crust previously generated in an arc setting would also imprint an arc signature. Due to the thick continental crust of the Central Andes, significant amounts of magma storage, assimilation, and fractional crystallization likely occurs at multiple levels in the crust, regardless of the original melting mechanism. Consequently, it can be difficult to unravel arc and non-arc magmatic processes in the Central Andes and it is within this context that we evaluate the spatial, temporal, elemental, and isotopic differences within the Intersalar Range to search for clues into the underlying magmatic sources and melting triggers.

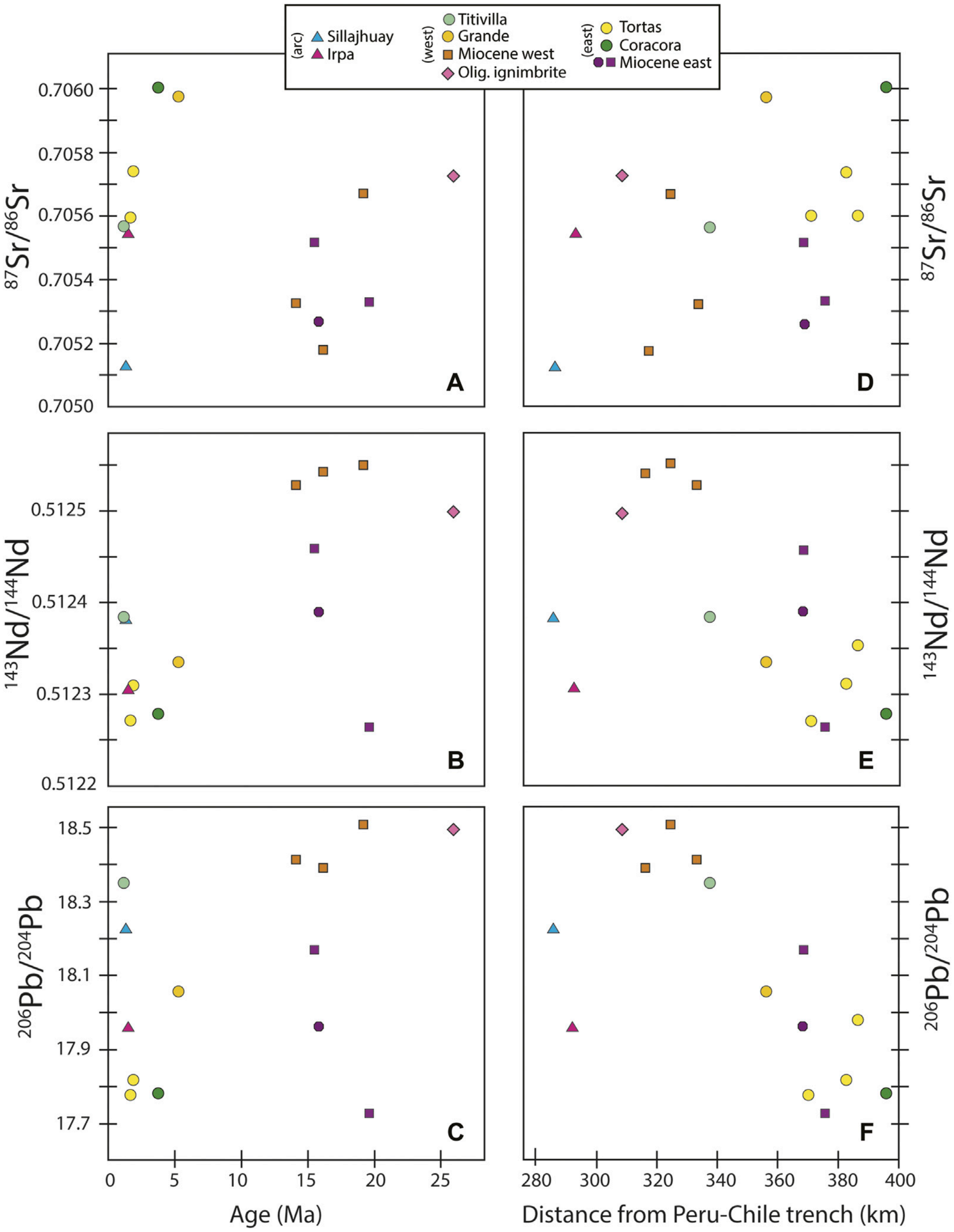

FIGURE 12
Isotope data from the Intersalar Range plotted against age **(A–C)** and distance **(D–F)**.

Volcanism, deformation, and crustal thickening in the Intersalar Range

The apparent pulsing of magmatism in the eastern Intersalar Range (>100 km from the contemporaneous arc front) in the Miocene and the Plio-Pleistocene is consistent with at least two separate melting events, most likely related to partial removal of the mantle lithosphere and lower crust. The first pulse began with the relatively low-volume eruptions of Cosoxaya and Irpani in the Early Miocene and continued with a larger flux of volcanism in the same region between ~14 and 16 Ma with the eruption of lavas of the Huaña Amata composite center. This larger flux of volcanism may also include significant volumes of explosive volcanism as evidenced by two coincident K/Ar ages reported by Leytón and Jurado (1995)

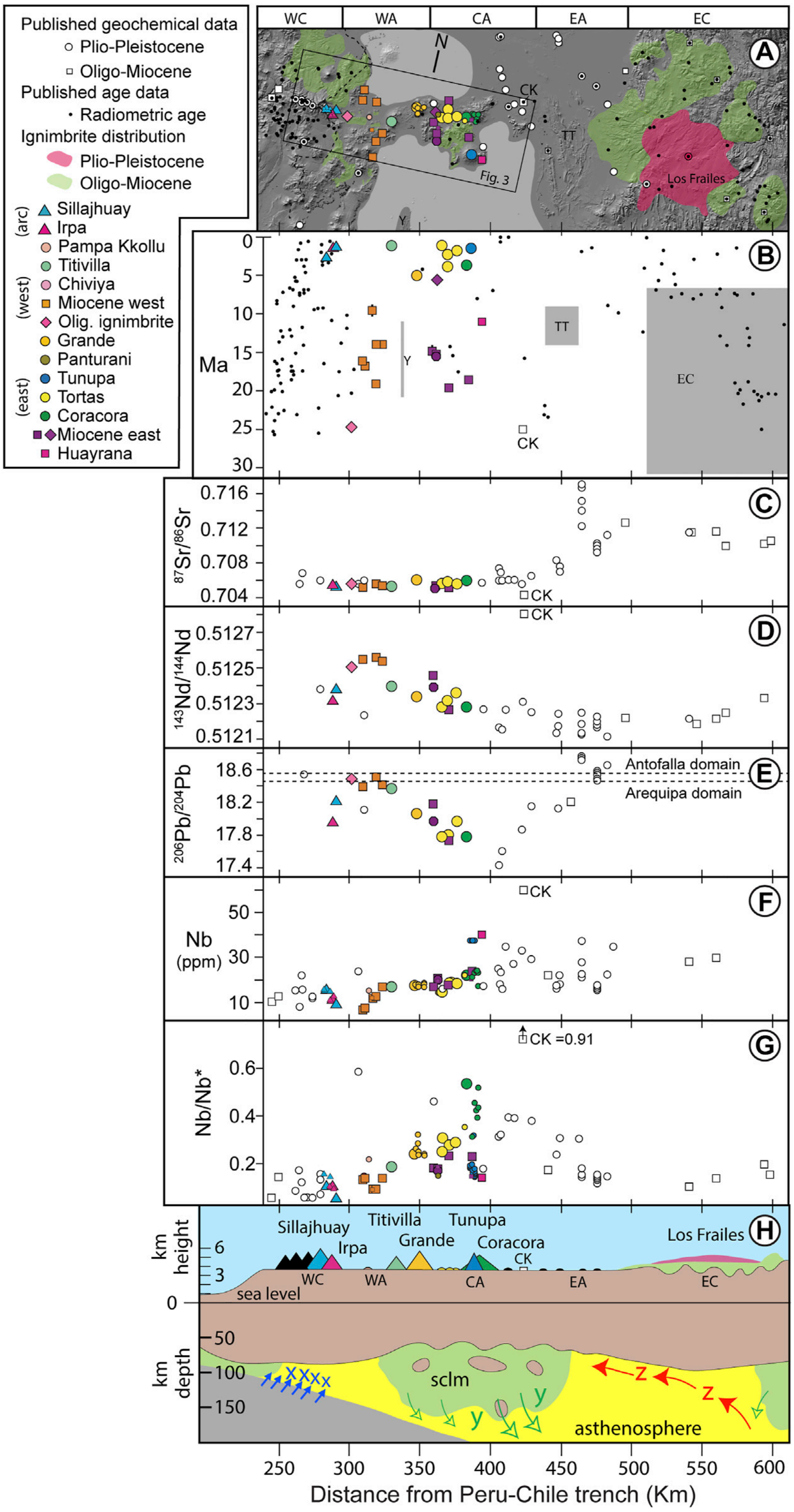

FIGURE 13
Arc-perpendicular compilation of available data collected within the larger bounding box of Figure 1. Note that north is offset approximately 12.5° to align perpendicular to the Peru-Chile trench and the trend of the CVZ arc (See Figure 1). Colored symbols from this study and Salisbury et al. (2015); larger symbols indicate samples with $^{49}Ar/^{39}Ar$ age data. Compositional data are restricted to <66 wt% SiO_2. **(A)** Sample localities of this study and all available published data within the confines of the image. The horizontal axis is shown in **(H)** and is the same in all graphs. WC, Western

(Continued)

FIGURE 13 (Continued)
Cordillera, WA, western Altiplano, CA, central Altiplano, EA, eastern Altiplano, EC, Eastern Cordillera, CK, Chiar Kkollu, Y, Yazón Anticline, TT, Tambo Tambillo fold and thrust belt. **(B)** Compilation of data from this study and published radiometric age data (Evernden et al., 1977; Grant et al., 1979; Almendras, 2002; Aitcheson et al., 1995; Kato, 2013; and references of Figure 4), sample localities shown in **(A)**. Shaded areas represent timing and width of exposed surface deformation of the Yazón anticline (Elger et al., 2005), Tambo Tambillo fold and thrust belt (Kennen et al., 1995) and the Eastern Cordillera (McQuarrie et al., 2005). **(C–E)** $^{87}Sr/^{86}Sr$, $^{143}Nd/^{144}Nd$, and $^{206}Pb/^{204}Pb$ isotope data from this study and published data (same references as Figure 11). The Pb isotope domains (based on Pb isotope values, not location) of Mamani et al. (2010) are shown for reference in **(E)**. **(F)** Nb concentrations plotted against distance from trench showing distinct eastward increase from the CVZ arc to the central Altiplano. Published data with multiple datapoints for single centers are shown as averages. **(G)** Nb/Nb* values plotted against distance from Peru-Chile trench. Higher values indicate smaller negative Nb anomalies. The highest Nb/Nb* values are found within igneous rocks of the central Altiplano and correlate spatially with the presence of the intact mantle lithospheric root shown in **(H)**. **(H)** Schematic cross section across the Central Andean Plateau showing proposed dominant melting triggers beneath each region. X = dehydration of subducting Nazca plate; y = foundering of subcontinental lithospheric mantle (sclm) and lower crust; Z = decompression melting of upwelling asthenosphere as described by Hoke and Lamb (2007). Following Hoke and Lamb (2007), foundering of the mantle lithosphere beneath the Eastern Altiplano/Eastern Cordillera likely occurred following the end of flat-slab subduction ~25 Ma. Lithospheric structure after Beck and Zandt (2002).

for the extensive ignimbrites of Chorca and Mokho. An apparent ~8 m.y. Hiatus of significant volcanism in the eastern Intersalar Range was then followed by the second pulse of magmatism, represented by eruptions of the Grande, Coracora, Tunupa, and the monogenetic tortas.

The timing of the Miocene pulse of volcanism in the Intersalar Range overlaps with deformation of the Yazón Anticline (Figure 13B), suggesting a possible relationship between these two events. There is no temporal relationship between Plio-Pleistocene volcanism and surface structures in the region. Trace element data are consistent with significant crustal thickening following the Miocene pulse and preceding the Plio-Pleistocene pulse. Higher Sr/Y values are recorded in the Plio-Pleistocene lavas compared to the Miocene samples in both the western and eastern parts of the range, with little to no observed spatial variation in either age group (Figures 10A,E). These higher values suggest magma equilibration in the presence of garnet and absence of plagioclase at the base of significantly thicker crust in the Plio-Pleistocene compared to the Miocene (e.g., Kay et al., 1994). Higher Dy/Yb in the Plio-Pleistocene group (Figure 10B) is also consistent with an increasing role of garnet, as opposed to amphibole, in the fractionation of the younger lavas. A thicker crust in the Plio-Pleistocene is further supported by steeper, chondrite-normalized REE patterns and higher $[La/Yb]_N$ values (Figure 9B), further indicating an increasing role of garnet fractionation in the younger samples. As the 9.49 ± 0.77 Ma Picacho lavas plot with the older samples, the crustal thickening implied by the trace element data likely occurred after this time. Figures 12A,B shows an apparent increase in $^{87}Sr/^{86}Sr$ and decrease in $^{143}Nd/^{144}Nd$ in the Plio-Pleistocene samples compared to the Miocene samples, although overlap is observed. This result is consistent with increased assimilation of continental crust in the younger, thicker crust. No systematic variations in Pb isotopes were observed between the two age groups. As the Late Miocene crustal thickening implied by the trace element data apparently occurred in the absence of local surface deformation, lower crustal flow from deformation of the Tambo Tambillo region (~14–5 Ma) and/or from the Eastern Cordillera (Husson and Sempere, 2003) may be invoked to resolve this discrepancy. The ductile flow of crust and, presumably, the mantle lithosphere below, is also consistent with the proposed foundering magmatic trigger of the Plio-Pleistocene volcanism of the eastern Intersalar Range.

Spatiotemporal and geochemical variations across the Intersalar Range and the Central Andean Plateau

To determine which elements showed the strongest east-west variation across the Intersalar Range, we plotted the concentration of all analyzed major and trace elements against distance from the Peru-Chile trench and quantified the correlations through least squares (r-squared) analysis. Only samples with age control and $SiO_2 < 63$ wt% were used in these calculations. Our results indicate that although overall systematic trace element variations across the Intersalar Range are limited, select elements, particularly Nb and other HFSEs, do show significant east-west correlations. For the Plio-Pleistocene group, Nb ($r^2 = 0.75$) shows the strongest correlation with distance from the trench and, thus, the arc front. For the Miocene group, the Nb correlation ($r^2 = 0.83$) is second only to Eu. Consequently, in the Plio-Pleistocene group, any ratio with Nb in the numerator increases with eastward distance in the Intersalar Range, and any ratio with Nb in the denominator will decrease. This observation suggests that the Nb values are not primarily controlled by lower amounts of partial melting in the reararc. The relative increase in Nb concentrations relative to other trace elements into the reararc is further demonstrated by correspondingly decreasing depths of the negative Nb anomaly on mantle-normalized spidergrams of Intersalar Range lavas (Figure 9A). The Nb anomaly can be quantified through calculation of Nb/Nb*, measured as the depth of the Nb anomaly relative to the adjacent LILEs of U and K. It is calculated here as $[Nb/Nb^* = Nb_N/(U_N^{2/3} * K_N^{1/3})]$ where Nb_N, U_N, and K_N are the mantle-normalized (Sun and McDonough, 1989) values of Nb, U, and K, respectfully; as for a similar calculation for Dy/Dy* by Davidson et al. (2007). We note that the choice of nearby trace elements to make this calculation makes little difference in the across-arc calculations of Figure 10H as Nb increases in the reararc are higher relative to all other trace elements analyzed.

Figure 10H demonstrates the significant increase of Nb/Nb* into the reararc in the Plio-Pleistocene samples, and to a lesser extent in the Miocene group. In the Plio-Pleistocene samples, no systematic east-west variations in isotopic ratios are observed, and only moderate differences are observed in the Miocene samples in ^{143}Nd/^{144}Nd and ^{206}Pb/^{204}Pb.

To better comprehend the spatiotemporal and geochemical differences across the Central Andean Plateau, we extended our across-arc analysis to include available published data between ~19ºS and 21.6ºS, spanning the Western Cordillera, Altiplano, and Eastern Cordillera and compare these data with a schematic cross section of the lithospheric structure modified from Beck and Zandt (2002) based on geophysical and geological studies at the latitude of the study area (Figure 13). The most intriguing result of this analysis is the correlation observed between the highest Nb/Nb* values of the Plio-Pleistocene lavas and the location of the mantle lithosphere root identified by Beck and Zandt (2002) beneath the central Altiplano (Figures 13G,H). In contrast, lower Nb/Nb* values (stronger negative Nb anomalies) correlate with the arc front of the Western Cordillera and the far reararc of the eastern Altiplano and Eastern Cordillera, both regions where subcontinental lithosphere mantle is hypothesized by Beck and Zandt (2002) to be absent. We note that the overall conical shape of this pattern is apparent in the relatively more mafic rocks of the tortas, Coracora, and the monogenetic flows of the central and eastern Altiplano, suggesting that fractionation of K and U is not a major factor. This observation is supported by the overall concentrations of Plio-Pleistocene Nb values, which are significantly higher in the eastern Intersalar Range lavas compared to the west (Figures 9A, 10G), and show almost no variation with wt% SiO_2 in the Intersalar Range (Figure 8H) or within individual centers (Salisbury et al., 2015).

Pb isotope values also appear to show a correlation with the presence of subcontinental mantle lithosphere as samples with the lowest ^{206}Pb/^{204}Pb are located in the central Altiplano (Figure 13E). ^{87}Sr/^{86}Sr values vary very little from the arc to the central Altiplano and are significantly higher in the east where the mantle lithosphere is absent (Figure 13C), including within the relatively mafic, olivine-bearing monogenetic centers of the eastern Altiplano (Davidson and de Silva, 1995; McLeod et al., 2013) and the ignimbrites of the Los Frailes volcanic complex (Kato, 2013). ^{143}Nd/^{144}Nd values are highest in the Intersalar Range, particularly in the Miocene samples, and are generally lower in the eastern Altiplano and Eastern Cordillera (Figure 13D).

Petrogenesis of Intersalar Range magmatism

Based on the spatial, temporal, and geochemical variations of this study and of those across the plateau, we consider the hypothesis of piecemeal foundering of enriched mantle lithosphere and eclogitized lower crust beneath the central Altiplano during the Miocene, and again during the Plio-Pleistocene, as the most likely explanation of reararc volcanism in the Intersalar Range. This hypothesis is primarily supported by the apparent pulsing of magmatism in the eastern Intersalar Range, and systematic differences in geochemistry between the arc and reararc regions, including elevated Nb and Nb/Nb* values in the eastern Intersalar compared to the western portion of the range and the arc front (Figure 9A, 10G-H, 13F-G). We expand on the model of Salisbury et al. (2015), which interpreted the anomalously high Nb concentrations of Tunupa volcano to reflect a significant component of the mantle lithosphere and suggested that the breakdown of the hydrous phases of amphibole and phlogopite as most likely responsible for the Nb signal. In this model, hydrous minerals such as amphibole and phlogopite strongly concentrate Nb-Ta-Ti during episodes of flat-slab subduction and metasomatism of the mantle lithosphere. Although HFSE are thought to be largely residual during slab dehydration, Nb-Ta-Ti may concentrate in hydrous minerals over multiple episodes of flat-slab subduction over 10s or 100s of millions of years. When the thickened mantle lithosphere and garnet-bearing lower crust become gravitationally unstable, detach, and founder (delaminate) into the asthenosphere, the increasing pressure forces the breakdown of amphibole and phlogopite, triggering wet melting and releasing their Nb-enriched trace element load. As vein amphibole in mantle xenoliths found elsewhere can contain higher concentrations of Nb and Ta relative to primitive mantle compared to all other trace elements, including K (Ionov et al., 1997), we consider this phase the most probable to control the observed Nb signal in the Intersalar Range and the broader arc-normal transect (Figure 13F). Fractionation of Ti-oxides such as rutile may also play a role in the Nb-Ta-Ti systematics, however, amphibole, and to a lesser extent phlogopite, are by far more common in mantle xenoliths in alkali basalts (Ionov et al., 1997). Cenozoic mantle xenoliths are essentially absent in the Cenozoic Central Andes (Lucassen et al., 2005), however, the extremely high Nb (>100 ppm) and Nb/Nb* values (>1) of Cretaceous-aged, extension-related alkaline magmatism from Ayopaya, Betanzos, and Vichacla (Schultz et al., 2004; Lucassen et al., 2007) in what is now the Eastern Cordillera of Bolivia suggest that the mantle lithosphere was already strongly metasomatized prior to the most recent flat-slab subduction between ~35 and 25 Ma. Partial removal of the lower lithosphere likely also triggers decompression melting in the upwelling asthenosphere. Following Blume-Oeste and Wörner (2016), we consider the lavas of the eastern Intersalar Range to be derived from a mixture of the mantle lithosphere and the convecting mantle asthenosphere, which then further assimilate and homogenize within the continental crust. Identification of precise compositions and the relative volume of endmember components is challenging as the few mafic magmas that erupted on the Central Andean Plateau are scattered across the plateau, and the composition of the mantle lithosphere, asthenosphere, and crust likely vary in both space and time.

We propose that Nb is particularly useful in recognizing a significant component of the mantle lithosphere even in magmas that are heavily influenced by crustal processing. Magmas thought to be derived from the mantle lithosphere are typically alkaline and defined by distinct Nb enrichments relative to most other trace elements (e.g., Pilet et al., 2008). In the Intersalar Range dataset, the basaltic trachyandesites from Coracora and the trachyandesitic monogenetic tortas west of Coracora, provide the strongest evidence for magmas with a significant component of enriched mantle lithosphere as a result of melting related to lithospheric foundering. The Coracora lavas erupted ~130 km east of the contemporaneous arc front (Figures 4, 13A,Figures 13B), are slightly alkaline (Figure 7), relatively high in TiO_2 (Figure 8D), and are characterized by the highest Nb/Nb* values analyzed in this study (Figures 9A, 10H). The mafic, isotopically depleted, trace-element enriched, ~25.1 Ma Chiar Kkollu sill (Davidson and de Silva, 1995; Hoke and Lamb, 2007) located in the central Altiplano ~20 km east of the Intersalar Range (Figures 1, 3) may represent the least-contaminated endmember of mantle lithosphere-derived magmatism in the Bolivian Altiplano, and data from this sample are shown in Figures 4, 7–9, 11, 13 for comparison with the newly collected data of this study. Chiar Kkollu has the highest measured Nb concentrations (60 ppm) and the highest Nb/Nb* values (0.91) of the Bolivian Altiplano and is also situated above the partially intact mantle lithospheric root of the central Altiplano (Figures 13F–H).

Elsewhere in the Central Andean Plateau, elevated Nb and Nb/Nb* values are observed in mafic lavas of the southern Puna of Argentina (Drew et al., 2009; Risse et al., 2013), and the phlogopite-bearing shoshonites and ultrapotassic mafic lavas of the northern Altiplano of Peru (Carlier et al., 2005), both of which show little to no evidence of crustal contamination and are interpreted to derive from the mantle lithosphere. The mafic rocks of the southern Puna of Argentina have long been hypothesized to be the result of lithospheric delamination (e.g., Kay and Kay, 1993; Kay et al., 1994; Drew et al., 2009; Murray et al., 2015) and we suspect a similar process in the central Altiplano of Bolivia, although with more crustal contamination in the Bolivian samples. The southern Puna and northern Altiplano reararc lavas are plotted in Figures 7–9, 11 to demonstrate the geochemical similarities with the lavas of the eastern Intersalar Range, particularly those of Coracora volcano.

Alternatively, or additionally, the source of the observed high Nb concentrations could be influenced by the breakdown of an amphibole-rich "sponge" that had accumulated in the middle to lower crust (Davidson et al., 2007), which filters these elements in addition to water. However, in volcanoes such as Mount Pelée where "cryptic amphibole fractionation" is suspected due to decreases in Dy/Yb with increasing SiO_2 (Davidson et al., 2007) a corresponding decrease in Nb is not observed, suggesting that Nb is not strongly concentrated in amphibole at crustal pressures. Furthermore, crustal compositions of exposed Andean basement and crustal xenoliths are typically lower in Nb concentrations than those observed in the central Altiplano lavas (e.g., Lucassen et al., 2005), suggesting that the mantle lithosphere is most likely responsible for the observed Nb signature in Intersalar Range lavas. Evidence against a crustal influence for the observed Nb signal is also found in the lack of north-south Nb and Nb/Nb* variations in lavas erupted on either side of the of the Pb-isotope-defined crustal boundary along the Quaternary CVZ arc (Aitcheson et al., 1995; Mamani et al., 2010), suggesting that the distinct crustal domains are not strongly affecting Nb trends.

The variations in Sr-Nd-Pb isotopes observed in this study preclude a simple interpretation with respect to the mantle source regions across the Intersalar Range and the broader plateau transect. Despite the limitations, the isotopic data show some consistency with our hypothesized petrogenetic model. A correlation is observed between Pb isotope values and the presence of the lithospheric root beneath the central Altiplano (Figure 13E), although these variations exist within the field of the Arequipa domain of Mamani et al. (2010) and may also be explained by local variations in the age of the contaminated continental crustal. The relatively low $^{87}Sr/^{86}Sr$ and somewhat high $^{143}Nd/^{144}Nd$ values of the Intersalar Range compared to other reararc lavas of the Central Andean Plateau (Figures 13C,D) are consistent with a component of mantle lithosphere as evidenced by correspondingly low $^{87}Sr/^{86}Sr$ and high $^{143}Nd/^{144}Nd$ values of regional magmas suspected to be derived from the mantle lithosphere, including those of Betanzos and Vichacla in Bolivia (Lucassen et al., 2007), and the shoshonites and ultrapotassic lavas of the Peruvian reararc (Carlier et al., 2005) (Figure 11). However, significant overlap in these values with lavas from the arc is also observed and we note that lavas from Coracora are characterized by the lowest $^{143}Nd/^{144}Nd$ values analyzed in this study. Despite a significant shift in Sr isotope values at the boundary between the central and eastern Altiplano, no clear correlation with the mantle lithosphere root in the central Altiplano is apparent in the data in either the Sr or Nd isotope data (Figures 13C,D). We suggest that in the absence of mafic magmatism and a correspondingly definitive isotopic signature, Nb and Nb/Nb* values may be useful in identifying a significant component of mantle lithosphere. Nb (and to a lesser extent Ta and Ti), may be one of the few elements that can effectively "see through" the effects of crustal contamination in silicic rocks and can aid in the identification of primary characteristics of the underlying mantle source.

Conclusion

The Intersalar Range provides a unique opportunity to assess a temporally constrained transect spanning the arc and rear arc regions of the Bolivian Altiplano. Twenty-three new $^{40}Ar/^{39}Ar$ age dates reveal a discontinuous eruptive history in the reararc region with primary magmatic phases in the Miocene (~20–11 Ma, dominantly between 14–16 Ma) and the Plio-Pleistocene (~5–1 Ma). The distinct eruptive phases contrast with the more continuously active volcanism in the Western and Eastern Cordilleras and are suggestive of distinct, non-arc magmatic triggers beneath the central Altiplano at these times. We interpret these data within the context of previous studies (e.g., Beck and Zandt, 2002; Barnes and Ehlers, 2009; Drew et al., 2009) which favor a model of localized, piecemeal foundering events over the timespan of construction of the Central Andean Plateau to explain the relative lack of mantle lithosphere and lower mafic crust, and the apparent slow and steady uplift of the plateau. Although the Miocene volcanism coincides temporally with surface deformation to the south of the Intersalar Range, significant crustal thickening between ~9.5 Ma and ~5 Ma is implied by elevated Sr/Y, Dy/Yb, and $[La/Yb]_N$ in the Plio-Pleistocene samples, consistent with ductile lower crustal flow as a mechanism to thicken the crust and to promote lithospheric foundering. Relatively high Nb concentrations (>~15 ppm) compared to the arc, and high Nb/Nb* values (>0.3) correlating with the presence of intact mantle lithosphere beneath the central Altiplano, are interpreted as reflecting dehydration melting triggered by the breakdown of hydrous minerals within the partially removed mantle lithosphere. This Nb signature is most apparent in the Plio-Pleistocene phase of volcanism of the eastern Intersalar Range of the central Altiplano, particularly in the lavas of Coracora volcano, although also recognizable in the Miocene samples.

The remaining mantle lithospheric root beneath the central Altiplano suggests that the process of piecemeal founding is either ongoing, and/or represents a potential location of future lithospheric foundering. High $^3He/^4He$ values of geothermal spring water near Coracora volcano in the eastern Intersalar Range, as well as in the broader region, indicate that mantle melting and storage beneath the Altiplano is either recent (<< 1 Ma) or active (Hoke and Lamb, 2007), suggesting an ongoing melting trigger beneath the plateau.

Although alternative explanations can be invoked, relatively low $^{87}Sr/^{86}Sr$ values hint at a contribution of isotopically depleted mantle lithosphere (e.g., Rogers and Hawkesworth, 1989) and share similarities with alkaline magmatism related to lithospheric foundering in the southern Puna and northern Altiplano reararc regions of the Central Andean Plateau. Pb isotope variations also show correlation with the mantle lithospheric root beneath the central Altiplano, however, variations in crustal Pb compositions may also explain these data. Decompression melting of the asthenosphere and magma mixing, crustal assimilation, and homogenization of magmas in the thick Andean crust all obscure the contributions of the mantle lithosphere in Central Andean lavas. In the absence of mafic magmatism and clear isotopic signatures, Nb systematics may provide important clues of the mantle source components.

Data availability statement

The original contributions presented in the study are included in the article/Supplementary Material, further inquiries can be directed to the corresponding author.

Author contributions

MS Principle Investigator. Developed the project in collaboration with NJ and Jon P. Davidson. Wrote the grants for funding, led the field investigations, performed the majority of sample preparation, coordinated all analytical analyses, interpreted the results, primary author of manuscript. NJ Collaborated with the overall development of the project. Coordinated field excursions. Participated in discussions regarding results and interpretations and contributed input and text for the manuscript. DB led the investigations of the $^{40}Ar/^{39}Ar$ age data. Wrote sections of the manuscript regarding the Ar-Ar data. Reviewed manuscript and contributed to interpretations and conclusions of the study.

Funding

This research was performed by MS as part of the International Junior Research Fellowship program at Durham University. The Department of Earth Sciences at Durham University provided additional funding for fieldwork, thin section preparation, and isotope analyses. Funding for 40Ar/39Ar age determinations was provided by the Natural Environmental Research Council (NERC). The Instituto de Investigaciones Geológicas y del Medio Ambiente at the Universidad Mayor de San Andrés provided vehicles for fieldwork.

Acknowledgments

We are extremely grateful for the mentorship of Jon P. Davidson at Durham University, whose lifetime of work in the Central Andes laid the foundation for this study. We also thank three anonymous reviewers for their helpful comments which greatly improved this manuscript.

Conflict of interest

The authors declare that the research was conducted in the absence of any commercial or financial relationships that could be construed as a potential conflict of interest.

Publisher's note

Supplementary material

The Supplementary Material for this article can be found online at: https://www.frontiersin.org/articles/10.3389/feart.2022.917488/full#supplementary-material

References

Aitcheson, S. J., Harmon, R. S., Moorbath, S., Schneider, A., Soler, P., Soria-Escalante, E., et al. (1995). Pb isotopes define basement domains of the Altiplano, central Andes. *Geol.* 23 (6), 555–558. doi:10.1130/0091-7613(1995)023<0555:pidbdo>2.3.co;2

Allmendinger, R. W., Jordan, T. E., Kay, S. M., and Isacks, B. L. (1997). The evolution of the Altiplano-Puna Plateau of the central Andes. *Annu. Rev. Earth Planet. Sci.* 25, 139–174. doi:10.1146/annurev.earth.25.1.139

Allmendinger, R. W., Smalley, R., Jr., Bevis, M., Caprio, H., and Brooks, B. (2005). Bending the Bolivian orocline in real time. *Geol.* 33 (11), 905–908. doi:10.1130/g21779.1

Almendras, O. (2002). Rio mulato quadrangle, SE 19-16: Thematic maps of mineral resources of Bolivia, publication SGB serie II-MTB-10B, GEOBOL-SGAB, scale 1:250,000, 1 sheet.

Baker, M., and Francis, P. (1978). Upper cenozoic volcanism in the central Andes – ages and volumes. *Earth Planet. Sci. Lett.* 41, 175–187. doi:10.1016/0012-821X(78)90008-0

Barnes, J. B., and Ehlers, T. A. (2009). End member models for Andean Plateau uplift. *Earth-Science Rev.* 97, 105–132. doi:10.1016/j.earscirev.2009.08.003

Beck, S. L., and Zandt, G. (2002). The nature of orogenic crust in the central Andes. *J. Geophys. Res.* 107, ESE 7-1–ESE 7-16. doi:10.1029/2000JB000124

Blum-Oeste, M., and Wörner, G. (2016). Central Andean magmatism can be constrained by three ubiquitous endmembers. *Terra nova.* 28, 434–440. No. 6. doi:10.1111/ter.12237

Cahill, T., and Isacks, B. L. (1992). Seismicity and shape of the subducted Nazca plate. *J. Geophys. Res.* 97, 17503529. . B12503–17. doi:10.1029/92JB00493

Carlier, G., Lorand, J. P., Liegeois, J. P., Fornari, M., Soler, P., Carlotto, V., et al. (2005). Potassic–ultrapotassic mafic rocks delineate two lithospheric mantle blocks beneath the southern Peruvian Altiplano. *Geol.* 33, 601–604. doi:10.1130/g21643.1

Correa, N. A. (2011).Evolución Geológica y Petrológica del complejo volcánico Quimsachata – aroma, Región de Tarapacá, Andes Centrales del Norte de Chile. Santiago, Chile: Universidad de Chile, 210. [Ph.D. thesis].

Davidson, J. P., and de Silva, S. L. (1995). Late cenozoic magmatism of the Bolivian Altiplano. *Contr. Mineral. Pet.* 119, 387–408. doi:10.1007/bf00286937

Davidson, J. P., and de Silva, S. L. (1992). Volcanic rocks from the Bolivian Altiplano: Insights into crustal structure, contamination, and magma Genesis in the central Andes. *Geol.* 20, 1127–1130. doi:10.1130/0091-7613(1992)020<1127:vrftba>2.3.co;2

Davidson, J. P., Turner, S., Handley, H., Macpherson, C., and Dosseto, A. (2007). Amphibole "sponge" in the arc crust? *Geol.* 35 (9), 787–790. doi:10.1130/g23637a.1

de Silva, S., Davidson, J. P., Croudace, I. W., and Escobar, A. (1993). Volcanological and petrological evolution of volcan Tata Sabaya, SW Bolivia. *J. Volcanol. Geotherm. Res.* 55, 305–335. doi:10.1016/0377-0273(93)90043-q

DeCelles, P. G., Zandt, G., Beck, C. A., Currie, C. A., Ducea, M. N., Kapp, P., et al. (2015). "Cyclical orogenic processes in the cenozoic central Andes," in *Geodynamics of a cordilleran orogenic system: The central Andes of Argentina and northern Chile*. Editors P. G. DeCelles, M. N. Ducea, B. Carrapa, and P. A. Kapp (USA: Geological Society of America Memoir), 212, 459–490. doi:10.1130/2015.1212(22

Deino, A. L. (2015). Berkeley geochronology center, mass spec, 40Ar/39Ar data measurement and reduction software. Available at: http://www.bgc.org/facilities/other_facil.html.

Drew, S. T., Ducea, M. N., and Schoenbohm, M. L. (2009). Mafic volcanism on the Puna Plateau, NW Argentina: Implications for lithospheric composition and evolution with an emphasis on lithospheric foundering. *Lithosphere* 1 (5), 305–318. doi:10.1130/L54.1

Elger, K., Oncken, O., and Glodny, J. (2005). Plateau-style accumulation of deformation: Southern Altiplano. *Tectonics* 24, TC4020. doi:10.1029/2004TC001675

Elkins-Tanton, L. T. (2005). "Continental magmatism caused by lithospheric delamination," in *Plates, plumes, and paradigms*. Editors G. R. Foulger, J. H. Natland, D. C. Presnall, and D. L. Anderson (USA: Geological Society of America Special Paper), 388, 449–461.

Evernden, J., Kriz, S., and Cherroni, C. (1977). Potassium-Argon ages of some Bolivian rocks. *Econ. Geol.* 72, 1042–1061. doi:10.2113/gsecongeo.72.6.1042

Feeley, T. C., and Davidson, J. P. (1994). Petrology of Calc-Alkaline Lavas at Volc n Ollag e and the Origin of Compositional Diversity at Central Andean Stratovolcanoes. *J. Petrology* 35, 1295–1340. doi:10.1093/petrology/35.5.1295

Gardeweg, M., and Sellés, D. (2017). "Characterization of the last volcanic products erupted in the Pica Gap (Northern Chile)," in *Actas XX congreso geológico argentino* (Sesión Técnica: Universidad de Chile), 7, 60–67.

GeoROC Database. ANDEAN_ARC.csv, 2012, Availabe at: http://georoc.mpch-mainz.gwdg.de/georoc.

Grant, J., Halls, C., Salinas, W., and Snelling, N. (1979). K-Ar ages of igneous rocks and mineralization in part of the Bolivian Tin Belt. *Econ. Geol.* 74, 838–851. doi:10.2113/gsecongeo.74.4.838

Handley, H. K., Macpherson, C. G., Davidson, J. P., Berlo, K., and Lowry, D. (2007). Constraining fluid and sediment contributions to subduction-related magmatism in Indonesia: Ijen volcanic complex. *J. Petrology* 48, 1155–1183. doi:10.1093/petrology/egm013

Hildreth, W., and Moorbath, S. (1988). Crustal contributions to arc magmatism in the Andes of central Chile. *Contr. Mineral. Pet.* 98, 455–489. doi:10.1007/BF00372365

Hoke, L., and Lamb, S. (2007). Cenozoic behind-arc volcanism in the Bolivian Andes, South America: Implications for mantle melt generation and lithospheric structure. *J. Geol. Soc. Lond.* 164, 795–814. doi:10.1144/0016-76492006-092

Hora, J. M., Singer, B. S., Wörner, G., Beard, B. L., Jicha, B. R., and Johnson, C. M. (2009). Shallow and deep crustal control on differentiation of calc-alkaline and tholeiitic magma. *Earth Planet. Sci. Lett.* 285, 75–86. doi:10.1016/j.epsl.2009.05.042

Husson, L., and Sempere, T. (2003). Thickening the Altiplano crust by gravity-driven crustalchannel flow. *Geophys. Res. Lett.* 30. doi:10.1029/2002GL016877

Ionov, D. A., Griffin, W. L., and O'Reilly, S. Y. (1997). Volatile- bearing minerals and lithophile trace elements in the upper mantle. *Chem. Geol.* 141, 153–184. doi:10.1016/S0009-2541(97)00061-2

Irvine, T. N., and Baragar, W. R. A. (1971). A guide to the chemical classification of the common volcanic rocks. *Can. J. Earth Sci.* 8 (5), 523–548. doi:10.1139/e71-055

James, D. E., and Sacks, I. S. (1999). "Cenozoic formation of the central Andes: A geophysical perspective," in *Geology and ore deposits of the central Andes*. Editor B. J. Skinner (Tulsa, Oklahoma: SEPM Special Publication), 1–25.

Jiménez, N., and López-Velásquez, S. (2008). Magmatism in the Huarina belt, Bolivia, and its geotectonic implications. *Tectonophysics* 459, 85–106. doi:10.1016/j.tecto.2007.10.012

Johnson, D. M., Hooper, P. R., and Conrey, R. M. (1999). XRF analysis of rocks and minerals for major and trace elements on a single low-dilution Li-tetraborate fused bead. *Adv. X-Ray Analysis* 41, 117–132.

Kato, J. J. (2013). *Geochemistry of the neogene Los Frailes ignimbrite complex of the central andean Altiplano plateau [ph.D. Thesis*. Ithaca, New York: Cornell University, 173.

Kay, R. M., and Kay, S. M. (1993). Delamination and delamination magmatism. *Tectonophysics* 219 (13), 177–189. doi:10.1016/0040-1951(93)90295-u

Kay, S. M., Coira, B. L., Caffe, P. J., and Chen, C. (2010). Regional chemical diversity, crustal and mantle sources and evolution of central Andean Puna plateau ignimbrites. *J. Volcanol. Geotherm. Res.* 198, 81–111. doi:10.1016/j.jvolgeores.2010.08.013

Kay, S. M., Coira, B., and Viramonte, J. (1994). Young mafic back arc volcanic rocks as indicators of continental lithospheric delamination beneath the Argentine Puna Plateau, central Andes. *J. Geophys. Res.* 99, 24323–24339. doi:10.1029/94JB00896

Kennen, L., Lamb, S., and Rundle, C. (1995). K-Ar dates from the Altiplano and Cordillera oriental of Bolivia: Implications for cenozoic stratigraphy and tectonics. *J. South Am. Earth Sci.* 8, 163–186. doi:10.1016/0895-9811(95)00003-x

Knaack, C., Cornelius, S. B., and Hooper, P. R. (1994). *Technical notes: Trace element analyses of rocks and minerals by ICP-ms: Pullman*. Washington: GeoAnalytical Laboratory, Washington State University Open-File Report.

Le Maitre, R. W., Bateman, P., Dudek, A., Keller, J., Lameyre Le Bas, M. J., Sabine, et al. (1989). *A classification of igneous rocks and glossary of terms*. Oxford: Blackwell, 193.

Leytón, F., and Jurado, E. (1995). Salinas de Garci Mendoza quadrangle, SE 19-15: Thematic maps of mineral resources of Bolivia, publication SGB serie II-MTB-4B, GEOBOL-SGAB, scale 1:250,000, 1 sheet.

Lindsay, J. M., Schmitt, A. K., Trumbull, R. B., de Silva, S. L., Siebel, W., and Emmermann, R. (2001). Magmatic evolution of the La Pacana caldera system, Central Andes, Chile: Compositional variation of two cogenetic, large-volume felsic ignimbrites. *J. Petrology* 42 (3), 459–486. doi:10.1093/petrology/42.3.459

Lucassen, F., Franz, G., Romer, R. L., Schultz, F., Dulski, P., and Wemmer, K. (2007). Pre-Cenozoic intra-plate magmatism along the Central Andes (17-34S): Composition of the mantle at an active margin. *Lithos* 99, 312–338. doi:10.1016/j.lithos.2007.06.007

Lucassen, F., Franz, G., Viramonte, J., Romer, R. L., Dulski, P., and Lang, A. (2005). The late Cretaceous lithospheric mantle beneath the Central Andes:

Evidence from phase equilibria and composition of mantle xenoliths. *Lithos* 82, 379–406. doi:10.1016/j.lithos.2004.08.002

Mamani, M., Wörner, G., and Sempere, T. (2010). *Geochemical variations in igneous rocks of the central Andean orocline (13°S to 18°S): Tracing crustal thickening and magma generation through time and space*, 122. USA: Geological Society of America Bulletin, 162–182. 1–2. doi:10.1130/B26538.1

Mark, D., Barfod, D., Stuart, F., and Imlach, J. (2009). The ARGUS multicollector noble gas mass spectrometer: Performance for ^{40}Ar/^{39}Ar geochronology. *Geochem. Geophys. Geosyst.* 10, Q0AA02. doi:10.1029/2009gc002643

Maro, G., Caffe, P. J., Romer, R. L., and Trumbull, R. B. (2017). Neogene mafic magmatism in the northern Puna Plateau, Argentina: Generation and evolution of a back-arc volcanic suite. *J. Petrology* 58 (8), 1591–1617. doi:10.1093/petrology/egx066

McGlashan, N., Brown, L., and Kay, S. (2008). Crustal thickness in the central Andes from teleseismically recorded depth phase precursors. *Geophys. J. Int.* 175 (3), 1013–1022. doi:10.1111/j.1365-246X.2008.03897.x

McLeod, C. L., Davidson, J. P., Nowell, G. M., and de Silva, S. L. (2012). Disequilibrium melting during crustal anatexis and implications for modeling open magmatic systems. *Geology* 40, 435–438. doi:10.1130/G33000.1

McLeod, C. L., Davidson, J. P., Nowell, G. M., de Silva, S. L., and Schmitt, A. K. (2013). Characterizing the continental basement of the Central Andes: Constraints from Bolivian crustal xenoliths. *Geol. Soc. Am. Bull.* 125 (5-6), 985–997. doi:10.1130/B30721.1

McQuarrie, N., Horton, B. K., Zandt, G., Beck, S., and DeCelles, P. G. (2005). Lithospheric evolution of the Andean fold-thrust belt, Bolivia, and the origin of the central Andean Plateau. *Tectonophysics* 399, 15–37. doi:10.1016/j.tecto.2004.12.013

Murray, K. E., Ducea, M. N., and Schoenbohm, L. (2015). "Foundering-driven lithospheric melting: The source of central Andean mafic lavas on the Puna Plateau (22°S-27°S)," in *Geodynamics of a cordilleran orogenic system: The central Andes of Argentina and northern Chile*. Editors P. G. DeCelles, M. N. Ducean, B. Carrapa, and P. A. Kapp (USA: Geological Society of America Memoir), 212, 139–166. doi:10.1130/2015.1212(08

Niespolo, E. M., Rutte, D., Deino, A. L., and Renne, P. R. (2017). Intercalibration and age of the Alder Creek sanidine 40Ar/39Ar standard. *Quat. Geochronol.* 39, 205–213. doi:10.1016/j.quageo.2016.09.004

Oncken, O., Hindle, D., Kley, J., Elger, K., Victor, P., and Schemmann, K. (2006). "Deformation of the central andean upper plate system — Facts, fiction, and constraints for plateau models," in *The Andes: Active subduction orogeny*. Editors O. Oncken, G. Chong, G. Franz, P. Giese, H.-J. Gotze, V. A. Ramos, et al. (Berlin: Springer-Verlag), 3–27.

Peccerillo, A., and Taylor, S. R. (1976). Geochemistry of Eocene calc-alkaline volcanic rocks from the Kastamonu area, Northern Turkey. *Contr. Mineral. Pet.* 58, 63–81. doi:10.1007/BF00384745

Pilet, S., Baker, M. B., and Stolper, E. M. (2008). Metasomatized lithosphere and the origin of alkaline lavas. *Science* 320, 916–919. N. 5878no. 5878. doi:10.1126/science.1156563

Polanco, E., and Gardeweg, M. (2000). "Antecedentes Preliminares de la Estratigrafía volcánica del Cenozoico Superior en los Cuadrangulos Pampa Lirima y Cancosa, Altiplano de la I Región," in *Chile (19°45'–20°00'S Y 69°00–68°30'W), congreso geológico chileno, 9* (Puerto Varas, Chile, 324–328. 31 Julio – 4 Agosto.

Risse, A., Trumbull, R. B., Kay, S. M., Coira, B., and Romer, R. L. (2013). Multi-stage evolution of late neogene mantle-derived magmas from the central Andes back-arc in the southern Puna Plateau of Argentina. *J. Petrology* 54 (10), 1963–1995. doi:10.1093/petrology/egt038

Rogers, G. R., and Hawkesworth, C. J. (1989). A geochemical traverse across the north Chilean Andes: Evidence for crust generation from the mantle wedge. *Earth Planet. Sci. Lett.* 91, 271–285. doi:10.1016/0012-821X(89)90003-4

Rollinson, H. R. (1993). *Using geochemical data: Evaluation, presentation, interpretation*. Essex: Longman, 102–170.

Salisbury, M. J., Jicha, B. R., de Silva, S. L., Singer, B. S., Jiménez, N. C., and Ort, M. H. (2011). 40Ar/39Ar chronostratigraphy of Altiplano-Puna volcanic complex ignimbrites reveals the development of a major magmatic province. *Geol. Soc. Am. Bull.* 123, 821–840. 5–6. doi:10.1130/B30280.1

Salisbury, M. J., Kent, A. J. R., Jiménez, N., and Jicha, B. R. (2015). Geochemistry and ^{40}Ar/^{39}Ar geochronology of lavas from Tunupa volcano, Bolivia: Implications for plateau volcanism in the central Andean Plateau. *Lithosphere* 7 (2), 95–107. doi:10.1130/l399.1

Schultz, F., Lehmann, B., Tawackoli, S., Rössling, R., Belyatsky, B., and Dulski, P. (2004). Carbonatite diversity in the central Andes: The Ayopaya alkaline province, Bolivia. *Contrib. Mineral. Pet.* 148, 391–408. doi:10.1007/s00410-004-0612-0

Sellés, D., Gardeweg, M., and Gartibaldi, N. (2016). *Geología de Área Pampa lirima-cancosa, región de Tarapacá, servicio nacional de Geología y minería (SERNAGEOMIN), serie geología básica, No. 182. 1 sheet, 1:100,000 scale*. Santiago, Chile. doi:10.13140/RG.2.2.35023.18086

Sparks, R. S. J., Folkes, C. B., Humphreys, M. C. S., Barfod, D. N., Clavero, J., Sunagua, M. C., et al. (2008). Uturuncu volcano, Bolivia: Volcanic unrest due to mid-crustal magma intrusion. *Am. J. Sci.* 308 (6), 727–769. doi:10.2475/06.2008.01

Sun, S., and McDonough, W. F. (1989). "Chemical and isotopic composition of oceanic basalts: Implications for mantle compositions and processes," in *Magmatism in the ocean basins*. Editors A. D. Saunders and M. J. Norry (London: Geological Society of London Special Publication), 42, 313–345.

Trumbull, R. B., Ulrich, R., Oncken, O., Ekkehard, S., Munier, K., and Hongn, F. (2006). "The time–space distribution of cenozoic volcanism in the south-central Andes: A new data compilation and some tectonic implications," in *The Andes: Active subduction orogeny*. Editors O. Oncken, G. Chong, G. Franz, P. Giese, H.-J. Gotze, V. A. Ramos, et al. (Berlin: Springer-Verlag), 29–43.

Victor, P., Oncken, O., and Glodny, J. (2004). Uplift of the Western Altiplano plateau: Evidence from the Precordillera between 20 and 21°S (northern Chile). *Tectonics* 23, TC4004. doi:10.1029/2003TC001519

Walker, B. A. (2011). "The geochemical evolution of the Aucanquilcha volcanic cluster: Prolonged magmatism and its crustal consequences," (Corvallis, Oregon: Oregon State University), 199. [Ph.D. thesis].

Wendt, I., and Carl, C. (1991). The statistical distribution of the mean squared weighted deviation. *Chem. Geol. Isot. Geosci. Sect.* 86, 275–285. doi:10.1016/0168-9622(91)90010-t

Wörner, G., Moorbath, S., and Harmon, R. S. (1992). Andean Cenozoic volcanic centers reflect basement isotopic domains. *Geol.* 20, 1103–1106. doi:10.1130/0091-7613(1992)020<1103:acvcrb>2.3.co;2

Wörner, G., Moorbath, S., Horn, S., Entenmann, J., Harmon, R. S., Davidson, J. P., et al. (1994). "Large geochemical variations along the Andean arc of northern Chile (17.5–22°S)," in *Tectonics of the southern central Andes: Structure and evolution of an active continental margin*. Editors K. J. Reutter, E. Scheuber, and P. J. Wigger (Berlin: Springer-Verlag), 77–91.

Yuan, X., Sobolev, S. V., and Kind, R. (2002). Moho topography in the central Andes and its geodynamic implications. *Earth Planet. Sci. Lett.* 199, 389–402. doi:10.1016/S0012-821X(02)00589-7

frontiers | Frontiers in Earth Science

TYPE Original Research
PUBLISHED 13 January 2023
DOI 10.3389/feart.2022.961130

EDITED BY
Gary Michelfelder,
Missouri State University, United States

REVIEWED BY
Robert Trumbull,
GFZ German Research Centre for Geosciences, Germany
Ian Ernest Masterman Smith,
The University of Auckland, New Zealand

*CORRESPONDENCE
Dale H. Burns,
✉ dhburns@stanford.edu

SPECIALTY SECTION
This article was submitted to Geochemistry, a section of the journal Frontiers in Earth Science

RECEIVED 04 June 2022
ACCEPTED 22 November 2022
PUBLISHED 13 January 2023

CITATION
Burns DH and de Silva SL (2023), Andesites and evolution of the continental crust: Perspectives from the Central Volcanic Zone of the Andes.
Front. Earth Sci. 10:961130.
doi: 10.3389/feart.2022.961130

Andesites and evolution of the continental crust: Perspectives from the Central Volcanic Zone of the Andes

Dale H. Burns[1]* and Shanaka L. de Silva[2]

[1]Department of Earth and Planetary Sciences, Stanford University, Stanford, CA, United States, [2]College of Earth, Oceanic, and Atmospheric Sciences, Oregon State University, Corvallis, OR, United States

Named for the Andes, andesites (53%–63% SiO_2) are the archetypal magma erupted at magmatic arcs. They have been established as the average composition of continental crust and as such are integral to the growth and evolution of the continental crust. However, andesites are quite variable in trace element and isotopic composition reflecting disparate paths of origin. Herein we return to the original site of their identification, the Central Andes, and use a comprehensive dataset of published and unpublished trace elements and isotopes to show that during the past 6 Myr two distinct types of andesite have erupted in the Central Volcanic Zone (CVZ), which correspond with different geodynamic conditions. Consistent with previous work, we confirm that major composite cones and minor centers of the steady state (low magmatic flux) Quaternary CVZ arc have trace element and isotopic characteristics consistent with magma generation/fractionation in the lower crust. Within the Quaternary arc centers, there are also significant latitudinal variations that correspond with the age, composition, and P-T conditions of the lower crust. However, in contrast to this prevailing model, in the 21–24°S segment 6–1 Ma andesites from ignimbrites and lava domes associated with the peak of the regional Neogene ignimbrite flare-up have compositions that indicate these andesites are hybrids between mantle-derived basalts and *upper crustal lithologies*. Since ~1 Ma, andesites in young silicic lava domes associated with the regional flare-up are compositionally indistinguishable from proximal Quaternary arc centers, indicating a return to steady-state magmatism and lower crustal production of andesites. We propose that the transition from upper crustal to lower crustal andesite production results from a decrease in mantle heat input and subsequent relaxation of the regional geotherm during the waning of the flare-up event. The two modes of andesite production have significant implications for the production and evolution of the CVZ arc crust. During the flare-up, prodigious amounts of basalt were emplaced into the mid-crust, resulting in the production of large volumes of hybrid intermediate magmas in the mid and upper crust. In contrast, the lower crustal differentiation recorded in the Quaternary steady state arc andesites would result in the formation of a dense crystalline residue in the lower crust and an overall densification of the lower crust. Over time, gravity instabilities associated with this densification may ultimately aid in the delamination of the dense lower crustal root, triggering flare-ups. These differences in andesite production may help explain the cyclicity (flare-up cycles) observed in mature continental arcs and emphasizes that andesite is not a monotonous composition and can vary with depth-dependent intra-crustal differentiation related to magmatic flux.

KEYWORDS

MASH processes, continental crust formation, lower crustal melting and recycling, crustal magmatism, continental arc magmatism, flare-up andesites, andesite petrogenesis, crustal andesites

Introduction

Andesite was a name first coined in 1836 by German geologist Leopold von Buch to describe "trachytes" from the Central Andes of Chile and Bolivia (Thorpe, 1982). Originally, andesites were defined as an intermediate volcanic rock containing between 53% and 63% SiO_2 (Thorpe et al., 1981; Gill, 1981). More recently, this classification was sub-divided (see Le Bas and Streckeisen, 1991), based on major element chemistry, into basaltic andesite (53–57 wt.% SiO_2) and andesite (57–63 wt.% SiO_2) rock types. Andesites are the most common magma type erupted at continental magmatic arcs and are compositionally analogous to the bulk composition of the continental crust on Earth (Taylor and McLennan, 1985). These compositional similarities have led to the recognition that andesites play a critical role in the evolution and growth of continental crust (e.g., Thorpe et al., 1981; Thorpe, 1982; Taylor and McLennan, 1985; Reubi and Müntener, 2022). However, although andesites have been studied for two centuries, there is still debate surrounding whether continental arc andesites are produced in the subarc mantle (see Straub et al., 2011 and references therein) or within the overlying continental crust (e.g., Eichelberger, 1978; Hildreth and Moorbath, 1988). Importantly, these two scenarios differ significantly with respect to the transfer of mass from the Earth's mantle to the crust, the rate of crustal growth, and the long-term recycling/fractionation of continental crust.

The Central Andes, the home of andesite, are a unique natural laboratory because the arc has been active and erupting andesitic compositions since the Jurassic (Thorpe et al., 1981; Rogers and Hawkesworth, 1989) and has an episodic history related to major tectonic changes that have impacted the production and storage of magma in the region (Coira et al., 1982; Kay and Coira, 2009). Much of this long history is characterized by andesitic magmatism and the construction of a volcanic arc dominated by composite volcanoes (Coira et al., 1982; Kay and Coira, 2009) classified as normal, low-flux, or steady state (e.g., de Silva, 2008; Burns et al., 2015). However, starting in the middle Miocene, ~25 Ma, changes in the geometry of the subducting plate triggered a high flux magmatic "flare-up" event during which prodigious volumes of dacite were erupted forming one of the largest silicic volcanic provinces on Earth (de Silva et al., 2006; Kay and Coira, 2009; Freymuth et al., 2015). Since the Quaternary, the arc has returned to steady-state activity represented by the modern active volcanic arc (Burns et al., 2015). These magmatic excursions connote fundamental changes in the role of andesite magmatism with significant implications for the production and potential destruction of continental crust. For instance, it has been proposed that >50% of new continental crust created at convergent boundaries is created during flare-up events (Coleman and Glazner, 1997). This is at odds with previous studies that have hypothesized that flare-up events are associated with the delamination of deep mafic cumulates from the lower crust resulting in a net loss of crust (e.g., Kay and Kay, 1993; Kay and Coira, 2009; de Silva and Kay, 2018).

In this study, we seek to understand the evolution of continental crust in the Central Andes using the composition of erupted andesites. We focus on basaltic andesites and andesites (53–63 wt.% SiO_2; herein referred to as andesites; Le Bas and Streckeisen, 1991) erupted in the last 6 Ma as they record two distinct modes of andesite production that correspond to distinct geodynamic states and specific magmatic processes occurring at distinct levels in the crust. We show that andesites are not a monotonous group and have distinct trace element and isotopic compositions depending on their depth of production as a function of the arc magmatic flux. A corollary of this is that the location at which andesites are produced has a significant impact on the production and long-term differentiation of continental crust.

Geological background

The Central Volcanic Zone (CVZ) is one of four active volcanic arc segments that make up the Andean Cordillera in South America (Stern, 2004). Subduction-related arc magmatism has occurred continuously in the CVZ for the past ca. 200 Ma in response to the subduction of the Nazca plate beneath the South American continent (Thorpe et al., 1981; Coira et al., 1982). At ~25 Ma, magmatism in the CVZ migrated eastward and then back west to its current position in response to changes in the dip of the subducting Nazca plate. The arc migration coincided with crustal shortening, which continued until at least 10 Ma, resulting in crustal thicknesses >70 km beneath parts of the CVZ (Allmendinger et al., 1997). The later history of crustal shortening was broadly synchronous with a dramatic shift in the style and characteristics of magmatism in the CVZ, as an arc-scale magmatic flare-up resulted in the production and eruption of large volumes of silicic "crustal" magmas in the CVZ. The most intense surface expression of this is the Altiplano-Puna Volcanic Complex (APVC) between 21 and 24°S (Figure 1; de Silva, 1989). Between 10 and 1 Ma, estimated magmatic fluxes appear to have increased by more than an order-of-magnitude relative to steady-state CVZ magmatism (de Silva et al., 2006; de Silva and Gosnold, 2007; Burns et al., 2015), resulting in the eruption of >15,000 km^3 of mainly crystal-rich dacite magma (de Silva and Gosnold, 2007). After the peak of the flare-up, ~4 Ma, eruptive activity in the region appears to start waning and the re-emergence of composite volcanoes, small-volume lava domes, and volumetrically dominant andesite (de Silva et al., 1994; Watts et al., 1999; Grunder et al., 2008; Tierney et al., 2016; Godoy et al., 2019) has signaled a return to steady-state conditions (Burns et al., 2015; Burns et al., 2020). In addition to major tectono-magmatic events causing arc-scale changes in crustal architecture and processes, the CVZ arc is built on multiple temporally and compositionally distinct crustal domains that play a significant role in the generation and evolution of the subduction-derived magmas (e.g., Barreiro and Clark, 1984; Aitcheson et al., 1995; Wörner et al., 1994; Mamani et al., 2008).

Methods and data filtration

In this paper we compile all available geochemical data from major and minor centers from Quaternary arc and back-arc centers

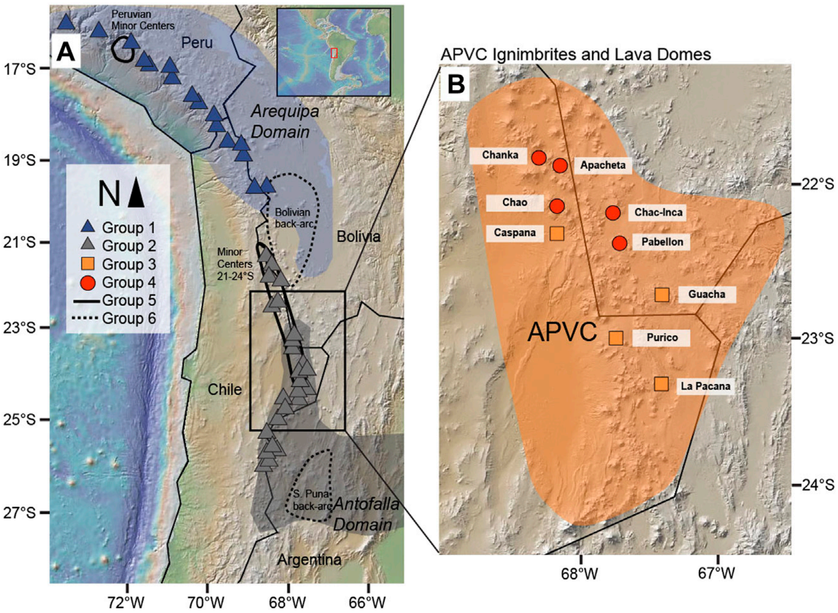

FIGURE 1
Maps showing the various types of andesite-bearing eruptive centers in the CVZ. Diagram includes Symbols for all panels are explained in panel D. These include major eruptive centers (i.e., composite cones) associated with the Quaternary arc (groups 1 and 2), eruptive centers associate the peak of the APVC ignimbrite flare-up (group 3), small volume centers associated with the waning stages of the APVC flare-up (group 4), minor centers associated with the arc (group 5), and minor centers found behind the arc (group 6). The large blue and grey fields in **(A)** show differences in the proposed basement terrains that underly the two arc segments (Mamani et al., 2010). Map in **(B)** shows the distribution of APVC flare-up related ignimbrites and domes (orange field) and locations of APVC units discussed in the text.

in the CVZ. We also present 17 new major and trace element analyses, and three new $^{87}Sr/^{86}Sr$ isotope measurements from the Purico-Chascon volcanic complex in N. Chile. New samples are restricted to the 1 Ma Purico ignimbrite, Cerro Purico lava dome, and Dome D (Hawkesworth et al., 1982; Schmitt et al., 2001; Burns et al., 2015; Burns et al., 2020). These new analyses represent andesites associated with the peak of the regional ignimbrite flare-up and fill a critical gap in understanding of andesites in the CVZ.

The new major element and select trace element concentrations were measured at the Washington State University Geoanalytical Laboratory. Major and select trace element concentrations were collected using a ThermoARL X-ray fluorescence (XRF) spectrometer, and rare-earth element concentrations were measured using an Agilent 7700 inductively coupled plasma mass spectrometer (ICP-MS). A detailed methodology is presented by Johnson et al. (1999). Whole-rock powders from three samples were analyzed for $^{87}Sr/^{86}Sr$ using thermal ionization mass spectrometry (TIMS) at New Mexico State University following the methodology of Ramos (1992). Although new data was collected as part of this work, it is important to emphasize that the Purico-Chascon samples are not the primary focus of this work, but rather help to fill out a critical group of samples that are paramount to this study (i.e., flare-up andesites).

We have limited our compiled database to samples with SiO_2 contents between 50 and 63 wt.% SiO_2 (volatile-free). In addition to including large composite volcanoes associated with the arc front, we also include geographically related minor centers and small volcanic fields. These centers and small fields include within-arc minor centers from both major arc segments (16–19°S and 21–26°S), back-arc centers from Bolivia (19–21°S) and back-arc centers from the Southern Puna in Argentina (25–27°S). Although we have compiled a comprehensive chemical database as part of the study, we have omitted REE concentration measured *via* instrumental neutron activation analysis from figures and discussion when possible. This is due to a lack of reproducibility when compared with replicate analyses made using modern ICP-MS techniques. We have also excluded samples from the northern Puna back-arc (Maro et al., 2017) as they erupt through older, more radiogenic crust. The complete dataset, including references, are provided in the Supplementary Data Table.

Results

Six different groups of andesites can be identified based on their spatiotemporal distributions, surface morphologies, eruptive characteristics (i.e., explosive vs. effusive), and compositions (Figures 1–3): 1) Andesitic lavas erupted from the major Quaternary arc composite cones between 19 and 16 °S; 2) Quaternary arc andesites from major composite cones between 21 and 26°S; 3) Ubiquitous but volumetrically minor lavas and pumices of calderas and ignimbrites erupted during the peak of the APVC flare-up from 6 to 1 Ma (herein referred to as peak flare-up); 4) Andesite enclaves and mingled magma in lava domes and ignimbrites from the waning stage of the flare-up <1 Ma (herein referred to as waning flare-up); 5) Andesites from minor centers spatially associated with the Quaternary arc; 6) Andesites from Quaternary back-arc minor centers.

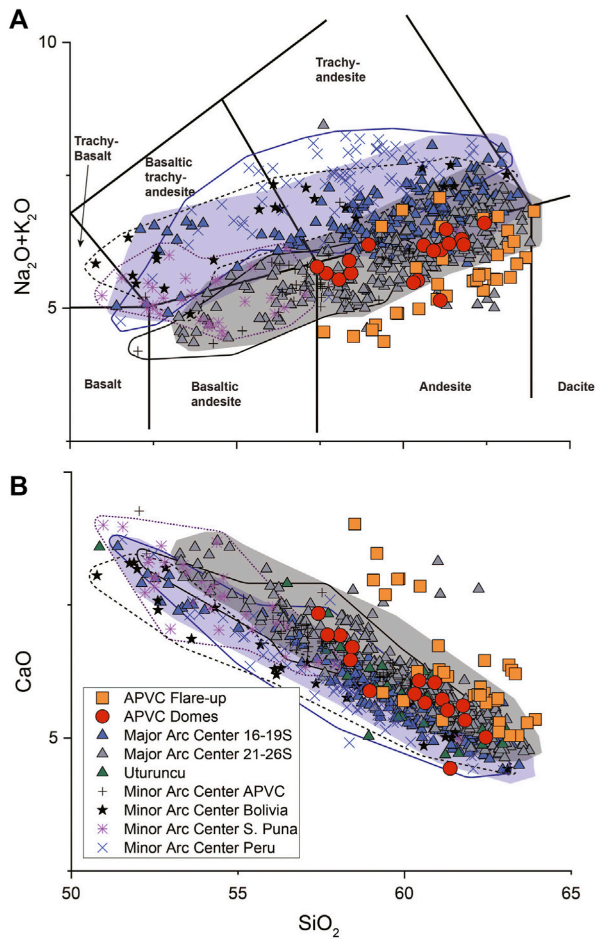

FIGURE 2
(A) Plot of SiO_2 vs. total alkali concentrations and **(B)** SiO2 vs. CaO concentrations. Panel A includes TAS classification grid following Le Maitre (1989). All plotted data has been filtered to only include SiO_2 concentrations between 50 and 63 wt.% SiO_2. Description of symbols and units for all panels are included in panel **(B)**. Individual groups are outlined to aid in visualization.

Quaternary arc andesites of the CVZ (groups 1 and 2)

Quaternary arc andesites from the CVZ define two compositionally distinct groups that correlate with latitude (e.g., Wörner et al., 1992; Wörner et al., 1994; Mamani et al., 2008; Mamani et al., 2010). Andesites from between 16 and 19°S (Group 1) have higher total alkali and lower CaO concentrations at a given SiO_2 content when compared to andesites from 21 to 26°S (Group 2; Figure 2). Group 1 andesites also have distinct REE concentrations characterized by much higher LREE abundances and considerably steeper REE patterns (Figure 4; i.e., higher La/Yb, La/Sm, and Sm/Yb ratios). REE abundances also show strong correlations with Sr/Y (Figure 3B), with group 1 andesites displaying considerably higher Sm/Yb and Sr/Y than their counterparts in group 2. Isotopically, there are similarities between andesites from the two segments defining a near-vertical trend in $^{87}Sr/^{86}Sr$ vs. trace element ratio-space (Figures 3B,C).

Andesites of the peak APVC flare-up 6 Ma to 1 Ma (group 3)

Andesites from the peak of the APVC flare-up (group 3) are compositionally distinct from other andesites in the CVZ. Group 3 andesites define a relatively narrow range of silica contents (58–63 wt.% SiO_2) and show no obvious trends when plotted against other major elements (Figure 2). One of the more striking features of the flare-up andesites is that they there show considerably more major element variations at a given SiO_2 concentration. This is illustrated in Figure 2A where total alkali concentrations vary by ~2 wt.% between 59 and 60 wt.% SiO_2. Group 3 andesites also have some of the lowest total alkali concentrations in CVZ.

The group 3 andesites also have distinct trace element characteristics relative to the rest of the CVZ. These differences are pronounced on the chondrite normalized trace element diagrams presented in Figure 4. The group 3 andesites have relatively flat REE patterns which are recorded in significantly lower La/Yb and La/Sm and lower Sr/Y than other major and minor centers in the CVZ. The shallow REE patterns are also characterized by relatively high HREE abundances relative to the group 1 and group 2 andesites. One of the most compelling compositional features observed in the group 3 andesites are their elevated Sr isotope ratios. ($^{87}Sr/^{86}Sr$ = .708–.711). They are considerably higher than any of the other andesites in the CVZ, including the waning stage APVC (group 4) andesites (.7055–.7060). These differences result in two distinct trends in Sr isotope-trace element ratio-space (Figures 3B,C). While most of the CVZ andesites show major variations in Sr/Y and Sm/Yb at relatively constant $^{87}Sr/^{86}Sr$, group 3 andesites show significant variations in Sr isotope ratios with only minimal changes in Sr/Y and Sm/Yb.

Waning stage APVC andesites <1 Ma (group 4)

The <1 Ma andesites from the waning stage of the APVC are distinct from the flare-up andesites and show considerable compositional overlap with the andesites of group 2 (21–26°S). These andesites have significantly steeper REE patterns (i.e., higher La/Yb, La/Sm, and Sm/Yb ratios) relative to the group 3 andesites with concentrations that are broadly similar to the andesites of group 2 (Figure 4). Andesites from group 4 define tight vertical trends in Figures 3B,C characterized by significant variations in Sr/Y and Sm/Yb with no significant change in Sr isotope ratios.

CVZ minor center andesites (group 5)

Andesites from minor centers in the CVZ show a high degree of compositional diversity that correlates with latitude. Arc minor centers located in Peru are very similar to the major composite cones in the region (group 1). These andesites show elevated total alkali concentrations at a given SiO_2 concentration, enriched LREE abundances/steep REE patterns, high Sr/Y concentrations, and Sr isotope ratios indistinguishable from the major composite cones. The only notable difference between the Peruvian minor centers and their major arc counterparts (i.e., group 1) is that the minor centers appear to

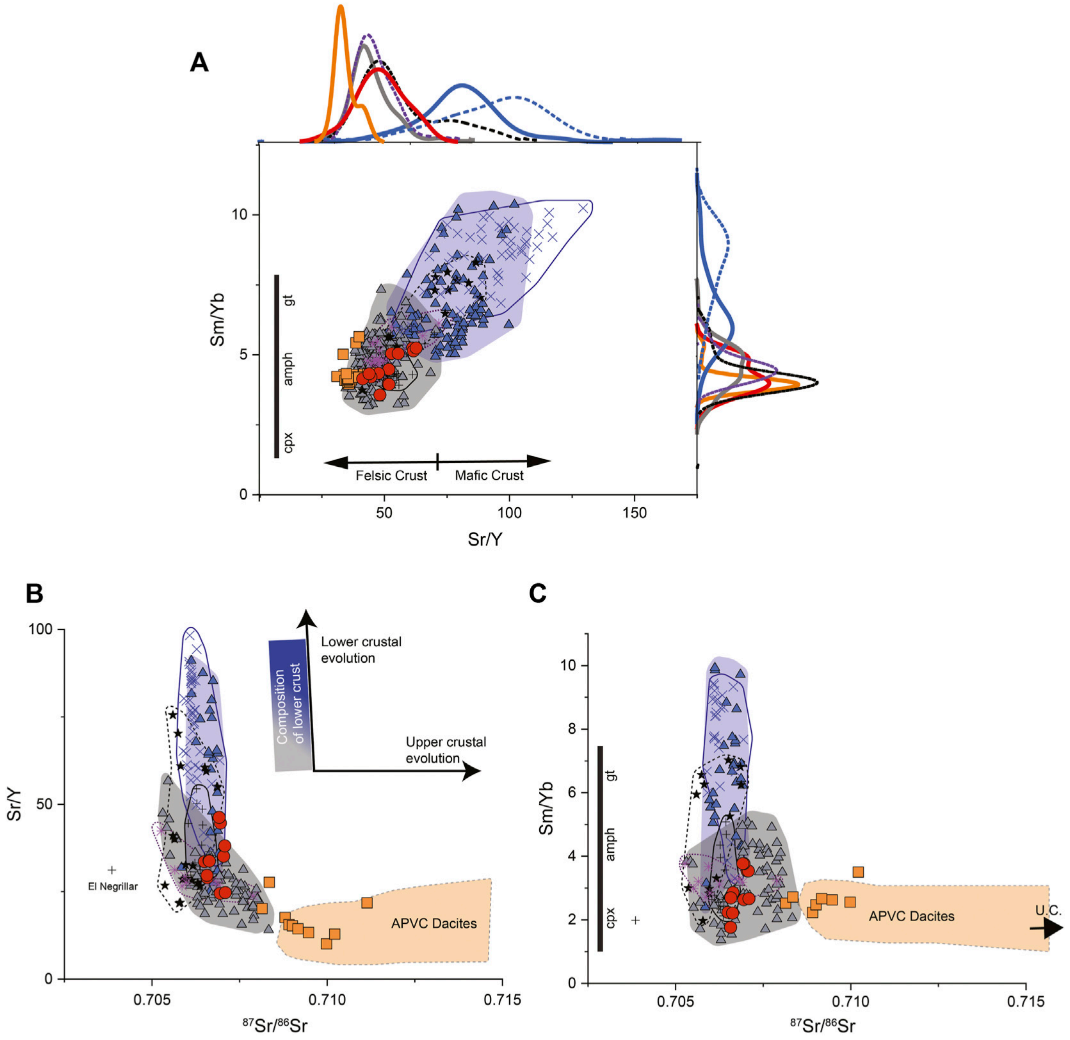

FIGURE 3
(A) Plot showing Sr/Y vs. Sm/Yb. Kernel density estimates (KDEs) for each trace element ratio and group are presented on the top and right side of the plot. KDE bandwidths were calculated using the Silverman method. Arrows show expected Sr/Y ratios in mafic vs. felsic lower crust. The vertical line shows the pressure-dependent relationship between Sm/Yb ratios and pyroxene, amphibole, and garnet after Kay and Mpodozis (2001). **(B, C)** Diagrams show $^{87}Sr/^{86}Sr$ vs. the trace element ratios in panel **(A)**. Both panels include an orange field showing the compositions of flare-up related dacite ignimbrites from the APVC. Arrows in Figure 3B show the mineralogically and compositionally dependent evolutionary pathways of lower vs. upper crustal magmas. The vertical bar in Figure 3C is discussed in the text.

be slightly more enriched in incompatible elements resulting in slightly higher LREE and incompatible element abundances (Figure 4).

Arc minor centers near the APVC between 21 and 24°S have lower total alkali concentrations, and higher CaO than the Peruvian centers. The minor center andesites also have relatively shallow REE patterns and low Sr/Y ratios, appearing indistinguishable from major arc centers between 21 and 26°S (Figures 3, 4). These andesites are also isotopically indistinguishable from group 2 andesites. One of the minor centers, Cerro Overo, is worth discussing in further detail. Although lavas from Cerro Overo are similar to other minor centers in the region with, bulk compositions ranging from ~52 to 57 wt.% SiO_2, olivine-hosted melt inclusions in the lavas record some of the most primitive mafic compositions erupted in the CVZ. The olivine-hosted melt inclusions are high-Mg basalts and have the lowest $^{87}Sr/^{86}Sr$ ratios (<.7040) recorded in the CVZ during the past 6 Ma (van Alderwerelt et al., 2021).

CVZ back-arc andesites (group 6)

In this study, we also include back-arc centers from two regions: 1) lavas from the Bolivian back-arc between 19 and 21°S and 2) andesites from the Southern Puna Plateau in Argentina (25–27°S). Andesites from the Southern Puna are the most compositionally restricted group included in this study. There do not appear to be any systematic variations between SiO_2 and total alkali concentrations. Andesites from the Southern Puna back-arc define steep REE patterns characterized by enrichments in LREEs (Figure 4). However, they differ from the group 1 and group 2 andesites as they do not show a depletion in HREEs. Isotopically, these andesites are indistinguishable from andesites from the major arc centers. Andesites from the Bolivian back-arc are perhaps the most interesting minor center lavas included in this

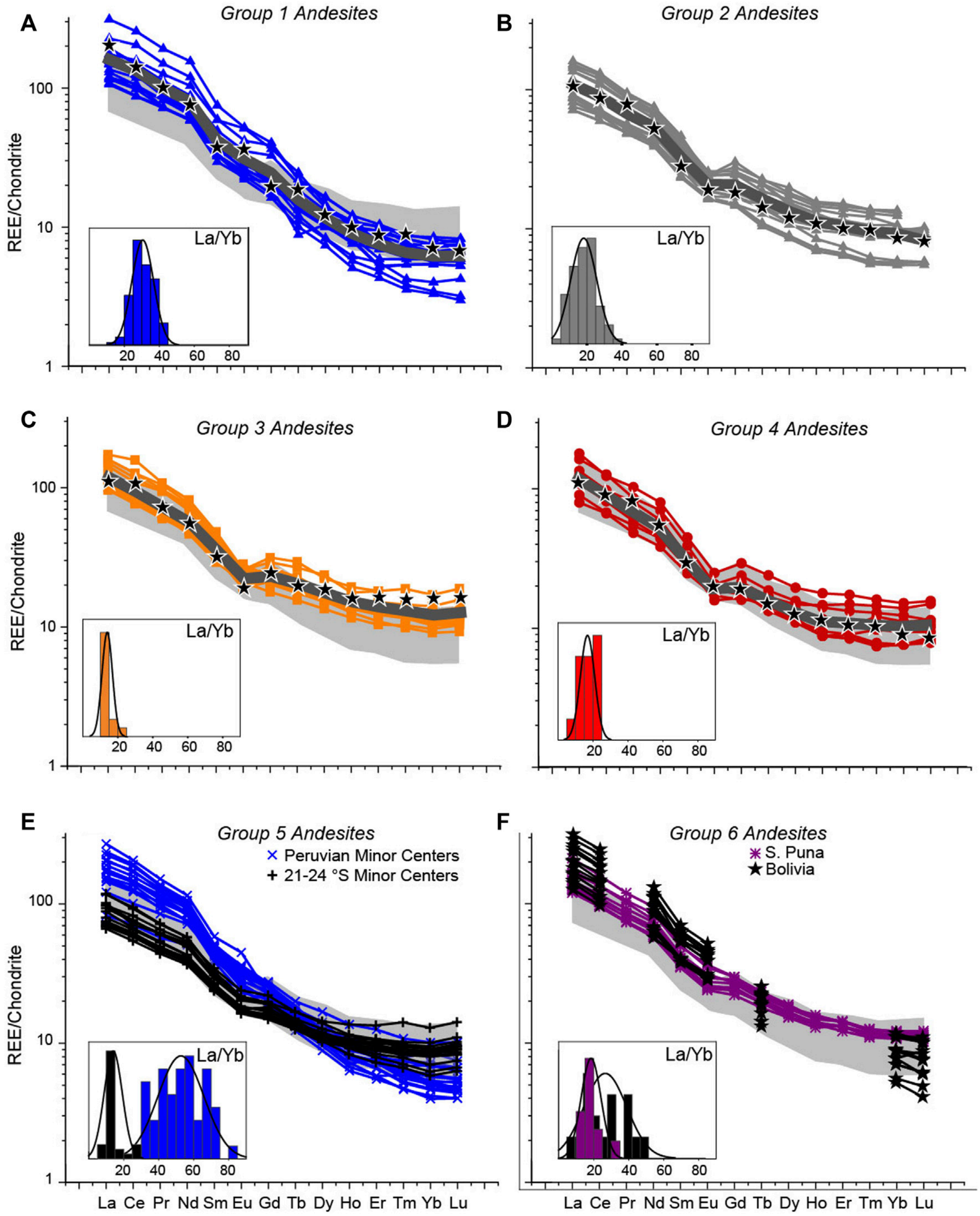

FIGURE 4
Chondrite-normalized (Sun and McDonough, 1989) REE diagrams showing compositional differences between CVZ andesites. The thick black lines represent averages, and the black stars show the crustal melting/mixing models discussed in the text and in Supplementary Appendix SA1. The inset boxes show the distribution(s) of La/Yb ratios in each group of andesite. The La/Yb histograms are overlain with normal distribution curves. Note that the group 1 andesites have considerably steeper REE patterns than other CVZ andesites. The grey field on panels **(A, C, D, E, and F)** show the range of REE patterns from group 2 **(B)**.

study. Not only do they occupy an area in space that is transitional between the two major arc segments in the CVZ, but they are also compositionally unique. In major element space (Figure 2), they overlap with group 1 andesites. However, REE abundances and Sr/Y ratios span the compositional gap between the two arc segments (Figures 3, 4).

Discussion

In the following sections, we discuss specific trace elements and trace element ratios that record the presence of distinct crystalline phases during the fractionation/evolution of the arc-related magmas. Central to our discussion of andesite generation in the CVZ are the ratios of Sr/Y and Sm/Yb. Both ratios are influenced by multiple crystalline phases (i.e., garnet, pyroxene, and plagioclase) present in the early evolution of CVZ magmas, and both ratios are highly sensitive to the presence of garnet, providing constraints on the depths and mechanisms responsible for early fractionation events (Chapman et al., 2015; Kay and Mpodozis, 2002; Wörner et al., 2018). For example, Kay and Mpodozis (2002), following Kay and Kay (1991), proposed that Sm/Yb variations in mafic to intermediate magmas in the Central Andes are mostly controlled by pressure-dependent changes from clinopyroxene to amphibole to garnet stability in the mineral residue in equilibrium with evolving magmas. Owing to the sensitivity of these ratios to the composition of the mineral residuum, they serve as critical tools for distinguishing upper *versus* lower crustal differentiation the CVZ. We also develop isotopically constrained trace element and AFC models to help fingerprint the sources and locations at which various magmatic processes are occurring within the CVZ crust (for a detailed description of the modeling techniques and parameters, see appendix 1). Thus far, we have discussed six distinct groups of andesites based largely on spatiotemporal distributions, surface morphologies, and eruptive characteristics (i.e., explosive vs. effusive). In the previous section, we provided a detailed comparison of the compositional similarities and differences between these groups. Following this comparison, we can now re-group the andesites into two groups based on compositional characteristics. Importantly, the compositional differences between the two groups appear to record disparate evolutionary pathways controlled by arc-scale geodynamic changes.

Upper Crustal andesites: The APVC peak flare-up (group 3)

Group 3 andesites (peak APVC flare-up) are compositionally distinct from all the other andesites in the CVZ and show strong upper crustal affinities characterized by distinctly lower Sr/Y and Sm/Yb and considerably higher $^{87}Sr/^{86}Sr$ ratios. The physical and compositional characteristics of ignimbrites of the APVC have been studied in detail (e.g., Schmitt et al., 2001; Lindsay et al., 2001; de Silva et al., 2006; Kay et al., 2010; Brandmeier and Wörner, 2016; Grocke et al., 2017; 2018). However, most of this work has been focused on the large, crystal-rich, high-K dacite ignimbrites that dominate the region (de Silva, 1989; de Silva et al., 2006; Salisbury et al., 2011). Dacites associated with the peak of the APVC flare-up lack the HREE depletion characteristic of magmas derived in the garnet-bearing lower crust (e.g., Schmitt et al., 2001; de Silva et al., 2006), and Schmitt et al. (2001) argued that this observation paired with Sr trace element systematics in 1.0 Ma Purico ignimbrite constrain the region of melt production/fractionation for the APVC ignimbrites to between 15 and 35 km. Importantly, isotope mixing models indicate that the large dacite ignimbrites of the APVC require at least 50% mid to upper crust (Lindsay et al., 2001; Schmitt et al., 2001; Soler et al., 2007; Kay et al., 2010; Freymuth et al., 2015). Andesites associated with the APVC (group 3) share some compositional similarities with dacite ignimbrites from the APVC (i.e., low Sr/Y and Sm/Yb). However, elevated $^{87}Sr/^{86}Sr$ isotope ratios and mineral associations and compositions indicate that the dacites experienced protracted histories in the upper crust (4–8 km depth; de Silva et al., 1994; Lindsay et al., 2001; Schmitt et al., 2001; Soler et al., 2007; Burns et al., 2015). In contrast, the APVC andesites have bulk rock and mineral compositions that appear to record a snapshot into the deeper reaches of the mid to upper crustal magmatic system.

Two-pyroxene thermobarometry from the Purico andesite (group 3) pumice yielded a total range in crystallization/equilibration pressures from 6 to 11 kbars (22–40 km depth) with a higher-pressure subset between 8 and 11 kbars, the former corresponding to crustal depths between 29 and 40 km (see Supplementary Figure S3). Rare-earth element patterns recorded in the group 3 andesites are nearly indistinguishable from the Paleozoic metamorphic rocks that are thought to make up the upper crust in the region (Lucassen et al., 2001). While this could indicate that the andesites are pure crustal melts, this would require nearly 100% melting and the bulk composition would have silica contents exceeding 68% (Lucassen et al., 2001). In addition, the range of $^{87}Sr/^{86}Sr$ isotope ratios recorded in the andesites are far lower and more restricted than the regional upper crustal basement (.7081–.7111 vs. .7241–1.123). Most of the group 3 andesites do not display significant Eu anomalies (Figure 4), and the few samples that do, we interpret as overprinting due to plagioclase fractionation at higher levels in the upper crust. This is consistent with plagioclase becoming a stable phase at ~20–17 km depth (Burns et al., 2015). The apparent lack of plagioclase in the host rock is also interesting, as the upper crust in the region is thought to be dominated by plagioclase-bearing gneiss (Lucassen et al., 2001). However, dehydration melting experiments conducted on biotite + plagioclase + quartz gneiss starting compositions (Gardien et al., 2000) show that at 10 kbars plagioclase is readily consumed in hydrous (4 wt.% added H_2O), high temperature (900°C) conditions. Beneath the APVC, increased mantle heat input in response to large-scale geodynamic changes (see de Silva et al., 2006; Kay and Coira, 2009; de Silva and Kay, 2018) would have resulted in the ascent and accumulation of large volumes of basalt in the lower to middle crust (~55–30 km). This basalt would provide the thermal energy required to initiate both the dehydration melting of the biotite and the subsequent break-down of plagioclase. Both the crystallization of basalt and the dehydration of biotite would liberate large volumes of water into the overlying crust, resulting in decreased crustal solidus temperatures, and, overtime, the generation of the prodigious volumes of crustal magma seen during the magmatic flare-up. We propose that the group 3 andesites are mixtures of ascending mafic magmas and the mid to upper crustal melts. The model presented in Figure 4C represents a mixture of 60% high-Al basalt and 40% partial melt of the regional upper crustal basement. For details of the modeling parameters, see Appendix 1.

Lower crustal andesites: Quaternary CVZ arc and minor centers (groups 1, 2, 4, 5, and 6)

Andesites associated with the Quaternary CVZ arc, including both major composite cones (groups 1 and 2) and minor eruptive centers (group 5), do not share the same upper crustal origin recorded in the group 3 andesites. Instead, these andesites record predominantly lower crustal origins with compositional differences that can be correlated with distinct crustal domains (e.g., Wörner et al., 1992; Wörner et al., 1994; Aitcheson et al., 1995; Mamani et al., 2008; Mamani et al., 2010). As illustrated in Figures 3, 4, andesites erupted between 16 and 19°S have distinctly higher Sr/Y, higher Sm/Yb, and steeper REE patterns than andesites erupted between 21 and 26°S. Davidson et al. (1988)

attributed the trace element enrichments and Sr systematics in the northern arc segment (based on observations in Nevados de Payachata region of the CVZ at ~18°S) to fractionation/assimilation in a garnet-bearing plagioclase-free environment. More recently, Blum-Oeste and Wörner (2016); Wörner et al. (2018) proposed that some of the trace element enrichment in the northern arc segment might reflect an enriched mantle wedge beneath the region (either an enriched lithospheric mantle lithosphere or the melting of foundering amphibole-bearing crustal cumulates). While this could help to explain some of the more pronounced enrichments (i.e., Sr and LREEs), the HREEs and elevated Sr isotope ratios are still best reconciled with a lower crustal origin. For this study, in keeping with most other previous works (Davidson et al., 1988; Wörner et al., 1992; Wörner et al., 1994; Aitcheson et al., 1995; Mamani et al., 2008; Mamani et al., 2010), we assume that the major compositional differences between the two arc segments correspond to differences in the composition of the lower crust. We find it probable that there are source heterogeneities along-strike within the CVZ arc, but a quantitative assessment of this is beyond the scope of this work.

Mamani et al. (2008; Mamani et al., 2010), following the work of Wörner et al. (1992, Wörner et al. 1994) and Aitcheson et al. (1995), proposed that various geochemical tracers, including Pb isotopes, delineate multiple distinct crustal domains beneath the CVZ with a transitional terrain boundary at ~20°S (Arequipa domain above 20°S and Antofalla domain below 20°S. This has been supported by multiple geophysical studies (Schmitz et al., 1997; Yuan et al., 2002), and one of the key features appears to be a significant change in the composition of the lowermost crust between 21 and 22°S. To the north of 20°S, the crust appears to have a significantly larger portion of mafic lower crust. Mamani et al. (2008) proposed that the larger proportion of mafic crust north of 20°S was the cause of the high Sr/Y ratios recorded in young volcanoes in the region. These interpretations are supported by petrophysical models which indicate that garnet stability is inversely correlated with SiO_2 contents (Tassara, 2006). In this case, a more mafic lower crust north of 20°S would contain more garnet and impart a stronger garnet signature during lower crustal fractionation processes (Tassara, 2006). South of 20°S, there is additional evidence indicating the lower crust is significantly more felsic. A rare slice of Paleozoic lower crust exposed at ~22°S in northern Chile (Sierra de Limon Verde) contains a high-grade metamorphic assemblage that includes amphibolite, eclogite, and granulite facies rocks that are largely felsic in composition (~62–68 wt.% SiO_2; Lucassen et al., 2001).

Trace element variations presented in Figure 3 are consistent with the lower crustal differences discussed above. Andesites from 16 to 19°S are consistent with lower crustal fractionation and the mixing between mantle-derived basaltic magmas melt and melts-derived from eclogitic lower crust. In addition, to be devoid of plagioclase, the REE patterns are best reproduced by a lower crustal phase assemblage dominated by garnet and clinopyroxene. In contrast, andesites from 21 to 26°S appear to be derived from a more mineralogically diverse source region. Although depleted HREE concentrations indicate that garnet played a role in the formation of these andesites, depleted MREE concentrations record a strong amphibole signal. There is also evidence for minor amounts of plagioclase. However, this could represent a later stage of crystallization overprinting the deeper signals.

Minor centers from the CVZ arc (group 5) generally share similar compositional characteristics with regional major arc centers. Minor arc centers from Peru define trends similar to those observed in the major arc systems between 16 and 19 °S. The Peruvian minor centers seem to be slightly enriched in incompatible trace elements relative to their major center counterparts (i.e., LREE, Sr, K_2O). However, this enrichment could simply be recording a slight decrease in the degree of partial melting in the source region.

Back-arc andesites (group 6)

Some of the best support for major changes in crustal composition controlling the early evolution of CVZ magmas come from minor centers from the Bolivian back-arc (e.g., Davidson and de Silva, 1995). Samples from these centers have REE concentrations and trace element ratios (i.e., Sr/Y and Sm/Yb) that are transitional between the two arc segments. This is significant, as these centers are located in the proposed transition zone between the Arequipa and Antofalla domains (located between 19 and 21°S) and appear to display distinct geochemical signatures characteristic of both domains. This is consistent with the work of Wörner et al. (1994), who conducted a geochemical traverse along the CVZ in this region (17.5–22°S) and showed that compositions erupted on the surface record the boundary. Wörner et al. (1994) also proposed that the boundary is not sharp, but a southward dipping wedge characterized by the southern Antofalla terrain overlying the older Arequipa terrain. In some cases, they observed that volcanic centers could record characteristic of both terrains.

Lavas from the S. Puna have slightly different compositional characteristics than other andesites in the CVZ, including LREE enrichments and high concentrations of incompatible HFSE (Kay et al., 1994; Risse et al., 2013). Some of these differences have been attributed to delamination-driven melting of asthenospheric mantle beneath the Southern Puna (Kay et al., 1994). On a broader scale, the differences between the Quaternary frontal arc lavas and the back-arc may be related to lower degrees of partial melting in the back arc in response to less fluid fluxing from the subduction slab (Burns et al., 2020).

Andesite production and evolution in the CVZ through space and time: The role of mantle flux

Since the Pliocene, two distinct types of andesites have erupted in the CVZ. Between 6 and 1 Ma, during the peak of the APVC flare-up, crustal melting in response to the influx of large volumes of mantle-derived basalt (likely high-Al basalt; Burns et al., 2020) into the middle and upper crust resulted in the production of voluminous hybrid upper crustal andesites (group 3; Figure 5). In contrast, Quaternary andesites associated with the modern CVZ arc (groups 1 and 2) and andesites from the waning stage of the flare-up (group 4) record a distinct lower crustal evolution. Davidson et al. (1991) proposed that the composition(s) of the most primitive lavas erupted in the CVZ represent a compositional "baseline" imparted on mantle-derived magmas in a deep, lower crustal MASH zone (Hildreth and Moorbath, 1988). In this scenario, ascending mantle-derived magmas stall (near the base of the crust), partially melt the lower crust, fractionate, and create hybrid magmas with compositions that reflect a combination of these processes. Recent geophysical studies in

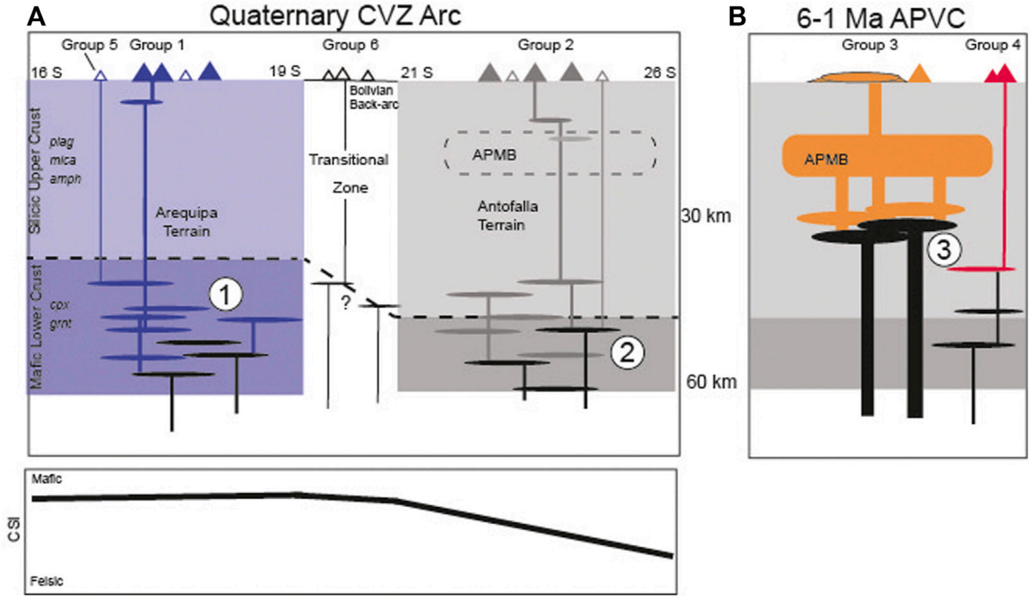

FIGURE 5
Schematic diagrams illustrating the different mechanisms for andesite formation in the CVZ. **(A)** includes Quaternary andesites from the frontal arc. Diagrams highlight difference in the composition of the crust. Crust between 16 and 19°S contains a significantly higher proportion of mafic crust than the crust between 21 and 26°S. CSI (Crustal Structure Index) is a measure of the proportion of mafic to felsic crust in the basement beneath the CVZ (based on gravity modeling) and is discussed in detail by Mamani et al. (2008). The APMB is the geophysically imaged Altiplano-Puna Magma Body proposed to reside in the upper crust between 21 and 24°S (e.g.; Chmielowski et al., 1999; Ward et al., 2017). **(B)** includes andesites associated with the peak and waning stages of the regional ignimbrite flare-up. The numbers included in both panels shows location(s) of proposed andesite generation in the crust. See the text for details.

other arc settings (e.g., Taupo Volcanic Zone; Harrison and White, 2004), along with numerical simulations (Dufek and Bergantz, 2005; Annen et al., 2006), have shown that this zone likely extends through most of the lower crust in typical continental arc settings.

A fundamental question that arises when comparing andesites from the Quaternary arc centers with those from the peak APVC flare-up is whether the “upper crustal” APVC andesites can be derived from the “lower crustal” CVZ andesites. There are multiple lines of evidence that indicate that this cannot be the case. First, there are significant compositional differences between the two groups of andesites at a given SiO_2 content (i.e., total alkali and CaO concentrations; Figure 2). In addition, peak APVC flare-up andesites have considerably higher Sr isotope ratios, precluding a scenario wherein the peak APVC flare-up andesites could have differentiated from a basaltic andesite-andesite precursor similar to those erupted from the Quaternary CVZ arc. These differences could indicate distinct processes, different source magmas, or similar processes occurring at different levels of the crust. If these interpretations are correct, and the upper crustal flare-up andesites are not related to the deeper Quaternary arc andesites, two questions arise: 1) What are the mafic magmas fueling the flare-up, and 2) how were they able to escape the lower crust MASH zone without fractionating and evolving to more silicic (basaltic andesite to andesite) compositions? We propose that the answer to this lies in the elevated mantle heat and material flux associated with the regional magmatic flare-up.

Following the work of Shaw (1980), Hildreth (1981) proposed that the injection of basalt into the crust can significantly impact crustal stress regimes resulting in extensional fracturing of the overlying crust, promoting the upward propagation of magma. Once fracturing is initiated, subsequent injections of basalt, and the resulting increase in pore pressure, accelerate crustal failure and result in a focusing of basaltic magma upward with time. With sufficient time and an elevated basalt flux, progressive weakening of the crust can result in the delivery of basalts to higher crustal levels. The crustal depth at which the ascending magmas stall is likely controlled by the density of the crust and perhaps a density-controlled mid-crustal decollement. In the case of Andean crust, 20 and 30 km appears to be a critical depth (Lucassen et al., 2001). Once these basaltic magmas stall, partial melting of the crust and subsequent mixing and fractionation result in the formation of the hybrid intermediate magmas common in large continental magmatic systems (Hildreth, 1981). In the case of the flare-up andesites, asthenospheric upwelling in response to crustal-scale delamination (e.g., Kay and Coira, 2009) and the production of large volumes of basalt are thought to have caused major perturbations of the crustal geothermal gradient (de Silva, 1989; de Silva and Gosnold, 2007). In addition to the changes in the regional stress regimes resulting from the upwelling basalt, the removal of the high density lithospheric “root” would have removed a major mechanical barrier from the lower crust, significantly weaking the crust. These changes would have allowed large volumes of mantle-derived basalt to ascend into the high levels within the crust before stalling, fractionating, and providing the thermal energy necessary to induce crustal melting.

The production of large volumes of andesite in the mid and upper crust beneath the APVC was first proposed by de Silva (1989), who proposed that high basalt flux into the crust resulted in the development of a large mid to upper crustal MASH zone. Once established, this large upper crustal processing center acted as a thermomechanical barrier trapping ascending magmas and creating a positive feedback loop between magma input, crustal melting, and the thermomechanical state of the crust (de Silva and Gosnold, 2007; de Silva and Gregg, 2014). Importantly, these changes were proposed to result in the production of copious amounts of andesite in the upper crust. Recent geophysical studies (Ward et al., 2014; Ward et al., 2017) focused on the crust beneath the APVC have revealed a large low velocity zone extending from ~25 to 4 km depth that has been interpreted as a large, melt-rich crystal mush, which previous authors coined the Altiplano-Puna Magma Body (APMB; Chmielowski et al., 1999; Zandt et al., 2003). The extent of this low velocity zone is of particular importance here, as the deeper depths correspond well with our estimated andesite generation depths beneath the APVC. We propose that basalts are delivered to a depth of ~35–25 km where they stall and interact with the continental crust in the lower reaches of the upper crustal MASH zone. During this time intermediate andesite magmas are formed and propagate through the crust, where they accumulate between ~17 and 20 km depth (see Burns et al., 2015). Our geochemical models here support these previous conceptual models that the deeper reservoir (17–20 km) is andesitic and serves as the magmatic "mothership" feeding the large, predominantly dacitic, upper crustal magma reservoirs feeding the APVC ignimbrite-forming eruptions (de Silva et al., 2006). This scenario is quite distinct from the prevailing model of lower crustal andesite genesis that explains the steady state andesites.

Andesite magmatism and the growth of continental growth

Continental magmatic arcs are one of the primary locations where new continental crust is created on Earth (e.g., Eichelberger, 1978; Thorpe et al., 1981), with the intermediate composition(s) characteristic of subduction zone magmas closely resembling the bulk composition of the Earth's crust (Taylor and McLennan, 1985). During the past 6 My, andesites from the CVZ record two distinct types of crustal growth. Steady-state andesites, herein represented by the Quaternary arc systems and minor eruptive centers associated with the modern frontal arc, record the fractionation and evolution of mafic, mantle-derived magmas (likely high-Al basalt) in the lower crust. Importantly, this lower crustal fractionation would result in the crystallization and subsequent accumulation of high-density mafic phase assemblages dominated by olivine, clinopyroxene, and possibly garnet at higher pressures (see Burns et al., 2020 for additional discussion of deep crystallizing assemblage), favoring the production of a dense, mafic lower crust. During this deep fractionation, intermediate melts would be produced, extracted, and delivered to the upper crust. However, the physical result of this entire process would be the densification and eventual loss of the lower crust. In contrast, andesites from the APVC flare-up record the delivery of basalts to higher levels in the crust and subsequent generation of upper crustal hybrid magmas. These magmas likely added significant volume to the mid to upper crust but did not result in the same densification of the crust.

It has been well established that continental magmatic arcs experience distinct magmatic episodes throughout their histories that appear to occur in response to major changes in crustal structure/composition (e.g., Kay et al., 1999; Ducea et al., 2005; DeCelles et al., 2009; Kay and Coira, 2009; Chapman et al., 2021). These cyclic episodes are characterized by punctuated short-term periods of intense magmatism (5–20 Myr) wherein mantle power input can increase by more than an order-of-magnitude relative to steady-state arc magmatism (de Silva et al., 2006; Burns et al., 2015). Importantly, it has been proposed that an overwhelming amount of the continental crust formed in continental subduction zones is created during these periods (some estimates are >50% of the total plutonic volume during a single period; Coleman and Glazner, 1997). For the Cretaceous Sierra Nevada arc in California, multiple authors (Ducea et al., 2005; DeCelles et al., 2009; Chapman et al., 2021) have proposed that these high intensity events (flare-ups) occur following periods of crustal shortening where convergence-driven thrusting behind the arc thicken the continental crust. The thickening results in the delivery of melt-fertile lower crust and mantle lithosphere into the melting region beneath the arc, providing fuel for a flare-up. Melting of the lower crustal/mantle lithosphere results in the formation of large volumes of dense residual granulite and eclogite (garnet pyroxenite) facies residuum and the formation of a dense arc "root." Consequently, the high density of this root results in a density inversion with the underlying asthenosphere and can result in foundering and delamination of the root (Kay and Kay, 1993). In the model for the Sierra Nevada arc, this has been proposed to cause the termination of the flare-up (e.g., Ducea et al., 2005). A critical feature of the model proposed for the Sierra Nevada is that it coincides with the crustal thickening events. This is not applicable to the Neogene Central Andean ignimbrite flare-up that includes the APVC, as there is clear evidence that the crustal thickening and delamination occurred prior to the flare-up (Kay et al., 1999).

Our findings indicate that steady-state magmatism in the Central Andes (on the already thickened crust) results in the deep crystallization of mantle-derived basalts and the dense residuum in the lower crust. During the mid-Miocene, gravity instabilities resulting from the dense root, in concert with changing subducting plate geometry, resulted in the delamination of the deep root and the initiation of the flare-up. An important observation is that although continental crust is being produced during both stages of magmatism in the CVZ (flare-up and steady state) the increase in new crust added during the flare-up may be balanced by loss of lower crust through delamination. In a recent compilation, de Silva and Kay (2018) calculated that in the case of the Central Andes from 21 to 24°S, delamination coupled with forearc subduction erosion has resulted in ~5.5% loss of continental crust during the flare-up. It is worth noting that to maintain an andesitic continental crust (~61% SiO_2; Taylor and McLennan, 1985), the foundering of mafic to ultramafic materials from the base of the crust is likely a critical process. Within the framework of continental arc cyclicity, it appears that andesitic continental crust is being produced on a nearly continuous basis. However, the long-term survival of the crust created may be heavily dependent on the processes and thermal conditions in which the magmas are generated.

Concluding summary

During the past 6 My, andesites in the Central Andes record two distinct modes of andesite magmatism that correspond with large-scale geodynamic changes in the region. From ca. 6–1 Ma, andesites associated with the peak of the APVC ignimbrite flare-up have geochemical and isotopic signatures consistent with the emplacement of mantle-derived basalts into the upper crust and subsequent melting and mixing

(Assimilation-Fractional Crystallization) with upper crustal lithologies. The emplacement of large volumes of basalt into the upper crust result from delamination-driven asthenospheric mantle upwelling following major changes in the geometry of the subducting Nazca plate.

In contrast, major composite cones and minor centers associated with the Quaternary CVZ arc have distinctive trace element and isotopic characteristics showing a clear lower crustal origin. Within the Quaternary centers, there are also distinct latitudinal variations that reflect changes in the age and composition of the lower crust. The transition from upper crustal to lower crustal magmatism during the past 6 My reflects the waning of regional flare-up and a return to steady state arc magmatism. Importantly, this transition from prodigious melt production in the mid to upper crust to lower crustal magma production has significant implications for the density structure and evolution of the crust. During the flare-up, considerable mass is added to the mid to upper crust potentially, resulting in the vertical expansion of the crust. In contrast, during steady state magmatism, lower crustal MASH processes result in the crystallization of large volumes of deep, mafic phases in the lower most crust, creating a dense crystalline residuum and effectively "densifying" the lower crust. This densification may ultimately aid in the delamination of the dense lower crustal root and the triggering of future flare-ups. These differences in andesite production may help to explain the cyclicity observed in mature continental arcs.

Data availability statement

The original contributions presented in the study are included in the article/Supplementary Material, further inquiries can be directed to the corresponding author.

Author contributions

DB and SdS compiled the data for this project. DB organized, plotted, and interpreted the data and wrote the initial draft of the manuscript. SdS provided comments and unpublished data for this work. SdS also helped with the conceptualization of this project.

Funding

The manuscript submission fees will be covered by the Stanford College of Earth, Energy, and Environmental Sciences.

Acknowledgments

Our ideas about andesites and CVZ magmatism have been influenced heavily by many colleagues, too numerous to fully acknowledge, but we wish to call out Peter Francis, Jon Davidson, Anita Grunder, Gerherd Wörner, Sue Kay, and Axel Schmitt, among them. Any shortcomings in our analysis and logic are our own failing. The journal reviews by Ian Smith and Bob Trumbull are gratefully acknowledged for keeping us honest and improving the final product. Editorial handling of Gary Michelfelder and Valerio Acocella is also appreciated. We would also like to thank Cerise Burns for proofreading multiple versions of this manuscript.

Conflict of interest

The authors declare that the research was conducted in the absence of any commercial or financial relationships that could be construed as a potential conflict of interest.

Publisher's note

Supplementary material

The Supplementary Material for this article can be found online at: https://www.frontiersin.org/articles/10.3389/feart.2022.961130/full#supplementary-material

References

Aitcheson, S. J., Harmon, R. S., Moorbath, S., Schneider, A., Soler, P., Soria-Escalante, E., et al. (1995). Pb isotopes define basement domains of the Altiplano central Andes. *Geology* 23, 555–558. doi:10.1130/0091-7613(1995)023<0555:pidbdo>2.3.co;2

Allmendinger, R. W., Jordan, T. E., Kay, S. M., and Isacks, B. L. (1997). The evolution of the Altiplano-Puna plateau of the central Andes. *Annu. Rev. Earth Planet Sci.* 25, 139–174. doi:10.1146/annurev.earth.25.1.139

Annen, C., Blundy, J. D., and Sparks, S. J. (2006). The Genesis of intermediate and silicic magmas in deep crustal hot zones. *J. Petrol.* 47, 505–539. doi:10.1093/petrology/egi084

Barreiro, B. A., and Clark, A. H. (1984). Lead isotopic evidence for evolutionary changes in magma-crust interaction, Central Andes, southern Peru. *Earth Planet. Sci. Lett.* 69, 30–42.

Blum-Oeste, M., and Wörner, G. (2016). Central Andean magmatism can be constrained by three ubiquitous end-members. *Terra nova.* 28, 434–440. doi:10.1111/ter.12237

Brandmeier, M., and Wörner, G. (2016). Compositional variations of ignimbrite magmas in the central Andes over the past 26 Ma — a multivariate statistical perspective. *Lithos* 262, 713–728. doi:10.1016/j.lithos.2016.07.011

Burns, D. H., de Silva, S. L., Tepley, F. J., and Schmitt, A. K. (2020). Chasing the mantle: Deciphering cryptic mantle signals through Earth's thickest continental magmatic arc. *Earth Planet Sci. Lett.* 531, 115985. doi:10.1016/j.epsl.2019.115985

Burns, D. H., de Silva, S. L., Tepley, F. T., Schmitt, A. K., and Loewen, M. L. (2015). Recording the transition from flare-up to steady-state arc magmatism at the Purico-Chascon volcanic complex, northern Chile. *Earth Planet Sci. Lett.* 422, 75–86. doi:10.1016/j.epsl.2015.04.002

Chapman, J. B., Ducea, M. N., DeCelles, P. G., and Profeta, L. (2015). Tracking changes in crustal thickness during orogenic evolution with Sr/Y: An example from the North American Cordillera. *Geology* 43, 919–922.

Chapman, J. B., Shields, J. E., Ducea, M. N., Paterson, S. R., Attia, S., and Ardill, K. E. (2021). The causes of continental arc flare ups and drivers of episodic magmatic activity in Cordilleran orogenic systems. *Lithos* 398-399, 106307–106399. doi:10.1016/j.lithos.2021.106307

Chmielowski, J., Zandt, G., and Haberland, C. (1999). The central andean altiplano-puna magma body. *Geophys Res. Lett.* 26, 783–786. doi:10.1029/1999gl900078

Coira, B., Davidson, J., Mpodozis, C., and Ramos, V. (1982). Tectonic and magmatic evolution of the Andes of northern Argentina and Chile. *Earth-sci Rev.* 18, 303–332. doi:10.1016/0012-8252(82)90042-3

Coleman, D. S., and Glazner, A. F. (1997). The Sierra crest magmatic event: Rapid formation of juvenile crust during the late cretaceous in California. *Int. Geol. Rev.* 39, 768–787. doi:10.1080/00206819709465302

Davidson, J. P., and de Silva, S. L. (1995). Late cenozoic magmatism of the Bolivian Altiplano. *Contrib. Mineral. Petrol* 119, 387–408. doi:10.1007/bf00286937

Davidson, J. P., Harmon, R. S., and Wörner, G. (1991). "The source of central Andean magmas; Some considerations," in *Andean magmatism and its tectonic setting*. Editors R. S. Harmon and C. W. Rapela (Boulder, Colorado: Geological Society of America Special). Paper 265.

Davidson, J. P., McMillan, N. J., Moorbath, S., Wörner, G., Harmon, R. S., and Lopez-Escobar, L. (1988). The Nevados de Payachata volcanic region (18 °S/69 °W, N. Chile) II. Evidence for widespread crustal involvement in Andean magmatism. *Contrib. Mineral. Petrol* 105, 412–432. doi:10.1007/bf00286829

de Silva, S. L. (1989). Altiplano-Puna volcanic complex of the central Andes. *Geology* 17, 1102–1106. doi:10.1130/0091-7613(1989)017<1102:apvcot>2.3.co;2

de Silva, S. L. (2008). Arc magmatism, calderas, and supervolcanoes. *Geology* 36, 671–42.

de Silva, S. L., and Gosnold, W. D. (2007). Episodic construction of batholiths: Insights from the spatiotemporal development of an ignimbrite flare-up. *J. Volcanol. Geoth Res.* 167, 320–335. doi:10.1016/j.jvolgeores.2007.07.015

de Silva, S. L., and Gregg, P. M. (2014). Thermomechanical feedbacks in magmatic systems: Implications for growth, longevity, and evolution of large caldera-forming magma reservoirs and their supereruptions. *J. Volcanol. Geoth Res.* 282, 77–91. doi:10.1016/j.jvolgeores.2014.06.001

de Silva, S. L., and Kay, S. M. (2018). Turning up the heat: High-flux magmatism in the central Andes. *Elements* 14, 245–250. doi:10.2138/gselements.14.4.245

de Silva, S. L., Self, S., Francis, P. W., Drake, R. E., and Carlos Ramirez, R. (1994). Effusive silicic volcanism in the central Andes: The chao dacite and other young lavas of the altiplano-puna volcanic complex. *J. Geophys. Res.* 99 (B9), 17805–17825. doi:10.1029/94jb00652

de Silva, S. L., Zandt, G., Trumbull, R., Viramonte, J. G., Salas, G., and Jiméz, N. (2006). "Large ignimbrite eruptions and volcano-tectonic depressions in the central Andes: A thermomechanical perspective,". Editors C. Troise, G. De Natale, and C. R. J. Kilburn (London: Geological Society), 269, 47–63.*Mech. Activity Unrest A. T. Large Calderas.*

DeCelles, P. G., Ducea, M. N., Kapp, P., and Zandt, G. (2009). Cyclicity in Cordilleran orogenic systems. *Nat. Geosci.* 2, 251–257. doi:10.1038/ngeo469

Ducea, M. N., Paterson, S. R., and DeCelles, P. G. (2005). High-volume magmatic events in subduction systems. *Elements* 11, 99–104. doi:10.2113/gselements.11.2.99

Dufek, J., and Bergantz, G. W. (2005). Lower crustal magma genesis and preservation: A stochastic framework for the evaluation of basalt–crust interaction. *J. Petrol* 46, 2167–2195. doi:10.1093/petrology/egi049

Eichelberger, J. C. (1978). Andesitic volcanism and crustal evolution. *Nature* 275, 21–27. doi:10.1038/275021a0

Freymuth, H., Brandmeier, M., and Wörner, G. (2015). The origin and crust/mantle mass balance of Central Andean ignimbrite magmatism constrained by oxygen and strontium isotopes and erupted volumes. *Contrib. Mineral. Petr* 169, 58. doi:10.1007/s00410-015-1152-5

Gardien, V., Thompson, A. B., and Ulmer, P. (2000). Melting of biotite + plagioclase + quartz gneisses: The role of H2O in the stability of amphibole. *J. Petrol* 41, 651–666. doi:10.1093/petrology/41.5.651

Gill, J. B. (1981). *Orogenic andesites and plate tectonics- Minerals and Rocks No. 16*. Berlin Heidelberg: Springer.

Godoy, B., Taussi, M., Gonzalez-Maurel, O., Renzulli, A., Hernandez-Prat, L., le Roux, P., et al. (2019). Linking the mafic volcanism with the magmatic stages during the last 1 Ma in the main volcanic arc of the Altiplano-Puna Volcanic Complex (Central Andes). *J. S Am. Earth Sci.* 95, 102295. doi:10.1016/j.jsames.2019.102295

Grocke, S. B., de Silva, S. L., Iriate, R., Lindsay, J. M., and Cottrell, E. (2017). Catastrophic Caldera-Forming (CCF) Monotonous Silicic Magma Reservoirs: Geochemical and Petrological Constraints on Heterogeneity, Magma Dynamics, and Eruption Dynamics of the 349 Ma Tara Supereruption, Guacha II Caldera, SW Bolivia. *J. Petrol.* 58, 227–260.

Grunder, A. L., Klemetti, E. W., Feeley, T. C., and McKee, C. M. (2008). Eleven million years of arc volcanism at the aucanquilcha volcanic cluster, northern Chilean Andes: Implications for the life span and emplacement of plutons. *Trans. R. Soc. Edinb Earth Sci.* 97, 415–436. doi:10.1017/s0263593300001541

Harrison, A. J., and White, R. S. (2004). Crustal structure of the Taupo volcanic zone, New Zealand: Stretching and igneous intrusion. *Geophys Res. Lett.* 31. doi:10.1029/2004GL019885

Hawkesworth, C. J., Hammill, M., Gledhill, A. R., van Calsteren, P., and Rogers, G. (1982). Isotope and trace element evidence for late-stage intra-crustal melting in the High Andes. *Earth Planet S. C. Lett.* 58, 240–254. doi:10.1016/0012-821x(82)90197-2

Hildreth, W. (1981). Gradients in silicic magma chambers: Implications for lithospheric magmatism. *J. Geophys Res. Solid Earth* 86, 10153–10192. doi:10.1029/jb086ib11p10153

Hildreth, W., and Moorbath, S. (1988). Crustal contributions to arc magmatism in the Andes of Central Chile. *Contrib. Mineral. Petrol* 98, 455–489. doi:10.1007/bf00372365

Johnson, D., Hooper, P., and Conrey, R. (1999). XRF analysis of rocks and minerals for major and trace elements on a single low dilution Li-tetraborate fused bead. *Adv. X-ray Analysis* 41, 843–867.

Kay, R. W., and Kay, S. M. (1993). Delamination and delamination magmatism. *Tectonophysics* 219, 177–189. doi:10.1016/0040-1951(93)90295-u

Kay, S. M., Coira, B. L., Caffe, P. J., and Chen, C.-H. (2010). Regional chemical diversity, crustal and mantle sources and evolution of central Andean Puna plateau ignimbrites. *J. Volcanol. Geoth Res.* 198, 81–111. doi:10.1016/j.jvolgeores.2010.08.013

Kay, S. M., and Coira, B. L. (2009). "Shallowing and steepening subduction zones, continental lithospheric loss, magmatism, and crustal flow under the Central Andean Altiplano-Puna Plateau," in *Backbone of the americas: Shallow subduction, plateau uplift, and ridge and terrane collision*. Editors S. M. Kay, V. A. Ramos, and W. R. Dickinson (Boulder, CO: Geological Society of America), 229–259.

Kay, S. M., Coira, B., and Viramonte, J. (1994). Young mafic back arc volcanic rocks as indicators of continental lithospheric delamination beneath the Argentine Puna Plateau, central Andes. *J. Geophys Res. Solid Earth* 99, 24323–24339. doi:10.1029/94jb00896

Kay, S. M., Mpodozis, C., and Coira, B. (1999). "Neogene magmatism, tectonism, and mineral deposits of the Central Andes (22°-33°S latitude),". Editor B. J. Skinner (Littleton, CO, USA: Society of Economic Geology Special Publication), 7, 27–59. *Geol. Ore Deposits Central Andes*.

Kay, S. M., and Mpodozis, C. (2001). Central Andean ore deposits linked to evolving shallow subduction systems and thickening crust. *GSA Today* 11, 4–9.

Kay, S. M., and Mpodozis, C. (2002). Magmatism as a probe to the Neogene shallowing of the Nazca plate beneath the modern Chilean flat-slab. *J. S Am. Earth Sci.* 15, 39–57. doi:10.1016/s0895-9811(02)00005-6

Kay, R. W., and Kay, S. M (1991). Creation and destruction of lower continental crust. *Geologische Rundschau* 80, 259–278.

Le Bas, M. J., and Streckeisen, A. L. (1991). The IUGS systematics of igneous rocks. *J. Geol. Soc. Lond.* 148, 825–833. doi:10.1144/gsjgs.148.5.0825

Le Maitre, R. W. (1989). *A classification of igneous rocks and glossary terms*. 2nd Edition. Oxford: Blackwell Scientific Publications.

Lindsay, J. M., Schmitt, A. K., Trumbull, R. B., de Silva, S. L., Siebel, W., and Emmermann, R. (2001). Magmatic evolution of the La pacana caldera system, central Andes, Chile: Compositional variation of two cogenetic, large-volume felsic ignimbrites. *J. Petrol* 42, 459–486. doi:10.1093/petrology/42.3.459

Lucassen, F., Becchio, R., Harmon, R., Kasemann, S., Franz, G., Trumbull, R., et al. (2001). Composition and density model of the continental crust at an active continental margin—The central Andes between 21° and 27°S. *Tectonophysics* 341, 195–223. doi:10.1016/s0040-1951(01)00188-3

Mamani, M., Tassara, A., and Wörner, G. (2008). Composition and structural control of crustal domains in the central Andes. *Geochem. Geophys. Geosyst* 9. doi:10.1029/2007GC001925

Mamani, M., Wörner, G., and Sempere, T. (2010). Geochemical variations in igneous rocks of the Central Andean orocline (13°S to 18°S): Tracing crustal thickening and magma generation through time and space. *GSA Bull.* 122, 162–182. doi:10.1130/b26538.1

Maro, G., Caffe, P. J., Romer, R. L., and Trumbull, R. B. (2017). Neogene mafic magmatism in the northern Puna Plateau, Argentina: Generation and evolution of a back-arc volcanic suite. *J. Petrol* 58, 1591–1617. doi:10.1093/petrology/egx066

Ramos, F. C. (1992). *Isotope geology of the metamorphic core of the central grouse creek mountains, Box Elder County*. University of California Los Angeles.

Reubi, O., and Müntener, O. (2022). Making andesites and the continental crust: Mind the step when wet. *J. Petrol.* 63 (6). doi:10.1093/petrology/egac044

Risse, A., Trumbull, R. B., Kay, S. M., Coira, B., and Romer, R. L. (2013). Multi-stage evolution of late Neogene mantle-derived magmas from the central Andes back-arc in the southern Puna Plateau of Argentina. *J. Petrol* 54, 1963–1995. doi:10.1093/petrology/egt038

Rogers, G., and Hawkesworth, C. J. (1989). A geochemical traverse across the north Chilean Andes: Evidence for crust generation from the mantle wedge. *Earth Planet Sci. Lett.* 91, 271–285. doi:10.1016/0012-821x(89)90003-4

Salisbury, M. J., Jicha, B. R., de Silva, S. L., Singer, B. S., Jiménez, N. C., and Ort, M. H. (2011). 40Ar/39Ar chronostratigraphy of Altiplano-Puna volcanic complex ignimbrites reveals the development of a major magmatic province. *Geol. Soc. Am. Bull.* 123, 821–840. doi:10.1130/b30280.1

Schmitt, A., Silva, S. D., Trumbull, R., and Emmermann, R. (2001). Magma evolution in the Purico ignimbrite complex, northern Chile: Evidence for zoning of a dacitic magma by injection of rhyolitic melts following mafic recharge. *Contrib. Mineral. Petrol* 140, 680–700. doi:10.1007/s004100000214

Schmitz, M., Heinsohn, W.-D., and Schilling, F. R. (1997). Seismic, gravity and petrological evidence for partial melt beneath the thickened Central Andean crust (21° – 23°S). *Tectonophysics* 270, 313–326. doi:10.1016/s0040-1951(96)00217-x

Shaw, H. R. (1980). "The fracture mechanisms of magma transport from the mantle to the surface," in *Physics of magmatic processes*. Editor R. B. Hargraves (Princeton, N.J: Princeton University Press), 201–264.

Soler, M. M., Caffe, P. J., Coira, B. L., Onoe, A. T., and Kay, S. M. (2007). Geology of the vilama caldera: A new interpretation of a large-scale explosive event in the central andean plateau during the upper Miocene. *J. Volcanol. Geoth Res.* 164, 27–53. doi:10.1016/j.jvolgeores.2007.04.002

Stern, C. R. (2004). Active Andean volcanism: Its geologic and tectonic setting. *Rev. Geol. Chile* 31, 161–206. doi:10.4067/s0716-02082004000200001

Straub, S. M., Gómez, -Tuena, A., Stuart, F. M., Zellmer, G. F., Espinasa-Perena, R., Cai, Y., et al. (2011). Formation of hybrid arc andesites beneath thick continental crust. *Earth Planet Sci. Lett.* 303, 337–347. doi:10.1016/j.epsl.2011.01.013

Sun, S., and McDonough, W. F. (1989). Chemical and isotopic systematics of oceanic basalts: Implications for mantle composition and processes. *Geol. Soc. Lond Spec. Publ.* 42, 313–345. doi:10.1144/gsl.sp.1989.042.01.19

Tassara, A. (2006). Factors controlling the crustal density structure underneath active continental margins with implications for their evolution. *Geochem. Geophys. Geosyst* 7, Q01001. doi:10.1029/2005GC001040

Taylor, S. R., and McLennan, S. M. (1985). *The continental crust: Its composition and evolution*. Oxford, UK: Blackwell.

Thorpe, R. S. (1982). *Andesites: Orogenic andesites and related rocks*. Norwich, UK: John Wiley & Sons.

Thorpe, R. S., Francis, P. W., and Harmon, R. S. (1981). Andean andesites and crustal growth. *Phil. Trans. R. Soc. Lond. A*, 305–320.

Tierney, C. R., Schmitt, A. K., Lovera, O. M., and de Silva, S. L. (2016). Voluminous plutonism during volcanic quiescence revealed by thermochemical modeling of zircon. *Geology* 44, 683–686. doi:10.1130/g37968.1

van Alderwerelt, B., Ukstins, I. A., and Ramos, F. C. (2021). Sr isotopes and geochemistry of Cerro Overo maar provide a unique window into arc magma Genesis in the Central Volcanic Zone of the Andes. *Lithos* 386, 105978. doi:10.1016/j.lithos.2021.105978

Ward, K. M., Delph, J. R., Zandt, G., Beck, S. L., and Ducea, M. N. (2017). Magmatic evolution of a Cordilleran flare-up and its role in the creation of silicic crust. *Sci. Rep-uk* 7, 9047. doi:10.1038/s41598-017-09015-5

Ward, K. M., Zandt, G., Beck, S. L., Christensen, D. H., and McFarlin, H. (2014). Seismic imaging of the magmatic underpinnings beneath the Altiplano-Puna volcanic complex from the joint inversion of surface wave dispersion and receiver functions. *Earth Planet S. C. Lett.* 404, 43–53. doi:10.1016/j.epsl.2014.07.022

Watts, R. B., de Silva, S. L., de Rios, G. J., and Croudace, I. (1999). Effusive eruption of viscous silicic magma triggered and driven by recharge: A case study of the Cerro chascon-runtu jarita dome complex in southwest Bolivia. *B Volcanol.* 61, 241–264. doi:10.1007/s004450050274

Wörner, G., Mamani, M., and Blum-Oeste, M. (2018). Magmatism in the central Andes. *Elements* 14, 237–244. doi:10.2138/gselements.14.4.237

Wörner, G., Moorbath, S., Horn, S., Entenmann, J., Harmon, R. S., Davidson, J. P., et al. (1994). “Large and fine-scale geochemical variations along the Andean arc of northern Chile (17.5° to 22°S),” in *Tectonics of the southern central Andes, structure and evolution of an active continental margin*. Editors K. J. Ruetter, E. Scheuber, and P. J. Wigger (Berlin: Spinger).

Wörner, G., Moorbath, S., and Harmon, R. S. (1992). Andean Cenozoic volcanic centers reflect basement isotopic domains. *Geology* 20, 1103–1106. doi:10.1130/0091-7613(1992)020<1103:acvcrb>2.3.co;2

Yuan, X., Sobolev, S., and Kind, R. (2002). Moho topography in the central Andes and its geodynamic implications. *Earth Planet Sci. Lett.* 199, 389–402. doi:10.1016/s0012-821x(02)00589-7

Zandt, G., Leidig, M., Chmielowski, J., Baumont, D., and Yuan, X. (2003). Seismic detection and characterization of the altiplano-puna magma body, central Andes. *Pure Appl. Geophys* 160, 789–807. doi:10.1007/pl00012557

Frontiers in
Earth Science

Investigates the processes operating within the major spheres of our planet

Advances our understanding across the earth sciences, providing a theoretical background for better use of our planet's resources and equipping us to face major environmental challenges.

Discover the latest Research Topics

See more →

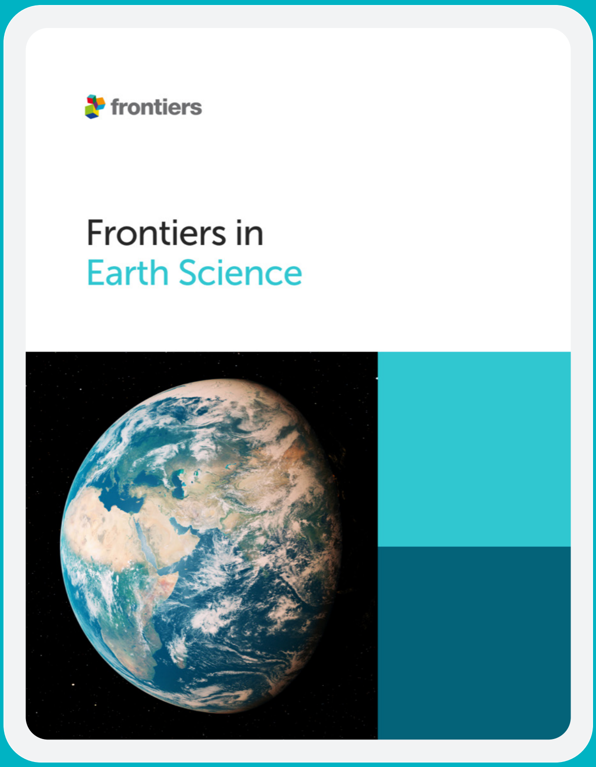

frontiers

Frontiers in
Earth Science

Frontiers

Avenue du Tribunal-Fédéral 34
1005 Lausanne, Switzerland
frontiersin.org

Contact us

+41 (0)21 510 17 00
frontiersin.org/about/contact